

Investigations about the Chemistry of Tetraarylethene- and Iridium-Based Luminophores

Présentée le 29 février 2024

Faculté des sciences de base
Laboratoire de chimie supramoléculaire
Programme doctoral en chimie et génie chimique

pour l'obtention du grade de Docteur ès Sciences

par

Anastasia GITLINA

Acceptée sur proposition du jury

Prof. S. Gerber, présidente du jury
Prof. K. Severin, directeur de thèse
Prof. E. Zysman-Colman, rapporteur
Prof. R. Alberto, rapporteur
Prof. M. K. Nazeeruddin, rapporteur

Table of Contents

Acknowledgements	5
Abstract	7
Résumé	8
List of Abbreviations and Designations	10
Chapter 1. Introduction	15
1.1 Aggregation-Induced Emission (AIE)	15
1.1.1 Introduction	15
1.1.2 Mechanisms of AIE	17
1.1.3 Applications	20
1.1.4 Synthesis of AIE Luminophores Using Triazenes.....	22
1.2 Polymeric Tri- and Tetraarylethene-Based Luminophores	24
1.2.1 Synthesis and Properties of Poly(Tri- and Tetraarylethene)s	24
1.2.2 Applications	30
1.3 Ir(III) Luminophores with Orthometalated Ligands	33
1.3.1 Introduction	33
1.3.2 Synthesis of Ir(C ^N) ₃ and Ir(C ^C :) ₃ Complexes. <i>fac</i> and <i>mer</i> Isomers.....	35
1.3.3 <i>mer</i> → <i>fac</i> Isomerization of Ir(C ^N) ₃ and Ir(C ^C :) ₃	41
1.3.4 Photophysical Properties and Applications of Ir(C ^N) ₃ and Ir(C ^C :) ₃ Complexes	45
1.4 Objectives of the Thesis.....	51
Chapter 2. Synthesis of Hyperbranched Polyarylethenes by C–H Vinylations with a Triazene	52
2.1 Introduction	53
2.2 Synthesis of Poly(triphenylethene)s by C–H Vinylations	54
2.3 Characterization of the Polymers	56
2.4 Optical and Photophysical Properties of the Polymers	58

2.5 Application	63
2.6 Conclusions	67
2.7 Attempted C–H Vinylation of <i>fac</i> -Ir(ppy) ₃	68
Chapter 3. Acid-Base-Induced <i>fac</i>→<i>mer</i> Isomerization of Ir Complexes with Orthometalated Ligands	71
3.1 Introduction	72
3.2 Microwave Synthesis of <i>fac</i> -Ir(C [^] N) ₃ Complexes.....	72
3.3 Protonation of Ir(ppy) ₃ with Strong Acids and Study of the <i>fac</i> → <i>mer</i> Isomerization	75
3.4 Repetitive <i>fac</i> ↔ <i>mer</i> Switching	77
3.5 Scope	78
3.6 Investigations of Ligand Exchange	80
3.7 Stereoselectivity Studies and Possible Mechanism	82
3.8 Applications	85
3.9 Conclusions	90
3.10 Towards Autonomous Switching	91
3.11 Attempted <i>fac</i> → <i>mer</i> Isomerization of Other Ir Complexes	99
Chapter 4. Acid-Base-Induced <i>fac</i>→<i>mer</i> Isomerization of Ir Complexes with Cyclometalated NHC Ligands	104
4.1 Introduction	105
4.2 Protonation of <i>fac</i> -Ir(C [^] C:) ₃ Complexes and Possible Mechanism of the <i>fac</i> → <i>mer</i> Isomerization.....	106
4.3 Investigation of Ligand Exchange	110
4.4 Isomerization of a Mixture of <i>fac</i> and <i>mer</i> Isomers	111
4.5 Isomerization of a Sterically Hindered Ir(C [^] C:) ₃ Complex.....	112
4.6 Conclusions	117
Chapter 5. Summary and Outlook.....	119
Chapter 6. Experimental Part	121

6.1 Materials and Methods	122
6.2 Experimental Part for Chapter 2	125
6.3 Experimental Part for Chapter 3	159
6.4 Experimental Part for Chapter 4	296
References	338
Curriculum Vitae	356

Acknowledgements

My four and a half years in Switzerland have provided me with a unique and invaluable experience, and this journey would not have been possible without the multifaceted support I have received. Throughout this time, every person I have encountered left a lasting impression on me. Although I cannot individually mention everyone, I am exceptionally grateful to each of you.

First and foremost, I give my heartfelt appreciation to Prof. Kay Severin, who graciously welcomed me into his laboratory and allowed me to pursue my doctoral studies under his guidance. Throughout my PhD journey, I gained invaluable insights from Kay. His extensive scientific perspective and profound knowledge of chemistry provided me with the foundation to engage in several exciting research projects. He granted me the autonomy to explore independently while providing constructive supervision. Observing his dedication of time and effort in leading the research group has been an invaluable learning experience. I extend my thanks for his unwavering support and confidence in both me and my research endeavors.

I acknowledge and deeply respect Prof. Eli Zysman-Colman, Prof. Roger Alberto, Prof. Mohammad Khaja Nazeeruddin, and Prof. Sandrine Gerber for dedicating time of their schedules to be part of the jury for my PhD defence, and for reading, providing feedback, and engaging in fruitful discussions on the written thesis.

I am thankful to Dr. Farzaneh Fadaei-Tirani for her exceptional skills in X-ray crystallography and knowledge transfer. My gratitude extends to Dr. Aurélien Borne and the NMR team, the MS platform, and the chemical store of BCH for their invaluable services at the EPFL. I also thank Anne Lene Odegaard and Christina Zamanos-Epreman for their administrative support.

I am grateful to all collaborators who supported and enriched my doctoral studies with important experiments. Thanks to Dr. Albert Ruggi for conducting photophysical studies, Dr. Łukasz Woźniak for help with the chiral HPLC measurements, the Protein Production and Structure Core Facility of the EPFL for support with the ECD spectroscopy measurements, Dr. Yann Lavanchy for help with the TGA and GPC measurements, and Dr. Natalia Gasilova for help with the DLS measurements.

I express my gratitude to the members of the Severin group, both past and present, for fostering a welcoming atmosphere, organizing exciting group trips, offering help, and engaging in interesting discussions within and outside the laboratory.

I acknowledge my former supervisors, Prof. Elena Grachova (St. Petersburg State University) and Prof. Igor Koshevoy (University of Eastern Finland), for their pivotal roles in my early education as a chemist and researcher.

I am grateful to my friends who supported me from a distance, residing in Russia, Finland, Denmark, the UK, the Netherlands, Germany, Austria, Spain, Israel, and the US, and particularly to those who visited me in Switzerland and physically delivered their support.

Last but certainly not least, I am sincerely grateful to my parents and family, whose enduring love, support, and unwavering belief in me have been a constant presence throughout my life, warming my heart and contributing to my achievements. I express my immense gratitude and admiration to the person who stands by me as I reach this milestone and with whom I have started my own family: my beloved husband, Ivan. Your dedication to being by my side, everlasting support, and undoubtful belief in me are what I will be eternally grateful for. Words cannot express how much I love you, and I feel truly blessed to have you in my life.

Abstract

The work described in this thesis focuses on two classes of luminophores: tetraarylethene-based polymers and Ir(III) complexes with orthometalated ligands. Tetraarylethene-based polymers show aggregation-induced emission (AIE) and they are of interest for applications in sensing, imaging, and material science. Ir(III) complexes with orthometalated ligands, on the other hand, can be used as components for light-emitting diodes, and they have been employed as photocatalysts, as building blocks for supramolecular complexes, and as chemo- and bio-sensors.

Chapter 2 describes a novel procedure for the synthesis of hyperbranched polyarylethenes *via* successive electrophilic C–H vinylation reactions of aromatic cores with a triazene. The hyperbranched polyarylethenes display size-dependent luminescence and unusual ratiometric AIE behaviour and they can be applied as sensors for alkali metal cations.

In Chapter 3, a clean, fast, and simple procedure for the conversion of *fac*-Ir(C^N)₃ complexes into the thermodynamically less stable *mer* isomers by a consecutive reaction with first acid (TFA or HNTf₂) and then base (NEt₃) is reported. The process enables the interconversion of luminophores with distinct photophysical properties and allows accessing *mer* complexes, which are difficult to synthesize with standard procedures. The possibility of the autonomous *fac*↔*mer* switching was also studied.

Chapter 4 describes that the *fac* isomers of Ir(III) complexes with metalated *N*-heterocyclic carbene ligands, Ir(C^C)₃, can be converted cleanly into the *mer* isomers when solutions of the complexes are treated with first HNTf₂ and then NEt₃. The procedure allows obtaining *mer*-Ir(C^C)₃ in high yields and enables the direct conversion of the mixture of *fac* and *mer* isomers of Ir(C^C)₃ into the pure *mer* isomers. The substituent effect was also studied, and acid-base-induced *fac*→*mer* isomerization of the bulky Ir(C^C)₃ complex was investigated.

Key words: aggregation-induced emission, polyarylethenes, vinylation, triazene, Iridium complexes, isomerization, facial isomer, meridional isomer, luminescence, photophysical properties

Résumé

Les travaux décrits dans cette thèse se concentrent sur deux classes de luminophores: les polymères à base de tétraaryléthène et les complexes d'Ir(III) contenant des ligands orthométalisés. Les polymères à base de tétraaryléthène présentent une Emission Induite par Agrégation (AIE) et sont intéressants pour des applications dans les domaines de la détection, de l'imagerie et de la science des matériaux. Les complexes d'Ir(III) avec des ligands orthométalisés, d'autre part, peuvent être utilisés comme composants pour les diodes électroluminescentes, et ils ont été employés comme photocatalyseurs, comme éléments constitutifs de complexes supramoléculaires, et comme biocapteurs et chimiodétecteurs.

Le chapitre 2 décrit une nouvelle procédure de synthèse de polyaryléthènes hyperbranchés *via* des réactions de vinylation C-H électrophiles successives de noyaux aromatiques avec un triazène. Les polyaryléthènes hyperbranchés présentent une luminescence dépendante de la taille et un comportement AIE ratiométrique inhabituel, et ils peuvent être utilisés comme capteurs de cations de métaux alcalins.

Le chapitre 3 présente une procédure propre, rapide et simple pour la conversion des complexes *fac*-Ir(C^N)₃ en isomères *mer* thermodynamiquement moins stables par une réaction consécutive avec un acide (TFA ou HNTf₂) puis une base (NEt₃). Le processus permet l'interconversion de luminophores aux propriétés photophysiques distinctes et permet d'accéder aux complexes *mer*, qui sont difficiles à synthétiser avec des procédures standard. La possibilité d'une commutation autonome *fac*↔*mer* a également été étudiée.

Le chapitre 4 décrit que les isomères *fac* des complexes Ir(III) contenant des ligands carbènes N-hétérocycliques métallisés, Ir(C^C)₃, peuvent être convertis purement en isomères *mer* lorsque les solutions des complexes sont traitées d'abord avec HNTf₂ et ensuite avec NEt₃. Cette procédure permet d'obtenir des *mer*-Ir(C^C)₃ avec des rendements élevés, et de convertir directement le mélange d'isomères *fac* et *mer* d'Ir(C^C)₃ en isomères *mer* uniquement. L'effet du substituant a également été étudié, et l'isomérisation *fac*→*mer* acid/base induite du complexe volumineux Ir(C^C)₃ a été étudiée.

Mots clés: émission induite par agrégation, polyaryléthènes, vinylation, triazène, complexes d'iridium, isomérisation, isomère facial, isomère méridional, luminescence, propriétés photophysiques.

List of Abbreviations and Designations

A	absorption
Ac	acyl
acac	acetylacetonate
ACQ	aggregation-caused quenching
AIE(E)	aggregation-induced emission (enhancement)
APPI	atmospheric pressure ionization
Ar	aryl
<i>b</i>	light path, cm
BET	Brunauer-Emmett-Teller
bpy	2,2'-bipyridyl
<i>c</i>	molar concentration, M
CHCA	α -cyano-4-hydroxycinnamic acid
CI	conical intersection
CIE	commission Internationale de l'éclairage
COD	1,5-cyclooctadiene
COE	<i>cis</i> -cyclooctene
DBU	1,8-diazabicyclo(5.4.0)undec-7-ene
DCDPP	dicyanodiphenylpyrazine
DCM	dichloromethane
DCTB	<i>trans</i> -2-[3-(4- <i>tert</i> -butylphenyl)-2-methyl-2-propenylidene]malononitrile
DLS	dynamic light scattering
DMAC	dimethylacetamide
DMF	<i>N,N</i> -dimethylformamide
DMSO	dimethylsulfoxide
DNA	deoxyribonucleic acid
DNT	2,4-dinitrotoluene
DPDHP	diphenyl dihydrophenanthrene
ECD	electronic circular dichroism
<i>ee</i>	enantiomeric excess, %
EQE	external quantum efficiency, %

ESI	electrospray ionization
Et	ethyl
F	fluorescein
<i>f</i>	solvent fraction, vol. %
<i>fac</i>	facial isomer
FE-SEM	field-emission scanning electron microscopy
GB	Glovebox
GPC	gel permeation chromatography
Hbtpy	2-(benzo[<i>b</i>]thiophen-2-yl)pyridine
Hbuppy	2-(4- <i>tert</i> -butylphenyl)pyridine
Hbzq	benzo[<i>h</i>]quinoline
HC [^] C:	cyclometalating ligand with C _{Ar} and C _{carbene} donors
HC [^] N	cyclometalating ligand with C _{Ar} and N donors
Hdfppy	2-(2,4-difluorophenyl)pyridine
HFIP	hexafluoroisopropanol
Hfppy	2-(4-fluorophenyl)pyridine
Hmeppy	2-(4-methoxyphenyl)pyridine
HNTf ₂	bistriflimidic acid, bis(trifluoromethanesulfonyl)imide
HOMO	highest occupied molecular orbital
HOTf	triflic acid, trifluoromethanesulfonic acid
Hpbb	1-phenyl-3-benzylbenzimidazolin-2-ylidene
HPLC	high-pressure liquid chromatography
Hpmb	1-phenyl-3-methylbenzimidazolin-2-ylidene
Hppy	2-phenylpyridine
Hppz	1-phenylpyrazole
HRMS	high-resolution mass spectrometry
HR-TEM	high resolution tunneling electron spectroscopy
HPS	hexaphenylsilole
Htppy	2-([1,1':4',1''-terphenyl]-4-yl)pyridine
Htpy	2-(4-methylphenyl)pyridine
Htpz	1-phenyl-1,2,4-triazolo[4,3- <i>f</i>]phenanthridine
<i>I</i>	photoluminescence intensity
<i>ISC</i>	intersystem crossing

<i>IC</i>	internal conversion
IR	infrared
<i>J</i>	coupling constant, Hz
<i>k</i>	slope for linear approximation
LC	ligand centered charge transfer
LUMO	lowest occupied molecular orbital
<i>m</i>	mass, mg
<i>M_n</i>	number average molecular weight, g/mol
<i>M_w</i>	weight average molecular weight, g/mol
<i>M_z</i>	Z-average molecular weight, g/mol
[M]	molecular ion
<i>m/z</i>	molecular weight/charge ratio
MALDI	matrix-assisted laser desorption/ionization
MC	metal centered charge transfer
Me	methyl
<i>mer</i>	meridional isomer
MLCT	metal-to-ligand charge transfer
MO	molecular orbital
MOF	metal-organic framework
<i>n</i>	number of monomer units in a polymer
N [^] N	diimine ligand
<i>n/s</i>	not soluble
NHC	<i>N</i> -heterocyclic carbene
NMR	nuclear magnetic resonance
O [^] O	cyclometalating ligand with O donors
OLED	organic light-emitting diode
<i>P_s</i>	solvent density, g/mL
PA	picric acid
<i>PDI</i>	polydispersity index
Ph	phenyl
PLED	polymeric light-emitting diode
PMMA	poly(methyl methacrylate)
ppb	parts per billion

ppm	parts per million
py	pyridyl
<i>p/s</i>	partially soluble
Q	quinine sulfate
QS	Quartz Suprasil
RACI	restricted access to CI
<i>Rl</i>	refractive index
RIM	restriction of intramolecular motions
RIR	restriction of intramolecular rotation
RIV	restriction of intramolecular vibrations
r.t.	room temperature
S	solubility, mg/mL
S ₀	ground singlet electronic state
S ₁	excited singlet electronic state
SERS	surface-enhanced Raman spectroscopy
SOC	spin-orbit coupling
T ₁	excited triplet electronic state
^t Bu	<i>tert</i> -butyl
<i>T_d</i>	temperature of degradation, °C
TFA	trifluoroacetic acid
TGA	thermal gravimetric analysis
THBA	10,10',11,11'-tetrahydro-5,5'-bidibenzo[<i>a,d</i>][7]annulenyldiene
THF	tetrahydrofuran
TLC	thin-layer chromatography
TNT	2,4,6-trinitrotoluene
TPE	tetraphenylethylene
UV	ultraviolet
V(V')	volume (corrected volume), mL
VR	vibrational relaxation
VT	variable-temperature
wt%	weight yield, %
XRD	X-ray diffraction
Δ	ligand-field splitting parameter

Δ	delta isomer
δ	chemical shifts, ppm
$\Delta\varepsilon$	molar extinction coefficient, $M^{-1}\cdot\text{cm}^{-1}$
θ	ellipticity, mdeg
Λ	lambda isomer
λ_{abs}	absorption maximum, nm
λ_{ex}	excitation maximum, nm
λ_{em}	emission maximum, nm
τ	photoluminescence lifetime, ns
Φ	photoluminescence quantum yield, %

Chapter 1. Introduction

For this thesis, two classes of luminophores have been investigated: polymeric tetraarylethenes and Ir(III) complexes with orthometalated ligands. Tetraarylethenes show aggregation-induced emission (AIE), and the concept of AIE will be introduced in subchapter 1.1 with a discussion of examples, mechanisms, and applications. The commonly used synthetic methods, properties, and applications of AIE-active polyarylethenes will be reviewed in subchapter 1.2. The synthesis, the photophysical and photochemical properties, and applications of Ir(III) complexes with orthometalated ligands will be discussed in subchapter 1.3.

1.1 Aggregation-Induced Emission (AIE)

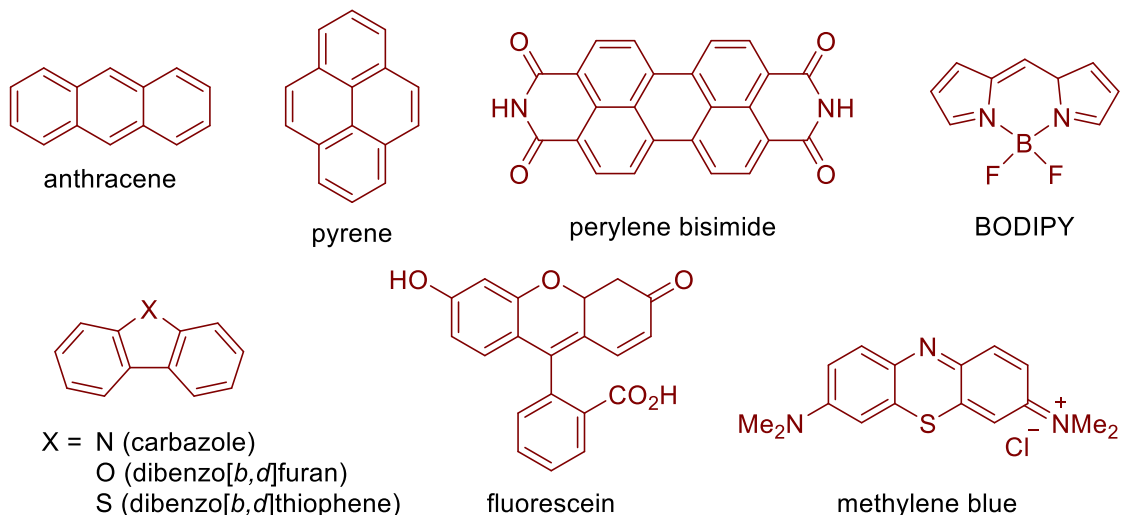
This subchapter aims to briefly introduce the AIE phenomenon, which is relevant to the work described in this thesis. The broader picture of AIE with more examples, mechanistic investigations, and applications is given in thorough reviews by B. Z. Tang,^{1,2} B. Liu³, and A. Chakravarthy.⁴ A historical perspective by F. Würthner illustrating the origins of AIE also deserves attention.⁵ Finally, a bibliometric analysis by H. Lin clearly demonstrates the 'hot' research status of AIE since its introduction to the scientific community.⁶

1.1.1 Introduction

Many conventional aromatic luminophores (anthracene, pyrene, perylene bisimide, BODIPY, fluorescein, methylene blue, Fig. 1.1a) emit with high photoluminescence quantum yield when molecularly isolated, *e.g.* in dilute solution. In the aggregate or solid state, they experience aggregation-caused quenching (ACQ) of luminescence due to formation of intermolecular π - π stacking interactions responsible for non-radiative relaxation of the excited states. The ACQ effect was reported for pyrene by T. Förster and K. Kasper in 1954.⁷ Subsequently, it was generalized to a vast majority of planar luminophores,⁸ leading to substantial limitations in their applications in aggregate and solid form, *e.g.* sensing, imaging, and OLEDs.⁹⁻¹¹ The opposite photophysical behaviour of 1-methyl-1,2,3,4,5-pentamethylsilole, which is non-emissive in solution and highly luminescent in aggregate and solid state, was accidentally discovered by B. Z. Tang and co-workers in 2001.¹² In 2007, they reported

a similar behaviour for tetraphenylethylene (TPE).¹³ This phenomenon has been termed “aggregation-induced emission (AIE)”. Nowadays, numerous solid-state luminophores with high photoluminescence quantum yields are known, for example hexaphenylsilole (HPS), dicyanodiphenylpyrazine (DCDPP), 10,10',11,11'-tetrahydro-5,5'-bidibenzo[*a,d*][7]annulenyliene (THBA) shown in Fig. 1.1b.

a) Aggregation-caused quenching (ACQ) luminophores



b) Aggregation-induced emission (AIE) luminogens

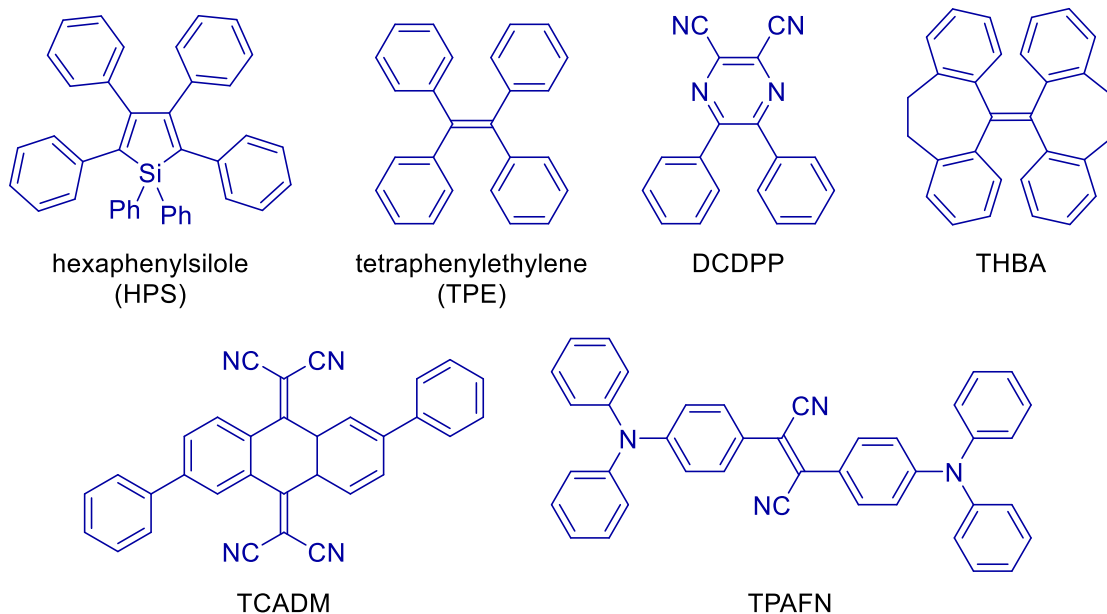
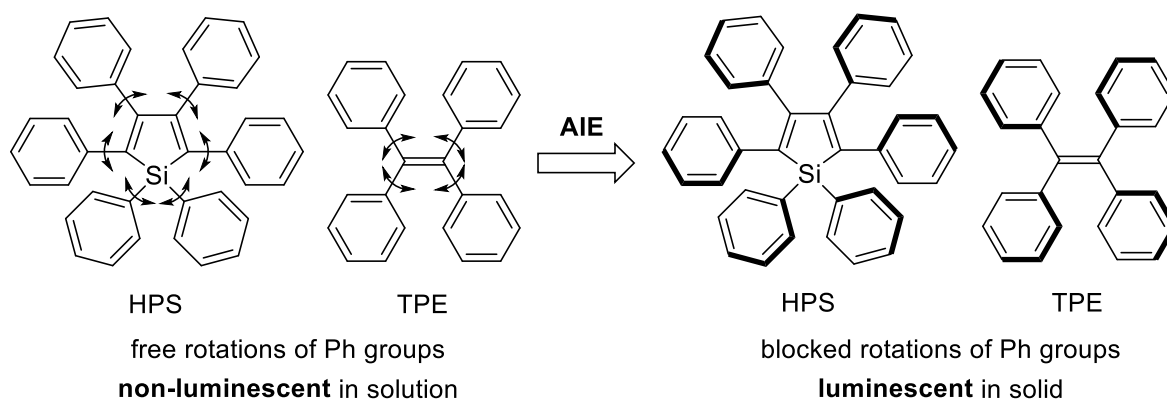


Figure 1.1 Selected examples of compounds with ACQ (a) and AIE (b).

1.1.2 Mechanisms of AIE

The first mechanistic insights into AIE were obtained by B. Z. Tang and co-workers in 2009.¹⁴ To explain the AIE behaviour of HPS, they introduced and experimentally confirmed the concept of restriction of intramolecular rotations (RIR). HPS is decorated with six phenyl rings freely rotating around C–C and Si–C bonds in dilute solution making the molecule conformationally flexible. The fast rotations dissipate the excited state energy *via* non-radiative ways, e.g. thermally. In the crystal state, HPS adopts a highly twisted propeller-like conformation, which causes intramolecular repulsion and slows down the intramolecular rotations due to the steric constraints. The non-radiative pathways are thus blocked, and the emission turns on (Fig. 1.2a).

a) Aggregation-induced emission (AIE)



b) Restriction of intramolecular motion (RIM):

restriction of intramolecular rotations (RIR) + restriction of intramolecular vibrations (RIV)

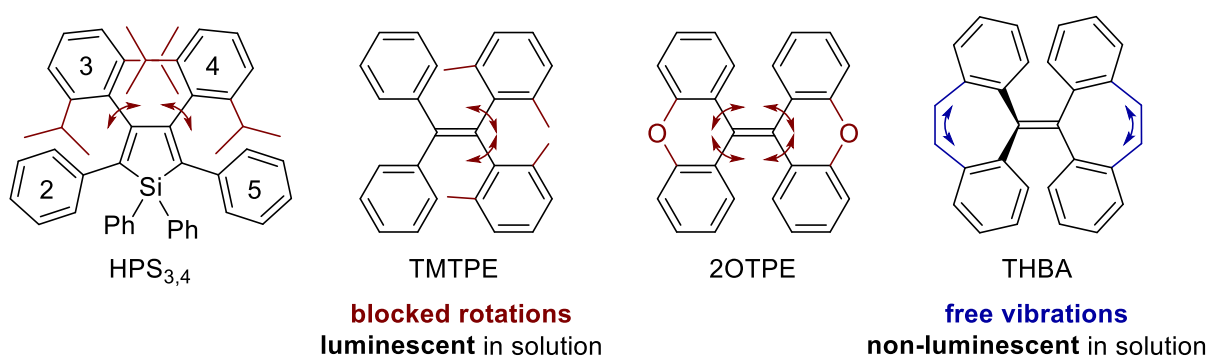


Figure 1.2 AIE concept (a) and the RIM mechanism of AIE (b).

In a similar fashion, the AIE behaviour of TPE was proposed to be the result of RIR of the phenyl rings preventing the formation of π - π stacking interactions in solid state leading to bright luminescence (Fig. 1.2a).¹³ The RIR mechanism was supported by

several control experiments, such as study of the viscosity, temperature, pressure effects, and photoluminescence lifetime measurements.¹⁴

The RIR mechanism was further supported by studies of B. Z. Tang, M.-Q. Zhu, Y. Liu, Q. Miao, and co-workers done on a series of structurally modified HPS and TPE. The introduction of bulky isopropyl groups at the *ortho* positions of phenyl rings 3 and 4 of HPS (HPS_{3,4}) leads to luminescence of this compound in solution (Fig. 1.2b).¹⁵ A similar approach on blocking the rotations with methyl groups at the *ortho* positions of geminal phenyl rings of TPE (TMTPE) resulted in turning on the luminescence in solution (Fig. 1.2b).¹⁶ Locking the rotors by means of covalent bonding is also an effective way to activate the RIR. It was shown that the locking of the *ortho* positions of two pairs of geminal phenyl rings of TPE with 'O'-bridges (2OTPE) makes this compound highly emissive in solution (Fig. 1.2b).¹⁷ A similar effect was observed when vicinal phenyl rings of TPE were hooked up by photo-induced cyclization.¹⁸ However, locking the geminal phenyls of TPE with ethylene bridges (THBA) did not lead to solution-based luminescence, but to solid-state emission (Fig. 1.2b).¹⁹ The AIE behaviour of THBA cannot be explained by the RIR mechanism because it does not have rotatable units. Instead, THBA possesses intramolecular vibrational motions. The restriction of intramolecular vibrations (RIV) was suggested to be responsible for the AIE properties of THBA.²⁰ The RIV mechanism was supported by other non-TPE-based molecules (for example, TCADM, TPAFN, Fig. 1.1b), which vibrations (bending, flapping, stretching, scissoring, etc.) are restricted in solid state leading to AIE.^{21,22}

Thus, the suggested general mechanism behind AIE is restriction of intramolecular motions (RIM), including rotations (RIR) and vibrations (RIV).²⁰ The RIM concept clearly demonstrates the design strategies for AIE compounds, from which introducing multiple free rotating aryl rings (polyarylation) is one of the most efficient.²³ Following this strategy, numerous molecules with AIE have been synthesized, including hydrocarbon, heteroatom (boron, Schiff bases, nitrile compounds), macromolecule (main/side chain polymers, dendrimers, hyperbranched polymers, metal-organic frameworks), bio- (cyclodextrines, DNA), and metal-complex (Zn(II), Au(I), Cu(I), Pt(II), Pd(II), Ir(III)) based compounds.¹

Additional studies on the mechanism of AIE were provided by B. Z. Tang and co-workers in 2015.²⁴ They showed that along with rotations of the phenyl rings, photo-

induced *E/Z* isomerization of the central C=C bond of TPE is responsible for quenching of its luminescence in solution, although to a smaller extent. Having distinguished the two processes and measured photoluminescence quantum yields of each, they determined that the emission is quenched 10% by *E/Z* photoisomerization and 81% by free rotation of phenyl groups, evidencing that the RIR mechanism is dominant. Shortly later, the RIM mechanism was questioned by theoretical and experimental studies. C. Corninboeuf and co-workers proposed that ultrafast relaxation achieving through a conical intersection (CI) and restricted access to CI (RACI) are possible mechanisms for turning OFF and ON the luminescence of TPE in dilute solution and in the solid state, respectively.^{25,26} In the application of the CI concept to TPE, excitation from the ground state (S_0) to the first excited state (S_1) causes a reduction of the ethylenic C=C bond order, which initiates the twisting dynamics of the phenyl rings. These motions stabilize S_1 and destabilize S_0 , causing the two states to degenerate and be closer energetically, *i.e.* crossing referred to CI. In the following experimental work, the structural evolution of TPE crossing the CI has been visualized using frequency and polarization resolved UV/IR spectroscopy. It was shown that upon passing the CI, TPE undergoes Woodward-Hoffmann 6- π photocyclization of one pair of vicinal phenyl rings to give diphenyl dihydrophenanthrene, DPDHP (Fig. 1.3).²⁷

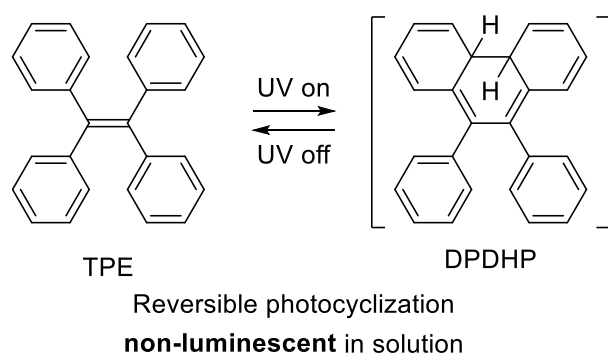


Figure 1.3 Luminescence quenching of TPE in solution is associated with photocyclization.²⁷

Over 80% of the excited TPE molecules were converted into DPDHP within 7–10 ps depending on the solvent. According to calculations, the photocyclization process is barrierless and requires a low structural reorganization. DPDHP is not stable (lifetime is 300 ps) and further converts to the TPE ground state. Remarkably, the photocyclization has been reported over 40 years ago as the first step in photo-

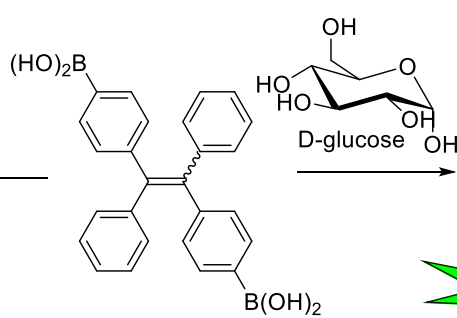
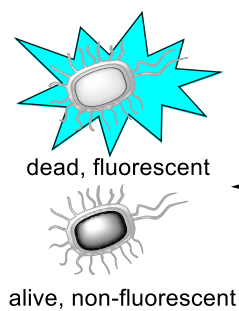
induced oxidation of TPE to diphenyl phenanthrene.^{28,29} The cyclized isomer DPDHP was shown to be unstable and, if not trapped, reverts back to the starting material.³⁰

Given that the non-radiative decay of the TPE excited state occurs on the picosecond timescale, it is inconsistent with rotation- or vibration-mediated decays, which happen on the nano- to microsecond timescale.³¹ The latter observations are not in agreement with the previously suggested mechanism of intramolecular rotations and vibrations for dissipating the excited state energy non-radiatively. The luminescence of TPE in the solid state can now be explained by the RACI, which preserves the electronic energy for radiative decay *via* light emission.

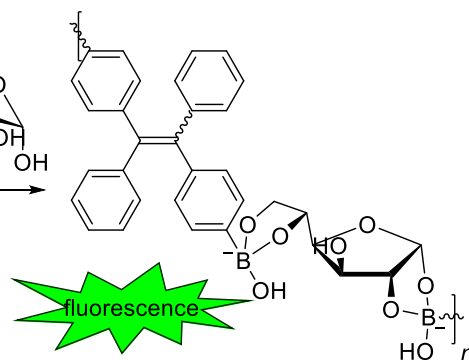
1.1.3 Applications

Compounds with AIE properties have found numerous applications, including fluorescent sensing,³² electroluminescent devices,³³ cancer theranostics,³⁴ and fluorescent bio-imaging.³⁵ TPE is a prototype AIE compound. TPE and its derivatives are widely used owing to their concise synthesis, stability, and intensive luminescence in the solid state. Reviews about applications of TPE-based compounds are referenced.³⁶⁻³⁹ Some examples are shown in Fig. 1.4. A TPE with two boronic acid groups was employed as a selective fluorescent sensor for D-glucose.⁴⁰ The same compound can be used for fluorescent discrimination of dead and living bacteria.⁴¹ A probe containing 1,3-indandione-functionalized TPE undergoes fluorescent quenching in the presence of basic amino acids, such as arginine and lysine.⁴² TPE conjugated to a specifically hybridized DNA strands gives different fluorescent responses.⁴³ Fluorescence of the TPE-based linear polymer quenches in the presence (from ppm to ppb) of various explosive nitro-compounds, such as picric acid (PA), 2,4-di-, and 2,4,6-trinitrotoluene (DNT, TNT), making it good explosive detector.⁴⁴ TPE itself can be used as fluorescent visualizing agent for the detection of latent fingerprints on wet non-porous surfaces.⁴⁵ An electroluminescent device based on TPE-dimer with *para* linkage was found to show sky-blue emission at 488 nm with current efficiency up to 7.3 cd/A, bright luminance up to 11180 cd/m² at 15 V, and external quantum efficiency (EQE) of 3.2%.⁴⁶ A probe based on piperazine-functionalized TPE was used in selective visualization of lysosomes.⁴⁷ A TPE functionalized with a pyridinium group is a good fluorescent visualizer for selective staining of mitochondria in living cells.⁴⁸

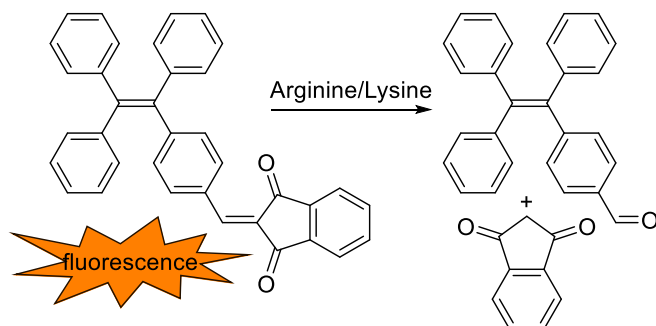
Discrimination of dead/alive bacteria



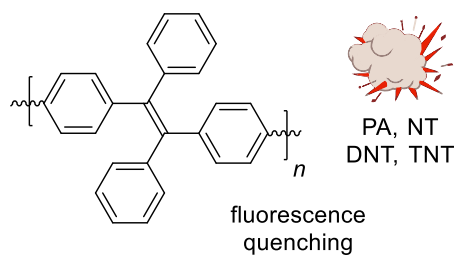
Selective sensor for glucose



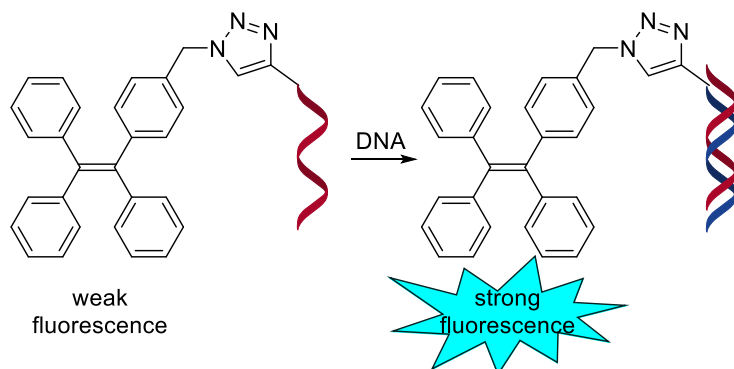
Sensing of basic amino acids



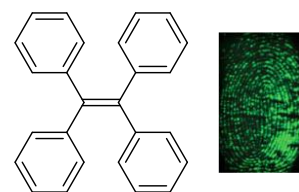
Explosives detection



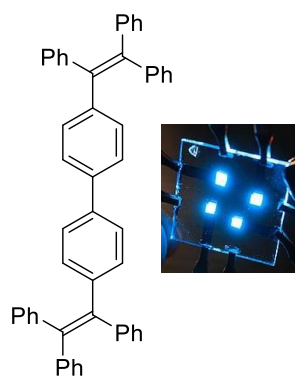
Nucleic acid hybridization detection



Visualization of latent fingerprints



Sky-blue OLEDs



Selective imaging of organelles

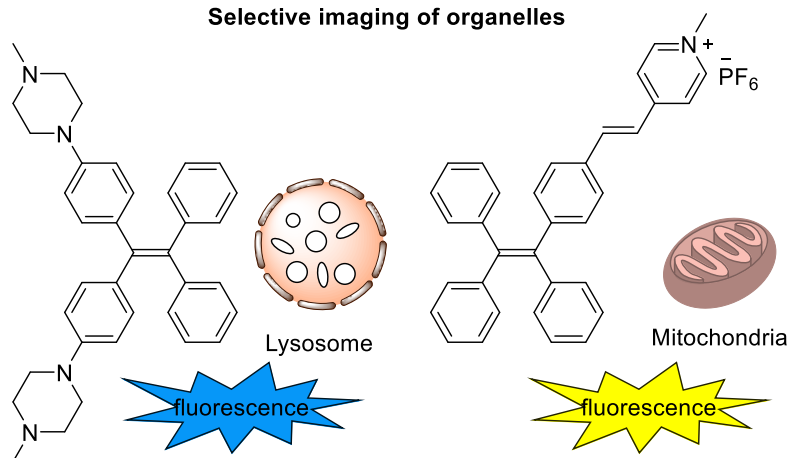


Figure 1.4 Overview of applications of TPE derivatives.

1.1.4 Synthesis of AIE Luminophores Using Triazenes

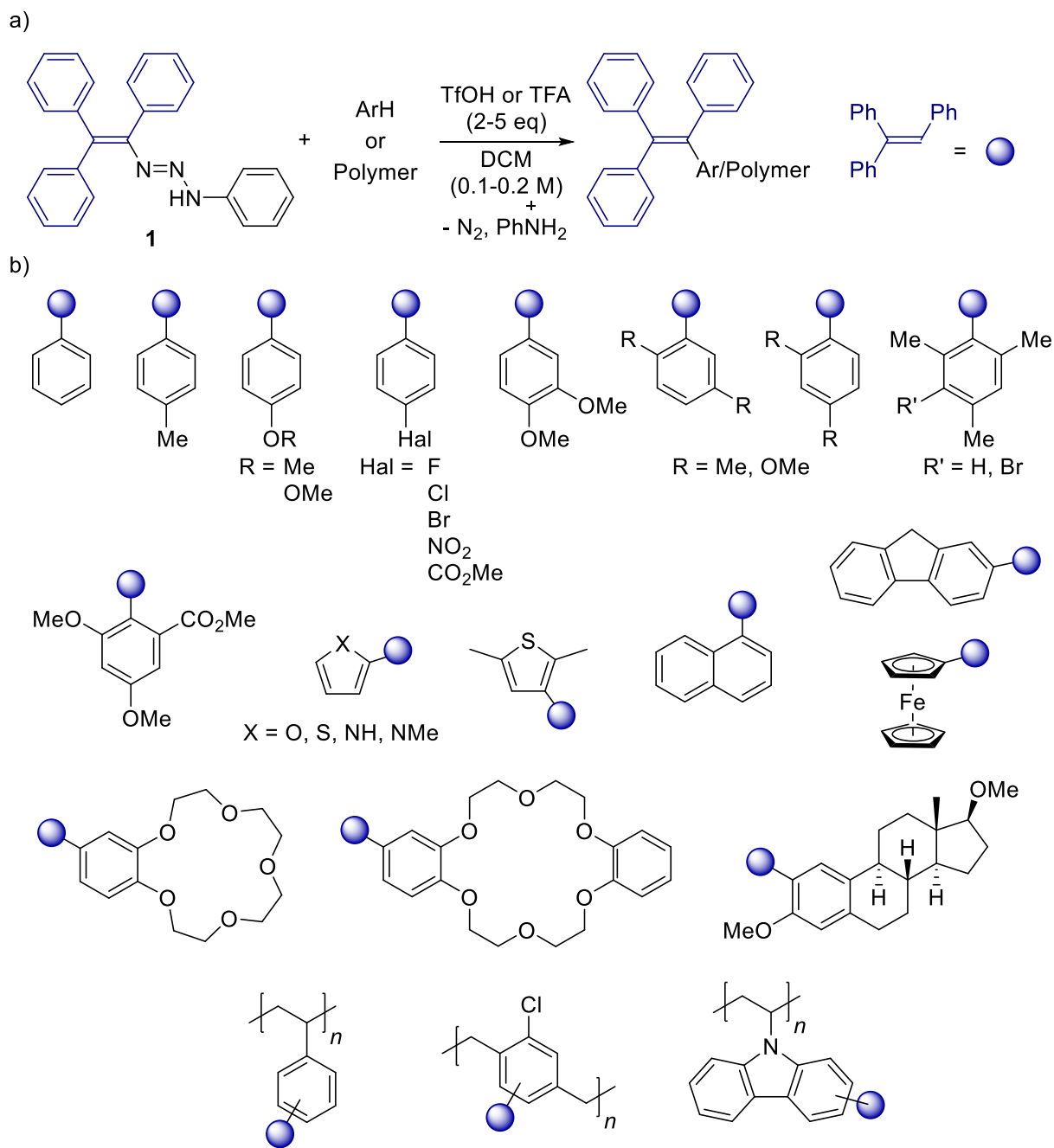
This subchapter describes a method for grafting of triarylethene group onto aromatic compounds.⁴⁹ This procedure was a starting point for the work described in this thesis.

Tetraarylethenes can be conventionally synthesized *via* McMurry^{50,51} or Wittig^{52–54} reactions, addition of lithiated benzylic species to benzophenone derivatives,^{55,56} Pd-catalyzed cross-coupling reactions between triarylethenyl bromides and arylboronic acids, or transition metal-catalyzed coupling of arylmetal compounds to alkynes.^{57,58} However, the conventional procedures often give moderate yields and selectivity, and they typically require chromatographic purification of the products. They are also not metal-free and demand highly reactive aryl/benzyl organometallic reagents.

Recently, a metal-free approach to tetraarylethenes relying on the acid-induced C–H vinylation of aromatic compounds with triazenes was developed by Severin's group.⁴⁹ Scheme 1.1a shows the use of triazene **1** for the synthesis of aryl(triphenyl)ethenes. The optimized procedure requires a treatment of a solution of the triazene (1–2.5 equiv.) and arene (1–20 equiv.) in DCM (0.1–0.2 M) with HOTf or TFA (2–5 equiv.) with following stirring for 1 h at r.t. The triazene function of **1** cleaves in the presence of Brønsted acids and can be replaced by different nucleophiles. The reaction is proposed to proceed *via* highly reactive triphenylvinyl cation, which is formed after acid-induced N–N bond cleavage and release of N₂.⁵⁹ When aromatic compounds are used as nucleophiles, aryl(triphenyl)ethenes are obtained (Scheme 1.1a).

This C–H activation route is fast, versatile, and simple to perform. Importantly, it can be used for the direct grafting of AIE-active triarylvinyl group onto non-AIE-active compounds. Thus, a broad scope of aromatic compounds including heterocycles, supramolecular hosts, biologically relevant molecules, and commercial polymers can be functionalized with the triarylvinyl group, and they become AIE-active (Scheme 1.1b).

Based on this procedure, a method to access polymeric tetraarylethenes was developed (Chapter 2).



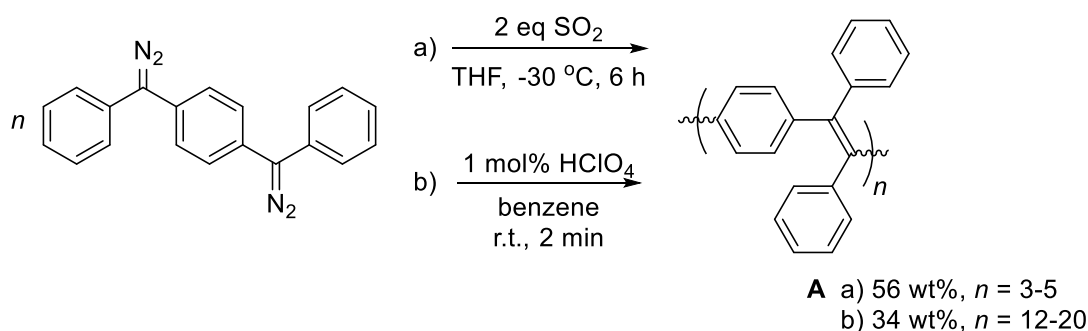
Scheme 1.1 Synthesis of AIE-active aryl(triphenyl)ethenes by C–H vinylation of different arenes with triazene **1**.⁴⁹

1.2 Polymeric Tri- and Tetraarylethene-Based Luminophores

Conjugated polymers composed of phenylene units connected by C=C bonds in various topologies are known since the 1970s.^{60,61} The synthesis and properties of these compounds have been described in numerous research articles. Since the 2000s, highly phenylated polymers have attracted renewed interest due to applications originating from the discovery of aggregation-induced emission (AIE) of tetraphenylethene (TPE). For the discussion of the mechanism of AIE and applications of AIE-active compounds, see subchapters 1.1.2 and 1.1.3, respectively. Below, we review the synthetic approaches to poly(tri- and tetraarylethene)s. Their unique properties make them useful compounds for many applications, which are also discussed in more detail in subchapter 1.2.2.

1.2.1 Synthesis and Properties of Poly(Tri- and Tetraarylethene)s

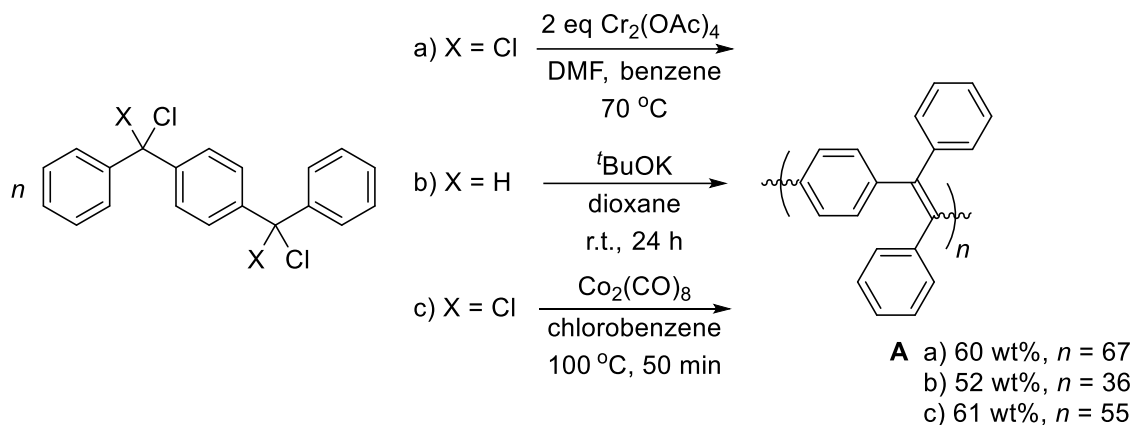
Linear poly(triphenylethylene)s of type **A** (Scheme 1.2) were first described in 1968 by T. Nagai and co-workers.⁶¹ They showed that **A** can be obtained in good yield by reductive olefination of 1,4-bis(α -diazobenzyl)benzene in the presence of SO₂ gas (Scheme 1.2a). Using the same monomer, L. de Koninck and G. Smets (1969) obtained **A** with increased molecular weights by employing acid catalysis (Scheme 1.2b).⁶²



Scheme 1.2 Synthetic routes to linear poly(triarylethene) **A** through reductive olefination of a monomer with diazo groups.

Another route to poly(triphenylethylene) **A** starting with a chlorinated monomer was developed by H.-H. Hörhold and co-workers (1977).⁶³ Reductive olefination of 1,4-bis(α, α -dichlorobenzyl)benzene by chromium(II) acetate gave polymer **A** in 60% yield

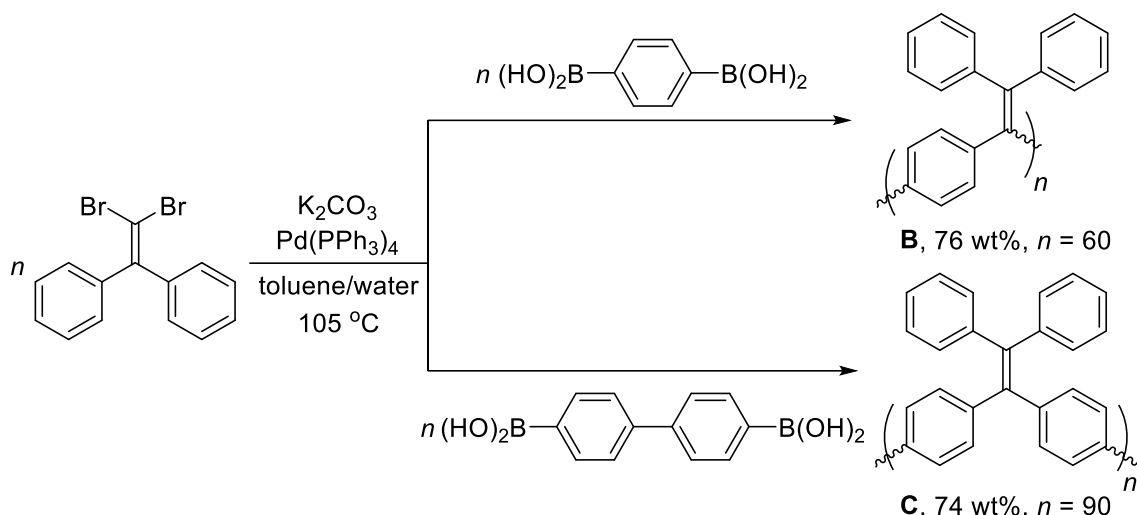
(Scheme 1.3a). The films based on this polymer display outstanding photoconductive properties, which are better than those for poly(*N*-vinylcarbazole)⁶⁴ known as one of the best photoconductive materials.⁶⁵



Scheme 1.3 Synthetic routes to linear poly(triarylethene) **A** via reductive olefination of monomers with halogen groups.

Reductive olefination can be carried out under basic conditions using potassium *tert*-butoxide⁶⁶ (Scheme 1.3b) or utilizing different reducing agents, such as dicobalt octacarbonyl⁶⁷ (Scheme 1.3c). The photoluminescence quantum yield of **A** in a neat film was first measured by M. R. Andersson and co-workers (2000), and a value of 19% was reported.⁶⁶ While a value of 37% was measured by U. Scherf and co-workers (2016) for a polymer of type **A** with a higher molecular weight ($n = 55$).⁶⁷ In both publications, the films were reported to exhibit bright green luminescence.

B. Z. Tang, J. Xu and co-workers (2016) have employed Suzuki cross-coupling reactions to obtain linear polymeric tri- (**B**) and tetraarylethenes (**C**) in good yields from monomers containing halogen and boronic acid functional groups (Scheme 1.4).⁶⁸

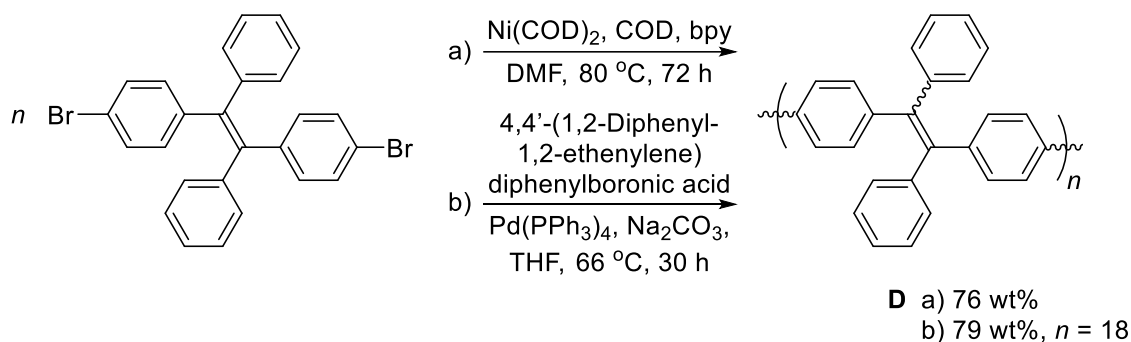


Scheme 1.4 Synthetic routes to linear poly(triphenylethene) **B** and poly(tetraphenylethene) **C** using Suzuki cross-coupling reactions.

The AIE properties of the linear polymer **A** with OPh functional groups synthesized by reductive polyolefination were described by H.-H. Hörhold and co-workers (February 19th, 2001),⁶⁹ shortly before than the term ‘Aggregation-Induced Emission’ was introduced for 1-methyl-1,2,3,4,5-pentaphenylsilole by B. Z. Tang and co-workers (August 14th, 2001).¹² Since the discovery of the AIE properties of TPE in 2007,¹³ poly(tri- and tetraarylethene)s attracted renewed interest. In a THF-water mixture (1:9, v/v), the polymers **B** and **C** show photoluminescence quantum yields (Φ_{agg}) of 14% and 18%, respectively. Usually, the emission spectra of TPE-based polymers are bathochromically shifted compared to that of TPE due to the extended electronic conjugation. In aggregate state, TPE emits at around 470 nm, whereas **B** and **C** emit at 506 and 480 nm, respectively.

Further, the luminescence of poly(tri- and tetraarylethene)s in aggregated and solid state was found sensitive to the presence of hazardous aromatic amino and nitro compounds. For example, the luminescence of the aggregates of **B** in a THF-water mixture (1:9, v/v) undergoes quenching by vapours, solutions (detection limit 5 ppb), and powders (detection limit 1 ng) of various nitro-compounds, such as PA and TNT, making this polymer an attractive candidate for sensing applications.

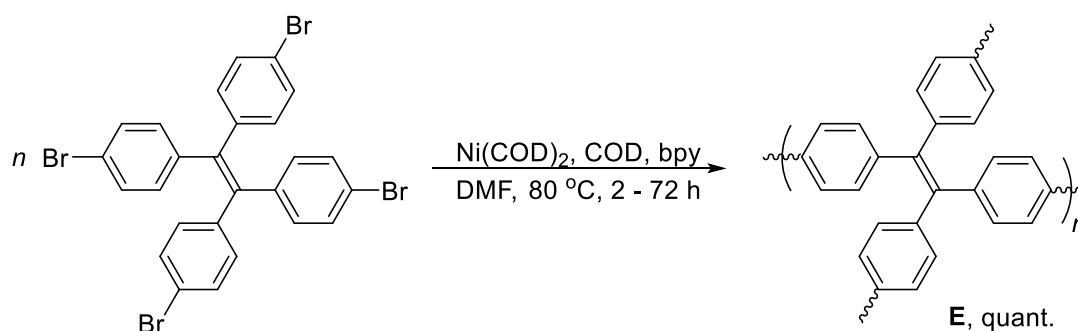
Linear poly(tetraphenylethene) of type **D** was first obtained in 2011 by D. Jiang and co-workers from 1,2-bis(4-bromophenyl)-1,2-diphenylethene in 76% yield using polymerization based on Yamamoto coupling reaction (Scheme 1.5a).⁷⁰



Scheme 1.5 Synthetic routes to linear poly(tetraarylethene) **D** using C–C coupling reactions.

The aggregates of **D** in THF-water mixtures showed a maximal Φ_{agg} value of 22%, which is higher than that for **B** and **C**.⁷⁰ In the next year, B. Z. Tang and co-workers reported a procedure to obtain **D** by cross-coupling TPE derivatives with halogen and boronic acid functional groups (Scheme 1.5b).⁷¹ A refractive index (R_I) of the polymer was measured, and, remarkably, a thin film of **D** displayed a very high R_I values of 1.7649–1.6873 in a wide optical region of 400–1700 nm, which is much higher than those of commercial plastics (e.g. 1.49 for poly(methyl methacrylate), PMMA).

A polymer network of type **E** was obtained quantitatively by Yamamoto coupling of tetrakis(4-bromophenyl)ethene (Scheme 1.6).⁷⁰



Scheme 1.6 Synthesis of polymer network **E** by Yamamoto coupling reactions.

In comparison to the linear analogue **D**, the polymer **E** demonstrates a higher photoluminescence quantum yield in solid state (Φ_{solid}) of 40%. Due to the 3D network

structure, the polymer **E** also possesses microporosity with a large Brunauer-Emmett-Teller (BET) surface area. Nitrogen sorption isotherm measurements at 77 K have shown reversible curves for BET surface area increasing from 753 m²g⁻¹ to 1665 m²g⁻¹ with increasing the polymerization reaction time from 2 h to 72 h. The microporous structure was also confirmed with field-emission scanning electron microscopy (FE-SEM), showing the average particle size from 25 nm to 255 nm increasing with the polymerization reaction time. The micropores have also been visualized by high-resolution tunneling electron microscopy (HR-TEM), showing the homogeneous distribution of the micropores, which have similar size regardless of the polymerization reaction time.

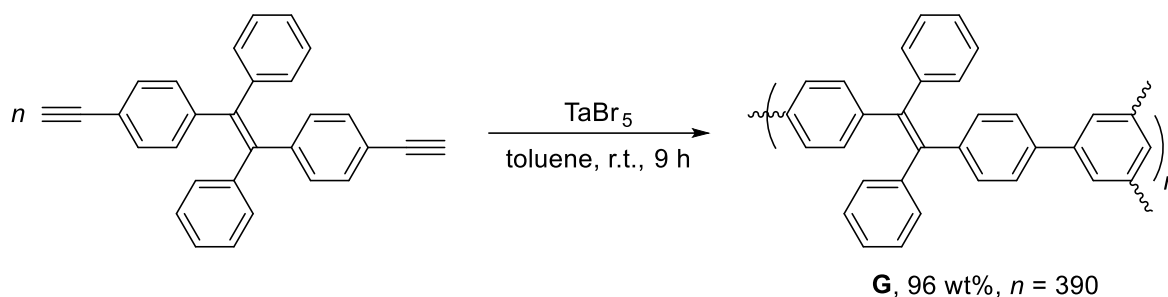
A microporous polymer network of type **F** was synthesized by U. Scherf and co-workers (2015) by reductive olefination of tris(α,α -dichlorobenzyl)benzene using dicobalt octacarbonyl or chromium(II) acetate (Scheme 1.7).⁷²



Scheme 1.7 Synthesis of the microporous polymer network **F** by reductive olefinations.

It was suggested that the bulky architecture of branched polymers always bring some restriction on the intramolecular motions (RIM) of the AIE-active units even in the molecularly isolated state, making the polymers luminescent in solution and further reducing the overall AIE effect.¹ Branched polymers are intrinsically crowded in their molecular structures. Obtaining a hyperbranched polymer which is non-emissive in solution but strongly luminescent in the aggregate and solid state is thus challenging. Polymer **F** shows yellow emission in the solid state with Φ_{solid} of 3.5%, which is lower than that of all previously mentioned polymer types. Additionally, the polymer network **F** possesses a moderately high BET surface area of 462 m²g⁻¹.

A hyperbranched polymer of type **G** with a high molecular weight ($n = 390$) was obtained by B. Z. Tang and co-workers (2012) by polycyclotrimerization of 1,2-bis(4-ethenylphenyl)-1,2-diphenylethene using TaBr_5 as catalyst (Scheme 1.8).⁷³



Scheme 1.8 Synthesis of hyperbranched polymer **G** by [2+2+2]-cyclotrimerizations.

Gel permeation chromatography (GPC) of polymer **G** showed a large M_w of 157800 with a PDI of 2.7. Thermal gravimetric analysis (TGA) showed a high thermal stability with a degradation temperature (T_d) of 462 °C. Polymer **G** is highly soluble in common organic solvents such as DCM, chloroform, toluene, and THF.

When **G** is dissolved in THF, a weak cyan luminescence is observed with photoluminescence quantum yield in solution (Φ_{sol}) of ~3.1%. The weak emission can be explained by the rigid and crowded architecture of **G**. Despite the cavities inside the polymer, the proximity of neighboring TPE moieties imposes some steric hindrance on the aryl rings. Because of that, part of the excited state energy cannot be non-radiatively dissipated, leading to weak emission in solution. It provides evidence to the fact that flexibility in molecular structure is of particular importance to the successful design of AIE-active hyperbranched polymers. Polymer **G** shows strong AIE enhancement (AIEE) in THF-water mixtures with 11-fold increase of emission intensity for the aggregates in 95% water content. In the solid state, $\Phi_{\text{solid}} = 47\%$ was observed, which is larger than that of all previously discussed structure types. Upon increasing the water fraction, the macromolecules most probably adopt a more compact structure to reduce the surface area in contact with water. Such compression leads to the bright emission in aggregate state.

The emission of the aggregates of **G** undergoes quenching by a solution of PA (detection limit 1 ppm). Due to the presence of unreacted triple bonds on the periphery,

the polymer can be cross-linked upon UV irradiation with the formation of well-resolved photopatterns. This feature allows the use of this polymer in photolithography.

To summarize, the synthetic approaches to polymeric tri- or tetraarylethenes of types **A–G** include polymerizations based on C–C (cross)coupling reactions, reductive olefination and cyclotrimerization reactions. These procedures are efficient for synthesizing the polymers **A–G** in good yields with different molecular weights. However, they have a number of drawbacks, such as:

1. Requirement of catalytic or stoichiometric amounts of metal-based catalysts, which are expensive and environmentally unfriendly, and cannot always be completely removed after work-up;
2. Requirement for using monomers with reactive functional groups, *i.e.* halogen, boronic acid, terminal alkyne, which remain present in the polymeric products and can compromise their chemical and photochemical stability.

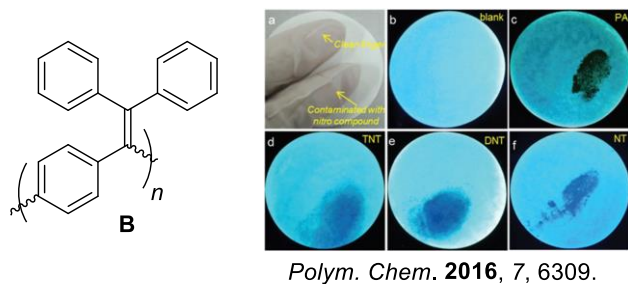
Thus, new synthetic methods for polymeric tri- or tetraarylethenes are of high interest. In Chapter 2, we describe a novel approach to hyperbranched poly(tetraarylethene)s based on successive C–H vinylation reactions with a triazene, which addresses the stated problems.

1.2.2 Applications

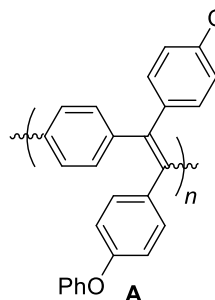
As discussed above, polymeric tri- or tetraarylethenes of types **A–G** feature large molecular weights, high photoconductivity, thermal stability, good solubility in common organic solvents, good tendency to film formation, and very high refractive indexes of the films. In addition, they possess AIE (AIEE), and the emission of their aggregates is sensitive to the presence of different additives, such as solvents, amino and nitro aromatics, or metal cations. In solid state, tri- or tetraarylethenes **A–G** show green-to-yellow luminescence with moderate to good Φ_{solid} .

Applications of polymeric tri- or tetraarylethenes of types **A–G** include the fluorescent sensing of vapors, solutions and solids of aromatic nitro^{68,71,74} and amine⁷² compounds, metal cations,⁷⁴ the composition of emitting layers of electroluminescent devices,⁷⁵ the sorption of N₂ and H₂ gases,^{70,72,76} and the formation of films with high refractive indexes.^{71,74} Selected examples are shown in Fig. 1.5.

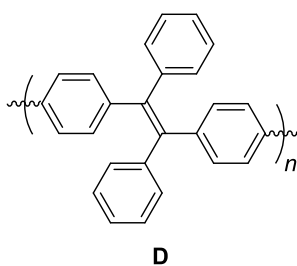
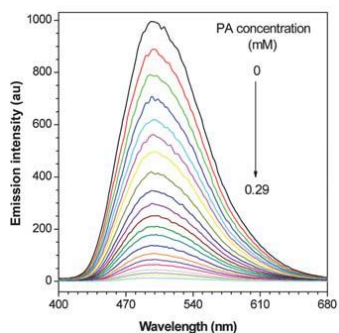
Sensing of explosives in solid state



Electroluminescent devices



Sensing of explosives using aggregates

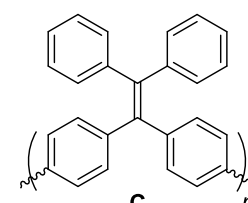
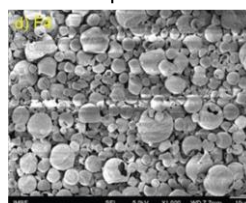


ACS Appl. Polym. Mater. **2019**, *1*, 11, 3039.

J. Mater. Chem. **2012**, *22*, 232.

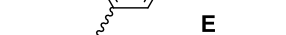
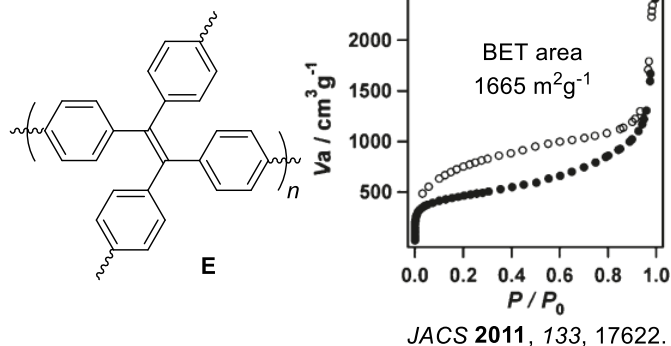
Films with high refractive indexes

RI up to 1.8



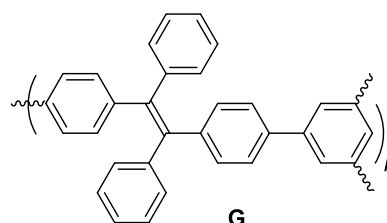
Polym. Chem. **2016**, *7*, 6309.

Sorption of N₂

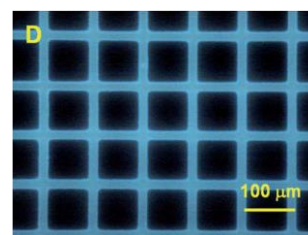
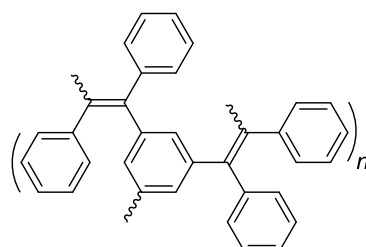
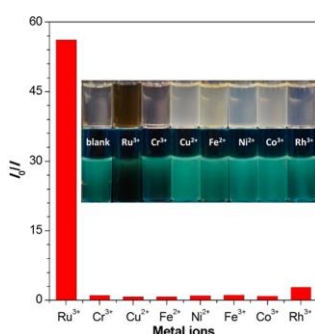


JACS **2011**, *133*, 17622.

Photopatterning



Selective sensing of Ru³⁺



Polym. Chem. **2012**, *3*, 1481.

Macromolecules **2015**, *48*, 8098.

Figure 1.5 Overview of the applications of polyarylethenes **A–G**. Sources of images are indicated. Adapted and reproduced with permissions of Royal Society of Chemistry and American Chemical Society.

Polyarylethenes were used as components of emissive layers of polymeric light-emitting diodes (PLEDs). Based on a derivative of the linear polymer **A** with OPh donor groups, a series of electroluminescent solar-harvesting devices with different emission colours and photoluminescence quantum yields in film (Φ_{film}) up to 45% was fabricated.⁷⁵ Fast, low-cost, and highly sensitive detection of explosive nitro-compounds can be achieved using polyarylethenes. An effective sensor for explosive nitro-compounds PA, DNT, and TNT (detection limit < 1 ng) was prepared by spraying the suspension of aggregates of the linear polymer **B** onto a filter paper (surface concentration 1 $\mu\text{g}/\text{cm}^2$).⁶⁸ The sensing of these compounds can also be done using a suspension of the aggregates of the polymer **D** directly.⁷¹ Polyarylethenes possess good film-forming ability, and their thin films show *R*/s up to 1.8, which are higher than those of commercial polymers, such as PMMA (1.49), polycarbonate (1.58) and polystyrene (1.59).⁷⁴ The polymeric network **E** shows a unique microporous structure with a very large BET surface area of 1665 m^2/g measured with respect to N_2 gas, making **E** an efficient absorbent.⁷⁰ The polymeric network **F** is a highly selective fluorescent sensor for detecting Ru^{3+} ions.⁷⁴ Due to the terminal alkyne groups remaining on the periphery of the hyperbranched polymer **G** after its synthesis, they are able for UV-induced crosslinking, which reflect as the appearance of contrast patterns known as imaging by 'photopatterning'.⁷³

1.3 Ir(III) Luminophores with Orthometalated Ligands

1.3.1 Introduction

With the advent of the digital era, mankind has become more dependent on electronic technologies, many of which owe their existence to rare elements. Among these elements, iridium is less common in the surrounding world – its content in the Earth's crust is about 40 times less than that of gold.

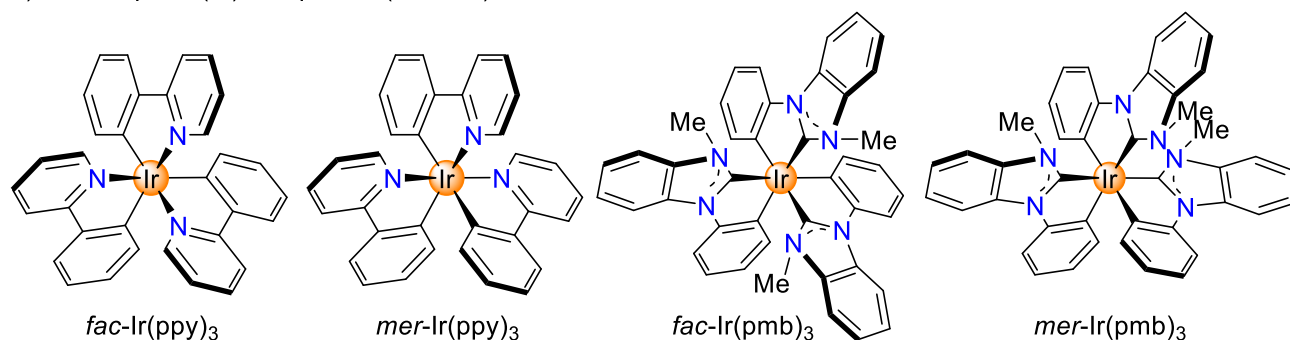
Iridium was discovered in 1803 by the British chemist Smithson Tennant as an impurity extracted from nugget platinum. In the first years after its discovery, the noble metal was considered useless due to its chemical inertness and challenging processing.⁷⁷ However, rapid progress in metallurgy, chemistry, physics and material science has made it possible to process and use iridium-based compounds in a various human activities. Thus, iridium itself and its alloys, inorganic compounds and organometallic complexes found a wide range of applications, from the crucibles for melting and re-crystallization, the tips of ballpoint pens and contacts in spark plugs to the catalysts for photochemical reactions and components of electroluminescent devices.

Iridium is a transition metal of the platinum group with atomic number 77. It is located in period 6 and group 9 in the Periodic Table and has a configuration of $[\text{Xe}]4f^{14}5d^76s^2$ in the ground state. After its discovery, the chemistry of iridium have been developing very rapidly, and soon compounds with oxidation states from -1 to $+9$,⁷⁸ including complexes with coordination numbers from 3 to 6 and different geometry of the ligand environment, were obtained. The most stable oxidation states are $+1$, $+3$ and $+4$. In case of Ir(I), the d^8 configuration is realized, and complexes with coordination numbers 4 or 5 adopt a square or trigonal bipyramidal geometry, respectively. In case of Ir(III), the d^6 configuration is realized, and complexes with coordination number 6 adopt an octahedral geometry. The ligands in the coordination sphere of iridium can be of diverse electronic and steric nature. The following types of octahedral Ir(III) complexes are of relevance for the work described in the thesis (Scheme 1.9):

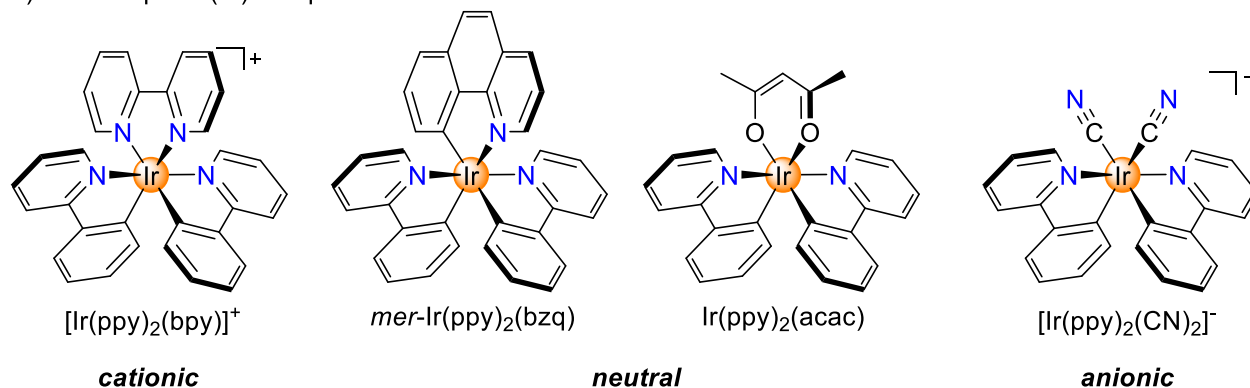
1. Homoleptic Ir(III) complexes with three monoanionic orthometalated ligands ($\text{C}^{\wedge}\text{N}$ or $\text{C}^{\wedge}\text{C}$:). The complexes are charge neutral (Fig. 1.9a).

2. Heteroleptic Ir(III) complexes with monoanionic orthometalated ligands (C[^]N or C[^]C:) and a heteroligand. Depending on the heteroligand, the complexes can be cationic (N[^]N), neutral (C[^]N, O[^]O) or anionic (C≡N) (Fig. 1.9b).

a) Homoleptic Ir(III) complexes (*neutral*)



b) Heteroleptic Ir(III) complexes



Scheme 1.9 Selected examples of homoleptic (a) and heteroleptic (b) Ir(III) complexes.

These photoactive iridium(III) complexes have found numerous applications as therapeutic and bio-imaging probes,^{79,80} photocatalysts in water splitting^{81,82} and various organic reactions,^{83–85} photosensitizers for the production of singlet oxygen,^{86–88} luminescent sensors for oxygen,⁸⁹ metal cations^{90,91} and anions, pH, volatile organic compounds, and biomolecules.^{92–94} Materials based on iridium(III) complexes have been widely used for the development of organic light-emitting diodes (OLEDs) with different characteristics.^{95–97} The applications are enabled by the unique properties of these compounds. Advantageous features are:

1. High chemical, physical (thermal) and photochemical stability;
2. Versatility in ligands design, fine tuning of spectral characteristics by changing steric and electronic properties of ligands;

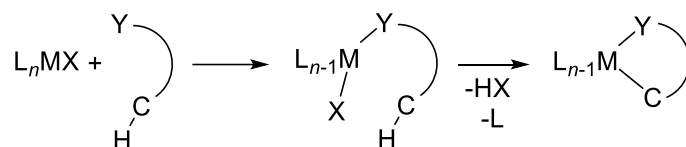
3. Intensive luminescence over a wide spectral range from near-UV to near-IR;
4. Longer excited state lifetimes compared to organic fluorophores;
5. Shorter excited state lifetimes compared to other organometallic phosphors;
6. High photoluminescence quantum yields in solutions, films and solid state;
7. Increased internal quantum efficiency compared to conventional fluorophores;
8. Electroluminescent properties.

Homoleptic Ir(III) complexes with orthometalated arylpyridine ($\text{Ir}(\text{C}^{\wedge}\text{N})_3$) or aryl *N*-heterocyclic carbene (NHC) ligands ($\text{Ir}(\text{C}^{\wedge}\text{C}:)_3$) can form two isomers: *fac* and *mer* (Scheme 1.9a). The work described in this thesis focuses on the chemical and photochemical isomerization of these complexes, and not on their photophysical properties. Consequently, synthetic procedures and previously used isomerization conditions will be discussed in detail in subchapters 1.3.2 and 1.3.3. The electronic structure and the luminescent properties of these complexes will only briefly be introduced in subchapter 1.3.4. Finally, applications of $\text{Ir}(\text{C}^{\wedge}\text{N})_3$ and $\text{Ir}(\text{C}^{\wedge}\text{C}:)_3$ will be reviewed in the end of subchapter 1.3.4.

1.3.2 Synthesis of $\text{Ir}(\text{C}^{\wedge}\text{N})_3$ and $\text{Ir}(\text{C}^{\wedge}\text{C}:)_3$ Complexes. *fac* and *mer* Isomers.

Chemistry of Ir(III) complexes with orthometalated ligands has been developing for more than 40 years. Many synthetic routes leading to good yields of target $\text{Ir}(\text{C}^{\wedge}\text{N})_3$ and $\text{Ir}(\text{C}^{\wedge}\text{C}:)_3$ complexes have been proposed and optimised. However, classical (or conventional) methods to access these complexes are firmly established in practice. The search for cost-efficient methods is also an active direction of research, since iridium in metal state and, even more so, its compounds are expensive.

The conventional methods for the synthesis of $\text{Ir}(\text{C}^{\wedge}\text{N})_3$ rely on a cyclometalation of $\text{HC}^{\wedge}\text{N}$ ligand (the archetypal example of $\text{HC}^{\wedge}\text{N}$ is 2-phenylpyridine) with Ir metallocenter. The cyclometalation reactions are known since 1955 from the studies by G. Bähr and G. Müller on chelated organoaluminium compounds.⁹⁸ The term 'cyclometalation' was coined by S. Trofimenko in 1973 after his studies on chelated organopalladium compounds.⁹⁹ In general, the mechanism of cyclometalation involves pre-coordination of the ligand donor atom Y to the metal center M, activation of the C–H bond by M and its heterolytic cleavage with following a pseudo-covalent M–C σ -bond formation, leading to a closure of a metallocycle (Scheme 1.10).¹⁰⁰



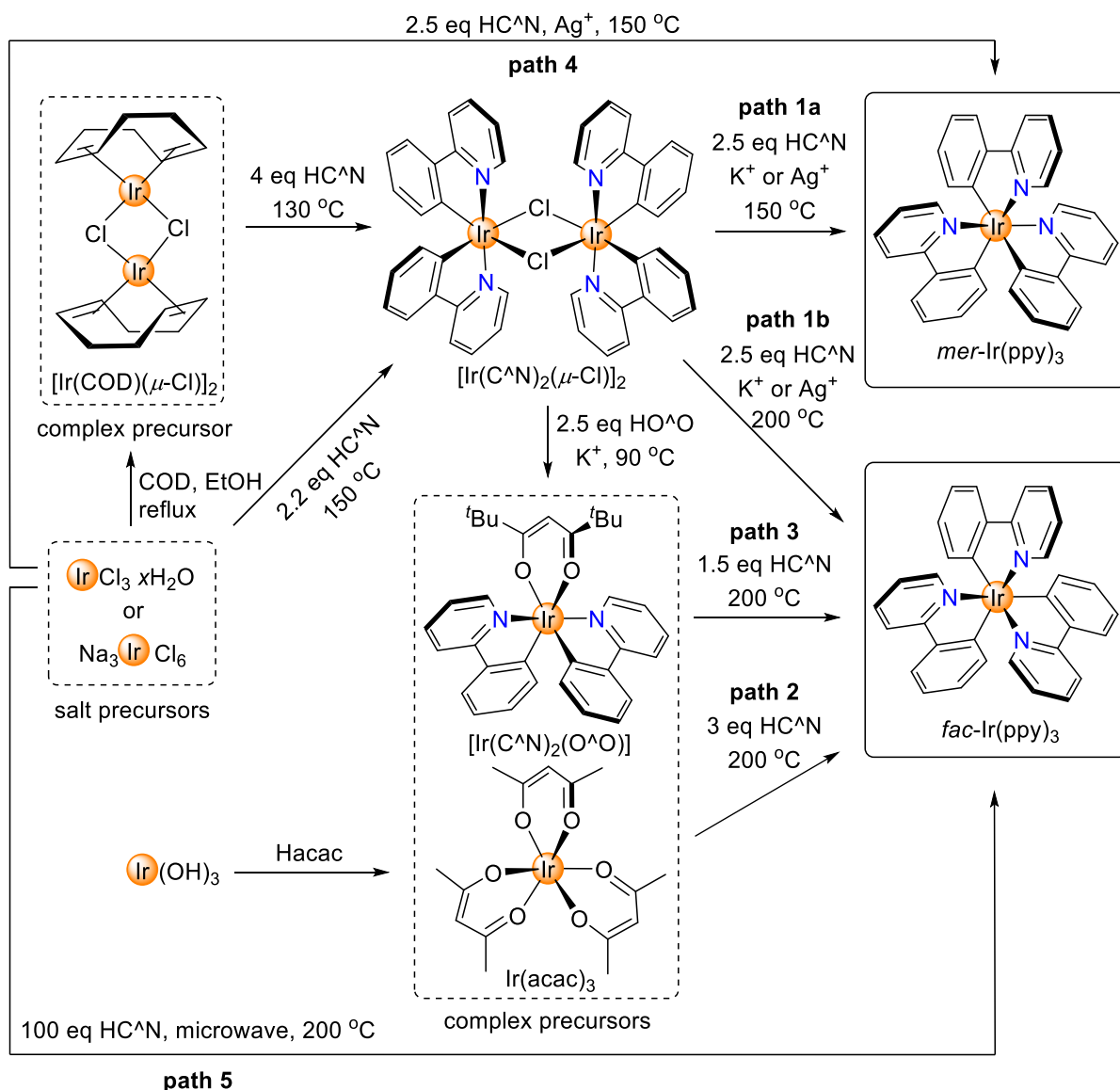
C = aryl, alkyl, alkenyl
 Y = group V (N, P, As) and VI (O, S) donor atoms
 M = metal (Ir, Pd, Pt, Rh, Ru, Au, Re)
 X = leaving group (Cl, OAc)
 L = labile ligand (water, DMSO, MeCN, CO)

Scheme 1.10 General scheme for cyclometalation reactions.

Typically, $\text{IrCl}_3 \cdot x\text{H}_2\text{O}$ or Na_3IrCl_6 are used as iridium salt precursors for the direct cyclometalation of $\text{HC}^{\wedge}\text{N}$ ligands or for the preparation of the iridium complex precursors such as $\text{Ir}(\text{acac})_3$, (acac = acetylacetonate). Three conventional methods for the synthesis of $\text{Ir}(\text{C}^{\wedge}\text{N})_3$ can be distinguished (Scheme 1.11):

1. Cleavage of chloro-bridged dimer complexes $[\text{Ir}(\text{C}^{\wedge}\text{N})_2(\mu\text{-Cl})]_2$ with base and further cyclometalation of added $\text{HC}^{\wedge}\text{N}$ ligand (Scheme 1.11, **paths 1a** and **1b**).
2. Exchange of acac ligands in $\text{Ir}(\text{acac})_3$ to $\text{C}^{\wedge}\text{N}$ ligands (Scheme 1.11, **path 2**).
3. Change of $\text{O}^{\wedge}\text{O}$ ligand in $\text{Ir}(\text{C}^{\wedge}\text{N})_2(\text{O}^{\wedge}\text{O})$ to $\text{C}^{\wedge}\text{N}$ ligand (Scheme 1.11, **path 3**).

The first chloro-bridged iridium dimer complex of type $[\text{Ir}(\text{C}^{\wedge}\text{N})_2(\mu\text{-Cl})]_2$ was described in 1974 by M. Nonoyama.¹⁰¹ He reported that a reaction between Na_3IrCl_6 (1 equiv.) and Hbzq (benzo[*h*]quinoline, 3 equiv.) in 2-methoxyethanol (0.04 mM) under reflux for 24 h resulted in 11% yield of $[\text{Ir}(\text{bzq})_2(\mu\text{-Cl})]_2$. This technique for $[\text{Ir}(\text{C}^{\wedge}\text{N})_2(\mu\text{-Cl})]_2$ preparation has been called the Nonoyama method, and the conditions have been further optimized and generalized for other cyclometalating ligands. The standard procedure involves combining $\text{IrCl}_3 \cdot x\text{H}_2\text{O}$ or Na_3IrCl_6 with 2–3 equiv. $\text{HC}^{\wedge}\text{N}$ in pure 2-methoxyethanol, 2-ethoxyethanol or their mixtures with water (3:1, v/v) at refluxing temperatures (120–140 °C) for 24 h.^{102,103} It was further reported that $[\text{Ir}(\text{C}^{\wedge}\text{N})_2(\mu\text{-Cl})]_2$ complexes adopt an *N,N-trans* configuration of the cyclometalated ligands (Scheme 1.11).¹⁰⁴



Scheme 1.11 Syntheses of *fac* and *mer* isomers of Ir(C^N)₃. The scheme is simplified by drawing C^N as metalated 2-phenylpyridine.

In general, the Nonoyama method gives good yields of [Ir(C^N)₂(μ-Cl)]₂ complexes. However, the purity and the yields strongly depend on the nature of the C^N ligand. For example, for benzo[*h*]quinolines and some substituted phenylpyridines, the yield of [Ir(C^N)₂(μ-Cl)]₂ did not exceed 50%.^{101,105} To overcome this issue, it was suggested to use chloro-bridged iridium(I) alkenyl complexes [Ir(COD)(μ-Cl)]₂^{106,107} and [Ir(COE)₂(μ-Cl)]₂,¹⁰⁸ where COD = 1,5-cyclooctadiene, COE = *cis*-cyclooctene, as complex precursors for the high-yield synthesis of [Ir(C^N)₂(μ-Cl)]₂. The cyclometalation between [Ir(COD)(μ-Cl)]₂ and 4 equiv. HC^N ligand was carried out in 2-ethoxyethanol at 130 °C for 3 h in a sealed flask filled with argon (Scheme 1.11).¹⁰⁹

The yields of $[\text{Ir}(\text{C}^{\wedge}\text{N})_2(\mu\text{-Cl})]_2$ using this method exceed 90%. A quick and facile method to access $[\text{Ir}(\text{C}^{\wedge}\text{N})_2(\mu\text{-Cl})]_2$ complexes was reported in 2020 by B. Orwat, I. Kownacki and co-workers.¹¹⁰ They showed that $[\text{Ir}(\text{C}^{\wedge}\text{N})_2(\mu\text{-Cl})]_2$ can be synthesized quantitatively by microwave-accelerated heating of a solution of $\text{IrCl}_3 \cdot x\text{H}_2\text{O}$ and 2.2 equiv. $\text{HC}^{\wedge}\text{N}$, including 2-phenylpyridines, benzo[*h*]quinoline and 2-phenoxy pyridine, in 2-methoxyethanol (0.06 M) at 150 °C for 10 min. The method tolerates a variety of functional groups (Me, OMe, OPh, NMe_2 , F, Br, CF_3 , C_6F_5 , NPh_2 , $\text{C}_6\text{H}_4\text{NPh}_2$). This procedure was chosen for the synthesis of $[\text{Ir}(\text{C}^{\wedge}\text{N})_2(\mu\text{-Cl})]_2$ in the work described in this thesis.

Remarkably, *fac*- $\text{Ir}(\text{ppy})_3$ (ppy = metalated 2-phenylpyridine) was first isolated in 1985 by R. J. Watts and co-workers as a 10% impurity during the synthesis of $[\text{Ir}(\text{ppy})_2(\mu\text{-Cl})]_2$ using the Nonoyama procedure.¹¹¹ Then, in 2003, M. Thompson and co-workers reported that $\text{Ir}(\text{C}^{\wedge}\text{N})_3$ complexes can be obtained by reaction of $[\text{Ir}(\text{C}^{\wedge}\text{N})_2(\mu\text{-Cl})]_2$ with 2 equiv. $\text{HC}^{\wedge}\text{N}$ ligand in the presence of K_2CO_3 (Scheme 1.11, **paths 1a** and **b**).¹⁰³ They also found that at lower temperatures (140–150 °C), meridional isomers of $\text{Ir}(\text{C}^{\wedge}\text{N})_3$ predominantly formed (Scheme 1.11, **path 1a**), while heating the reaction mixture at higher temperatures (200 °C) resulted in mostly *fac*- $\text{Ir}(\text{C}^{\wedge}\text{N})_3$ (Scheme 1.11, **path 1b**). These observations evidence that *mer* and *fac* isomers are the kinetically and thermodynamically favored products, respectively. In *fac* isomer, all nitrogen donors are in *trans* positions with respect to the carbon donors, while in *mer* isomer, one pair of nitrogen donors is in *trans* position to each other. *fac* isomers have higher symmetry than *mer* ones, thus their NMR spectra are simpler. Generally, the solubility of *mer* isomers is higher than that of the corresponding *fac* isomers. Consequently, the separation can be achieved by re-crystallization or flash column chromatography.¹⁰³

The **path 1** gives $\text{Ir}(\text{C}^{\wedge}\text{N})_3$ complexes in yields between 65 and 80%. To facilitate the cleavage of the Ir–Cl bond in dimer complexes, AgOTf salt can be used.¹¹² Additionally, a synthesis of *mer* and *fac* isomers can be achieved directly from $\text{IrCl}_3 \cdot x\text{H}_2\text{O}$, $\text{HC}^{\wedge}\text{N}$ and AgOTf at corresponding temperatures without the isolation of $[\text{Ir}(\text{C}^{\wedge}\text{N})_2(\mu\text{-Cl})]_2$ (Scheme 1.11, **path 4**).^{113–115} A quick microwave-accelerated reaction to access high yields of *fac*- $\text{Ir}(\text{ppy})_3$ and *fac*- $\text{Ir}(\text{tpy})_3$ from $\text{IrCl}_3 \cdot x\text{H}_2\text{O}$ and Hppy and Htpy (*p*-tolylpyridine), respectively, without the use of AgOTf and avoiding the isolation of $[\text{Ir}(\text{C}^{\wedge}\text{N})_2(\mu\text{-Cl})]_2$ was reported in 2003 by H. Konno and Y. Sasaki (Scheme 1.11, **path**

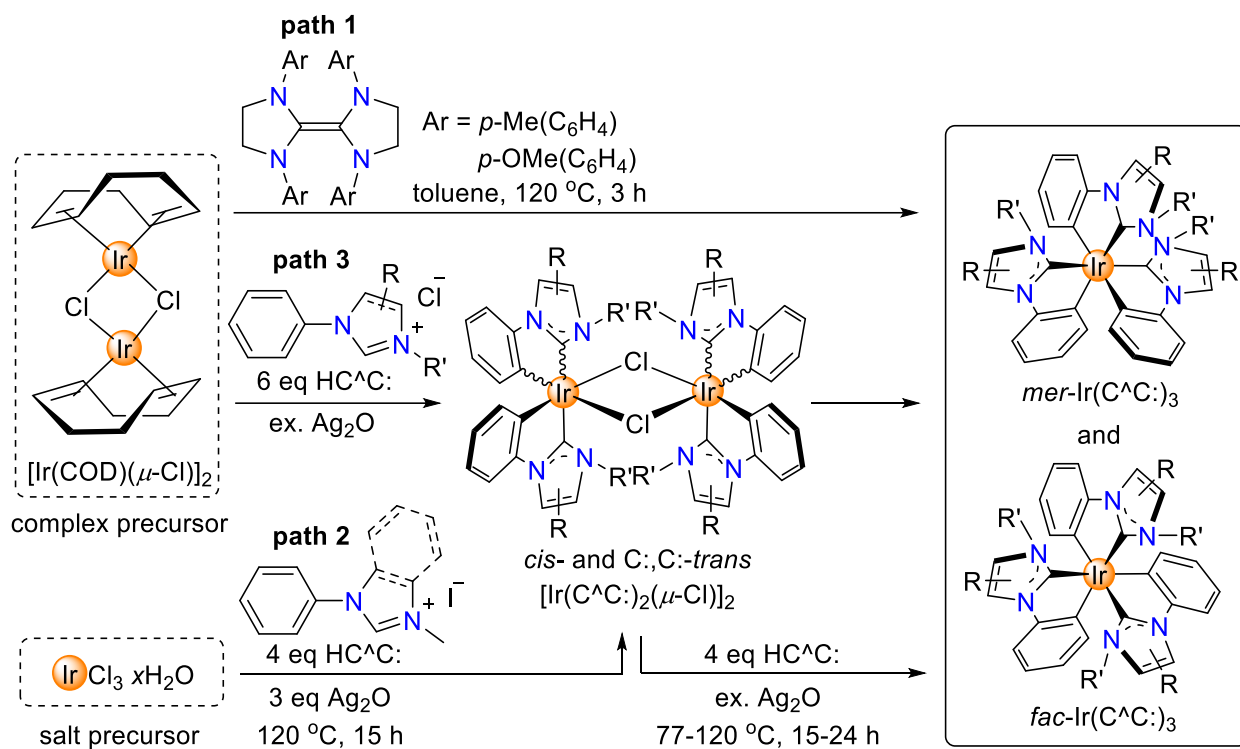
5).¹¹⁶ This method was generalized to other substituted 2-phenylpyridines and further used for the synthesis of *fac*-Ir(C[^]N)₃ in the work described in this thesis. A detailed discussion of the procedure and our studies are provided in subchapter 3.2.

Another conventional route to *fac*-Ir(ppy)₃ starting from Ir(acac)₃ was reported by R. J. Watts and co-workers in 1991.¹¹⁷ They showed that refluxing Ir(acac)₃ with Hppy in glycerol resulted in 45% *fac*-Ir(ppy)₃ (Scheme 1.11, **path 2**). Subsequently, the Ir(acac)₃ route was employed for synthesizing other *fac*-Ir(C[^]N)₃ complexes.^{103,118} However, the yields were still modest (< 50%). Moreover, the method is limited by the access to Ir(acac)₃, which is either quite expensive or can be synthesized in low yield (10%) from Ir(OH)₃ and acetylacetonone.¹¹⁹

In 2003, M. Thompson and co-workers reported that [Ir(C[^]N)₂(μ-Cl)]₂ complexes react with dipivaloylmethane (HO[^]O) in the presence of K₂CO₃ to give neutral hetero-complexes [Ir(C[^]N)₂(O[^]O)] (Scheme 1.11, **path 3**).¹⁰³ Heating a solution of these intermediates with HC[^]N in glycerol under reflux resulted in 60–80% of *fac*-Ir(C[^]N)₃. Even though an additional step between [Ir(C[^]N)₂(μ-Cl)]₂ and Ir(C[^]N)₃ is included, it leads to higher yields of the target complexes compared to the direct synthesis from Ir(acac)₃.

Ir(C[^]C:)₃ complexes gained recognition after their structural analogues Ir(C[^]N)₃ have been explored for the application in OLEDs. However, the first Ir(C[^]C:)₃ complex bearing an orthometalated NHC ligand was reported in 1982 by M. Lappert and co-workers,¹²⁰ several years earlier than Ir(ppy)₃. *fac*-Ir(C[^]C:)₃ was synthesized in “satisfactory yield” from [Ir(COD)(μ-Cl)]₂ and an electron-rich olefin as a carbene precursor by refluxing in toluene for 3 h (Scheme 1.12, **path 1**). Further NMR studies by M. Thompson, S. Forrest and co-workers (2005) revealed that the reaction proceeds through the formation of a dimer [Ir(C[^]C:)₂(μ-Cl)]₂,¹²¹ structurally similar to [Ir(C[^]N)₂(μ-Cl)]₂. In their work, they used IrCl₃·xH₂O as the iridium precursor, imidazolium iodides as the carbene precursors, and Ag₂O in 2-ethoxyethanol at 120 °C for 15 h (Scheme 1.12, **path 2**). Besides [Ir(C[^]C:)₂(μ-Cl)]₂ (< 13%), they isolated 10% of mixed *fac*- and *mer*-Ir(C[^]C:)₃. Reactions of other [Ir(C[^]C:)₂(μ-Cl)]₂ complexes with HC[^]C: and Ag₂O also led to mixtures of isomers, chromatographic separation of which resulted in *fac*- and *mer*-Ir(C[^]C:)₃ in a varied yield (8 – 77%). The role of Ag₂O

in these cyclometalation reactions was investigated.¹²¹ Ag₂O helps to generate the carbene ligand by deprotonating the imidazolium salt, stabilizes the carbenes *via* the formation of Ag(I) carbene complexes,¹²² acts as a transmetalating agent,¹²³ and helps to cleave the formed [Ir(C[^]C:)₂(μ-Cl)]₂ by chloride abstraction.



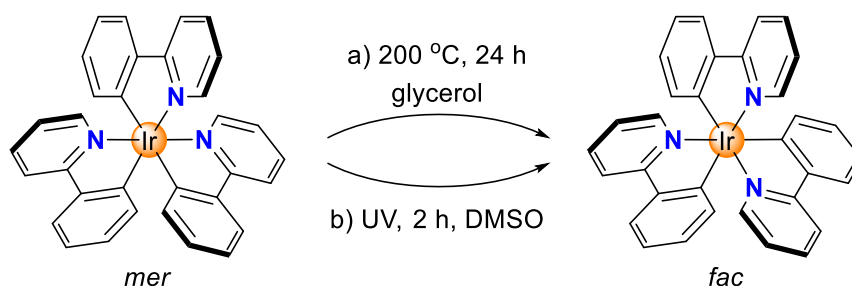
Scheme 1.12 Syntheses of *fac* and *mer* isomers of Ir(C[^]C:)₃.

A step towards higher yields of Ir(C[^]C:)₃ (58 – 78%) was taken by K. Mashima and co-workers (2008), who combined [Ir(COD)(μ-Cl)]₂ with HC[^]C: and Ag₂O in a stepwise and in one-pot fashion (Scheme 1.12, **path 3**).¹²⁴ They also obtained isomer mixtures with predominant formation of *mer*-Ir(C[^]C:)₃. Remarkably, when stepwise cyclometalation was carried out, and the intermediate [Ir(C[^]C:)₂(μ-Cl)]₂ complexes were isolated and characterized by XRD analysis, the latter showed a C:,C:-*trans* configuration of the cyclometalated ligands, similar to what was found for [Ir(C[^]N)₂(μ-Cl)]₂. However, M. Nazzerruddin and co-workers (2015) obtained indirect evidence that [Ir(C[^]C:)₂(μ-Cl)]₂ can adopt both a *cis*- and a C:,C:-*trans* configuration of the cyclometalated ligands (Scheme 1.12).¹²⁵ After reaction of crude [Ir(C[^]C:)₂(μ-Cl)]₂ with a diimine ligand (N[^]N) in DCM at r.t., they observed the formation of two heteroleptic complexes, [Ir(C[^]C:)₂(N[^]N)]PF₆ with *cis*- and C:,C:-*trans* configuration of C[^]C: ligands.

To summarize, the main route towards *fac* and *mer* isomers of $\text{Ir}(\text{C}^{\wedge}\text{N})_3$ and $\text{Ir}(\text{C}^{\wedge}\text{C}:)_3$ complexes involves orthometalation of iridium precursors ($\text{IrCl}_3 \cdot x\text{H}_2\text{O}$ and $[\text{Ir}(\text{COD})(\mu\text{-Cl})_2]$) with aryl pyridines or aryl NHCs and proceeds through chloro-bridged dimer of type $[\text{Ir}(\text{C}^{\wedge}\text{N})_2(\mu\text{-Cl})_2]$ or $[\text{Ir}(\text{C}^{\wedge}\text{C}:)_2(\mu\text{-Cl})_2]$. The yields are generally higher for $\text{Ir}(\text{C}^{\wedge}\text{N})_3$ than for $\text{Ir}(\text{C}^{\wedge}\text{C}:)_3$. $\text{Ir}(\text{C}^{\wedge}\text{C}:)_3$ complexes are obtained as mixtures of *fac* and *mer* isomers, while some $\text{Ir}(\text{C}^{\wedge}\text{N})_3$ complexes are accessible as single isomers under optimized reactions conditions.

1.3.3 *mer*→*fac* Isomerization of $\text{Ir}(\text{C}^{\wedge}\text{N})_3$ and $\text{Ir}(\text{C}^{\wedge}\text{C}:)_3$

As mentioned in the previous subchapter, *mer*- $\text{Ir}(\text{C}^{\wedge}\text{N})_3$ is the kinetically controlled product, while *fac*- $\text{Ir}(\text{C}^{\wedge}\text{N})_3$ is the thermodynamic product. Thermal and photochemical *mer*→*fac* isomerizations of $\text{Ir}(\text{C}^{\wedge}\text{N})_3$ complexes were reported for the first time by M. Thompson and co-workers in 2003 (Scheme 1.13a and b).¹⁰³ Upon refluxing *mer*- $\text{Ir}(\text{tpy})_3$ in glycerol for 24 h, they observed a conversion into *fac*- $\text{Ir}(\text{tpy})_3$ with 70% yield. After testing the thermal isomerization for other $\text{Ir}(\text{C}^{\wedge}\text{N})_3$ complexes, they found that *mer*- $\text{Ir}(\text{dfppy})_3$ (dfppy = metalated 2-(2,4-difluorophenyl)pyridine) did not isomerize at elevated temperatures. However, irradiation of a solution of *mer*- $\text{Ir}(\text{dfppy})_3$ in DMSO by UV light for 2 h gave an almost quantitative conversion (> 95%) to *fac*- $\text{Ir}(\text{dfppy})_3$. All other studied $\text{Ir}(\text{C}^{\wedge}\text{N})_3$ complexes showed similar results towards photo-induced *mer*→*fac* isomerization.¹⁰³ Calculations showed that the *mer* isomers are about 30 kJ/mol less stable than the corresponding *fac* isomers. It was proposed that the thermal and photochemical instability of the *mer* isomers is related to the strong trans influence of the aryl donors placed opposite to each other.¹⁰³



Scheme 1.13 Thermal and photochemical *mer*→*fac* isomerizations of $\text{Ir}(\text{ppy})_3$.¹⁰³

Valuable insights into the mechanism of thermal *mer*→*fac* isomerizations were obtained by G. van Koten and co-workers (2008).¹²⁶ They observed no isomerization

and recovery of the starting materials in non-alcoholic solvents (1,2-dichlorobenzene, benzonitrile), while heating solutions of *mer* isomers in glycerol, phenol, and decane-glycerol mixture resulted in conversion to *fac* isomers. Using NMR kinetic studies, they confirmed that the isomerization proceeds *via* elimination of one ligand, formation of an intermediate Ir(III) alkoxide complex, which can further react with the eliminated ligand, and the product adopts a *fac* coordination at the metal center. Ligand elimination was suggested to proceed either dissociatively (*via* nucleophilic attack of the hydroxyl group onto Ir and loss of the ligand) or associatively (*via* oxidative addition of the coordinated alcohol with the formation of Ir(IV) and reductive elimination of the ligand). They also provided a series of thermal *mer*→*fac* isomerizations with heteroleptic complexes and detected the formation of mixtures of *fac* isomers using NMR and mass spectroscopy. Altogether, these observations evidence that thermal *mer*→*fac* isomerization proceeds with ligand exchange.¹²⁶

In the same work by G. van Koten and co-workers,¹²⁶ it was investigated that photochemical *mer*→*fac* isomerizations proceed completely differently from the thermally induced ones, *i.e.* without ligand dissociation/scrambling. In the earlier work by T. Karatsu and co-workers (2003),¹²⁷ a quantitative *mer*→*fac* isomerizations of Ir(dfpp)₃ was achieved by irradiation of an acetonitrile solution for 200 min. It was also observed that the isomerization is facilitated in polar solvents (MeOH, MeCN) and slowed down in non-polar solvents (cyclohexane). The photo-induced *mer*→*fac* conversion was followed by UV/vis spectroscopy and excited state lifetime measurements. The absorption spectra showed several isobestic points when going from *mer* to *fac*, and the photon-counting experiments evidenced the existence of a triplet excited state, which mediates the isomerization.

The mechanism of the photochemical *mer*→*fac* isomerization was examined by DFT calculations performed in the following work by T. Karatsu and co-workers (2009).¹²⁸ They prepared *mer*-Ir(ppz)₃, where ppz is metalated 1-phenylpyrazole. The optical isomers Δ -*mer*-Ir(ppz)₃ and Λ -*mer*-Ir(ppz)₃ were separated using preparative chiral high-pressure liquid chromatography (HPLC). The irradiation of a solution of Δ -*mer*-Ir(ppz)₃ in MeCN by 366 nm Hg lamp for 700 s resulted in a racemic mixture of Δ -*fac*-Ir(ppz)₃ and Λ -*fac*-Ir(ppz)₃, as shown by HPLC and electronic circular dichroism (ECD) spectroscopy. Ligand detachment could not be observed. Quantum chemical

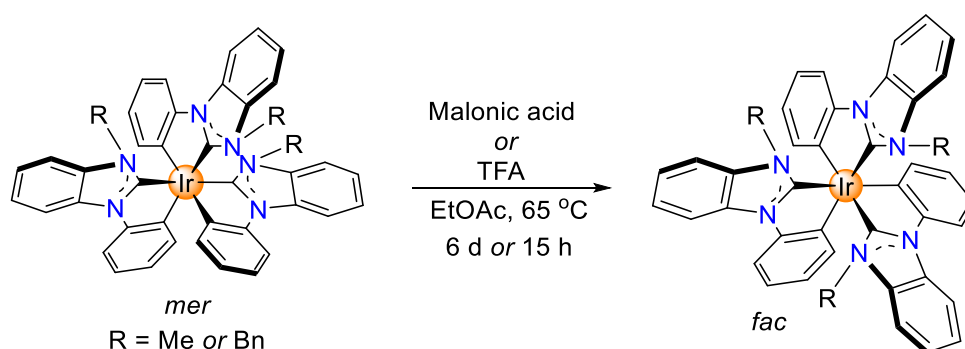
calculations confirmed that *trans* N–Ir–N bonds in *mer* isomer are elongated, suggesting that *trans* N–Ir–N bonds are likely sites for photo-induced bond rupture. Taking the experimental observations and theoretical calculations into account, the mechanism of the photochemical *mer*→*fac* isomerization was suggested to involve rupture of one of the *trans* N–Ir–N bonds, re-organization of the five-coordinated trigonal bipyramidal complex, and re-coordination of the ‘free’ N-donor to restore a *fac* octahedral geometry.

The *in-situ* visualization of both thermal and photochemical *mer*→*fac* isomerizations of Ir(ppy)₃ using surface-enhanced Raman spectroscopy (SERS) was reported by I.-C. Chen and co-workers (2018).¹²⁹ To quench the strong phosphorescence of the complex and carry out efficient monitoring, Ir(ppy)₃ was enclosed with a surfactant and coated with a thin layer of silica and then bonded to the surface of Ag nanoparticles. The SERS spectra showed that photoinduced *mer*→*fac* conversion proceeds through axial Ir–N bond rupture, without attachment to the surface and formation of any intermediates. In contrast, thermal *mer*→*fac* isomerization involves equatorial Ir–N bond rupture with the formation of Ir(III) siloxide intermediate of ‘*mer*’ geometry with ppy ligand coordinated *via* C donor. Upon further heating the intermediate eliminates siloxide ligand, undergoes re-organization and re-coordination of the ‘free’ N donor, resulting in *fac*-Ir(ppy)₃.

A detailed mechanistic study of the photochemical *mer*→*fac* isomerization of Ir(ppy)₃ was provided by D. Escudero (2019).¹³⁰ Using calculations for optimization of the geometry of triplet metal-centered (³MC) excited states and for energetic profiles of the isomerization, he showed the existence of a non-radiative ³MC state for *mer*-Ir(ppy)₃, which is responsible for the isomerization. The ³MC state has a significantly elongated one of the Ir–N bonds in *trans* position and adopts pseudo-trigonal bipyramidal geometry. Calculated energetic profiles showed that this geometry allows the ppy ligand with the elongated Ir–N bond to make a 180° rotation around the Ir–C bond, resulting in *fac*-Ir(ppy)₃. The population analysis confirmed that the ³MC state is highly populated at room temperature, and its activation barrier is 9 kcal/mol with the global barrier of the photoisomerization being 28.9 kcal/mol, confirming the thermodynamic feasibility of *mer*→*fac* photoconversion. The activation barrier of the back *fac*→*mer* isomerization was calculated to be 31.8 kcal/mol, evidencing that

mer→*fac* photoisomerization is irreversible. It is worth noting that *fac*→*mer* isomerizations of Ir(C[^]N)₃ complexes have not been reported so far.

Compared to Ir(C[^]N)₃ complexes, Ir(C[^]C:)₃ do not undergo thermal or photochemical *mer*→*fac* isomerizations and decompose upon prolonged light irradiation.¹²¹ A Brønsted acid-mediated *mer*→*fac* isomerization of Ir(pmb)₃ and Ir(pbb)₃, where pmb is metalated 1-phenyl-3-methylbenzimidazolin-2-ylidene and pbb is – 1-phenyl-3-benzylbenzimidazolin-2-ylidene, was reported in 2017 by H.-H. Johannes and co-workers (Scheme 1.14).¹³¹ Heating a solution of *mer*-Ir(pmb)₃ (or *mer*-Ir(pbb)₃) in ethyl acetate with malonic acid (or TFA, 1M solutions in water) at 65 °C for 6 d (or 15 h) resulted in conversion into *fac*-Ir(pmb)₃ in 54% yield (or *fac*-Ir(pbb)₃ in 76% yield). The authors were not able to characterize the intermediates, but quantum chemical calculations of the possible mechanism were conducted employing *mer*-Ir(pmb)₃ and TFA as reagents. It was shown that upon TFA addition to *mer*-Ir(pmb)₃, one of the C_{Ph} donors in *trans* position gets protonated, and trifluoroacetate coordinates to the Ir center. Next, the monodentate pmb ligand undergoes a 180° rotation around the Ir–C_{carbene} bond, and the complex experiences de-coordination of trifluoroacetate and passes through a penta-coordinated trigonal bipyramidal transition state. Further reorganization leads to a complex of pseudo-octahedral geometry stabilized *via* agostic interactions. Finally, the ‘free’ trifluoroacetate acts as a base and abstracts the acidic proton involved in agostic interactions, which facilitates a re-metalation step and results in *fac*-Ir(pmb)₃.



Scheme 1.14 The acid-mediated *mer*→*fac* isomerization of Ir(C[^]C:)₃ complexes.¹³¹

This procedure is attractive from a synthetic point of view because it allows obtaining *fac* isomers of Ir(C[^]C:)₃ in high yield. Thus, it has been utilized in a number of recent studies.^{132–136} However, the method has limitations when using bulky Ir(C[^]C:)₃

complexes.¹³⁷ Remarkably, in this work, another Brønsted acid HCl was attempted to mediate *mer*→*fac* isomerization. However, the authors observed degradation of both *fac* and *mer* isomers of Ir(pmb)₃ and Ir(pbb)₃ upon HCl addition and related it to the increased strength of HCl compared to malonic acid and TFA.

Interestingly, in the work by M. Lappert and co-workers, reporting the first *fac*-Ir(C[^]C:)₃ complexes, HCl gas was added to a solution of *fac*-Ir(C[^]C:)₃ complex in benzene–Et₂O mixture at r.t. for 30 min. They observed the formation of a protonated complex [Ir(C[^]C:)₂(HC[^]C:)]Cl with meridional arrangement of the C:-donors.¹²⁰ Notably, C_{Ph} and not C_{carbene} got protonated upon HCl addition. S. Kang and co-workers (2022) were able to detect small amounts of *mer*-Ir(C[^]C:)₃ after a train sublimation of *fac*-Ir(C[^]C:)₃.¹³⁸ Usually, the train sublimation method requires very high temperatures (> 400 °C), which can potentially induce *fac*→*mer* isomerization. Nevertheless, no controlled *fac*→*mer* isomerization of Ir(C[^]C:)₃ has been reported.

We managed to find the conditions for controlled *fac*→*mer* isomerization of Ir(C[^]N)₃ and Ir(C[^]C:)₃ complexes, and our studies are discussed in Chapters 3 and 4.

1.3.4 Photophysical Properties and Applications of Ir(C[^]N)₃ and Ir(C[^]C:)₃ Complexes

The electronic structure of octahedral d⁶ Ir(III) complexes can be described by the ligand-field theory. As a result of the interaction of d-metal with ligands, the d-orbitals of the metal become energetically non-degenerate and are splitted by the field of ligands with the splitting parameter Δ . The energy level diagram for Ir(C[^]N)₃ is presented in Figure 1.6.

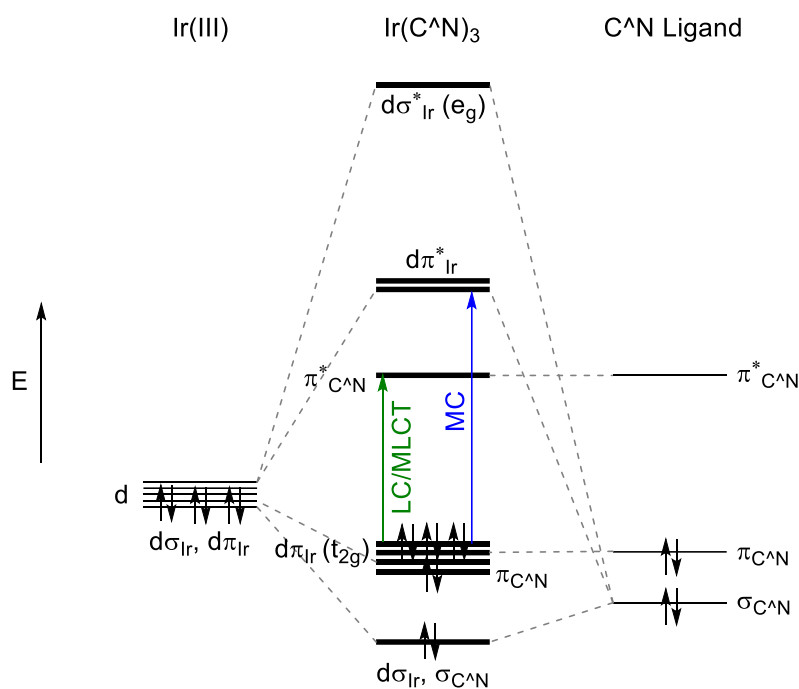


Figure 1.6 Simplified electronic energy level diagram for $\text{Ir}(\text{C}^{\wedge}\text{N})_3$. $\text{C}^{\wedge}\text{N}$ = cyclometalated ligand, MC = metal centered, LC = ligand centered and MLCT = metal-to-ligand charge transfer, respectively. Adapted with permission of RSC.¹³⁹

Quantitatively, the ligand-field splitting parameter Δ is equal to the energy difference between t_{2g} and e_g orbitals. Also, Δ depends on the atomic number and oxidation state of the metal as well as on the position of the ligands in the spectrochemical series.¹⁴⁰ Large values of Δ can be achieved with σ -donor ligands (aryl, carbene). Based on the nature and relative position of the molecular orbitals (MOs) of iridium and surrounding ligands in homoleptic $\text{Ir}(\text{C}^{\wedge}\text{N})_3$ complexes, the following electronic transitions are fundamentally possible: ligand centered (or intraligand) $\pi-\pi^*$ transitions (LC), $d\pi-d\pi^*$ metal centered transitions (MC), and charge transfer from the $d\pi$ -orbital of iridium to the π^* -orbital of the $\text{C}^{\wedge}\text{N}$ ligand (MLCT).

In order to schematically represent the processes of energy absorption and emission by an iridium complex, a Jablonski diagram is used (Fig. 1.7). Absorption of light by $\text{Ir}(\text{C}^{\wedge}\text{N})_3$ causes LC and MLCT transitions from the ground singlet electronic state (\mathbf{S}_0) to vibrational levels of the excited singlet state (\mathbf{S}_1). From \mathbf{S}_1 the molecule can potentially relax *via* the radiative $\mathbf{S}_1 \rightarrow \mathbf{S}_0$ transition (fluorescence), the radiationless internal conversion (IC) and vibrational relaxation (VR); the radiationless intersystem crossing (ISC) followed by the radiative excited singlet state (\mathbf{T}_1) to \mathbf{S}_0 transition

(phosphorescence). Generally speaking, ISC and the $T_1 \rightarrow S_0$ transition are forbidden by the multiplet selection rules. However, the restriction is partially lifted, and the probability of such processes increases due to strong spin-orbit coupling (SOC), which is the stronger the heavier the metal is (Ru, Rh, Os, Ir, etc.). For Ir(III) complexes, SOC is very strong, and ISC is faster than fluorescence, thus they are triplet emitters.

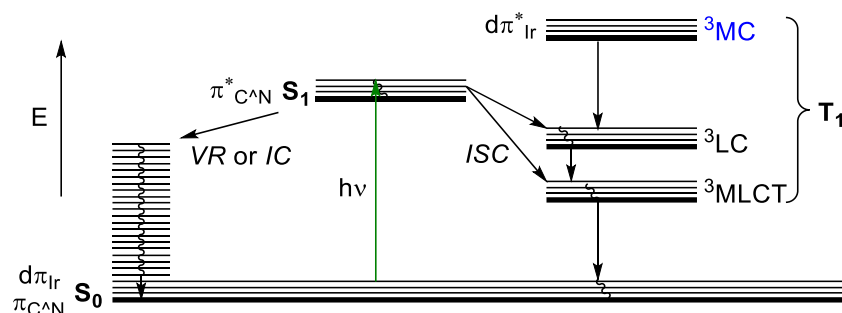


Figure 1.7 Simplified Jablonski diagram for $Ir(C^N)_3$. Designations: S_0 – ground singlet state; S_1 and T_1 – excited singlet and triplet states; ISC – intersystem crossing; IC – internal conversion, VR – vibrational relaxation (potential processes); 1LC and 1MLCT – S_1 obtained as a result of LC (solid arrow in pink) and MLCT (solid arrow in green) transitions, respectively; 3MC , 3MLCT , and 3MC – T_1 obtained as a result of ISC from S_1 . Dashed arrows in pink and green represent potential fluorescence. Adapted with permission of RSC.¹³⁹

For the most studied iridium complex fac - $Ir(ppy)_3$, the highest occupied molecular orbital (HOMO) and lowest unoccupied molecular orbital (LUMO) were determined. Using high-resolution spectroscopy¹⁴¹ and quantum chemical calculations,¹⁴² it was shown that S_0 (HOMO) of fac - $Ir(ppy)_3$ is a mixture of the $d\pi$ -orbitals of iridium and the π -orbitals of the aryl ring of ppy ligand. On the other hand, T_1 (LUMO) is localised on the π^* -orbitals of the pyridyl ring of ppy ligand. The T_1 of fac - $Ir(ppy)_3$ can be described as a mixed of $^3LC/MLCT$ state. The relative position of 3MLCT and 3LC depends on the nature of the ligand(s). The 3LC state can be energetically the lowest within T_1 for some homoleptic¹²¹ and heteroleptic Ir(III) complexes.¹⁴³

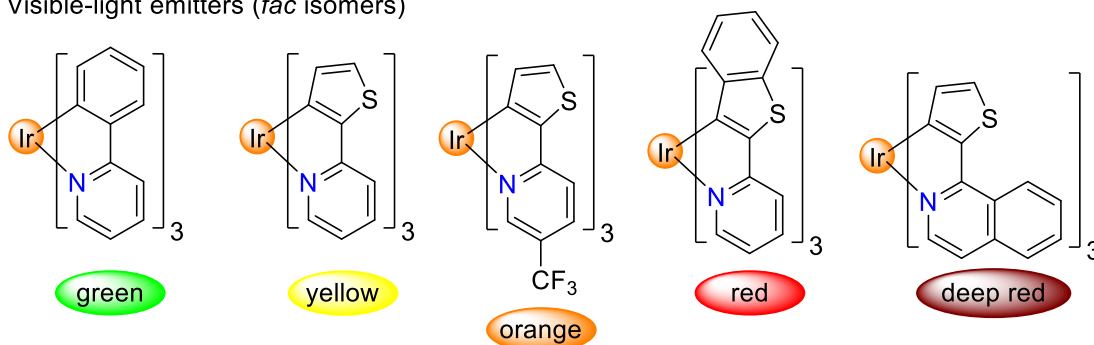
The photophysical properties (absorption, excitation and emission spectra, photoluminescence quantum yields and lifetimes) of the fac and mer isomers of $Ir(C^N)_3$ are different.^{103,127} Generally, the absorption spectra have lower resolution and smaller molar extinction coefficients, and the emission spectra of the mer isomers

are broader and bathochromically shifted compared to those of the *fac* isomers. This was explained by non-equivalence of three C[^]N ligands in *mer*.¹⁰³ Elongation of the N–Ir–N bonds in *trans* position in the *mer* isomers is responsible for reaching low-lying non-radiative ³MC excited state, which causes lower photoluminescence quantum yields and larger non-radiative rate constants of *mer* isomers compared to those of *fac*.^{103,130} Overall, *fac* isomers of Ir(C[^]N)₃ are more attractive for applications.

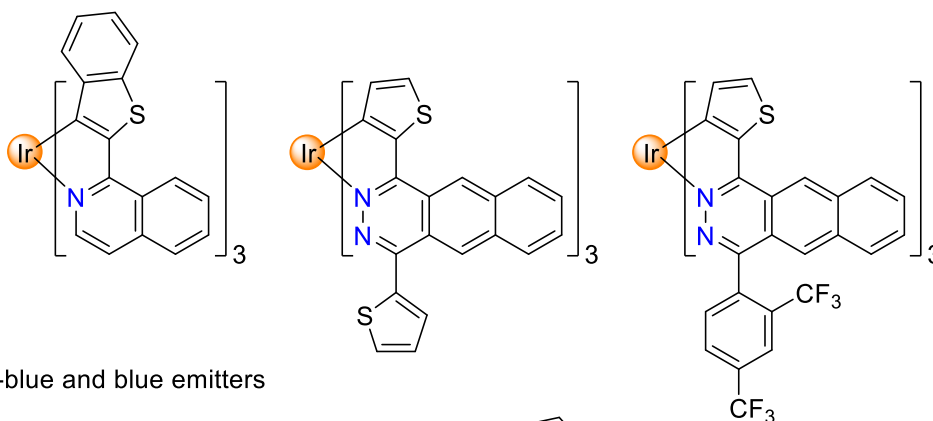
The photophysical properties of Ir complexes can be fine-tuned by changing the energy difference between HOMO and LUMO. As mentioned above, for Ir(C[^]N)₃, the HOMO is localised on the d π -orbitals of Ir and the π -orbitals of the aryl ring of the C[^]N ligand, and the LUMO is localized on the π^* -orbitals of the pyridyl ring of the C[^]N ligand. Therefore, on the one hand, the introduction of electron acceptors (or donors) on the aryl ring of the C[^]N ligand can alter the HOMO energy, resulting in a hypsochromic (or bathochromic) shift of the emission maximum. On the other hand, functionalization of the pyridyl ring with electron-accepting (or donating) groups can alter the LUMO energy, leading to bathochromic (or hypsochromic) shift of the emission spectrum. Alternatively, the use of C[^]N ligands with a larger (or smaller) ligand-field splitting, which can shift the emission maximum to the blue (or red) region, altering the HOMO.

These approaches have been used for obtaining Ir-based OLEDs of different colour (Fig. 1.8).⁹⁶ For example, based on a series of *fac*-Ir(C[^]N)₃ complexes, electroluminescent devices of green to deep red colours have been obtained (Fig. 1.8a).¹¹⁸ *fac*-Ir(C[^]N)₃ complexes with ligands containing fused aromatic system have been applied as near-IR emitters (Fig. 1.8b).¹⁴⁴

a) Visible-light emitters (*fac* isomers)



b) Near-IR emitters (*fac* isomers)



c) Deep-blue and blue emitters

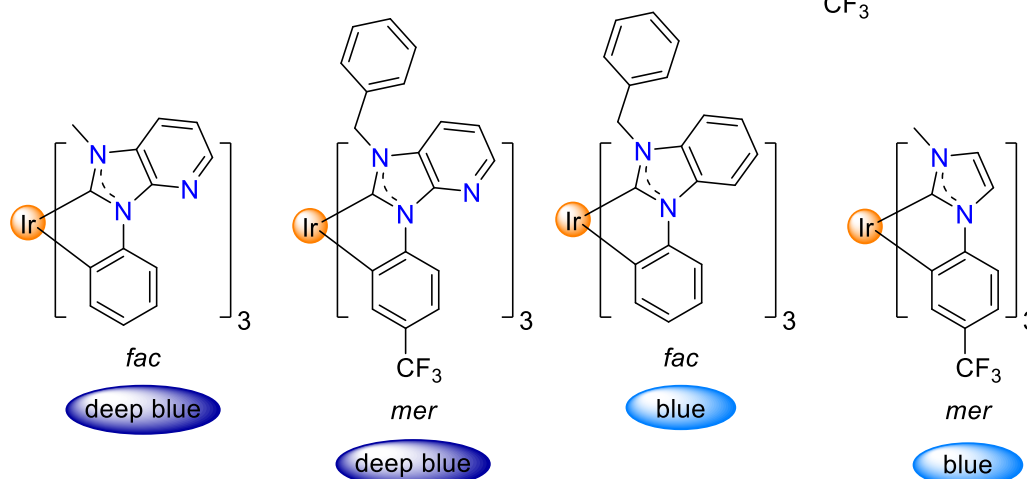


Figure 1.8 Structures of selected Ir(C[^]N)₃ and Ir(C[^]C:)₃ luminophores.

As a consequence of using C[^]C: ligands with strongly σ -donating and weakly π -accepting properties (larger ligand-field splitting) instead of C[^]Ns (smaller ligand-field splitting), Ir(C[^]C:)₃ complexes feature blue and even near-UV emission.^{121,124} Numerous NHC-based complexes have been prepared and incorporated into OLEDs.^{96,134,145} Selected examples of deep-blue and blue Ir(C[^]C:)₃ emitters are shown in Fig. 1.8c. In a recent publication by E. Zysman-Colman and co-workers, four new examples of bulky Ir(C[^]C:)₃ complexes featuring deep-blue emission are

reported.¹³⁷ Electroluminescent devices prepared with the *mer* isomers demonstrated the potential of such complexes for commercial displays.

Low quantum yields were reported for some $\text{Ir}(\text{C}^{\wedge}\text{C}:)_3$ complexes.¹²¹ However, cooling the sample and rigidification of the complex in a solid matrix was helpful to increase the quantum yields.^{121,134} Some *mer*- $\text{Ir}(\text{C}^{\wedge}\text{C}:)_3$ complexes show higher photoluminescence quantum yields than the corresponding *fac*-isomers.^{121,137,146} Electroluminescent devices fabricated on the basis of *mer*- $\text{Ir}(\text{C}^{\wedge}\text{C}:)_3$ were found to display favourable characteristics, e.g. higher EQE, compared to *fac*- $\text{Ir}(\text{C}^{\wedge}\text{C}:)_3$.^{135,137,146,147}

Apart from applications in OLEDs, $\text{Ir}(\text{C}^{\wedge}\text{N})_3$ complexes have been used extensively as photoredox catalysts.^{148,149} These catalysts are commonly used for construction of challenging C–C or C–heteroatom bonds.¹⁴⁸

Water-soluble $\text{Ir}(\text{C}^{\wedge}\text{N})_3$ complexes have been used as biological probes for cellular imaging, *in vivo* imaging, and therapeutic applications.^{93,150} Furthermore, derivatives of $\text{Ir}(\text{C}^{\wedge}\text{N})_3$ complexes have been applied as chemosensors for a wide range of compounds, including Brønsted and Lewis acids, cations, anions, amines, O_2 gas, and amino acids.¹⁵¹ $\text{Ir}(\text{C}^{\wedge}\text{N})_3$ bearing various functional groups have also been used as building blocks for supramolecular assemblies.^{152,153}

1.4 Objectives of the Thesis

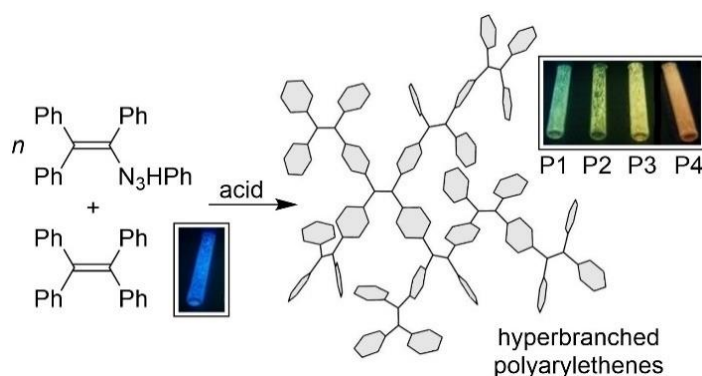
Polymeric tri- and tetraarylethenes are AIE-active compounds with numerous potential applications. The first part of this thesis is devoted to the development of a novel synthetic approach to polyarylethenes and to study of the properties of the resulting polymers (Chapter 2). More specific objectives include:

- Development of a 'traceless' synthetic method to access hyperbranched polyarylethenes.
- Investigation of the chemical and the photophysical properties of hyperbranched polyarylethenes.
- Application of hyperbranched polyarylethenes as fluorescent chemosensors.

Iridium complexes of the general formula $\text{Ir}(\text{C}^{\wedge}\text{N})_3$ and $\text{Ir}(\text{C}^{\wedge}\text{C}:)_3$ are important luminophores. They form two stable isomers with distinct photophysical and electrochemical properties: *fac* and *mer*. Isomerizations from *mer* to the more stable *fac* form have been described in the literature, whereas the inverse *fac*→*mer* conversion was not known. The second part of this thesis deals with development of such a *fac*→*mer* isomerization reaction (Chapters 3 and 4). More specifically, the objectives include:

- Development of the conditions for *fac*→*mer* isomerization of $\text{Ir}(\text{C}^{\wedge}\text{N})_3$ and $\text{Ir}(\text{C}^{\wedge}\text{C}:)_3$ complexes.
- Study of the isomerization mechanism and characterization of intermediates.
- Scope screening and study of substituent effects.
- Proof-of-concept applications of the *fac*→*mer* isomerization.

Chapter 2. Synthesis of Hyperbranched Polyarylethenes by C–H Vinylation with a Triazene



This chapter is based on a publication:

A.Yu. Gitlina, A. Ruggi, K. Severin “Synthesis of hyperbranched polyarylethenes by consecutive C–H vinylation reactions”, *Polym. Chem.* **2023**, 14 (36), 4182–4187. [DOI: 10.1039/D3PY00803G](https://doi.org/10.1039/D3PY00803G)

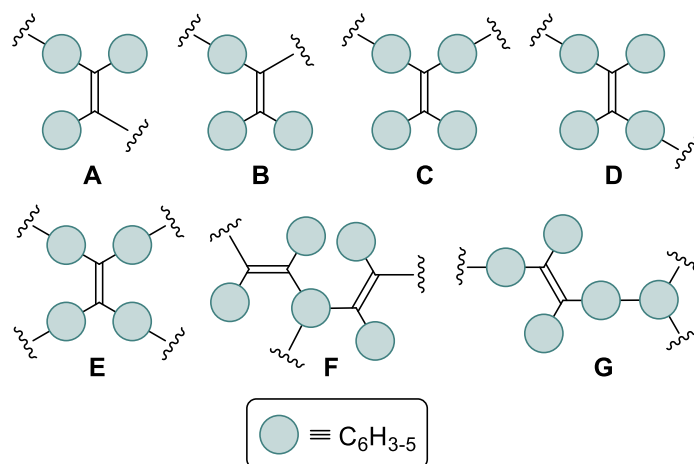
Reprinted and adapted version with permission from The Royal Society of Chemistry.

Author contributions: **A.Yu. G.** and K. S. conceived the idea. **A.Yu. G.** carried out the experiments. A. R. performed the solid-state photophysical measurements. K. S. obtained funding for the project and supervised the study. **A.Yu. G.**, A. R., and K. S. co-wrote the manuscript. All authors discussed the results and commented on the manuscript.

2.1 Introduction

Linear polymers composed of $-\text{C}(\text{Ph})=\text{C}(\text{Ph})-\text{C}_6\text{H}_4-$ units (Scheme 2.1, **A**) are known for more than 50 years,^{61–63} and several articles^{154,155} review their synthesis and properties (for more references, see subchapter 1.2.1). Conjugated poly(arylene-1,2-diphenylethene)s show high thermal stability, the tendency to form films with high photoconductivity, and good solubility in common organic solvents.

As it was discussed in subchapter 1.2.1, the discovery of the AIE¹ properties of TPE¹³ and related applications¹⁵⁶ triggered further interest in highly phenylated conjugated polymers. It is worth pointing out that the AIE properties of a polymer of type **A**, poly[1,4-phenylene-1,2-di(phenoxyphenyl)vinylene], was reported before the term ‘Aggregation-Induced Emission’ was coined.⁶⁹ Polymers with different topologies were synthesized and characterized, from linear structures **B–D** to microporous polymer networks **E** and **F** and hyperbranched polymers of type **G** (Scheme 2.1, and subchapter 1.2.1). Applications of these materials are discussed in subchapter 1.2.2.

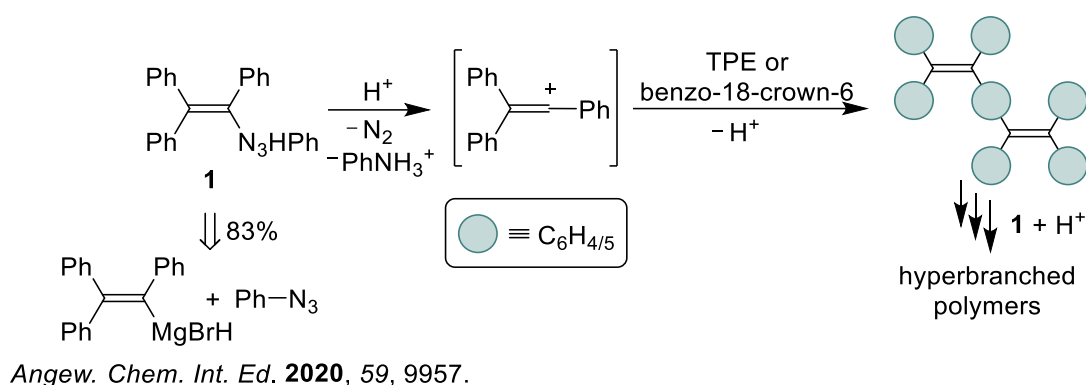


Scheme 2.1 Structures of polymers with tri- and tetraphenylethene repeat units.

The synthesis of polymeric tri- or tetraphenylethenes **A–G** was achieved by vinyl–aryl or aryl–aryl (cross)coupling reactions, by reductive olefinations, or by [2+2+2] cycloaddition reactions. The required monomers feature reactive functional groups such as halogens, boronic acids, or alkynes. A fraction of these functional groups will be present in the final polymers at the terminal sites. These groups can be employed for further functionalization reactions. For example, the residual alkyne groups in a polymer of type **G** were used for light-induced crosslinking of thin films.⁷³ On the other

hand, the remaining functional groups can compromise the chemical and photochemical stability of the polymers.

Below, we describe a novel approach for synthesizing polyarylethenes. Our procedure relies on electrophilic vinylation reactions with triazene **1** (Scheme 2.2). This polymerization *via* C–H activation is ‘traceless’ because the resulting polymers do not feature reactive groups in their periphery. The branched polyarylethenes show molecular weight-dependent luminescence and unusual ratiometric AIE.



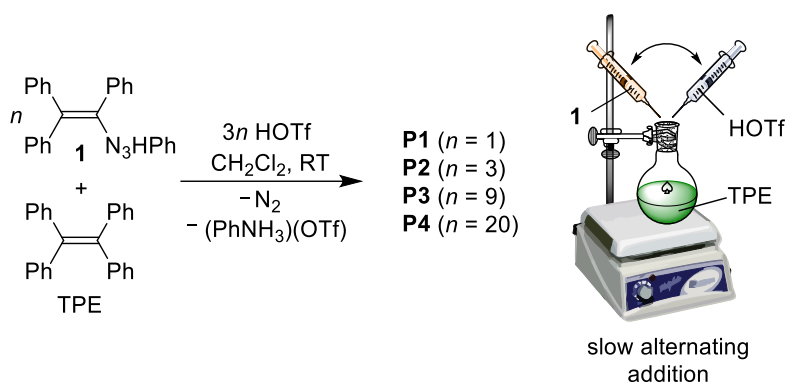
Scheme 2.2 Synthesis of a hyperbranched polymers by consecutive vinylation of TPE or benzo-18-crown-6 with triazene **1**.

2.2 Synthesis of Poly(triphenylethene)s by C–H Vinylations

Triphenylethenyl triazene **1** is easily accessible in a high yield by the reaction of triphenylethenyl magnesium bromide with phenyl azide (Scheme 2.2).^{49,59} In the presence of Brønsted acids, the triazene function can be replaced by different nucleophiles. The reaction is thought to proceed *via* highly reactive triphenylvinyl cation, which is formed after acid-induced N–N bond cleavage and release of dinitrogen.⁵⁹ When aromatic compounds are used as nucleophiles, aryl(triphenyl)ethenes are obtained.⁴⁹ In a similar fashion, we hypothesized that consecutive C–H vinylation reactions with **1** would provide facile access to hyperbranched polyarylethenes.

In order to optimize the polymerization conditions, we performed test reactions with CH₂Cl₂ solutions containing TPE (134 mM) and excess of triazene **1** (5 or 10 equiv.). Coupling reactions were initiated by the slow dropwise addition of triflic acid (HOTf). After a basic work-up, the product mixture was analyzed by mass spectrometry, which

showed that oligomers with high molecular weight were not detected (for details, see the Experimental part, subchapter 6.2.2). Presumably, the excess of **1** hampers the coupling chemistry, which is in line with our earlier observations that reactions with **1** are best performed with an excess of the aromatic coupling partner.⁴⁹ Consequently, we examined different synthetic procedures. Various parameters were altered, such as acid strength and concentration, addition sequence, TPE and triazene **1** concentration, and the addition method (for details, see the Experimental part, subchapter 6.2.10). The polyvinylation of TPE was achieved in CH₂Cl₂ (0.134 M according to TPE) by slow alternating addition of first **1** (*n* equiv.) and then HOTf (3*n* equiv., Scheme 2.3).



Scheme 2.3 Syntheses of the polymers **P1–P4**.

A total of *n* equivalents of **1** were added in *n* steps, and a reaction time of one hour was used for each step. After completion of the polymerization, a basic work-up was performed. The products **P1** (*n* = 1), **P2** (*n* = 3), **P3** (*n* = 9), and **P4** (*n* = 20) were isolated in the form of yellow to orange powders by precipitation with methanol, followed by washing with diethyl ether/hexane (1:1, v/v). All four compounds were found to display good solubility in standard organic solvents such as DCM, ethyl acetate, acetone, and THF.

The coupling chemistry that we have employed is expected to give branched oligomers/polymers with high structural diversity. Our earlier studies with **1** had shown that reactions with substituted benzenes can result in C–H activation at the *ortho* and *para* positions.⁴⁹ For the coupling of triphenylethene fragments to polyarylethenes, steric interactions may lead to higher *para* selectivity, but coupling at the *ortho* position cannot be excluded. Furthermore, the terminal phenyl groups of the growing polymer

are expected to display similar reactivity, so the attachment of new triphenylethene groups will occur in a random fashion.

2.3 Characterization of the Polymers

The polyarylethenes **P1–P4** were analyzed by mass spectrometry with atmospheric pressure photoionization (APPI) in positive mode. Oligomers with up to seven triphenylethene groups per TPE were detected for **P1**, and oligomers with up to 11 $\text{Ph}_2\text{C}=\text{C}(\text{Ph})$ groups were detected for **P4** (for mass spectra, see the Experimental part, subchapter 6.2.2). Polymers with larger molecular weights were likely present as well, but we were not able to detect them by mass spectrometry, regardless of the ionization technique used (ESI, APPI, or MALDI).

GPC measurements performed using a viscometer detector showed the expected increase in the weight average molecular weight, M_w , when going from **P1** to **P4** (Fig. 2.1). The polydispersity index, PDI , increases along with the molecular weight, reaching a value of 3.27 for **P4**.

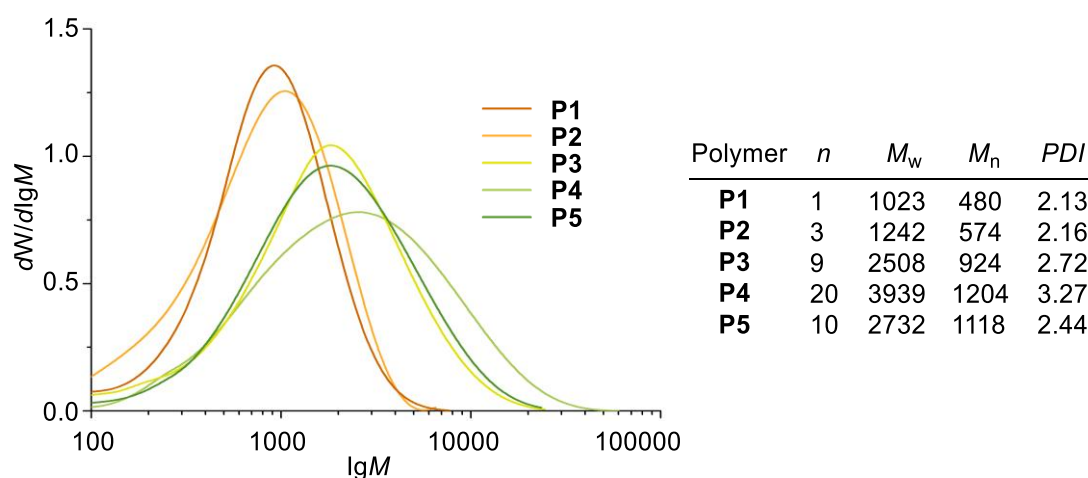


Figure 2.1 Results of GPC measurements of **P1–P5** (polymer **P5** is discussed in subchapter 2.5).

The polymerization *via* C–H activation was expected to be traceless, meaning that residual triazene functions should not be found in the final polymers. Elemental analyses of **P1–P4** confirmed the absence of nitrogen-containing compounds in the products (for details, see the Experimental part, subchapter 6.2.1). The ^{13}C NMR spectrum of **P4** showed peaks in the area between 115 and 146 ppm, which can be

attributed to aromatic or olefinic C_{sp2} atoms (Fig. 2.2). Peaks for aliphatic C_{sp3} atoms could not be detected. The lack of signals in the ¹⁹F NMR spectrum confirmed that nucleophilic OTf groups were not incorporated during the coupling reactions (Fig. 2.3).

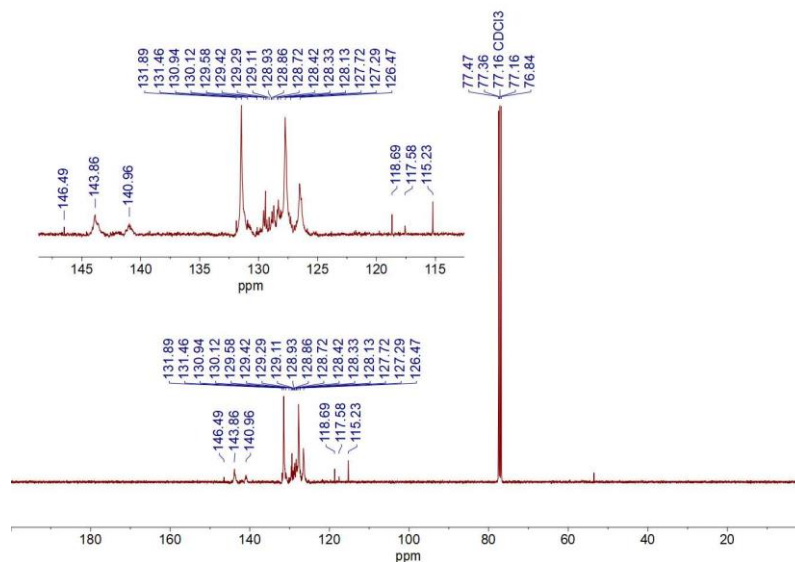


Figure 2.2 ¹³C NMR (101 MHz, CD₂Cl₂, 298 K) spectrum of **P4**. The spectrum resembles that of TPE.¹⁵⁷

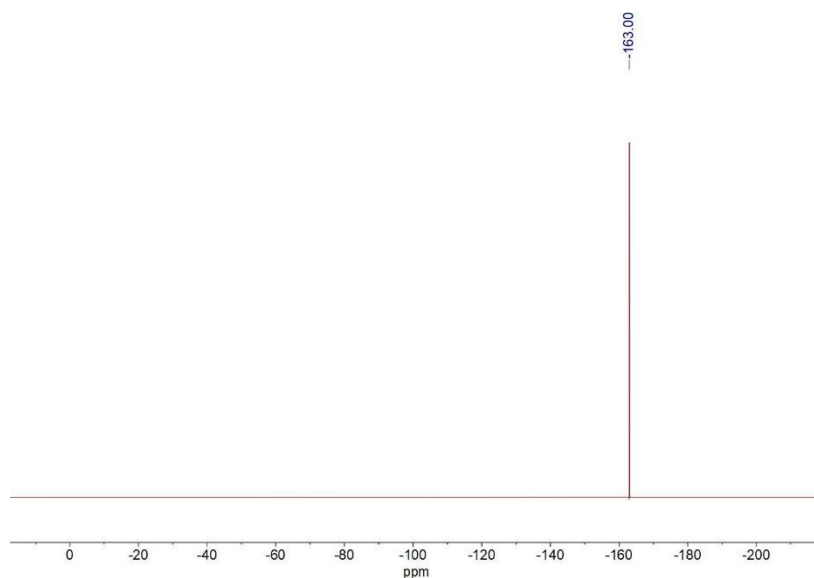


Figure 2.3 ¹⁹F NMR (376 MHz, CDCl₃, 298 K) spectrum of **P4** with C₆F₆ as a standard ($\delta_{\text{C}_6\text{F}_6} = -163.0$ ppm). The absence of other peaks than that of C₆F₆ confirms that there are no -CF₃ groups in **P4** ($\delta_{\text{F}}(-\text{SO}_3\text{CF}_3)$ is -50 to -80 ppm).^{158,159}

TGA revealed that **P2–P4** are thermally robust compounds, with degradation temperatures (5% weight loss) between 332 °C (**P2**) and 420 °C (**P4**) (Fig. 2.4). The latter value is comparable to what was found for linear poly(triphenylethene)s (402 °C) and poly(tetraphenylethene)s (400 °C).⁶⁸ The TGA data for **P1** were compromised by its low melting point.

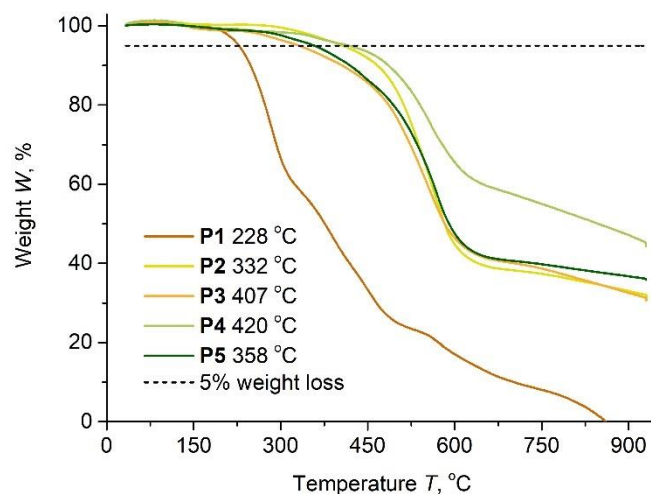


Figure 2.4 TGA profiles of polymers **P1–P5** (polymer **P5** is discussed in subchapter 2.5). Program: N₂, 30 °C to 900 °C with step 10 °C/min, flow rate: 20 mL/min.

2.4 Optical and Photophysical Properties of the Polymers

The absorption spectra of **P1–P4** in THF showed a broad band with a maximum between 300 and 325 nm (Fig. 2.5, top). For the larger polymers **P2–P4**, the band extended up to ~450 nm, suggesting that the conjugation exerts influence on the electronic structure of the polymers compared to that of free TPE.¹⁶⁰ The normalized UV-vis absorption spectra of **P2–P4** were similar, indicating a comparable degree of π -conjugation in these structures (Fig. 2.5, bottom).

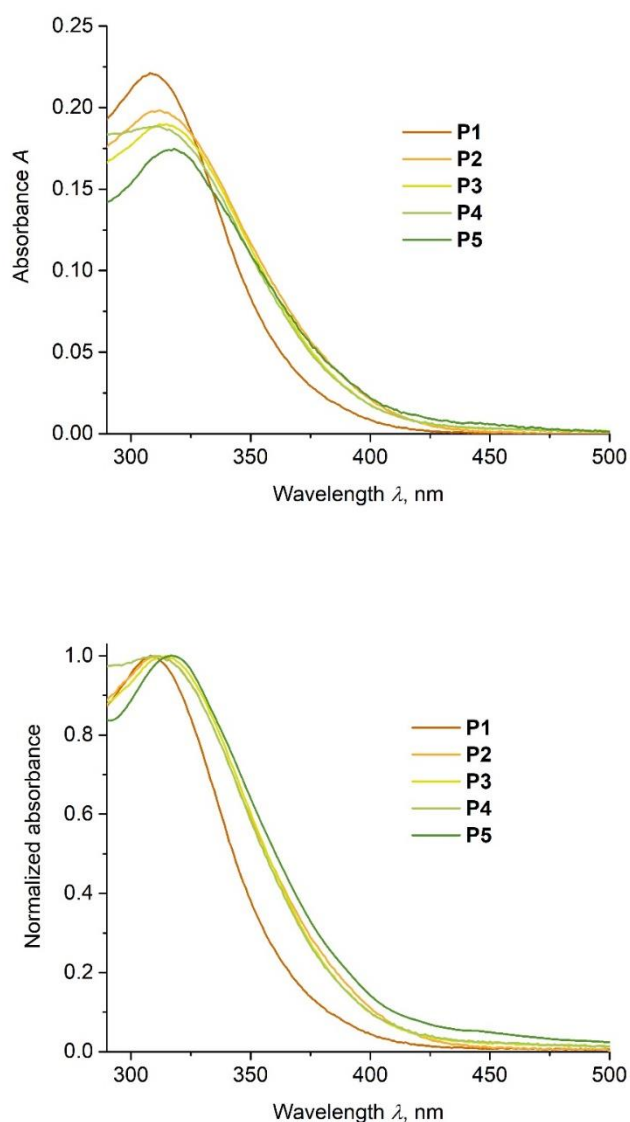


Figure 2.5 Absolute (top) and normalized (bottom) absorption spectra of the polymers **P1–P5** (polymer **P5** is discussed in subchapter 2.5) in THF, [**P1–P5**] = 0.4 $\mu\text{g/mL}$.

In THF, **P1** is weakly luminescent, with an emission maximum at 499 nm and a quantum yield of 0.05% (Fig. 2.6 and Table 2.1). A bathochromic shift was observed for the larger polymers, but the difference is very small (**P4**: $\lambda_{\text{em}} = 502$ nm). The solution-based luminescence intensity increased with molecular weight, and the quantum yield of **P4** ($\Phi_{\text{sol}} = 0.46\%$) was ten times higher than that of **P1**.

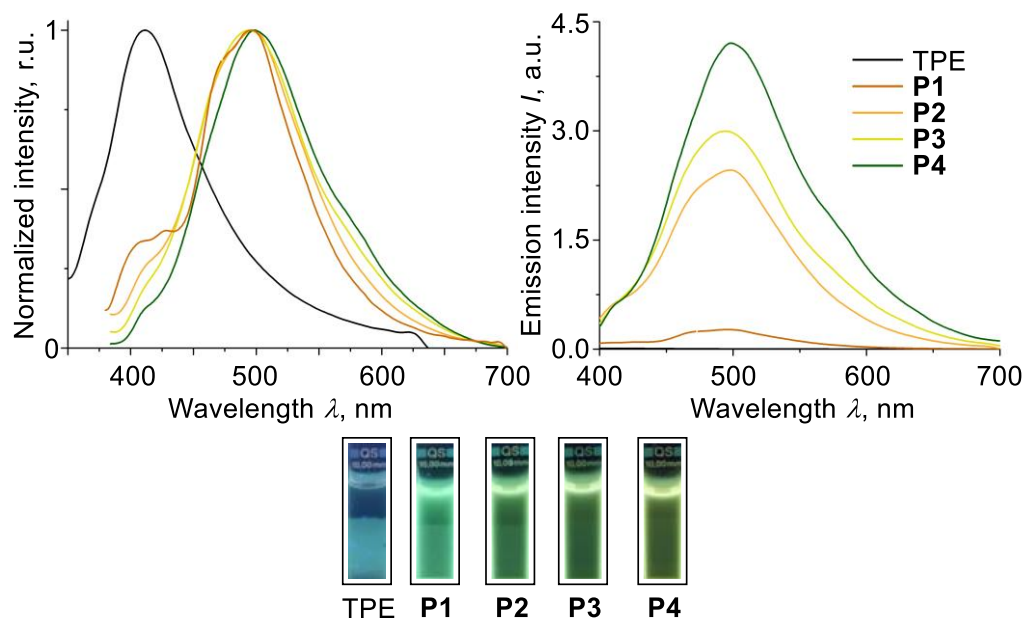


Figure 2.6 Normalized (left) and absolute (right) luminescence spectra ($\lambda_{\text{exc}} = 365 \text{ nm}$) of solutions of **P1–P4** in THF, $[\text{P1–P4}] = 0.4 \mu\text{g/mL}$.

Table 2.1 Optical properties and photoluminescence quantum yields of the compounds.

Compound	λ_{abs} , nm	$\lambda_{\text{em}}^{\text{sol}}$, nm	$\lambda_{\text{em}}^{\text{solid}}$, nm	Φ_{solid} , %	$\Phi_{\text{sol}}^{\text{a}}$, %
TPE	309	414	443	23.0 ¹⁶¹	0.24 ¹
P1	308	499	488	14.8	0.05
P2	312	498	505, 575sh	10.4	–
P3	315	494	503, 574	5.24	–
P4	316	502	515, 579	1.91	0.46
P5	318	425sh, 490, 575sh	500sh, 600	5.42	0.32

^a Photoluminescence quantum yields in solution were measured relatively to quinine sulphate in 0.5 M H₂SO₄, $\lambda_{\text{ex}} = 366 \text{ nm}$, 298 K.

The luminescence of TPE in solution is quenched by photoisomerization of the central C=C double bond and by photocyclization.¹⁶² Recent experimental results suggest that the former relaxation pathway is dominant.¹⁶³ The enhanced solution-based luminescence when going from **P1** to **P4** implies that ethylenic twisting becomes increasingly difficult for the larger polymers. It should be noted that hyperbranched polymer **G** (Scheme 2.1) was also found to be luminescent in solution, albeit weakly

($\Phi_{\text{sol}} = 0.46\%$ measured relatively to fluorescein in 0.1 M NaOH as standard, $\Phi_{\text{F}} = 97\%$).⁷³

While the normalized emission spectra of **P1–P4** are very similar (Fig. 2.6), we observed pronounced differences in the solid-state emission of the four compounds (Fig. 2.7). For the main emission band, we found a bathochromic shift when going from **P1** ($\lambda_{\text{em}} = 488$ nm) to **P4** ($\lambda_{\text{em}} = 515$ nm). In addition, one could observe a second band at ~ 575 nm, which was most pronounced for polymer **P4**. The different photophysical properties of solid **P1–P4** are clearly visible when solid samples are irradiated with UV light. **P1** appears green/yellow, whereas **P4** appears as an orange solid (Fig. 2.7). The quantum yields of the polyarylethenes decrease with size, with a value of $\Phi_{\text{solid}} = 14.8\%$ for **P1** and $\Phi_{\text{solid}} = 1.9\%$ for **P4** (Table 2.1).

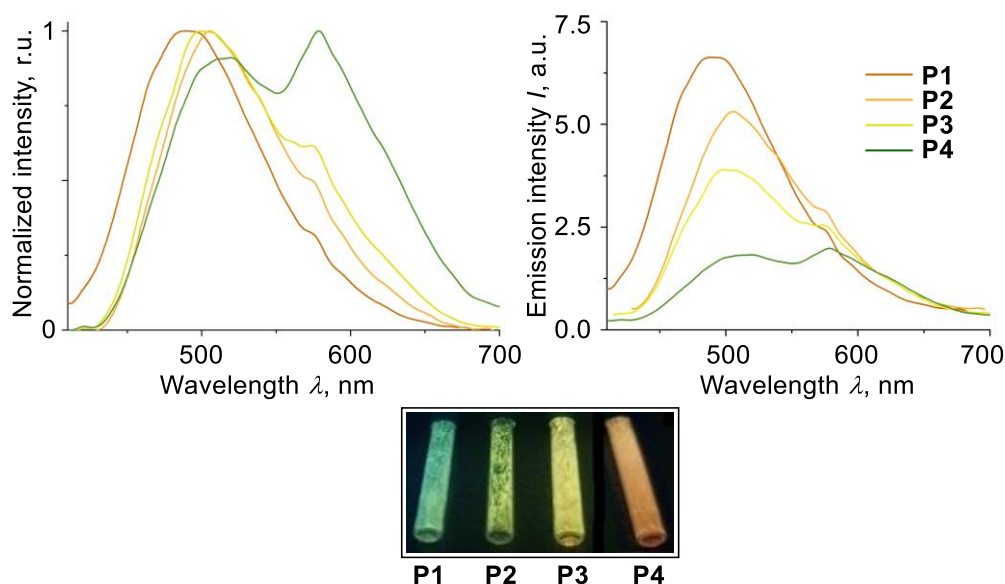


Figure 2.7 Normalized (left) and absolute (right) luminescence spectra of solid TPE and solid **P1–P4** and a photo of the samples when irradiated at $\lambda = 365$ nm.

The double emission of solid **P4** was also evident in AIE studies. The luminescence spectra of **P4** in THF solutions containing an increasing amount of water showed an augmented emission at 500 nm along with an even steeper increase in emission at 575 nm (Fig. 2.8). A similar behaviour was observed when using dioxane–water or DMF–water solvent mixtures (for luminescence spectra, see the Experimental part, subchapter 6.2.6). The results suggest that the ensemble of compounds representing **P4** contains two luminophores (or luminophore substructures) with distinct AIE

behaviour. The luminophore (or the luminophore substructure) emitting at 500 nm shows weak AIE, whereas the one emitting at 575 nm shows a much stronger AIE effect. The net result is a ratiometric response upon aggregation.

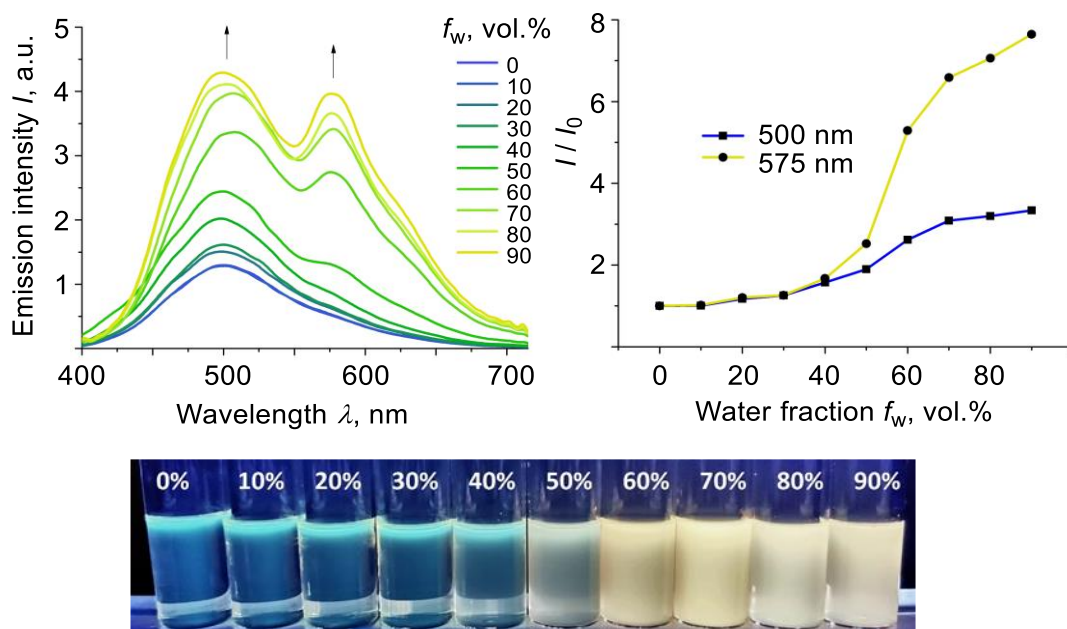


Figure 2.8 AIE behaviour of **P4** in THF–water mixtures ($[P4] = 0.25$ mg/mL) and a photo of the samples when irradiated at $\lambda = 365$ nm.

The presence of the luminophore (or the luminophore substructure) with distinct photophysical behaviour was also evidenced by the measurements of excited state lifetimes for **P1–P5** (polymer **P5** is discussed in subchapter 2.5) in solid state using time-correlated photon counting method (Table 2.2). The luminophore (or the luminophore substructure) emitting at 500 nm and at 575 nm show double exponential decay with short (0.79 to 1.92 ns) and long (1.85 to 8.49 ns) excited state lifetime components, which is probably a result of the overlapping of two independent emission spectra of the luminophores (or the luminophore substructures).

Table 2.2 Photoluminescence lifetimes of the polymers in solid state.

Compound	τ^a , ns ($\lambda_{em} = 500$ nm)	τ , ns ($\lambda_{em} = 600$ nm)
P1	1.23 (24.3); 4.03 (76.7)	1.92 (29.1); 8.49 (70.9)
P2	1.28 (28.0); 4.11 (72.0)	1.27 (15.0); 6.18 (85.0)
P3	794 ps (60.4); 2.93 (39.6)	1.11 (18.2); 5.57 (81.8)
P4	753 ps (45.9); 2.83 (54.1)	1.27 (15.9); 5.68 (84.1)

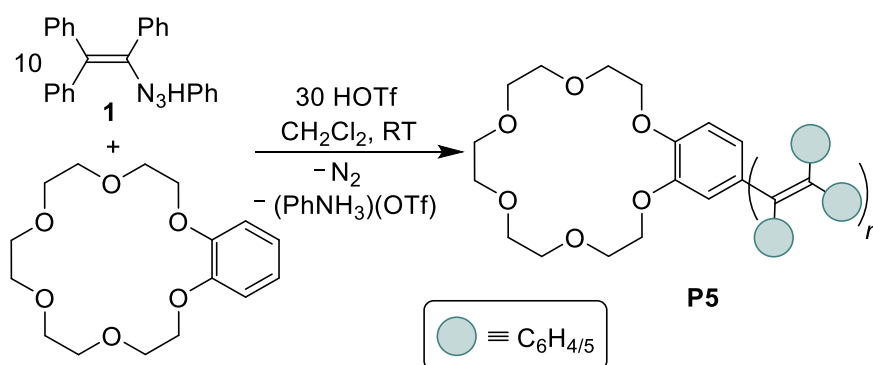
P5 0.49 (50.0); 1.85 (50.0) 1.00 (16.8); 5.65 (83.2)

^a The relative contributions of the components of the double exponential decay are given in parenthesis.

2.5 Application

Luminogens with a ratiometric response are of interest for sensing applications because relative changes in luminescence can often be measured more precisely than absolute changes. NIR and visible-light ratiometric fluorophores and phosphors have been overviewed in several review articles and found applications in the sensing of cations, anions, and biomolecules, as well as, in imaging and in biomedicine.^{164–167} Ratiometric AIE can be achieved by combining dyes that show aggregation-caused quenching (ACQ) with AIE luminogens.^{168–170} In these systems, one observes the quenching of one emission band with a concomitant increase of a second emission band upon aggregation. The response of **P4** is distinct in that we see an increased emission for two bands, albeit to a different extent.

For the syntheses of the polymers **P1–P4**, we used TPE as the core (Scheme 2.2). Since the C–H vinylation chemistry is compatible with a range of aromatic compounds,⁴⁹ other cores can be used as well. To demonstrate this point, we prepared a polymer **P5** using benzo-18-crown-6 (Scheme 2.4). Hyperbranched poly(triphenylethene) was grown from the crown ether using the optimized procedure for consecutive C–H vinylation with triazene **1**. A total of 10 equivalents of **1** were added in 10 steps, with a reaction time of one hour for each step.



Scheme 2.4 Synthesis of the crown ether conjugate **P5**.

GPC measurements of **P5** (Fig. 2.1) revealed a weight average molecular weight of $M_w = 2732$. This value is slightly higher than what was found for **P3**, for which we had used 9 equivalents of triazene **1**. The thermal stability of **P5** is good, with a 5% weight loss at 358 °C (Fig. 2.4).

A solution of **P5** in THF emits at 490 nm when excited at 365 nm (for the emission spectrum, see the Experimental part, subchapter 6.2.5) with the quantum yield of 0.32%. This value is slightly lower than what we found for **P4** ($\Phi_{\text{sol}} = 0.46\%$). The quantum yield of **P5** in the solid state was 5.4%. The luminescence spectra of **P5** in THF solutions containing an increasing amount of water showed the appearance of a second emission band at 575 nm (Fig. 2.9). A new band in this region was also observed in THF–hexane and THF–methanol mixtures (for the luminescence spectra, see the Experimental part, subchapter 6.2.6). Qualitatively, the AIE behaviour of **P5** is similar to what we observed for **P4** (Fig. 2.8) and **P3** (for the luminescence spectra, see the Experimental part, subchapter 6.2.6). However, the relative intensity of the band at 575 nm is more pronounced, resulting in more red-shifted emission upon aggregation.

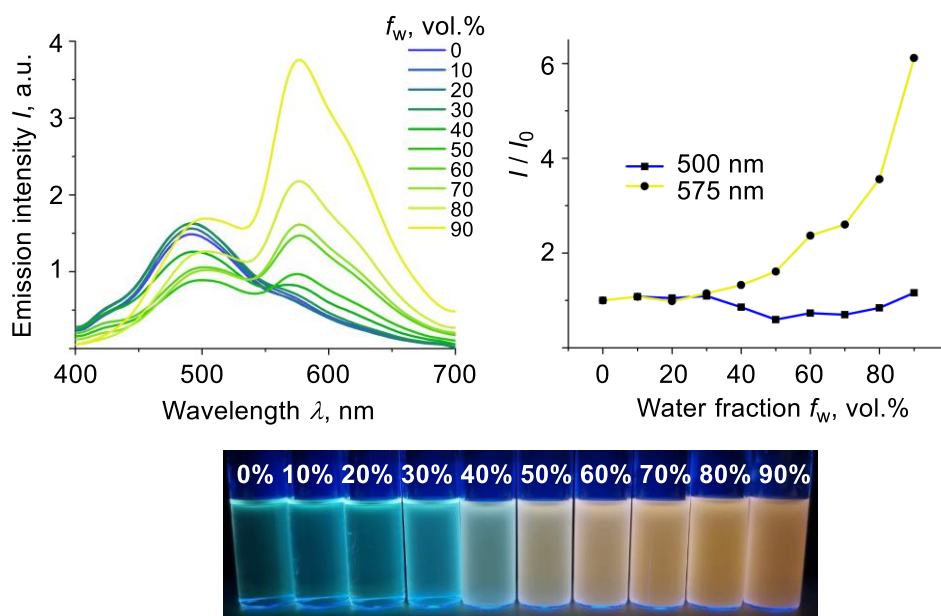


Figure 2.9 AIE behaviour of **P5** in THF–water mixtures ($[\text{P5}] = 0.25 \text{ mg/mL}$) and a photo of the samples when irradiated at $\lambda = 365 \text{ nm}$.

The presence of a benzo-18-crown-6 unit in **P5** gives a cation-responsive material. When alkali metal chlorides ($[MCl]_{\text{final}} = 0.3 \text{ mM}$, $M = \text{Li, Na, K, Rb, and Cs}$) were added to the aggregates of **P5** in THF/water (1:1, v/v), pronounced changes in the luminescence spectra were observed (Fig. 2.10).

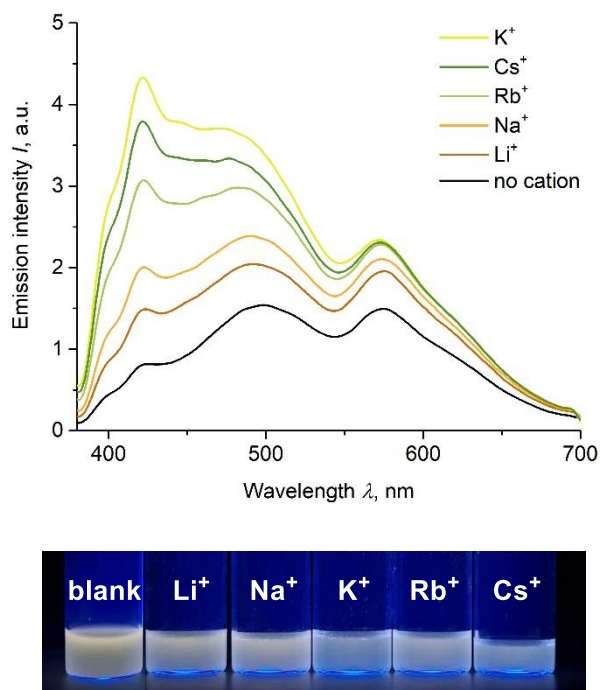


Figure 2.10 Emission spectra ($\lambda_{\text{exc}} = 365 \text{ nm}$) of **P5** in THF–water ($v/v = 1:1$, $[\text{P5}] = 0.25 \text{ mg/mL}$) after the addition of aliquots of aqueous MCl solutions ($[MCl]_{\text{final}} = 0.3 \text{ mM}$) and photographs of the samples when irradiated at $\lambda = 365 \text{ nm}$.

The overall emission intensity was found to increase, with the most pronounced changes occurring for the bands at 422 and 500 nm. The largest emission increase was observed for KCl, followed by the heavy alkali chlorides CsCl and RbCl. This response is in line with the known selectivity of benzo-18-crown-6 for alkali metal ions.¹⁷¹ No pronounced anion effect on the emission was detected (Fig. 2.11).

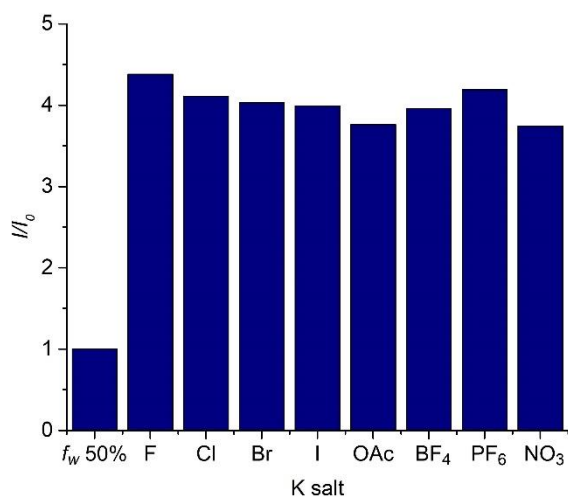
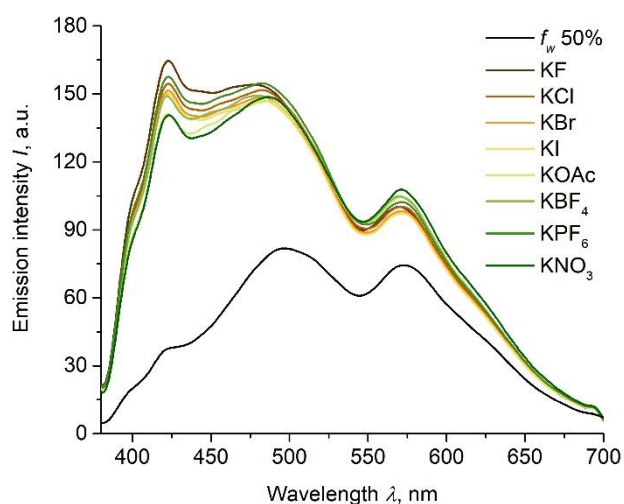


Figure 2.11 Emission spectra ($\lambda_{exc} = 365$ nm, top) and column chart for I/I_0 vs K salt at 423 nm (bottom) for **P5** in THF–water ($v/v = 1:1$) with and without different K salts ($[KX]_{final} = 0.3$ mM).

Interestingly, we also observed a luminescence response when solid **P5** was ground in a mortar together with solid KCl. The normalized emission spectrum of the mixture after grinding displayed an increased emission at 513 nm when compared to the main band at 590 nm (Fig. 2.12, left). The altered emission is clearly visible by the naked eye.

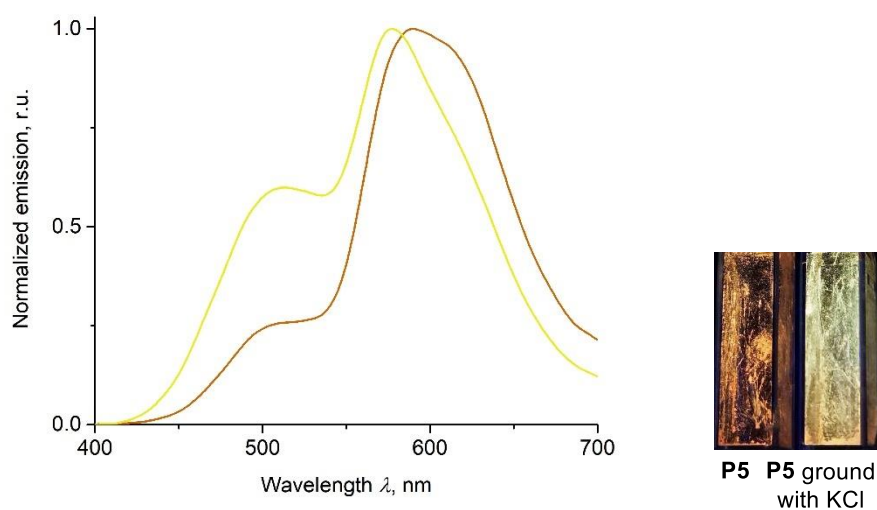


Figure 2.12 Normalized luminescence spectra ($\lambda_{exc} = 365$ nm) of solid **P5** (orange curve) and of **P5** after it was ground with KCl (yellow curve), and a photo of the samples when irradiated at $\lambda = 365$ nm.

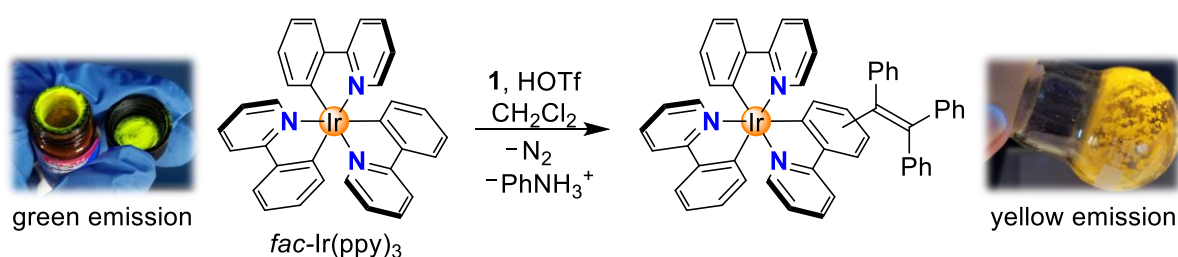
2.6 Conclusions

A novel procedure for the grafting of hyperbranched poly(triphenylethene)s to aromatic compounds was described. The polymers are grown by consecutive C–H activation reactions using triphenylethenyl triazene **1**. This reagent shows vinyl cation-like reactivity after acid-mediated cleavage of the triazene functional group. In contrast to other procedures for the synthesis of polyarylethenes, our methodology is ‘traceless’, and functional groups are not found in the products. The products show size-dependent luminescence. The polymers with higher molecular weight display increased luminescence quantum yield in solution but decreased luminescence quantum yield in the solid state. Upon aggregation or in the solid state, the polymers show a second, red-shifted emission band. As a result, they exhibit unusual ratiometric aggregation-induced emission. For the present study, we grafted hyperbranched poly(triphenylethene) to TPE and to benzo-18-crown-6. However, it is clear from our earlier study that the C–H vinylation methodology is compatible with numerous other aromatic compounds including heterocycles, biologically relevant molecules, and commercial polymers. Consecutive C–H vinylation reactions could thus be used to prepare AIE-active polyarylethenes for diverse potential applications.

2.7 Attempted C–H Vinylation of *fac*-Ir(ppy)₃

Compared to many purely organic AIE luminogens obtained so far,¹ there are fewer examples of metal-based compounds showing AIE properties.¹⁷² Usually, metal-based AIE luminogens are made *via* coordination of “naked” metal cations or complexes to organic AIE-active ligands^{173–176} or by post-synthetic modification of metal complexes with AIE-active groups.¹⁷² We were interested if luminescent Ir complexes can be functionalized with a triphenylethenyl group using the C–H vinylation procedure described above.

First, we performed a test reaction using the optimized conditions for C–H vinylation from our previous work.⁴⁹ A solution containing green-emissive *fac*-Ir(ppy)₃ (5 equiv.) and triazene **1** (1 equiv.) was prepared in CH₂Cl₂ (0.04 M) and then treated with HOTf (5 equiv.), see Scheme 2.5. Gas evolution was observed, indicating cleavage of the triazene function. The coupling chemistry that we attempted was expected to give a vinylation product with functionalization at the aryl ring as the more nucleophilic site of *fac*-Ir(ppy)₃.



Scheme 2.5 Expected C–H vinylation of *fac*-Ir(ppy)₃ with triazene **1**.

After a basic work-up and purification by flash chromatography on silica, a yellow-emissive powder was isolated. While performing thin-layer chromatography (TLC), we noticed that the crude contains traces of the starting material when eluted with pure CH₂Cl₂ (Fig. 2.13a, green spot). The product was purified by elution with a mixture CH₂Cl₂–MeOH (3:1, v/v, Fig. 2.13a, yellow spot), indicating its different polarity. The isolated product was analyzed by mass spectrometry, which showed that the structure with proposed molecular mass was not detected (Fig. 2.13b). Instead, we observed a molecular ion corresponding to the starting material. However, the latter had been removed during the chromatographic purification.

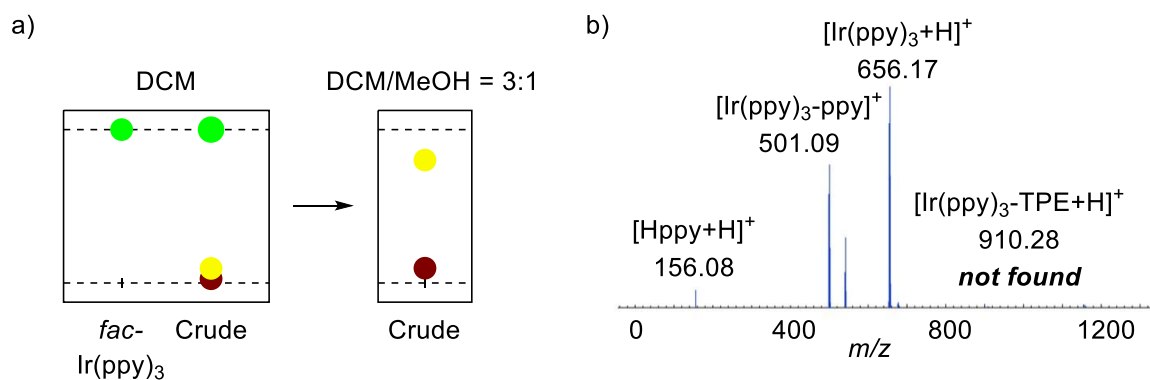


Figure 2.13 Results of a) TLC of the crude obtained after attempted C–H vinylation of *fac*-Ir(ppy)₃ and b) mass spectrometry of the isolated product.

The ¹H NMR spectroscopy revealed that the isolated product is *mer*-Ir(ppy)₃ (Fig. 2.14a and b). Thus, a *fac*→*mer* isomerization had occurred during the attempted C–H vinylation of *fac*-Ir(ppy)₃ with triazene **1** (Scheme 2.6).

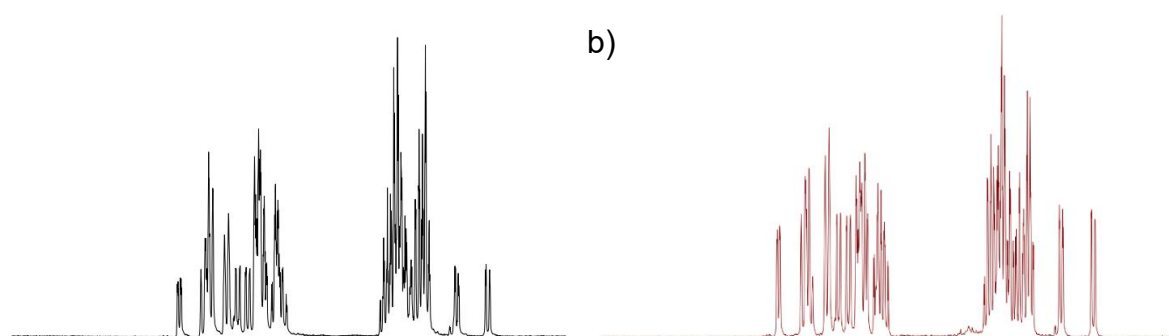
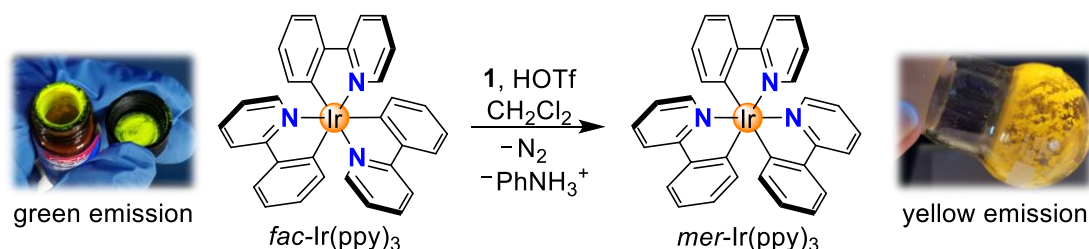


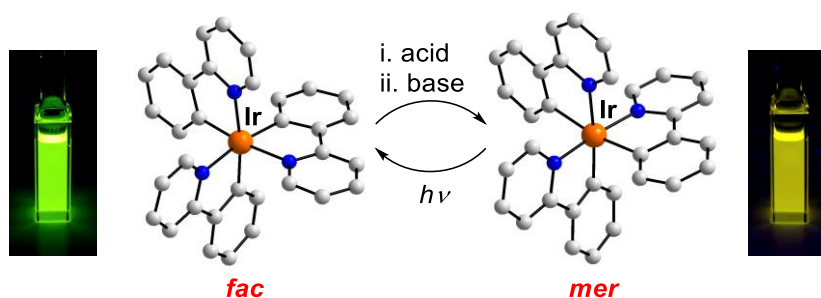
Figure 2.14 ¹H NMR (CD₂Cl₂, 298 K) spectrum of a) *mer*-Ir(ppy)₃ reported by M. E. Thompson and co-workers (adapted and reproduced with permission of ACS)¹⁰³ and b) the product of attempted C–H vinylation of *fac*-Ir(ppy)₃ with triazene **1**.



Scheme 2.6 *fac*→*mer* conversion of Ir(ppy)₃ during an attempted C–H vinylation reaction.

As it was discussed in subchapter 1.3, *fac* and *mer* isomers of Ir(ppy)₃ have distinct photophysical properties, which explains the observed change of emission colour after the reaction. The *mer*→*fac* isomerization of Ir(C^N)₃ complexes has been studied extensively (for references, see subchapter 1.3.3), whereas the inverse *fac*→*mer* conversion was not known. The accidental finding described above was the starting point for more detailed investigations, which are summarized in the next two chapters of this thesis.

Chapter 3. Acid-Base-Induced *fac*→*mer* Isomerization of Ir Complexes with Orthometalated Ligands



This chapter is based on a publication:

A.Yu. Gitlina, F. Fadaei-Tirani, A. Ruggi, C. Plaice, K. Severin “Acid-base-induced *fac*→*mer* isomerization of luminescent iridium(III) complexes”, *Chem. Sci.* **2022**, 13 (35), 10370–10374. [DOI: 10.1039/D2SC02808E](https://doi.org/10.1039/D2SC02808E)

Reprinted and adapted version with permission from The Royal Society of Chemistry.

This publication was highlighted by S. Greed “Making a *mer*-isomer” in *Nat. Rev. Chem.* **2022** ([DOI: 10.1038/s41570-022-00429-y](https://doi.org/10.1038/s41570-022-00429-y))¹⁷⁷ and included in the themed collection of *Chem. Sci.* [Most popular 2022 main group, inorganic and organometallic chemistry articles](#).

A.Yu. G. and K. S. initiated the study, **A.Yu. G.** performed the experiments and analyzed the data, F. F.-T. collected and processed the X-ray data, A. R. performed the photophysical measurements, C. P. helped with the synthesis and the analysis of the heteroleptic Ir(dfppy)₂(tpy) complexes, and **A.Yu. G.** and K. S. co-wrote the manuscript. All authors discussed the results and commented on the manuscript.

3.1 Introduction

Iridium(III) complexes with cyclometalated arylpyridine ligands (C[^]N ligands) display intriguing photophysical and chemical properties (for details, see subchapters 1.3.3 and 1.3.4). Noteworthy characteristics include high photoluminescence quantum yields, reversible redox transitions, a pronounced chemical and thermal stability, and the possibility to tune the emission colour, the phosphorescence lifetime, and the redox properties by structural modifications.⁹⁵ The unique properties of Ir(C[^]N)₃ complexes have led to diverse applications including emitters in phosphorescent OLEDs, photoredox catalysts, chemical or biological probes, and building blocks for supramolecular assemblies (for references, see subchapter 1.3.4).

Ir(C[^]N)₃ complexes form two stable isomers with distinct photophysical and electrochemical properties: *fac* and *mer*.^{103,178} The synthesis of these isomers and their chemical, photochemical and photophysical properties are described in more detail in subchapters 1.3.2, 1.3.3 and 1.3.4. Briefly, the *mer* isomers are thermodynamically less stable than the *fac* isomers. By adjusting the reaction conditions, it is possible to obtain the *mer* isomers in a kinetically controlled reactions.^{103,178–181} A *mer*→*fac* isomerization can be achieved at high temperature or by irradiation.^{103,127,128,130,178} The inverse *fac*→*mer* isomerization, which is thermodynamically uphill, has not been reported so far.

Herein, we show that a *fac*→*mer* isomerization can be achieved by a consecutive reaction of Ir(C[^]N)₃ complexes with first acid and then base. The chemically induced isomerization allows using highly luminescent Ir(C[^]N)₃ complexes as molecular switches.

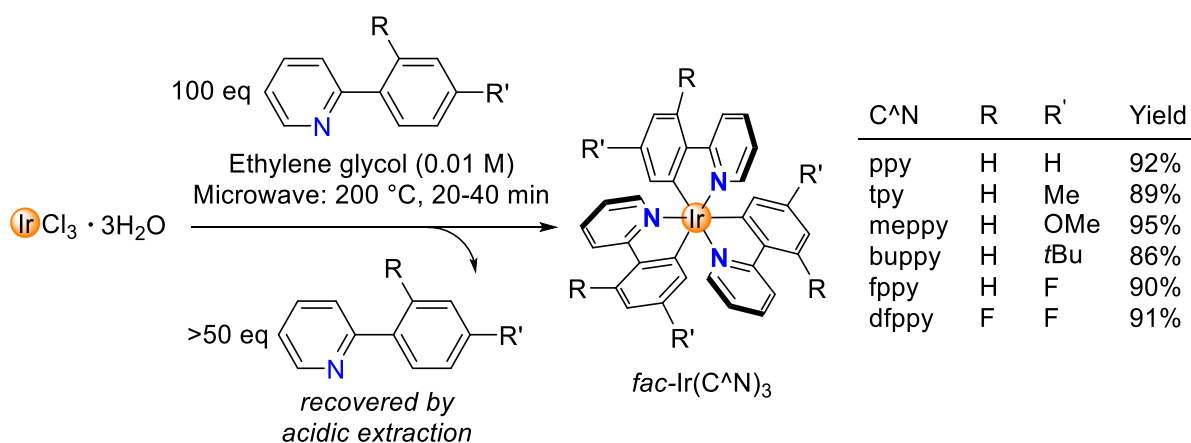
3.2 Microwave Synthesis of *fac*-Ir(C[^]N)₃ Complexes

The synthetic approaches to Ir(C[^]N)₃ complexes are discussed in detail in subchapter 1.3.2. Ir(C[^]N)₃ complexes are typically synthesized by cyclometalation of Ir precursors, such as IrCl₃·xH₂O, Ir(acac)₃, Ir(C[^]N)₂(O[^]O) (O[^]O = dipivaloylmethane) with HC[^]N ligands. These methods include additional steps for the synthesis and purification of Ir(C[^]N)₂(O[^]O) and [Ir(C[^]N)₂(μ-Cl)]₂ complexes. To selectively produce the *fac* isomer, the conventional procedures requires refluxing in glycerol for at least 24 h, and the

yields are sometimes low.¹¹⁶ Moreover, chromatographic separation is needed for further purification of the *fac* complexes. High amounts of acrolein, which is highly toxic and irritative for human body,¹⁸² are formed during these procedures.

In 2003, H. Konno and Y. Sasaki reported an approach to *fac*-Ir(ppy)₃ and *fac*-Ir(tpy)₃, where ppy = 2-phenylpyridyl and tpy = 2-(4-methylphenyl)pyridyl, from IrCl₃·xH₂O and the corresponding ligand by microwave irradiation-assisted cyclometalation.¹¹⁶ The reaction proceeds in ethylene glycol (0.01 M with respect to IrCl₃·3H₂O) for 1–3 min and gives *fac*-Ir(ppy)₃ and *fac*-Ir(tpy)₃ in 75% and 67% yield, respectively. This reaction is highly selective, and no traces of the *mer* isomers were found in the products. However, the main limitation is using 100 equiv. of the cyclometalating ligand compared to IrCl₃·xH₂O. Although the authors have mentioned that the synthetic method can be applied to other orthometalated iridium complexes, no further studies were reported.

Below, we show that this procedure can be used for the nearly quantitative and highly selective synthesis of six complexes featuring different ligands: *fac*-Ir(ppy)₃, *fac*-Ir(tpy)₃, *fac*-Ir(meppy)₃, *fac*-Ir(buppy)₃, *fac*-Ir(fppy)₃, and *fac*-Ir(dfppy)₃, where meppy = 2-(4-methoxyphenyl)pyridyl, buppy = 2-(4-*tert*-butylphenyl)pyridyl, fppy = 2-(4-fluorophenyl)pyridyl, dfppy = 2-(2,4-difluorophenyl)pyridyl (Scheme 3.1).



Scheme 3.1 Synthesis of the *fac* isomers of Ir(ppy)₃, Ir(tpy)₃, Ir(meppy)₃, Ir(buppy)₃, Ir(fppy)₃ and Ir(dfppy)₃ by microwave irradiation.

The nearly quantitative yield is achieved by prolongation of the reaction time to 20–40 min. Furthermore, we have developed a procedure for the recovery of the

cyclometalating ligand, which is still used in high excess (for details, see the Experimental part, subchapter 6.3.1). After completing the reaction in a microwave, the products precipitate from the reaction mixture (Fig. 3.1a and b). Their isolation requires simple filtration, washing with solvents (methanol and diethyl ether, successively) and drying under high vacuum.

Our procedure offers *quick* (1 hour for performing the synthesis from loading the reagents into a microwave vial to isolating the dried product), *facile* (no chromatography at the purification step), *near-quantitative yielding* (no by-products, no *mer* isomers detected, purity > 97% by NMR as for commercially available *fac* complexes), *reliable* (a scope of iridium complexes tolerates) and *non-toxic* (no acrolein was formed because ethylene glycol is used) pathway to larger quantities (80–90 mg, Fig. 3.1c) of *fac*-Ir(C^N)₃ from commercially available IrCl₃·xH₂O and HC^N ligands.

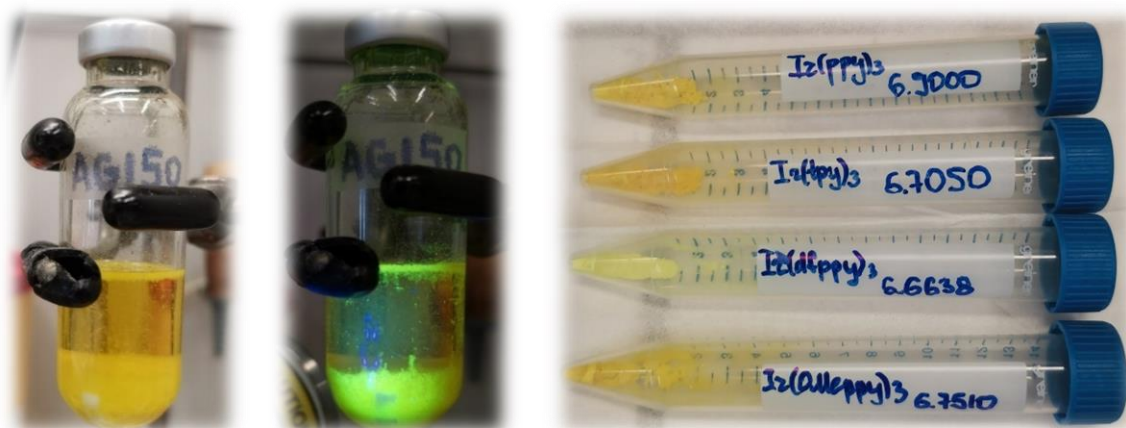
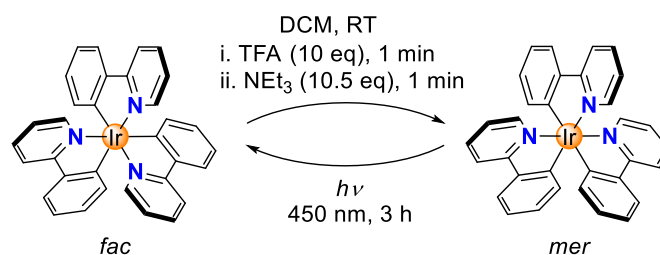


Figure 3.1 Photos of a microwave vial containing the *fac*-Ir(ppy)₃ precipitate after completing the reaction taken a) under day light and b) when irradiated at $\lambda = 365$ nm. c) Photo of freshly prepared *fac* isomers of Ir(ppy)₃, Ir(tpy)₃, Ir(dfppy)₃, and Ir(meppy)₃ using the microwave method.

Cost analysis of the synthetic methods showed that the microwave irradiation-assisted method is comparable in price with the conventional synthetic procedures, and favorable in terms of time consumed for the synthesis. It is worth using this procedure instead of buying the *fac* complexes from chemical suppliers (for details, see the Experimental part, subchapter 6.3.1).

3.3 Protonation of Ir(ppy)₃ with Strong Acids and Study of the *fac*→*mer* Isomerization

While investigating the chemistry of *fac*-Ir(ppy)₃, we made a surprising observation: when a solution of *fac*-Ir(ppy)₃ in CH₂Cl₂ was treated in a successive fashion with first TFA (10 equiv.) and then with NEt₃ (10.5 equiv.), a quantitative conversion into the *mer* isomer was observed (Scheme 3.2).



Scheme 3.2 Interconversion of *fac*-Ir(ppy)₃ and *mer*-Ir(ppy)₃.

The chemically induced transformation of *fac*-Ir(ppy)₃ into *mer*-Ir(ppy)₃ was followed by ¹H NMR spectroscopy using CD₂Cl₂ as solvent. The TFA treatment resulted in the rapid (< 1 min) formation of a defined complex of low symmetry, with three sets of signals for the three ligands (Fig. 3.2a). Furthermore, the NMR data indicated that protonation had occurred at one of the phenyl groups, thereby converting a chelating, anionic C[^]N ligand into a monodentate, neutral N-donor ligand.

Attempts to characterize the TFA adduct by single crystal X-ray crystallography were not successful. However, when using bistriflimidic acid (HNTf₂) instead of TFA, we were able to crystallize the ‘open form’. The result of a crystallographic analysis is depicted in Fig. 3.2b. In line with the NMR data, the cationic Ir complex features two orthometalated 2-phenylpyridine ligands and one neutral 2-phenylpyridine ligand, which is bound *via* the pyridine group to the metal. One C–H group of the phenyl ring forms an agostic interaction¹⁸³ with the cationic Ir center (Ir⋯H ~ 1.97 Å; Ir–H–C ~ 115°). When the agostic interaction is taken into account, the coordination environment around Ir can be described as distorted octahedral.

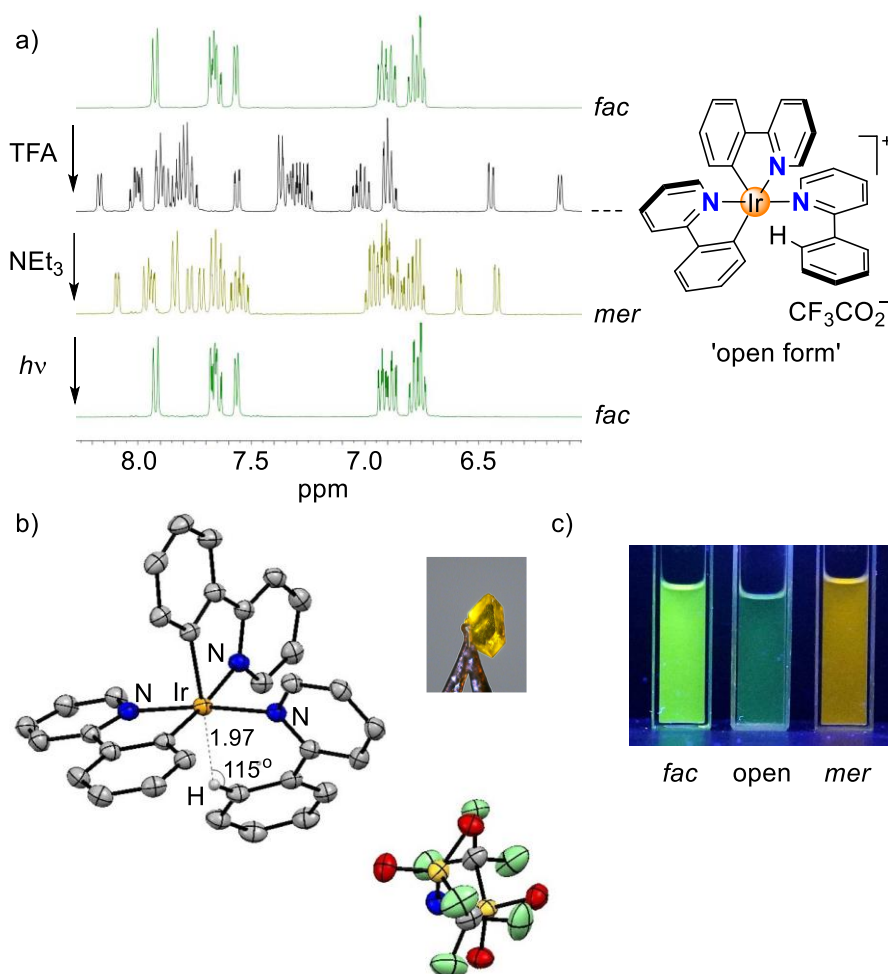


Figure 3.2 a) ^1H NMR spectra (400 MHz, CD_2Cl_2 , aromatic region) for the conversion of *fac*- $\text{Ir}(\text{ppy})_3$ into *mer*- $\text{Ir}(\text{ppy})_3$ and back. b) Molecular structure of $[\text{Ir}(\text{ppy})_2(\text{Hppy})](\text{NTf}_2)$ in the crystal with thermal ellipsoids at 50% probability and a photo of the crystal picked for XRD analysis. c) Photos of solutions containing *fac*- $\text{Ir}(\text{ppy})_3$, $[\text{Ir}(\text{ppy})_2(\text{Hppy})](\text{O}_2\text{CCF}_3)$ ('open form'), and *mer*- $\text{Ir}(\text{ppy})_3$ under UV-light ($\lambda_{\text{ex}} = 366 \text{ nm}$).

The open form has a meridional arrangement of the three N-donor atoms, and a base-induced metalation is primed to give the *mer* isomer of $\text{Ir}(\text{ppy})_3$, as found experimentally. Within one minute after the addition of NEt_3 , a quantitative formation of *mer*- $\text{Ir}(\text{ppy})_3$ was observed (Fig. 3.2a). To simplify the deprotonation step and minimize the presence of by-products, solid inorganic salts, such as KHCO_3 and Cs_2CO_3 , were tested. However, NEt_3 gave the best result. Optimization of the protonation step was also carried out, including acid strength and acid concentration effect (for optimization details, see the Experimental part, subchapter 6.3.15).

As described in the literature (for references, see subchapter 1.3.3), it is possible to convert the *mer* isomer back into the *fac* isomer by irradiation. For this purpose, we have used a 90 W LED lamp with an emission maximum at 450 nm. A clean back-isomerization was achieved within 3 h, as evidenced again by ^1H NMR spectroscopy (Fig. 3.2a). The *fac* and the *mer* isomer of $\text{Ir}(\text{ppy})_3$ show distinct emission colours and intensities, with a weaker, red-shifted emission for the *mer* form (Fig. 3.2c). The open form $[\text{Ir}(\text{ppy})_2(\text{Hppy})](\text{O}_2\text{CCF}_3)$ is largely non-luminescent.

3.4 Repetitive *fac*↔*mer* Switching

The acid-base reaction accompanying the transformation of *fac*- $\text{Ir}(\text{ppy})_3$ to *mer*- $\text{Ir}(\text{ppy})_3$ results in the formation of salt $(\text{HNEt}_3)(\text{O}_2\text{CCF}_3)$ (Fig. 3.3a). In order to examine if the presence of this salt would compromise subsequent isomerization steps, we have performed multiple *fac*→*mer*→*fac* cycles in the same reaction flask without separation/purification steps. The conversion efficiency was monitored by recording the emission spectra after each isomerization. The results indicate that for ten cycles, neither the chemically induced *fac*→*mer* isomerization nor the photochemical *mer*→*fac* isomerization is compromised to a significant extent by the presence of accumulating amounts of salt (Fig. 3.3b). The robustness of the switching process was substantiated by ^1H NMR studies in CD_2Cl_2 . After three *fac*→*mer*→*fac* cycles, only trace amounts of side products could be detected by ^1H NMR spectroscopy (for the spectra, see the Experimental part, subchapter 6.3.5).

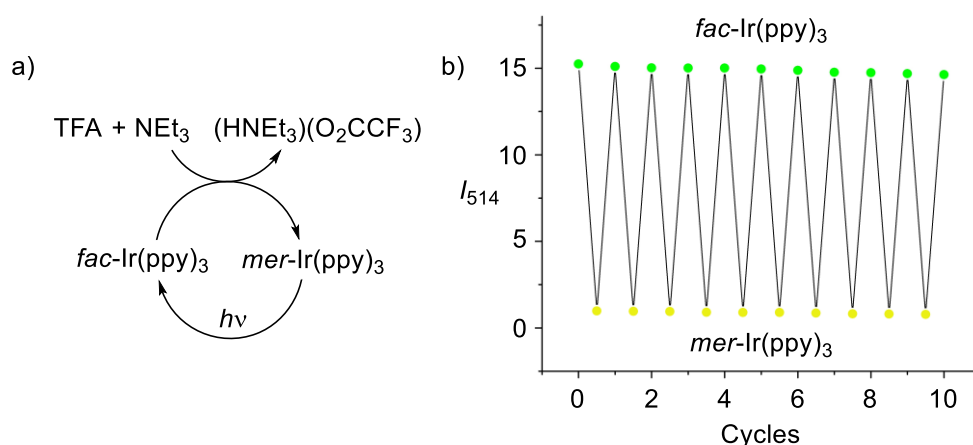
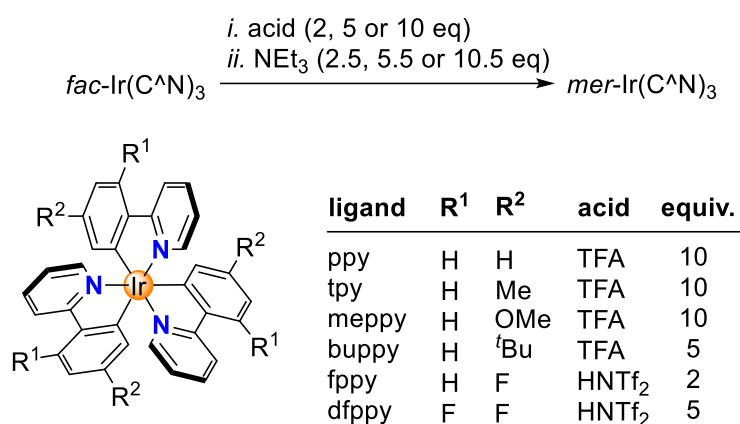


Figure 3.3 a) Acid-base treatment followed by irradiation allows repetitive cycling between *fac*- and *mer*- $\text{Ir}(\text{ppy})_3$ with releasing $(\text{HNEt}_3)(\text{O}_2\text{CCF}_3)$. b) The interference of accumulating salt is low for first ten cycles, as evidenced by spectroscopic monitoring.

3.5 Scope

Next, we examined if other Ir(C[^]N)₃ complexes would also undergo acid-base-induced *fac*→*mer* isomerizations. Complexes with orthometalated *p*-tolylpyridine (tpy), 2-(4-methoxyphenyl)pyridine (meppy), and 2-(4-*tert*-butylphenyl)pyridine (buppy) ligands behaved in a similar fashion as Ir(ppy)₃: a clean and fast *fac*→*mer* conversion could be induced by consecutive addition of TFA (5–10 equiv.) and NEt₃ (5.5–10.5 equiv.) (Scheme 3.3). A quantitative back-isomerization was achieved by irradiation with blue light (for NMR monitoring, see the Experimental part, subchapter 6.3.5). For complexes based on metalated 2-(4-fluorophenyl)pyridine (fppy) and 2-(2,4-difluorophenyl)pyridine (dfppy), on the other hand, TFA addition did not result in the formation of the open form. We hypothesized that the reduced basicity of the fluorinated phenyl group was responsible for the lack of reactivity. Indeed, the *fac*→*mer* isomerization of *fac*-Ir(fppy)₃ and *fac*-Ir(dfppy)₃ was achieved with the stronger acid HNTf₂ (2 and 5 equiv., Fig. 3.4 and 3.5, respectively). The back *mer*→*fac* conversion for these complexes was achieved by light irradiation.



Scheme 3.3 Chemically induced *fac*→*mer* isomerizations are possible for different Ir(C[^]N)₃ complexes using either TFA or HNTf₂ for the protonation step.

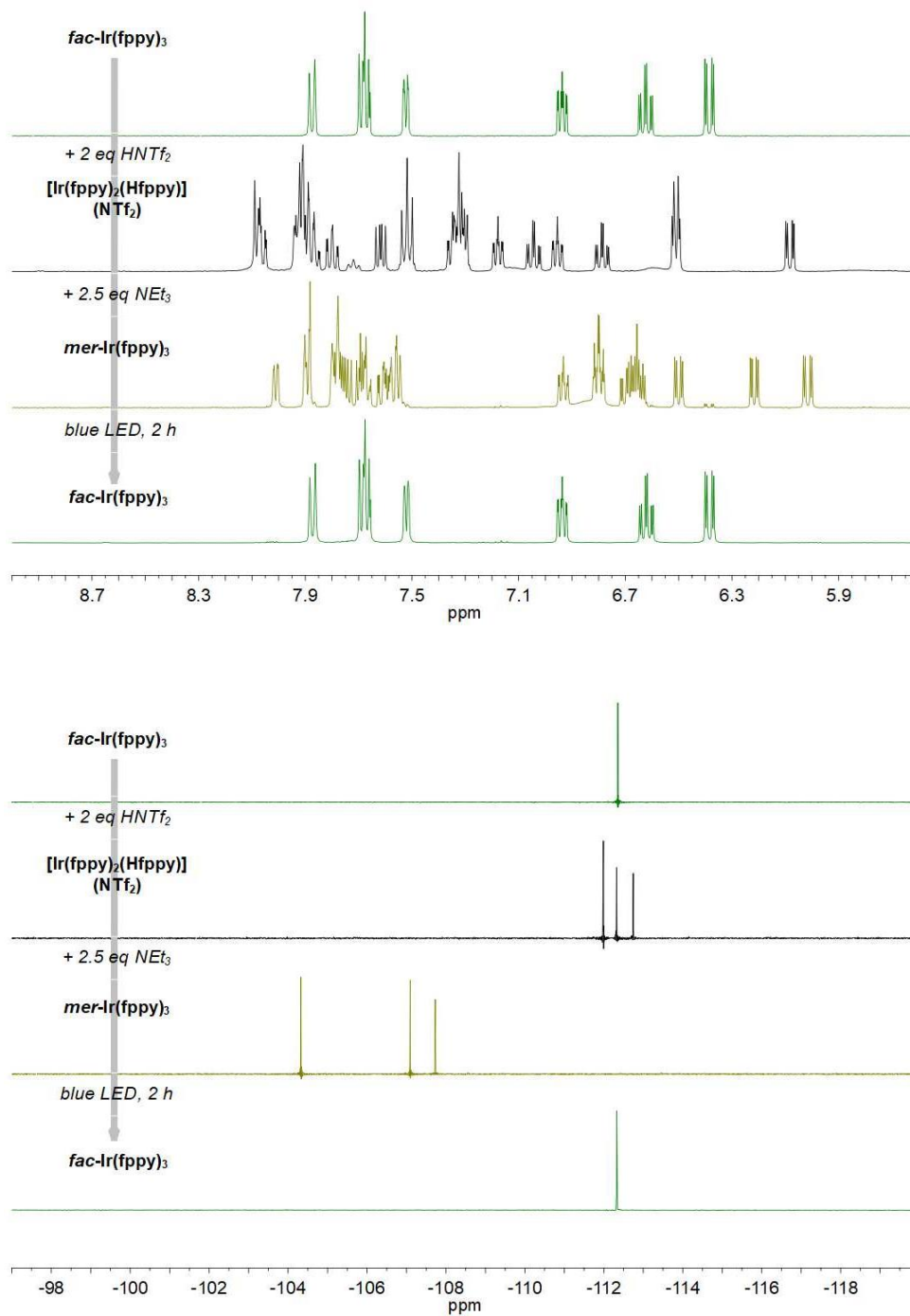


Figure 3.4 ¹H and ¹⁹F NMR spectra for *fac* → *mer* → *fac* isomerization of Ir(fppy)₃.

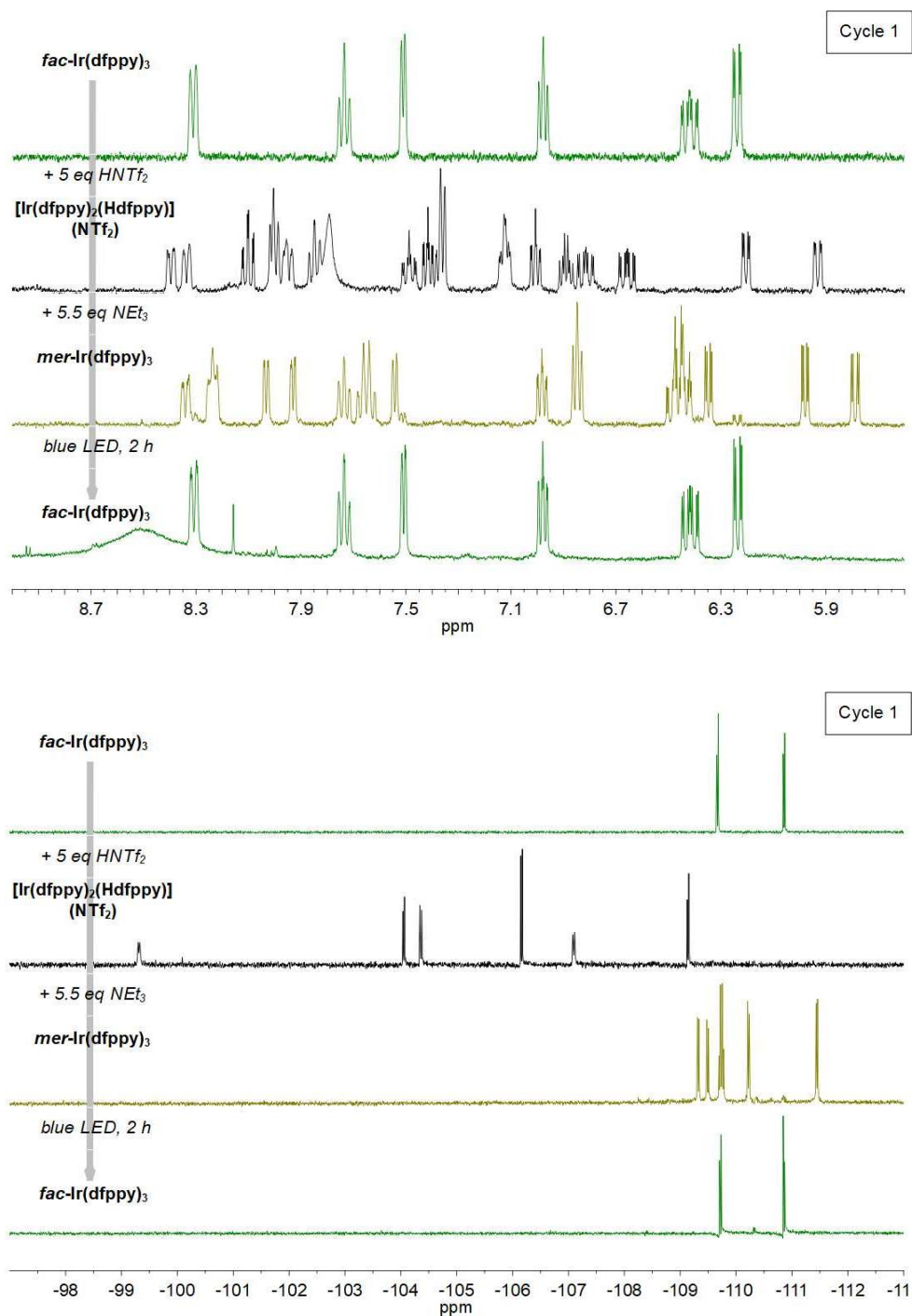
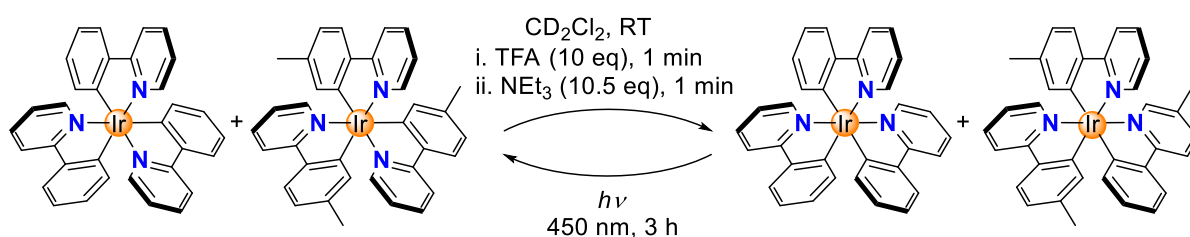


Figure 3.5 ^1H and ^{19}F NMR spectra for $fac \rightarrow mer \rightarrow fac$ isomerization of $\text{Ir}(\text{dfppy})_3$.

3.6 Investigations of Ligand Exchange

The protonated complexes $[\text{Ir}(\text{C}^{\wedge}\text{N})_2(\text{HC}^{\wedge}\text{N})]^+$ feature a monodentate N-donor ligand. This ligand is expected to be more labile than the chelating $\text{C}^{\wedge}\text{N}$ ligands. It was therefore conceivable that ligand exchange processes can occur during isomerization at the stage of the ‘open form’. In order to evaluate if ligand scrambling can happen,

we have examined the *fac*→*mer*→*fac* isomerization of an equimolar mixture of *fac*-Ir(ppy)₃ and *fac*-Ir(tpy)₃ in CD₂Cl₂. Analysis of the mixture after TFA/NEt₃ treatment by ¹H NMR spectroscopy showed the clean formation of the homoleptic complexes *mer*-Ir(ppy)₃ and *mer*-Ir(tpy)₃ (Scheme 3.4 and for the NMR spectra, see Experimental part, subchapter 6.3.9). The results of the NMR analysis were supported by high-resolution mass spectrometry (HRMS): signals of the heteroleptic complexes *mer*-Ir(ppy)₂(tpy) and *mer*-Ir(ppy)(tpy)₂ were not detected, indicating the absence of ligand exchange (Fig. 3.6). In line with literature reports,¹⁷⁸ the photochemical *mer*→*fac* back isomerization also proceeds without ligand scrambling.



Scheme 3.4 A *fac*→*mer*→*fac* isomerization sequence with a mixture of Ir(ppy)₃ and Ir(tpy)₃ does not lead to ligand scrambling.

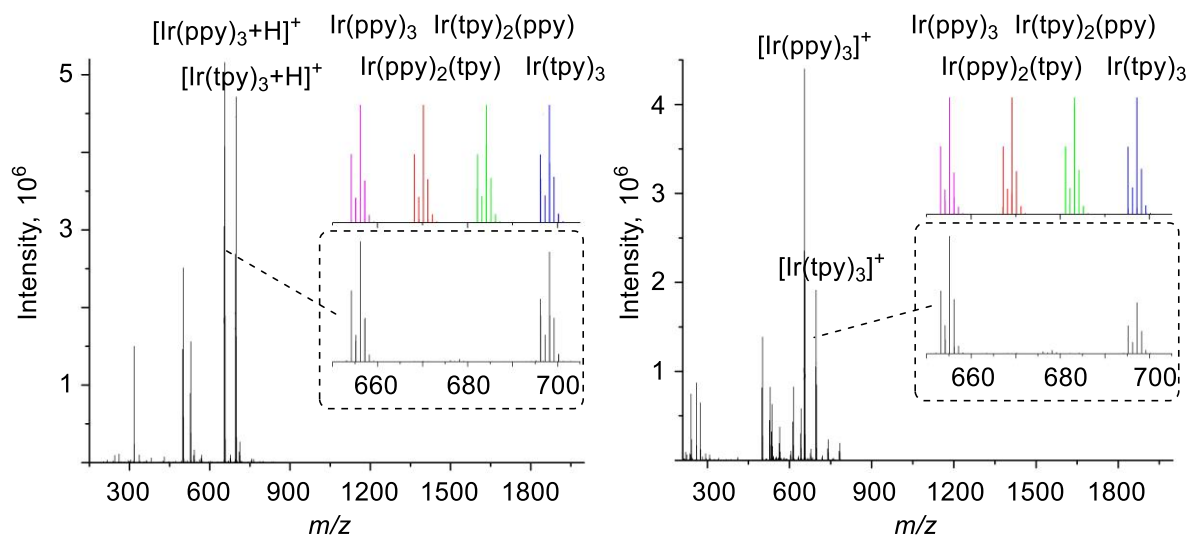
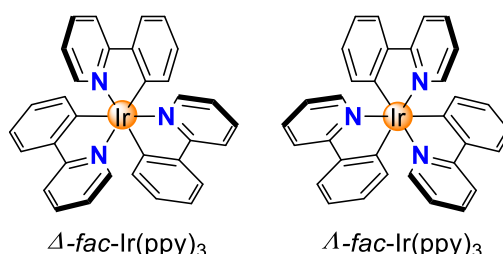


Figure 3.6 HRMS of the product mixture after the *fac*→*mer* isomerization (ESI⁺, left), and after the photochemical *mer*→*fac* isomerization (APPI⁺, right). Simulated spectra of the hypothetical heteroleptic complexes are shown in colour.

3.7 Stereoselectivity Studies and Possible Mechanism

Several publications describe methods for chiral HPLC-based separation of the Δ and Λ enantiomers of *fac*-Ir(C[^]N)₃ (Scheme 3.5).^{184–187}



Scheme 3.5 Enantiomers of *fac*-Ir(ppy)₃.

The conditions employed for the separation involve using Chiralpak[®] IA column with hexane–CHCl₃–CH₂Cl₂ (75:20:5, v/v/v) as eluent¹⁸⁶ or Chiralpak[®] ID column with hexane–isopropanol (90:10, v/v) as eluent.¹⁸⁷ In fact, the use of chlorinated solvents is not recommended for these traditional coated columns, because such solvents can solubilize the polysaccharide at the head of it, resulting in a plugged column. Thus, we made optimizations of the conditions for chiral separation of *fac*-Ir(ppy)₃ towards using hexane–isopropanol mixtures as eluent (for optimization details, see the Experimental part, subchapter 6.3.10). The following conditions were chosen: Chiralpak[®] IA column (size 4.6×250 mm, temperature 35 °C), eluent hexane–isopropanol 95:5, injection volume 10 μL, flow 1 mL/min, detection at $\lambda = 254$ nm, run time 30 min, sample solution: 2.5 mg/mL in DCM.

As determined in literature reports,^{184–187} Δ -*fac*-Ir(ppy)₃ is eluted first and Λ -*fac*-Ir(ppy)₃ is eluted second. The assignment of the chromatographic peaks for Δ -*mer*-Ir(ppy)₃ and Λ -*mer*-Ir(ppy)₃ has not been reported. To be able to investigate the stereoselectivity of acid-base-induced *fac*→*mer* isomerization, we performed an assignment of the stereoisomers of *mer*-Ir(ppy)₃ using a combination of chiral HPLC separation and XRD analysis. The first eluted enantiomer with an enantiomeric excess (*ee*) of 92% was obtained, and its HPLC profile and electronic circular dichroism (ECD) spectra are shown in Fig. 3.7a and b, respectively. Then, single crystals of this fraction were obtained by slow vapor diffusion of pentane into the CH₂Cl₂ solution at room temperature, and the absolute configuration was determined XRD analysis as Δ -*mer*-

$\text{Ir}(\text{ppy})_3$ (Fig. 3.7c). To exclude an error in picking a crystal of wrong configuration (4% of all crystals), the ECD spectrum of the crystal analyzed by XRD was recorded (Fig. 3.7d). The ECD spectra of the fraction and the crystal are similar in structure, which indicates that the first eluted enantiomer is Δ -*mer*- $\text{Ir}(\text{ppy})_3$. Consequently, the second eluted enantiomer is Λ -*mer*- $\text{Ir}(\text{ppy})_3$.

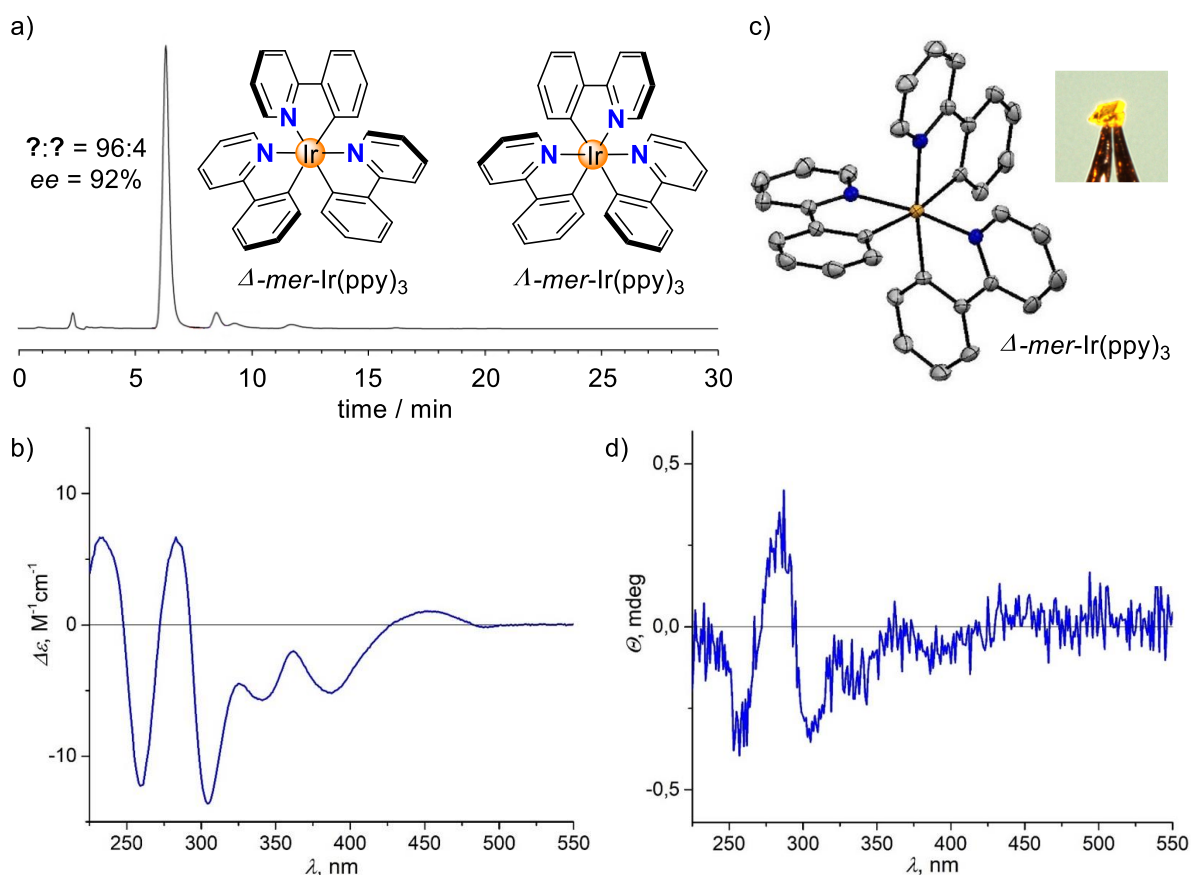


Figure 3.7 a) HPLC profile of the fraction enantio-enriched by the enantiomer of *mer*- $\text{Ir}(\text{ppy})_3$ with unknown configuration. b) ECD spectrum of the enantio-enriched fraction. c) Crystal structure of Δ -*mer*- $\text{Ir}(\text{ppy})_3$ determined by XRD analysis of the crystal obtained by the crystallization of the enantio-enriched fraction. Inset: photo of the single crystal. d) ECD spectrum of the Δ -*mer*- $\text{Ir}(\text{ppy})_3$ crystal.

To study further the stereoselectivity of the acid-base-induced *fac*→*mer* isomerization, we have prepared enantio-enriched fractions of *fac*- $\text{Ir}(\text{ppy})_3$ (for details, see the Experimental part, subchapter 6.3.10). Analysis of the sample before and after the TFA/ NEt_3 treatment showed the same enantiomeric ratio of Δ : Λ = 83:17, implying that the *fac*→*mer* isomerization proceeds without racemization (Fig. 3.8a and b). The

photochemical back *mer*→*fac* isomerization of Ir(ppy)₃ proceeded with partial racemization (Fig. 3.8c) in agreement with previously reported results.¹²⁸

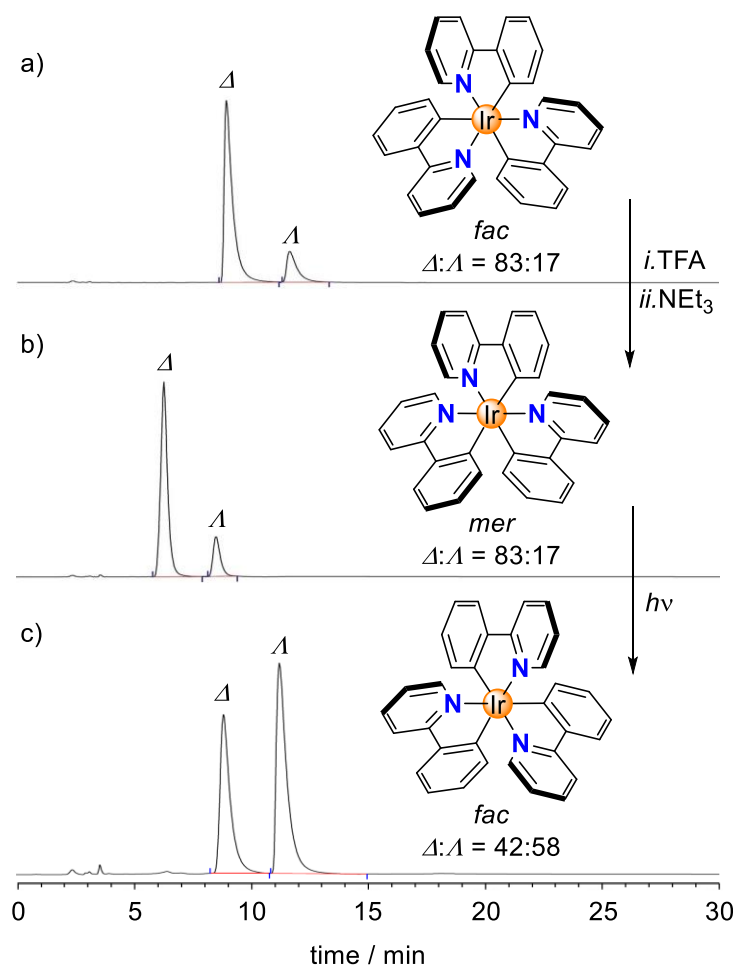
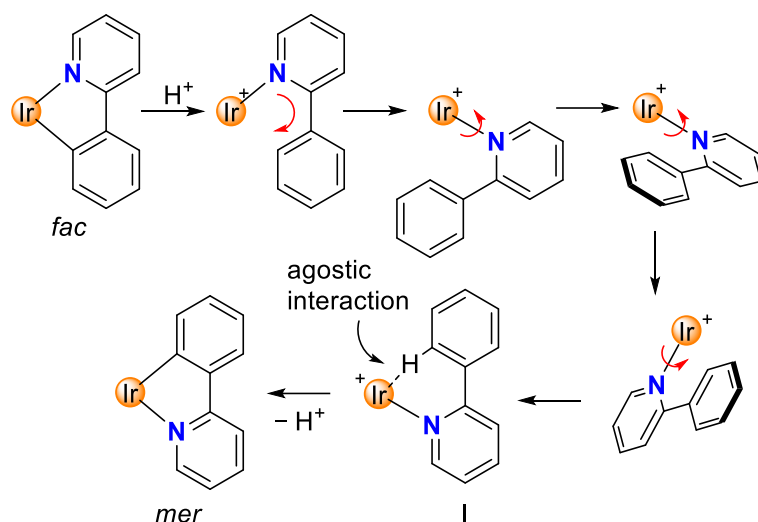


Figure 3.8 HPLC profiles of a sample containing enantio-enriched *fac*-Ir(ppy)₃ a) before, b) after acid-base-induced *fac*→*mer* isomerization, and c) after light-induced *mer*→*fac* isomerization.

The high stereoselectivity indicates that the isomerization involves a selective reorientation of one of the three ppy ligands. Most likely, this reorientation occurs upon protonation. The protonated Hppy ligand needs to undergo an in-plane movement along with a 180° rotation around the Ir–N bond to give to pre-meridional form **I** (Scheme 3.6). Base-induced Ir–C bond formation could then occur with minor structural rearrangements. This proposition is supported by the crystallographic analysis of the protonated complex [Ir(ppy)₂(Hppy)](NTf₂), which shows a pseudo-*mer* orientation of the three ligands and an agostic interaction between the aromatic C–H group and the cationic Ir center (Fig. 3.2b). It is worth mentioning that the

photochemical *mer*→*fac* back-isomerization proceeds through a different pathway, namely *via* Ir–N bond rupture¹²⁸ rather than Ir–C bond rupture. Therefore, Ir(C[^]N)₃ complexes could be considered as molecular motors performing a complex molecular motion, e.g. rotation of the ligand.^{188,189}



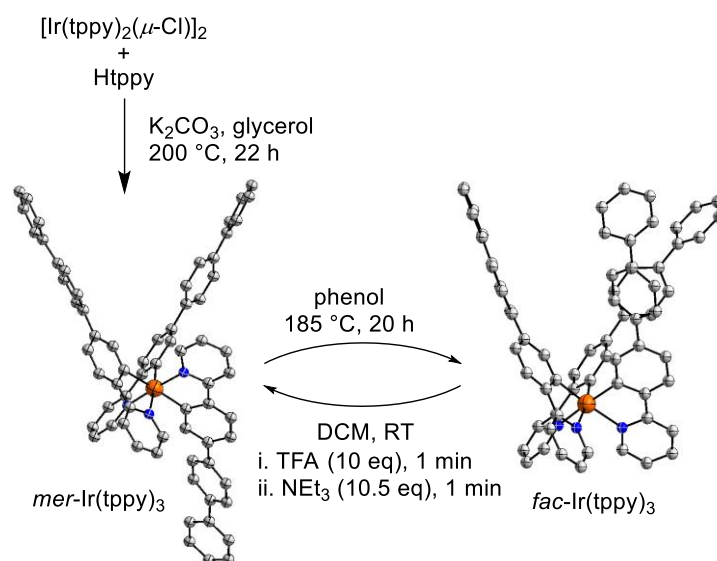
Scheme 3.6 Plausible mechanism for the isomerization involving an in-plane movement of the protonated Hppy ligand and a 180° rotation around the Ir–N bond. A sequential movement–rotation is shown for illustrative purposes.

3.8 Applications

Geometrical Switches

Compounds, which can be cycled between two (meta)stable states A and B, are often referred to as ‘molecular switches’.^{190–192} Some applications of molecular switches rely on the geometric differences between the forms A and B. In order to demonstrate that large structural changes can be achieved with *fac*→*mer* isomerizations, we have prepared an Ir(C[^]N)₃ complex with a long 4-(2-pyridyl)-*p*-terphenyl ligand (tppy) (Scheme 3.7). The free ligand Htppy was obtained in 85% yield by Pd-catalyzed cross-coupling of 2-(4-bromophenyl)pyridine with 4-biphenylboronic acid. In analogy to a reported procedure,¹¹⁰ we then synthesized the chloro-bridged dimer [Ir(tppy)₂(μ-Cl)]₂ by reaction of Htppy with IrCl₃·xH₂O in 2-ethoxyethanol-water (3:1, v/v) using microwave heating (150 °C, 20 min, yield: 82%, for details, see the Experimental part, subchapter 6.3.2). The homoleptic complex *mer*-Ir(tppy)₃ was obtained in 67% yield by reaction of [Ir(tppy)₂(μ-Cl)]₂ with Htppy and K₂CO₃ in glycerol at 200 °C (Scheme

3.7). Quantitative isomerization into *fac*-Ir(tppy)₃ was achieved by refluxing of a phenol solution of *mer*-Ir(tppy)₃ for 20 h.



Scheme 3.7 Synthesis of *fac*-Ir(tppy)₃ and *mer*-Ir(tppy)₃. The structures of the products are based on crystallographic analyses, with thermal ellipsoids at the 50% probability level. Hydrogen atoms are not shown for clarity.

Complex *fac*-Ir(tppy)₃ can be converted cleanly into the *mer* form using an acid-base treatment with TFA and NEt₃ (Fig. 3.9). Crystallographic analyses of the two isomers show the pronounced differences in geometry upon isomerization (Scheme 3.7). It is worth noting that a conversion of *mer*-Ir(tppy)₃ into *fac*-Ir(tppy)₃ was only achieved thermally, and not with light (Fig. 3.9). Apparently, the bulky ligands inhibit the photochemical isomerization, which was suggested to involve the rupture of one Ir–N bond.^{128,130}

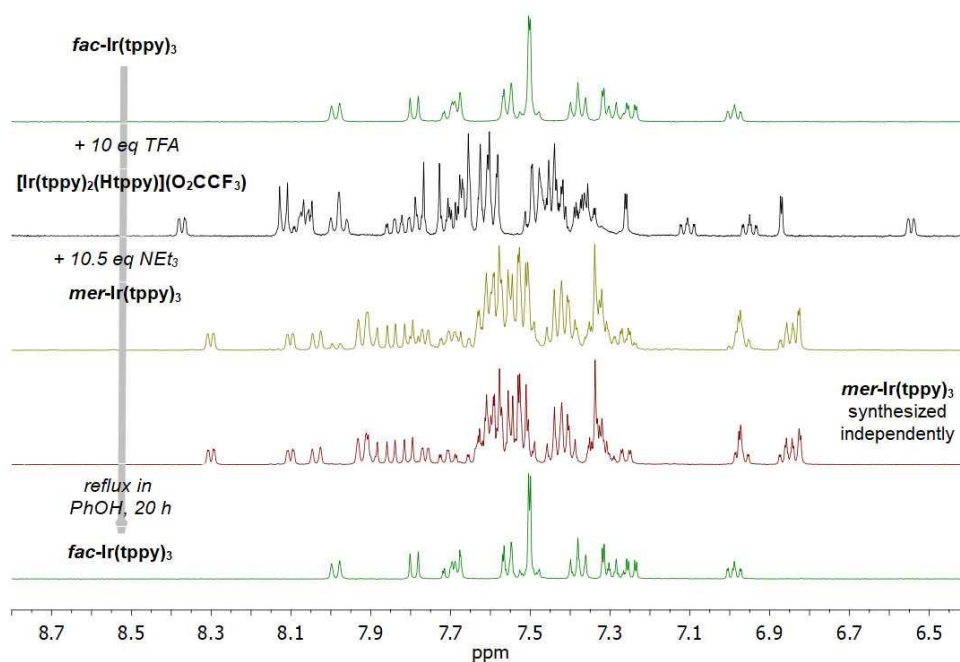
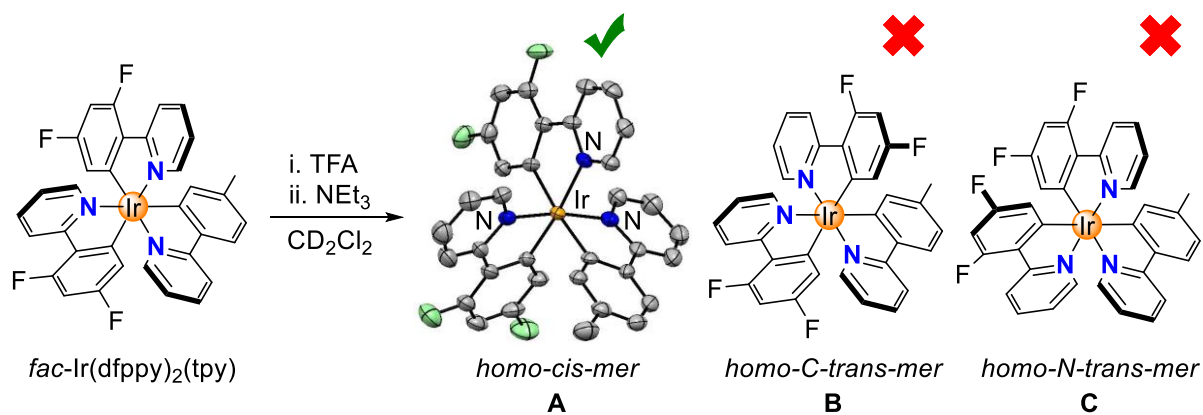


Figure 3.9 ^1H NMR spectra of a cycle for $fac \rightarrow mer \rightarrow fac$ for $\text{Ir}(\text{tppy})_3$ and a spectrum of $mer\text{-Ir}(\text{tppy})_3$ for visual comparison.

A synthetic pathway to new mer isomers

Having established that homoleptic $fac\text{-Ir}(\text{C}^{\wedge}\text{N})_3$ complexes can be isomerized chemically, we turned our attention to a heteroleptic complex, $fac\text{-Ir}(\text{dfppy})_2(\text{tpy})$.^{193,194} In principle, three different complexes could form during the chemically induced $fac \rightarrow mer$ isomerization (Scheme 3.8). Switching the orientation of the tpy ligand would give isomer **A**, whereas switching the orientation of one of the dfppy ligands would give isomer **B** or **C**. In view of the lower basicity of the fluorinated dfppy ligands, we anticipated that protonation of tpy with TFA would be preferred. Indeed, ^1H and ^{19}F NMR spectroscopic analysis of a mixture of $fac\text{-Ir}(\text{dfppy})_2(\text{tpy})$ and TFA (100 equiv.) in CD_2Cl_2 revealed that the more basic tpy ligand was protonated selectively (Fig. 3.10 and 3.11, respectively). Subsequent ring closure with NEt_3 gave a single isomer, and a crystallographic analysis of the product revealed that isomer **A** had formed (Scheme 3.8). Isomer **B** has not been detected, and no reports in the literature were found. Isomers **A** and **C** have different NMR spectra and slightly different optical and photophysical properties. For comparison, see the Experimental part (subchapter 6.3.13) and the publications.^{193,194}



Scheme 3.8 Isomerization of *fac*-Ir(dfppy)₂(tpy) gives selectively complex **A**. The structure of the product is based on XRD analysis, with thermal ellipsoids at the 50% probability level. Hydrogen atoms are not shown for clarity.

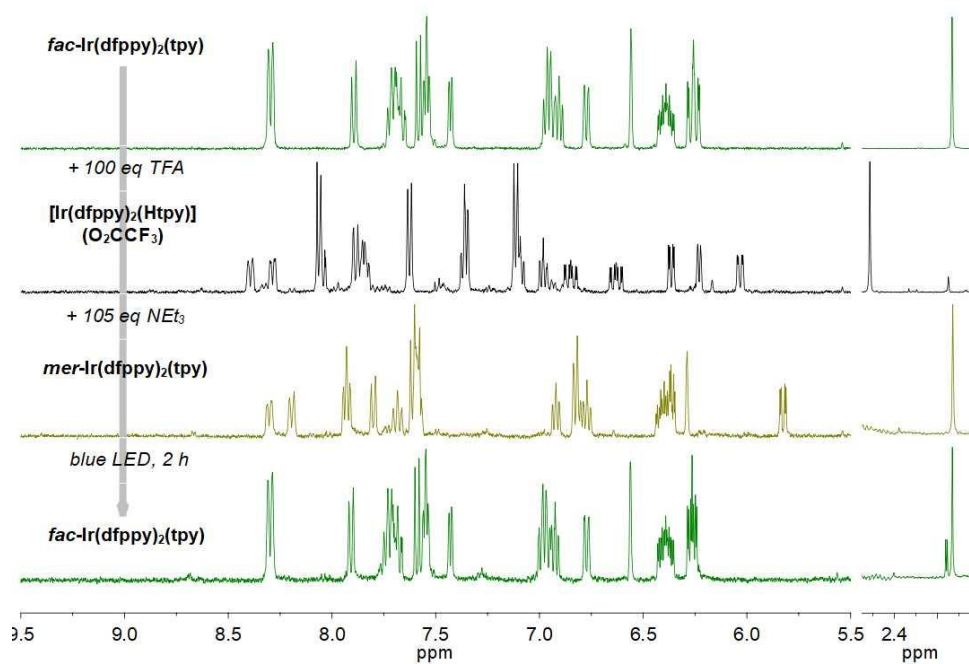


Figure 3.10 ¹H NMR spectra for *fac*→*mer*→*fac* isomerization of Ir(dfppy)₂(tpy).

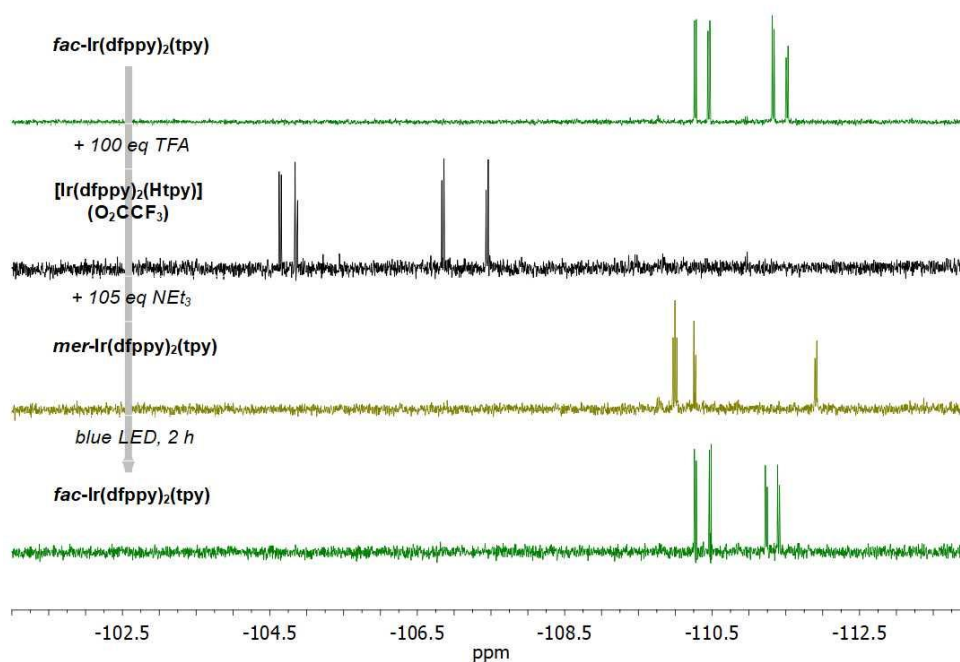


Figure 3.11 ^{19}F NMR spectra for $fac \rightarrow mer \rightarrow fac$ isomerization of $\text{Ir}(\text{dfppy})_2(\text{tpy})$.

New materials for data storage devices

The possibility to interconvert fac - and mer - $\text{Ir}(\text{C}^{\wedge}\text{N})_3$ complexes provides the opportunity to use these highly luminescent complexes for rewritable data storage devices.^{195,196} As a proof-of-concept, we have used a well plate filled with *o*-dichlorobenzene solutions of fac - $\text{Ir}(\text{ppy})_3$ as a luminescent display. The text 'Iridium' was written chemically by addition of TFA (green-black contrast) and then NEt_3 (green-orange contrast), and reset was achieved by light (Fig. 3.12).

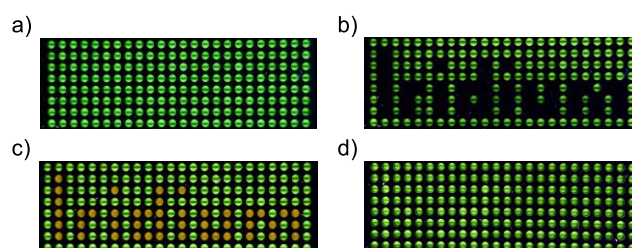


Figure 3.12 Photos of a well plate filled with solutions of a) fac - $\text{Ir}(\text{ppy})_3$ in *o*-dichlorobenzene, b) after addition of TFA to selected wells, c) after addition of NEt_3 to the same wells, and d) after irradiation with blue light. Details of the procedure and the photos of full well plates are given in the Experimental part, subchapter 6.3.8.

3.9 Conclusions

In conclusion, we have demonstrated that *fac*-Ir(C[^]N)₃ complexes can be converted cleanly into the thermodynamically less stable *mer* isomers by sequential treatment with first acid and then base. Spectroscopic and structural data indicate that the acid protonates a phenyl group of one ligand, resulting in Ir–C bond rupture. The intermediate protonated complex displays a *mer* arrangement of the N-donor atoms, priming the system for the kinetically controlled formation of *mer*-Ir(C[^]N)₃ in the presence of base. Notably, the structural rearrangement of the protonated HC[^]N ligand does not change the relative orientation of the two other C[^]N ligands. As a consequence, the isomerization is completely stereoselective, *i.e.* we observe conversion of Δ -*fac* into Δ -*mer*, and of Λ -*fac* into Λ -*mer*. The *mer* isomers can be converted back into the *fac* isomers by irradiation with light, and it is possible to perform multiple *fac*→*mer*→*fac* cycles with minor decomposition of the complexes.

fac-Ir(C[^]N)₃ and *mer*-Ir(C[^]N)₃ complexes are thermally highly stable, and the possibility to switch between these two stable forms opens numerous potential applications. One possible direction is rewritable data storage devices, and the luminescent display shown in Fig. 3.12 is a first proof-of-principle that such devices are feasible. Another possibility of the utilization of Ir(C[^]N)₃ complexes as geometric switches is in more complex nanostructures. The results obtained for Ir(tppy)₃ are evidence that large structural changes can be realized when converting *fac* isomers into *mer* isomers, and *vice versa*.

Finally, the results are also of interest from a synthetic point of view. Our new method allows preparing *mer* isomers of Ir(C[^]N)₃ complexes in a clean and fast fashion from the corresponding *fac* isomers. Notably, it is possible to access *mer* isomers, which are difficult to prepare otherwise. For example, the standard procedure to prepare the heteroleptic complex *mer*-Ir(dfppy)₂(tpy) gives isomer **C** with *homo-cis* configuration of the cyclometalated ligands (Scheme 3.8) rather than isomer **A** with *homo-N-trans* configuration.^{178,193,194}

3.10 Towards Autonomous Switching

Having explored the switching of $\text{Ir}(\text{C}^{\wedge}\text{N})_3$ complexes from *fac* to *mer* isomers by successive addition of two chemicals (first acid and then base), we turned our attention to processes that can be driven autonomously by addition of a chemical ‘fuel’.¹⁹⁷ Such processes are of particular interest nowadays because they trigger the cycles of oriented motion of artificial molecular machines, drawing them closer to the molecular machines originated by nature, such as myosin, kinesin, or dynein.

Artificial molecular machines capable of mimicking some features of natural systems have attracted great research interest, which was emphasized by the Nobel Prize for Chemistry awarded in 2016 to J.-P. Sauvage, F. Stoddard, and B. Feringa “*for the design and synthesis of molecular machines*”.^{198–200} To date, numerous molecular machines have been synthesized, and their actions, such as oriented rotations²⁰¹ and back-and-forth motions,²⁰² are triggered by light irradiation, electrochemically,²⁰³ or *via* a sequential addition of an acid and a base, or *vice versa*.^{204–206} Although these examples represent undoubtedly great scientific achievements in designing artificial molecular machines, their operation is not autonomous. A machine can be considered ‘autonomous’ if it is able to perform motions continuously as long as chemical fuel is present, without involvement of an external operator.¹⁹⁷ In the past decades, a number of abiotically originated small-molecule reagents (reagent systems) called ‘fuels’ have been developed and used for triggering whole cycles of motions of molecular machines. Examples of autonomously operated systems are discussed in the minireview by C. Biagini and S. Di Stefano.¹⁹⁷ Below, we describe one of them.

In 2017, D. Leigh and co-workers reported the use of trichloroacetic acid (HO_2CCCl_3) as a fuel to operate a rotary [2]catenane-based molecular motor.²⁰⁷ The [2]catenane depicted in Fig. 3.13 is composed of a ‘stator’ macrocycle with base-labile/acid-locked disulfide group and an acid-labile/base-locked hydrazone group, preventing free moving of a ‘rotor’ crown ether macrocycle. The crown ether can perform a 360° clockwise rotation around the stator, shuttling between two binding stations, a benzylammonium and a methyltriazolium group. The rotation of the [2]catenane is triggered by adding in one pulse HO_2CCCl_3 with co-fuels: thiol, disulfide, hydrazide (all depicted in Fig. 3.13), and catalytic amount of NEt_3 for promoting decarboxylation of HO_2CCCl_3 . The co-fuels are needed to exchange the acid- and base-labile groups,

temporarily detached from the [2]catenane, allowing the crown ether to shuttle between the binding stations. In the presence of the NEt_3 co-fuel, HO_2CCCl_3 undergoes decarboxylation resulting in CHCl_3 as the only waste product.

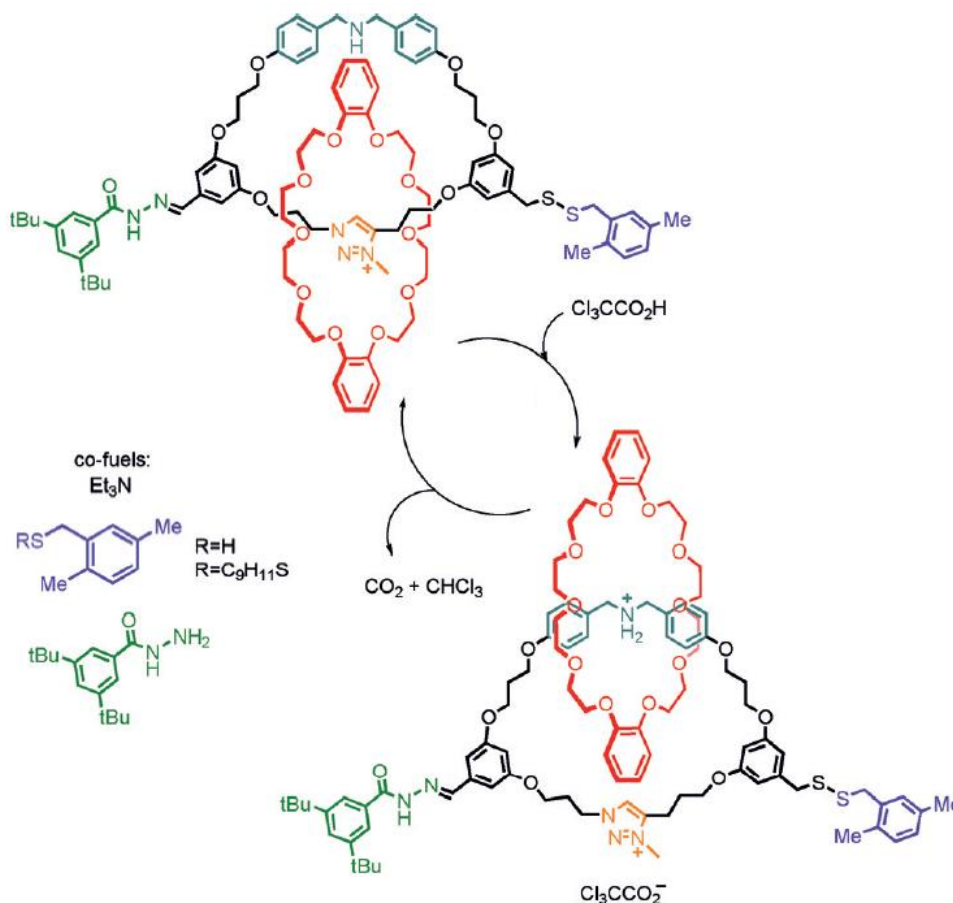
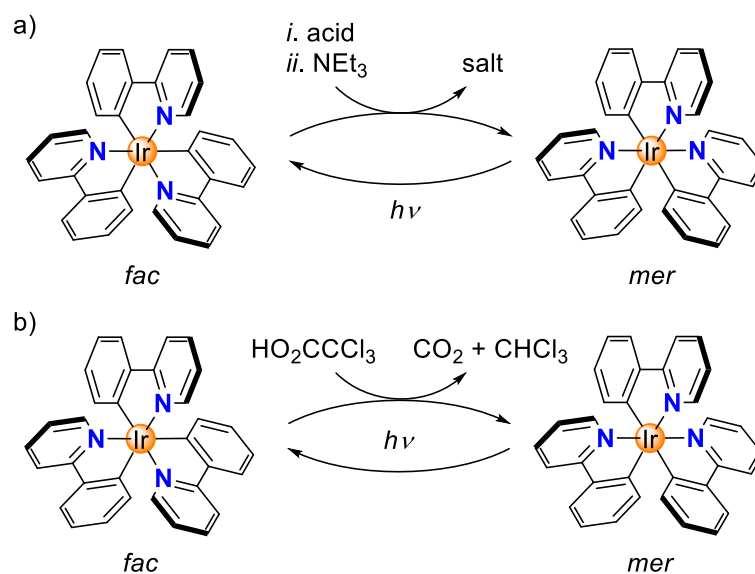


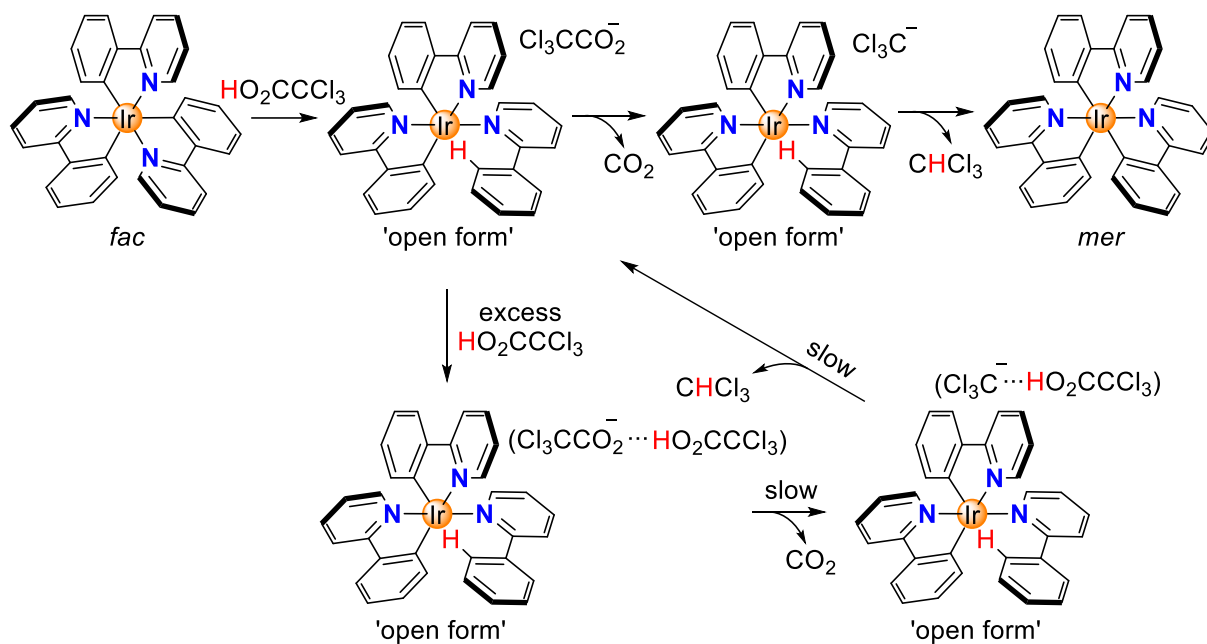
Figure 3.13 Oriented 360° rotation of [2]catenane driven by HO_2CCCl_3 and co-fuels.^{197,207} Adapted and reproduced with permission of John Wiley & Sons, Inc.¹⁹⁷

Earlier, we have shown that $\text{Ir}(\text{C}^{\wedge}\text{N})_3$ complexes could be considered as molecular motors performing a 180° rotation of one ligand during the acid-base-induced *fac*→*mer* isomerization (Scheme 3.9a, for details, see subchapters 3.4, 3.6 and 3.7). We were interested if it is possible to make this system autonomous. Triggering a 180° rotation of one ligand might be achieved by adding one equivalent of the “traceless” decarboxylative acid HO_2CCCl_3 in a single pulse under continuous light irradiation, allowing the system to reset to the original *fac* state (Scheme 3.9b).



Scheme 3.9 Switching between *fac* and *mer* isomers of $\text{Ir}(\text{C}^{\wedge}\text{N})_3$ complexes achieved by a) acid-base reaction with following light irradiation and by b) single-pulse addition of HO_2CCl_3 under continuous light irradiation.

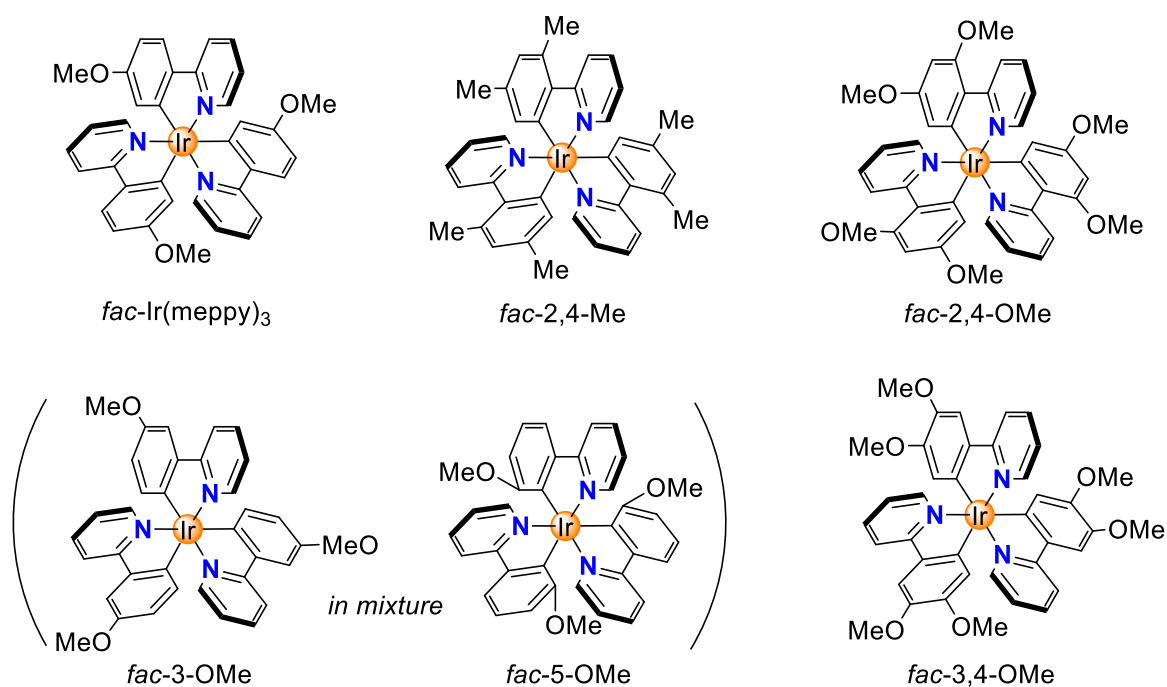
A possible mechanism of the *fac*→*mer* isomerization induced by HO_2CCl_3 is shown in Scheme 3.10. It involves protonation of *fac*- $\text{Ir}(\text{C}^{\wedge}\text{N})_3$ with formation of the ‘open form’ with *mer* arrangement of nitrogen atoms, and following decarboxylation of trichloroacetate with releasing trichloromethanide, which is a strong base. The latter deprotonates the ‘open form’ resulting in the *mer* isomer and CHCl_3 . The importance of using one equivalent of HO_2CCl_3 is demonstrated by the side process shown in Scheme 3.10. In the presence of an excess amount of the acid, the decarboxylation process is hampered by the interaction of trichloroacetate with the acid, which slows down the process.



Scheme 3.10 Proposed mechanism for the *fac*→*mer* isomerization of Ir(C^N)₃ triggered by decarboxylative acid HO₂CCCl₃.

During optimization studies for the protonation of different Ir(C^N)₃ complexes with TFA or HNTf₂, we found that the basicity of the aryl ring (the one being protonated) is an important parameter for the reactivity of the complex towards acids. Ir(C^N)₃ complexes with electron-donating groups on the aryl ring (4-Me, 4-OMe, 4-^tBu) can be protonated by the weaker acid TFA, while Ir(C^N)₃ with electron-withdrawing groups on the aryl ring (4-F, 2,4-diF) are protonated with the stronger acid HNTf₂. Thus, to be able to be protonated by HO₂CCCl₃, the weakest acid in the row HNTf₂ > TFA > HO₂CCCl₃, an iridium complex should possess an increased basicity of the aryl ring.

We have synthesized several substituted *fac*-Ir(C^N)₃ complexes with increased basicity of the aryl ring (Scheme 3.11 and the Experimental part, subchapter 6.3.16). During the test reactions with HO₂CCCl₃, we found that complex *fac*-Ir(meppy)₃ can be protonated with 10 equiv. of HO₂CCCl₃. Complex *fac*-2,4-Me undergoes partial decomposition when treated with HO₂CCCl₃. Complex *fac*-2,4-OMe was found to be inert towards all acids (HO₂CCCl₃, TFA, HNTf₂), and rupture of the Ir–C bond could not be detected by NMR spectroscopy. Attempts to synthesize *fac*-3-OMe led to isolating a mixture of the complexes *fac*-3-OMe and *fac*-5-OMe in 3:1 ratio. Unfortunately, it was not possible to separate them by re-crystallization or by column chromatography.



Scheme 3.11 *fac*-Ir(C^N)₃ complexes selected for the study of *fac*→*mer* isomerization induced by HO₂CCCl₃.

Complex *fac*-3,4-OMe showed somewhat more promising results. As shown by ¹H NMR spectroscopy, the complex undergoes protonation by an equimolar amount of HO₂CCCl₃ with the formation of one species (Fig. 3.14a). The number of signals in the aliphatic region, their multiplicity, and the values of the integrals evidence that the protonated form has a lower symmetry than *fac*-3,4-OMe, yet a higher symmetry than the expected 'open form' with agostic interactions (discussed in subchapter 3.3). Thus, we proposed that the protonation of *fac*-3,4-OMe with HO₂CCCl₃ resulted in a symmetrical adduct with trichloroacetate coordinated to the Ir center (Fig. 3.14b).

These results provoked further investigations on the isomerization of *fac*-3,4-OMe. We examined if the *fac*→*mer* isomerization could be induced by other acids. Indeed, ¹H NMR spectroscopy evidenced that a *fac*→*mer* isomerization occurs after TFA/NEt₃ treatment, and the corresponding 'open form' of low symmetry was formed upon addition of TFA (Fig. 3.15).

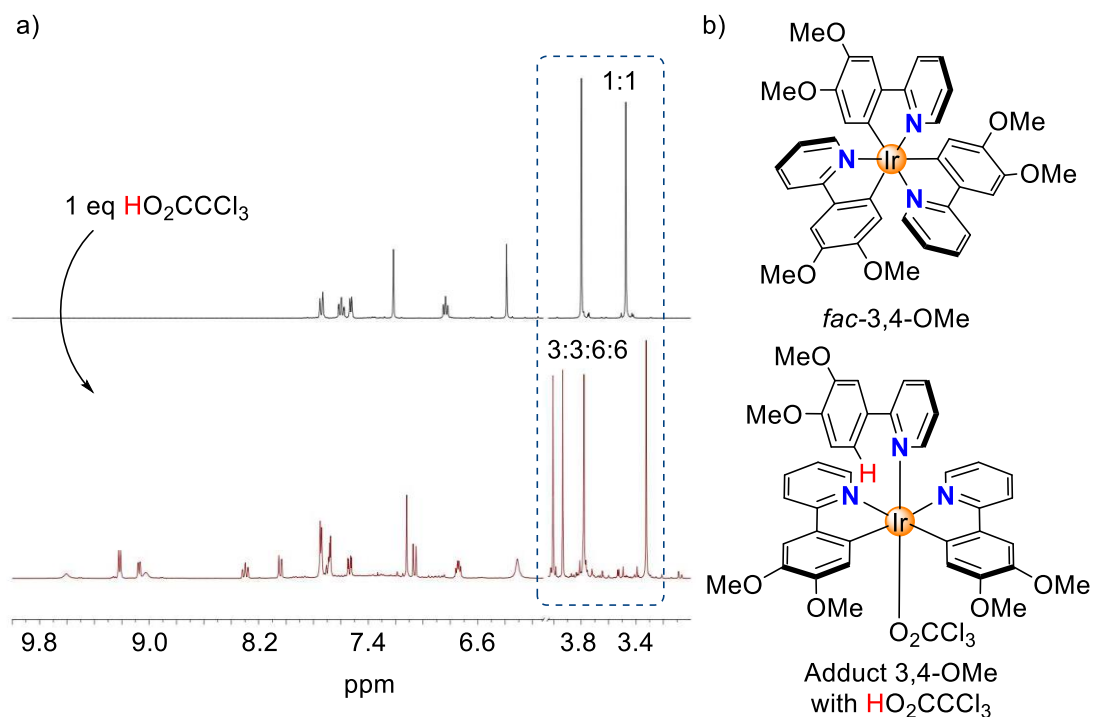


Figure 3.14 a) ^1H NMR spectra (400 MHz, CD_2Cl_2) for the conversion of complex *fac*-3,4-OMe into the acid adduct (b) upon protonation by 1 equiv. HO_2CCCl_3 .

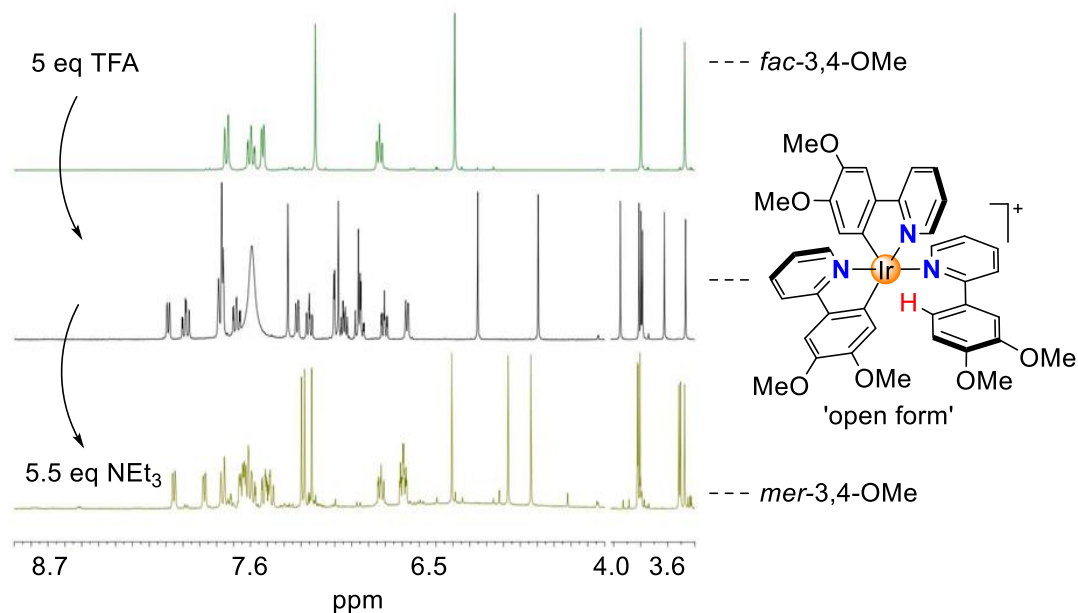


Figure 3.15 ^1H NMR spectra (400 MHz, CD_2Cl_2) for the conversion of *fac*-3,4-OMe into *mer*-3,4-OMe with structure of the 'open form' obtained by protonation of *fac*-3,4-OMe with TFA.

To optimize the conditions for the isomerization with HO_2CCCl_3 and to direct the protonation towards the formation of the ‘open form’ instead of coordination of trichloroacetate to the Ir center, we carried out a solvent screening. After addition of an equimolar amount of HO_2CCCl_3 to *fac*-3,4-OMe in different solvent, we observed that the ‘open form’ can be formed only in deuterated hexafluoroisopropanol (HFIP- d_2), while in other solvents (THF- d_8 , acetone- d_6 , DMSO- d_6), no protonation was detected (Fig. 3.16). Presumably, HFIP solvates trichloroacetate better than CD_2Cl_2 , which hampers its coordination to the Ir center and results in the formation of the ‘open form’. Also, strong solvatochromism was observed when *fac*-3,4-OMe was dissolved in HFIP, resulting in a dark green solution (for photos of the samples, see the Experimental part, subchapter 6.3.16).

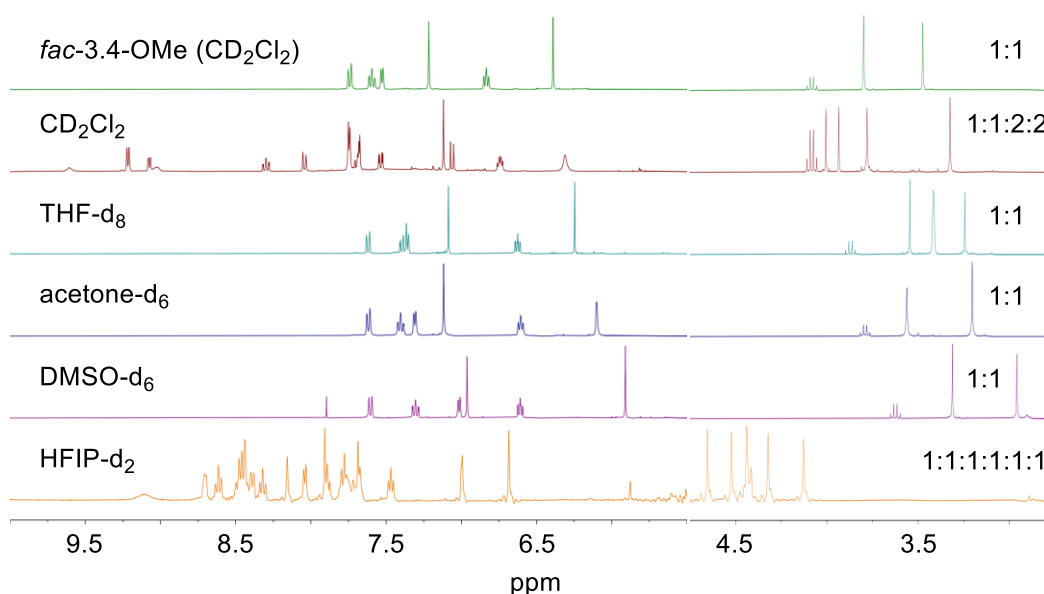


Figure 3.16 ^1H NMR spectra (400 MHz) for *fac*-3,4-OMe and its protonation with 1 equiv. HO_2CCCl_3 in different deuterated solvents.

HFIP- d_2 is a very expensive solvent (122 CHF per 1 g on Sigma Aldrich on September 15th, 2023) with the density of 1.615 g/mL, so one bottle of the commercial solvent is barely enough to prepare two samples for NMR studies. Thus, to follow the test reactions provided in pure HFIP- d_2 by NMR measurements, an aliquot of the reaction mixture (100 μL) was taken and then diluted with CD_2Cl_2 (400 μL). A clean *fac*→*mer* isomerization of 3,4-OMe was achieved after sequential $\text{HO}_2\text{CCCl}_3/\text{NEt}_3$ treatment.

However, according to the ^1H NMR spectra, the protonation step in HFIP- d_2 is slowed down (Fig. 3.17).

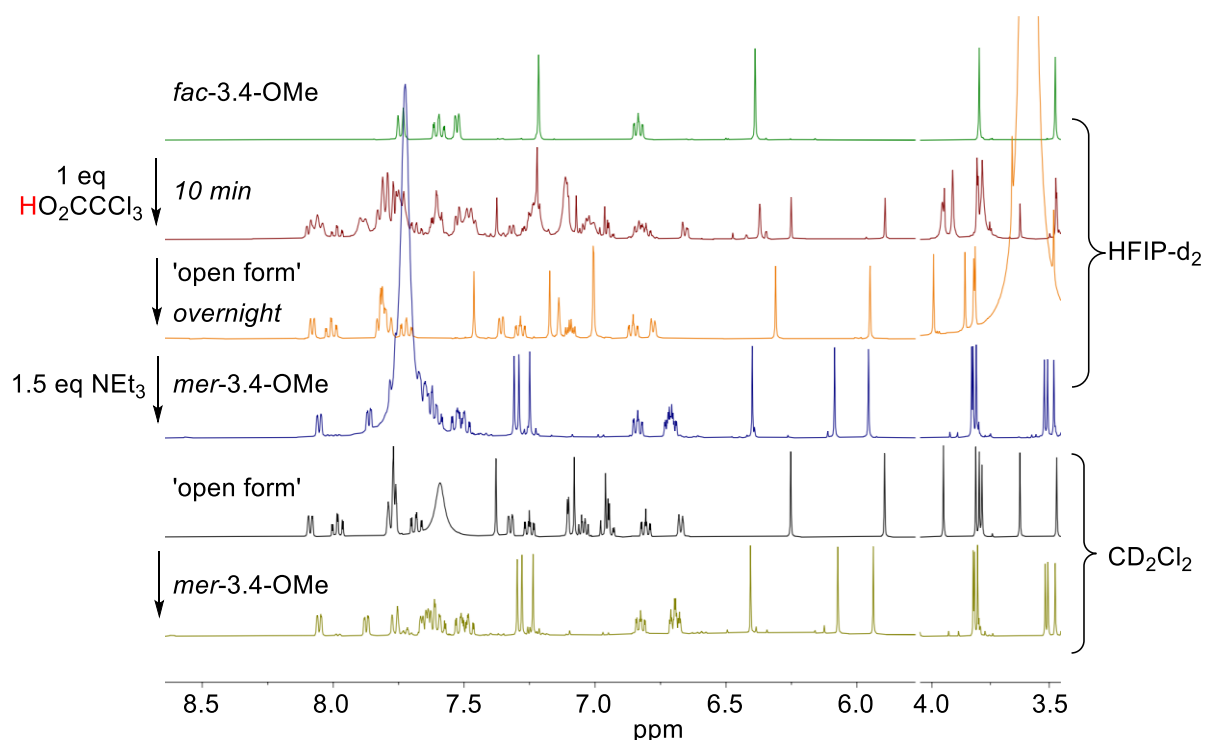


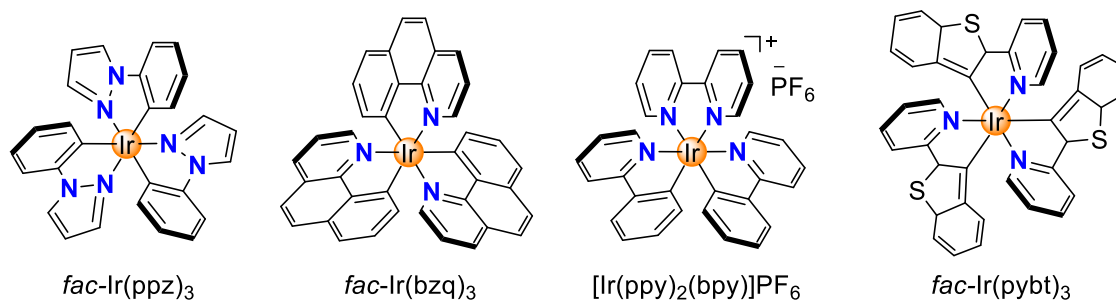
Figure 3.17 ^1H NMR spectra (400 MHz) for *fac*-3,4-OMe and *fac*→*mer* isomerization in HFIP- d_2 – CD_2Cl_2 and in pure CD_2Cl_2 .

Then, we investigated if the decarboxylation of trichloroacetate is possible to drive the deprotonation reaction autonomously. To our disappointment, neither varying the reaction time at room temperature (1–7 days), nor stirring at higher temperatures (40–50 °C, 1–2 h), nor using catalytic amount of co-fuel (10 mol. % NEt_3) led to the decarboxylation of trichloroacetate (for the NMR spectra, see the Experimental part, subchapter subchapter 6.3.16).

To summarize, we managed to find an iridium complex, 3,4-OMe, for which the *fac*→*mer* isomerization can be induced by 1 equiv. of HO_2CCl_3 . However, an autonomous decarboxylation was not achieved.

3.11 Attempted *fac*→*mer* Isomerization of Other Ir Complexes

Next, we were interested if other Ir complexes would undergo acid-base-induced *fac*→*mer* isomerizations. The complexes that we have used are shown in Scheme 3.12.



Scheme 3.12 Ir complexes which were used for attempted acid-base-induced isomerizations.

The facial isomers of the neutral complexes Ir(ppz)₃, Ir(bzq)₃, and Ir(btpy)₃ (ppz = metalated 1-phenylpyrazole, bzq = benzo[*h*]quinoline, and btpy = 2-(benzo[*b*]thiophen-2-yl)pyridine), and the cationic complex [Ir(ppy)₂(bpy)]PF₆ (bpy = 2,2'-bipyridyl) were synthesized (for details, see the Experimental part, subchapter 6.3.17). Subsequently, we examined successive reactions with strong acids (TFA, HNTf₂, HO₂CCCl₃, HBF₄) and then bases (NEt₃, 1,8-Diazabicyclo(5.4.0)undec-7-ene (DBU)).

Protonation of *fac*-Ir(ppz)₃ with clean formation of the corresponding 'open form' was achieved by adding 5 equiv. HNTf₂ (Fig. 3.18, spectrum in black). However, the addition of 5.5 equiv. NEt₃ resulted in a mixture of *mer*-Ir(ppz)₃ and by-products (Fig. 3.18, spectrum in maroon). We attempted varying the base strength at the re-metalation step (NEt₃ vs DBU), but a clean conversion to *mer*-Ir(ppz)₃ was not achieved (for details, see the Experimental part, subchapter 6.3.17). Work-up of the mixture allowed isolation of *mer*-Ir(ppz)₃ in 54% yield (Fig. 3.18, spectrum in yellow). Thus, the HNTf₂/NEt₃-induced *fac*→*mer* isomerization of Ir(ppz)₃ is possible but not quantitative, and an additional work-up step is required. Presumably, the conversion proceeds *via* the protonation of the aryl ring of one ppz ligand, similarly to the acid-base isomerization of Ir(C[^]N)₃ complexes. The quantitative back *mer*→*fac* isomerization was achieved by light irradiation (Fig. 3.18, bottom spectrum in green).

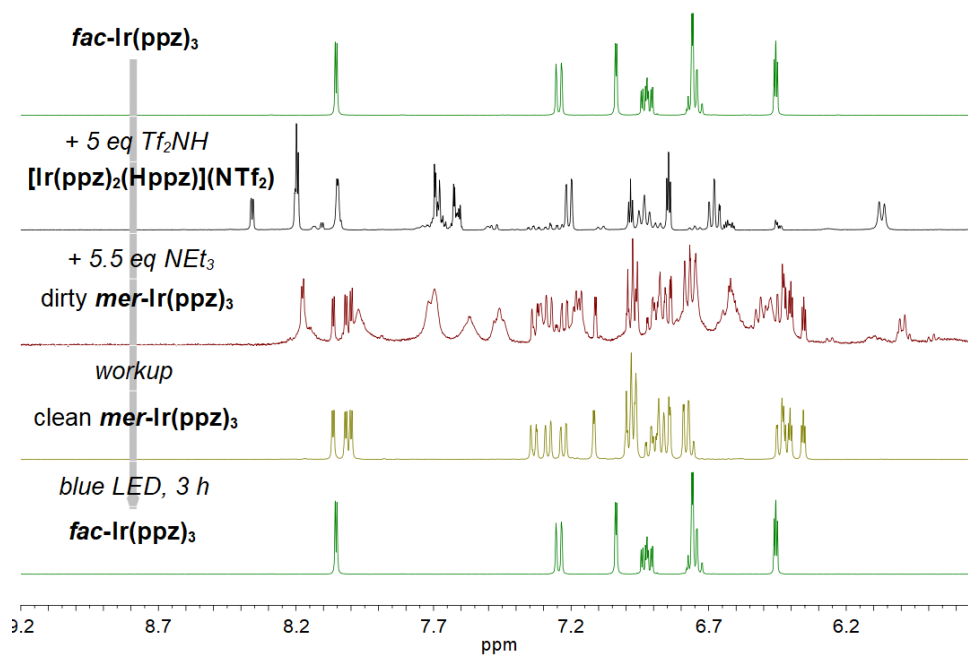


Figure 3.18 ^1H NMR (400 MHz, CD_2Cl_2) spectra for $\text{fac} \rightarrow \text{mer} \rightarrow \text{fac}$ isomerization of $\text{Ir}(\text{ppz})_3$.

The complex $\text{fac-Ir}(\text{bzq})_3$ was poorly soluble in several deuterated solvents, which made the NMR studies complicated and finally not representative. However, we observed the protonation of $\text{fac-Ir}(\text{bzq})_3$ with TFA, although the spectrum appeared quite complicated for analysis.

The cationic complex $[\text{Ir}(\text{ppy})_2(\text{bpy})]\text{PF}_6$ could not be protonated by TFA or by HNTf_2 (Fig. 3.19).

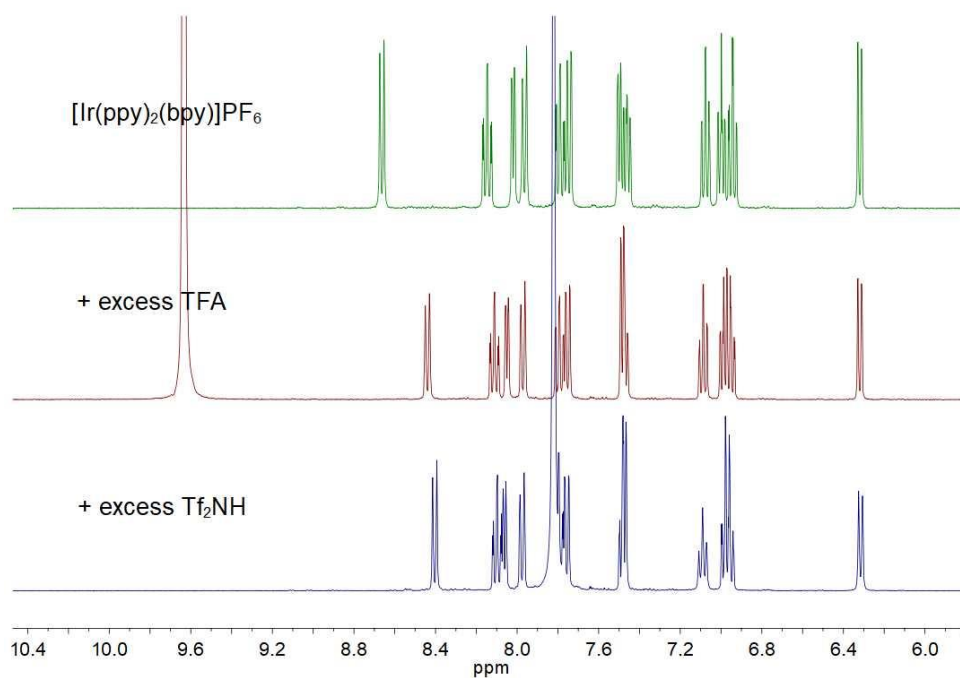


Figure 3.19 ^1H NMR (400 MHz, 298 K) spectra for $[\text{Ir}(\text{ppy})_2(\text{bpy})]\text{PF}_6$ in CD_2Cl_2 and after addition of excess amount TFA and HNTf_2 .

Upon TFA/ NEt_3 or $\text{HO}_2\text{CCCl}_3/\text{NEt}_3$ treatment, the complex $\text{Ir}(\text{btpy})_3$ restored its *fac* configuration (Fig. 3.20 and 3.21). When HNTf_2 or HBF_4 were added, *fac*- $\text{Ir}(\text{btpy})_3$ quantitatively converts into a stable compound of lower symmetry, which is inert to NEt_3 , and its' NMR spectrum does not match that of *mer*- $\text{Ir}(\text{btpy})_3$ (Fig. 3.22 and 3.23, spectra in black). We suppose that an acid adduct is formed, similar to what was observed for complex *fac*-3,4-OMe protonated by HO_2CCCl_3 in CD_2Cl_2 (Fig. 3.14b).

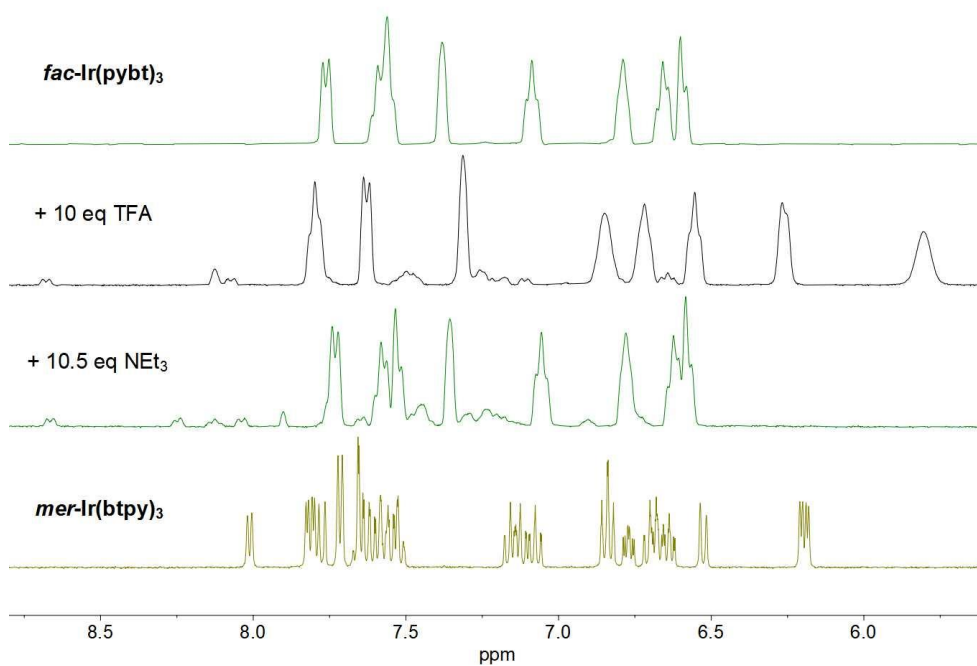


Figure 3.20 ^1H NMR (400 MHz, 298 K) spectra for $\text{fac-Ir}(\text{btpy})_3$ in CD_2Cl_2 and after successive addition of 10 equiv. TFA and 10.5 equiv. NEt_3 .

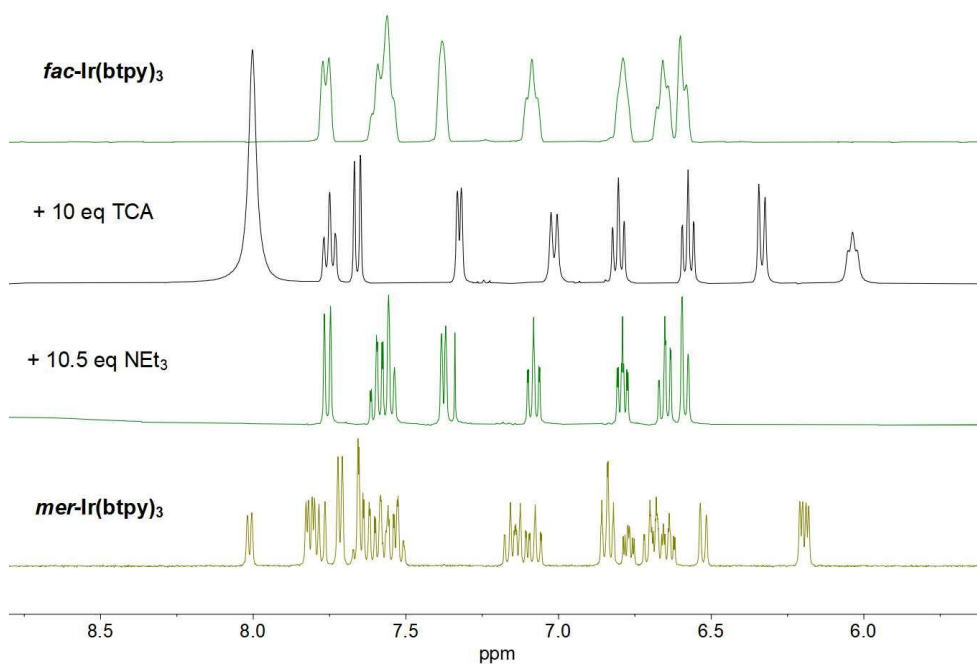


Figure 3.21 ^1H NMR (400 MHz, 298 K) spectra for $\text{fac-Ir}(\text{btpy})_3$ in CD_2Cl_2 and after successive addition of 10 equiv. HO_2CCl_3 and 10.5 equiv. NEt_3 .

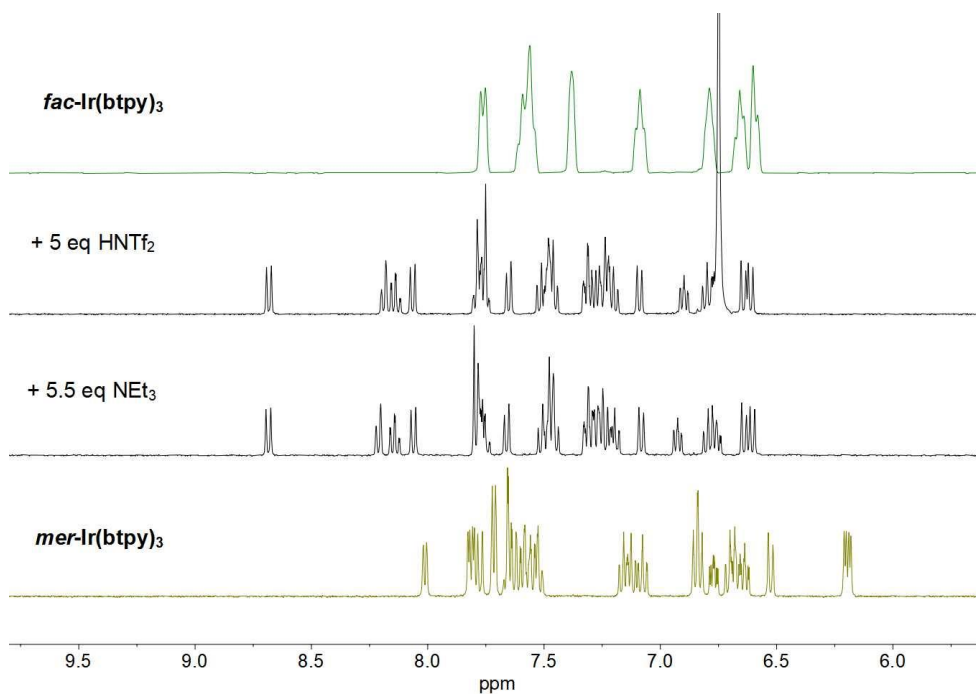


Figure 3.22 ¹H NMR (400 MHz, 298 K) spectra for *fac*-Ir(btpy)₃ in CD₂Cl₂ and after successive addition of 5 equiv. HNTf₂ and 5.5 equiv. NEt₃.

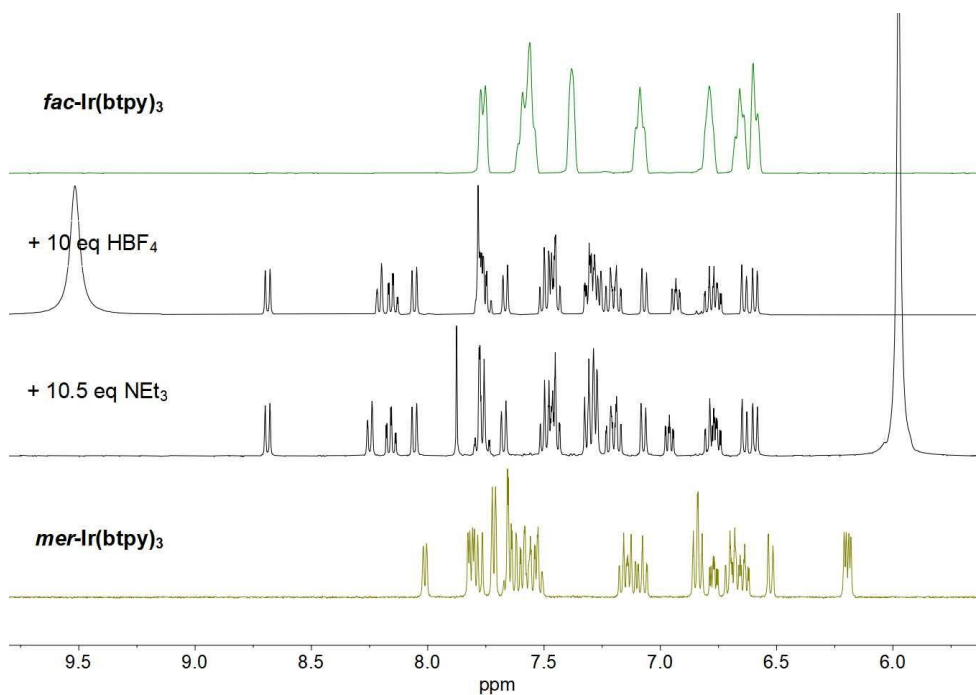
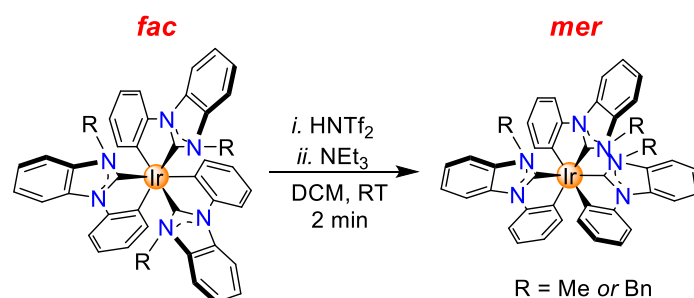


Figure 3.23 ¹H NMR (400 MHz, 298 K) spectra for *fac*-Ir(btpy)₃ in CD₂Cl₂ and after successive addition of 10 equiv. HBF₄ and 10.5 equiv. NEt₃.

Chapter 4. Acid-Base-Induced *fac*→*mer* Isomerization of Ir Complexes with Cyclometalated NHC Ligands



This chapter is based on a publication:

A.Yu. Gitlina, F. Fadaei-Tirani, K. Severin “The acid-mediated isomerization of iridium(III) complexes with cyclometalated NHC ligands: kinetic vs thermodynamic control”, *Dalton Trans.* **2023**, 52 (9), 2833–2837. [DOI: 10.1039/D2DT04039E](https://doi.org/10.1039/D2DT04039E)

Reprinted and adapted version with permission from The Royal Society of Chemistry.

A.Yu. G. and K. S. initiated the study, **A.Yu. G.** performed the experiments and analyzed the data, F. F.-T. collected and processed the X-ray data. **A.Yu. G.** and K. S. co-wrote the manuscript. All authors discussed the results and commented on the manuscript.

4.1 Introduction

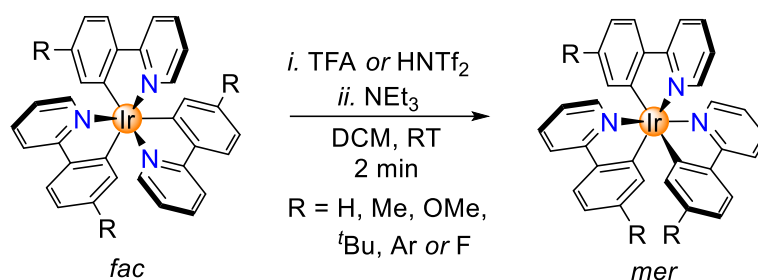
Iridium(III) complexes bearing three cyclometalated NHC ligands, $\text{Ir}(\text{C}^{\wedge}\text{C})_3$, were first described in 1982 by M. Lappert and co-workers.¹²⁰ The interest in these compounds was renewed by a study of S. Forrest and M. Thompson in 2005, in which they showed that $\text{Ir}(\text{C}^{\wedge}\text{C})_3$ complexes can display blue phosphorescence.¹²¹ Blue emitters are important for OLEDs, and $\text{Ir}(\text{C}^{\wedge}\text{C})_3$ complexes have been widely investigated in this context (for details and more references, see subchapter 1.3.4).²⁰⁸

To date, a limiting factor for studies with $\text{Ir}(\text{C}^{\wedge}\text{C})_3$ complexes is synthetic access. A review about synthetic methods for $\text{Ir}(\text{C}^{\wedge}\text{C})_3$ complexes is provided in subchapter 1.3.2. Briefly, the preparation of the ligand precursors can be demanding, and also the final metalation step often gives moderate yields.¹²¹ In addition, the complexes are typically obtained as a mixture of *fac* and *mer* isomers.

For the structurally related $\text{Ir}(\text{C}^{\wedge}\text{N})_3$ complexes ($\text{C}^{\wedge}\text{N}$ = cyclometalated arylpyridyl ligand), a *mer*→*fac* isomerization can be achieved thermally or by light irradiation.^{103,127,128,130,178} As mentioned in subchapter 1.3.3, attempts to use this procedure for $\text{Ir}(\text{C}^{\wedge}\text{C})_3$ complexes were not successful.¹²¹ In 2017, H.-H. Johannes and co-workers reported that $\text{Ir}(\text{C}^{\wedge}\text{C})_3$ complexes with metalated 1-phenyl-3-methylbenzimidazolin-2-ylidene (pmb) or 1-phenyl-3-benzylbenzimidazolin-2-ylidene (pbb) ligands can be isomerized with Brønsted acids (for procedure details, see subchapter 1.3.3).¹³¹ The acid-catalyzed *mer*→*fac* isomerization is interesting from a preparative point of view, because it allows increasing the overall yield of the *fac* isomer. The methodology can be used for other $\text{Ir}(\text{C}^{\wedge}\text{C})_3$ complexes, as reported in a series of recent publications.^{132–136}

To date, there is no procedure for the controlled conversion of *fac*- $\text{Ir}(\text{C}^{\wedge}\text{C})_3$ complexes into the corresponding *mer* isomers. Small amounts of *mer*- $\text{Ir}(\text{C}^{\wedge}\text{C})_3$ were detected after sublimation of a *fac*- $\text{Ir}(\text{C}^{\wedge}\text{C})_3$ complex.²⁰⁹ Studies with *mer* isomers, therefore, require chromatographic separation of the *fac* isomers. In this context, it is worth noting that *mer*- $\text{Ir}(\text{C}^{\wedge}\text{C})_3$ complexes can display favorable characteristics for applications in phosphorescent OLEDs (for details, see subchapter 1.3.4).^{135,146,147,209}

We have recently reported a method for clean and fast *fac*→*mer* isomerization of Ir(C[^]N)₃ complexes (Scheme 4.1 and Chapter 3).²¹⁰ The transformation can be achieved by the addition of a strong Brønsted acid (TFA or bistriflimidic acid, HNTf₂), followed by neutralization with base (NEt₃). The reaction was shown to involve protonated complexes of type [Ir(C[^]N)₂(HC[^]N)]⁺ as intermediates (for structural details, see subchapter 3.3).

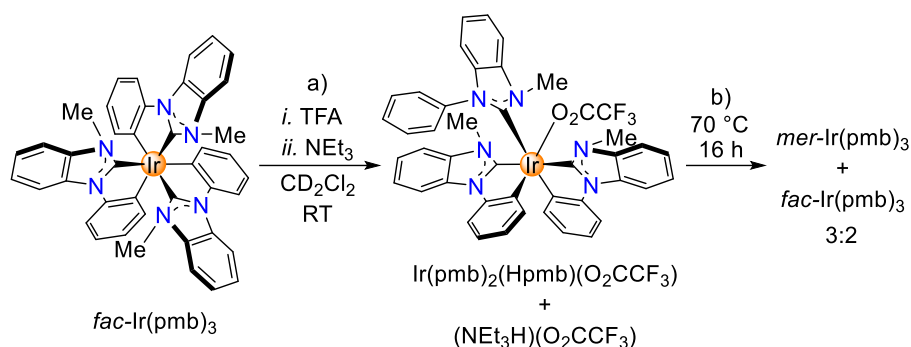


Scheme 4.1 The acid-mediated *mer*→*fac* isomerization of Ir(C[^]C:)₃ complexes.²¹⁰

Given that Brønsted acids can mediate the *mer*→*fac* isomerization of Ir(C[^]C:)₃ complexes, it may seem unlikely that the inverse *fac*→*mer* isomerization can be achieved with an acid/base treatment. However, we show below that such an isomerization is indeed possible if the reaction is performed under kinetic control.

4.2 Protonation of *fac*-Ir(C[^]C:)₃ Complexes and Possible Mechanism of the *fac*→*mer* Isomerization

We started our investigations with *fac*-Ir(pmb)₃.¹²¹ In order to induce a *fac*→*mer* isomerization, we examined the conditions that we had developed for Ir(C[^]N)₃ complexes (for details, see subchapter 3.3). A solution of *fac*-Ir(pmb)₃ in CD₂Cl₂ was first treated with TFA (5 equiv.) and then with NEt₃ (5.5 equiv.) (Scheme 4.2a). The ¹H NMR spectrum of the resulting solution was complex, and it did neither match the spectrum of the desired *mer*-Ir(pmb)₃ nor that of the starting material *fac*-Ir(pmb)₃ (Fig. 4.1a).



Scheme 4.2 a) The sequential addition of TFA (5 equiv.) and NEt₃ (5.5 equiv.) to a solution of *fac*-Ir(pmb)₃ in CD₂Cl₂ results in the formation of the TFA adduct Ir(pmb)₂(Hpmb)(O₂CCF₃). b) Heating for 16 h at 70 °C gives a mixture of *fac*-Ir(pmb)₃ and *mer*-Ir(pmb)₃.

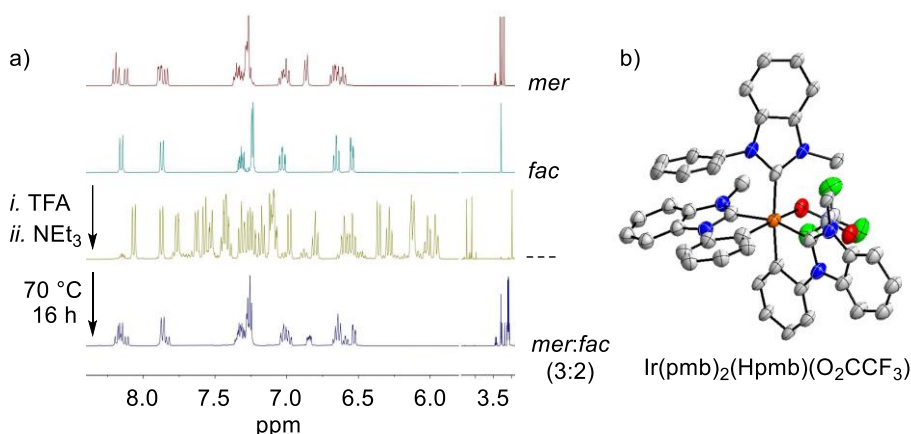


Figure 4.1 a) ¹H NMR spectra (400 MHz) of a solution of *fac*-Ir(pmb)₃ in CD₂Cl₂ (spectrum in teal), after sequential addition of TFA (5 equiv.) and NEt₃ (5.5 equiv.; spectrum in dark-yellow), and after heating at 70 °C for 16 h (spectrum in navy). The spectrum of *mer*-Ir(pmb)₃ in CD₂Cl₂ is given for comparison (in maroon). b) Crystal structure of Ir(pmb)₂(Hpmb)(O₂CCF₃) with thermal ellipsoids at 50% probability; hydrogen atoms and co-crystallized (NEt₃H)(O₂CCF₃) are not shown for clarity.

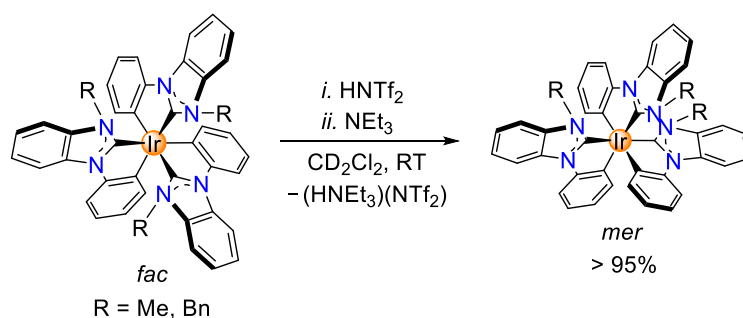
Gas phase diffusion of pentane into the CD₂Cl₂ solution of the obtained compound resulted in the formation of single crystals, which were analyzed by XRD. X-ray crystallography revealed that the TFA adduct Ir(pmb)₂(Hpmb)(O₂CCF₃) had formed (Fig. 4.1b). This complex shows three chemically distinct carbene ligands, only two of which are orthometalated. The third ligand binds exclusively *via* the carbene and displays a ‘free’ phenyl group. The structure of Ir(pmb)₂(Hpmb)(O₂CCF₃) in the solid

state matches what was observed by ^1H NMR spectroscopy. The structure is also in line with a computational study, which had concluded that protonation of *fac*-Ir(pmb) $_3$ should occur at the phenyl group rather than at the carbene.²¹¹

The three carbene donors in Ir(pmb) $_2$ (Hpmb)(O $_2$ CCF $_3$) show a meridional arrangement. The complex is therefore pre-organized to form *mer*-Ir(pmb) $_3$ upon orthometalation of the monodentate carbene ligand. We found that metalation could be induced by heating the CD $_2$ Cl $_2$ solution of Ir(pmb) $_2$ (Hpmb)(O $_2$ CCF $_3$) in a sealed NMR tube to 70 °C for 16 h without base addition. The ^1H NMR spectrum of the resulting solution showed that *mer*-Ir(pmb) $_3$ had indeed formed, but along with *fac*-Ir(pmb) $_3$ (*mer:fac* = 3:2) (Fig. 4.1a).

We hypothesized that forcing conditions for the re-metalation step by heating were responsible for the poor selectivity. Therefore, we replaced TFA with bistriflimidic acid (HNTf $_2$). The corresponding Tf $_2$ N $^-$ anion is a weaker ligand, and it is not expected to interact strongly with the Ir center.

When a solution of *fac*-Ir(pmb) $_3$ in CD $_2$ Cl $_2$ was first treated with HNTf $_2$ (1 equiv.) and then with NEt $_3$ (1.5 equiv.), we observed the clean formation of the *mer* isomer (Scheme 4.3). A similar isomerization was achieved with the structurally related complex *mer*-Ir(pbb) $_3$ having *N*-benzyl instead of *N*-methyl groups.



Scheme 4.3 A clean *fac*→*mer* isomerization can be achieved by the sequential addition of HNTf $_2$ (1 equiv.) and NEt $_3$ (1.5 equiv.) to a solution of *fac*-Ir(pmb) $_3$ or *fac*-Ir(pbb) $_3$ in CD $_2$ Cl $_2$.

In order to understand the different behaviour of the system when HNTf $_2$ is added compared to TFA, we analyzed the solution of *fac*-Ir(pmb) $_3$ after adding HNTf $_2$. The ^1H NMR spectrum showed that a complex with three chemically distinct carbene ligands

had formed (Fig. 4.2a). The signal multiplicity indicated that protonation had occurred at the phenyl group, as observed for TFA. Similar spectra were obtained for *fac*-Ir(pbb)₃ (for the NMR spectra, see the Experimental part, subchapter 6.4.3).

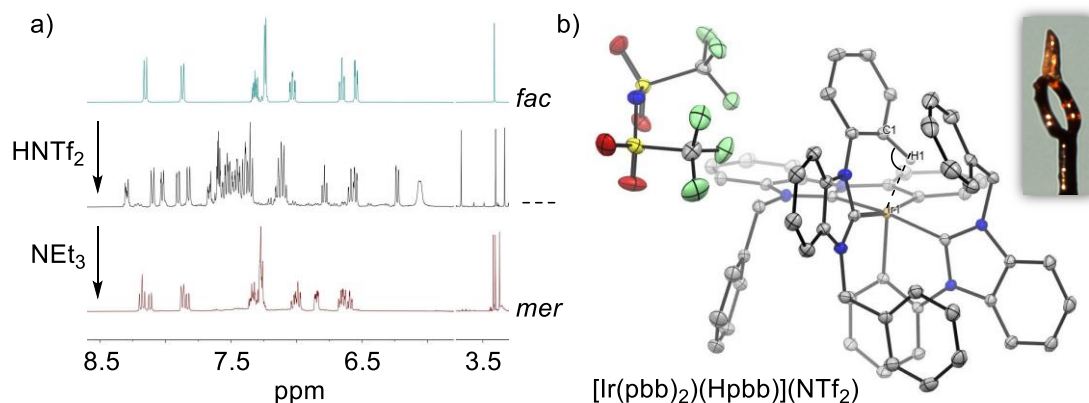


Figure 4.2 a) ¹H NMR spectra (400 MHz) of a solution of *fac*-Ir(pmb)₃ in CD₂Cl₂ (spectrum in teal), after sequential addition of HNTf₂ (1 equiv.; spectrum in black) and NEt₃ (1.5 equiv., spectrum in maroon). b) Crystal structure of [Ir(pbb)₂(Hpbb)](NTf₂) with thermal ellipsoids at 50% probability; other hydrogen atoms are omitted for clarity.

For the reaction with *fac*-Ir(pbb)₃, we obtained single crystals of the protonated form. The XRD analysis showed that a salt [Ir(pbb)₂(Hpbb)](NTf₂) (Fig. 4.2b) had formed. The ‘open form’ features two orthometalated carbene ligands and one monodentate carbene ligand with a ‘free’ phenyl group. One hydrogen of the phenyl group forms an agostic interaction¹⁸³ with the cationic Ir center (Ir⋯H ~ 1.85 Å; Ir–H–C ~ 109°). Overall, the coordination environment around Ir can be described as a distorted octahedral.

As observed for Ir(pmb)₂(Hpmb)(O₂CCF₃) (Fig. 4.1b), the three carbene C-donors in [Ir(pbb)₂(Hpbb)](NTf₂) adopt a meridional arrangement. It is worth noting that there are two possible isomers with a *mer* configuration of the carbene donors, namely an isomer **A** having the monodentate carbene in *trans* position to a phenyl group, and an isomer **B** with the monodentate carbene in *trans* position to another carbene donor (Fig. 4.3a). The structural data suggest that isomer **A** is preferred. This assumption is corroborated by the early work of M. Lappert and co-workers.¹²⁰ They had protonated an Ir(C[^]C:)₃ complex with anhydrous HCl, and they also observed a complex of type **A**. A different behaviour was observed during our earlier study with Ir(C[^]N)₃ complexes (for details, see subchapter 3.3). Protonation of *fac*-Ir(ppy)₃ had resulted in the

formation of a cationic complex $[\text{Ir}(\text{ppy})_2(\text{Hppy})]^+$, with the monodentate pyridyl ligand in *trans* position to another pyridyl ligand, which corresponds to an isomer of type **B** (Fig. 4.3b).

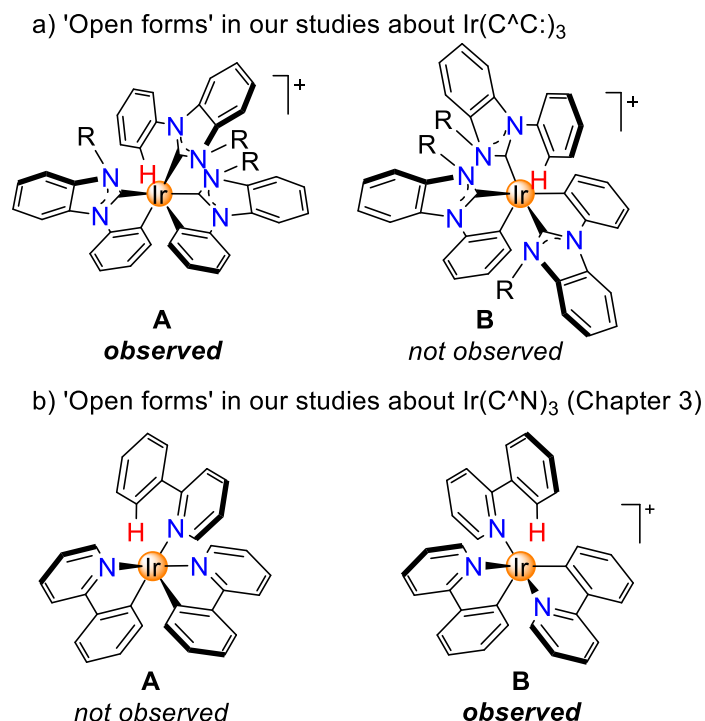
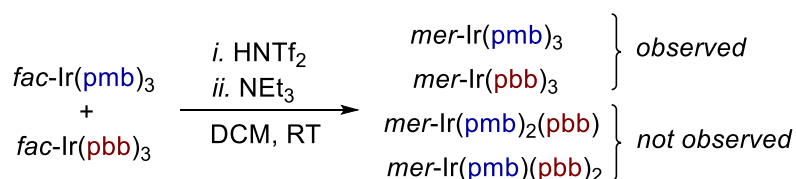


Figure 4.3 Possible isomers for protonated $[\text{Ir}(\text{C}^{\wedge}\text{C}:)_2(\text{HC}^{\wedge}\text{C}:)]^+$ (a) and $[\text{Ir}(\text{C}^{\wedge}\text{N})_2(\text{HC}^{\wedge}\text{N})]^+$ (b) complexes.

4.3 Investigation of Ligand Exchange

To examine if ligand scrambling can occur during the $\text{HNTf}_2/\text{NEt}_3$ -mediated *fac*→*mer* isomerization of $\text{Ir}(\text{C}^{\wedge}\text{C}:)_3$ complexes, we have performed the transformation with an equimolar amount of *fac*- $\text{Ir}(\text{pmb})_3$ and *fac*- $\text{Ir}(\text{pbb})_3$. Analysis of the mixture after the acid/base treatment by mass spectrometry showed peaks corresponding to $\text{Ir}(\text{pmb})_3$ and $\text{Ir}(\text{pbb})_3$, whereas peaks corresponding to the heteroleptic complexes $\text{Ir}(\text{pmb})_2(\text{pbb})$ and $\text{Ir}(\text{pmb})(\text{pbb})_2$ were not detected (Scheme 4.4, Fig. 4.4). These results imply negligible ligand scrambling during the isomerization process.



Scheme 4.4 The *fac*→*mer* isomerization of a mixture of Ir(pmbi)₃ and Ir(pbbi)₃ does not lead to ligand scrambling.

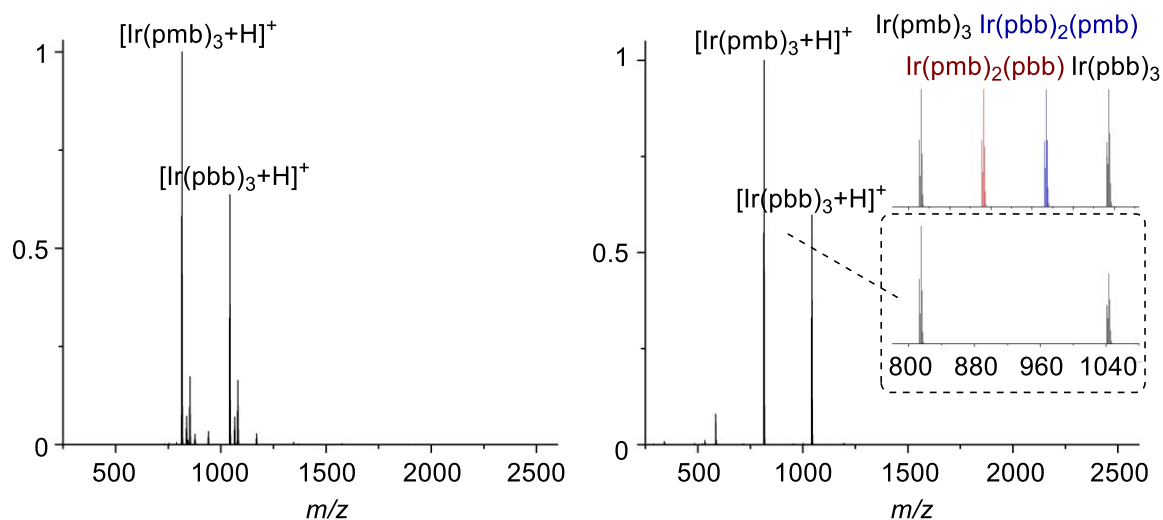
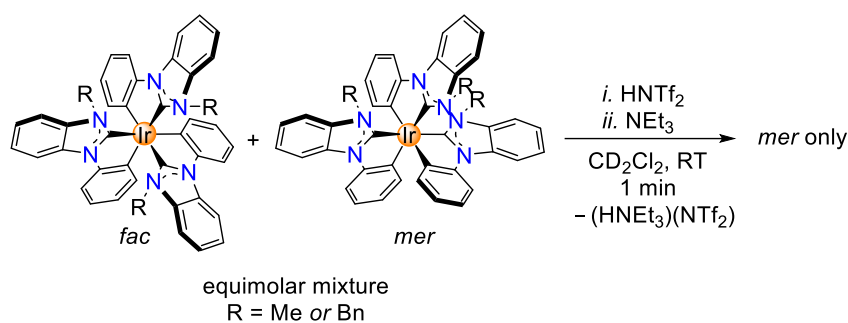


Figure 4.4 Nanochip-ESI⁺ HRMS of the starting mixture of *fac*-Ir(pmb)₃ and *fac*-Ir(pbb)₃ (left) and after its *fac*→*mer* isomerization (right). Simulated spectra of the hypothetical heteroleptic complexes are shown in colour.

4.4 Isomerization of a Mixture of *fac* and *mer* Isomers

A benefit of the acid-mediated *mer*→*fac* isomerization developed by H.-H. Johannes and co-workers (Scheme 4.1a) is the possibility to increase the overall yield of the *fac*-Ir(C[^]C:)₃ isomer. To demonstrate a similar advantage for our inverse *fac*→*mer* isomerization, we have started with an equimolar mixture of *fac*-Ir(pmb)₃ (or *fac*-Ir(pbb)₃) and *mer*-Ir(pmb)₃ (or *mer*-Ir(pbb)₃). This model combination simulates the isomeric mixture that can be obtained during the synthesis of Ir(C[^]C:)₃ complexes. Using the standard HNTf₂/NET₃ conditions, we were able to convert this mixture cleanly within 2 minutes into the pure *mer* isomer (Scheme 4.5, Fig. 4.5; for the spectra with Ir(pbb)₃, see the Experimental part, subchapter 6.4.6).



Scheme 4.5 An equimolar mixture of *fac*- and *mer*-Ir(C^AC:)₃ complexes is converted within two minutes into pure *mer*-Ir(C^AC:)₃ by sequential addition of HNTf₂ (2 equiv.) and NEt₃ (2.5 equiv.).

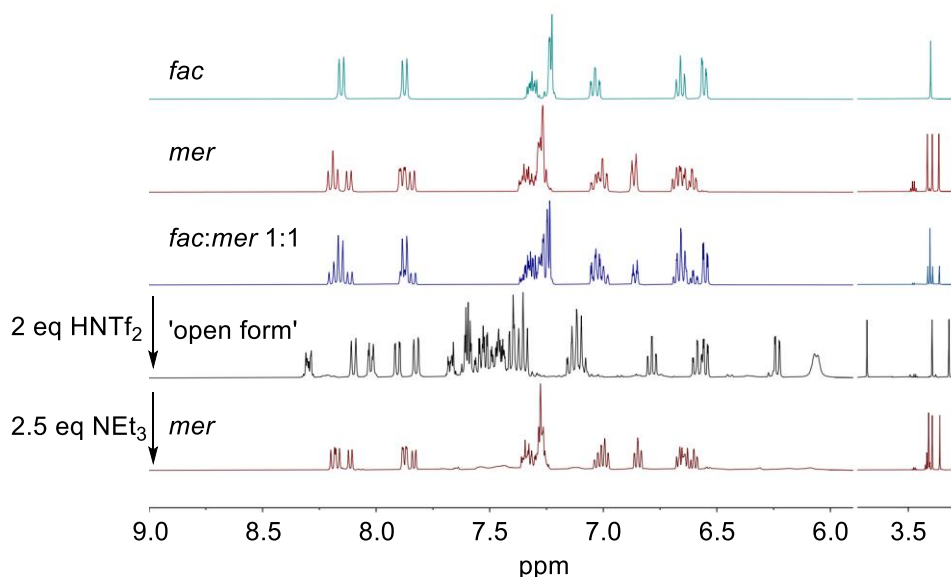


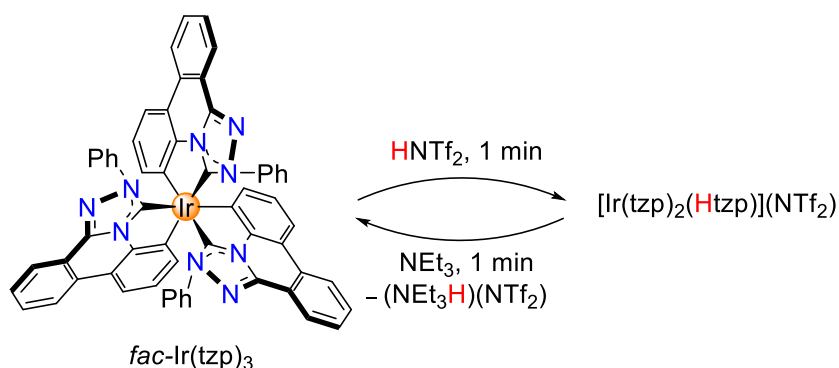
Figure 4.5 ¹H (400 MHz, CD₂Cl₂) NMR spectra for *fac*- and *mer*-Ir(pmb)₃ and for the acid-base-induced conversion of the mixture of the *fac* and *mer* isomers to the *mer* isomer through [Ir(pmb)₂(Hpmb)](NTf₂).

4.5 Isomerization of a Sterically Hindered Ir(C^AC:)₃ Complex

The acid/base-induced isomerization relies on a structural *fac*→*mer* reorganization upon protonation. Carbene ligands with pronounced steric demand and/or with reduced conformational flexibility are expected to impede such a reorganization. We have examined the isomerization of an iridium complex with three 1-phenyl-1,2,4-triazolo[4,3-*f*]phenanthridine based carbene ligands, Ir(tzp)₃.²¹² Due to the presence

of a rigid fused polycyclic aromatic system, the conformational flexibility of tzp ligand is strongly reduced when compared to pmb or pbb ligands.

In situ ^1H NMR spectroscopy (CD_2Cl_2) showed that *fac*-Ir(tzp) $_3$ can be converted cleanly into the protonated form $[\text{Ir}(\text{tzp})_2(\text{Htzp})](\text{NTf}_2)$ by the addition of one equivalent of HNTf_2 (Scheme 4.6 and Fig. 4.6). The protonation was accompanied by a colour change of the solution from pale yellow to orange.



Scheme 4.6 The addition of HNTf_2 (1 equiv.) to a solution of *fac*-Ir(tzp) $_3$ in CD_2Cl_2 leads to the formation of the protonated complex $[\text{Ir}(\text{tzp})_2(\text{Htzp})]^+$. The quick addition of NEt_3 (1.5 equiv.) does not lead to an isomerization but to re-formation of *fac*-Ir(tzp) $_3$.

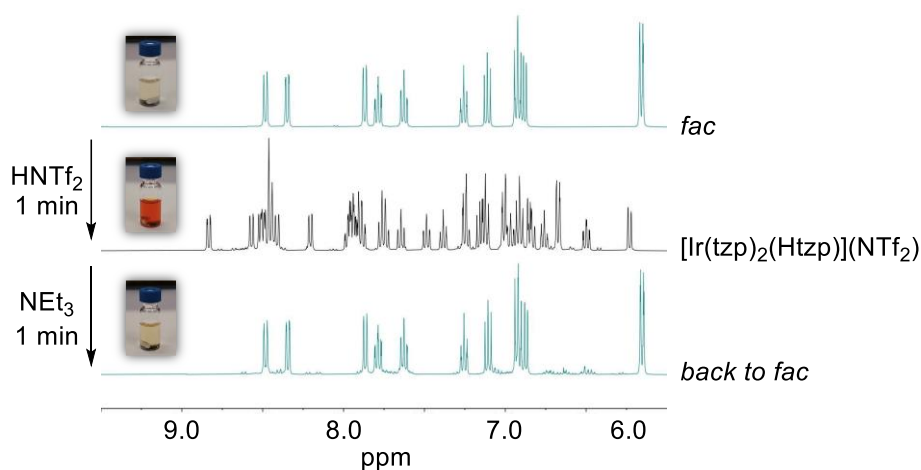


Figure 4.6 ^1H NMR spectra (400 MHz) of a solution of *fac*-Ir(tzp) $_3$ in CD_2Cl_2 (top spectrum in teal), after quick sequential addition of HNTf_2 (1 equiv.; spectrum in black) and NEt_3 (1.5 equiv., bottom spectrum in teal).

Deprotonation of $[\text{Ir}(\text{tzp})_2(\text{Htzp})](\text{NTf}_2)$ with NEt_3 (1.5 equiv.) did not result in the formation of the *mer* isomer. Instead, we observed the clean re-formation of *fac*-Ir(tzp) $_3$

(Fig. 4.6). Apparently, the reduced flexibility of tzp hampers a reorganization of *fac* to *mer* at the stage of the protonated complex. Based on these NMR studies, we assumed that the protonated complex is an ‘open form’ (two orthometalated carbene ligands and one monodentate carbene ligand with a ‘free’ phenyl group) with a facial arrangement of carbene donors, so-called ‘*fac*’-[Ir(tzp)₂(Htzp)](NTf₂). To verify this assumption, we crystallized the ‘open form’, and the XRD analysis revealed the ‘open form’ with *mer* arrangement of carbene donors (Fig. 4.7). In this structure, the hydrogen of the phenyl group also forms an agostic interaction¹⁸³ with the cationic Ir center (Ir···H ~ 1.90 Å; Ir–H–C ~ 131.9°). Additionally, polymorphism in the crystals of ‘*mer*’-[Ir(tzp)₂(Htzp)](NTf₂) was observed by XRD analysis (for details, see the Experimental part, subchapter 6.4.5). ¹H NMR spectroscopy showed that the spectrum of the crystals is different from what was measured once the solution of *fac*-Ir(tzp)₃ in CD₂Cl₂ was treated with HNTf₂ (Fig. 4.8). The NMR spectrum of the crystals dissolved in CD₂Cl₂ shows one major species, which is most probably ‘*mer*’-[Ir(tzp)₂(Htzp)](NTf₂), and traces of ‘*fac*’-[Ir(tzp)₂(Htzp)](NTf₂). It means that the *fac*→*mer* isomerization of Ir(tzp)₃ upon protonation is in fact possible but not clean and slowed down by the bulkiness and rigidity of the tzp ligands. The kinetics studies using NMR spectroscopy revealed that ‘*fac*’→‘*mer*’ isomerization of [Ir(tzp)₂(Htzp)](NTf₂) proceeds in 15 h with 82.5% yield (for the spectra, see the Experimental part, subchapter 6.4.5).

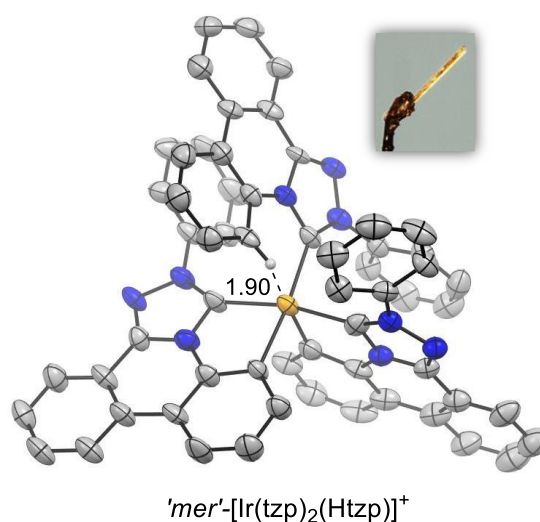


Figure 4.7 Photo of the crystal and crystal structure of ‘*mer*’-[Ir(tzp)₂(Htzp)](NTf₂). Thermal ellipsoids at 50% probability; other hydrogen atoms and counter anion Tf₂N⁻ are not shown for clarity.

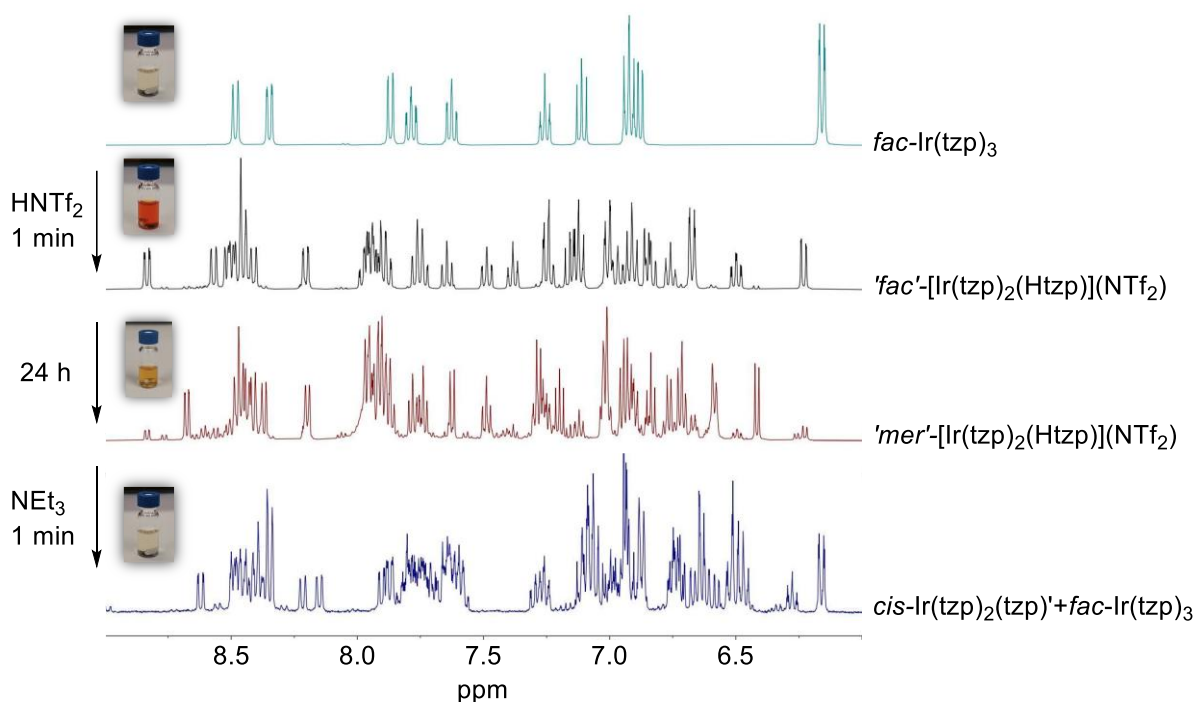


Figure 4.8 ^1H NMR spectra (400 MHz) of a solution of *fac*-Ir(tzp)₃ in CD_2Cl_2 (spectrum in teal), after quick addition of HNTf₂ (1 equiv.; spectrum in black), leaving this mixture for 24 h (spectrum in maroon), and after addition of NEt₃ (1.5 equiv., spectrum in navy).

However, the treatment of '*mer*'-[Ir(tzp)₂(Htzp)](NTf₂) with NEt₃ did not lead to formation of *mer*-Ir(tzp)₃. Instead, a mixture of a pseudo-heteroleptic complex *cis*-Ir(tzp)₂(tzp)' with abnormal coordination of one ligand (Fig. 4.9) and *fac*-Ir(tzp)₃ was obtained (Fig. 4.8). Earlier, the complex *cis*-Ir(tzp)₂(tzp)' was isolated during the synthesis of *fac*-Ir(tzp)₃ with 7% yield (work by H.-J. Son, S. Kang and co-workers).²¹²

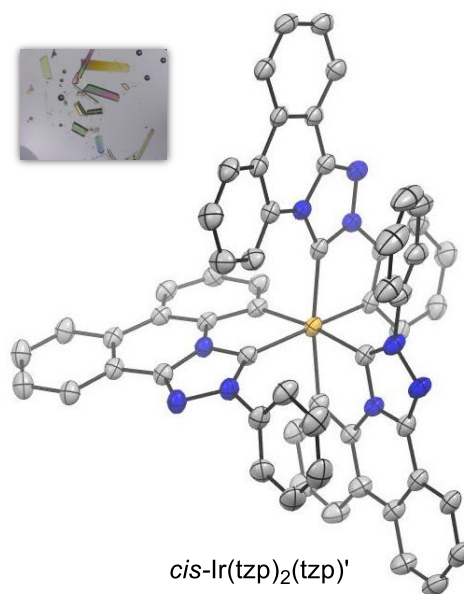
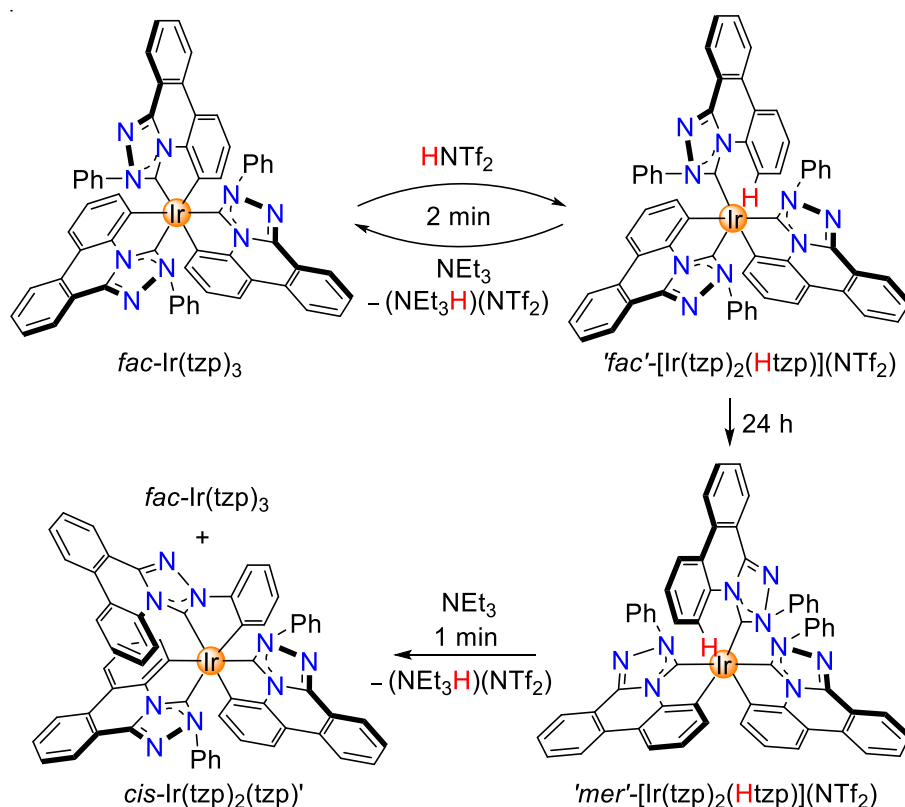


Figure 4.9 Photo of the crystals and crystal structure of *cis*-Ir(tzp)₂(tzp)' obtained after NEt₃-treatment of '*mer*'-[Ir(tzp)₂(Htzp)](NTf₂). Thermal ellipsoids at 50% probability, hydrogen atoms are not shown for clarity.

The reactions proceeding upon HNTf₂/NEt₃ addition to *fac*-Ir(tzp)₃ can be summarized in Scheme 4.7. When HNTf₂ is added to *fac*-Ir(tzp)₃, the unstable protonated complex, '*fac*'-[Ir(tzp)₂(Htzp)](NTf₂), is formed. If NEt₃ is added to it quickly, a back conversion to *fac*-Ir(tzp)₃ happens. With time (24 h), '*fac*'-[Ir(tzp)₂(Htzp)](NTf₂) converts to the stable protonated complex, '*mer*'-[Ir(tzp)₂(Htzp)](NTf₂), which upon addition of NEt₃ gives a mixture of the starting material *fac*-Ir(tzp)₃ and *cis*-Ir(tzp)₂(tzp)'. We attempted varying the conditions for the base-induced cyclization. However, we were not able to direct it towards the formation of *mer*-Ir(tzp)₃ (for the optimization, see the Experimental part, subchapter 6.4.5).



Scheme 4.7 The addition of HNTf₂ (1 equiv.) to a solution of *fac*-Ir(tzp)₃ in CD₂Cl₂ leads to the formation of the protonated complex 'fac'-[Ir(tzp)₂(Htzp)](NTf₂), which then slowly converts to 'mer'-[Ir(tzp)₂(Htzp)](NTf₂). The quick addition of NEt₃ (1.5 equiv.) to 'fac'-[Ir(tzp)₂(Htzp)](NTf₂) leads to re-formation of *fac*-Ir(tzp)₃, whereas the addition of it to 'mer'-[Ir(tzp)₂(Htzp)](NTf₂) leads to the mixture *fac*-Ir(tzp)₃ and *cis*-Ir(tzp)₂(tzp)'.

4.6 Conclusions

We have demonstrated that the *fac* isomers of Ir(C[^]C:)₃ complexes with pmb or pbb ligands can be converted cleanly into the *mer* isomers by treatment with first HNTf₂ and then NEt₃. The transformation can be accomplished within a few minutes and the side product (NEt₃H)(NTf₂) is easy to separate by a short filtration over silica gel. The use of HNTf₂ was found to be important because it allowed performing the re-metalation step with NEt₃ at room temperature. When TFA was employed, an elevated temperature and a longer reaction time was needed. The forcing conditions favored the thermodynamic product *fac*-Ir(C[^]C:)₃, thereby compromising the efficiency of the isomerization. A kinetically controlled deprotonation of [Ir(C[^]C:)₂(HC[^]C:)]⁺ is apparently essential for achieving a high selectivity.

In our investigations, we have focused on Ir(pmb)₃ and Ir(pbb)₃, and the full scope of the isomerization process needs to be evaluated in future studies. The results obtained with Ir(tzp)₃ indicate that conformationally restricted carbene ligands are not suited. However, there are numerous publications about Ir(C[^]C:)₃ complexes with ligands similar to pmb and pbb, and we anticipate that some of them are also susceptible to an acid/base-mediated *fac*→*mer* isomerization.

Our methodology is complementary to the procedure developed by H.-H. Johannes and co-workers,¹³¹ which allows the conversion of *mer*-Ir(C[^]C:)₃ complexes into the corresponding *fac* isomers. The Johannes process has already facilitated the synthetic work in several studies.^{132–136} We hope that our new procedure will also be helpful, in particular for investigations focusing on applications of *mer*-Ir(C[^]C:)₃ complexes.

Chapter 5. Summary and Outlook

The studies described in this thesis were devoted to two classes of luminophores: tetraarylethene-based polymers and homoleptic Ir(III) complexes with orthometalated ligands.

In Chapter 2, we reported a novel approach for the synthesis of hyperbranched polyarylethenes by successive C–H vinylations of aromatic compounds with a vinyl triazene. In the presence of Brønsted acid, the triazene function cleaves, and after releasing dinitrogen, the highly-reactive vinyl cation couples with tetraphenylethene. Multiple triazene/acid additions give hyperbranched polyarylethenes. Compared to other procedures, our methodology is ‘traceless’, and functional groups were not detected in the products. A series of polymers with different molecular weights was obtained. In solution, the polymers with higher molecular weight show more intensive emission, whereas in the solid state, the trend is reversed. In the aggregate and solid state, the polymers show an additional red-shifted emission band, and overall, the emission is enhanced compared to solution state. Consequently, the polymers show unusual ratiometric aggregation-induced emission (AIE). The aromatic core can be varied. We have demonstrated that alkali metal ions can be sensed with hyperbranched poly(triphenylethene) grafted onto benzo-18-crown-6. For future studies, we suggest that the C–H vinylation method can be used for connecting hyperbranched polyarylethenes to different functional aromatic compounds. The resulting ratiometric AIE probes could find diverse applications.

In Chapter 3, we showed that *fac*-Ir(C[^]N)₃ complexes can be quickly and quantitatively converted into the thermodynamically less stable *mer*-Ir(C[^]N)₃ isomers by successive addition of first a strong acid (TFA or HNTf₂) and then a base (NEt₃). Spectroscopic and structural analyses indicated that the acid protonates the C-donor of the C[^]N ligand. The protonated intermediate adopts a meridional arrangement of the N-donors and a pseudo-octahedral structure stabilized by agostic interactions. The addition of base to the protonated complex leads to the abstraction of the proton involved in the agostic interactions and promotes re-metalation, which results in the formation of *mer*-Ir(C[^]N)₃. A range of homoleptic Ir(C[^]N)₃ complexes with different substituents (Me, OMe, ^tBu, F) or with extended C[^]N ligands (tppy) as well as the heteroleptic complex

$\text{Ir}(\text{dfppy})_2(\text{tpy})$ undergo a clean acid-base-induced *fac*→*mer* isomerization. The novel isomerization was shown to be stereoselective and proceeded without ligand scrambling. The acid-base *fac*→*mer* conversion enabled switching between isomers of $\text{Ir}(\text{C}^{\wedge}\text{N})_3$ complexes with distinct photophysical properties. Thus, it can potentially be applied in data storage devices, as demonstrated by the preparation of a proof-of-concept luminescent display. The new isomerization reaction is also useful from a synthetic point of view since it enables obtaining *mer* isomers, that cannot be prepared using conventional methods. Another potential application is the use as a geometric switch in a more complex nanostructure, as demonstrated by the large structural changes observed during the *fac*↔*mer* conversion of $\text{Ir}(\text{tppy})_3$.

$\text{Ir}(\text{C}^{\wedge}\text{C}:)_3$ complexes with metalated *N*-heterocyclic carbene ligands are attractive for applications in OLEDs due to their blue emission. It appeared interesting to use the acid-base method for isomerization of these complexes as well. However, the literature showed that acids mediate the back *mer*→*fac* isomerization of $\text{Ir}(\text{C}^{\wedge}\text{C}:)_3$ complexes. *A priori*, the *fac*→*mer* direction triggered by acids seemed unlikely. However, as described in Chapter 4, the HNTf_2 - NEt_3 -induced *fac*→*mer* isomerization is possible for $\text{Ir}(\text{C}^{\wedge}\text{C}:)_3$ complexes under kinetic control. The intermediate was shown to be a protonated pseudo-octahedral complex with a meridional arrangement of C:-donors stabilized by agostic interactions. The use of HNTf_2 is important for achieving good selectivity towards the *mer* isomer because it allows for a fast NEt_3 -promoted re-metalation step at room temperature. Our procedure allows converting a mixture of *fac* and *mer* isomers into the pure *mer* isomer, and we think that it could be useful in accessing *mer*- $\text{Ir}(\text{C}^{\wedge}\text{C}:)_3$ complexes that are difficult to synthesize in high yields by conventional methods.

Chapter 6. Experimental Part

All the spectroscopic characterization, X-ray crystallographic data, photophysical characterization of the published compounds can also be found in the Electronic Supplementary Information placed on the websites of the corresponding publications.

Raw experimental data for Chapters 2–4 are available online in Zenodo:

Chapter 2: <https://zenodo.org/records/10034530>

Chapter 3: <https://zenodo.org/records/7002606>

Chapter 4: <https://zenodo.org/records/7660951>

6.1 Materials and Methods

Conditions, reagents, and solvents

Unless otherwise stated, all chemical reactions were carried out in oven-dried (110 °C) glassware under an atmosphere of dry N₂ using Schlenk or Glovebox (MBraun) techniques. All reagents and solvents were purchased from chemical suppliers (Precious Metals Online, Sigma Aldrich, Fluorochem, Acros Organics, TCI, Apollo, ABCR, Supelco) and used as received. Dry solvents were obtained from a solvent purification system with activated aluminum oxide columns (Innovative Technology).

Chromatography

Flash chromatography was performed using commercial silica gel 230–400 mesh (Silicycle) and MP alumina (Brockmann activity II–III, EcoChrom™). Preparative chiral high-pressure liquid chromatography (HPLC) was performed on a 1260 Infinity system (Agilent Technologies) operated in manual mode. Analytical chiral HPLC was performed on an automatic ultra-fast liquid chromatograph Prominence UFLC XR (Shimadzu) operating with LC-AD XR solvent delivery unit, SIL-20A XR autosampler, CMB-20A system controller, CTO-20A column oven, SPD-20A UV-Vis detector, RF-20A XS fluorescence detector, and Chromeleon software. Chiral columns Chiralpak IA, IB, IC ID, IF (4.6×250 mm) were used for screening in analytical HPLC, and chiral column Chiralpak IA (20×250 mm) was used for preparative HPLC.

NMR measurements

All NMR scale experiments were provided under the inert atmosphere of dry N₂ inside a Glovebox. Stock solutions of trifluoroacetic acid (TFA, 0.5 M), bistriflimidic acid (HNTf₂, 0.2 M), and triethylamine (NEt₃, 0.5 M) were prepared in CD₂Cl₂, which was passed through a column with basic alumina prior the experiments. Solution ¹H, ¹³C {¹H}, ¹⁹F {¹H}, ¹H–¹H COSY, ¹H–¹³C HSQC, and variable-temperature (VT) NMR spectra were recorded at indicated temperatures on a Bruker Avance 400 and on a Bruker Avance Neo 500 MHz spectrometers. All chemical shifts (δ) are reported in ppm and aligned with respect to the residual signal of the corresponding deuterated solvent.²¹³

Mass spectrometry

Electrospray-ionization (ESI) and nanochip-ESI high-resolution mass spectrometry (HRMS) data were acquired on a Q-ToF Ultima mass spectrometer (Waters), on a Q-ToF XEVO G2-XS mass spectrometer (Waters) and on a Linear Trap Quadrupole (LTQ) Orbitrap Elite ETD mass spectrometer (Thermo Fisher), operated in positive mode. Atmospheric pressure photoionization (APPI) and matrix-assisted laser desorption/ionization (MALDI) HRMS measurements were done on the LTQ Orbitrap Elite ETD spectrometer operated in positive mode. Data were processed using Mmass 5.5.0 software.

Gel permeation chromatography

Relative number (M_n), weight-average (M_w), high average (M_z) molecular weights and polydispersity indexes (PDI as M_w/M_n) of the products were measured on a Waters Associated gel permeation chromatography (GPC) system equipped with a viscometer as a detector. Dimethylacetamide (DMAC) + 0.1 wt% LiBr was used as an eluent at a flow rate of 1.0 mL/min and a temperature of 70 °C. A set of monodispersed linear polymethyl methacrylate (PMMA) covering the molecular range of 10^3 – 10^7 was used as a standard for the molecular weight calibrations.

Elemental analyses

Elemental analyses were performed on an organic elemental analyzer Flash 2000 (Thermo Scientific) on the samples, which were exposed to high vacuum prior to analysis using diffusion pump.

Microwave syntheses

Reactions accelerated by microwave irradiation were performed in an Initiator+ microwave synthesizer (Biotage) using glass microwave reaction vials (10–20 mL) equipped with stirring bars and sealed by metallic caps with septa.

Thermogravimetric analysis

Thermogravimetric analysis (TGA) was performed on a Flash 2000 Organic Elemental Analyzer (Thermo Scientific).

BET analysis

BET analysis was carried out on an Automated Gas Sorption Analyser (Autosorb IQ, 3P Instruments GmbH & Co.) operating with ASiQwin software. The sample was exposed to outgas procedure (120 °C, 600 min) prior measurement, and then N₂ sorption/desorption isotherms were recorded.

Dynamic light scattering (DLS)

The DLS measurements were provided on Zetasizer Nano ZS (Malvern) using a Quartz Suprasil (QS) cuvette (10×10 mm) at 25 °C.

Optical and photophysical measurements

UV-Vis absorption spectra were recorded on a Cary 60 spectrophotometer (Agilent Technologies) or on a Lambda 40 spectrometer (Perkin Elmer). Steady-state emission and excitation spectra were recorded on a Cary Eclipse fluorescence spectrometer (Varian) or an FS5 fluorometer using a Xe light source (Edinburgh). Screw-cap Quartz Suprasil (QS) cuvettes (10×10 mm) were used for solution photophysical measurements.

Photoluminescence lifetimes (τ) were measured on a time-correlated single photon counting Edinburgh LifeSpec II spectrometer using an Edinburgh Picosecond pulsed diode lasers ($\lambda_{exc} = 405$ nm) as excitation sources. The fitting of the emission decays was performed by using Fluoracle software. The quality of the fitting was evaluated *via* the analysis of the χ^2 parameter and of the residual distribution. Solid state quantum yields (Φ_{solid}) were measured with an integrating sphere module of the Edinburgh FS5, and quantum yield values were calculated with Fluoracle software.

Electronic circular dichroism (ECD) spectra were measured on a Chirascan V100 spectrometer (Applied Photophysics) in CD₂Cl₂ at 50 nm·min⁻¹ scan speed with a resolution of 1 nm and a response time of 1 s, sample temperature 22.5 °C, QS cuvette length 1 mm. The units in ECD spectra were transformed from ellipticity (θ , mdeg) into molar extinction coefficient ($\Delta\epsilon$, M⁻¹·cm⁻¹) by using the following equation: $\Delta\epsilon$ (M⁻¹·cm⁻¹) = θ (mdeg) / [32980 × b (cm) × c (M)], where b is the length of the light path, and c is the molar concentration of the sample solution.

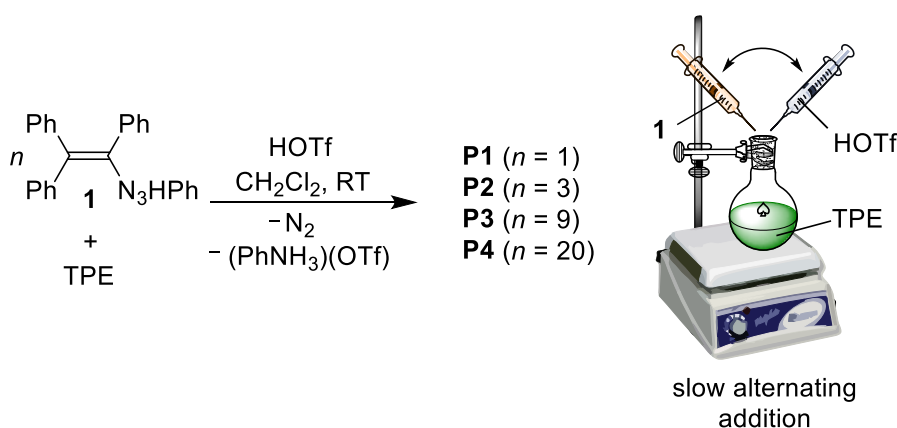
6.2 Experimental Part for Chapter 2

6.2.1 Synthesis of the Polymers

Triazene **1** was prepared according to the published procedure.⁴⁹

General procedure for the synthesis of hyperbranched polymers P1–P4.

Tetraphenylethylene (TPE, 1 equiv.) and triazene **1** (1 equiv.) were placed in a screw-cap vial equipped with a stirring bar, dissolved in dichloromethane (DCM, 0.133 M), and stirred for 10 min at r.t. Triflic acid (HOTf, 3 equiv.) was added slowly dropwise under vigorous stirring (1200 rpm) using a micropipette with a plastic tip. A colour change from yellow to dark red and gas release were observed. The mixture was stirred for 1 h at r.t. (the solution changed colour to dark green). Polymerization was achieved through the *n*-time dropwise addition of a solution of **1** (1 equiv.) in DCM (0.133 M) followed by the addition of HOTf (3 equiv.) and stirring for 1 h at r.t. after each addition. Subsequently, an excess of dry K₂CO₃ was added, and the dark green mixture was stirred until the colour changed to dark red. Then, the suspension was filtered through a pad of cotton wool, and the pad was subsequently washed by portions of DCM. The filtrate was evaporated to a minimum volume, and the product was precipitated with an excess of methanol and centrifuged. The crude product was exposed to 10-min sonication with methanol, washed with diethyl ether/hexane solvent mixture (1:1, v/v) and dried under high vacuum to give powders with a pale yellow to dark orange colour.



P1 (*n* = 1). Prepared from TPE (44.16 mg, 0.133 mmol, 1 equiv.), **1** (49.88 mg, 0.133 mmol, 1 equiv.) and HOTf (59.85 mg, 0.399 mmol, 35.29 μ L, 3 equiv.). Weight of dry

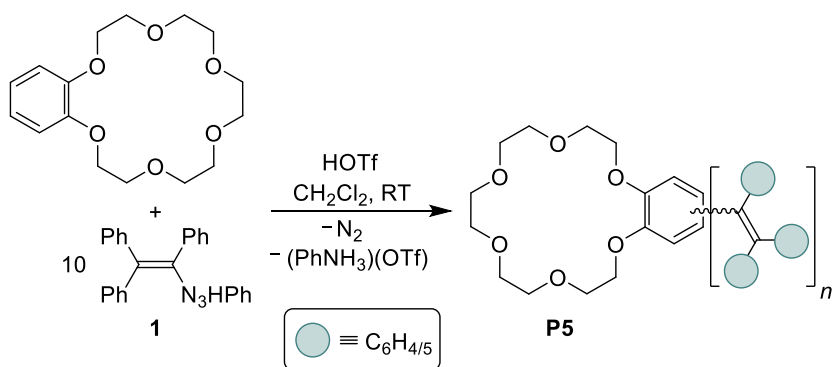
P1 (pale yellow powder): 14.1 mg. $M_w = 1023$ g/mol, $M_n = 480.2$ g/mol, $M_z = 1596$ g/mol, $PDI = 2.13$. Elem. anal. (%) C, 91.20; H, 3.26; N, 0.00.

P2 ($n = 3$). Prepared from TPE (44.16 mg, 0.133 mmol, 1 equiv.), **1** (149.6 mg, 0.399 mmol, 3 equiv.) and HOTf (179.6 mg, 1.197 mmol, 105.9 μ L, 9 equiv.). Weight of dry **P2** (yellow powder): 48.6 mg. $M_w = 1242$ g/mol, $M_n = 574.2$ g/mol, $M_z = 2183$ g/mol, $PDI = 2.16$. Elem. anal. (%) C, 87.35; H, 4.44; N, 0.00.

P3 ($n = 9$). Prepared from TPE (44.16 mg, 0.133 mmol, 1 equiv.), **1** (450 mg, 1.197 mmol, 9 equiv.) and HOTf (538.7 mg, 3.591 mmol, 317.6 μ L, 27 equiv.). Weight of dry **P3** (orange powder): 183.4 mg. $M_w = 2508$ g/mol, $M_n = 923.8$ g/mol, $M_z = 3998$ g/mol, $PDI = 2.72$. Elem. anal. (%) C, 93.01; H, 3.64; N, 0.00.

P4 ($n = 20$). Prepared from TPE (44.16 mg, 0.133 mmol, 1 equiv.), **1** (997.5 mg, 2.660 mmol, 20 equiv.) and HOTf (1197 mg, 7.980 mmol, 705 μ L, 60 equiv.). Weight of dry **P4** (dark orange powder): 520.2 mg. $M_w = 3939$ g/mol, $M_n = 1204$ g/mol, $M_z = 9524$ g/mol, $PDI = 3.27$. Elem. anal. (%) C, 94.62; H, 4.02; N, 0.00.

Synthesis of hyperbranched polymer P5. Benzo-18-crown-6 (100.0 mg, 0.320 mmol, 1 equiv.) and triazene **1** (102.2 mg, 0.320 mmol, 1 equiv.) were placed in a screw-cap vial equipped with a stirring bar, dissolved in DCM (0.320 M), and stirred for 10 min at r.t. HOTf (144.1 mg, 0.960 mmol, 85 μ L, 3 equiv.) was added slowly dropwise under vigorous stirring (1200 rpm) using a micropipette with a plastic tip. A colour change from yellow to dark red and gas release were observed. The mixture was stirred for 1 h at r.t. (the solution changed colour to dark green). Polymerization was achieved through 9-time dropwise addition of first a solution of **1** (102.2 mg, 0.320 mmol, 1 equiv.) in DCM (1.1 M) followed by the addition of HOTf (144.1 mg, 0.960 mmol, 85 μ L, 3 equiv.) and stirring for 1 h at r.t. after each addition. Then, the mixture was diluted with DCM to the volume of 100 mL, and the organic phase was washed with water (3 \times 200 mL) until neutral pH, and then with brine. The organic phase was dried over anhydrous Na₂SO₄ and filtered. The filtrate was evaporated to a minimum volume, and the product was precipitated with an excess of methanol and centrifuged. The crude product was exposed to 10-min sonication with methanol, washed with diethyl ether/hexane solvent mixture (1:1, v/v) and dried under high vacuum to give an orange powder.

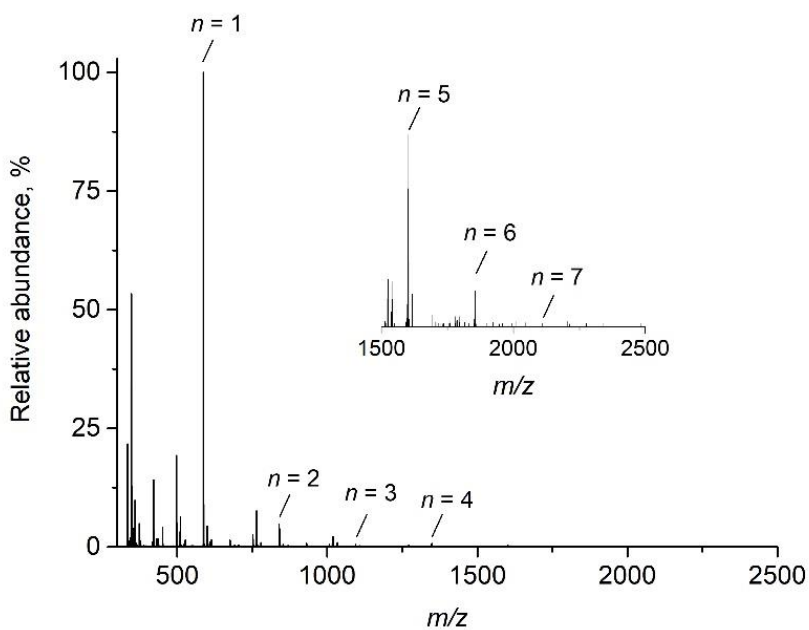


P5. Weight of dry **P5** (orange powder): 565.4 mg. $M_w = 2732$ g/mol, $M_n = 1118$ g/mol, $M_z = 5549$ g/mol, $PDI = 2.44$. Elem. anal. (%) C, 91.45; H, 5.90; N, 0.00.

6.2.2 Mass Spectra

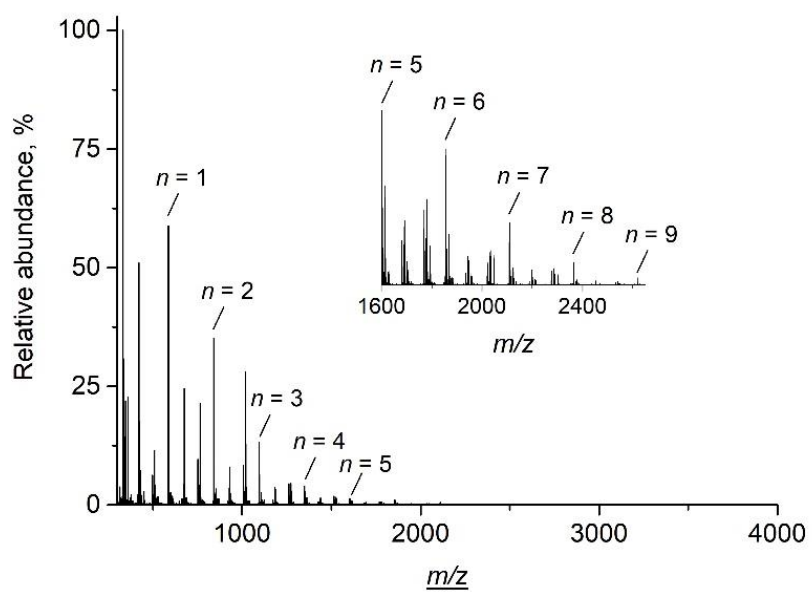
Summary table for APPI⁺ MS detection

Polymer	Products detected by MS, n
P1	up to 7
P2	up to 9
P3	up to 11
P4	up to 11
P5	up to 8

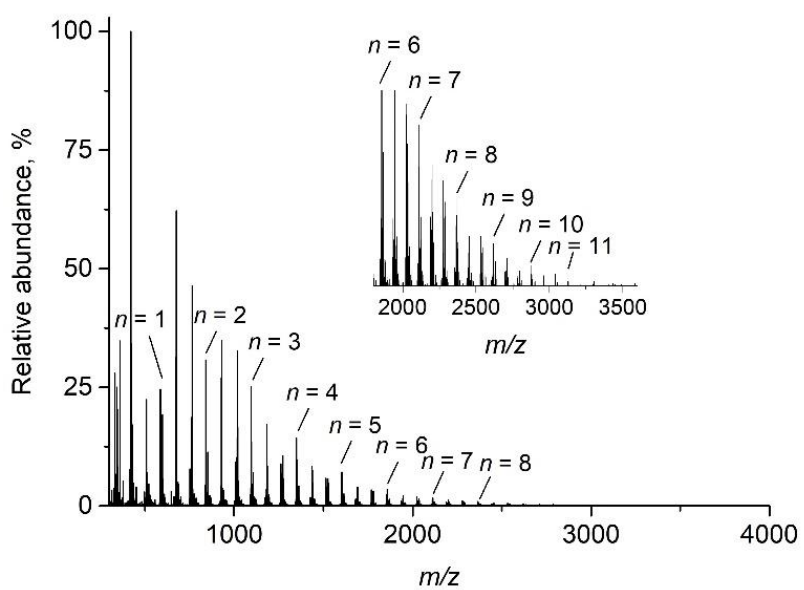


S

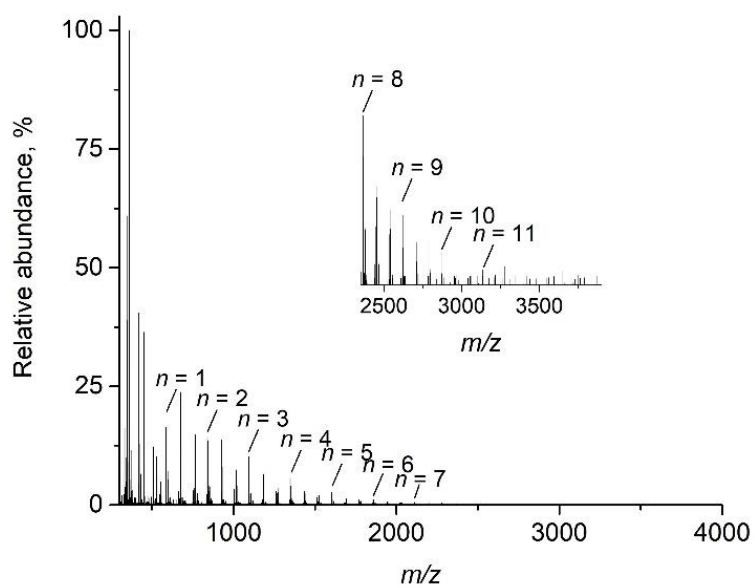
APPI⁺ HRMS of **P1**



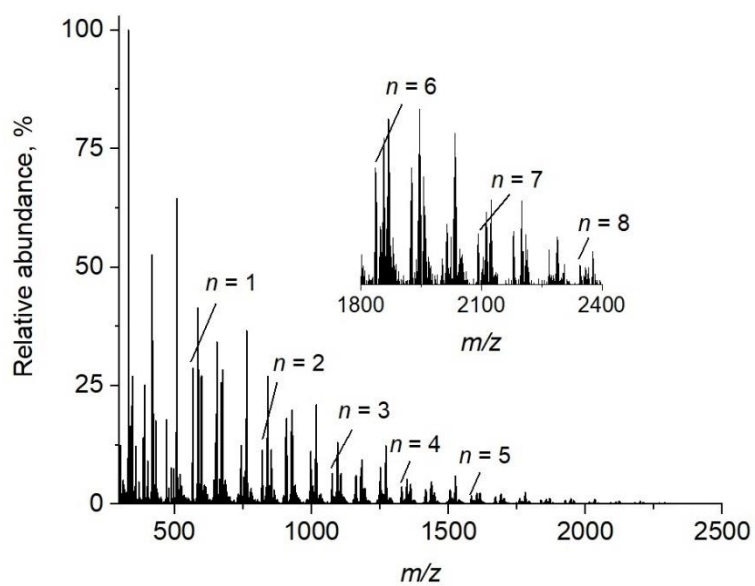
APPI+ HRMS of P2



APPI+ HRMS of P3



APPI⁺ HRMS of **P4**



APPI⁺ HRMS of **P5**

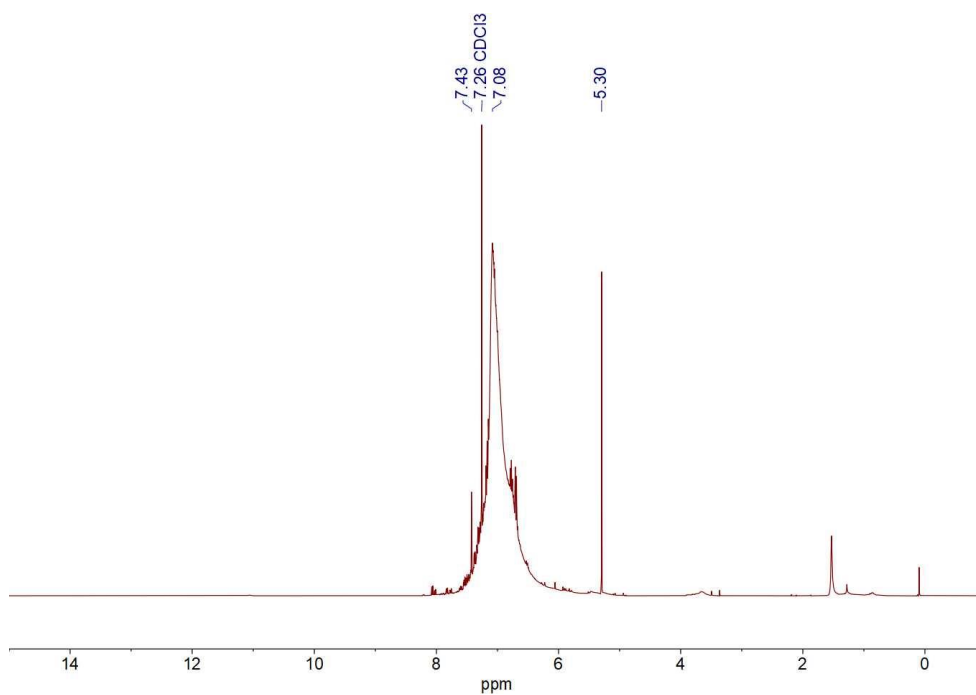
Summary of the HRMS data for the polymers **P1–P4**

<i>n</i>	Formula	Calculated [M] ⁺ , <i>m/z</i>	Found [M] ⁺ , <i>m/z</i>			
			P1	P2	P3	P4
1	C ₄₆ H ₃₄	586.2661	586.2713	586.2688	586.2664	586.2631
2	C ₆₆ H ₄₈	840.3756	840.3810	840.3808	840.3771	840.3717
3	C ₈₆ H ₆₂	1094.4852	1094.4902	1094.4900	1094.4868	1094.4802
4	C ₁₀₆ H ₇₆	1349.5981	1349.6011	1349.6026	1349.6006	1349.5938
5	C ₁₂₆ H ₉₀	1603.7076	1603.7122	1603.7117	1603.7111	1603.7025
6	C ₁₄₆ H ₁₀₄	1857.8172	1857.8274	1857.8176	1857.8206	1857.8104
7	C ₁₆₆ H ₁₁₈	2111.9267	2111.2572	2111.9277	2111.9297	2111.9166
8	C ₁₈₆ H ₁₃₂	2367.0396	–	2367.0550	2367.0436	2367.0294
9	C ₂₀₆ H ₁₄₆	2621.1492	–	2621.1434	2621.1504	2621.1481
10	C ₂₂₆ H ₁₆₀	2875.2587	–	–	2875.2715	2875.2658
11	C ₂₄₆ H ₁₇₄	3129.3683	–	–	3129.4014	3129.3880

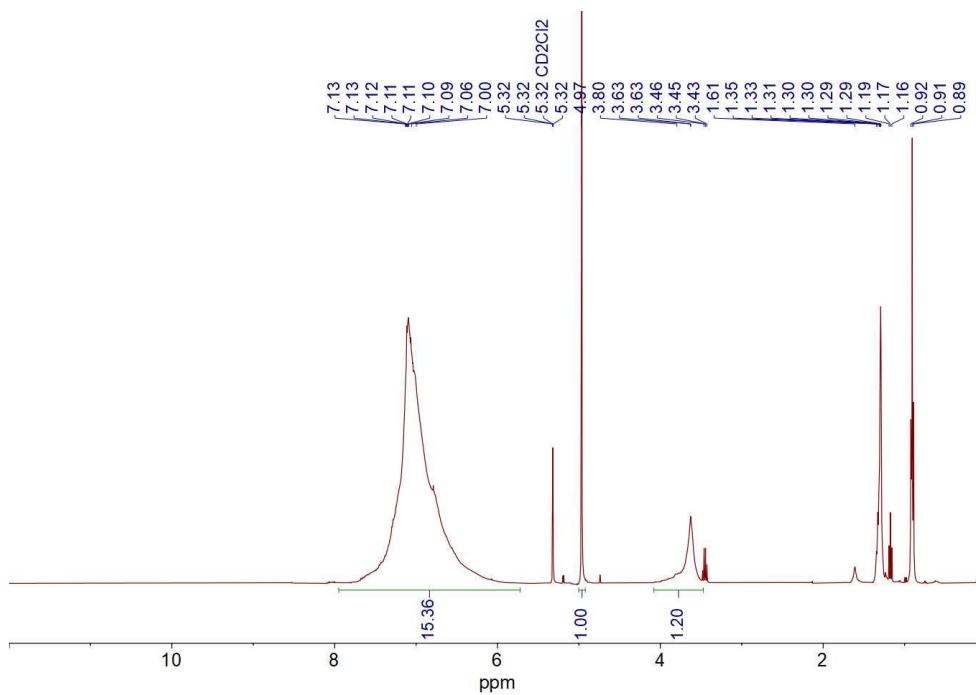
Summary of the HRMS data for polymer **P5**

<i>n</i>	Formula	Calculated [M] ⁺ , <i>m/z</i>	Found [M] ⁺ , <i>m/z</i>
1	C ₃₆ H ₃₈ O ₆	566.2668	566.2675
2	C ₅₆ H ₅₂ O ₆	820.3764	820.3769
3	C ₇₆ H ₆₆ O ₆	1074.4859	1074.4863
4	C ₉₆ H ₈₀ O ₆	1328.5955	1328.5938
5	C ₁₁₆ H ₉₄ O ₆	1583.7084	1583.7107
6	C ₁₃₆ H ₁₀₈ O ₆	1836.8146	1836.8144
7	C ₁₅₆ H ₁₂₂ O ₆	2090.9241	2090.9233
8	C ₁₇₆ H ₁₃₆ O ₆	2345.0337	2345.0370

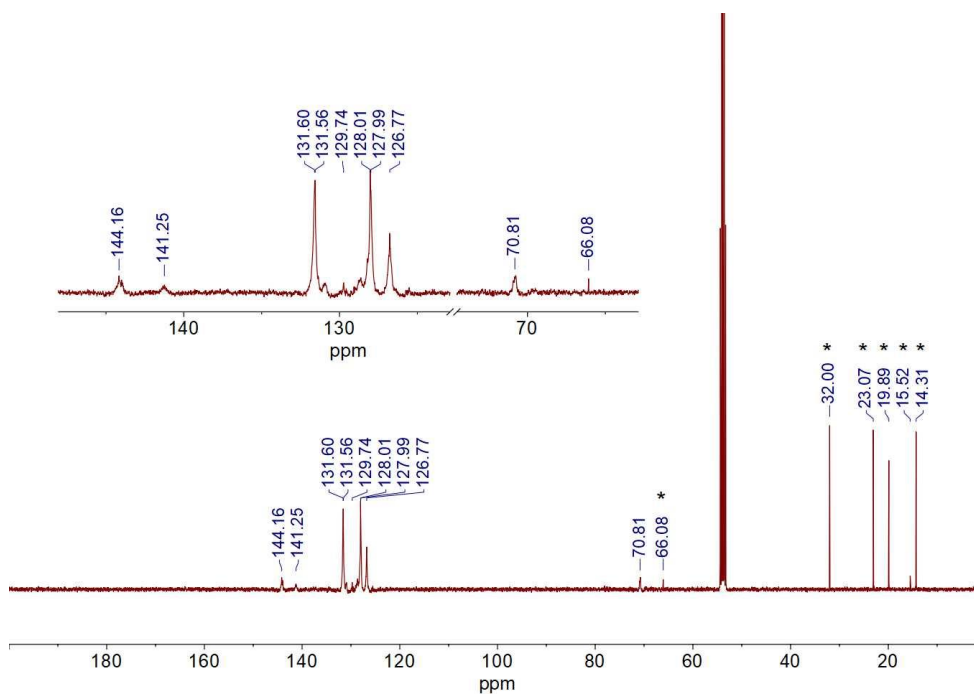
6.2.3 NMR Spectra



¹H NMR (400 MHz, CDCl₃, 298 K) spectrum of **P4**



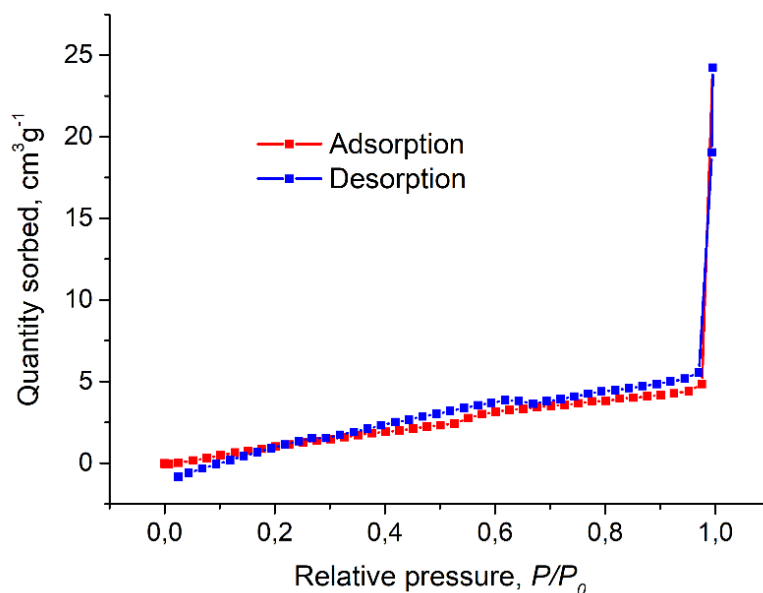
¹H NMR (400 MHz, CDCl₃, 298 K) spectrum of **P5**. The signal at 4.76 ppm belongs to the internal standard CH₂Br₂.



^{13}C NMR (101 MHz, CD_2Cl_2 , 298 K) spectrum of **P5**. The signals marked by asterisks belong to the internal standard CH_2Br_2 , and the solvents (Et_2O and *n*-hexane) which could not be removed after synthesis by drying under high vacuum.

6.2.4 Investigation of Gas Sorption Properties

Nitrogen sorption isotherm measurement at 77 K was performed to characterize the pore structure of **P4**.



N_2 sorption isotherm curve of **P4** (77 K)

The curve can be classified as type III isotherm with an absence of a knee. It can be concluded that **P4** does not possess porous structure, or the pores are too small to adsorb N_2 . The BET surface area of **P4** cannot be determined because the BET theory is not applicable to type III isotherm.

6.2.5 Photophysical Properties

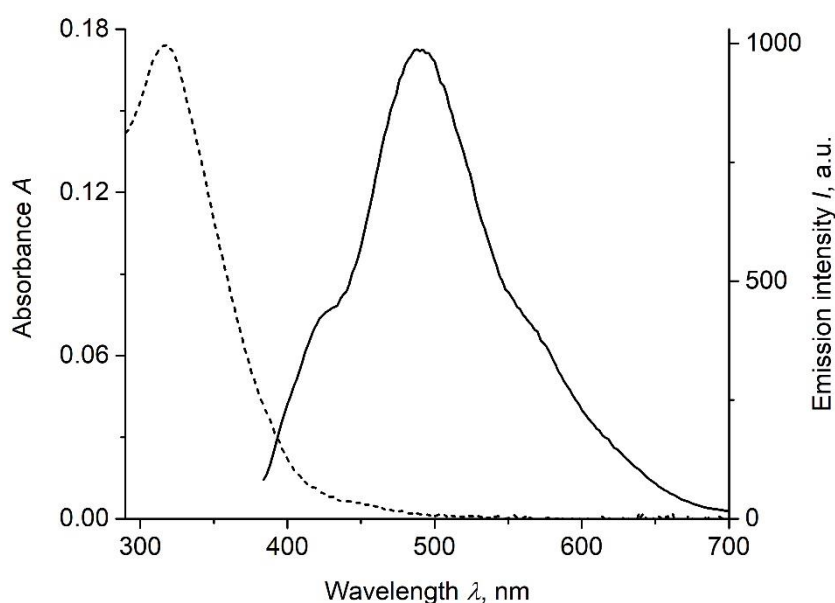
Photophysical measurements for TPE and for the polymers **P1–P5** were performed with aerated optically diluted solutions ($A < 0.1$) in spectrophotometric grade tetrahydrofuran (THF) placed in a QS cuvette (10×10 mm). The samples were prepared according to the following procedure: ≈ 1.1 mg of the polymer was weighted, placed in a vial, dissolved in 3 mL of THF and then the concentrated solution was diluted by taking a 50 μL aliquot of it and adding 4950 μL of THF to the aliquot.

Photoluminescence quantum yields of the polymers **P1**, **P4** and **P5** in aerated THF solutions were measured relative to quinine sulphate (Q) in 0.5 M H_2SO_4 . Following the standard procedures for determination of quantum yields,^{214,215} absorption and

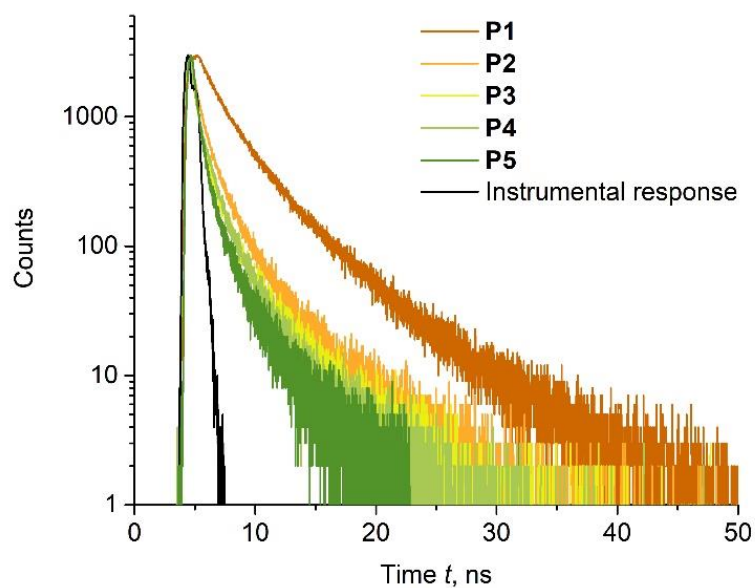
emission ($\lambda_{exc} = 366 \text{ nm}$) spectra were recorded for solutions of Q, **P1**, and **P4** with a gradual change of concentration. Then, a linear approximation of integral emission intensity vs absorbance was plotted, and a slope k was determined. The relative quantum yield of the polymers Φ_X was then calculated using the following equation:

$$\Phi_X = \Phi_Q \left(\frac{k_X}{k_Q} \right) \left(\frac{RI_X^2}{RI_Q^2} \right),$$

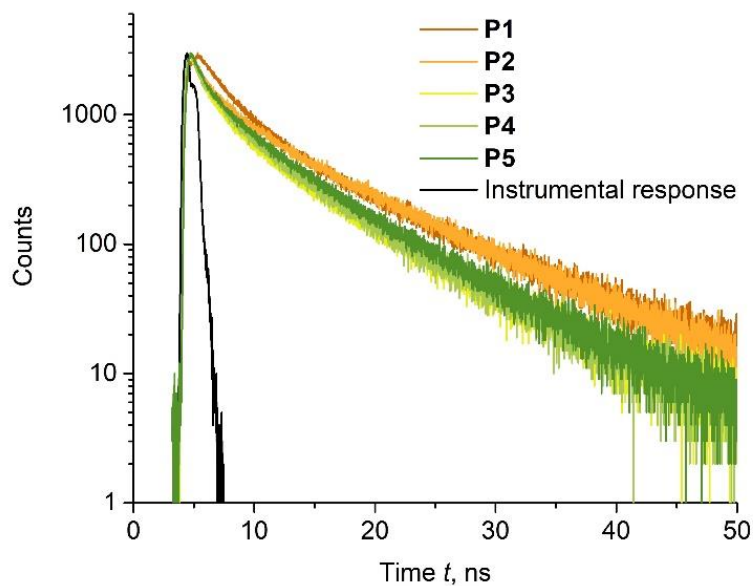
where Φ_Q is absolute quantum yield of the standard, $\Phi_Q = 0.546$ ($\lambda_{exc} = 366 \text{ nm}$),²¹⁶ k_X and k_Q are slopes for the linear approximation for the sample and the standard, respectively, $\frac{RI_X^2}{RI_Q^2}$ is refractive indexes ratio for sample solvent ($RI_{THF} = 1.404$)²¹⁷ and the standard ($RI_{0.5 \text{ M } H_2SO_4} = 1.346$)²¹⁸ at 25 °C.



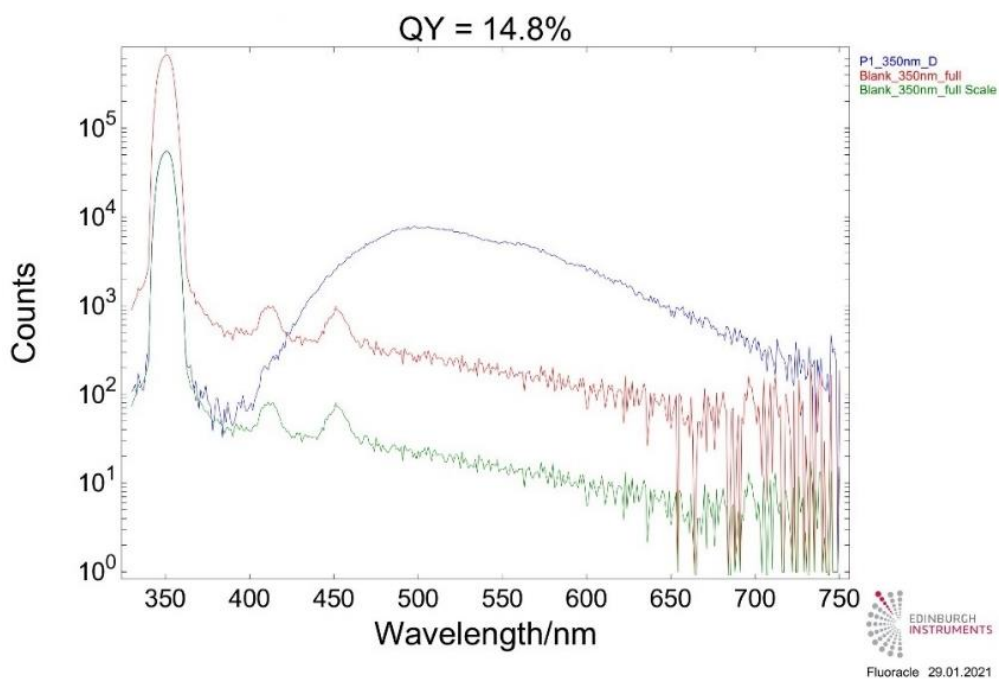
UV-Vis absorption (dashed) and photoluminescence (solid) spectra of polymer **P5** in THF ($\lambda_{exc} = 365 \text{ nm}$, $[P5] = 0.4 \mu\text{g/mL}$)



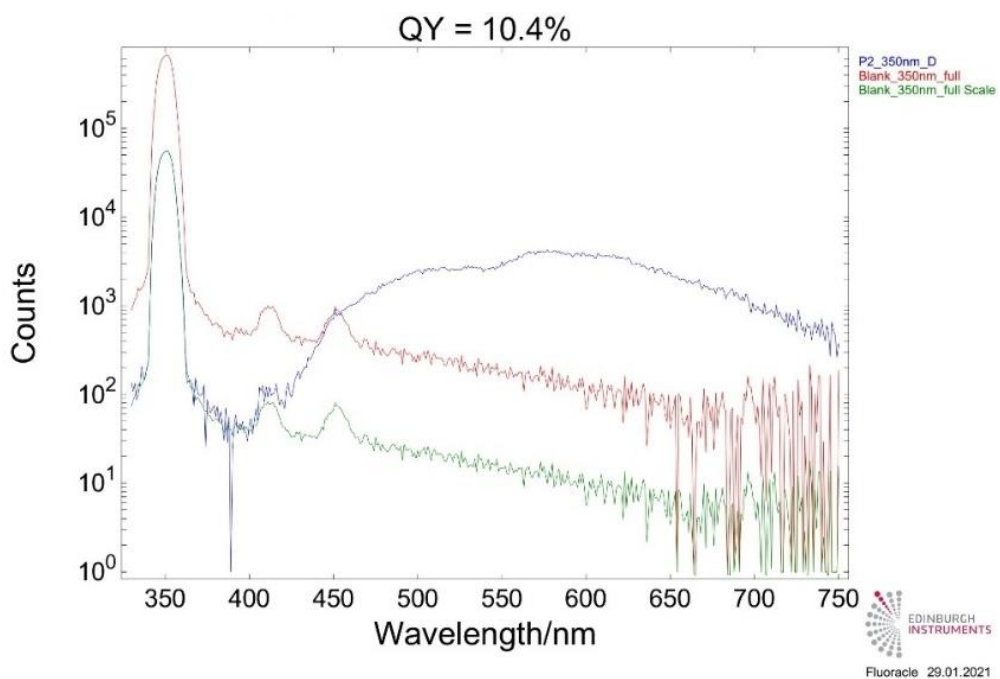
Photoluminescence decay curves at 500 nm for the polymers **P1–P5** recorded by time-correlated single photon counting ($\lambda_{exc} = 405$ nm)



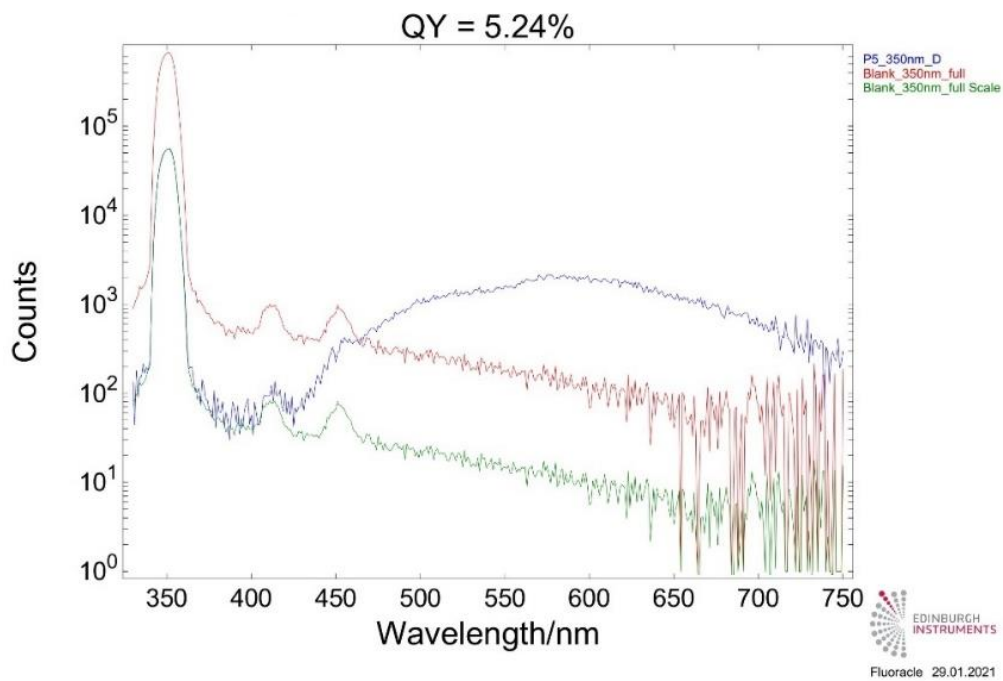
Photoluminescence decay curves at 600 nm for the polymers **P1–P5** recorded by time-correlated single photon counting ($\lambda_{exc} = 405$ nm)



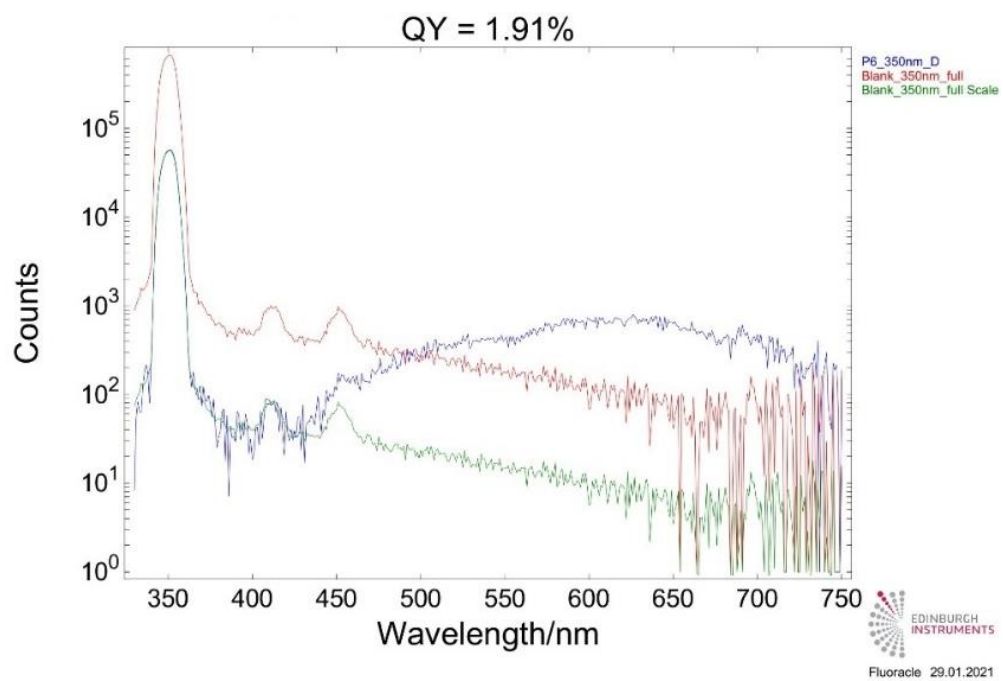
Solid state quantum yield calculation of **P1** ($\lambda_{exc} = 350$ nm)



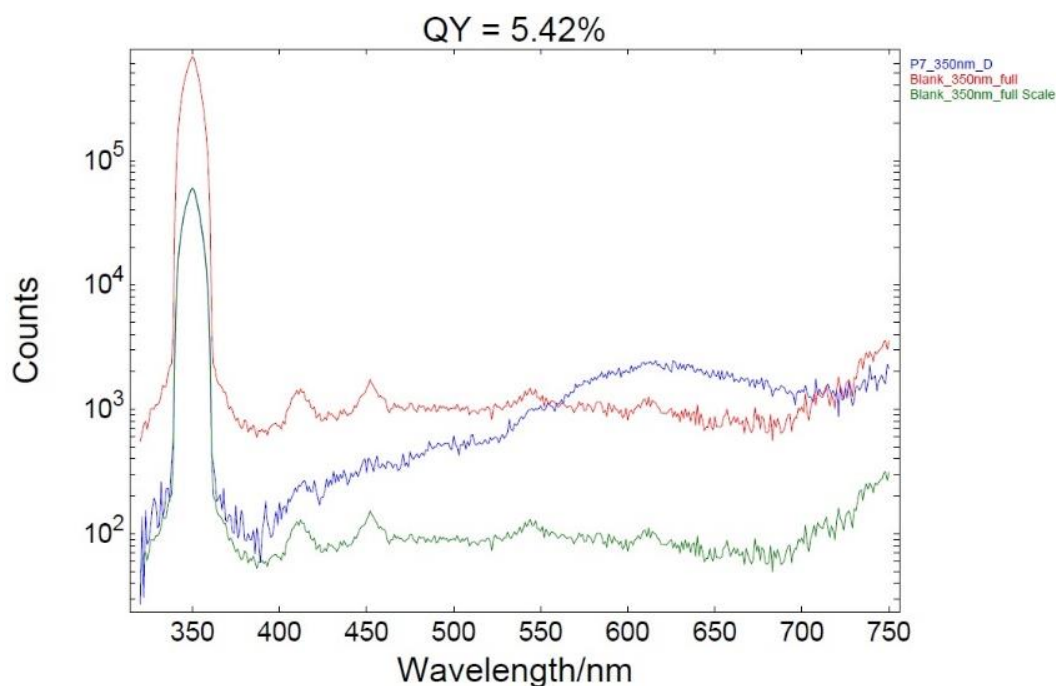
Solid state quantum yield calculation of **P2** ($\lambda_{exc} = 350$ nm)



Solid state quantum yield calculation of **P3** ($\lambda_{exc} = 350$ nm)



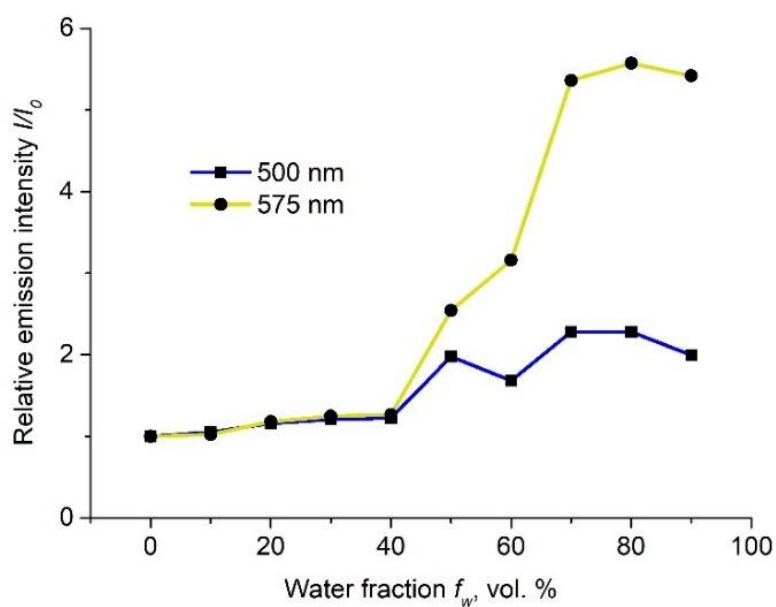
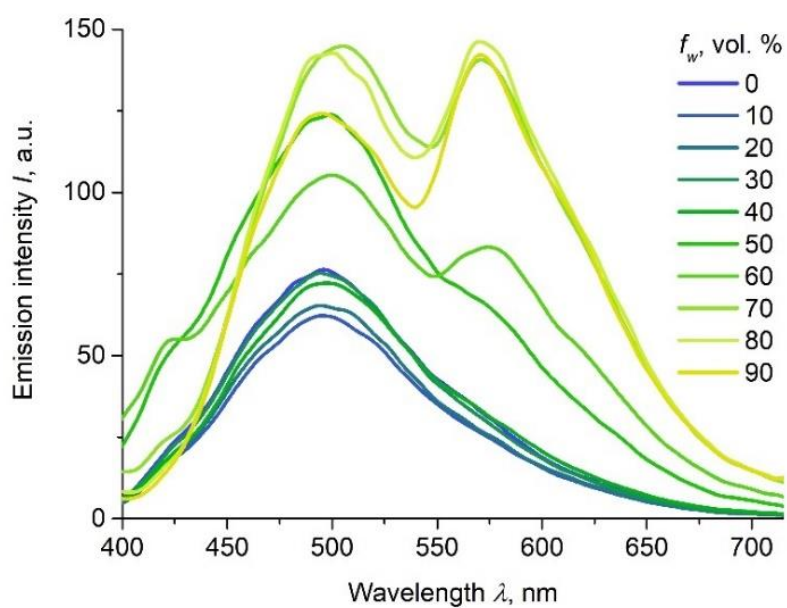
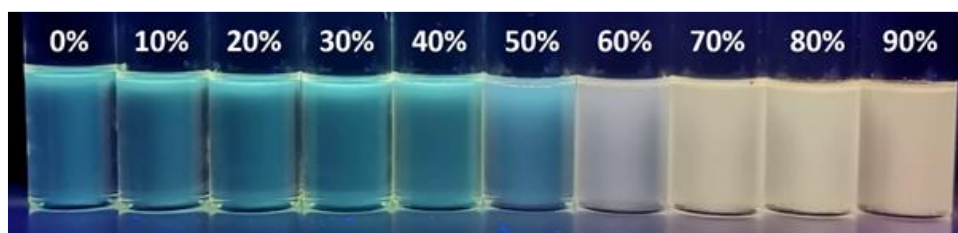
Solid state quantum yield calculation of **P4** ($\lambda_{exc} = 350$ nm)



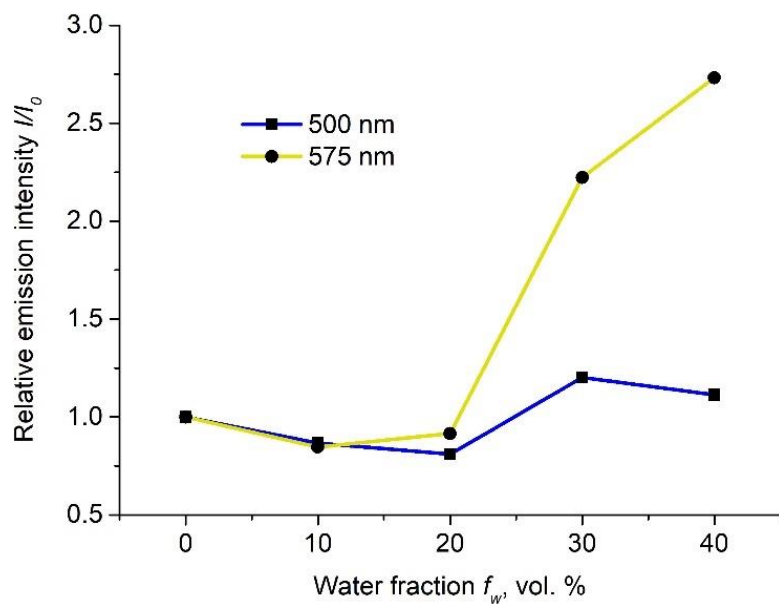
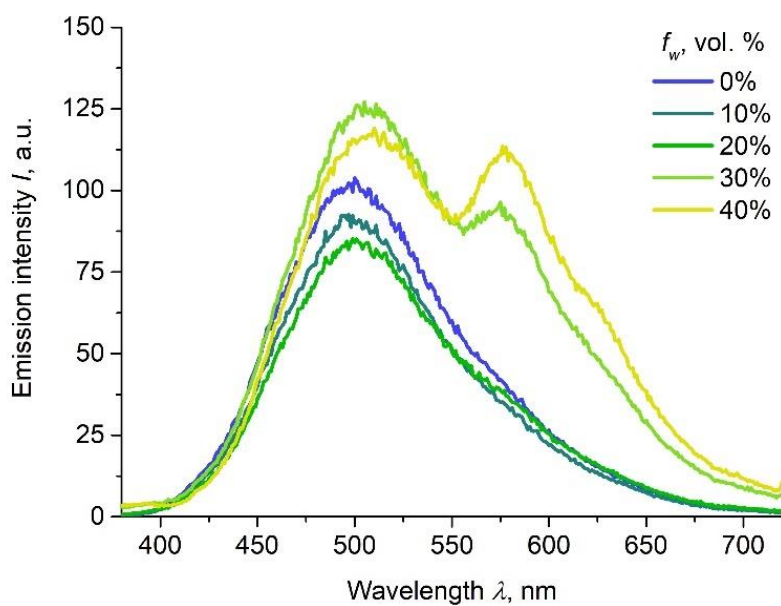
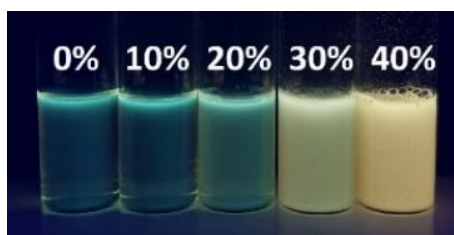
Solid state quantum yield calculation of **P5** ($\lambda_{exc} = 350 \text{ nm}$)

6.2.6 Aggregation-Induced Emission of the Polymers

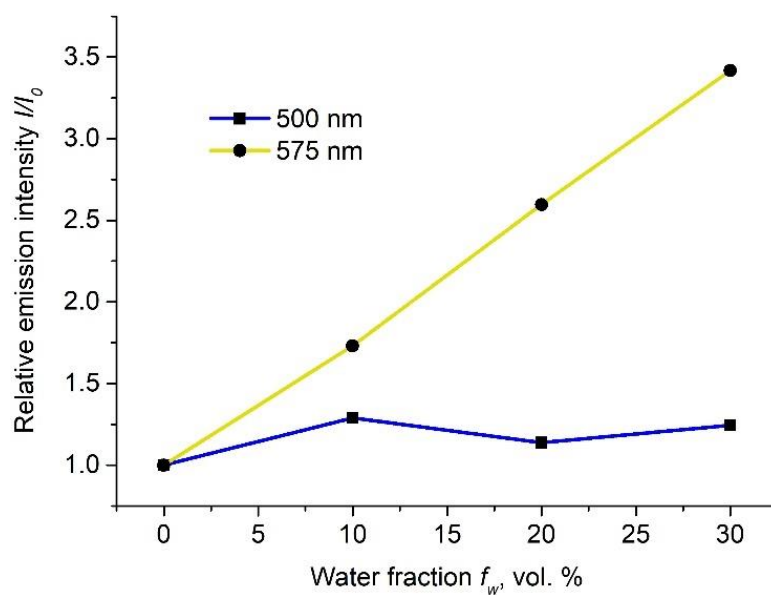
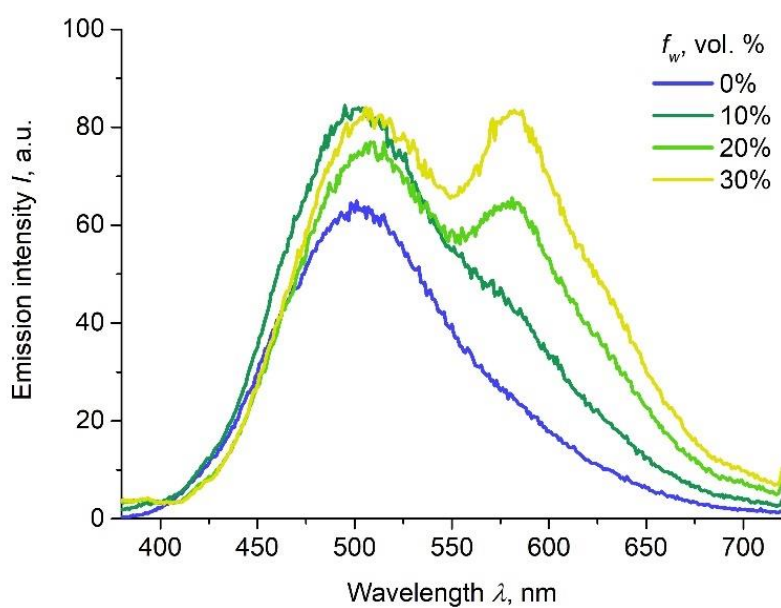
In a 15 mL screw-cap vial, 2.5 mg of the respective polymer was dissolved in a volume of THF, dioxane, or DMF according to indicated antisolvent (water, hexane or MeOH) fraction f , *i.e.* 10 mL – 0%, ..., 1 mL – 90%. A magnetic stirring bar was placed in the vial and the corresponding volume of antisolvent was added slowly (dropwise) under rapid stirring (1200 rpm), *i.e.* 1 mL – 10%, ..., 9 mL – 90%. Emission spectra were recorded immediately after the addition of antisolvent.



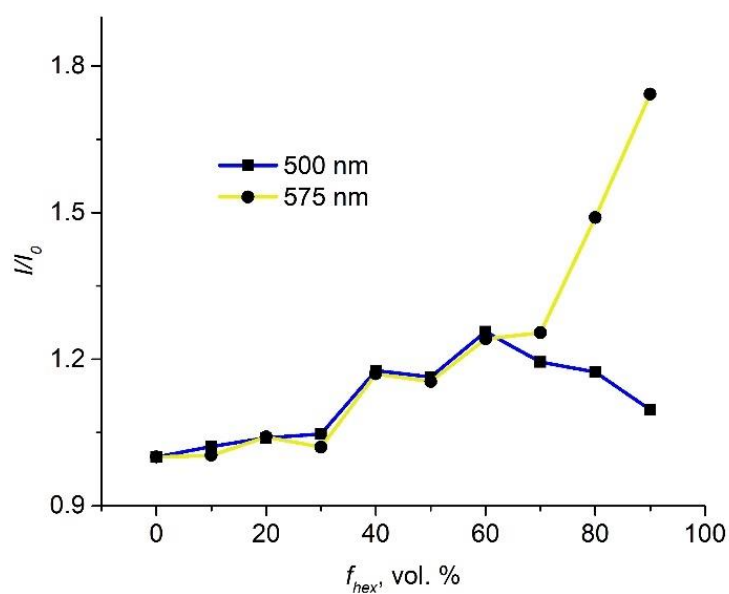
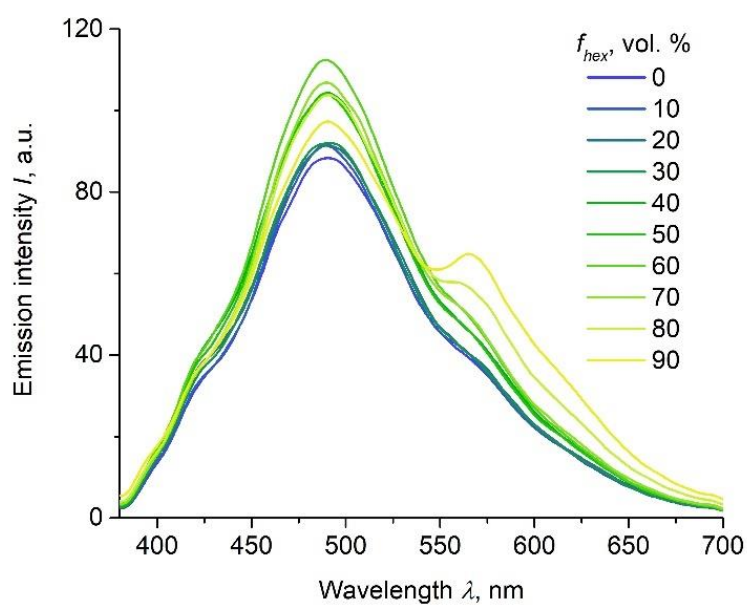
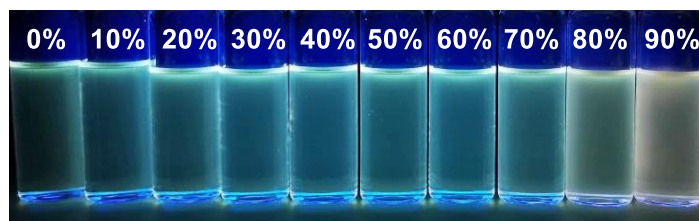
a) Photo images of **P3** in THF–water mixtures (f_w is indicated). b) Emission spectra and c) emission enhancement of **P3** in THF–water mixtures ($\lambda_{exc} = 365$ nm).



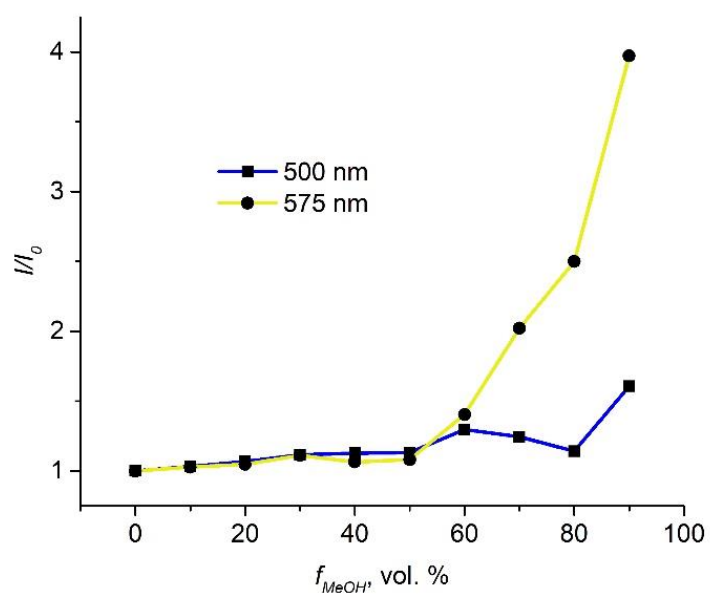
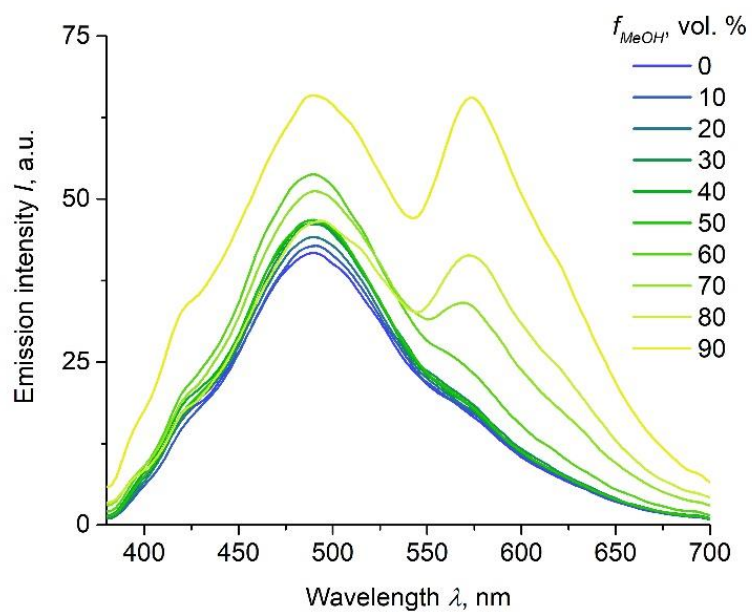
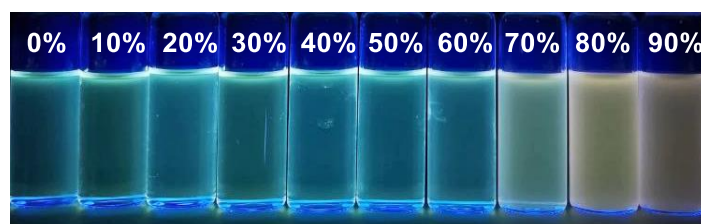
a) Photo images of **P4** in dioxane–water mixtures (f_w is indicated). b) Emission spectra and c) emission enhancement of **P4** in dioxane–water mixtures ($\lambda_{exc} = 365$ nm).



a) Photo images of **P4** in DMF–water mixtures (f_w is indicated). b) Emission spectra and c) emission enhancement of **P4** in DMF–water mixtures ($\lambda_{exc} = 365$ nm).



a) Photo images of **P5** in THF–hexane mixtures (f_{hex} is indicated). b) Emission spectra and c) emission enhancement of **P5** in THF–hexane mixtures ($\lambda_{exc} = 365$ nm).

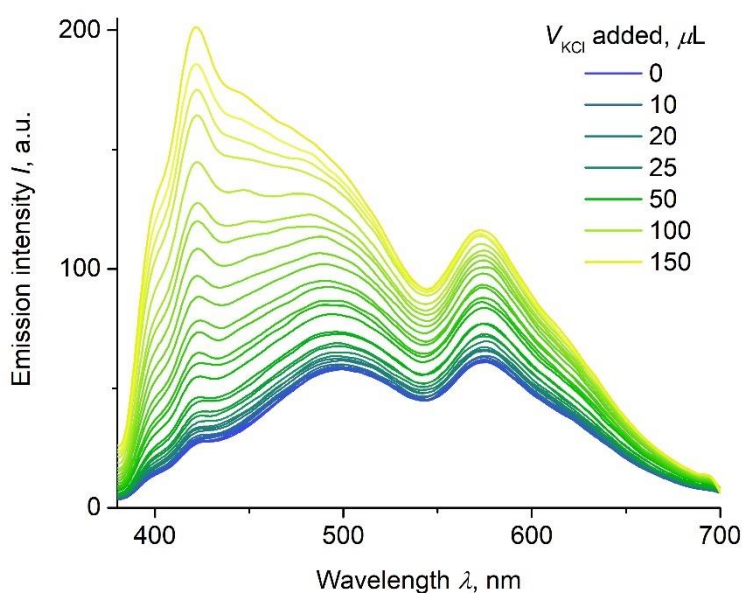


a) Photo images of **P5** in THF–MeOH mixtures (f_{MeOH} is indicated). b) Emission spectra and c) emission enhancement of **P5** in THF–MeOH mixtures ($\lambda_{exc} = 365$ nm).

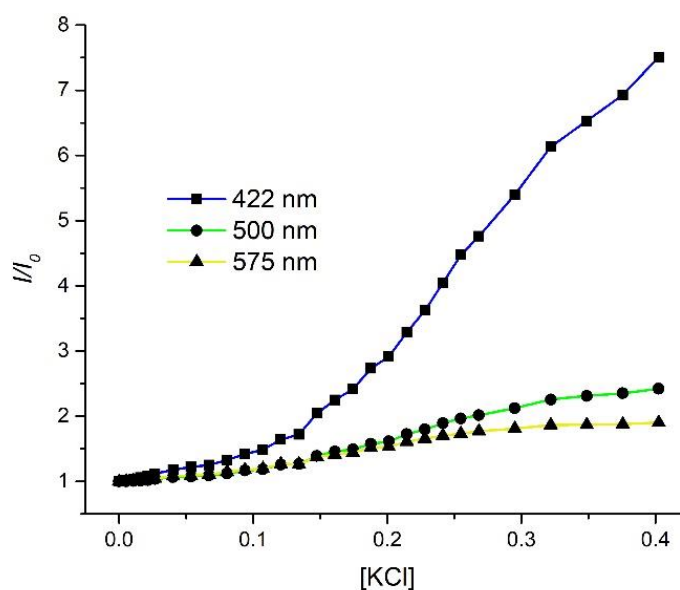
6.2.7 Sensing of Metal Ions

A photoluminescence titration was carried out by adding aliquots (μL) of an aqueous KCl solution (2 mg/mL) to a suspension of **P5** (2.5 mg) in THF–water (10 mL, $v/v = 1:1$). A concentration of $[\text{MCl}] = 0.3 \text{ mM}$ was chosen to study the photoluminescence response of **P5** for different alkali metal chlorides (Li, Na, Rb, or Cs) and potassium salts with various anions (F, Br, I, OAc, BF_4 , PF_6 , NO_3). For that, the volume equivalent to a final concentration of 0.3 mM of aqueous solutions of salts (2 mg/mL) was added to a suspension of **P5** (2.5 mg) in THF–water (10 mL, $v/v = 1:1$) under rapid stirring (1200 rpm).

Solid state sensing was carried out by grinding solid **P5** ($\sim 50 \text{ mg}$) with KCl ($\sim 50 \text{ mg}$) in an agate mortar. The photoluminescence response was measured by placing solid **P5** (not ground, ground, ground with KCl) on the walls of a QS cuvette ($10 \times 10 \text{ mm}$).



PL spectra ($\lambda_{\text{exc}} = 365 \text{ nm}$) of **P5** (2.5 mg) in THF–water (10 mL, $v/v = 1:1$) after addition of increasing amounts of aqueous KCl



Luminescence change vs [KCl] at different emission wavelengths. **P5** in THF-water ($v/v = 1:1$). I_0 = intensity at [KCl] = 0 mM. $\lambda_{exc} = 365$ nm.

6.2.8 DLS Measurements for P5 Aggregates

The aggregates of **P5** in THF-water (1:1, v/v) were freshly prepared according to the experiment described in subchapter 6.2.6 and diluted 25 times, so the final concentration of [**P5**] is 10 $\mu\text{g/mL}$. The diluted solution was placed in a QS cuvette 10×10 mm, and particles size distribution was determined by intensity-based method with three consequent measurements to follow the dynamics of the system.

The software report is provided below.

Sample Name: AG638_dil25times 1
SOP Name: THF-H2O.sop
File Name: 090823.dts
Record Number: 7
Material RI: 1.60
Material Absorbtion: 0.050

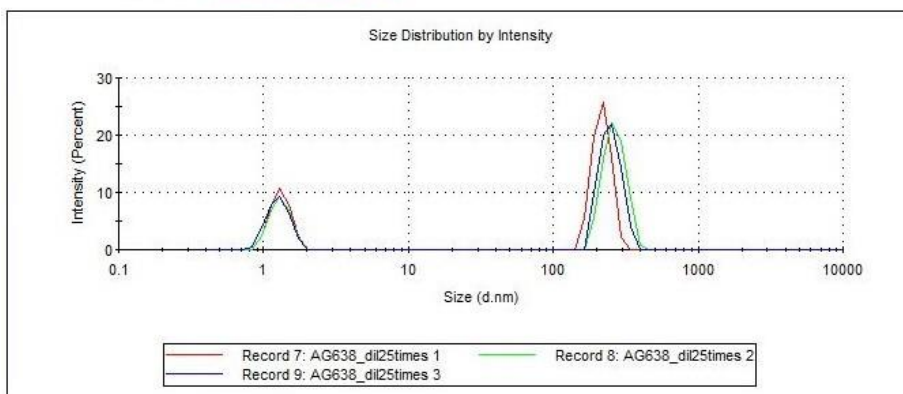
Dispersant Name: THF-H2O_50-50
Dispersant RI: 1.400
Viscosity (cP): 1.7000
Measurement Date and Time: Wednesday, August 09, 2023 11:06...

Temperature (°C): 24.9
Count Rate (kcps): 166.5
Cell Description: Low volume glass cuvette (45µL)

Duration Used (s): 70
Measurement Position (mm): 4.20
Attenuator: 10

	Size (d.nm):	% Intensity:	St Dev (d.nm):
Z-Average (d.nm): 297.0	Peak 1: 217.8	69.1	30.88
Pdl: 0.597	Peak 2: 1.310	30.9	0.2030
Intercept: 0.920	Peak 3: 0.000	0.0	0.000

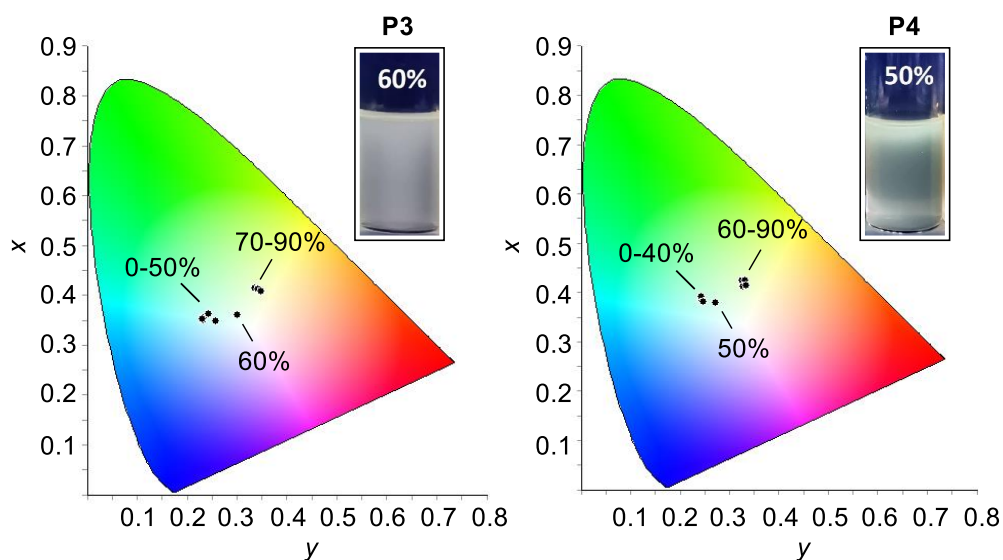
Result quality : Refer to quality report



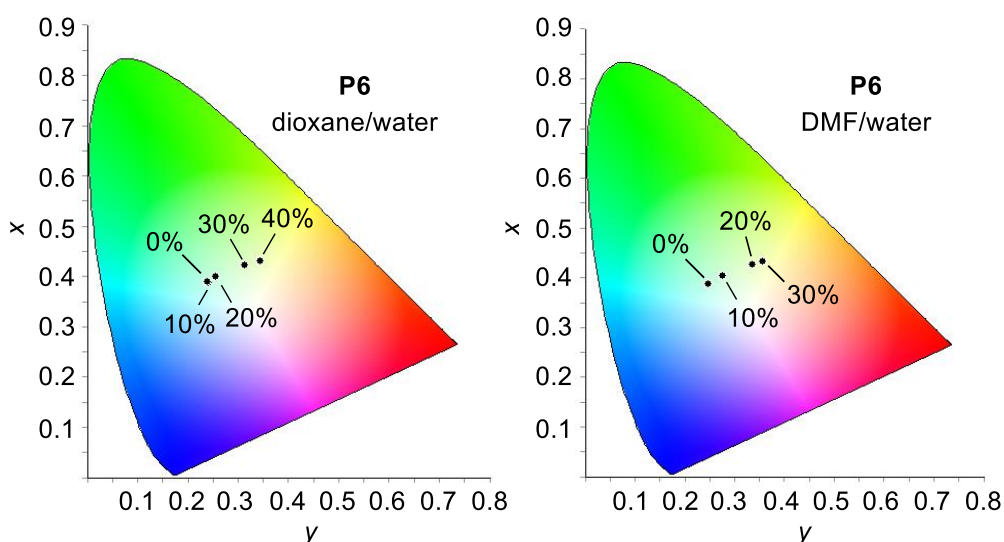
Software report for DLS based on intensity method

6.2.9 CIE Chromaticity Diagrams

The CIE chromaticity diagrams were created using the software ColourCalculator v. 7.77. In the software, the emission spectra were converted to the chromaticity coordinates (x,y) and placed in the CIE 1931 2° colour space.



CIE 1931 2° chromaticity diagrams of **P3** (left) and **P4** (right) in THF–water mixtures (f_w is indicated) and comparison of photo images of **P3** ($f_w = 60\%$) and **P4** ($f_w = 50\%$) under UV light ($\lambda_{exc} = 365\text{ nm}$)



CIE 1931 2° chromaticity diagrams of **P4** in dioxane/water and DMF–water mixtures (f_w is indicated)

6.2.10 Optimization of the Polymerization Reaction Conditions

The conditions for the polymerization were optimized by examination of the effects of different parameters including acid strength, addition sequence, concentration of TPE, of acid, and of triazene **1**, the addition method, and the technique used. The work-up procedure was selected based on the solubility of the polymers.

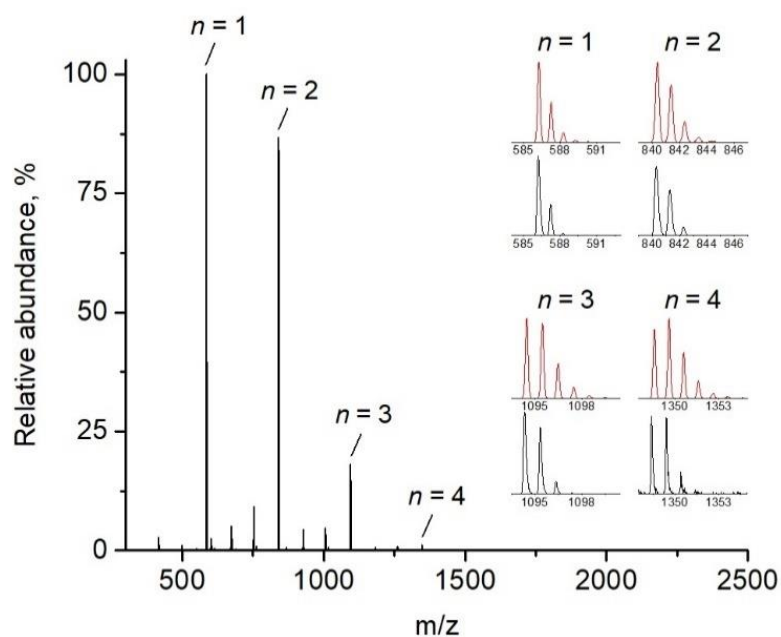
APPI and MALDI HRMS operating in positive mode were used to observe how the aforementioned parameters affect the polymerization by the detection of the products with low *n*. The results are summarized below.

Optimization of the polymerization conditions

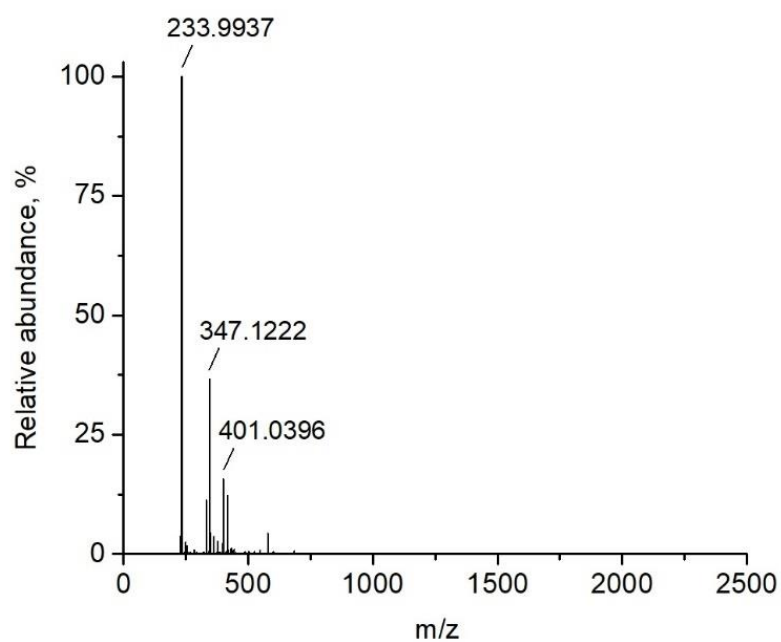
Entry	Effect	TPE ^a , equiv.	1 , equiv.	HOTf, equiv.	TFA, equiv.	Products, <i>n</i>					
						1	2	3	4	5	6
1	Acid strength ^b	1	1	5	–	+	+	+	+	–	–
2		1	1	–	5	–	–	–	–	–	–
3	Addition sequence ^b	1	1	5 (last)	–	+	+	+	+	–	–
4		1	1 (last)	5	–	+	+	–	–	–	–
5	TPE concentration ^b	5	1	5	–	+	+	–	–	–	–
6		0.5	1	5	–	+	+	+	+	–	–
7	HOTf concentration ^b	1	1	3	–	+	+	+	+	–	–
8		1	1	1.1	–	+	+	+	+	–	–
9	Addition method I ^b	1	5	5.5	–	–	–	–	–	–	–
10		1	10	11	–	–	–	–	–	–	–
11	Addition method II ^b	1	5	5.5	–	+	+	+	+	+	–
12		1	5	15	–	–	–	+	+	+	+
13	Schlenk line	1	5	15	–	+	+	+	+	+	+

^a [TPE] = 0.134 M (DCM), ^b performed in a glovebox

Acid strength: First, the influence of acid strength was investigated (Entry 1 and 2). The use of weaker TFA instead of HOTf did not give the desired products.

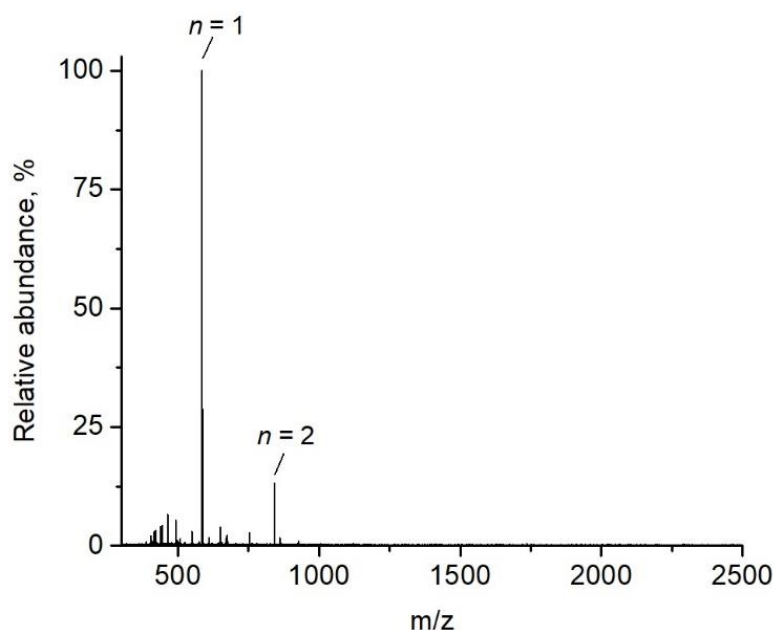


MALDI-TOF (DCTB matrix) HRMS of the product of Entry 1. The simulated spectra are shown in red.



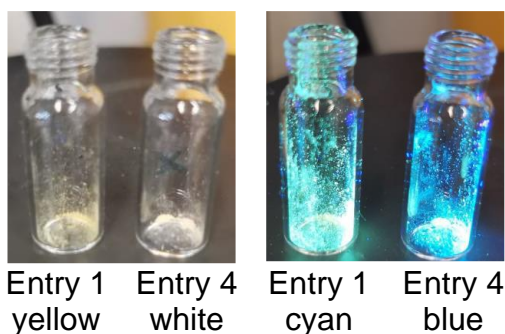
MALDI-TOF (CHCA matrix) HRMS of the product of Entry 2

Addition sequence: The polymerization was performed with two different addition sequences, with HOTf (Entry 3) or **1** (Entry 4) being added last to the reaction mixture. The MS results showed that an addition of HOTf after **1** is favorable.



MALDI-TOF (CHCA matrix) HRMS of the product of Entry 4

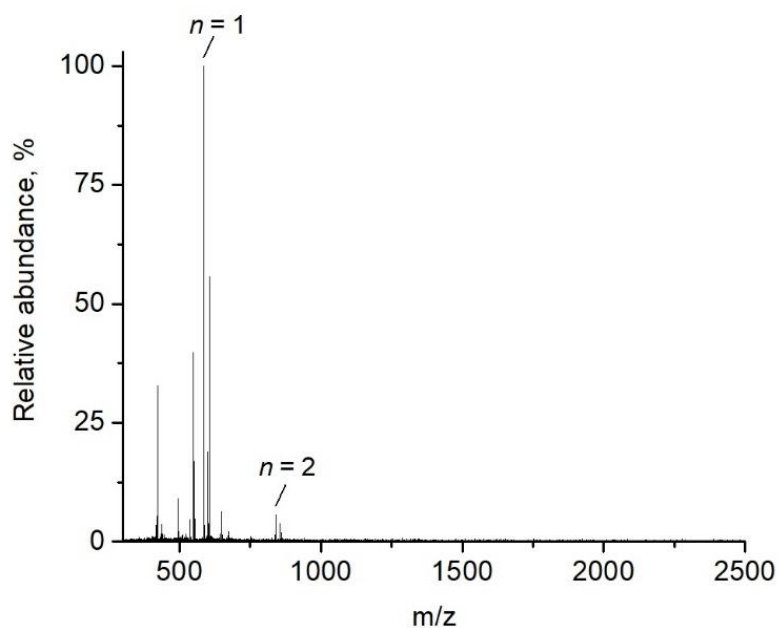
The MS results were supported by the difference in optical properties of the solid products of Entry 1 and 4. Going from Entry 4 to 1, the bathochromic shift of the emission colour of the product is clearly observed indicating the majority of the oligomers with higher molecular weights in the product of Entry 1.



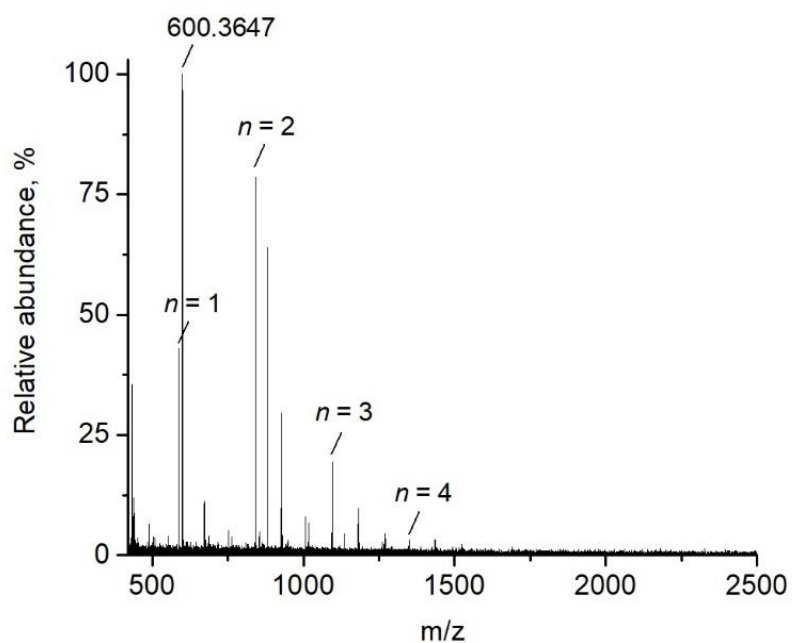
Entry 1 yellow Entry 4 white Entry 1 cyan Entry 4 blue

Photo images of the products of Entries 1 and 4 under ambient conditions (left) and under UV lamp (right, $\lambda_{exc} = 365$ nm).

TPE concentration: Subsequently, the influence of the TPE concentration was studied. An excess of TPE (Entry 5) suppressed the formation of oligomers. On the contrary, scaling down the TPE concentration (Entry 6) gave coupling products with $n = 1-4$.



MALDI-TOF (CHCA matrix) HRMS of the product of Entry 5



MALDI-TOF (CHCA matrix) HRMS of the product of Entry 6

These results can also be supported by the difference in optical properties of the products of Entry 5 and 6.

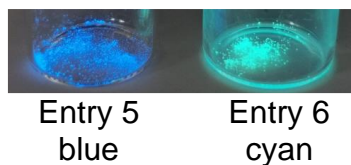
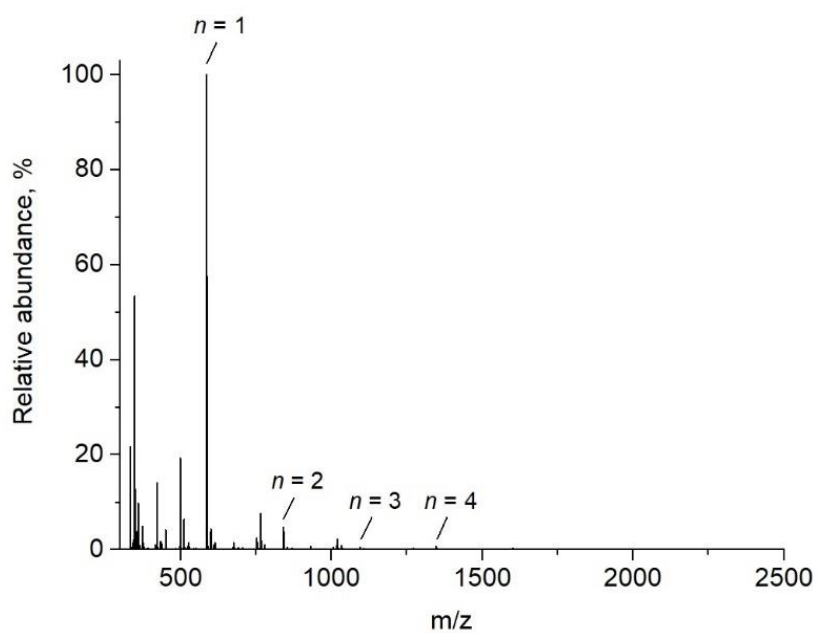
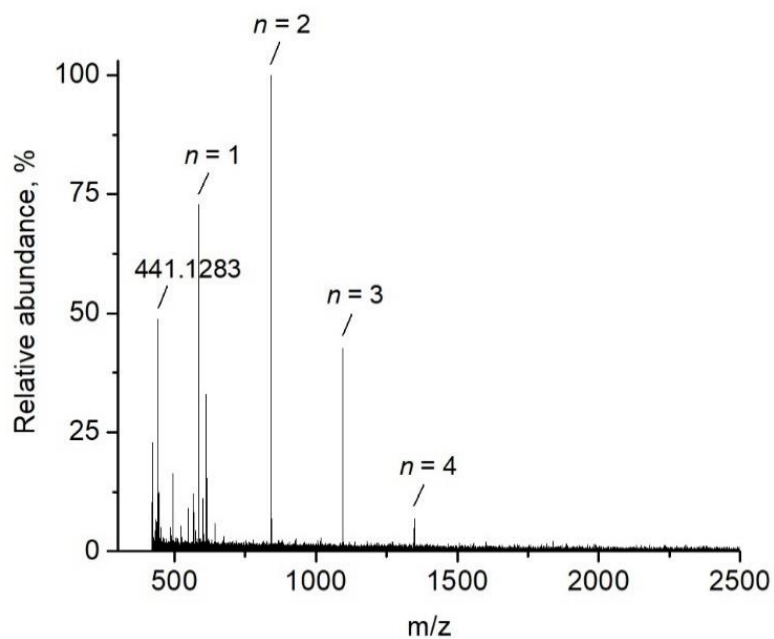


Photo images of the products of Entries 5 and 6 under UV lamp ($\lambda_{exc} = 365 \text{ nm}$)

HOTf concentration: Subsequently, the influence of HOTf concentration was investigated (Entry 7 and 8). A pronounced difference was not observed.

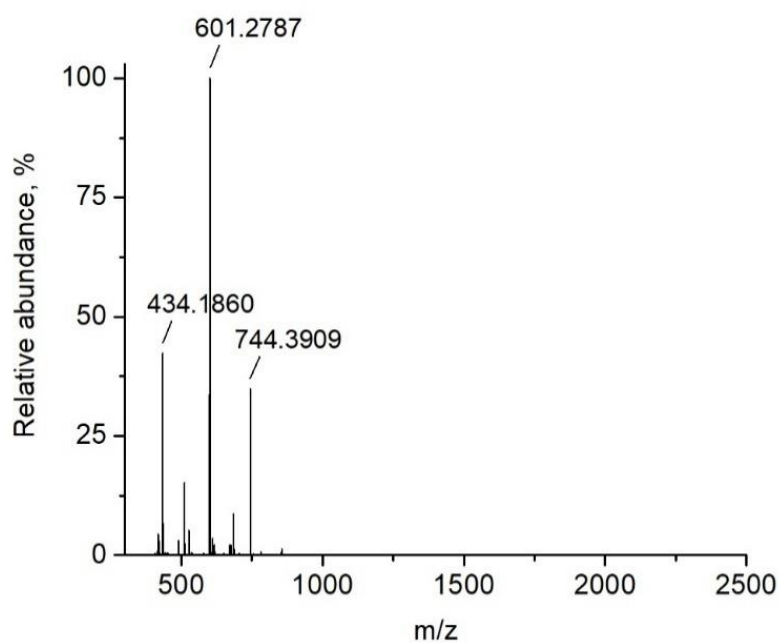


APPI HRMS of the product of Entry 7

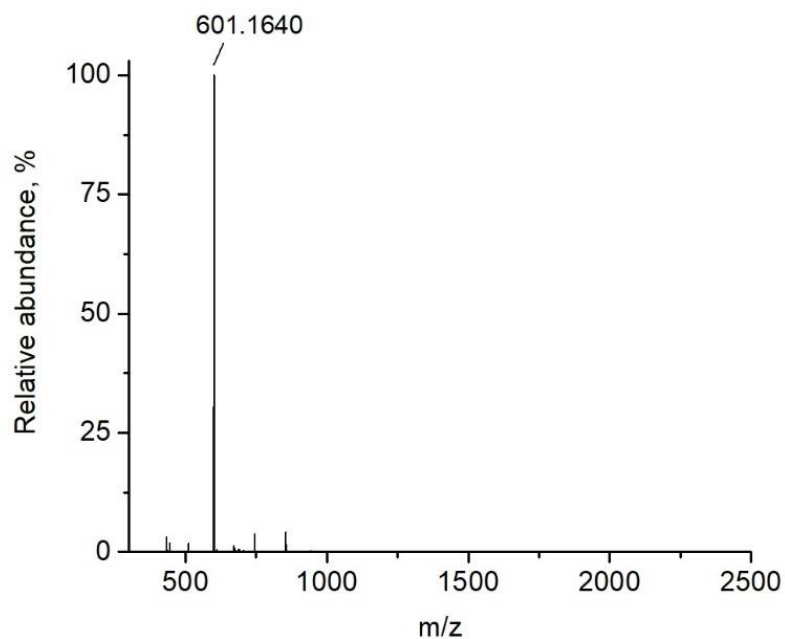


MALDI-TOF (CHCA matrix) HRMS of the product of Entry 8

Triazene concentration: Increasing the concentration of **1** along with that of HOTf suppressed the coupling reaction (Entry 9 and 10).



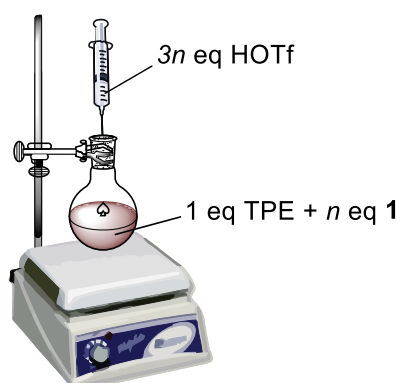
MALDI-TOF (CHCA matrix) HRMS of the product of Entry 9



MALDI-TOF (CHCA matrix) HRMS of the product of Entry 10

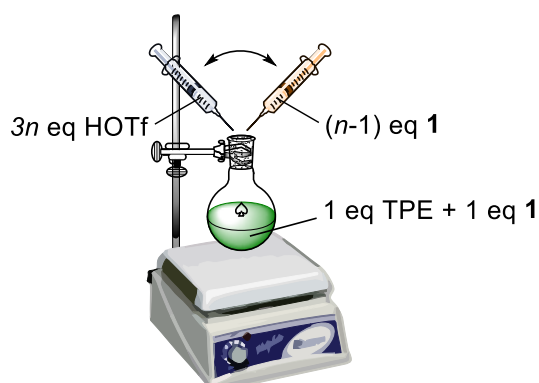
Addition method: The experiments using addition method I were performed in the following way: HOTf was added dropwise to a solution of **1** and TPE in DCM. In the presence of excess **1**, oligomers with higher molecular weights were not observed (Entry 9 and 10). Alternating addition of first **1** and then HOTf followed by stirring for 1 h (addition method II) gave improved results (Entry 11).

Addition method I

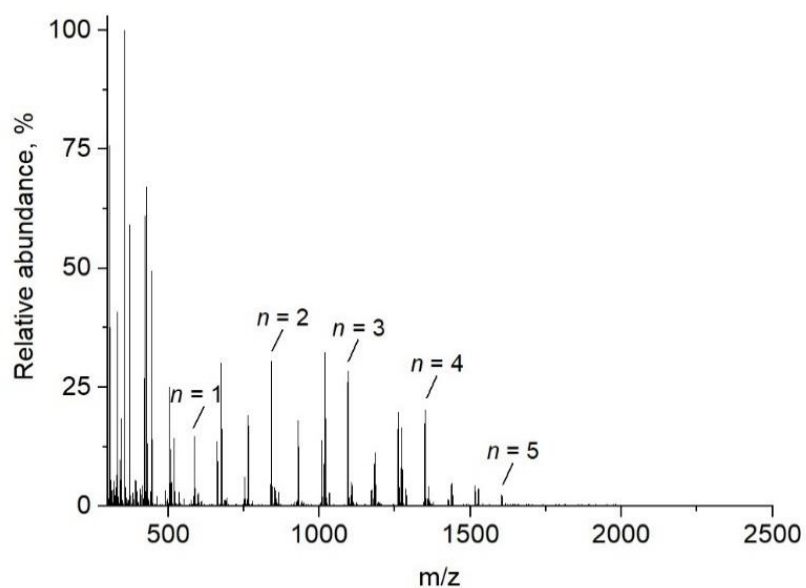


Slow addition of the acid ❌

Addition method II

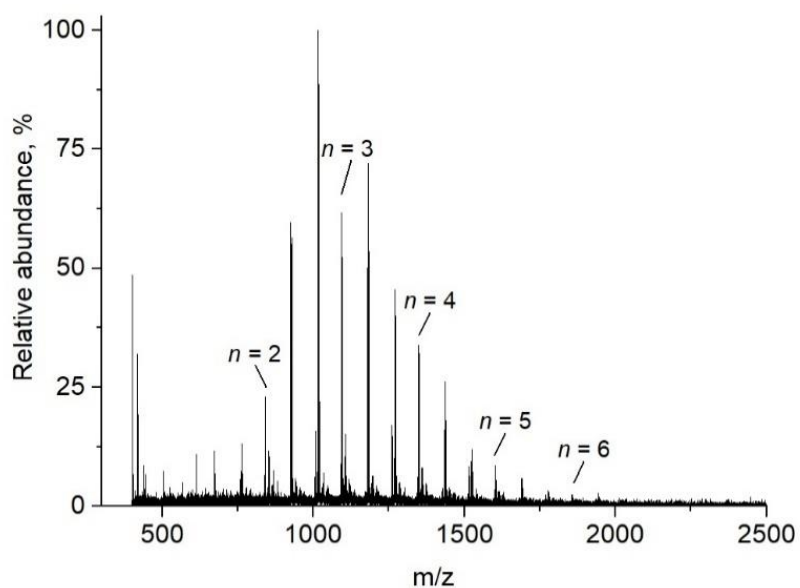


Slow alternating addition of both the triazene and the acid ✅



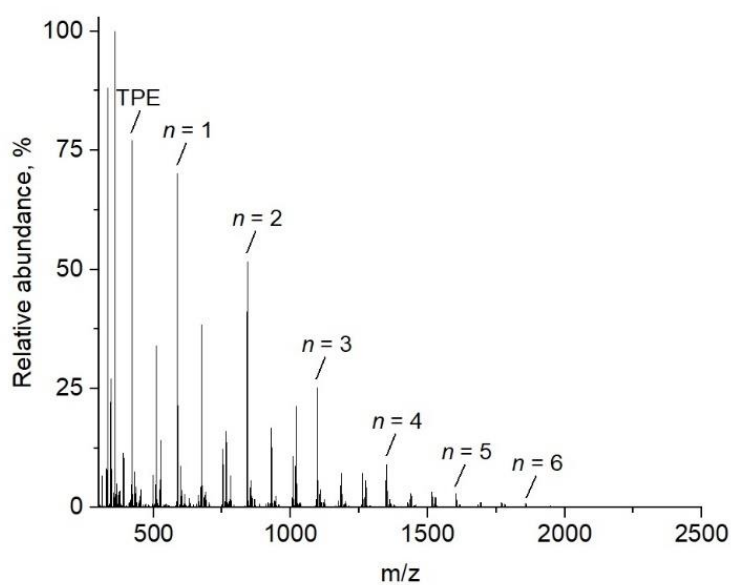
APPI HRMS of the product of Entry 11

Reconsidering the acid concentration: Using addition method II, the influence of the HOTf concentration was re-evaluated. In the experiments with addition method I, the HOTf concentration had a negligible effect (Entry 7 and 8). However, the relative amount of HOTf was found to have an influence when using addition method II (Entry 12). An MS analysis showed that a 3-fold excess of HOTf with respect to the triazene **1** was advantageous.



MALDI-TOF HRMS of the product of Entry 12

Glovebox vs. Schlenk line: A polymerization reaction was performed using Schlenk line techniques instead of a glovebox (Entry 13). An HRMS analysis of the product revealed a higher abundance of products with low masses.



APPI+ HRMS of the product of Entry 13

Solubility of the polymers: Solubility (S , mg/mL) of the product of Entry 12 in different solvents was investigated to develop an effective workup procedure. A sample was weighted (m , mg) in a vial, and a solvent (V , mL) was added using a micropipette (1000 μ L). The S was calculated using the corrected volume V' depending on the solvent density P_s .

$$V' = \frac{V \times P_s}{P_w}, S = \frac{m}{V'}$$

If the sample was partially soluble (**p/s**) or not soluble (**n/s**), the colour(s) of the precipitate(s) were noted. The solubility observations are summarized below (the rows are arranged accordingly to the relative polarity of the solvents from 0 to 1²¹⁹).

Solubility of the product of Entry 12 and colour(s) of precipitate(s)

Solvent	m , mg	V , mL	P_s , g/mL	V' , mL	S , mg/mL	Colour of precipitate
Cyclohexane	0.85	0.1	0.77	0.08	10.6	–
Pentane	1.89	>5	0.63	–	p/s	orange
Hexane	1.96	>5	0.66	–	p/s	orange
Heptane	1.49	>5	0.68	–	p/s	orange
Toluene	1.57	0.1	0.87	0.09	17.4	–
Et ₂ O	1.27	0.2	0.71	0.14	9.1	–
1,4-dioxane	0.92	0.1	1.03	0.10	9.2	–
Chlorobenzene	1.40	0.1	1.11	0.11	12.7	–
THF	1.02	0.1	0.88	0.09	11.3	–
Ethyl acetate	2.02	0.1	0.90	0.09	22.4	–
Chloroform	0.96	0.1	1.48	0.15	6.4	–
DCM	1.55	0.1	1.33	0.13	11.9	–
1,2-DCE	1.70	0.1	1.25	0.12	14.2	–
Acetone	1.45	0.2	0.78	0.16	9.1	–
DMF	1.81	0.1	0.94	0.09	20.1	–
Acetonitrile	1.93	>5	0.79	–	p/s	orange
MeNO ₂	1.72	>2	1.38	–	p/s	orange
<i>i</i> PrOH	1.23	>5	0.79	–	n/s	yellow + orange
Ethanol	1.33	>5	0.79	–	n/s	yellow + orange
Methanol	1.04	>5	0.79	–	n/s	yellow + orange
Water	1.69	>5	1.00	–	n/s	yellow + orange

According to the observations, the samples are **p/s** and **n/s** in non-polar and highly polar solvents. During the solubility experiment, a formation of two precipitates was observed – **yellow** which was better soluble, and **orange** which was mostly insoluble.

We attributed these precipitates to the products with low and high molecular weights, respectively. Thus, to develop an effective work-up procedure achieving separation of the mixture of oligomeric and polymeric products, the solvents leading to **p/s** (pentane, hexane, heptane, MeCN or MeNO₂) can be used. On the contrary, the samples were highly soluble in the solvents with medium polarity.

Work-up procedure: Based on solubility observations, the following work-up procedure was developed:

1. Addition of dry K₂CO₃ to the reaction mixture and stirring until the colour changed from dark green (probably HOTf adducts) to dark orange.
2. Precipitating the products with methanol followed by centrifugation.
3. Washing of the precipitate with methanol to remove phenyl ammonium triflate formed upon cleavage of the triazene group.
4. Washing of the precipitate with a mixture of diethyl ether and hexane (1:1, v/v) to remove shorter oligomers and traces of methanol;
5. Drying under high vacuum at least 3 h.

After applying this work-up procedure for the polymerization reaction with $n = 20$ (**P4**), an orange amorphous powder was obtained.



Photo of a sample of **P4**

6.3 Experimental Part for Chapter 3

6.3.1 Synthesis of Facial Isomers

Facial isomers of the complexes Ir(ppy)₃, Ir(tpy)₃, Ir(meppy)₃, Ir(buppy)₃, Ir(fppy)₃ and Ir(dfppy)₃, where metalated ppy = 2-phenylpyridine, tpy = 2-(4-methylphenyl)pyridine, meppy = 2-(4-methoxyphenyl)pyridine, buppy = 2-(4-*tert*-butylphenyl)pyridine, fppy = 2-(4-fluorophenyl)pyridine, dfppy = 2-(2,4-difluorophenyl)pyridine, were prepared according to the microwave irradiation-involved procedure described by H. Konno and Y. Sasaki for *fac*-Ir(ppy)₃ and *fac*-Ir(tpy)₃ with some modifications.¹¹⁶ The modified procedure was used for the synthesis of *fac*-Ir(meppy)₃, *fac*-Ir(buppy)₃, *fac*-Ir(fppy)₃, *fac*-Ir(dfppy)₃. Furthermore, we report a method for the recovery of the cyclometalating ligand, which is used in excess during the reaction.

General procedure for the synthesis of *fac* complexes. Ethylene glycol (10 mL) was added to a microwave reaction vial containing a stirring bar, IrCl₃·xH₂O (50.0 mg, 0.14 mmol, 1.00 equiv.), and the respective arylpyridine ligand (14.2 mmol, 100 equiv.). The vial was sealed by a metallic cap with a septum and degassed by multiple vacuum-N₂ purging cycles. The vial was placed in a microwave synthesizer, and the mixture was heated to 200 °C for 20–40 min. The resulting crystalline precipitate was isolated by centrifugation, washed with methanol (2×15 mL) and diethyl ether (2×15 mL), and dried under vacuum.

fac-Ir(ppy)₃. Obtained from IrCl₃·xH₂O and Hppy (2.20 g, 14.2 mmol) with the reaction time of 20 min. Yellow crystals, 84 mg (92%). ¹H NMR (400 MHz, CD₂Cl₂, 298 K) δ 7.92 (d, *J* = 8.2 Hz, 1H), 7.68–7.63 (m, 2H), 7.57 (m, 1H), 6.94–6.87 (m, 2H), 6.81–6.74 (m, 2H). ¹³C {¹H} NMR (101 MHz, CD₂Cl₂, 298 K) δ 167.0, 161.6, 147.8, 144.4, 137.3, 136.8, 130.2, 124.6, 122.7, 120.4, 119.4. The NMR spectra are in agreement with those reported in the literature.¹⁰³

fac-Ir(tpy)₃. Obtained from IrCl₃·xH₂O and Htpy (2.40 g, 14.2 mmol) with the reaction time of 20 min. Yellow crystals, 87 mg (89%). ¹H NMR (400 MHz, CD₂Cl₂, 298 K) δ 7.87 (d, *J* = 8.2 Hz, 1H), 7.63–7.55 (m, 2H), 7.48 (d, *J* = 5.4 Hz, 1H), 6.85 (t, *J* = 6.5 Hz, 1H), 6.71 (d, *J* = 7.9 Hz, 1H), 6.61 (s, 1H), 2.10 (s, 3H). ¹³C {¹H} NMR (101 MHz,

CD₂Cl₂, 298 K) δ 167.1, 162.0, 147.5, 141.8, 139.9, 137.9, 136.5, 124.5, 122.0, 121.6, 119.0, 22.0. The NMR spectra are in agreement with those reported in the literature.¹⁰³

fac-Ir(meppy)₃. Obtained from IrCl₃·xH₂O and Hmeppy (2.62 g, 14.2 mmol) with the reaction time of 40 min. Yellow crystals, 99 mg (95%). ¹H NMR (400 MHz, CD₂Cl₂, 298 K) δ 7.79 (d, *J* = 8.2 Hz, 1H), 7.69–7.45 (m, 3H), 6.94–6.77 (m, 1H), 6.47 (dd, *J* = 8.6, 2.7 Hz, 1H), 6.31 (d, *J* = 2.7 Hz, 1H), 3.55 (s, 3H). ¹³C {¹H} NMR (101 MHz, CD₂Cl₂, 298 K) δ 166.7, 164.1, 161.4, 147.6, 137.6, 136.5, 125.9, 121.6, 121.4, 118.7, 106.3, 55.0. The NMR spectra are in agreement with those reported in the literature.²²⁰

fac-Ir(buppy)₃. Obtained from IrCl₃·xH₂O and Hbuppy (2.99 g, 14.2 mmol) with the reaction time of 40 min. Yellow crystals, 100 mg (86%). ¹H NMR (400 MHz, CD₂Cl₂, 298 K) δ 7.90–7.81 (m, 1H), 7.71–7.49 (m, 3H), 6.91 (m, 3H), 1.07 (s, 9H). The NMR spectrum is in agreement with that reported in the literature.²²¹

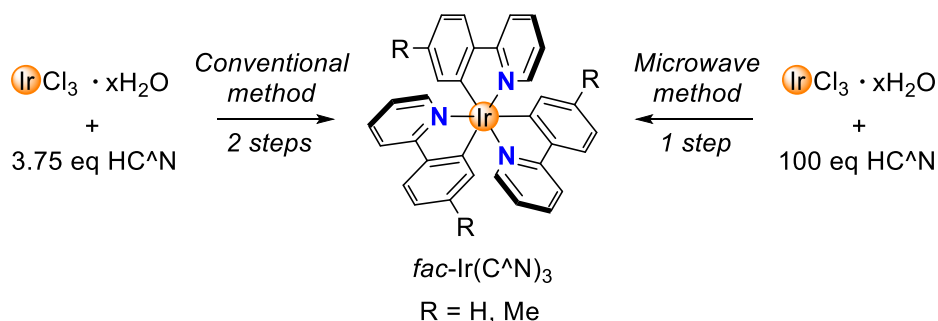
fac-Ir(fppy)₃. Obtained from IrCl₃·xH₂O and Hfppy (2.45 g, 14.2 mmol) with the reaction time of 40 min. Yellow crystals, 91 mg (90%). ¹H NMR (400 MHz, CD₂Cl₂, 298 K) δ 7.87 (d, *J* = 8.2 Hz, 1H), 7.74–7.64 (m, 2H), 7.52 (dq, *J* = 5.5, 1.6, 0.8 Hz, 1H), 6.94 (ddd, *J* = 7.1, 5.6, 1.3 Hz, 1H), 6.62 (td, *J* = 8.7, 2.7 Hz, 1H), 6.39 (dd, *J* = 10.3, 2.7 Hz, 1H). ¹⁹F {¹H} NMR (376 MHz, CD₂Cl₂, 298 K) δ -112.33 (s). The NMR spectra are in agreement with those reported in the literature.²²¹

fac-Ir(dfppy)₃. Obtained from IrCl₃·xH₂O and Hdfppy (2.71 g, 14.2 mmol) with the reaction time of 40 min. Light yellow crystals, 97 mg (91%). ¹H NMR (400 MHz, CD₂Cl₂, 298 K) δ 8.31 (d, *J* = 8.6 Hz, 1H), 7.73 (t, *J* = 7.9 Hz, 1H), 7.51 (d, *J* = 4.8 Hz, 1H), 6.98 (t, *J* = 6.5 Hz, 1H), 6.48–6.34 (m, 1H), 6.24 (dd, *J* = 9.2, 2.4 Hz, 1H). ¹⁹F {¹H} NMR (376 MHz, CD₂Cl₂, 298 K) δ -109.67 (d, *J* = 9.8 Hz), -110.86 (d, *J* = 10.3 Hz). The NMR spectra are in agreement with those reported in the literature.¹⁰³

The excess of ligand remaining in the ethylene glycol solution after centrifugation of the iridium complex was extracted with 2M aqueous H₂SO₄ (50 mL) by shaking the mixture in a separating funnel for 5 min. Subsequently, KHCO₃ (sat. aq., 100 mL) was added to the aqueous layer, and the ligand was extracted with ethyl acetate (3×50 mL). The organic layer was washed with distilled water (2×50 mL), brine (2×50 mL), and dried over anhydrous MgSO₄. The solvent was evaporated to give more than 50

equiv. of regenerated ligand. Flash column chromatography using a mixture of DCM–hexane (1:5 v/v) can be used for the purification of the ligand, if needed.

Cost analysis of the microwave method



To compare the cost efficiency of the conventional and microwave method, we estimated the cost of the products *fac*-Ir(ppy)₃ and *fac*-Ir(tpy)₃ per 1 mmol prepared by both methods. For this, we considered only the prices of starting materials per 1 mmol (taken from Sigma Aldrich for reagent grade chemicals by September 2023) taking into account the yields at each step and net time of synthesis without work-up.

Compound	Price, CHF	Quantity	Mol. weight, g/mol	Cost*, CHF
IrCl ₃ ·xH ₂ O	995	5 g	298.58	59.42
ppy	169	25 mL	155.2	0.996
tpy	237	25 g	169.2	1.604
<i>fac</i> -Ir(ppy) ₃	441	250 mg	654.78	1155
<i>fac</i> -Ir(tpy) ₃	158	100 mg	696.86	1101

* commercial cost per 1 mmol

Compound	Method	Yield dimer, %	Yield <i>fac</i> , %	Time, h	<i>fac</i> cost*, CHF
<i>fac</i> -Ir(ppy) ₃	Conventional ^a	88	79	48	90.47
	Microwave ^b	–	92	0.333	102.0
<i>fac</i> -Ir(tpy) ₃	Conventional	68	81	48	117.6
	Microwave	–	89	0.333	134.7

^a *i.* IrCl₃·xH₂O + 2.5 HC^N, 2-ethoxy-ethanol–water, 100 °C, 24h, inert atmosphere; *ii.*

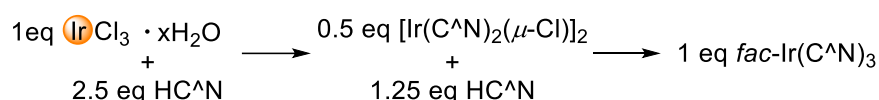
[Ir(C^N)₂(μ-Cl)]₂ + 2.5 HC^N, K₂CO₃, glycerol, 200 °C, 24 h, inert atmosphere. ^b

IrCl₃·xH₂O + 100 HC^N, ethylene glycol, 200 °C, 20 min, inert atmosphere, microwave.

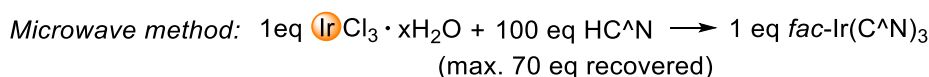
* synthetic cost per 1 mmol considering the yields.

The cost of the facial complexes per 1 mmol considering the yield was calculated using the formulae shown below.

Conventional method:



$$\text{Cost}^*(\text{fac}) = \frac{\text{Cost}^*(\text{IrCl}_3 \cdot x\text{H}_2\text{O}) + 2.5 \text{ Cost}^*(\text{HC}^{\wedge}\text{N})}{\text{Yield}([\text{Ir}(\text{C}^{\wedge}\text{N})_2(\mu\text{Cl})]_2)} + \frac{1.25 \text{ Cost}^*(\text{HC}^{\wedge}\text{N})}{\text{Yield}(\text{fac})} \quad (1)$$



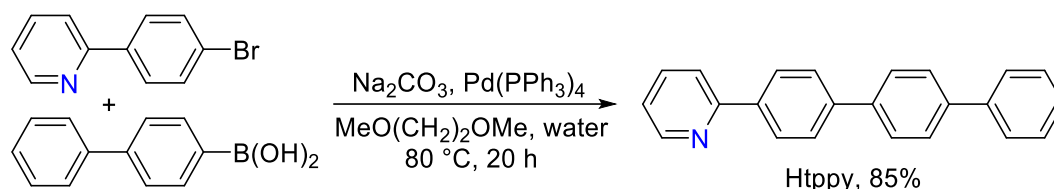
$$\text{Cost}^*(\text{fac}) = \frac{\text{Cost}^*(\text{IrCl}_3 \cdot x\text{H}_2\text{O}) + 100 \text{ Cost}^*(\text{HC}^{\wedge}\text{N})}{\text{Yield}(\text{fac})} - 70 \text{ Cost}^*(\text{HC}^{\wedge}\text{N}) \quad (2)$$

The conventional method consists of 2 steps, where the first one is the preparation of $[\text{Ir}(\text{C}^{\wedge}\text{N})_2(\mu\text{-Cl})]_2$, thus the formula (1) considers the yields of $[\text{Ir}(\text{ppy})_2(\mu\text{-Cl})]_2$ and $[\text{Ir}(\text{tpy})_2(\mu\text{-Cl})]_2$ and the coefficients in the corresponding chemical reactions. The microwave method consists of 1 step, so only the yields of $\text{fac-Ir}(\text{ppy})_3$ and $\text{fac-Ir}(\text{tpy})_3$ are considered in the formula (2). In addition, max. 70 equiv. of HC[^]H ligands can be recovered using the microwave method, which is also considered in the formula (2).

According to the cost analysis per 1 mmol, synthesizing $\text{fac-Ir}(\text{C}^{\wedge}\text{N})_3$ is around 10 times cheaper than buying them from chemical suppliers. Regarding the synthetic cost, the microwave method is slightly more expensive (11–17 CHF) than the conventional method, however the latter is much less time-consuming (0.333 h vs 48 h) and provides better yields (90% vs 80%). The microwave setup also allows carrying out several parallel syntheses of $\text{fac-Ir}(\text{C}^{\wedge}\text{N})_3$, which can be further combined and worked-up together using the simple procedure of filtration, washing the solid product with several solvents, and drying, which does not require column chromatography. Moreover, the excess of HC[^]N ligand can be recovered and used for further reaction. Thus, the microwave method may become advantageous to utilize for the synthesis of $\text{fac-Ir}(\text{C}^{\wedge}\text{N})_3$ compared to the conventional method.

6.3.2 Syntheses of the Complexes $\text{mer-Ir}(\text{tppy})_3$ and $\text{fac-Ir}(\text{tppy})_3$

The ligand 2-([1,1':4',1''-terphenyl]-4-yl)pyridine (Htppy) was synthesized by a Suzuki-Miyaura cross-coupling reaction.



Htpy. A mixture of 2-(4-bromophenyl)pyridine (871 mg, 3.72 mmol, 1.0 equiv.), 4-biphenylboronic acid (810 mg, 4.09 mmol, 1.1 equiv.), Na_2CO_3 (1.18 g, 11.1 mmol, 3.0 equiv.) and $\text{Pd}(\text{PPh}_3)_4$ (215 mg, 0.19 mmol, 5 mol. %) was placed in a 100 mL Schlenk flask equipped with a stirring bar and degassed. Subsequently, a degassed mixture of 1,2-dimethoxyethane-water (4:1 v/v, 50 mL) was added to the solids. The mixture was stirred under an atmosphere of N_2 at $80\text{ }^\circ\text{C}$ for 20 h. After cooling down to room temperature, the mixture was poured into NH_4Cl (sat. aq., 100 mL) and the product was extracted with dichloromethane (3×100 mL). The organic layer was washed with brine, dried over MgSO_4 , and concentrated *in vacuo*. The residue was purified from triphenylphosphine oxide by chromatography on silica and the product was eluted with dichloromethane ($R_f = 0.47$) to give a pale-yellow precipitate after solvent evaporation. The precipitate was rinsed with diethyl ether (2×7 mL) and dried under vacuum to give Htpy (971 mg, 85%) as a white crystalline solid. ^1H NMR (400 MHz, CD_2Cl_2 , 298 K) δ 8.70 (m, 1H), 8.14 (m, 2H), 7.85–7.77 (m, 6H), 7.73 (m, 2H), 7.68 (m, 2H), 7.48 (m, 2H), 7.38 (m, 1H), 7.27 (m, 1H). ^{13}C $\{^1\text{H}\}$ NMR (101 MHz, CDCl_3 , 298 K) δ 157.0, 149.6, 141.5, 140.8, 140.6, 139.5, 138.1, 137.2, 129.0, 127.7, 127.6, 127.6, 127.5, 127.2, 122.4, 120.8. HRMS (ESI/QTOF) m/z : $[\text{M}+\text{H}]^+$ calcd. for $\text{C}_{23}\text{H}_{18}\text{N}^+$ 308.1434; found 308.1431. Elem. anal. calcd. for $\text{C}_{23}\text{H}_{17}\text{N}$: C, 89.87; H, 5.57; N, 4.56; found: C, 89.59; H, 5.36; N, 4.48. Single crystals of Htpy were obtained by slow diffusion of hexane into DCM solution of Htpy at r.t. The compound was described in the literature without full characterization.²²²

The chloro-bridged dimer $[\text{Ir}(\text{tppy})_2(\mu\text{-Cl})]_2$ was obtained following the procedure described by B. Orwat and co-workers for the synthesis of the complexes $[\text{Ir}(\text{ppy})_2(\mu\text{-Cl})]_2$ and $[\text{Ir}(\text{dfppy})_2(\mu\text{-Cl})]_2$ with some modifications.¹¹⁰

$[\text{Ir}(\text{tppy})_2(\mu\text{-Cl})]_2$. A mixture of 2-ethoxyethanol-water (3:1 v/v, 20 mL) was added to a microwave reaction vial equipped with a stirring bar and containing $\text{IrCl}_3 \cdot x\text{H}_2\text{O}$ (705 mg, 2.00 mmol, 1.0 equiv.) and Htpy (1355 mg, 4.371 mmol, 2.2 equiv.). The vial was sealed by a cap with a septum and degassed by multiple vacuum- N_2 purging

cycles. The vial was placed in the microwave synthesizer and the reaction mixture was heated to 150 °C for 20 min. The resulting precipitate was isolated by centrifugation, washed with methanol (2×15 mL) and diethyl ether (2×15 mL), and dried under vacuum to give $[\text{Ir}(\text{tpyy})_2(\mu\text{-Cl})_2]$ (1378 mg, 82%) as an orange amorphous powder. ^1H NMR (400 MHz, CD_2Cl_2 , 298 K) δ 9.42 (d, J = 5.0 Hz, 1H), 8.02 (d, J = 8.0 Hz, 1H), 7.91–7.83 (m, 1H), 7.67 (d, J = 8.2 Hz, 1H), 7.59–7.55 (m, 2H), 7.50 (d, J = 8.4 Hz, 2H), 7.41 (d, J = 7.8 Hz, 2H), 7.34–7.30 (m, 3H), 7.15 (dd, J = 8.1, 1.8 Hz, 1H), 6.98–6.90 (m, 1H), 6.23 (d, J = 1.7 Hz, 1H).

fac- $\text{Ir}(\text{tpyy})_3$ was synthesized from *mer*- $\text{Ir}(\text{tpyy})_3$ by thermal *mer*-to-*fac* isomerization using the conditions described by G. van Koten and co-workers.¹⁷⁸ The complex *mer*- $\text{Ir}(\text{tpyy})_3$ was obtained following the standard conditions for the synthesis of facial isomers of homoleptic iridium(III) complexes from the corresponding chloro-bridged dimers in glycerol.¹⁰³

mer- $\text{Ir}(\text{tpyy})_3$. A mixture of $[\text{Ir}(\text{tpyy})_2(\mu\text{-Cl})_2]$ (200 mg, 0.12 mmol, 1.0 equiv.), Htpyy (91 mg, 0.3 mmol, 2.5 equiv.) and K_2CO_3 (164 mg, 1.19 mmol, 10 equiv.) was placed in a 100 mL Schlenk flask equipped with stirring bar and degassed. Subsequently, glycerol (20 mL) was added to the solids. The mixture was stirred under an atmosphere of N_2 at 200 °C for 22 h (*the utilization of a heating block instead of an oil bath is convenient*). After cooling down to room temperature, the mixture was poured into water (20 mL). The brown precipitate was isolated by centrifugation, washed with methanol (3×15 mL) and diethyl ether (2×15 mL) and dried under high vacuum. The residue was purified by flash chromatography on silica and the product was eluted with dichloromethane to give *mer*- $\text{Ir}(\text{tpyy})_3$ (177 mg, 67%) as an orange amorphous solid. ^1H NMR (400 MHz, CD_2Cl_2 , 298 K) δ 8.30 (dd, J = 5.9, 1.0 Hz, 1H), 8.10 (d, J = 4.6 Hz, 1H), 8.04 (d, J = 8.2 Hz, 1H), 7.96–7.22 (m, 40H), 7.01–6.93 (m, 2H), 6.85 (m, 3H). ^{13}C { ^1H } NMR (101 MHz, CD_2Cl_2 , 298 K) δ 155.5, 153.9, 148.6, 145.8, 141.9, 141.8, 141.2, 137.4, 136.9, 136.5, 136.4, 135.6, 135.1, 131.2, 129.4, 129.3, 129.3, 129.3, 129.2, 129.2, 128.1, 128.0, 127.9, 127.8, 127.7, 127.7, 127.6, 127.4, 127.4, 125.2, 125.2, 125.1, 123.1, 122.9, 122.2, 120.9, 120.8, 119.9, 119.7, 119.6, 119.4, 119.0. HRMS (ESI/QTOF) m/z : $[\text{M}+\text{H}]^+$ calcd. for $\text{C}_{69}\text{H}_{49}^{193}\text{IrN}_3^+$ 1112.3550; found 1112.3551. Elem. anal. calcd. for $\text{C}_{69}\text{H}_{48}\text{IrN}_3$: C, 74.57; H, 4.35; N, 3.78; found: C,

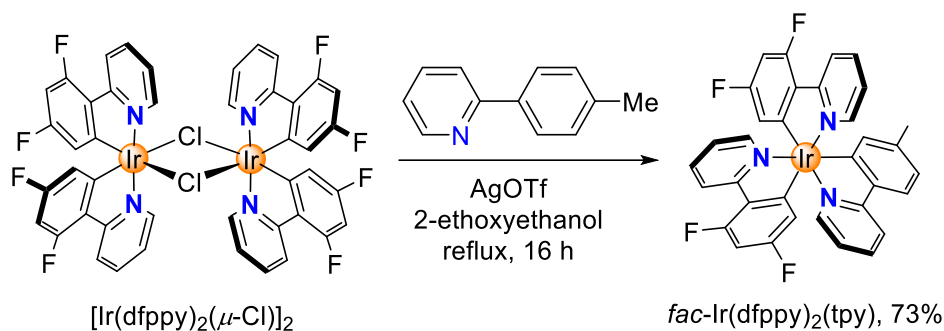
74.54; H, 4.38; N, 3.60. Single crystals of *mer*-Ir(tppy)₃ were obtained by slow gas phase diffusion of hexane into a solution of *mer*-Ir(tppy)₃ in DCM at r.t.

fac-Ir(tppy)₃. *mer*-Ir(tppy)₃ (170 mg, 0.15 mmol) and phenol (3 g) were added to a microwave reaction vial equipped with a stirring bar. The vial was sealed by a metallic cap with a septum and degassed by multiple vacuum-N₂ purging cycles. The vial was placed in a heating block and the mixture was stirred at refluxing temperature of phenol (185 °C) for 20 h. After cooling to room temperature, the brown solution was transferred to a 25 mL round-bottom flask, and phenol was completely removed by sublimation on a water-cooled condenser (47 °C). The brownish-yellow precipitate was purified by chromatography on silica and the product was eluted with DCM to give *fac*-Ir(tppy)₃ (170 mg, quant.) as an orange crystalline solid. ¹H NMR (400 MHz, CD₂Cl₂, 298 K) δ 7.99 (d, *J* = 8.2 Hz, 1H), 7.79 (d, *J* = 8.2 Hz, 1H), 7.69 (m, 2H), 7.62–7.44 (m, 6H), 7.38 (t, *J* = 7.6 Hz, 2H), 7.28 (m, 3H), 6.99 (t, *J* = 6.4 Hz, 1H). ¹³C {¹H} NMR (101 MHz, CD₂Cl₂, 298 K) δ 166.8, 161.9, 147.9, 144.2, 141.6, 141.6, 141.3, 139.9, 136.9, 135.6, 129.2, 127.9, 127.6, 127.6, 127.4, 125.0, 122.7, 119.7, 119.6. HRMS (ESI/QTOF) *m/z*: [M+H]⁺ calcd. for C₆₉H₄₉¹⁹³IrN₃⁺ 1112.3550; found 1112.3548. Elem. anal. calcd. for C₆₉H₄₈IrN₃: C, 74.57; H, 4.35; N, 3.78; found: C, 74.51; H, 4.34; N, 3.60. Single crystals of *fac*-Ir(tppy)₃ were obtained by slow gas phase diffusion of diethyl ether into a solution of *fac*-Ir(tppy)₃ in DCM at r.t.

6.3.3 Synthesis of the Heteroleptic Complex *fac*-Ir(dfppy)₂(tpy)

[Ir(dfppy)₂(μ-Cl)]₂ was synthesized analogously to [Ir(tppy)₂(μ-Cl)]₂ from IrCl₃·xH₂O (705 mg, 2.00 mmol, 1.0 equiv.) and Hdfppy (841 mg, 4.40 mmol, 2.2 equiv.). The dimer was isolated as light-yellow powder (1039 mg, 85%). ¹H NMR (400 MHz, CD₂Cl₂, 298 K) δ 9.12 (dd, *J* = 5.8, 0.9 Hz, 1H), 8.33 (d, *J* = 8.4 Hz, 1H), 7.95–7.78 (m, 1H), 6.87 (ddd, *J* = 7.3, 5.9, 1.3 Hz, 1H), 6.38 (ddd, *J* = 12.4, 9.2, 2.3 Hz, 1H), 5.29 (dd, *J* = 9.1, 2.3 Hz, 1H). ¹⁹F {¹H} NMR (376 MHz, CD₂Cl₂, 298 K) δ -108.42 (d, *J* = 9.6 Hz), -110.61 (d, *J* = 10.1 Hz). The NMR data are in agreement with those reported in the literature.²²³

The heteroleptic complex *fac*-Ir(dfppy)₂(tpy) was obtained from [Ir(dfppy)₂(μ-Cl)]₂ and Htpy as described by S. Aoki and co-workers²²⁴ with modifications regarding the purification.

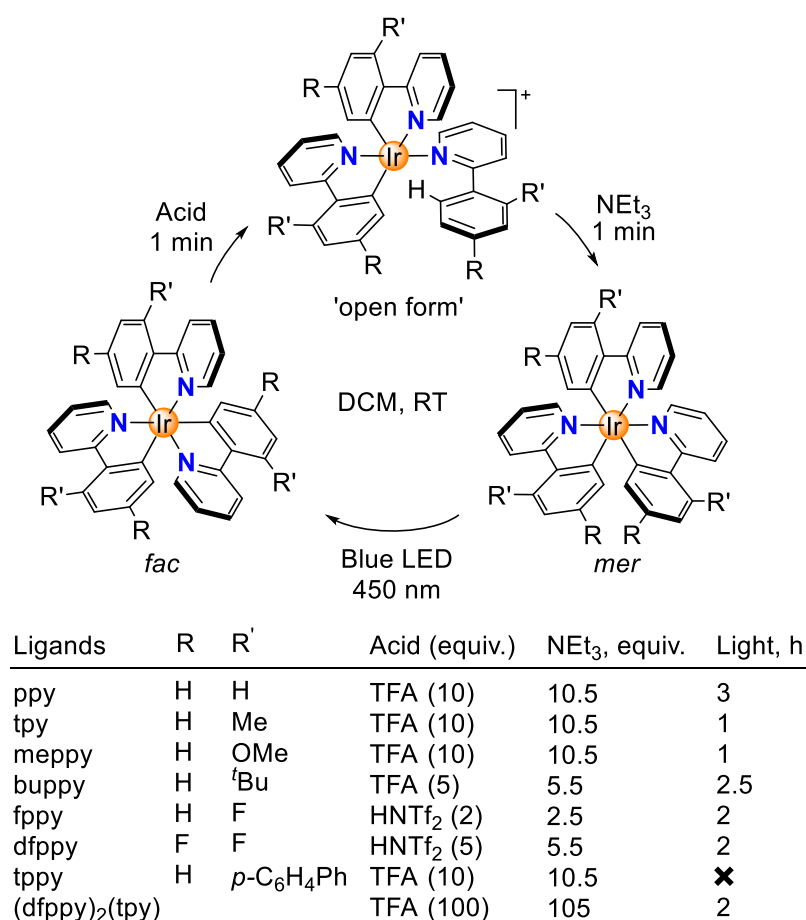


fac-Ir(dfppy)₂(tpy). A mixture of [Ir(dfppy)₂(μ-Cl)]₂ (455 mg, 0.37 mmol, 1.0 equiv.), Htpy (190 mg, 1.12 mmol, 3.0 equiv.) and AgOTf (201 mg, 0.79 mmol, 2.1 equiv.) was placed in a 50 mL Schlenk flask equipped with stirring bar and degassed. Subsequently, 2-ethoxyethanol (12 mL) was added to the solids. The mixture was stirred under N₂ atmosphere at refluxing temperature (135 °C) for 16 h. After cooling down to room temperature, the mixture was poured into water (20 mL). The yellow precipitate was isolated by centrifugation and suspended in DCM (150 mL). The organic layer was washed with water (2×50 mL), brine (50 mL), dried over MgSO₄, filtered, and concentrated *in vacuo*. The product was purified by column chromatography on silica and eluted with hexane/ethyl acetate (2:1, v/v) with *R_f* = 0.27 to give a yellow powder after solvent evaporation. The powder was recrystallized by slow diffusion of methanol into a solution of the product in DCM at room temperature to give *fac*-Ir(dfppy)₂(tpy) as yellow crystalline needles (405 mg, 73%). ¹H NMR (400 MHz, CD₂Cl₂, 298 K) δ 8.30 (d, *J* = 8.5 Hz, 2H), 7.89 (d, *J* = 8.2 Hz, 1H), 7.76–7.62 (m, 3H), 7.62–7.49 (m, 3H), 7.43 (d, *J* = 5.3 Hz, 1H), 6.93 (m, 3H), 6.77 (d, *J* = 7.9 Hz, 1H), 6.56 (s, 1H), 6.48–6.31 (m, 2H), 6.31–6.19 (m, 2H), 2.13 (s, 3H). ¹⁹F {¹H} NMR (376 MHz, CD₂Cl₂, 298 K) δ -109.06 (d, *J* = 10.2 Hz), -109.47 (d, *J* = 9.8 Hz), -111.01 (d, *J* = 9.7 Hz), -111.23 (d, *J* = 9.8 Hz). ¹³C {¹H} NMR (126 MHz, CD₂Cl₂, 298 K) δ 166.78 (s), 166.44 (dd, *J* = 34.4, 6.3 Hz), 165.36–165.07 (m), 163.62–163.05 (m), 161.28 (d, *J* = 12.5 Hz), 159.34 (s), 147.75 (d, *J* = 5.5 Hz), 147.48 (s), 141.57 (s), 140.70 (s), 137.63 (s), 137.47 (s), 137.30 (s), 128.26 (m), 124.72 (s), 123.65 (dd, *J* = 21.2, 7.9 Hz), 122.79 (d, *J* = 6.9 Hz), 122.44 (d, *J* = 20.9 Hz), 119.43 (s), 118.37 (ddd, *J* = 15.7, 10.1, 2.6 Hz), 96.94–96.27 (m), 21.95 (s). HRMS (ESI/QTOF) *m/z*: [M+H]⁺ calcd. for C₃₄H₂₃F₄¹⁹³IrN₃⁺ 742.1452; found 742.1451. Elem. anal. calcd. for C₃₄H₂₂F₄IrN₃: C, 55.13; H, 2.99; N, 5.67; found: C, 55.13; H, 2.98; N, 5.67. The NMR

spectra of *fac*-Ir(dfppy)₂(tpy) obtained are in agreement with those reported in the literature.^{194,224}

6.3.4 General Procedure for the Repetitive *fac*↔*mer* Isomerization

The *fac*↔*mer* isomerizations of the complexes Ir(ppy)₃, Ir(tpy)₃, Ir(meppy)₃, Ir(buppy)₃, Ir(fppy)₃, Ir(dfppy)₃, Ir(tppy)₃ and Ir(dfppy)₂(tpy) were performed in NMR scale following the General Procedure optimized for each complex and described below. The *mer*→*fac* isomerization of Ir(tppy)₃ was achieved thermally and not by light irradiation.

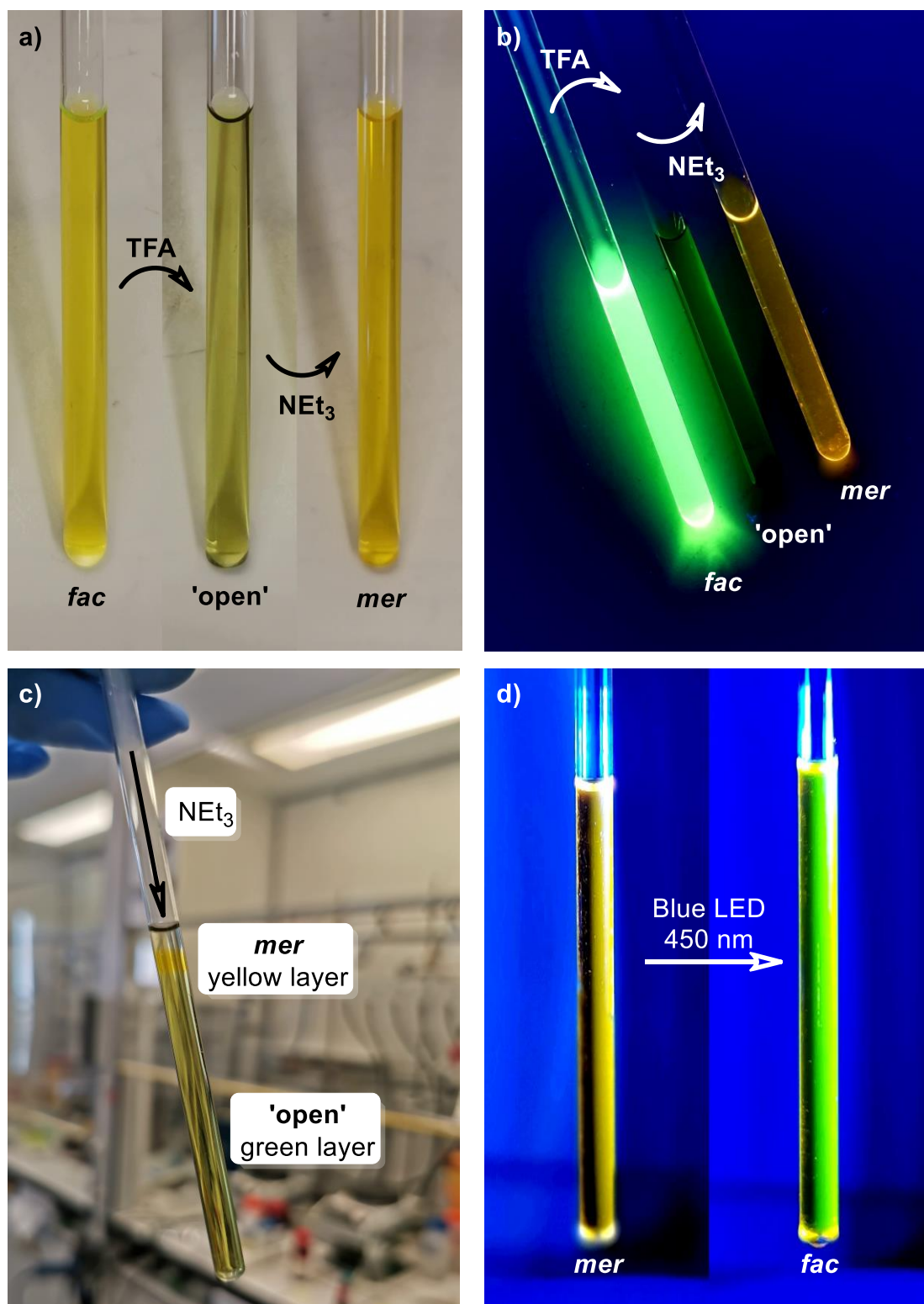


fac-Ir(C[^]N)₃ (1–5 mg, 1 equiv.) was placed in a 5 mL vial equipped with a stirring bar and dissolved in 0.5 mL of CD₂Cl₂ resulting in a yellow solution. Subsequently, the corresponding acid stock solution in CD₂Cl₂ (5, 10 or 100 molar equiv.) was added in one portion under vigorous stirring (1200 rpm). The reaction was accompanied by a change of colour to greenish-yellow and emission quenching. After 1 min of stirring at room temperature, the solution was transferred to an NMR tube, and a spectrum of the protonated complex ('open form') was recorded.

Subsequently, the solution of the open form was transferred back to the vial, and an aliquot of NEt₃ stock solution in CD₂Cl₂ (5.5, 10.5 or 105 molar equiv.) was added slowly dropwise under vigorous stirring (1200 rpm). The reaction was accompanied by a change of colour back to yellow and by an increased emission intensity. After 1 min of stirring at room temperature, the solution was transferred to an NMR tube, and a spectrum of *mer*-Ir(C^N)₃ was recorded.

Subsequently, the NMR tube containing the solution of *mer*-Ir(C^N)₃ was exposed to the blue light of a Kessil LED lamp ($\lambda_{em} = 450$ nm, 90 W, A360W E-series tuna blue https://kessil.com/aquarium/saltwater_A360.php) at room temperature for 1–3 h. Finally, a spectrum of *fac*-Ir(C^N)₃ was recorded.

Visualization of a simplified version of the General Procedure (under air, without stirring) for the isomerization of Ir(ppy)₃ is shown below.



Photos of NMR tubes during the *fac*→*mer*→*fac* isomerization of Ir(ppy)₃. a) Acid-base *fac*→*mer* isomerization of Ir(ppy)₃ under daylight and b) upon irradiation at 366 nm. c) Formation of a layer of the *mer* isomer upon addition of NEt₃ to the solution of the open form. d) Photochemical *mer*→*fac* isomerization of Ir(ppy)₃.

[Ir(ppy)₂(Hppy)](O₂CCF₃). A solution of the open form (greenish-yellow, weak green emission) was obtained upon addition of an aliquot of a stock solution of TFA in CD₂Cl₂ (0.5 M, 76.3 μL, 38.2 μmol, 10.0 equiv.) to a solution of *fac*-Ir(ppy)₃ (2.5 mg, 3.8 μmol, 1.0 equiv.) in 0.5 mL of CD₂Cl₂ (yellow, intensive green emission). ¹H NMR (400 MHz, CD₂Cl₂, 298 K) δ 8.17 (d, *J* = 5.8 Hz, 1H), 8.01 (ddd, *J* = 8.2, 6.4, 2.4 Hz, 2H), 7.94–7.73 (m, 8H), 7.56 (dd, *J* = 7.8, 1.4 Hz, 1H), 7.40–7.22 (m, 6H), 7.07–6.97 (m, 2H), 6.94–6.85 (m, 3H), 6.45 (dd, *J* = 7.9, 1.0 Hz, 1H), 6.14 (d, *J* = 5.5 Hz, 1H). ¹⁹F {¹H} NMR (376 MHz, CD₂Cl₂, 253 K) δ –76.03 (s). ¹³C {¹H} NMR (101 MHz, CD₂Cl₂, 253 K) δ 168.6, 162.5, 161.8, 152.7, 149.9, 149.1, 147.2, 146.6, 145.6, 142.6, 139.4, 139.4, 139.2, 136.5, 134.2, 134.1, 134.0, 133.0, 131.4, 131.2, 126.5, 125.6, 125.5, 125.0, 124.8, 124.7, 124.6, 123.5, 120.2, 120.1. HRMS (nanochip-ESI/LTQ-Orbitrap) *m/z*: [M]⁺ calcd. for C₃₃H₂₅IrN₃⁺ 656.1672; found 656.1679. Single crystals of [Ir(ppy)₂(Hppy)](NTf₂) were obtained by slow gas phase diffusion of hexane into a solution of *fac*-Ir(ppy)₃ (20 mg, 1.0 equiv.) and HNTf₂ (43 mg, 5.0 equiv.) in DCM at room temperature.

mer-Ir(ppy)₃. A solution of the *mer* isomer (yellow, yellow emission) was obtained upon addition of an aliquot of a stock solution of NEt₃ in CD₂Cl₂ (0.5 M, 80.2 μL, 40.1 μmol, 10.5 equiv.) to the solution of [Ir(ppy)₂(Hppy)](O₂CCF₃). ¹H NMR (400 MHz, CD₂Cl₂, 298 K) δ 8.09 (d, *J* = 5.0 Hz, 1H), 8.00–7.90 (m, 2H), 7.84 (d, *J* = 8.1 Hz, 2H), 7.78 (d, *J* = 7.3 Hz, 1H), 7.72 (d, *J* = 7.3 Hz, 1H), 7.69–7.60 (m, 3H), 7.60–7.50 (m, 2H), 7.03–6.73 (m, 10H), 6.59 (dd, *J* = 7.1, 1.1 Hz, 1H), 6.42 (d, *J* = 7.5 Hz, 1H). ¹³C {¹H} NMR (101 MHz, CD₂Cl₂, 298 K) δ 177.8, 175.6, 171.0, 168.9, 168.3, 160.1, 153.7, 151.8, 148.5, 146.1, 145.5, 143.0, 138.2, 137.3, 136.3, 134.9, 133.2, 131.1, 130.4, 130.4, 130.1, 124.9, 124.8, 124.5, 123.0, 122.7, 122.0, 121.9, 121.5, 119.7, 119.4, 119.3, 119.0. The NMR spectra of *mer*-Ir(ppy)₃ obtained *in situ* are in agreement with those reported in the literature.¹⁰³

[Ir(tpy)₂(Htpy)](O₂CCF₃). A solution of the open form (greenish-yellow, weak green emission) was obtained upon addition of an aliquot of a stock solution of TFA in CD₂Cl₂ (0.5 M, 57.5 μL, 28.7 μmol, 10.0 equiv.) to a solution of *fac*-Ir(tpy)₃ (2.0 mg, 2.9 μmol, 1.0 equiv.) in 0.5 mL of CD₂Cl₂ (yellow, intensive green emission). ¹H NMR (400 MHz, CD₂Cl₂, 298 K) δ 8.17 (d, *J* = 5.9 Hz, 1H), 7.97 (ddd, *J* = 21.8, 11.0, 4.9 Hz, 2H), 7.87–7.69 (m, 5H), 7.57 (d, *J* = 7.3 Hz, 2H), 7.43 (d, *J* = 7.9 Hz, 1H), 7.32–7.09 (m, 5H),

7.02–6.94 (m, 1H), 6.90–6.76 (m, 2H), 6.68 (s, 1H), 6.27 (s, 1H), 6.16 (d, $J = 5.7$ Hz, 1H), 2.50 (s, 3H), 2.31 (s, 3H), 2.12 (s, 3H). ^{19}F $\{^1\text{H}\}$ NMR (376 MHz, CD_2Cl_2 , 273 K) δ –75.95 (s). ^{13}C $\{^1\text{H}\}$ NMR (101 MHz, CD_2Cl_2 , 273 K) δ 169.1, 162.9, 162.2, 152.8, 149.9, 149.3, 147.5, 145.2, 143.8, 143.0, 142.1, 142.0, 139.9, 139.3, 139.2, 137.0, 134.9, 134.4, 133.9, 126.2, 125.9, 125.7, 125.7, 125.3, 125.0, 124.2, 122.9, 119.9, 119.8, 22.1, 21.9, 21.6.

mer-Ir(tpy)₃. A solution of the *mer* isomer (yellow, yellow emission) was obtained upon addition of an aliquot of a stock solution of NEt₃ in CD_2Cl_2 (0.5 M, 60.3 μL , 30.1 μmol , 10.5 equiv.) to the solution of [Ir(tpy)₂(Htpy)](O₂CCF₃). ^1H NMR (400 MHz, CD_2Cl_2 , 298 K) δ 8.06 (d, $J = 5.0$ Hz, 1H), 7.87 (dd, $J = 10.0, 4.5$ Hz, 2H), 7.77 (dd, $J = 8.0, 3.4$ Hz, 2H), 7.56 (m, 7H), 6.88–6.82 (m, 1H), 6.82–6.66 (m, 6H), 6.36 (s, 1H), 6.21 (s, 1H), 2.12 (s, 6H), 2.10 (s, 3H). The NMR spectrum of *mer*-Ir(tpy)₃ obtained *in situ* are in agreement those reported in the literature for individual compound.¹⁰³

[Ir(meppy)₂(Hmeppy)](O₂CCF₃). A solution of the open form (greenish-yellow, weak cyan emission) was obtained upon addition of an aliquot of a stock solution of TFA in CD_2Cl_2 (0.5 M, 134.4 μL , 67.2 μmol , 10.0 equiv.) to a solution of *fac*-Ir(meppy)₃ (5.0 mg, 6.7 μmol , 1.0 equiv.) in 0.5 mL of CD_2Cl_2 (yellow, intensive green emission). ^1H NMR (400 MHz, CD_2Cl_2 , 293 K) δ 8.16 (d, $J = 5.2$ Hz, 1H), 7.95 (td, $J = 7.9, 1.5$ Hz, 1H), 7.87 (d, $J = 8.7$ Hz, 2H), 7.81–7.67 (m, 4H), 7.50 (d, $J = 8.7$ Hz, 1H), 7.37–7.19 (m, 4H), 7.16 (d, $J = 8.2$ Hz, 2H), 6.98 (ddd, $J = 7.2, 5.8, 1.4$ Hz, 1H), 6.89 (dd, $J = 8.6, 2.5$ Hz, 1H), 6.86–6.78 (m, 1H), 6.59 (dd, $J = 8.6, 2.5$ Hz, 1H), 6.41 (d, $J = 2.5$ Hz, 1H), 6.29 (d, $J = 5.5$ Hz, 1H), 5.95 (d, $J = 2.5$ Hz, 1H), 3.87 (s, 3H), 3.78 (s, 3H), 3.62 (s, 3H). ^{19}F $\{^1\text{H}\}$ NMR (376 MHz, CD_2Cl_2 , 273 K) δ –76.13 (s). ^{13}C $\{^1\text{H}\}$ NMR (101 MHz, CD_2Cl_2 , 273 K) δ 168.5, 164.2, 162.5, 162.0, 161.3, 160.3, 152.4, 149.9, 149.8, 149.2, 139.4, 139.3, 139.3, 139.1, 138.8, 135.7, 135.6, 127.5, 126.6, 125.8, 125.1, 123.7, 122.5, 121.5, 119.7, 119.6, 119.5, 119.1, 109.7, 109.3, 56.5, 55.6, 55.5.

mer-Ir(meppy)₃. A solution of the *mer* isomer (yellow, intensive green emission) was obtained upon addition of an aliquot of a stock solution of NEt₃ in CD_2Cl_2 (0.5 M, 141.1 μL , 70.6 μmol , 10.5 equiv.) to the solution of [Ir(meppy)₂(Hmeppy)](O₂CCF₃). ^1H NMR (400 MHz, CD_2Cl_2 , 298 K) δ 8.05 (dd, $J = 5.9, 0.9$ Hz, 1H), 7.90 (dd, $J = 5.6, 0.9$ Hz, 1H), 7.82 (d, $J = 8.2$ Hz, 1H), 7.69 (dd, $J = 15.3, 8.6$ Hz, 4H), 7.63–7.45 (m, 5H), 6.83

(m, 1H), 6.69 (m, 2H), 6.57–6.46 (m, 3H), 6.40 (d, $J = 2.7$ Hz, 1H), 6.09 (d, $J = 2.6$ Hz, 1H), 5.89 (d, $J = 2.6$ Hz, 1H), 3.59 (s, 6H), 3.55 (s, 3H). The NMR spectrum of *mer*-Ir(meppy)₃ obtained *in situ* are analogous to those for *mer*-Ir(tpy)₃ reported in the literature.²²⁰

[Ir(buppy)₂(Hbuppy)](O₂CCF₃). A solution of the open form (greenish-yellow, weak green emission) was obtained upon addition of an aliquot of a stock solution of TFA in CD₂Cl₂ (0.5 M, 27.9 μL, 14.0 μmol, 5.0 equiv.) to a solution of *fac*-Ir(buppy)₃ (2.3 mg, 2.8 μmol, 1.0 equiv.) in 0.5 mL of CD₂Cl₂ (yellow, intensive green emission). ¹H NMR (400 MHz, CD₂Cl₂, 293 K) δ 8.09 (d, $J = 5.8$ Hz, 1H), 8.01 (td, $J = 7.9, 1.4$ Hz, 1H), 7.93 (d, $J = 8.0$ Hz, 1H), 7.87 (m, 2H), 7.83–7.69 (m, 5H), 7.45 (d, $J = 8.2$ Hz, 1H), 7.34 (m, 4H), 7.26 (ddd, $J = 7.4, 5.9, 1.4$ Hz, 1H), 7.08–6.95 (m, 2H), 6.94–6.82 (m, 2H), 6.36 (d, $J = 1.8$ Hz, 1H), 6.25 (d, $J = 5.6$ Hz, 1H), 1.33 (s, 9H), 1.22 (s, 9H), 1.03 (s, 9H).

mer-Ir(buppy)₃. A solution of the *mer* isomer (yellow, yellow emission) was obtained upon addition of an aliquot of a stock solution of NEt₃ in CD₂Cl₂ (0.5 M, 30.7 μL, 15.4 μmol, 5.5 equiv.) to the solution of [Ir(buppy)₂(buppy)](O₂CCF₃). ¹H NMR (400 MHz, CD₂Cl₂, 298 K) δ 8.07 (d, $J = 5.0$ Hz, 1H), 7.89 (dd, $J = 5.6, 3.4$ Hz, 2H), 7.76 (d, $J = 8.3$ Hz, 2H), 7.71–7.48 (m, 7H), 7.03 (dd, $J = 8.2, 2.1$ Hz, 1H), 7.00–6.91 (m, 3H), 6.91–6.84 (m, 1H), 6.82–6.70 (m, 2H), 6.67 (d, $J = 2.0$ Hz, 1H), 6.53 (d, $J = 1.9$ Hz, 1H), 1.14–1.13 (m, 18H), 1.08 (s, 9H).

[Ir(fppy)₂(Hfppy)](NTf₂). A solution of the open form (yellow, weak cyan emission) was obtained upon addition of an aliquot of a stock solution of HNTf₂ in CD₂Cl₂ (0.2 M, 35.7 μL, 7.1 μmol, 2.0 equiv.) to a solution of *fac*-Ir(fppy)₃ (2.5 mg, 3.6 μmol, 1.0 equiv.) in 0.5 mL CD₂Cl₂ (light-yellow, cyan emission). ¹H NMR (400 MHz, CD₂Cl₂, 293 K) δ 8.16–8.00 (m, 2H), 7.96–7.85 (m, 5H), 7.84–7.75 (m, 1H), 7.61 (dt, $J = 16.3, 8.1$ Hz, 1H), 7.58–7.47 (m, 2H), 7.42–7.25 (m, 4H), 7.18 (ddd, $J = 7.2, 5.7, 1.5$ Hz, 1H), 7.04 (td, $J = 8.7, 2.5$ Hz, 1H), 6.95 (ddd, $J = 7.4, 5.9, 1.4$ Hz, 1H), 6.79 (td, $J = 8.5, 2.5$ Hz, 1H), 6.51 (dd, $J = 9.1, 2.6$ Hz, 2H), 6.08 (dd, $J = 9.7, 2.5$ Hz, 1H). ¹⁹F {¹H} NMR (376 MHz, CD₂Cl₂, 293 K) δ -104.33 (s), -107.09 (s), -107.73 (s).

mer-Ir(fppy)₃. A solution of the *mer* isomer (yellow, intensive cyan emission) was obtained upon addition of an aliquot of a stock solution of NEt₃ in CD₂Cl₂ (44.6 μL, 8.9

μmol , 2.5 equiv.) to the solution of $[\text{Ir}(\text{fppy})_2(\text{Hfppy})](\text{NTf}_2)$. ^1H NMR (400 MHz, CD_2Cl_2 , 298 K) δ 8.01 (dd, $J = 5.9, 0.9$ Hz, 1H), 7.93–7.85 (m, 2H), 7.82–7.72 (m, 4H), 7.72–7.65 (m, 2H), 7.64–7.53 (m, 3H), 6.93 (m, 1H), 6.80 (m, 2H), 6.67 (m, 3H), 6.50 (dd, $J = 9.0, 2.8$ Hz, 1H), 6.22 (dd, $J = 8.8, 2.7$ Hz, 1H), 6.02 (dd, $J = 10.2, 2.6$ Hz, 1H). ^{19}F $\{^1\text{H}\}$ NMR (376 MHz, CD_2Cl_2 , 298 K) δ –111.99 (s), –112.32 (s), –112.75 (s).

$[\text{Ir}(\text{dfppy})_2(\text{Hdfppy})](\text{NTf}_2)$. A solution of the open form (yellow, weak cyan emission) was obtained upon addition of an aliquot of a stock solution of HNTf_2 in CD_2Cl_2 (0.2 M, 32.8 μL , 6.6 μmol , 5.0 equiv.) to a solution of *fac*- $\text{Ir}(\text{dfppy})_3$ (1.0 mg, 1.3 μmol , 1.0 equiv.) in 0.5 mL CD_2Cl_2 (light-yellow, intensive cyan emission). ^1H NMR (400 MHz, CD_2Cl_2 , 293 K) δ 8.37 (m, 2H), 8.10 (td, $J = 7.8, 1.5$ Hz, 1H), 8.05–7.93 (m, 3H), 7.86 (m, 1H), 7.52–7.45 (m, 1H), 7.44–7.34 (m, 3H), 7.12 (m, 2H), 7.06–6.97 (m, 1H), 6.92–6.76 (m, 2H), 6.66 (ddd, $J = 12.5, 8.8, 2.4$ Hz, 1H), 6.20 (dd, $J = 8.1, 2.3$ Hz, 1H), 5.98–5.88 (m, 1H). ^{19}F $\{^1\text{H}\}$ NMR (376 MHz, CD_2Cl_2 , 293 K) δ –99.30 (s), –104.05 (d, $J = 11.2$ Hz), –104.36 (d, $J = 11.8$ Hz), –106.16 (d, $J = 10.9$ Hz), –107.09 (d, $J = 11.9$ Hz), –109.14 (d, $J = 11.2$ Hz).

mer- $\text{Ir}(\text{dfppy})_3$. A solution of the *mer* isomer (yellow, intensive cyan emission) was obtained upon addition of an aliquot of a stock solution of NEt_3 in CD_2Cl_2 (14.4 μL , 7.2 μmol , 5.5 equiv.) to the solution of $[\text{Ir}(\text{dfppy})_2(\text{Hdfppy})](\text{NTf}_2)$. ^1H NMR (400 MHz, CD_2Cl_2 , 298 K) δ 8.34 (d, $J = 9.9$ Hz, 1H), 8.23 (d, $J = 6.9$ Hz, 2H), 8.03 (d, $J = 5.8$ Hz, 1H), 7.93 (d, $J = 5.6$ Hz, 1H), 7.74 (t, $J = 8.8$ Hz, 1H), 7.70–7.60 (m, 2H), 7.54 (d, $J = 5.8$ Hz, 1H), 7.01–6.96 (m, 1H), 6.85 (t, $J = 6.6$ Hz, 2H), 6.51–6.32 (m, 4H), 5.98 (dd, $J = 7.6, 2.4$ Hz, 1H), 5.79 (dd, $J = 9.1, 2.4$ Hz, 1H). ^{19}F $\{^1\text{H}\}$ NMR (376 MHz, CD_2Cl_2 , 298 K) δ –109.33 (d, $J = 10.0$ Hz), –109.48 (d, $J = 10.5$ Hz), –109.70 (d, $J = 9.7$ Hz), –109.77 (d, $J = 9.5$ Hz), –110.22 (d, $J = 9.6$ Hz), –111.43 (m). The NMR spectra of *mer*- $\text{Ir}(\text{dfppy})_3$ obtained *in situ* are in agreement with those reported in the literature.¹⁰³

$[\text{Ir}(\text{tpyy})_2(\text{Htpyy})](\text{O}_2\text{CCF}_3)$. A solution of the open form (greenish-yellow, weak white emission) was obtained upon addition of an aliquot of a stock solution of TFA in CD_2Cl_2 (0.5 M, 36.0 μL , 18.0 μmol , 10.0 equiv.) to a solution of *fac*- $\text{Ir}(\text{tpyy})_3$ (2.0 mg, 1.8 μmol , 1.0 equiv.) in 0.5 mL CD_2Cl_2 (yellow, greenish-yellow emission). ^1H NMR (400 MHz, CD_2Cl_2 , 298 K) δ 8.37 (d, $J = 5.0$ Hz, 1H), 8.09 (m, 5H), 7.98 (t, $J = 7.9$ Hz, 2H), 7.87–7.77 (m, 4H), 7.73–7.58 (m, 16H), 7.50–7.35 (m, 16H), 7.26 (d, $J = 1.7$ Hz, 1H), 7.11

(m, 1H), 6.95 (m, 2H), 6.87 (d, $J = 1.8$ Hz, 1H), 6.55 (d, $J = 4.8$ Hz, 1H). ^{19}F $\{^1\text{H}\}$ NMR (376 MHz, CD_2Cl_2 , 298 K) δ -75.87 (s).

mer-Ir(tppy)₃. A solution of the *mer* isomer (yellow, yellow emission) was obtained upon addition of an aliquot of a stock solution of NEt_3 in CD_2Cl_2 (37.8 μL , 18.9 μmol , 10.5 equiv.) to the solution of $[\text{Ir}(\text{tppy})_2(\text{Htppy})](\text{O}_2\text{CCF}_3)$. The spectroscopic data of *mer*-Ir(tppy)₃ obtained *in situ* are in agreement with those presented above.

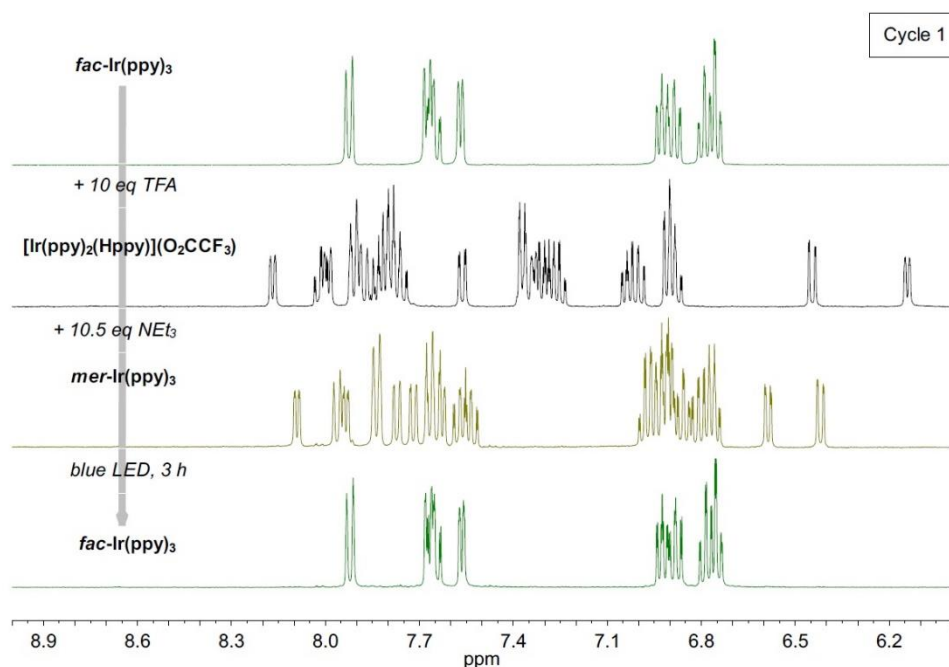
$[\text{Ir}(\text{dfppy})_2(\text{Htpy})](\text{O}_2\text{CCF}_3)$. A solution of the open form (greenish-yellow, green emission) was obtained upon addition of an aliquot of a stock solution of TFA in CD_2Cl_2 (0.5 M, 25.8 μL , 337 μmol , 100 equiv.) to a solution of *fac*-Ir(dfppy)₂(tpy) (2.5 mg, 3.4 μmol , 1.0 equiv.) in 0.5 mL CD_2Cl_2 (yellow, intensive green emission). ^1H NMR (400 MHz, CD_2Cl_2 , 298 K) δ 8.39 (d, $J = 8.9$ Hz, 1H), 8.29 (m, 1H), 8.05 (m, 2H), 7.91–7.82 (m, 3H), 7.63 (d, $J = 7.3$ Hz, 2H), 7.42–7.32 (m, 2H), 7.10 (m, 3H), 6.98 (m, 1H), 6.89–6.81 (m, 1H), 6.69–6.56 (m, 1H), 6.36 (dd, $J = 8.2, 2.3$ Hz, 1H), 6.23 (m, 1H), 6.03 (dd, $J = 8.9, 1.7$ Hz, 1H), 2.51 (s, 3H). ^{19}F $\{^1\text{H}\}$ NMR (376 MHz, CD_2Cl_2 , 298 K) δ -76.23 (s), -104.64 (d, $J = 11.0$ Hz), -104.86 (d, $J = 11.7$ Hz), -106.85 (d, $J = 11.0$ Hz), -107.45 (d, $J = 11.1$ Hz).

mer-Ir(dfppy)₂(tpy). A solution of the *mer* isomer (yellow, cyan emission) was obtained upon addition of an aliquot of a stock solution of NEt_3 in CD_2Cl_2 (49.3 μL , 335 μmol , 105 equiv.) to the solution of $[\text{Ir}(\text{dfppy})_2(\text{Htpy})](\text{O}_2\text{CCF}_3)$. ^1H NMR (400 MHz, CD_2Cl_2 , 298 K) δ 8.30 (m, 1H), 8.19 (m, 1H), 7.93 (m, 2H), 7.80 (d, $J = 8.0$ Hz, 1H), 7.68 (t, $J = 8.3$ Hz, 1H), 7.59 (m, 4H), 6.92 (m, 1H), 6.79 (m, 3H), 6.47–6.32 (m, 3H), 6.29 (s, 1H), 5.83 (dd, $J = 9.2, 2.4$ Hz, 1H), 2.13 (s, 3H). ^{19}F $\{^1\text{H}\}$ NMR (376 MHz, CD_2Cl_2 , 298 K) δ -110.00 (t, $J = 9.6$ Hz), -110.26 (d, $J = 9.2$ Hz), -111.91 (d, $J = 9.8$ Hz). ^{13}C $\{^1\text{H}\}$ NMR (126 MHz, CD_2Cl_2 , 298 K) δ 184.09–183.85 (m), 172.53 (s), 170.54 (s), 165.66 (d, $J = 10.5$ Hz), 165.47–165.21 (m), 164.99 (d, $J = 7.2$ Hz), 164.51 (d, $J = 6.2$ Hz), 164.10 (d, $J = 11.0$ Hz), 163.60 (d, $J = 10.5$ Hz), 163.33 (m), 162.01 (d, $J = 10.9$ Hz), 161.25 (d, $J = 13.0$ Hz), 153.14 (s), 151.80 (s), 148.55 (s), 142.52 (s), 140.70 (s), 137.99 (s), 137.00 (s), 135.88 (s), 133.80 (s), 129.17 (m), 127.19 (m), 124.90 (s), 123.86 (d, $J = 21.8$ Hz), 123.35 (s), 123.06 (m), 122.61 (s), 122.17 (s), 119.38 (s), 118.79 (dd, $J = 13.7, 2.7$ Hz), 112.45 (dd, $J = 16.3, 2.6$ Hz), 98.01 (t, $J = 27.3$ Hz),

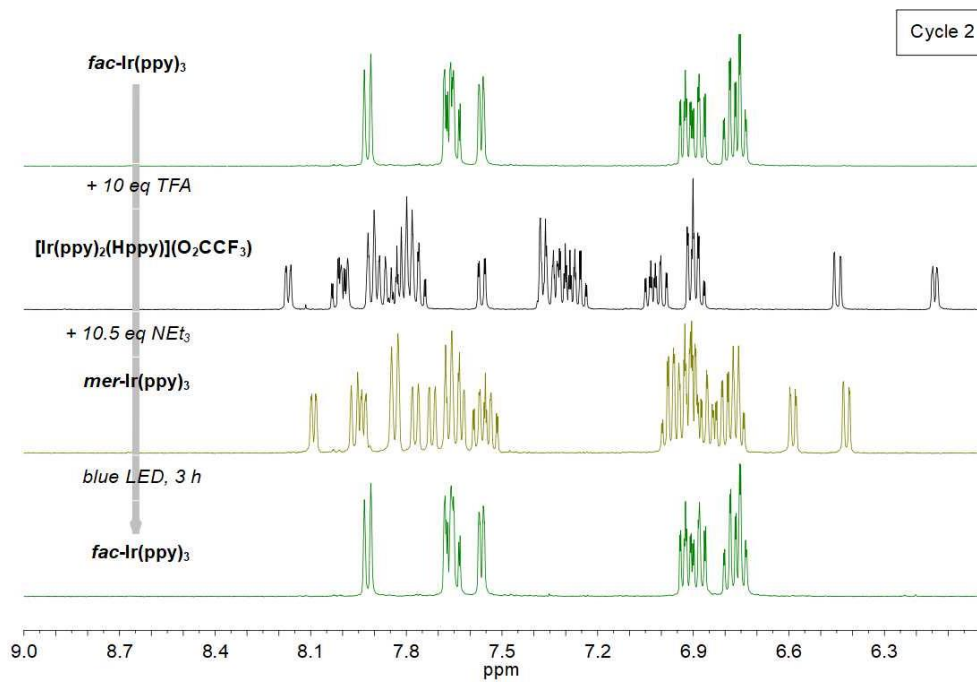
95.60 (t, $J = 27.2$ Hz), 22.06 (s). The spectroscopic data of a different isomer of *mer*-Ir(dfppy)₂(tpy) have been reported in the literature.¹⁹³

6.3.5 NMR Control of Repetitive *fac*↔*mer* Isomerization

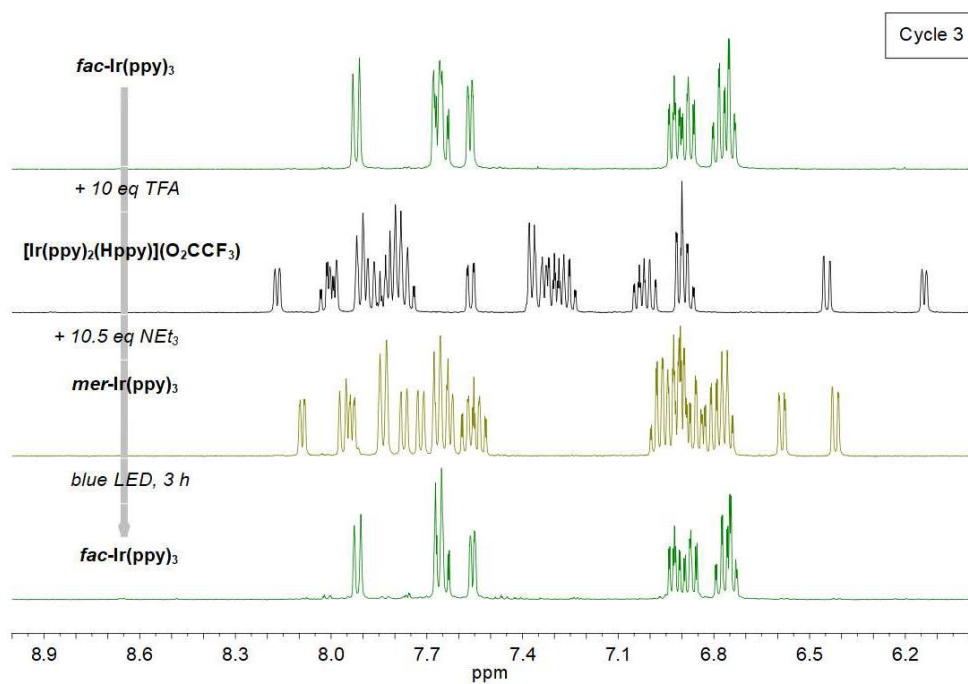
The General Procedure (for details, see subchapter 6.3.4) was used for multiple *fac*→*mer*→*fac* isomerizations of the complexes Ir(ppy)₃, Ir(tpy)₃, Ir(meppy)₃, and Ir(dfppy)₃. Three cycles for each compound were performed. ¹H (400 MHz) and ¹⁹F (376 MHz) NMR measurements were recorded in CD₂Cl₂ at 298 K. Each new cycle was started by the addition of acid to the solution from the previous cycle without additional purification steps.



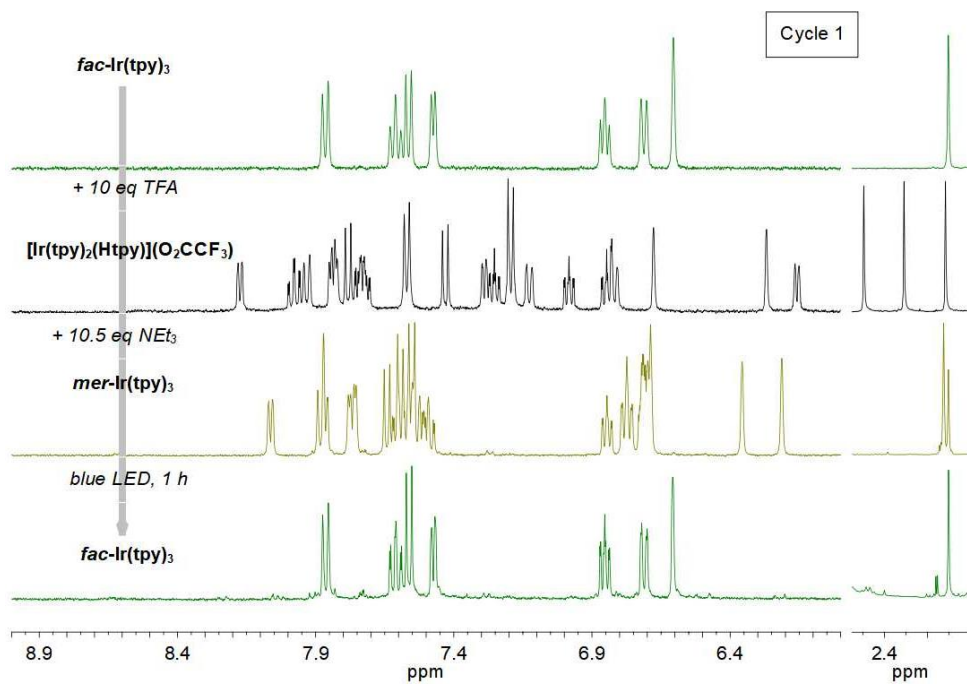
¹H NMR spectra for Cycle 1 *fac*→*mer*→*fac* for Ir(ppy)₃



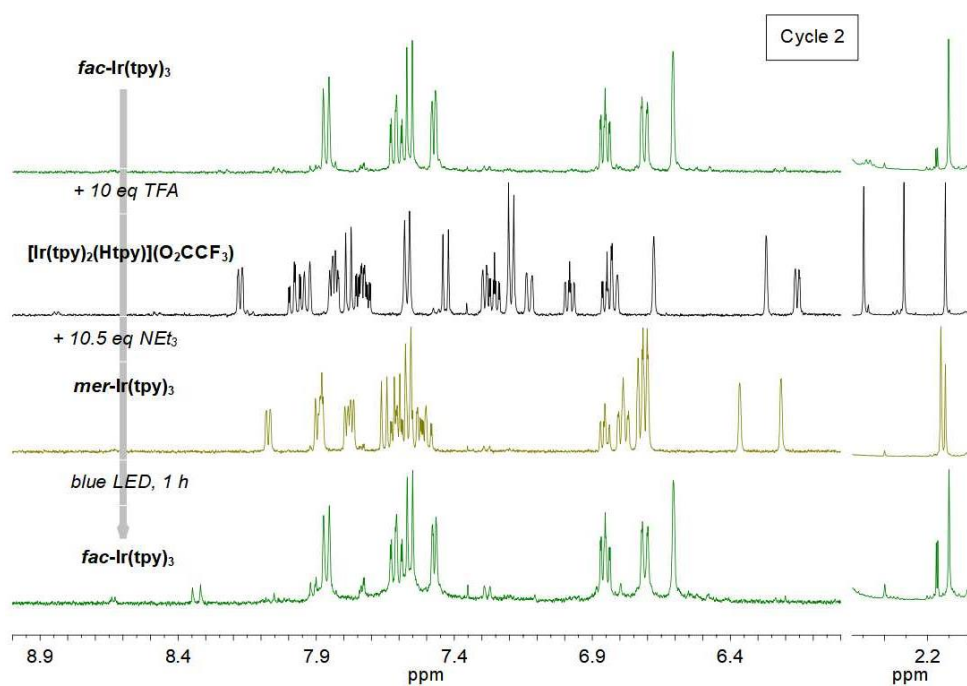
¹H NMR spectra for Cycle 2 *fac*→*mer*→*fac* for Ir(ppy)₃



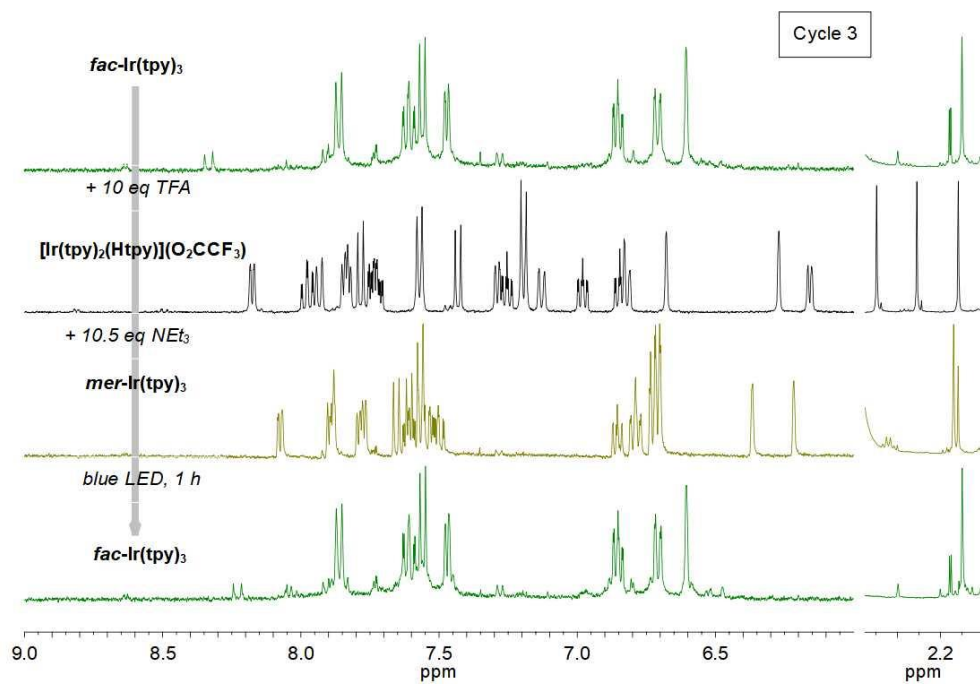
¹H NMR spectra for Cycle 3 *fac*→*mer*→*fac* for Ir(ppy)₃



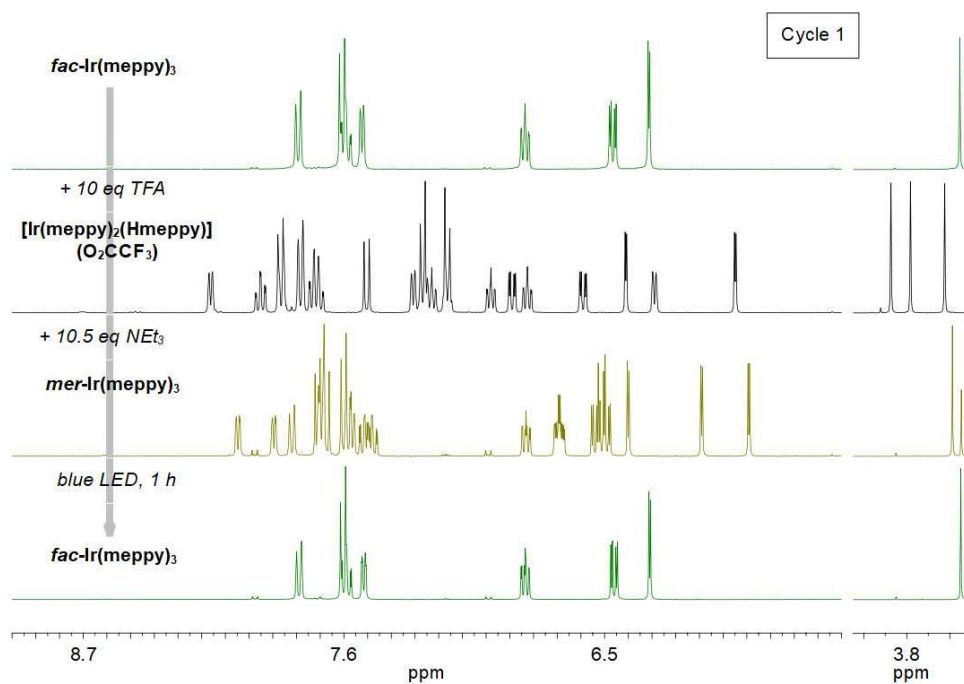
¹H NMR spectra for Cycle 1 *fac*→*mer*→*fac* for Ir(tpy)₃



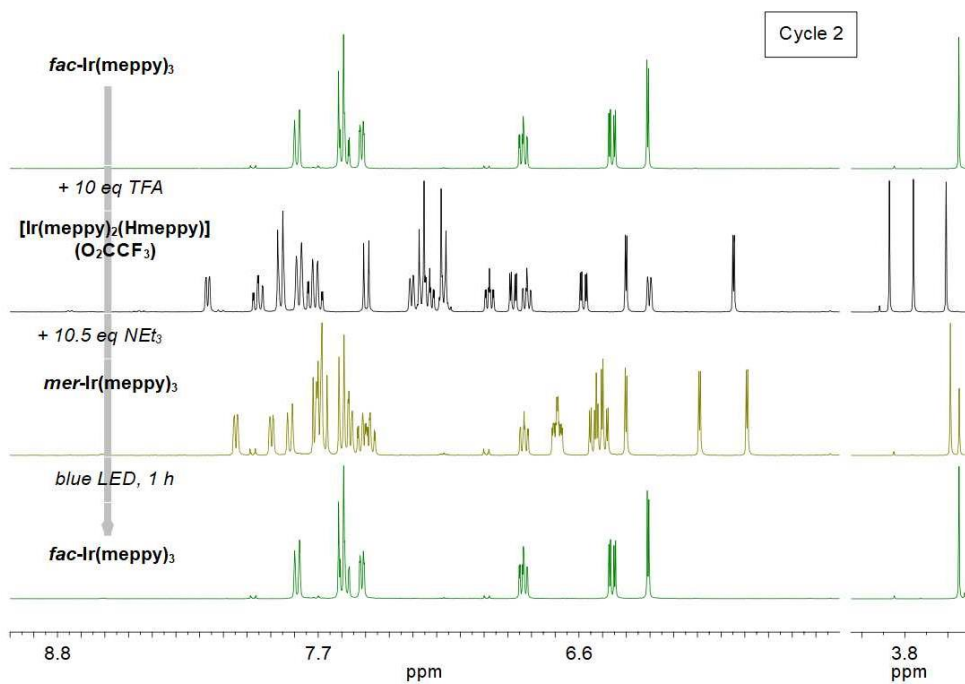
¹H NMR spectra for Cycle 2 *fac*→*mer*→*fac* for Ir(tpy)₃



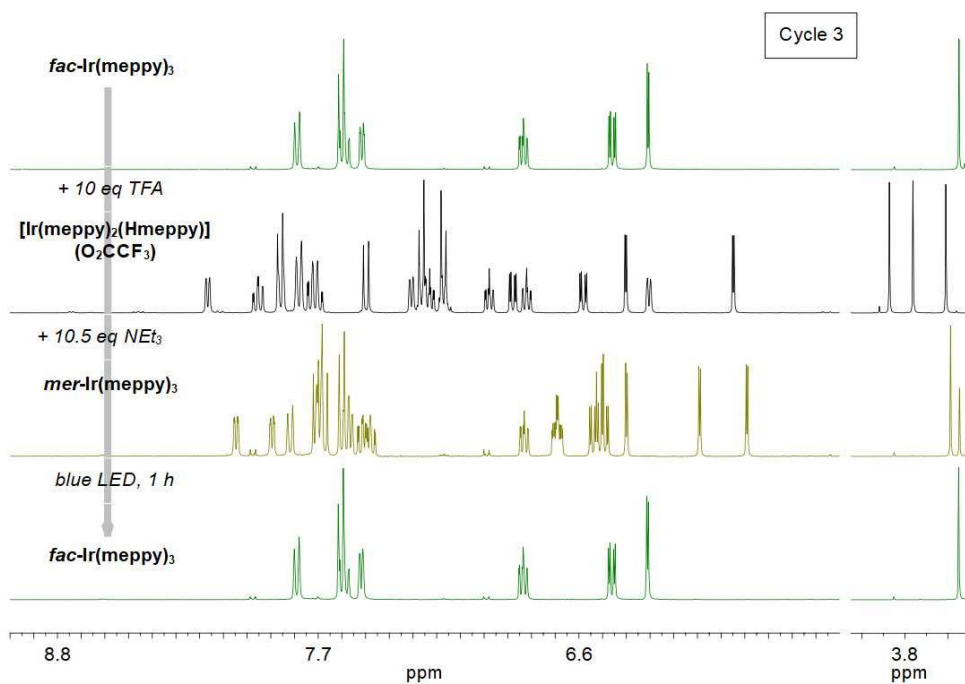
¹H NMR spectra for Cycle 3 *fac*→*mer*→*fac* for Ir(tpy)₃



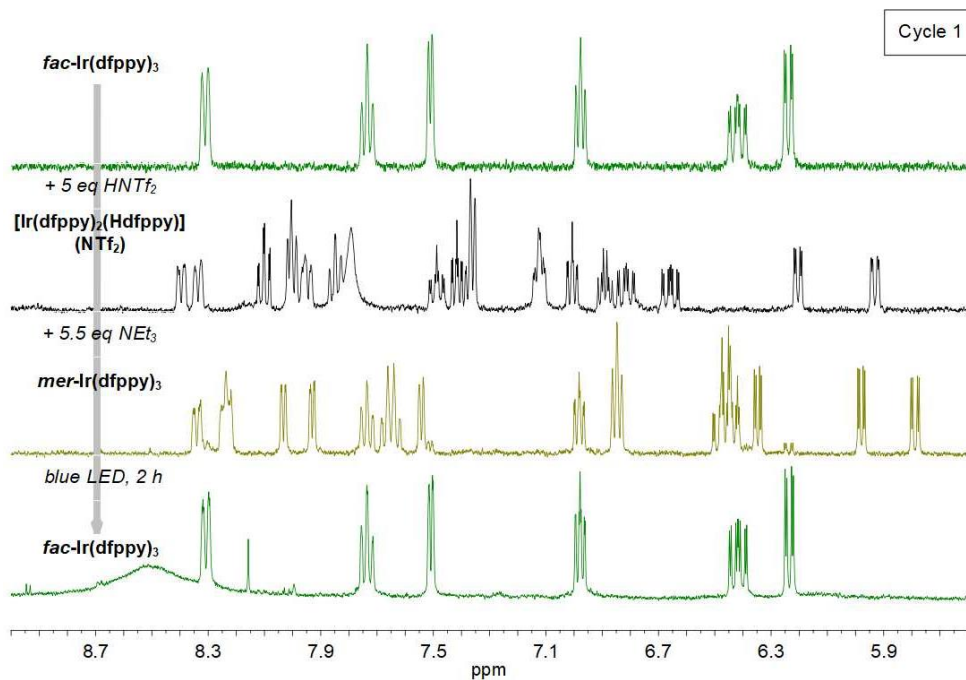
¹H NMR spectra for Cycle 1 *fac*→*mer*→*fac* for Ir(meppy)₃



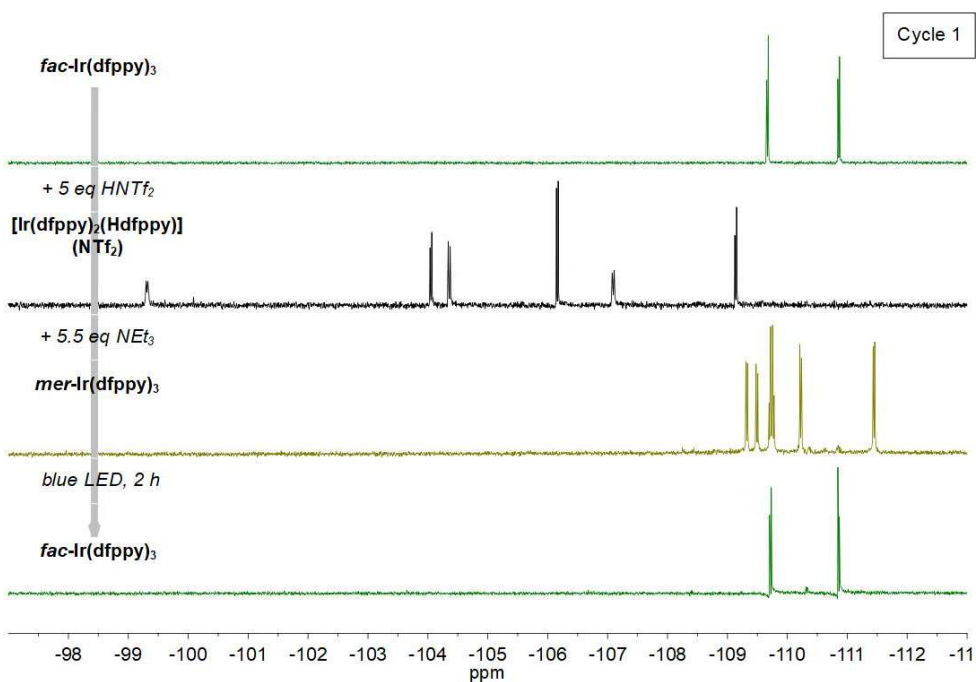
¹H NMR spectra for Cycle 2 *fac*→*mer*→*fac* for Ir(meppy)₃



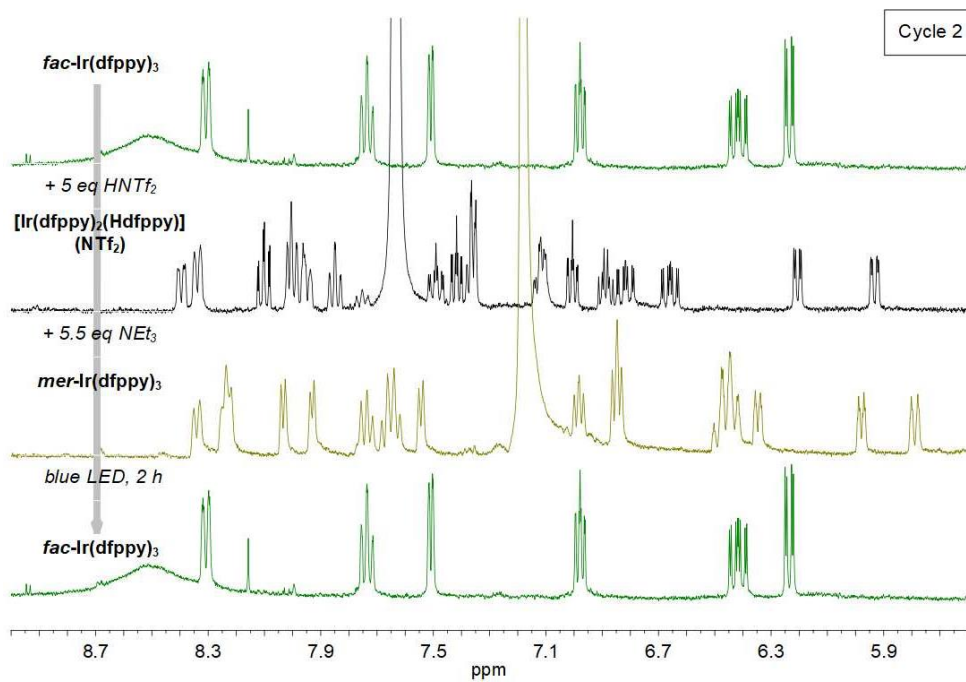
¹H NMR spectra for Cycle 3 *fac*→*mer*→*fac* for Ir(meppy)₃



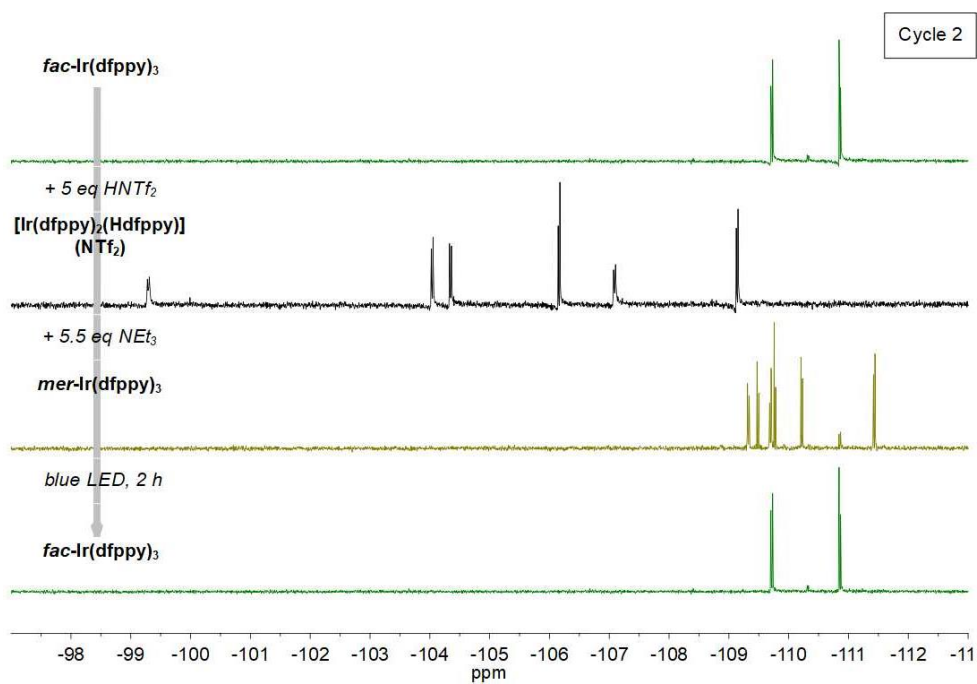
¹H NMR spectra for Cycle 1 *fac*→*mer*→*fac* for Ir(dfppy)₃



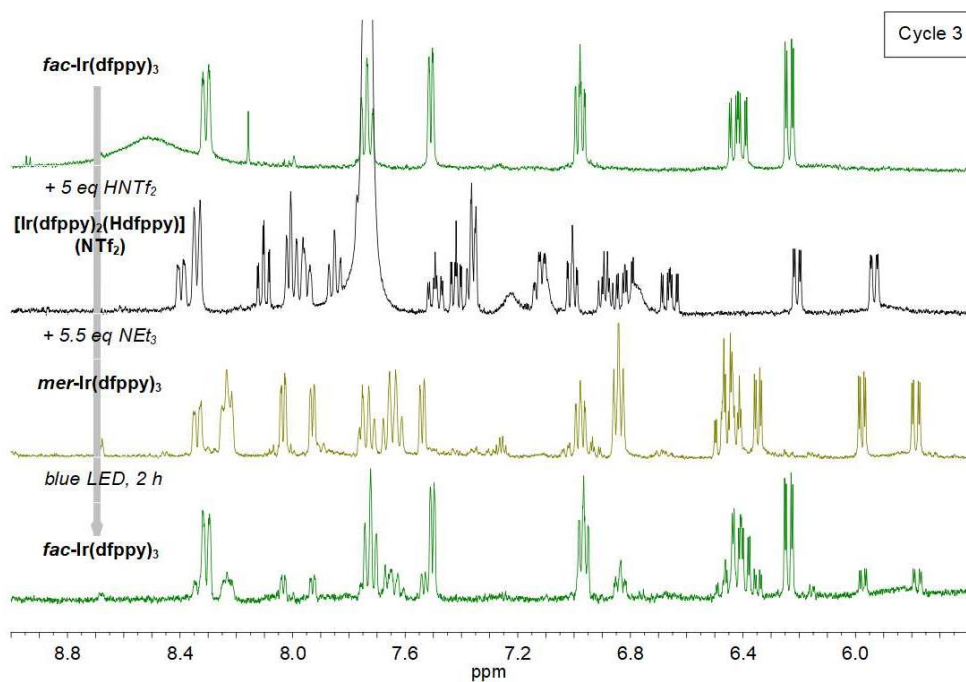
¹⁹F NMR spectra for Cycle 1 *fac*→*mer*→*fac* for Ir(dfppy)₃



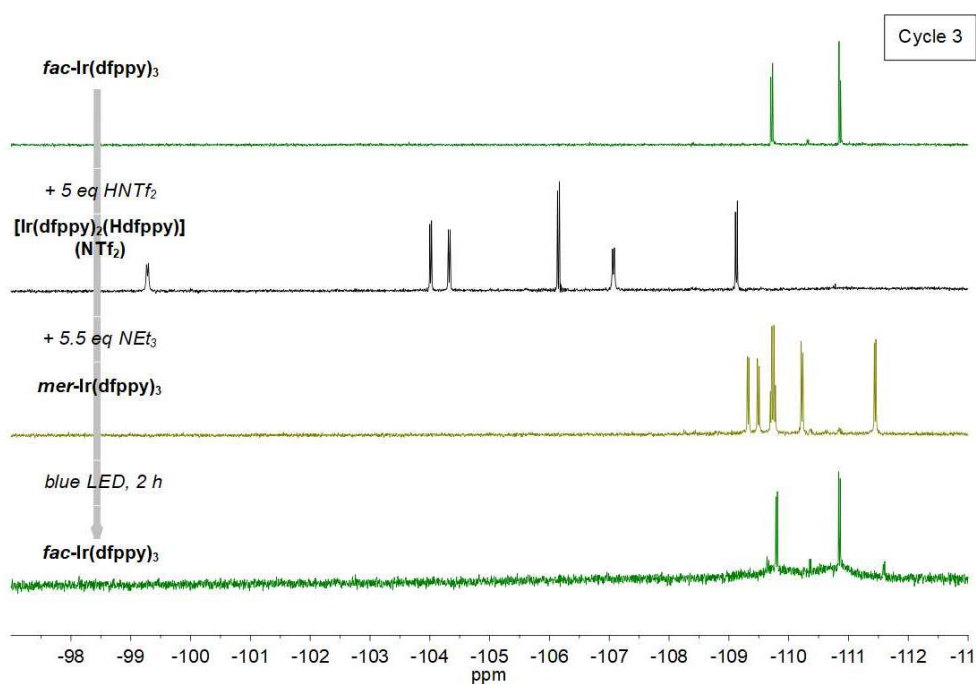
¹H NMR spectra for Cycle 2 *fac*→*mer*→*fac* for Ir(dfppy)₃



¹⁹F NMR spectra for Cycle 2 *fac*→*mer*→*fac* for Ir(dfppy)₃

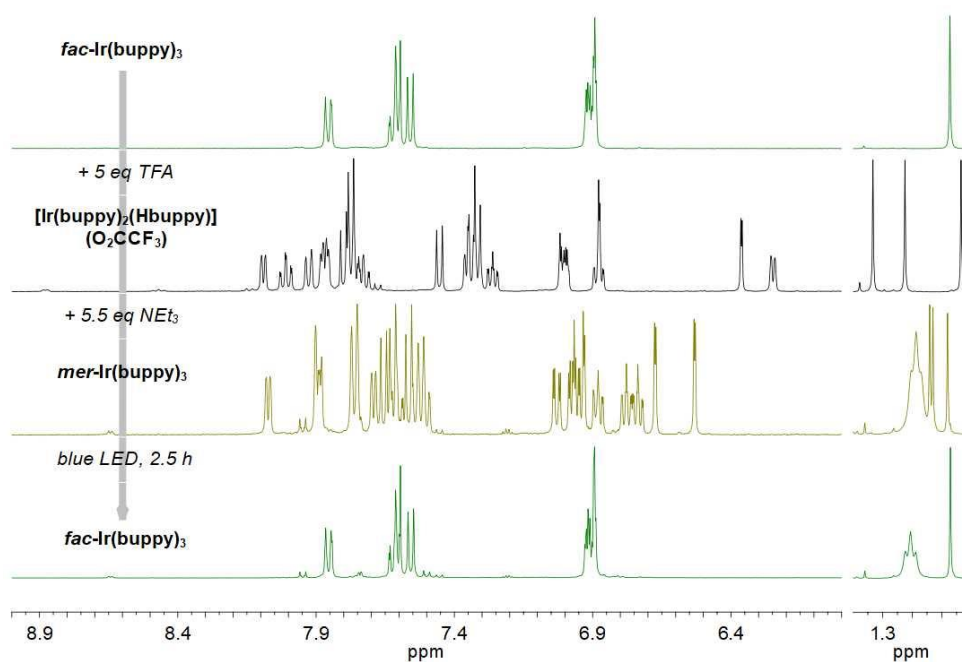


¹H NMR spectra for Cycle 3 *fac*→*mer*→*fac* for Ir(dfppy)₃



¹⁹F NMR spectra for Cycle 3 *fac*→*mer*→*fac* for Ir(dfppy)₃

A single *fac*→*mer*→*fac* isomerization was performed for the complexes Ir(buppy)₃, Ir(fppy)₃, Ir(tppy)₃ and Ir(dfppy)₂(tpy) using the General Procedure. The cycles were monitored by ¹H (400 MHz) and ¹⁹F (376 MHz) NMR spectroscopy (CD₂Cl₂, 298 K, the spectra for three latter compounds can be found in subchapters 3.5 and 3.8).



^1H NMR spectra for a cycle of *fac*→*mer*→*fac* for $\text{Ir}(\text{bppy})_3$

6.3.6 Photophysical Properties

The photophysical properties of the *fac* and the *mer* isomers of the complexes $\text{Ir}(\text{ppy})_3$, $\text{Ir}(\text{tpy})_3$, $\text{Ir}(\text{meppy})_3$, $\text{Ir}(\text{bppy})_3$, $\text{Ir}(\text{fppy})_3$ and $\text{Ir}(\text{dfppy})_3$ are reported.^{95,103,220}

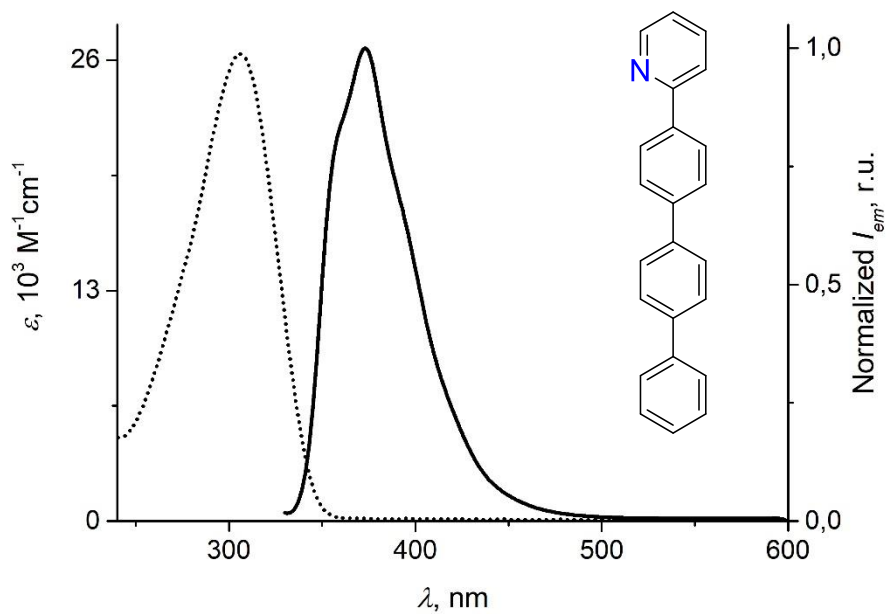
Photophysical measurements for the ligand Htpy and *fac*- $\text{Ir}(\text{tpy})_3$, *mer*- $\text{Ir}(\text{tpy})_3$, *fac*- $\text{Ir}(\text{dfppy})_2(\text{tpy})$, and *mer*- $\text{Ir}(\text{dfppy})_2(\text{tpy})$ were performed with aerated optically diluted ($A < 0.1$) solutions of spectrophotometric grade DCM (for Htpy) and THF (for Ir complexes).

Photoluminescence quantum yields in aerated THF solutions (Φ_{sol}) were measured relative to a solution of fluorescein (F) in 0.1 M NaOH ($\Phi_{\text{F}} = 0.92$). Optically diluted solutions were excited at an isoabsorptive wavelengths and quantum yields were calculated according to the equation:

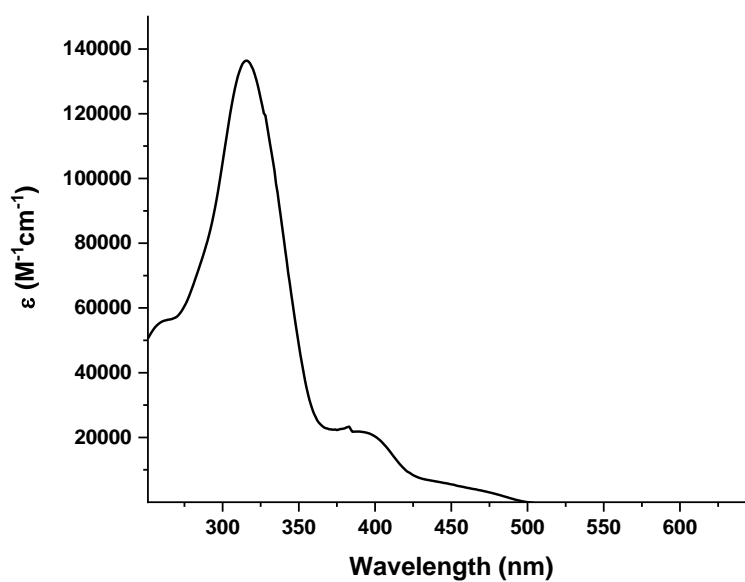
$$\Phi = \Phi_{\text{F}} \frac{A_{\text{F}} I}{A I_{\text{F}}} \left(\frac{RI}{RI_{\text{F}}} \right)^2$$

where I and I_{F} – the values of the integrated areas below the emission spectra of the Ir(III) complexes and reference, respectively, A and A_{F} – the absorbances at the excitation wavelength of the Ir(III) complexes and reference, respectively, RI and RI_{F}

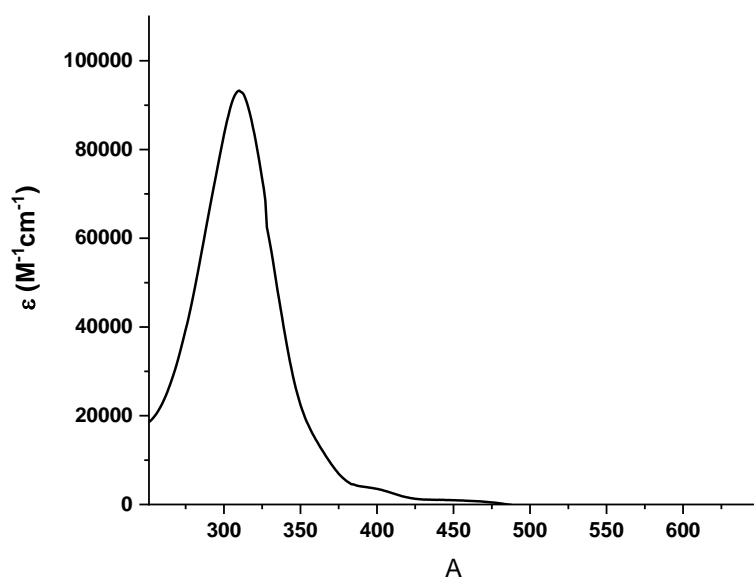
– the refractive indexes of the solvents used for Ir(III) complexes and reference, respectively.²²⁵



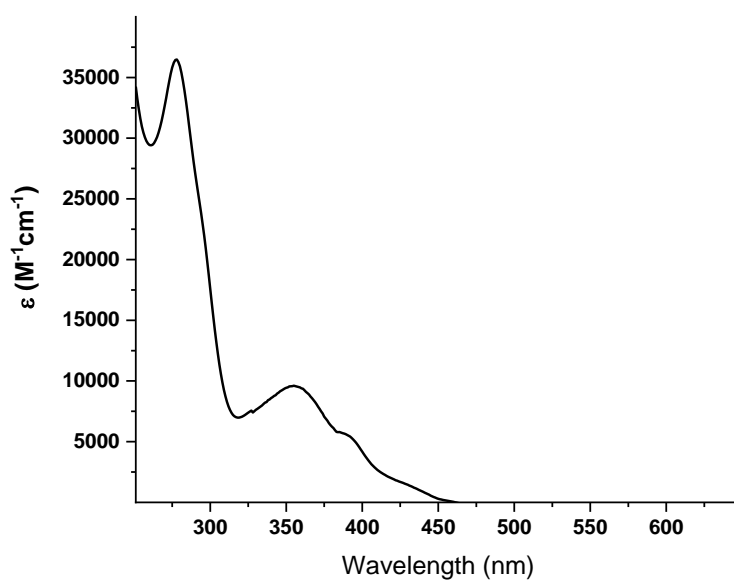
UV-Vis absorption (dotted line) and emission spectra (solid line, @315) of Htpy in DCM



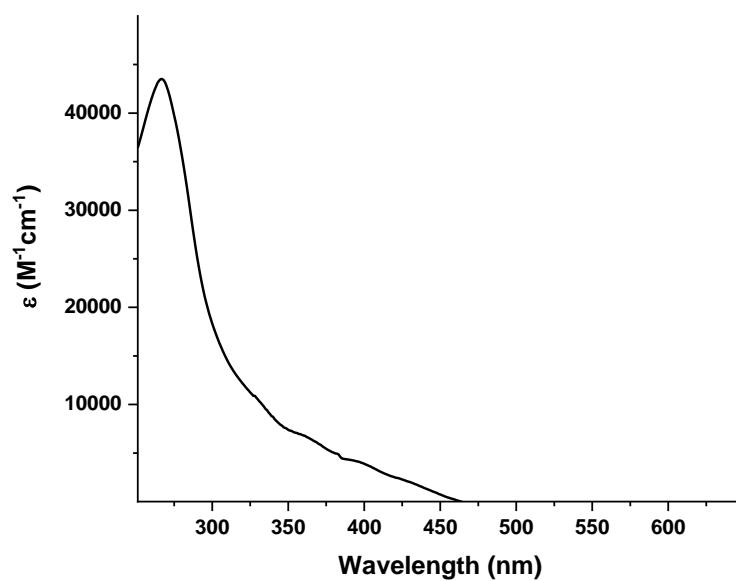
UV-Vis absorption spectrum of *fac*-Ir(tppy)₃ in THF



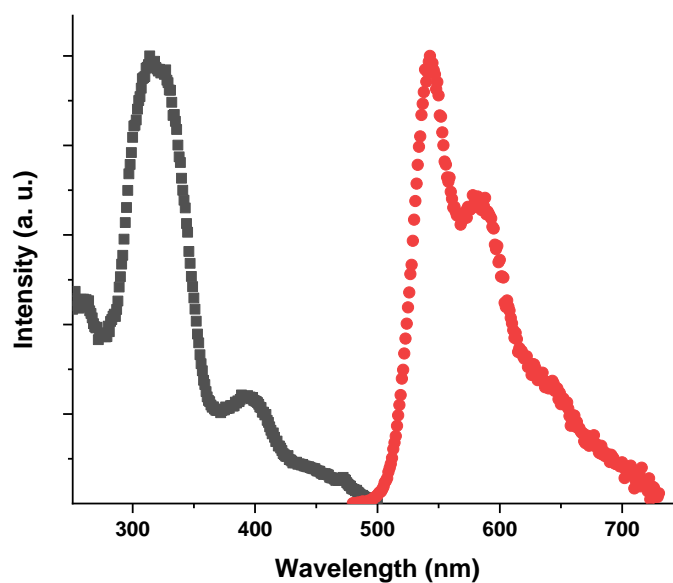
UV-Vis absorption spectrum of *mer*-Ir(tppy)₃ in THF



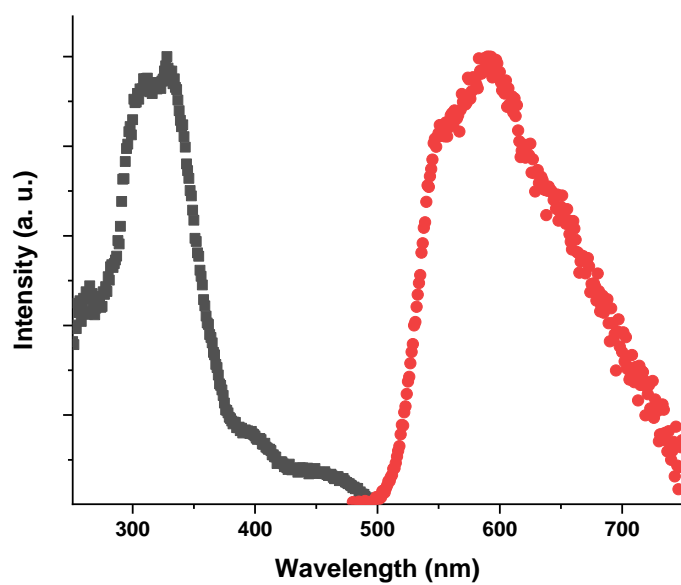
UV-Vis absorption spectrum of *fac*-Ir(dfppy)₂(tpy) in THF



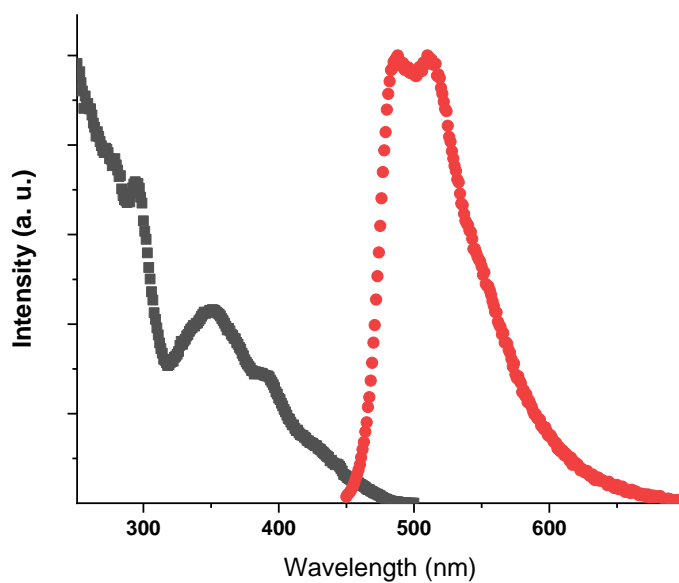
UV-Vis absorption spectrum of *mer*-Ir(dfppy)₂(tpy) in THF



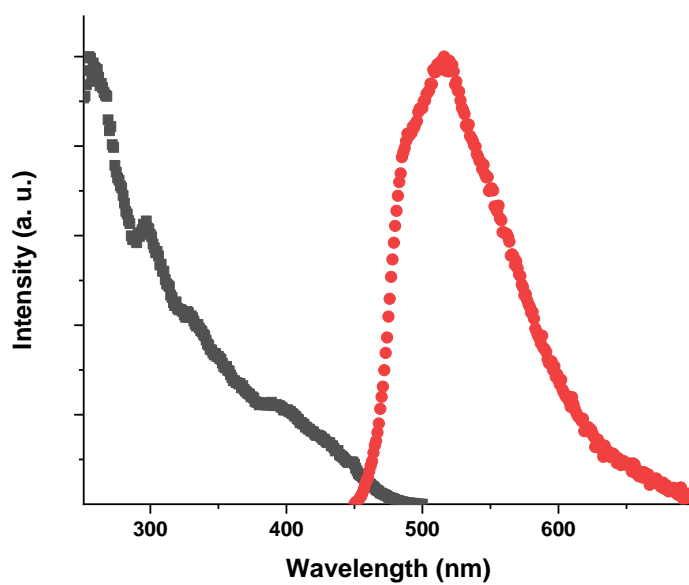
Excitation (black line, @550) and emission (red line, @400) spectra of *fac*-Ir(tppy)₃ in THF



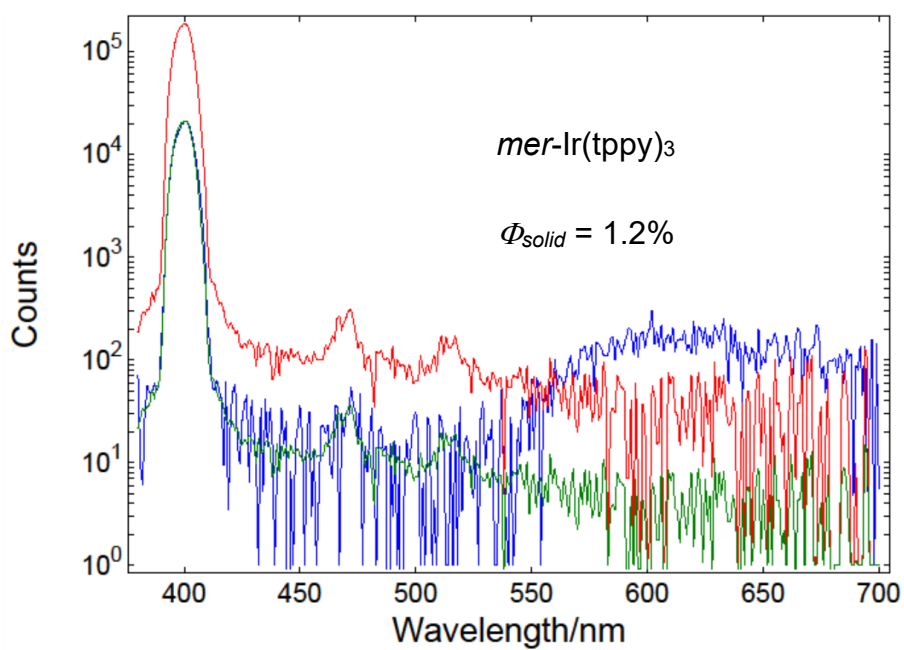
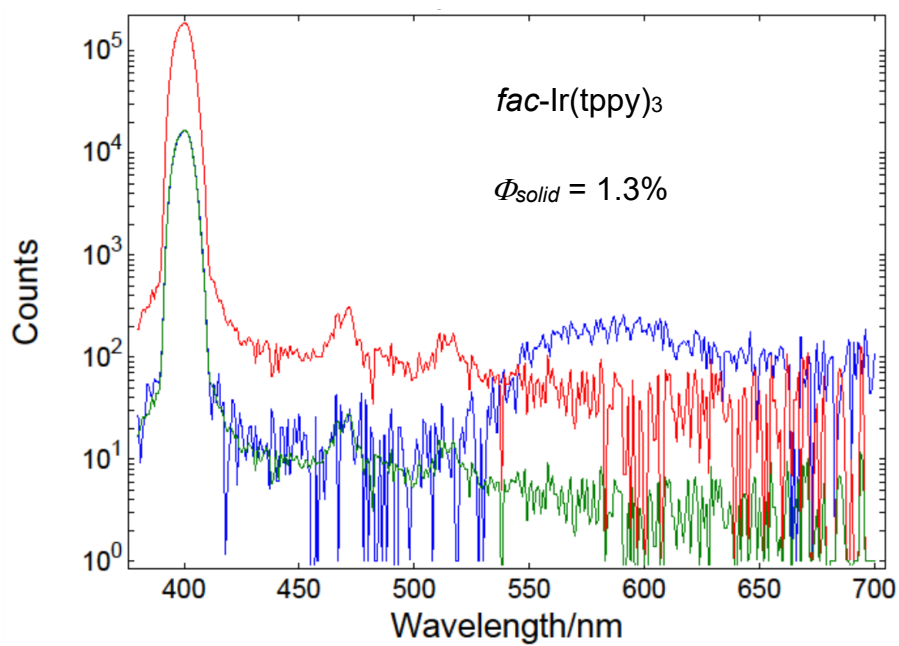
Excitation (black line, @590) and emission (red line, @400) spectra of *mer*-Ir(tpy)₃ in THF



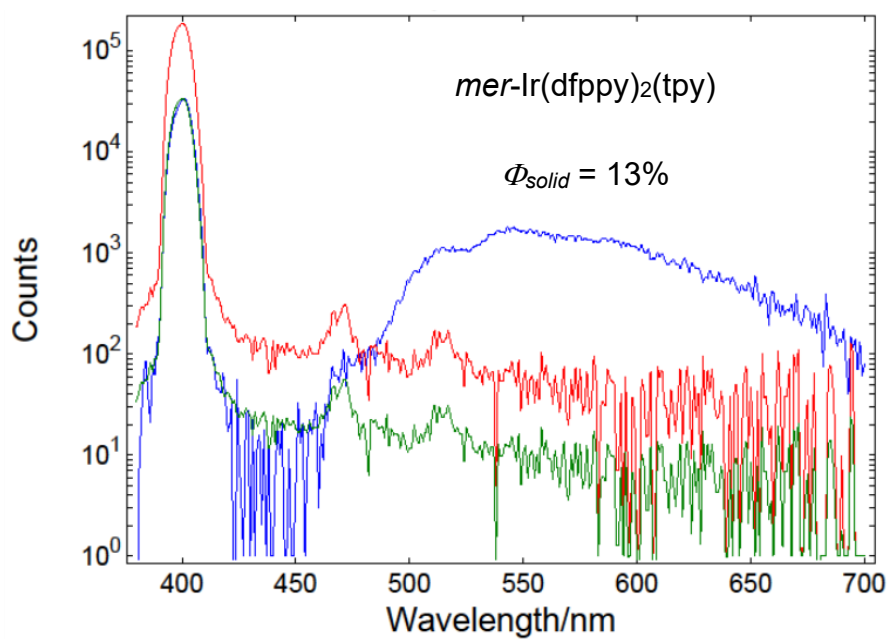
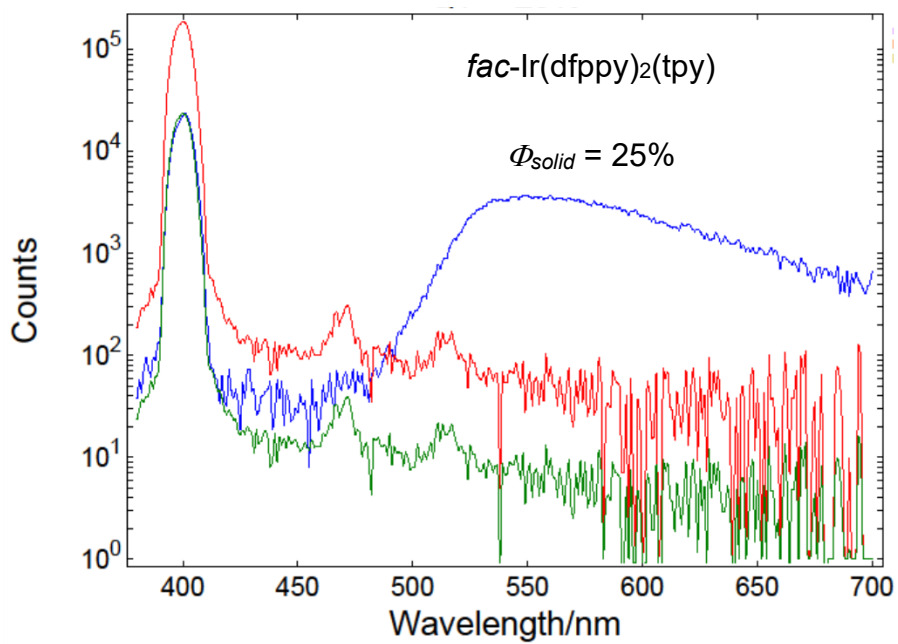
Excitation (black line, @511) and emission (red line, @390) spectra of *fac*-Ir(dfppy)₂(tpy) in THF



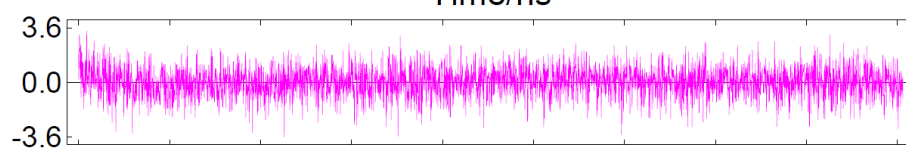
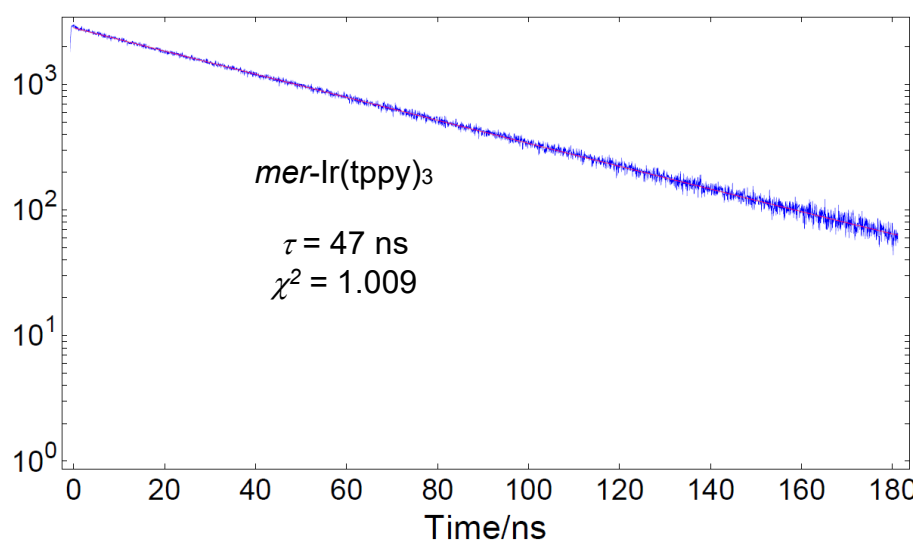
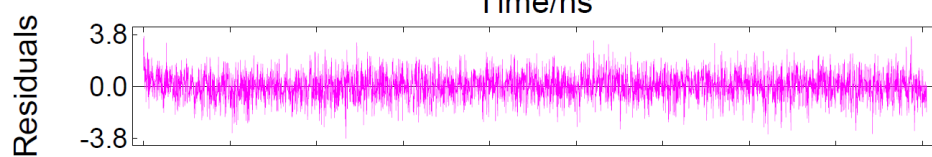
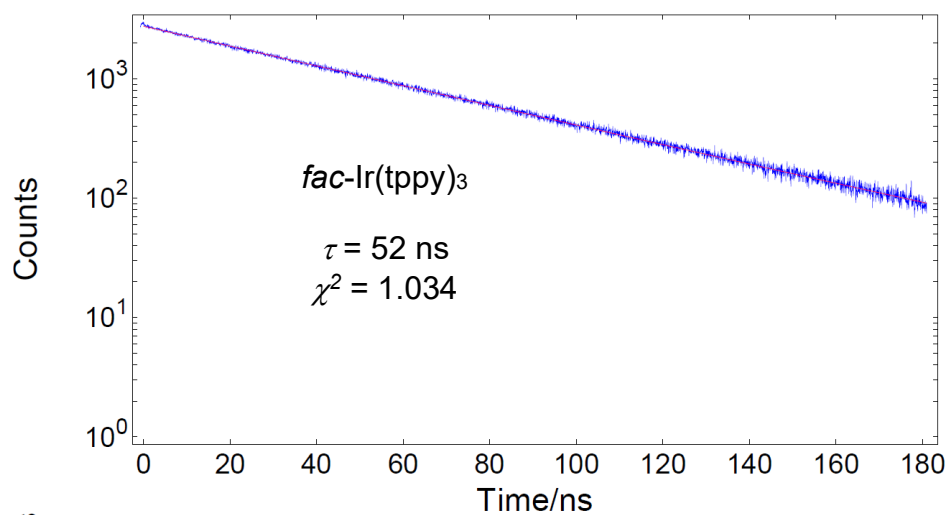
Excitation (black line, @517) and emission (red line, @390) spectra of *mer*-Ir(dfppy)₂(tpy) in THF



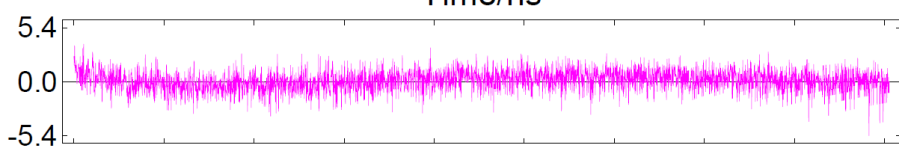
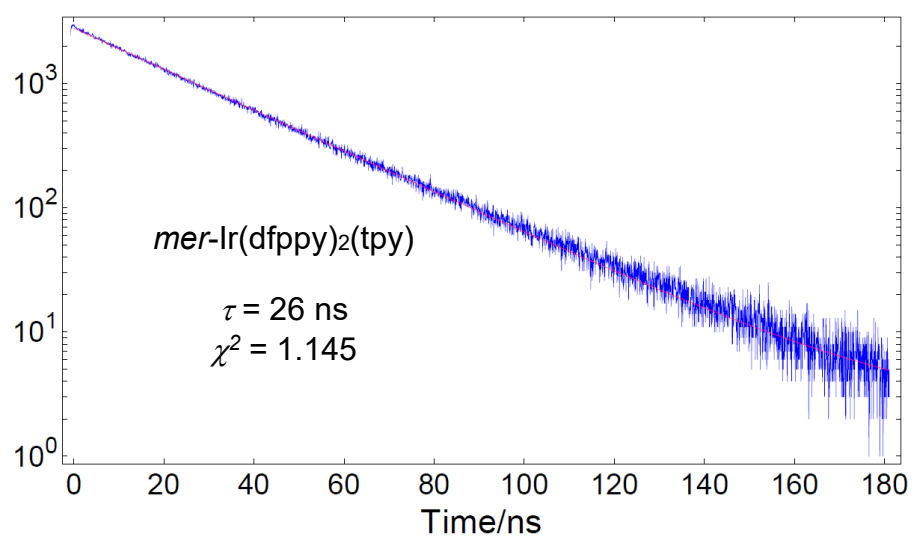
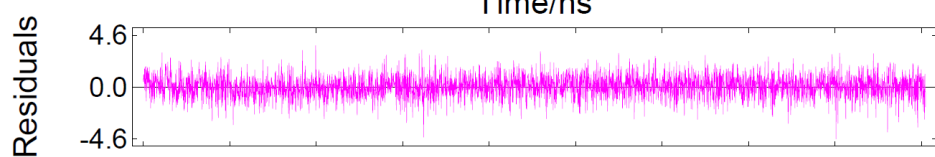
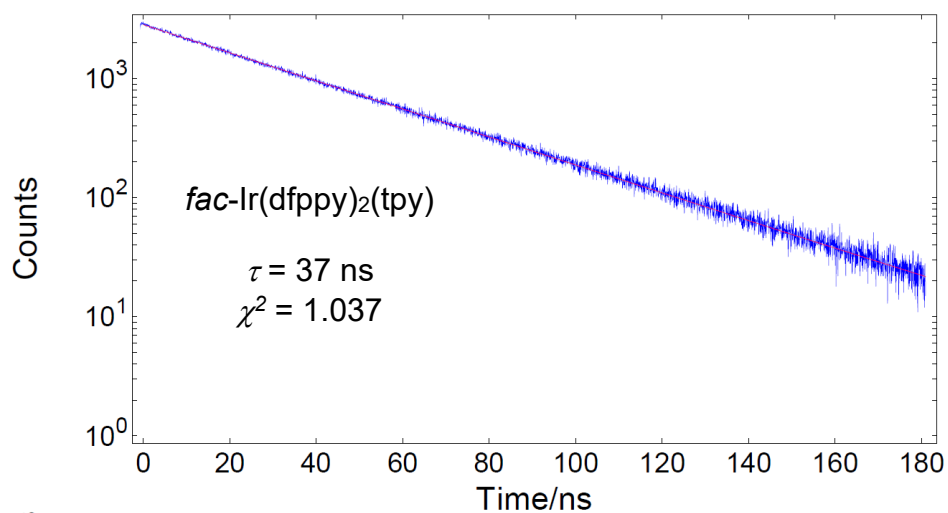
Solid state photon counting spectra of complexes $Ir(tppy)_3$ ($\lambda_{exc} = 405$ nm)



Solid state photon counting spectra of complexes $Ir(dfppy)_2(tpy)$ ($\lambda_{exc} = 405$ nm)



Photoluminescence decay curves of the Ir(tppy)₃ isomers recorded by time-correlated single photon counting ($\lambda_{exc} = 405 \text{ nm}$, THF)



Photoluminescence decay curves of the Ir(dfppy)₂(tpy) isomers recorded by time-correlated single photon counting ($\lambda_{exc} = 405 \text{ nm}$, THF)

Optical properties of the compounds

Compound	λ_{abs} , nm (ϵ , $10^4 \text{ M}^{-1}\cdot\text{cm}^{-1}$)	λ_{em} , nm (@ λ_{exc})
Htppy	306 (26)	373 (@315)
<i>fac</i> -Ir(tppy) ₃	314 (13.7), 391 (2.2), 454 (0.51)	543, 584, 642sh
<i>mer</i> -Ir(tppy) ₃	310 (9.3), 393 (0.39)	552, 590
<i>fac</i> -Ir(dfppy) ₂ (tpy)	278 (3.6), 354 (0.96), 389 (0.56), 425 (0.17)	488, 511, 545sh
<i>mer</i> -Ir(dfppy) ₂ (tpy)	266 (4.3), 325 (1.1)	487, 515, 552sh

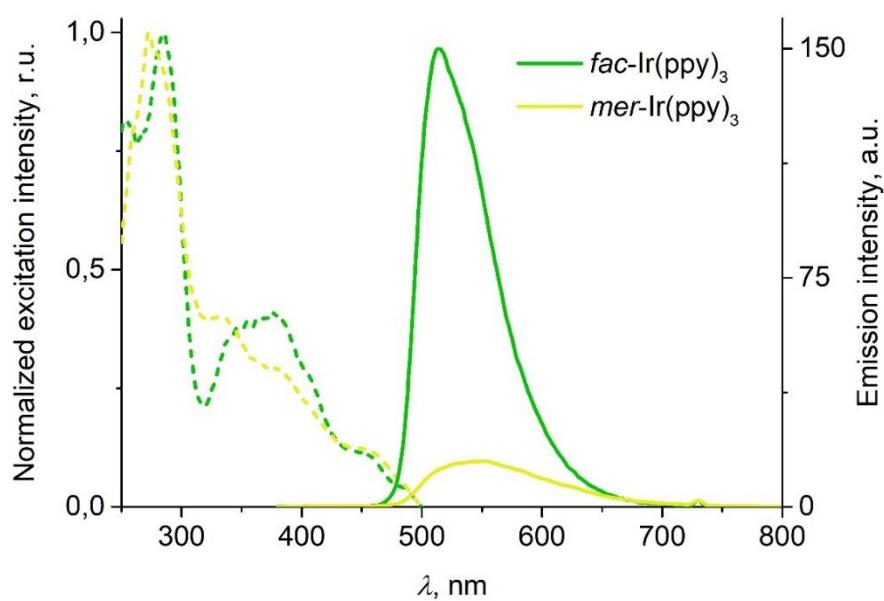
Photoluminescence quantum yields and lifetimes of Ir(III) complexes

Compound	$\Phi_{\text{solid}}^{\text{a}}$, %	$\Phi_{\text{sol}}^{\text{b}}$, %	τ^{c} , ns
<i>fac</i> -Ir(tppy) ₃	1.3	1.5	52
<i>mer</i> -Ir(tppy) ₃	1.2	1.3	47
<i>fac</i> -Ir(dfppy) ₂ (tpy)	25	2.4	37
<i>mer</i> -Ir(dfppy) ₂ (tpy)	13	1.4	26

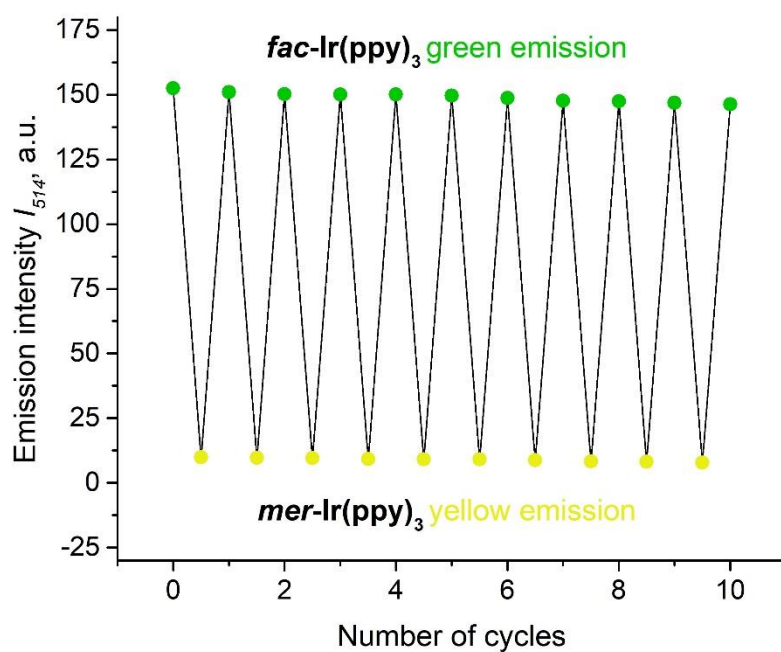
[a] Absolute photoluminescence quantum yields in solid state measured using integrating sphere. [b] Relative photoluminescence quantum yields in THF solution measured referring to the solution of fluorescein in aqueous 0.1 M NaOH ($\Phi_{\text{F}} = 0.92$). [c] Photoluminescence lifetime measured by time-correlated single photon counting in THF solution.

6.3.7 Spectroscopic Monitoring of the Acid-Base *fac*→*mer* Isomerization

To demonstrate reversibility of *fac*↔*mer* isomerizations, 10 cycles were performed for Ir(ppy)₃ using the General Procedure (for procedure details, see subchapter 6.3.4). The excitation and emission spectra of *fac*-Ir(ppy)₃ and *mer*-Ir(ppy)₃ during the first cycle are presented below. The emission intensity at $\lambda = 514 \text{ nm}$ was recorded after each isomerization. The solutions for the measurements were prepared in DCM by dilution to *ca.* 10^{-5} M .



Excitation (dashed lines, @ λ_{em}) and emission spectra (solid lines, @365) of Ir(ppy)₃ solution during the isomerization from *fac* to *mer*

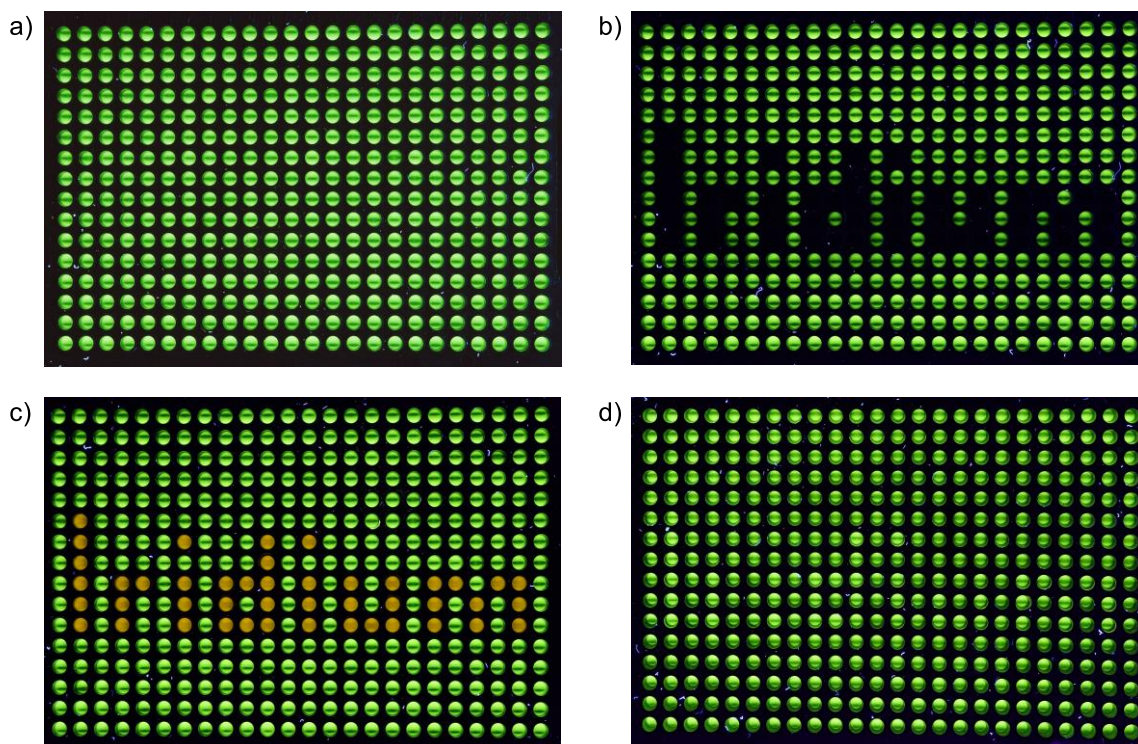


The luminescence intensity at 514 nm of a solution containing Ir(ppy)₃ during *fac*↔*mer* isomerization cycles ($\lambda_{ex} = 365$ nm)

6.3.8 A Simple Rewritable Data Storage Device Based on Ir(ppy)₃

To demonstrate the possibility of using Ir(C^N)₃ complexes for rewritable data storage devices, a simple luminescent display based on Ir(ppy)₃ was constructed.

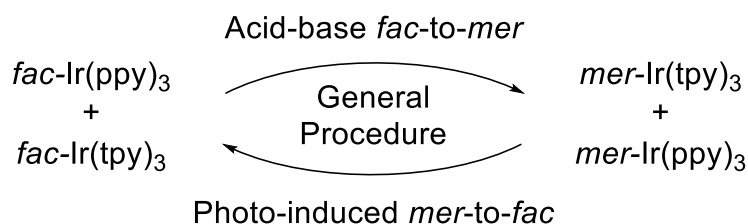
A Microseal 384-well black-coloured polypropylene-based PCR plate (Bio-Rad Laboratories, Inc.) was used as a matrix. *fac*-Ir(ppy)₃ was dissolved in *o*-dichlorobenzene (1.5 mg/mL) and aliquots of the solutions were pipetted into each well (20 μL per well) (a). Then, the word “Iridium” was written using a pipette “pen” with TFA (3 μL per well) as the black “ink” (b). The addition of NEt₃ to the ‘Iridium wells’ (7 μL per well) resulted in an orange emission (c). Finally, the word was erased by exposure to blue light for 7 h (d).



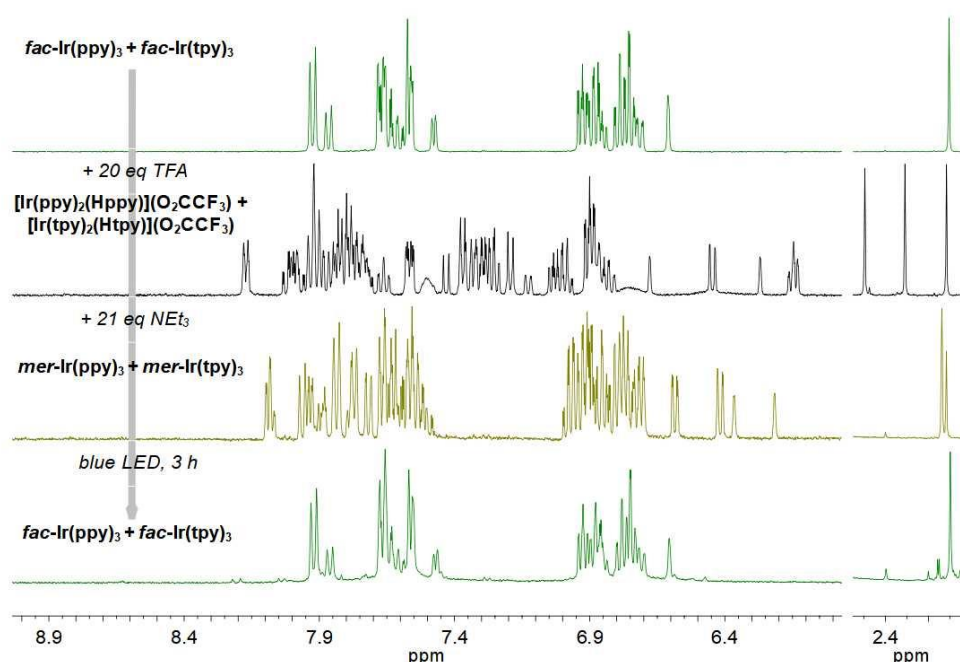
A rewritable luminescent display based on *fac*↔*mer* Ir(ppy)₃ isomerization

A short video showing the isomerization from *fac*-Ir(ppy)₃ to *mer*-Ir(ppy)₃ in the well plate is given as a Supplementary Movie on the webpage of the publication <https://doi.org/10.1039/D2SC02808E>.

6.3.9 Investigation of Ligand Exchange



A $\textit{fac} \rightarrow \textit{mer} \rightarrow \textit{fac}$ isomerization of a mixture of $\textit{fac}\text{-Ir(ppy)}_3$ and $\textit{fac}\text{-Ir(tpy)}_3$ using the General Procedure



^1H NMR (CD_2Cl_2 , 298 K) spectra for the $\textit{fac} \rightarrow \textit{mer} \rightarrow \textit{fac}$ isomerization of a mixture of $\textit{fac}\text{-Ir(ppy)}_3$ and $\textit{fac}\text{-Ir(tpy)}_3$

The NMR spectrum obtained after irradiation (bottom spectrum in green) is nearly identical to that of the starting mixture (top spectrum in green), indicating that ligand scrambling during isomerization is negligible.

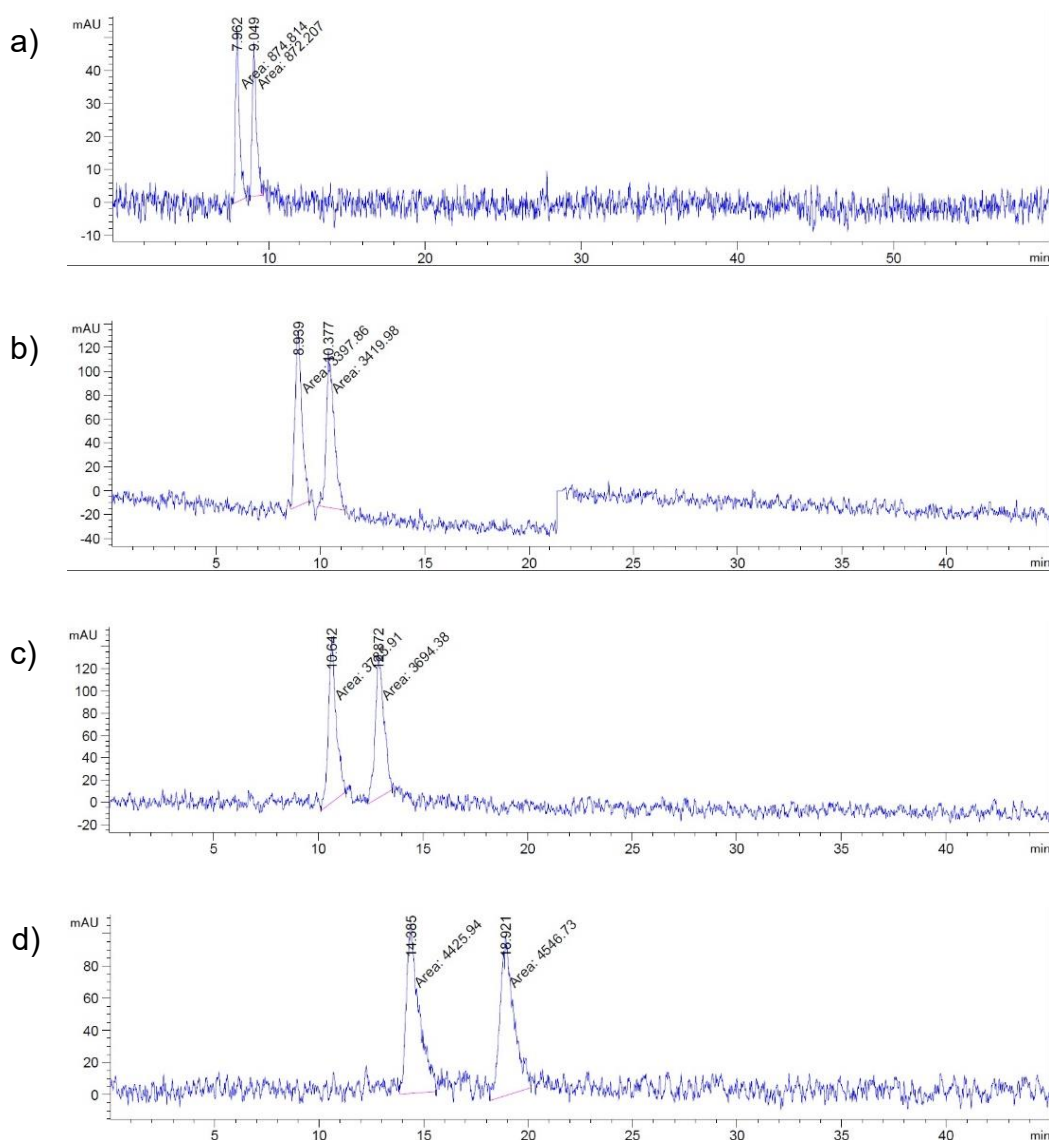
HRMS data

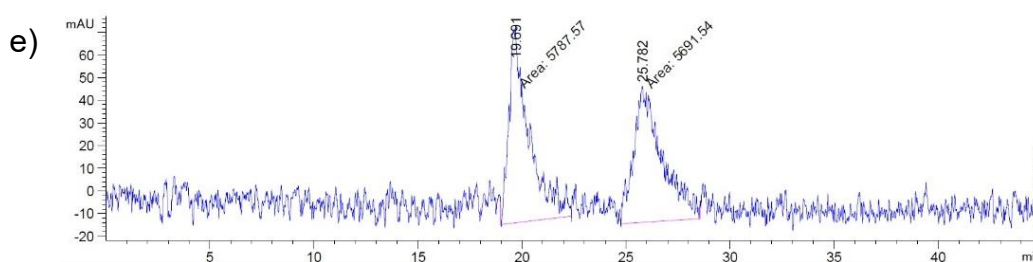
Compound	Formula	$\textit{fac} \rightarrow \textit{mer}$ (ESI $^+$)		$\textit{mer} \rightarrow \textit{fac}$ (APPI $^+$)	
		Calcd. $[\text{M}+\text{H}]^+$	Found	Calcd. $[\text{M}]^+$	Found
$^{193}\text{Ir(ppy)}_3$	$\text{C}_{33}\text{H}_{24}\text{IrN}_3$	656.1672	656.1687	655.1594	655.1603

$^{193}\text{Ir}(\text{ppy})_2(\text{tpy})$	$\text{C}_{34}\text{H}_{26}\text{IrN}_3$	670.1829	<i>n.f.</i>	669.1750	<i>n.f.</i>
$^{193}\text{Ir}(\text{tpy})_2(\text{ppy})$	$\text{C}_{35}\text{H}_{28}\text{IrN}_3$	684.1985	<i>n.f.</i>	683.1907	<i>n.f.</i>
$^{193}\text{Ir}(\text{tpy})_3$	$\text{C}_{36}\text{H}_{30}\text{IrN}_3$	698.2142	698.2153	697.2063	697.2064

6.3.10 Chiral HPLC Resolution of Δ and Λ Isomers and Stereoselectivity of the Acid-Base *fac*→*mer* and the Photochemical *mer*→*fac* Isomerizations

The conditions for optical resolution of racemic *fac*-Ir(ppy)₃ and *mer*-Ir(ppy)₃ into their Δ and Λ isomers were found using analytical chiral HPLC by screening the column type (Chiralpak IA, IB, IC, ID, IF) and the ratio of the solvents (hexane-*i*-PrOH from 80:20 to 98:2, v/v). The results of the screening using the column Chiralpak IA are shown below.





HPLC profiles of *rac-fac*-Ir(ppy)₃ eluted by hexane–*i*-PrOH solvent mixture with gradual decrease of *i*-PrOH volume fraction

HPLC screening summary (column Chiralpak IA, hexane–*i*-PrOH)

HPLC profile	Eluent, v/v	Retention time gap between peaks, min
a)	80:20	1
b)	85:15	1.5
c)	90:10	2.3
d)	95:5	4.5
e)	98:2	6.1

The following conditions were chosen and used for further enantiomeric excess (*ee*) analyses: column Chiralpak IA (size 4.6×250 mm, temperature 35 °C), eluent hexane–*i*-PrOH 95:5, injection volume 10 μL, flow 1 mL/min, detection at 254 nm, run time 30 min, sample solution: 2.5 mg/mL in DCM. The HPLC profiles of the racemic *fac*-Ir(ppy)₃ and *mer*-Ir(ppy)₃ separated in preparative HPLC mode are shown below.

For the stereoselectivity studies, racemic *fac*-Ir(ppy)₃ was separated into two enantiomerically enriched samples using preparative chiral HPLC. The following conditions were employed: preparative column Chiralpak IA, temperature 25 °C, eluent hexane/*i*-PrOH 95:5, injection volume 0.5 mL (6 iterative injections), flow 18 mL/min, detection at 254 nm, run time 45 min, sample solution: 2.5 mg/mL in DCM. The HPLC profiles of the enantiomerically enriched samples are shown below. The assignment of the peaks in the chromatogram of the *fac* isomer was made based on the work of J. Otsuki and co-workers.¹⁸⁶ The 1st eluted enantiomer is Δ -*fac*-Ir(ppy)₃ and the 2nd eluted enantiomer is Λ -*fac*-Ir(ppy)₃. The results of our separation are shown below.

1st eluted: Δ -*fac*-Ir(ppy)₃. 3.4 mg (45%), Δ : Λ = 83:17 (*ee* = 66%), $\tau_{\Delta\text{-}fac} \approx 8.9$ min.

2nd eluted: Λ -*fac*-Ir(ppy)₃. 2.8 mg (37%), Δ : Λ = 30:70 (*ee* = 40%), $\tau_{\Lambda\text{-}fac} \approx 11.3$ min.

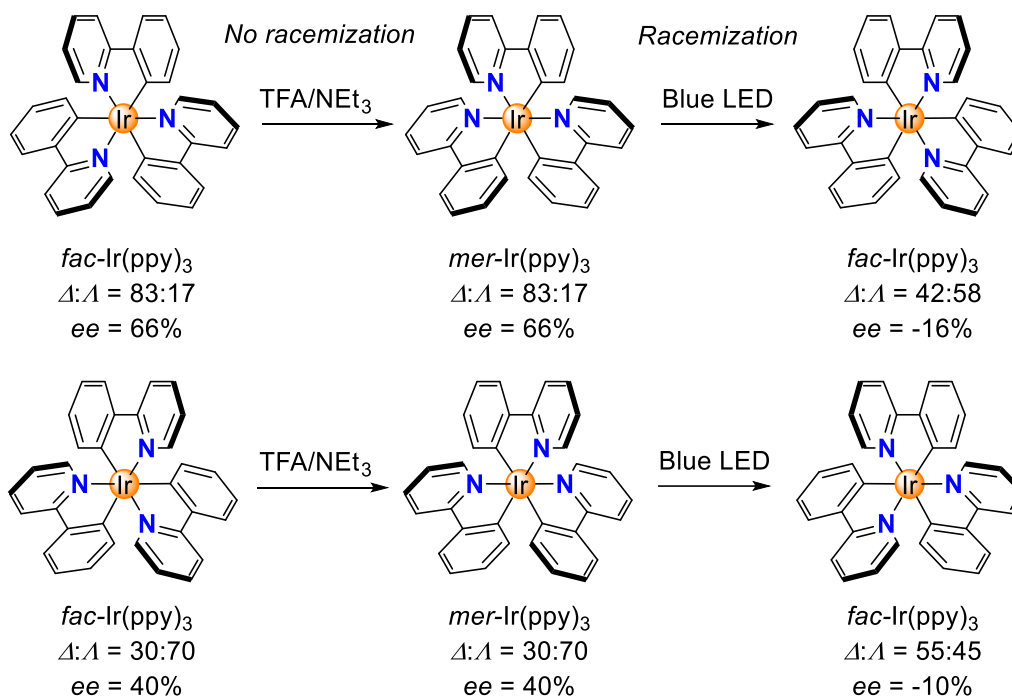
The assignment of the peaks in the chromatogram of the *mer* isomer was discussed in subchapter 3.7. The 1st eluted enantiomer (96:4, *ee* = 92%) was obtained using preparative chiral HPLC following the conditions described above. Its HPLC profile and CD spectrum are given below. Single crystals of this enantiomer were obtained by slow gas phase diffusion of pentane into a solution of the complex in DCM at room temperature. The absolute configuration was determined by X-ray crystallography as Δ -*mer*-Ir(ppy)₃. The CD spectra of the measured crystal and the whole sample with *ee* = 92% showed below and indicated the same absolute configuration. Thus, the 1st eluted enantiomer was assigned as Δ -*mer*-Ir(ppy)₃, and the 2nd eluted enantiomer was assigned as Λ -*mer*-Ir(ppy)₃. The results of our separation are shown below.

1st eluted: Δ -*mer*-Ir(ppy)₃. $\tau_{\Delta\text{-}mer} \approx 6.4$ min.

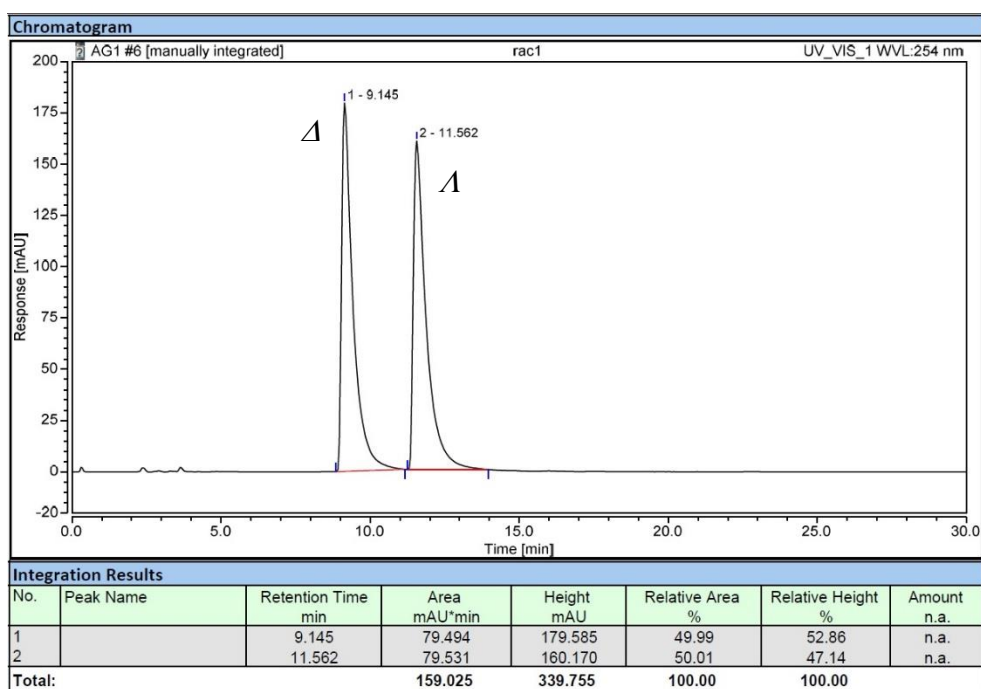
2nd eluted: Λ -*mer*-Ir(ppy)₃. $\tau_{\Lambda\text{-}mer} \approx 8.5$ min.

The enantiomerically enriched samples of Δ -*fac*-Ir(ppy)₃ (Δ : Λ = 83:17, *ee* = 66%) and Λ -*fac*-Ir(ppy)₃ (Δ : Λ = 30:70, *ee* = 40%) were isomerized to *mer* following the General Procedure. Subsequently, the *mer* isomers were isomerized back to *fac* isomers photochemically. The reactions were followed by analytical chiral HPLC and CD spectroscopy, and the spectra are shown below.

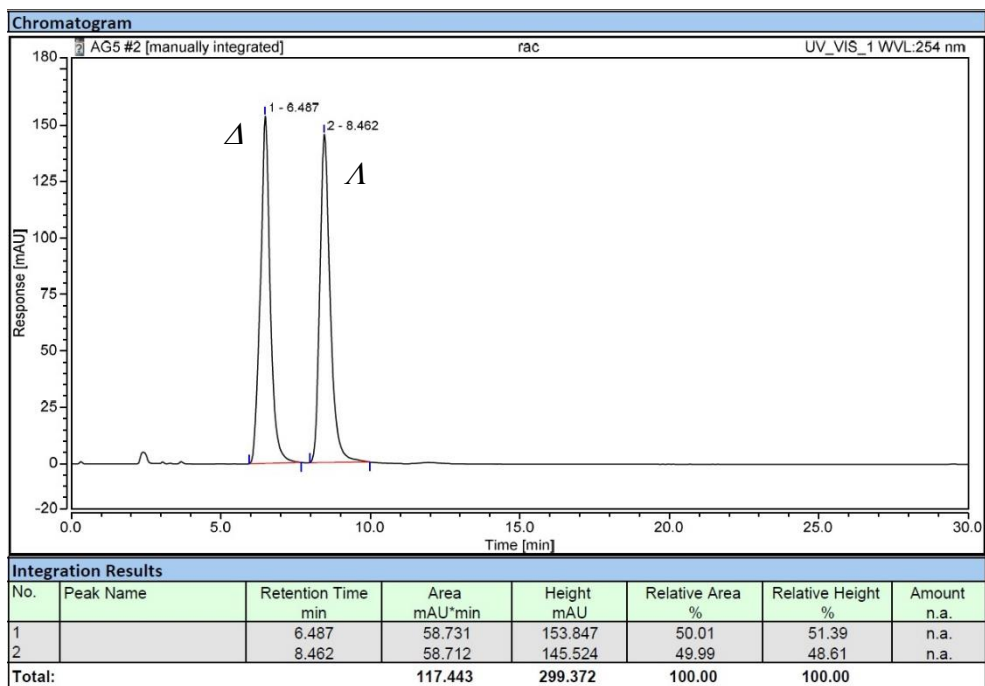
It was found that the acid-base-induced *fac*→*mer* isomerization proceeds stereoselectively with the same ratio Δ : Λ = 83:17 for the first sample and Δ : Λ = 30:70 for the second sample. In turn, the photochemical *mer*→*fac* isomerization proceeds with racemization in both cases. The summary of these results is shown below.



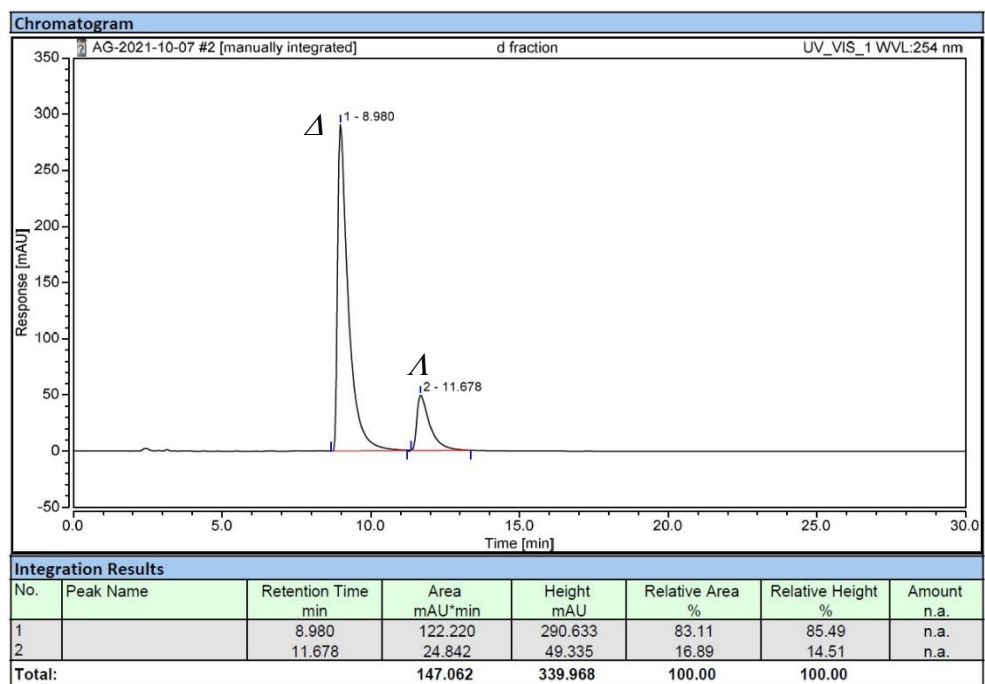
fac → *mer* → *fac* isomerization of enantiomerically enriched samples of *fac*-Ir(ppy)₃



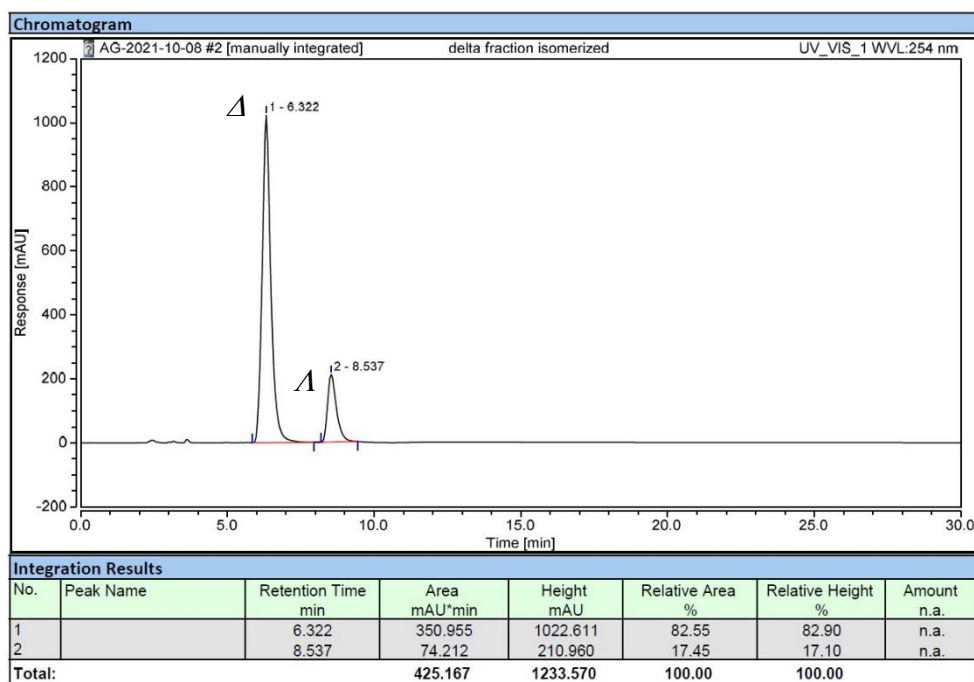
HPLC profile of racemic *fac*-Ir(ppy)₃



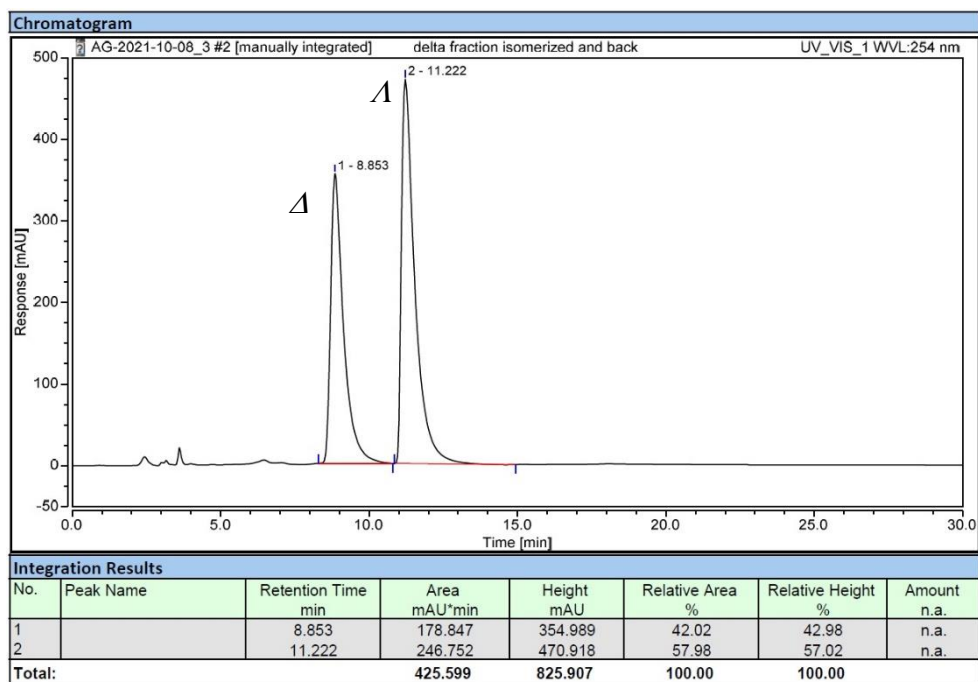
HPLC profile of racemic *mer*-Ir(ppy)₃



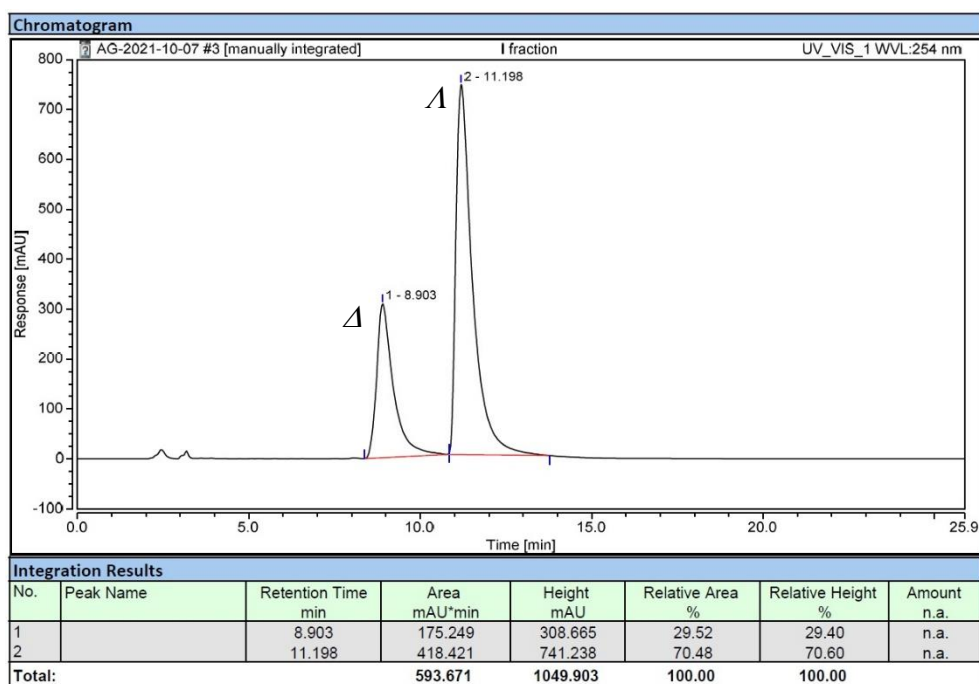
HPLC profile of enantioenriched Δ -*fac*-Ir(ppy)₃ before the *fac*→*mer* isomerization



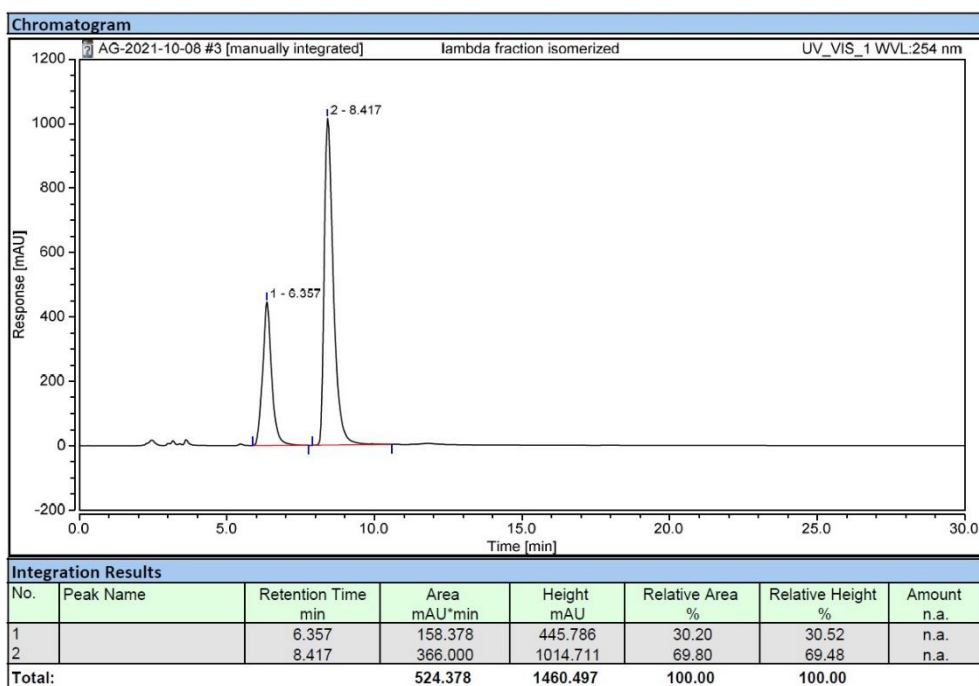
HPLC profile of enantioenriched Δ -*mer*-Ir(ppy)₃ obtained from Δ -*fac*-Ir(ppy)₃ via the acid-base *fac*→*mer* isomerization



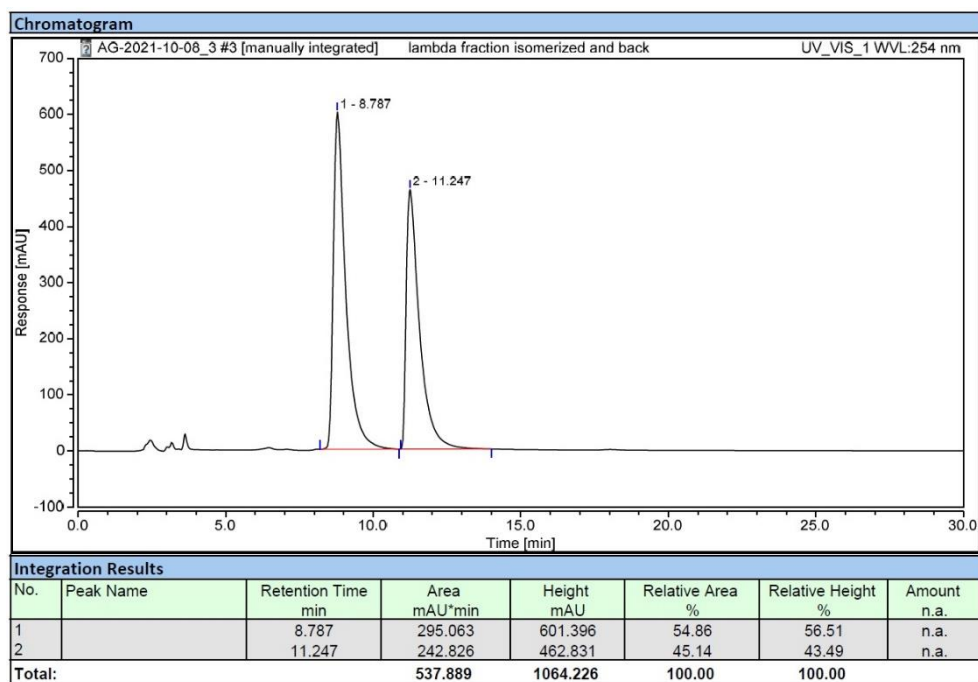
HPLC profile of the mixture after photochemical *mer*→*fac* isomerization



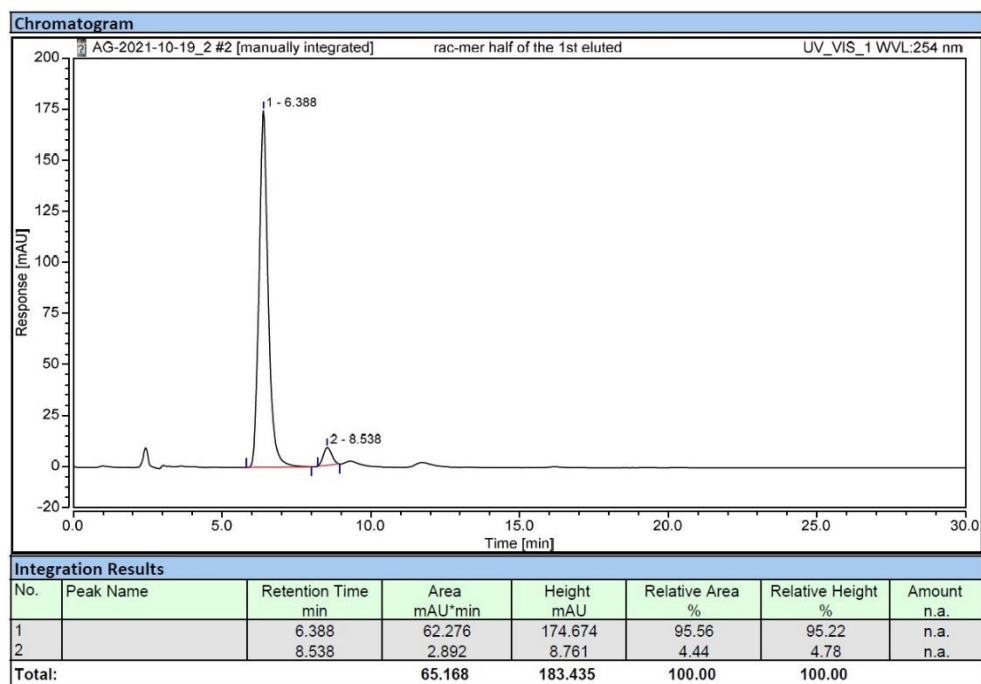
HPLC profile of enantioenriched Λ -*fac*-Ir(ppy)₃ before the *fac*→*mer* isomerization



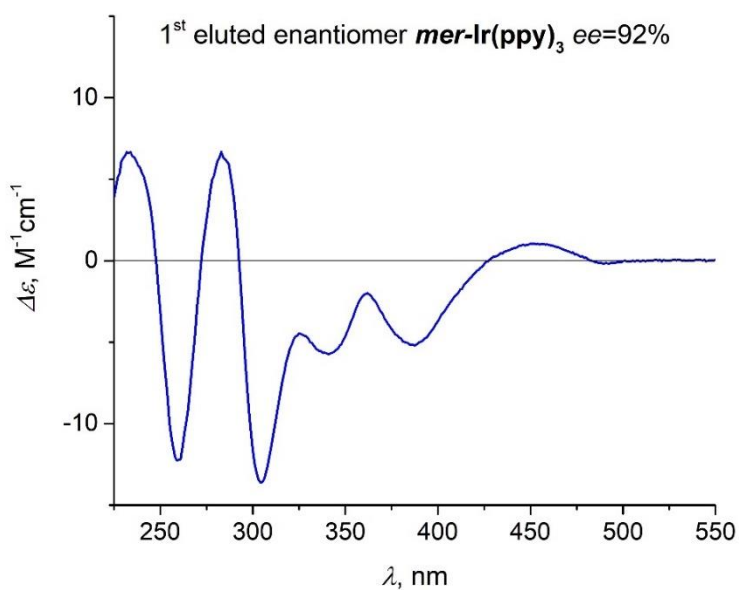
HPLC profile of enantioenriched Λ -*mer*-Ir(ppy)₃ obtained from Λ -*fac*-Ir(ppy)₃ via the acid-base *fac*→*mer* isomerization



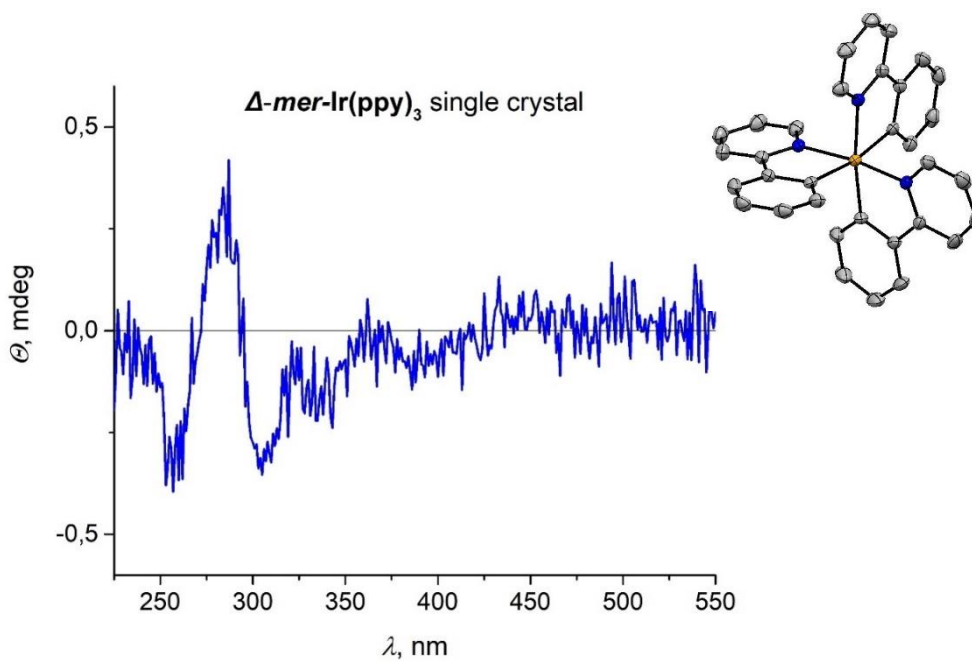
HPLC profile of the mixture after photochemical *mer*→*fac* isomerization



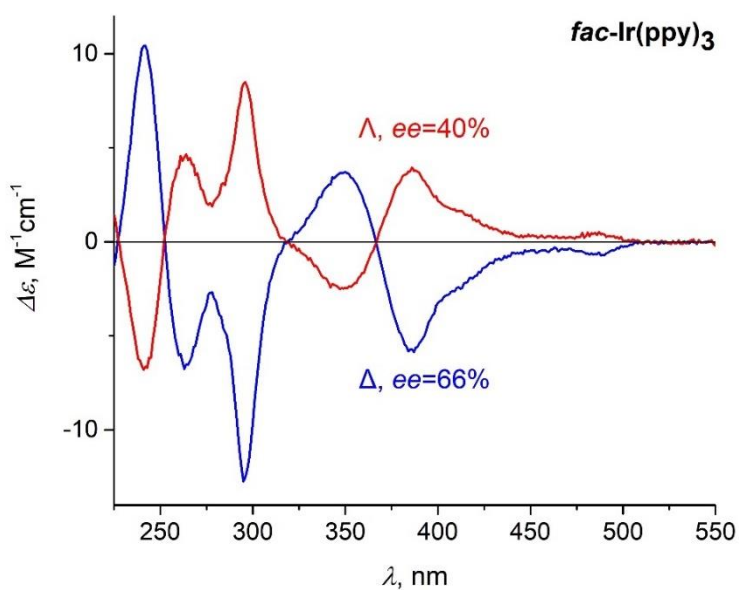
HPLC profile of the first eluted enantiomer of *mer*-Ir(ppy)₃



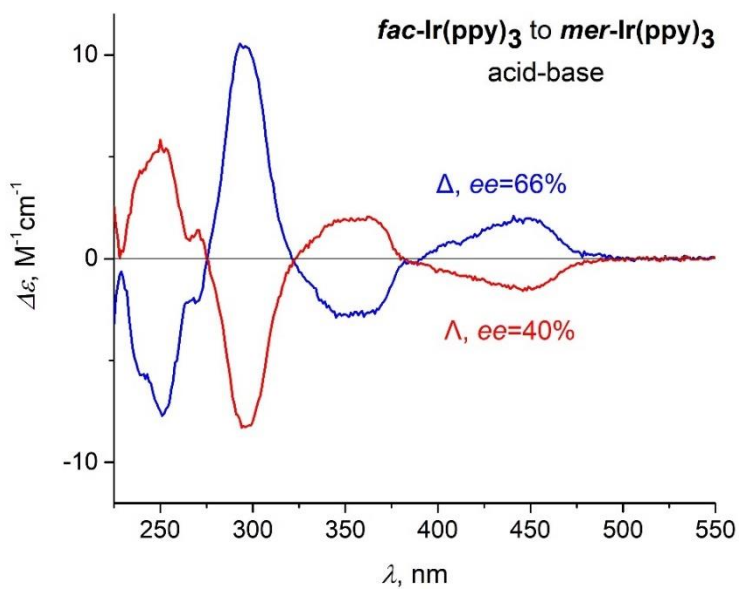
ECD spectrum (DCM) of the first eluted enantiomer of *mer*-Ir(ppy)₃



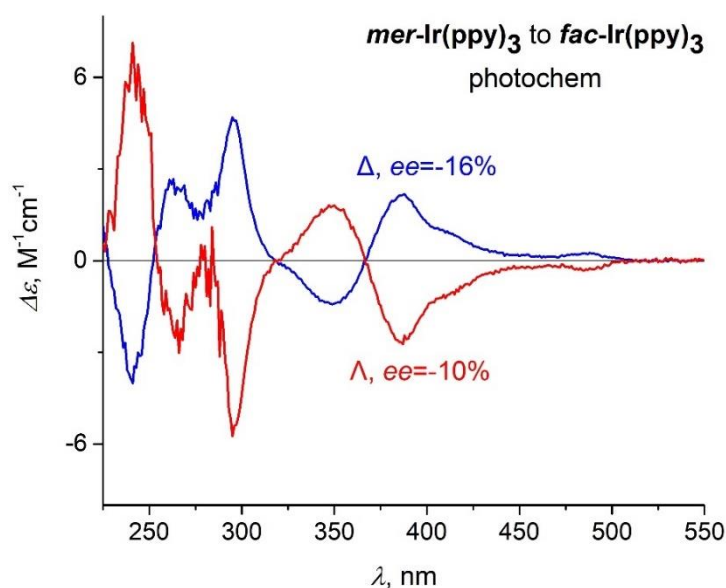
ECD spectrum of a solution (DCM) of the single crystal obtained after crystallization of the first eluted enantiomer of *mer*-Ir(ppy)₃. Inset: ORTEP view with 50% probability. Hydrogen atoms are not shown for clarity.



ECD spectra (DCM) of enantioenriched Δ -*fac*-Ir(ppy)₃ (blue line) and Λ -*fac*-Ir(ppy)₃ (red line) before the *fac*→*mer* isomerization



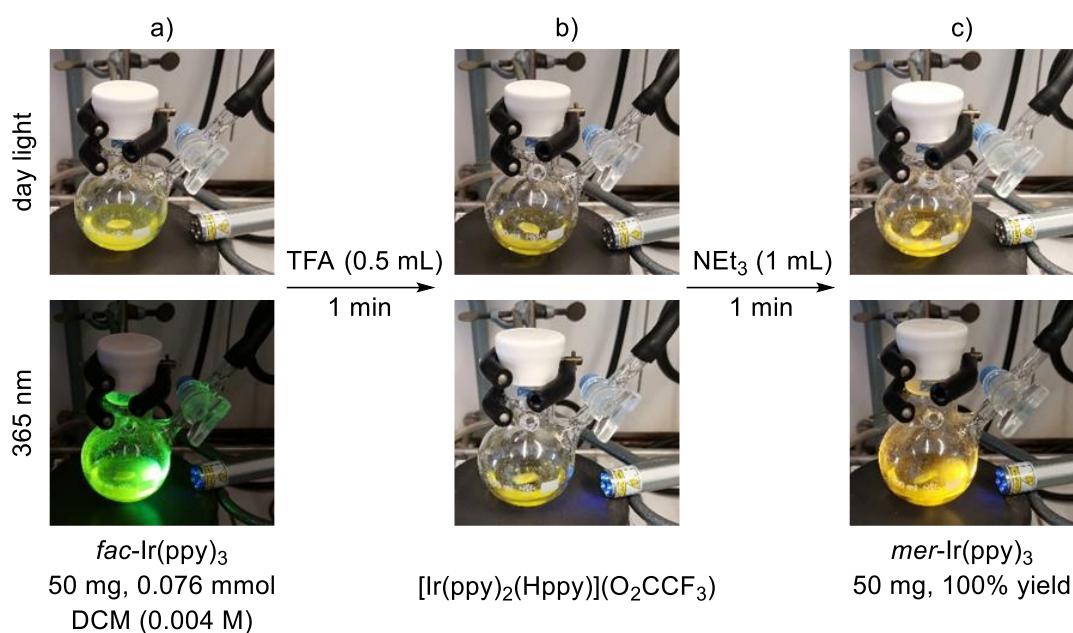
ECD spectra (DCM) of enantioenriched Δ -*mer*-Ir(ppy)₃ (blue line) and Λ -*mer*-Ir(ppy)₃ (red line) after the *fac*→*mer* isomerization



ECD spectra (DCM) of enantioenriched Δ -*fac*-Ir(ppy)₃ (blue line) and Λ -*fac*-Ir(ppy)₃ (red line) after the photochemical *mer*→*fac* isomerization

6.3.11 Large-Scale Synthesis of *mer*-Ir(ppy)₃ from *fac*-Ir(ppy)₃

fac-Ir(ppy)₃ (50 mg, 76 μ mol) was placed in a 100 mL Schlenk flask equipped with a stirring bar and dissolved under stirring in 20 mL of DCM (*yellow solution with green luminescence when irradiated at 365 nm*, a). Subsequently, pure TFA (0.5 mL) was added in one portion under mild stirring (350 rpm). The reaction was accompanied by a change of colour to greenish-yellow and quenching of the emission (b). After 1 min of stirring at room temperature, NEt₃ (1 mL) was added dropwise under fast stirring (650 rpm). The reaction was accompanied by a colour change back to yellow and a turn-on of the emission (c). After 1 min of stirring at room temperature, the solvent and the excess of NEt₃ were removed under vacuum. The resulting yellow crystalline precipitate was rinsed with methanol (2×15 mL) and diethyl ether (1×15 mL) to wash away the salt HNEt₃(O₂CCF₃) and dried under vacuum to give *mer*-Ir(ppy)₃ (50 mg, quant.). This procedure can be used for all other complexes mentioned in this work.

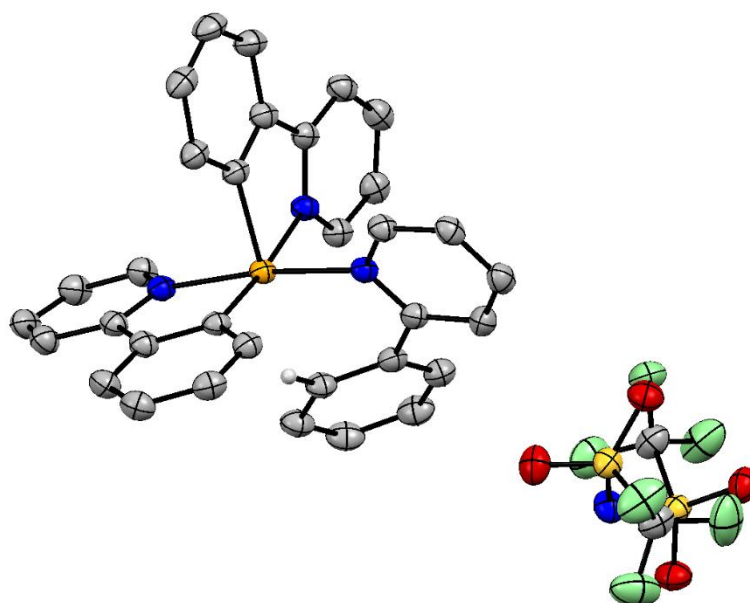


Stepwise visualization of the 50 mg synthesis of $mer\text{-Ir(ppy)}_3$ from $fac\text{-Ir(ppy)}_3$ via the acid-base $fac \rightarrow mer$ isomerization. a) The solution of $fac\text{-Ir(ppy)}_3$ in DCM before the addition of TFA, b) the mixture after the addition of TFA, and c) the mixture after the addition of NEt_3 .



Photo images of starting material $fac\text{-Ir(ppy)}_3$ and the product $mer\text{-Ir(ppy)}_3$ under daylight (left) and when irradiated at 365 nm (right).

6.3.12 Crystallographic Data



ORTEP view of $[\text{Ir}(\text{ppy})_2(\text{Hppy})](\text{NTf}_2)$ at the 50% probability level. Most hydrogen atoms are omitted for clarity.

A clear intense yellow hexagonal-shaped crystal with dimensions $0.42 \times 0.28 \times 0.12 \text{ mm}^3$ was mounted. Data were collected using a SuperNova, Dual, Cu at home/near, Atlas diffractometer operating at $T = 140.01(10) \text{ K}$.

Data were measured using ω scans using $\text{CuK}\alpha$ radiation. The diffraction pattern was indexed and the total number of runs and images was based on the strategy calculation from the program CrysAlis^{Pro} 1.171.41.110a (CrysAlis^{Pro} Software System, Rigaku Oxford Diffraction, 2021). The maximum resolution that was achieved was $\theta = 76.610^\circ$ (0.79 Å).

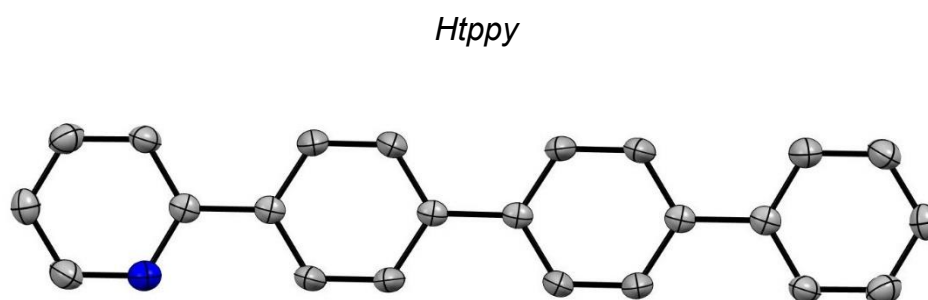
The unit cell was refined using CrysAlis^{Pro} 1.171.41.105a on 57568 reflections, 71% of the observed reflections.

Data reduction, scaling and absorption corrections were performed using CrysAlis^{Pro} 1.171.41.105a. The final completeness is 99.90% out to 76.610° in θ . A gaussian absorption correction was performed using CrysAlis^{Pro} 1.171.41.105a. Numerical absorption correction based on gaussian integration over a multifaceted crystal model

Empirical absorption correction using spherical harmonics, implemented in SCALE3 ABSPACK scaling algorithm. The absorption coefficient μ of this material is 9.913 mm^{-1} at this wavelength ($\lambda = 1.54184 \text{ \AA}$) and the minimum and maximum transmissions are 0.083 and 0.661.

The structure was solved and the space group $P2_1/c$ (№ 14) was determined by the ShelXT 2018/2²²⁶ structure solution program using dual methods and refined by full matrix least squares minimization on F^2 using version 2018/3 of ShelXL 2018/3.²²⁷ All non-hydrogen atoms were refined anisotropically. Hydrogen atom positions were calculated geometrically and refined using the riding model.

The value of Z' is 2. This means that there are two independent molecules in the asymmetric unit.



ORTEP view of Htppy at the 50% probability level

A colourless plate-shaped crystal with dimensions $0.32 \times 0.19 \times 0.02 \text{ mm}^3$ was mounted. Data were collected using a SuperNova, Dual, Cu at home/near, Atlas diffractometer operating at $T = 150.00(10) \text{ K}$.

Data were measured using ω scans using $\text{CuK}\alpha$ radiation. The diffraction pattern was indexed and the total number of runs and images was based on the strategy calculation from the program CrysAlis^{Pro} 1.171.41.110a (CrysAlis^{Pro} Software System, Rigaku Oxford Diffraction, 2021). The maximum resolution achieved was $\theta = 73.999^\circ$ (0.80 \AA).

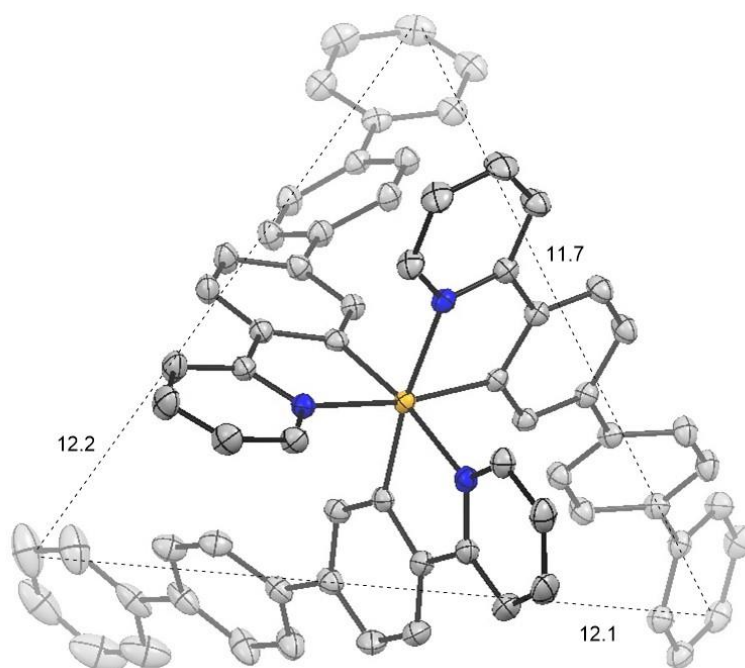
The unit cell was refined using CrysAlis^{Pro} 1.171.41.110a on 1539 reflections, 28% of the observed reflections.

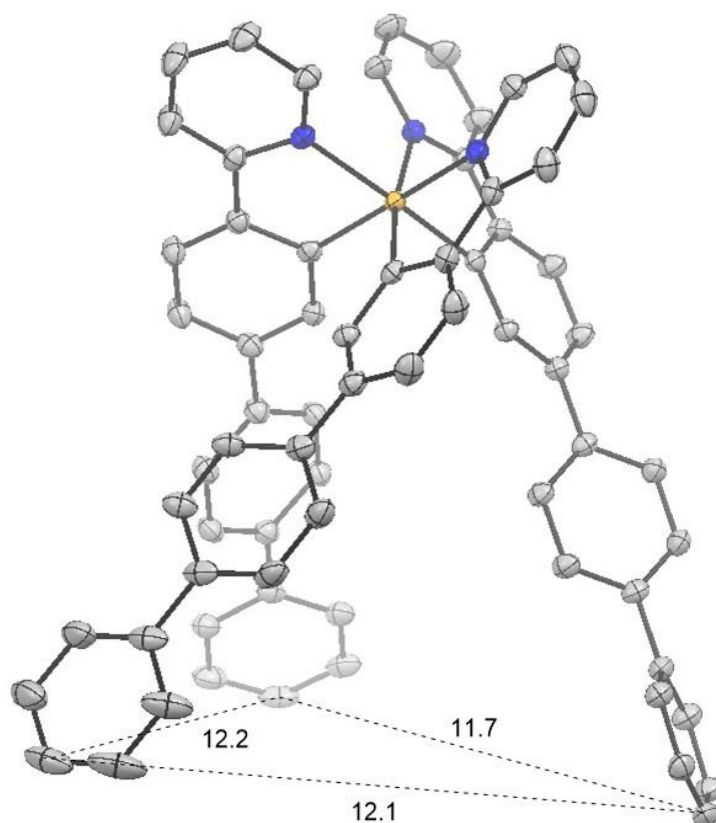
Data reduction, scaling and absorption corrections were performed using CrysAlis^{Pro} 1.171.41.110a. The final completeness is 99.80 % out to 73.999° in θ . A Gaussian absorption correction was performed using CrysAlis^{Pro} 1.171.41.110a. Numerical absorption correction based on Gaussian integration over a multifaceted crystal model. Empirical absorption correction using spherical harmonics as implemented in SCALE3 ABSPACK scaling algorithm. The absorption coefficient μ of this material is 0.585 mm⁻¹ at this wavelength ($\lambda = 1.54184$ Å) and the minimum and maximum transmissions are 0.635 and 1.000.

The structure was solved and the space group $P2_1/c$ (№ 14) was determined by the ShelXT 2018/2²²⁶ structure solution program using dual methods and refined by full matrix least squares minimization on F^2 using version 2018/3 of ShelXL 2018/3.²²⁷ All non-hydrogen atoms were refined anisotropically. Hydrogen atom positions were calculated geometrically and refined using the riding model. Due to the presence of inversion center in the structure, atoms C1 and N1 lie on the same positions with the s.o.f of half in the asymmetric unit.

The value of Z' is 0.5. This means that only half of the formula unit is present in the asymmetric unit, with the other half consisting of symmetry-equivalent atoms.

fac-Ir(tppy)₃





ORTEP views of *fac*-Ir(tppy)₃ with depth cue (50% probability level). Hydrogen atoms are omitted for clarity.

A clear dark orange prism-shaped crystal with dimensions 0.26×0.17×0.04 mm³ was mounted. Data were collected using a XtaLAB Synergy R, DW system, HyPix–Arc 150 diffractometer operating at $T = 139.99(10)$ K.

Data were measured using ω scans using CuK α radiation. The diffraction pattern was indexed and the total number of runs and images was based on the strategy calculation from the program CrysAlis^{Pro} 1.171.41.110a (CrysAlis^{Pro} Software System, Rigaku Oxford Diffraction, 2021). The maximum resolution achieved was $\theta = 76.166^\circ$ (0.79 Å).

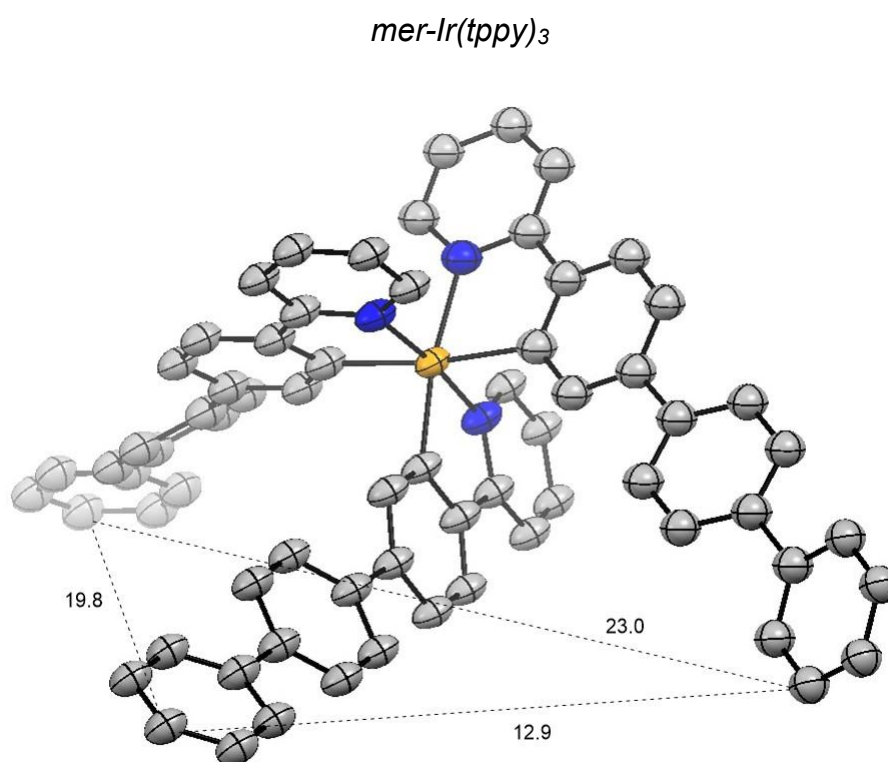
The unit cell was refined using CrysAlis^{Pro} 1.171.41.110a on 45783 reflections, 82% of the observed reflections.

Data reduction, scaling and absorption corrections were performed using CrysAlis^{Pro} 1.171.41.110a. The final completeness is 99.90 % out to 76.166° in θ . A Gaussian absorption correction was performed using CrysAlis^{Pro} 1.171.41.110a. Numerical

absorption correction based on Gaussian integration over a multifaceted crystal model. Empirical absorption correction using spherical harmonics as implemented in SCALE3 ABSPACK scaling algorithm. The absorption coefficient μ of this material is 6.173 mm^{-1} at this wavelength ($\lambda = 1.54184 \text{ \AA}$) and the minimum and maximum transmissions are 0.218 and 1.000.

The structure was solved and the space group $P\bar{1}$ (№ 2) was determined by the ShelXT 2018/2²²⁶ structure solution program using dual methods and refined by full matrix least squares minimization on F^2 using version 2018/3 of ShelXL 2018/3.²²⁷ All non-hydrogen atoms were refined anisotropically. Hydrogen atom positions were calculated geometrically and refined using the riding model.

There is a single molecule in the asymmetric unit, which is represented by the reported sum formula. In other words: Z is 2 and Z' is 1.



ORTEP view of *mer-Ir(tppy)₃* with depth cue (25% probability level). Hydrogen atoms are omitted for clarity.

A clear intense orange plate-shaped crystal with dimensions 0.18×0.06×0.01 mm³ was mounted. Data were collected using a XtaLAB Synergy R, DW system, HyPix-Arc 150 diffractometer operating at $T = 139.99(10)$ K.

Data were measured using ω scans using CuK α radiation. The diffraction pattern was indexed and the total number of runs and images was based on the strategy calculation from the program CrysAlis^{Pro} 1.171.41.110a (CrysAlis^{Pro} Software System, Rigaku Oxford Diffraction, 2021). The maximum resolution that was achieved was $\theta = 75.272^\circ$ (0.80 Å).

The unit cell was refined using CrysAlis^{Pro} 1.171.41.110a on 25613 reflections, 98% of the observed reflections.

Data reduction, scaling and absorption corrections were performed using CrysAlis^{Pro} 1.171.41.110a. The final completeness is 99.70% out to 75.272° in θ . A Gaussian absorption correction was performed using CrysAlis^{Pro} 1.171.41.110a. Numerical absorption correction based on Gaussian integration over a multifaceted crystal model. Empirical absorption correction using spherical harmonics as implemented in SCALE3 ABSPACK scaling algorithm. The absorption coefficient μ of this material is 5.255 mm⁻¹ at this wavelength ($\lambda = 1.54184$ Å) and the minimum and maximum transmissions are 0.425 and 1.000.

The structure was solved, and the space group $P\bar{1}$ (№ 2) was determined by the ShelXT 2018/2²²⁶ structure solution program using dual methods and refined by full matrix least squares minimization on F^2 using version 2018/3 of ShelXL 2018/3.²²⁷ All non-hydrogen atoms were refined anisotropically. Hydrogen atom positions were calculated geometrically and refined using the riding model.

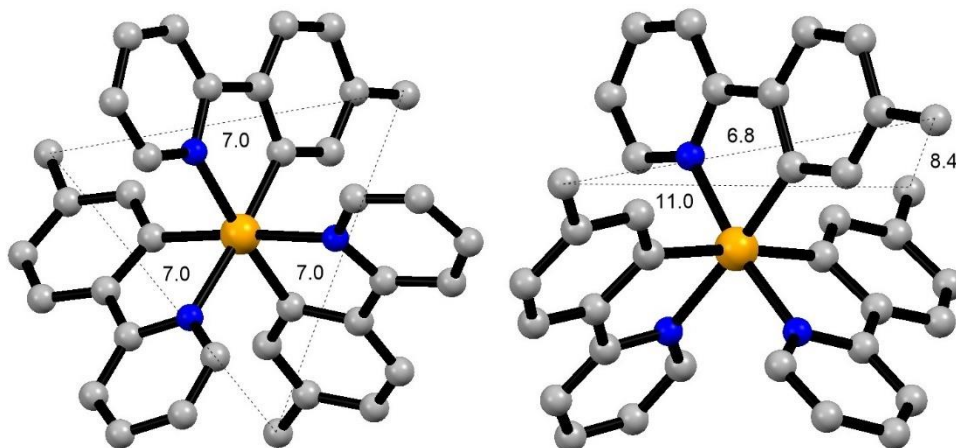
This structure was refined as a 2-component twin.

The value of Z' is 2. This means that there are two independent molecules in the asymmetric unit.

The crystal structures of *fac*-Ir(tpy)₃ and *mer*-Ir(tpy)₃ are presented below for comparison of how the 'short' ligand (tpy, instead of tppy) affects the change of the

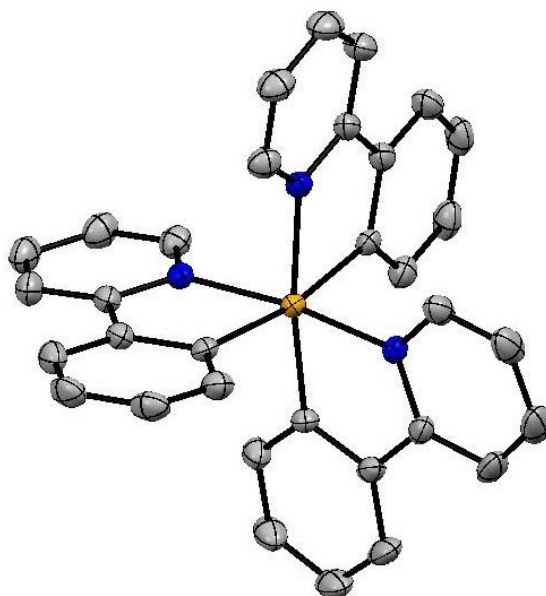
size of molecule upon *fac*→*mer* isomerization. In the complex Ir(tpy)₃, these geometrical changes are not pronounced, while in Ir(tppy)₃ they are clearly observed.

fac-Ir(tpy)₃ and *mer*-Ir(tpy)₃



Crystal structures of *fac*-Ir(tpy)₃ (CCDC 215418)²²⁸ and *mer*-Ir(tpy)₃ (CCDC 1290063).¹⁰³ Hydrogen atoms are not shown for clarity.

Δ -*mer*-Ir(ppy)₃



ORTEP view of Δ -*mer*-Ir(ppy)₃ at the 50% probability level. Hydrogen atoms are omitted for clarity.

A clear intense orange plate-shaped crystal with dimensions 0.15×0.12×0.03 mm³ was mounted. Data were collected using a XtaLAB Synergy R, DW system, HyPix-Arc 150 diffractometer operating at $T = 140.00(10)$ K.

Data were measured using ω scans with MoK α radiation. The diffraction pattern was indexed and the total number of runs and images was based on the strategy calculation from the program CrysAlis^{Pro} 1.171.41.118a (CrysAlis^{Pro} Software System, Rigaku Oxford Diffraction, 2021). The maximum resolution achieved was $\theta = 41.261^\circ$ (0.54 Å).

The unit cell was refined using CrysAlis^{Pro} 1.171.41.118a on 42711 reflections, 43% of the observed reflections.

Data reduction, scaling and absorption corrections were performed using CrysAlis^{Pro} 1.171.41.118a. The final completeness is 100.00 % out to 41.261° in θ . A Gaussian absorption correction was performed using CrysAlis^{Pro} 1.171.41.118a. Numerical absorption correction based on Gaussian integration over a multifaceted crystal model. Empirical absorption correction using spherical harmonics as implemented in SCALE3 ABSPACK scaling algorithm. The absorption coefficient μ of this material is 4.643 mm⁻¹ at this wavelength ($\lambda = 0.71073\text{Å}$) and the minimum and maximum transmissions are 0.593 and 1.000.

The structure was solved and the space group $P4_12_12$ (№ 92) was determined by the ShelXT 2018/2²²⁶ structure solution program using dual methods and refined by full matrix least squares minimization on F^2 using version 2018/3 of ShelXL 2018/3.²²⁷ All non-hydrogen atoms were refined anisotropically. Hydrogen atom positions were calculated geometrically and refined using the riding model.

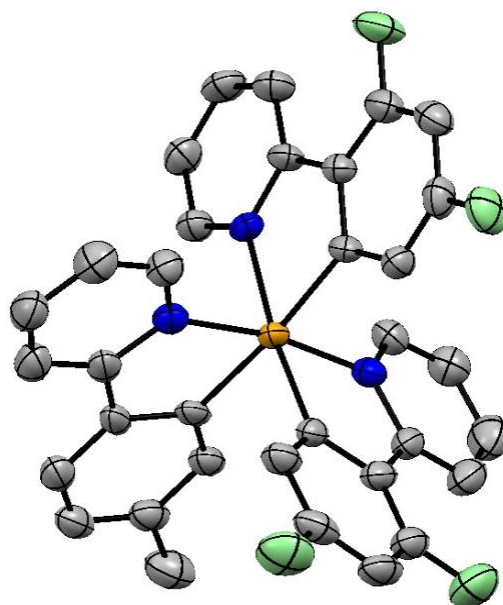
This structure was refined as a 2-component inversion twin.

The value of Z' is 0.5. This means that only half of the formula unit is present in the asymmetric unit, with the other half consisting of symmetrically equivalent atoms.

The Flack parameter was refined to 0.070(11). Determination of absolute structure using Bayesian statistics on Bijvoet differences using the Olex2 results in Note.

Note: The Flack parameter is used to determine chirality of the crystal studied, the value should be near 0, a value of 1 means that the stereochemistry is wrong, and the model should be inverted. A value of 0.5 means that the crystal consists of a racemic mixture of the two enantiomers.

mer-Ir(dfppy)₂(tpy)



ORTEP view of *mer*-Ir(dfppy)₂(tpy) at the 50% probability level. Hydrogen atoms are omitted for clarity.

A clear intense yellow plate-shaped crystal with dimensions 0.16×0.15×0.01 mm³ was mounted. Data were collected using a XtaLAB Synergy R, DW system, HyPix-Arc 150 diffractometer operating at $T = 140.00(10)$ K.

Data were measured using ω scans with CuK α radiation. The diffraction pattern was indexed and the total number of runs and images was based on the strategy calculation from the program CrysAlis^{Pro} 1.171.41.120a (CrysAlis^{Pro} Software System, Rigaku Oxford Diffraction, 2021). The maximum resolution achieved was $\theta = 75.533^\circ$ (0.80 Å).

The unit cell was refined using CrysAlis^{Pro} 1.171.41.120a on 20871 reflections, 46% of the observed reflections.

Data reduction, scaling and absorption corrections were performed using CrysAlis^{Pro} 1.171.41.120a. The final completeness is 100.00 % out to 75.533° in θ . A Gaussian absorption correction was performed using CrysAlis^{Pro} 1.171.41.120a. Numerical absorption correction based on Gaussian integration over a multifaceted crystal model. Empirical absorption correction using spherical harmonics as implemented in SCALE3 ABSPACK scaling algorithm. The absorption coefficient μ of this material is 10.238 mm⁻¹ at this wavelength ($\lambda = 1.54184 \text{ \AA}$) and the minimum and maximum transmissions are 0.218 and 1.000.

The structure was solved, and the space group *C2/c* (№ 15) was determined by the ShelXT 2018/2²²⁶ structure solution program using dual methods and refined by full matrix least squares minimization on F^2 using version 2018/3 of ShelXL 2018/3.²²⁷ All non-hydrogen atoms were refined anisotropically. Hydrogen atom positions were calculated geometrically and refined using the riding model.

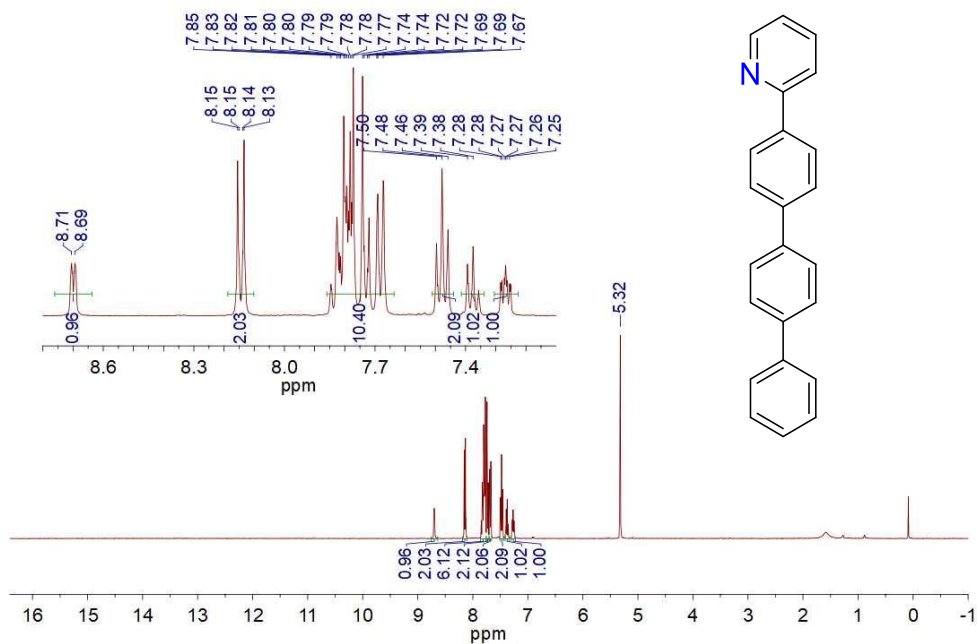
There is a single molecule in the asymmetric unit, which is represented by the reported sum formula. In other words: *Z* is 8 and *Z'* is 1.

Crystallographic data for the compounds

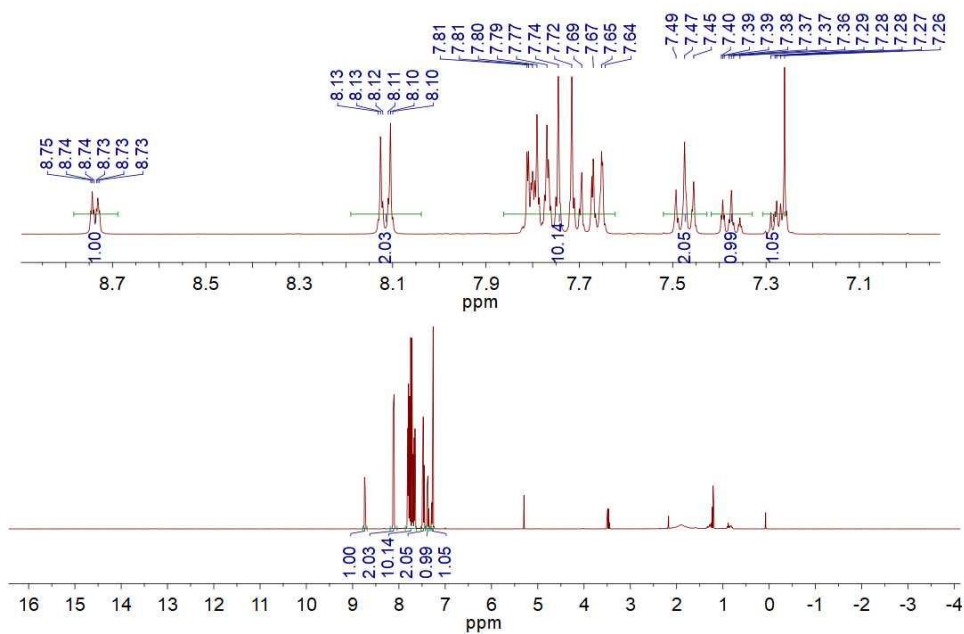
Compound	[Ir(ppy) ₂ (Hppy)](NTf ₂)	Htppy	fac-Ir(tppy) ₃
Formula	C _{35.5} H ₂₆ ClF ₆ IrN ₄ O ₄ S ₂	C ₂₃ H ₁₇ N	C ₇₀ H ₅₀ Cl ₂ IrN ₃
Formula Weight	978.37	307.38	1196.23
<i>D</i> _{calc.} , g cm ⁻³	1.858	1.327	1.501
<i>μ</i> , mm ⁻¹	9.913	0.585	6.173
Colour	intense yellow	colourless	dark orange
Shape	hexagonal	plate	prism
Size, mm ³	0.42×0.28×0.12	0.32×0.19×0.02	0.26×0.17×0.04
<i>T</i> , K	140.01(10)	150.00(10)	139.99(10)
Crystal System	monoclinic	monoclinic	triclinic
Space Group	P2 ₁ /c	P2 ₁ /c	P $\bar{1}$
<i>a</i> , Å	27.8756(2)	17.7468(11)	13.85396(12)
<i>b</i> , Å	12.70840(9)	5.5397(4)	14.21567(12)
<i>c</i> , Å	20.40752(14)	7.8676(5)	14.60645(14)
<i>α</i> , °	90	90	100.2746(8)
<i>β</i> , °	104.6080(7)	95.986(6)	100.6552(8)
<i>γ</i> , °	90	90	105.2857(7)
<i>V</i> , Å ³	6995.75(9)	769.26(8)	2647.62(4)
<i>Z</i>	8	2	2
<i>Z'</i>	2	0.5	1
<i>λ</i> , Å	1.54184	1.54184	1.54184
Radiation type	CuK α	CuK α	CuK α
<i>θ</i> _{min} , °	3.845	5.012	3.171
<i>θ</i> _{max} , °	76.610	73.999	76.166
Measured Refl.	81444	5478	56071
Independent Refl.	14600	1527	10852
Refl. <i>I</i> ≥ 2σ(<i>I</i>)	14192	1032	10760
<i>R</i> _{int}	0.0383	0.0430	0.0184
Parameters	964	109	704
Restraints	0	0	43
Largest Peak, e Å ⁻³	1.564	0.469	0.439
Deepest Hole, e Å ⁻³	-1.299	-0.213	-0.664
GooF	1.082	1.049	1.067
<i>wR</i> ₂ (all data)	0.0761	0.2065	0.0402
<i>wR</i> ₂	0.0754	0.1775	0.0401
<i>R</i> ₁ (all data)	0.0299	0.0857	0.0163
<i>R</i> ₁	0.0290	0.0612	0.0161
CCDC number	2101920	2102440	2096259

Compound	<i>mer</i> -Ir(tppy) ₃	Δ - <i>mer</i> -Ir(ppy) ₃	<i>mer</i> -Ir(dfppy) ₂ (tpy)
Formula	C ₆₉ H ₄₈ IrN ₃	C ₃₃ H ₂₄ IrN ₃	C ₃₄ H ₂₂ F ₄ IrN ₃
Formula Weight	1111.30	654.75	1.852
<i>D</i> _{calc.} , g cm ⁻³	1.402	1.504	10.238
μ , mm ⁻¹	5.255	4.643	740.74
Colour	intense orange	intense orange	intense yellow
Shape	plate	plate	plate
Size, mm ³	0.18×0.06×0.01	0.15×0.12×0.03	0.16×0.15×0.01
<i>T</i> , K	139.99(10)	140.00(10)	140.00(10)
Crystal System	triclinic	tetragonal	monoclinic
Space Group	<i>P</i> $\bar{1}$	<i>P</i> 4 ₁ 2 ₁ 2	<i>C</i> 2/ <i>c</i>
<i>a</i> , Å	18.0800(5)	9.72023(11)	33.9701(5)
<i>b</i> , Å	18.3585(7)	9.72023(11)	8.77822(19)
<i>c</i> , Å	19.0127(7)	30.5949(5)	18.0310(3)
α , °	68.335(3)	90	90
β , °	85.431(3)	90	98.8980(14)
γ , °	64.368(3)	90	90
<i>V</i> , Å ³	5263.6(3)	2890.70(8)	5312.07(16)
<i>Z</i>	4	4	8
<i>Z'</i>	2	0.5	1
λ , Å	1.54184	0.71073	1.54184
Radiation type	CuK α	MoK α	CuK α
θ_{min} , °	2.512	2.198	2.633
θ_{max} , °	75.272	41.261	75.533
Measured Refl.	26115	99418	45625
Independent Refl.	26115	8678	5386
Refl. $I \geq 2\sigma(I)$	15824	6667	4613
<i>R</i> _{int}	<i>n/a</i>	0.0786	0.0556
Parameters	1028	169	381
Restraints	2270	1	0
Largest Peak, e Å ⁻³	5.309	1.810	2.376
Deepest Hole, e Å ⁻³	-2.857	-2.757	-2.012
GooF	1.402	1.043	1.057
<i>wR</i> ₂ (all data)	0.3936	0.0720	0.1133
<i>wR</i> ₂	0.3576	0.0687	0.1092
<i>R</i> ₁ (all data)	0.1771	0.0594	0.0503
<i>R</i> ₁	0.1321	0.0357	0.0424
CCDC number	2102439	2118152	2122690
Flack parameter	–	0.070(11)	–

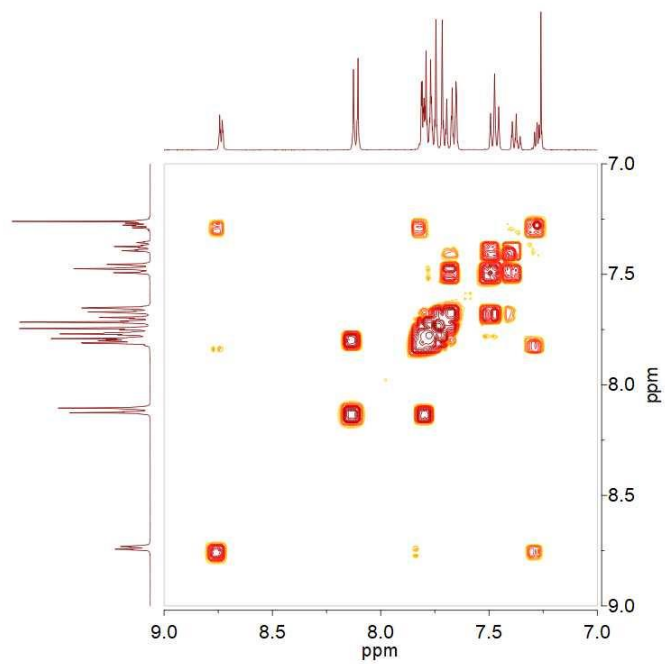
6.3.13 NMR Spectra



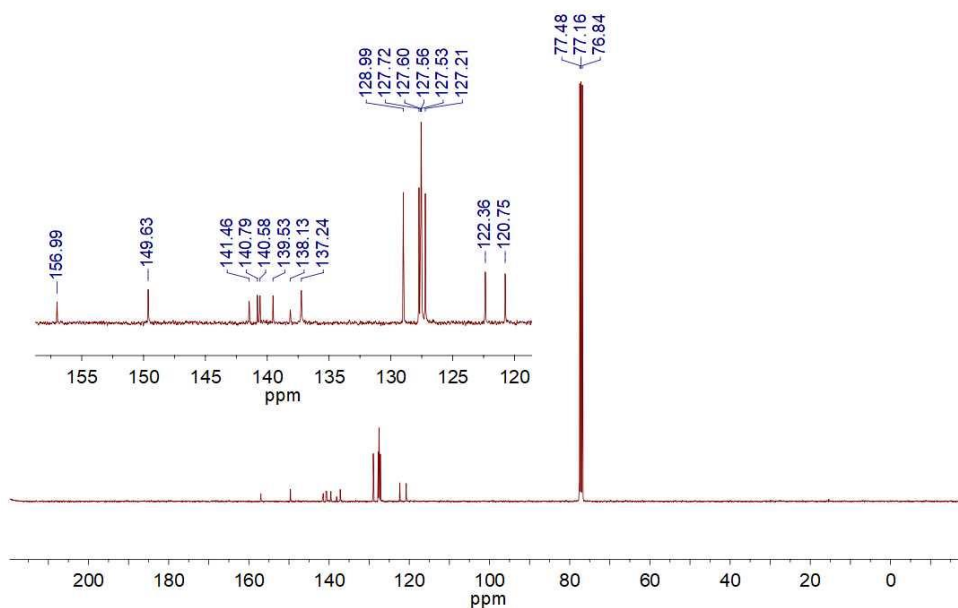
^1H NMR (400 MHz, CD_2Cl_2 , 298 K) spectrum of Hppy



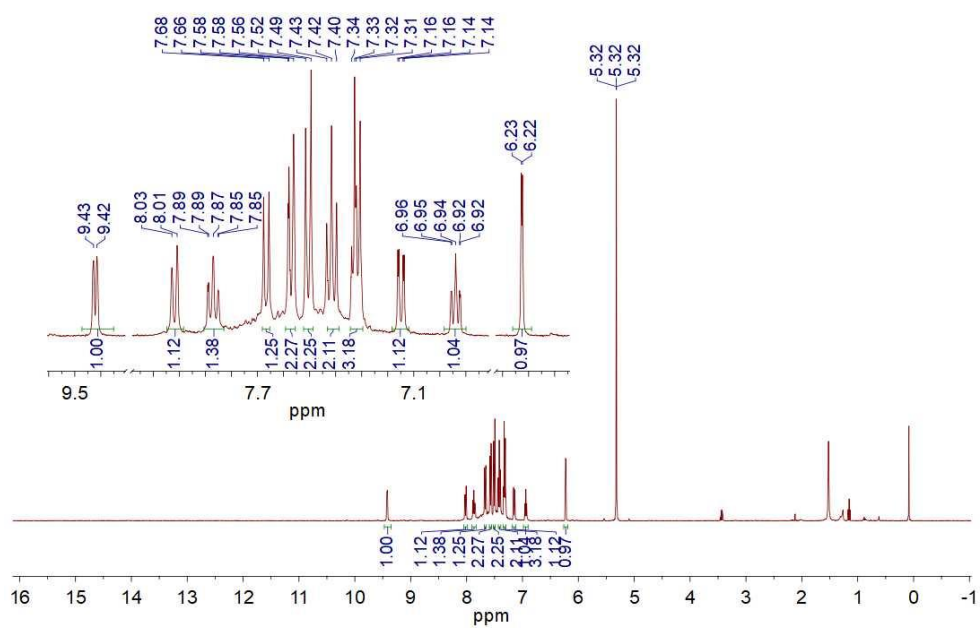
^1H NMR (400 MHz, CDCl_3 , 298 K) spectrum of Hppy



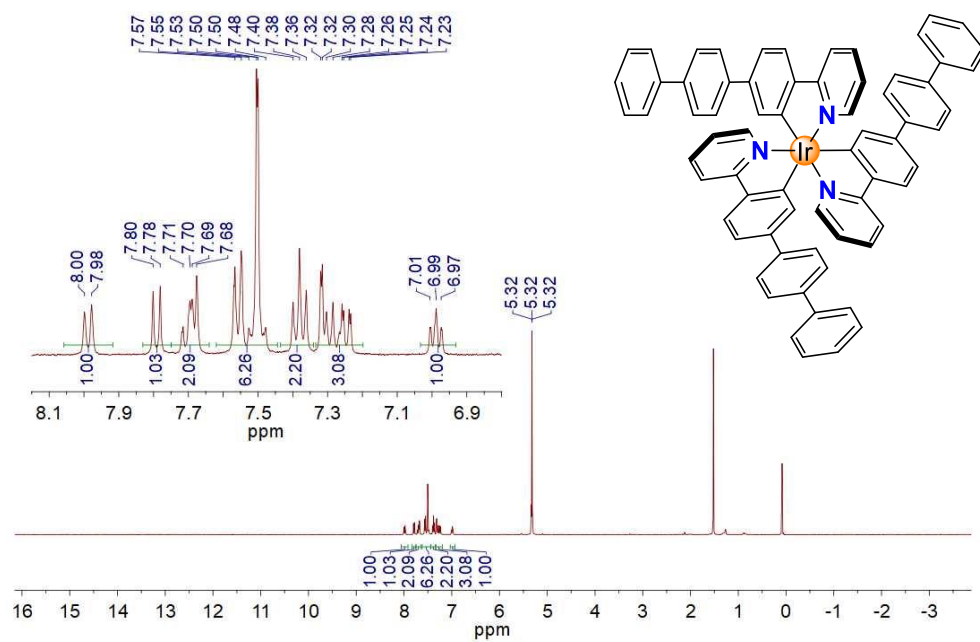
^1H - ^1H COSY NMR (400 MHz, CDCl_3 , 298 K) spectrum of Htpy



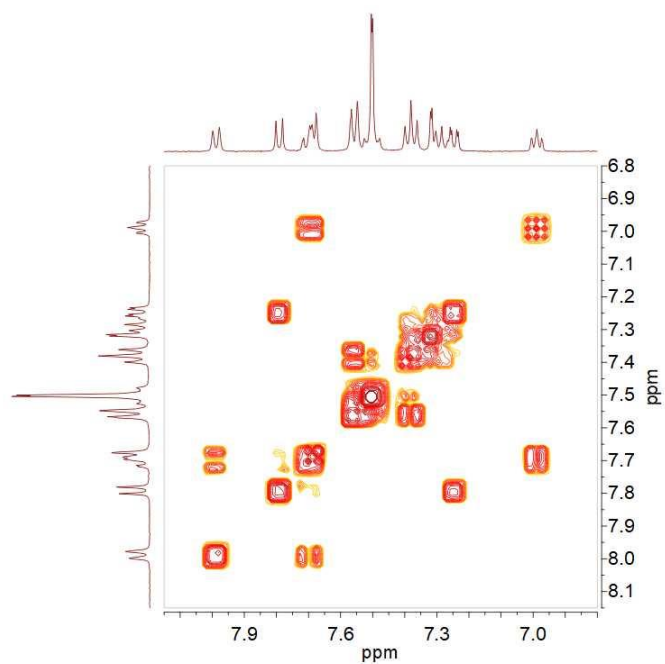
^{13}C NMR (101 MHz, CDCl_3 , 298 K) spectrum of Htpy



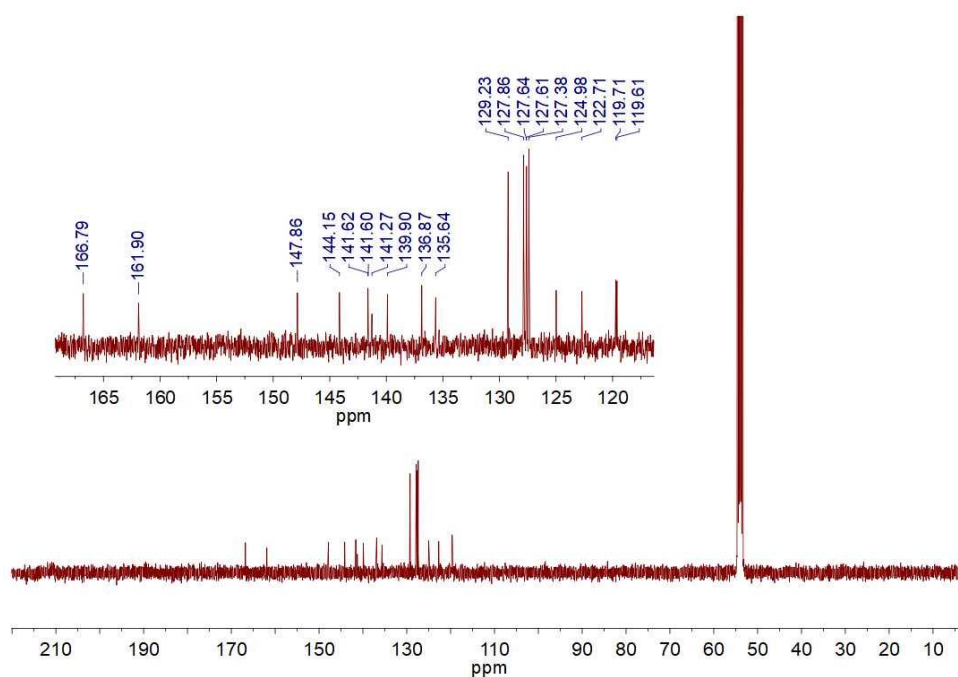
^1H NMR (400 MHz, CD_2Cl_2 , 298 K) spectrum of $[\text{Ir}(\text{tppy})_2(\mu\text{-Cl})]_2$



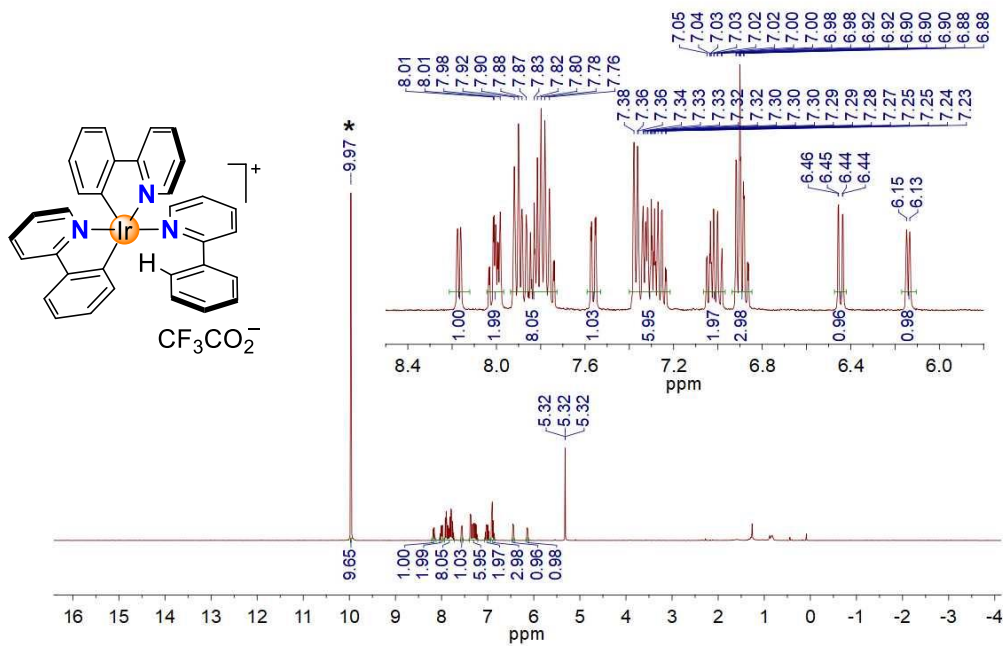
^1H NMR (400 MHz, CD_2Cl_2 , 298 K) spectrum of *fac*- $\text{Ir}(\text{tppy})_3$



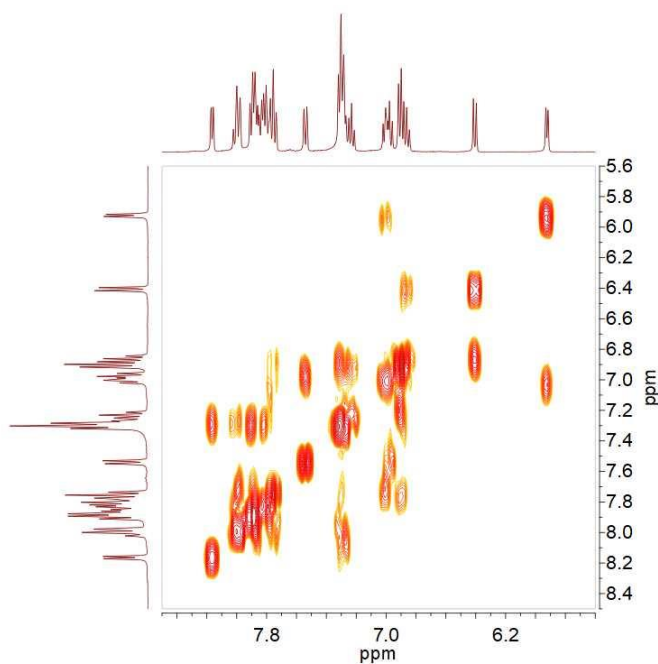
^1H - ^1H COSY NMR (400 MHz, CD_2Cl_2 , 298 K) spectrum of *fac*-Ir(tppy) $_3$



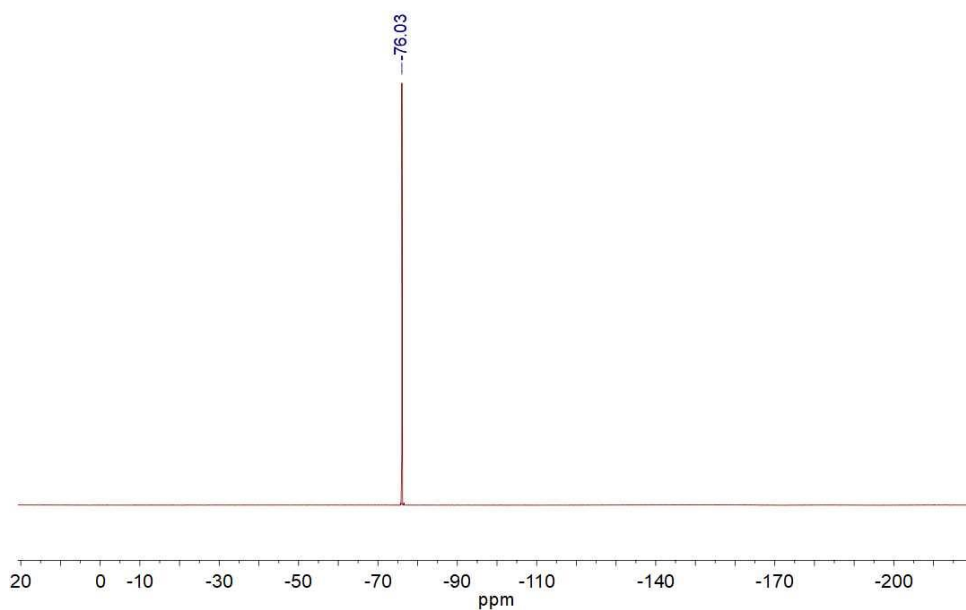
^{13}C NMR (101 MHz, CD_2Cl_2 , 298 K) spectrum of *fac*-Ir(tppy) $_3$



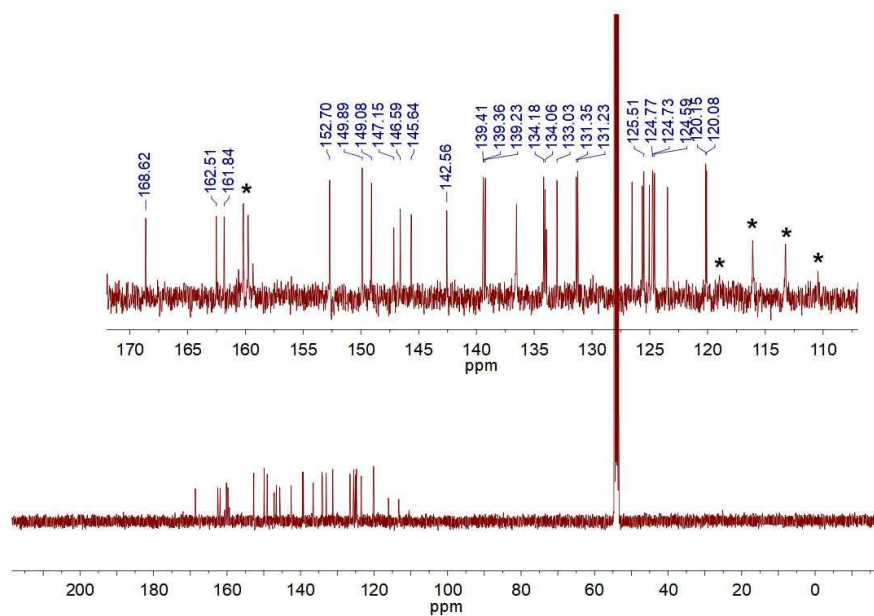
^1H NMR (400 MHz, CD_2Cl_2 , 298 K) spectrum of $[\text{Ir}(\text{ppy})_2(\text{Hppy})](\text{O}_2\text{CCF}_3)$. The TFA signal is marked by an asterisk.



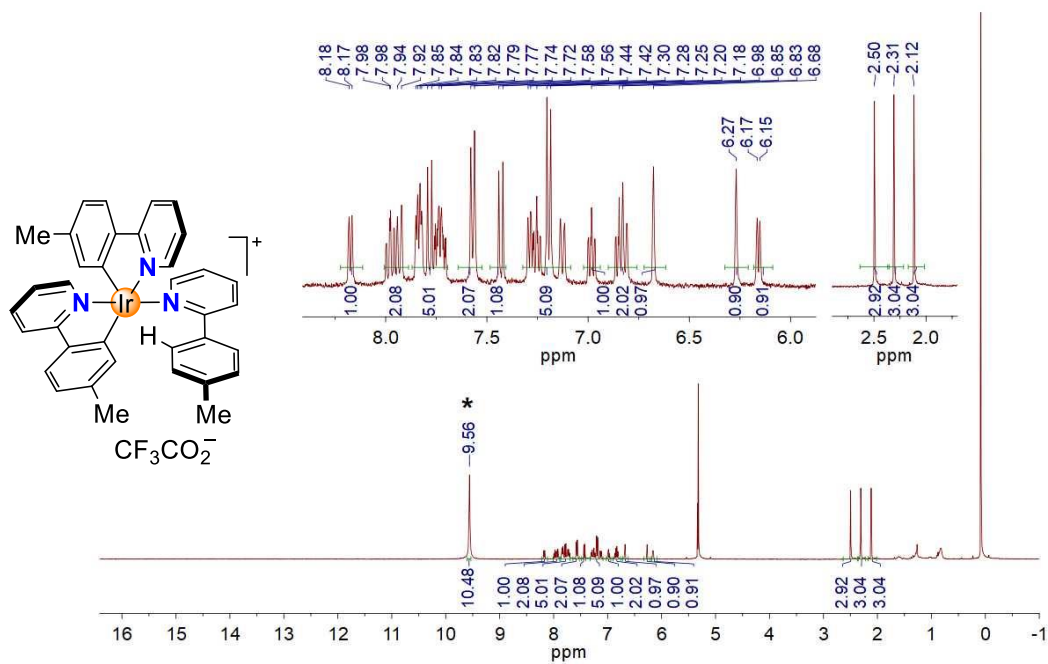
^1H - ^1H COSY NMR (400 MHz, CD_2Cl_2 , 253 K) spectrum of $[\text{Ir}(\text{ppy})_2(\text{Hppy})](\text{O}_2\text{CCF}_3)$



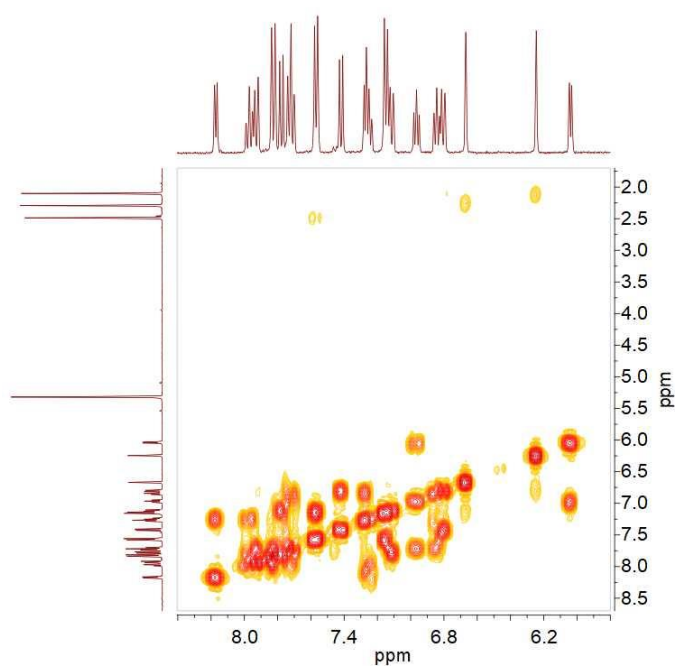
^{19}F NMR (376 MHz, CD_2Cl_2 , 253 K) spectrum of $[\text{Ir}(\text{ppy})_2(\text{Hppy})](\text{O}_2\text{CCF}_3)$



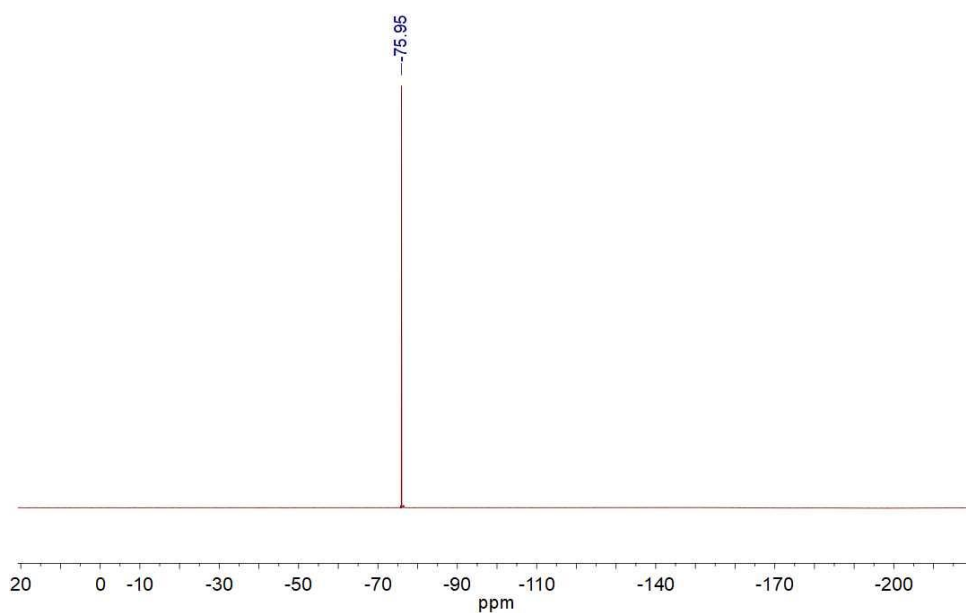
^{13}C NMR (101 MHz, CD_2Cl_2 , 253 K) spectrum of $[\text{Ir}(\text{ppy})_2(\text{Hppy})](\text{O}_2\text{CCF}_3)$. The TFA signals are marked by asterisks.



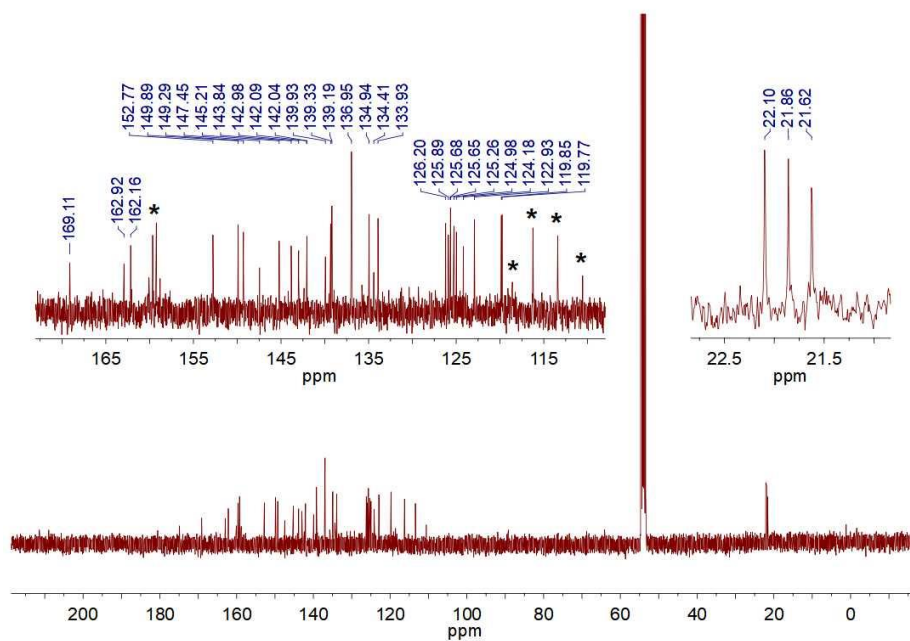
^1H NMR (400 MHz, CD_2Cl_2 , 298 K) spectrum of $[\text{Ir}(\text{tpy})_2(\text{Htpy})](\text{O}_2\text{CCF}_3)$. The TFA signal is marked by an asterisk.



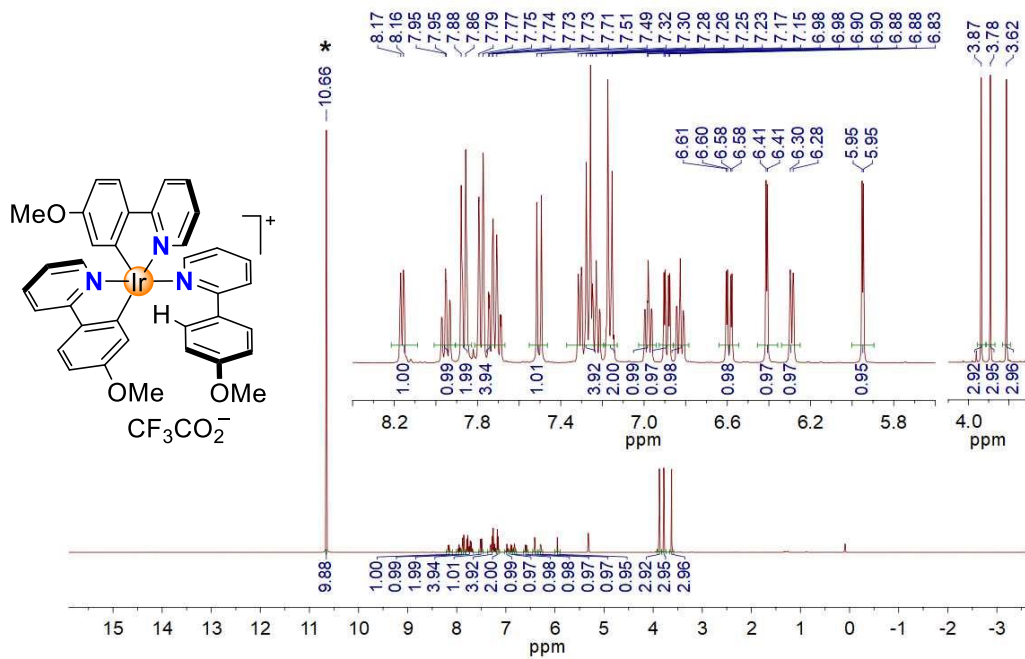
^1H - ^1H COSY NMR (400 MHz, CD_2Cl_2 , 273 K) spectrum of $[\text{Ir}(\text{tpy})_2(\text{Htpy})](\text{O}_2\text{CCF}_3)$



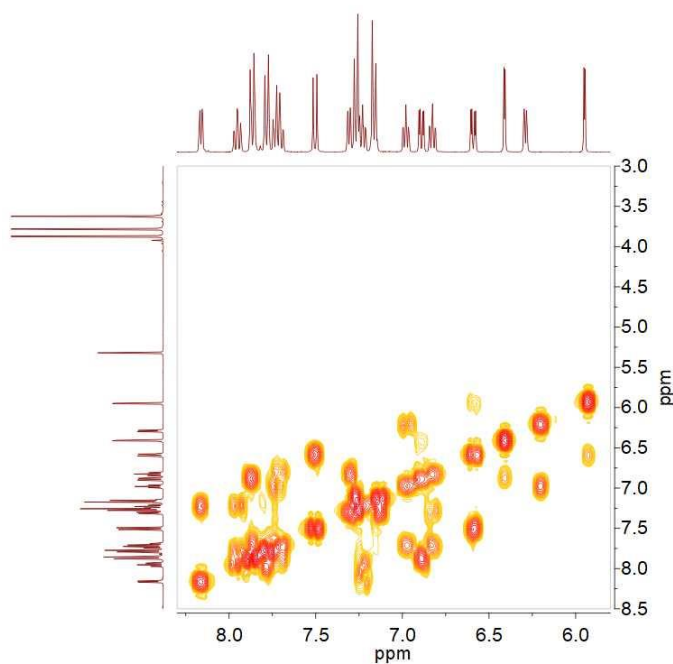
^{19}F NMR (376 MHz, CD_2Cl_2 , 273 K) spectrum of $[\text{Ir}(\text{tpy})_2(\text{Htpy})](\text{O}_2\text{CCF}_3)$



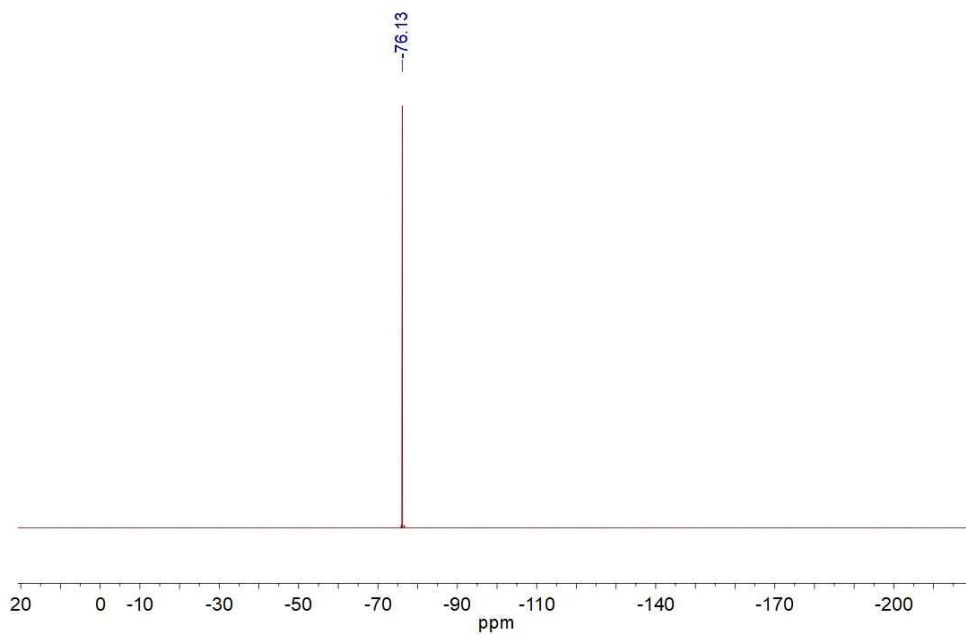
^{13}C NMR (101 MHz, CD_2Cl_2 , 273 K) spectrum of $[\text{Ir}(\text{tpy})_2(\text{Htpy})](\text{O}_2\text{CCF}_3)$. TFA signals are marked by asterisks.



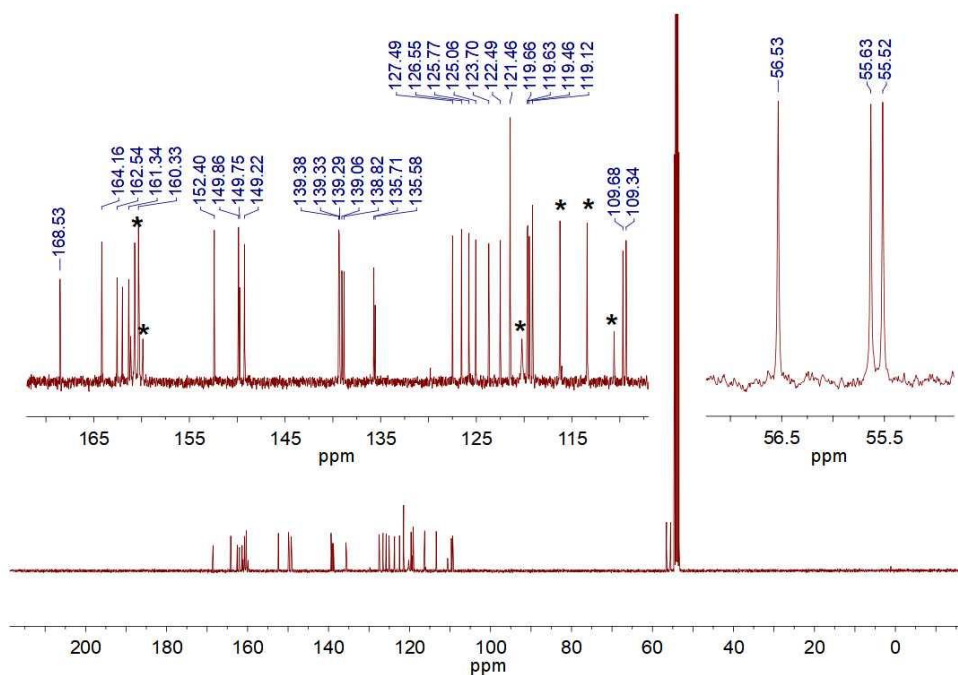
^1H NMR (400 MHz, CD_2Cl_2 , 298 K) spectrum of $[\text{Ir}(\text{meppy})_2(\text{Hmeppy})](\text{O}_2\text{CCF}_3)$. The TFA signal is marked by an asterisk.



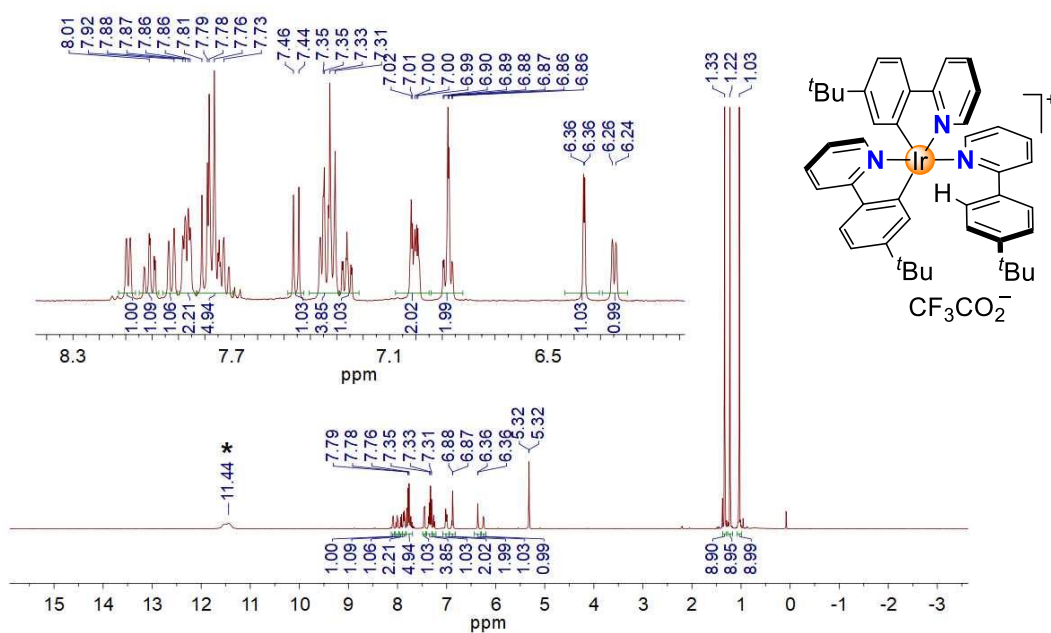
^1H - ^1H COSY NMR (400 MHz, CD_2Cl_2 , 273 K) spectrum of $[\text{Ir}(\text{meppy})_2(\text{Hmeppy})](\text{O}_2\text{CCF}_3)$



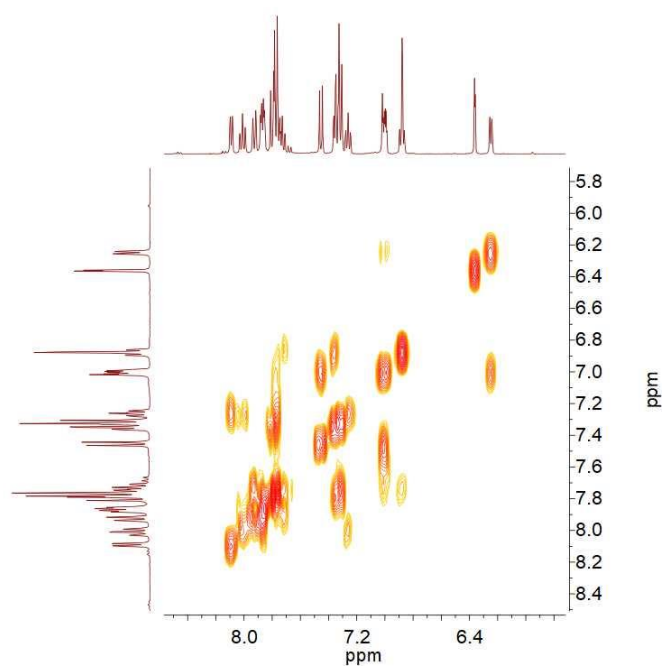
¹⁹F NMR (376 MHz, CD₂Cl₂, 273 K) spectrum of [Ir(meppy)₂(Hmeppy)](O₂CCF₃)



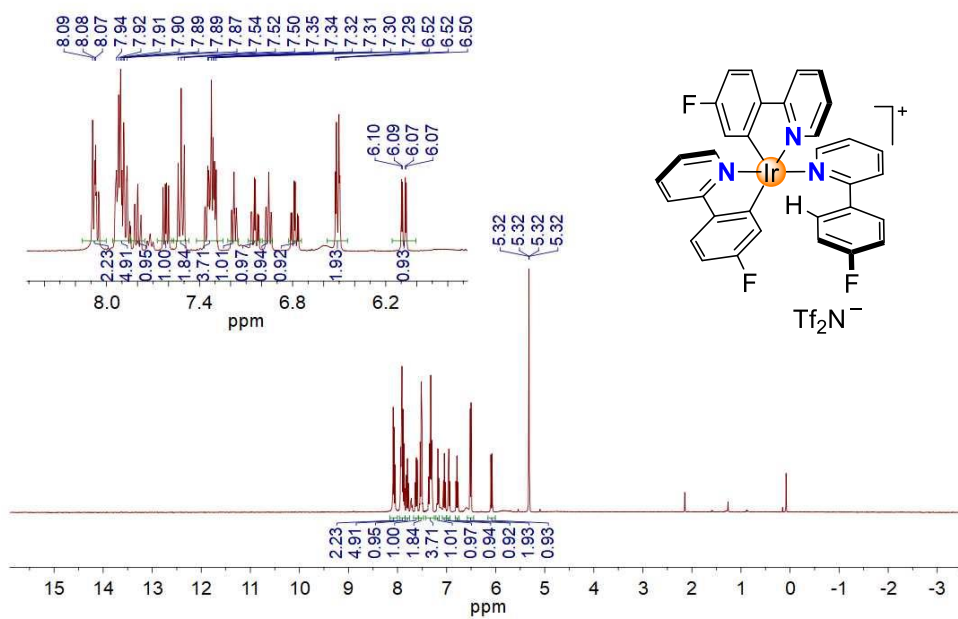
¹³C NMR (101 MHz, CD₂Cl₂, 273 K) spectrum of [Ir(meppy)₂(Hmeppy)](O₂CCF₃). TFA signals are marked by asterisks.



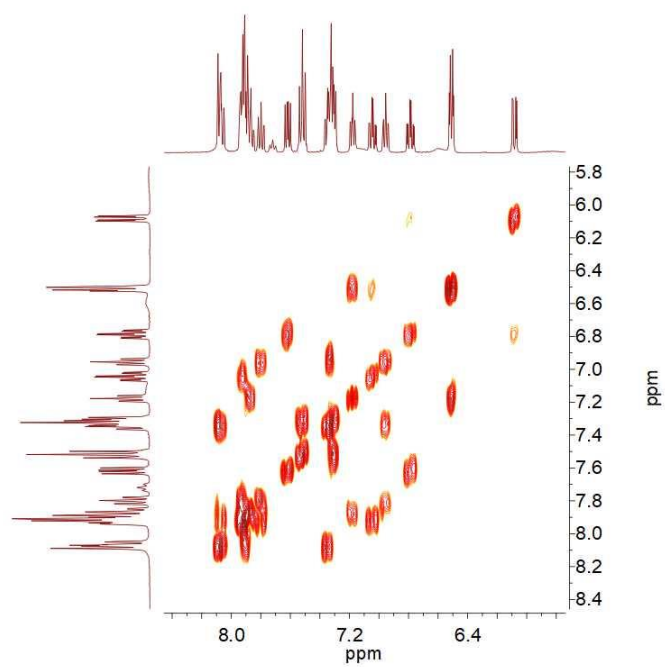
^1H NMR (400 MHz, CD_2Cl_2 , 298 K) spectrum of $[\text{Ir}(\text{buppy})_2(\text{Hbuppy})](\text{O}_2\text{CCF}_3)$. The TFA signal is marked by an asterisk.



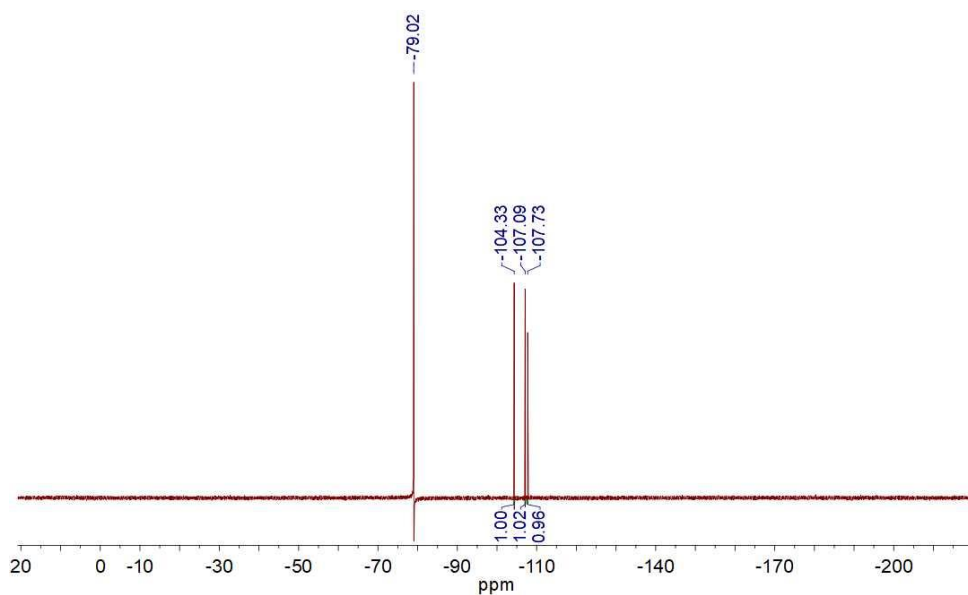
^1H - ^1H COSY NMR (400 MHz, CD_2Cl_2 , 273 K) spectrum of $[\text{Ir}(\text{buppy})_2(\text{Hbuppy})](\text{O}_2\text{CCF}_3)$



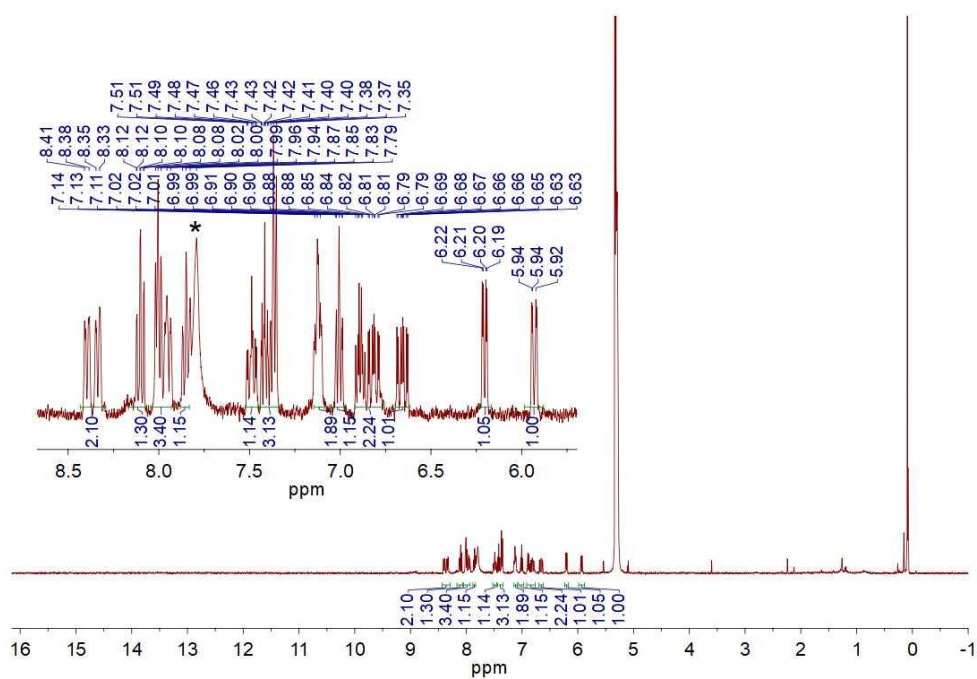
^1H NMR (400 MHz, CD_2Cl_2 , 298 K) spectrum of $[\text{Ir}(\text{fppy})_2(\text{Hfppy})](\text{NTf}_2)$



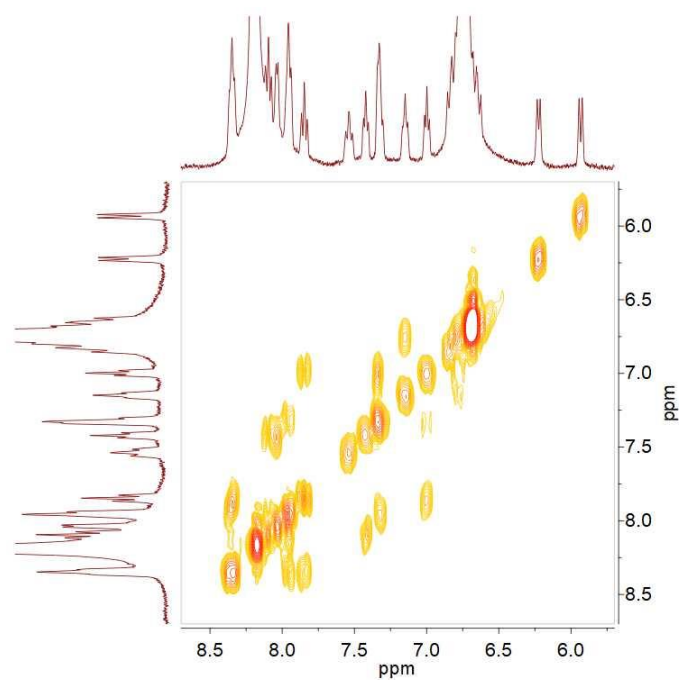
^1H - ^1H COSY NMR (400 MHz, CD_2Cl_2 , 273 K) spectrum of $[\text{Ir}(\text{fppy})_2(\text{Hfppy})](\text{NTf}_2)$



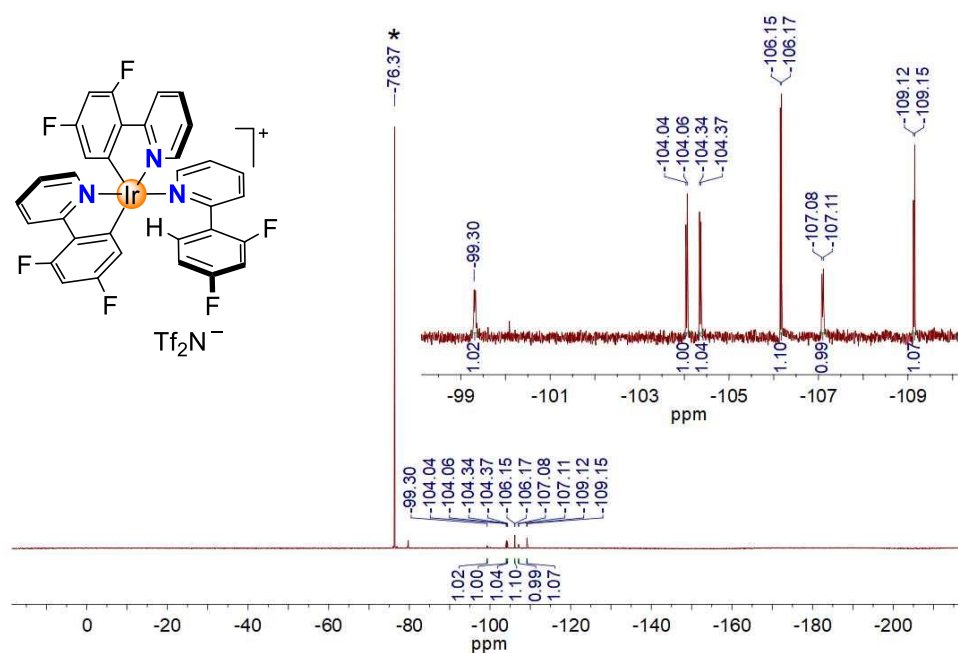
^{19}F NMR (376 MHz, CD_2Cl_2 , 298 K) spectrum of $[\text{Ir}(\text{fppy})_2(\text{Hfppy})](\text{NTf}_2)$



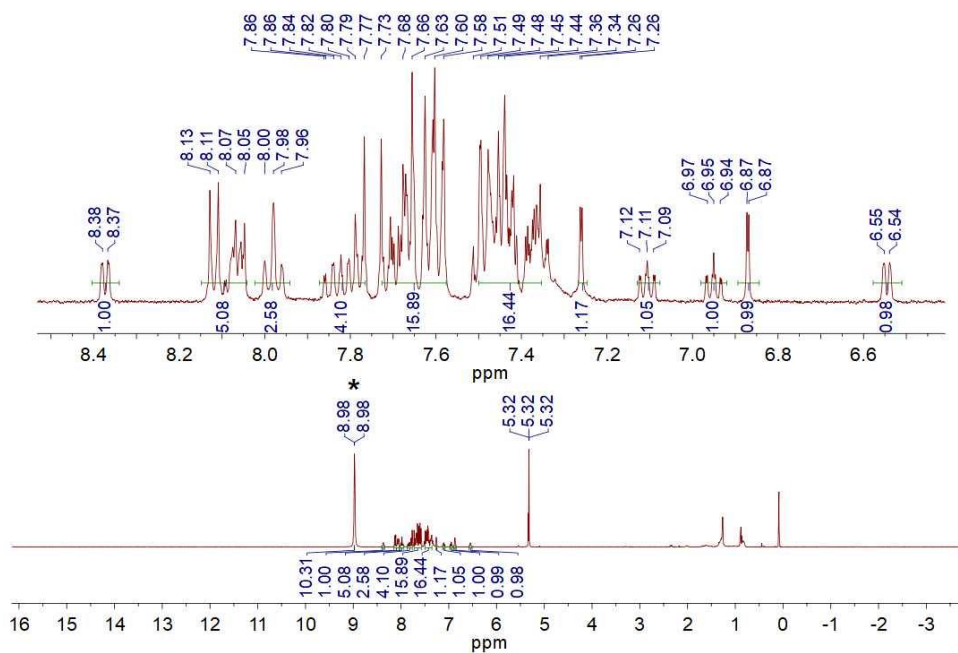
^1H NMR (400 MHz, CD_2Cl_2 , 298 K) spectrum of $[\text{Ir}(\text{dfppy})_2(\text{Hdfppy})](\text{NTf}_2)$. The Tf_2NH signal is marked by an asterisk.



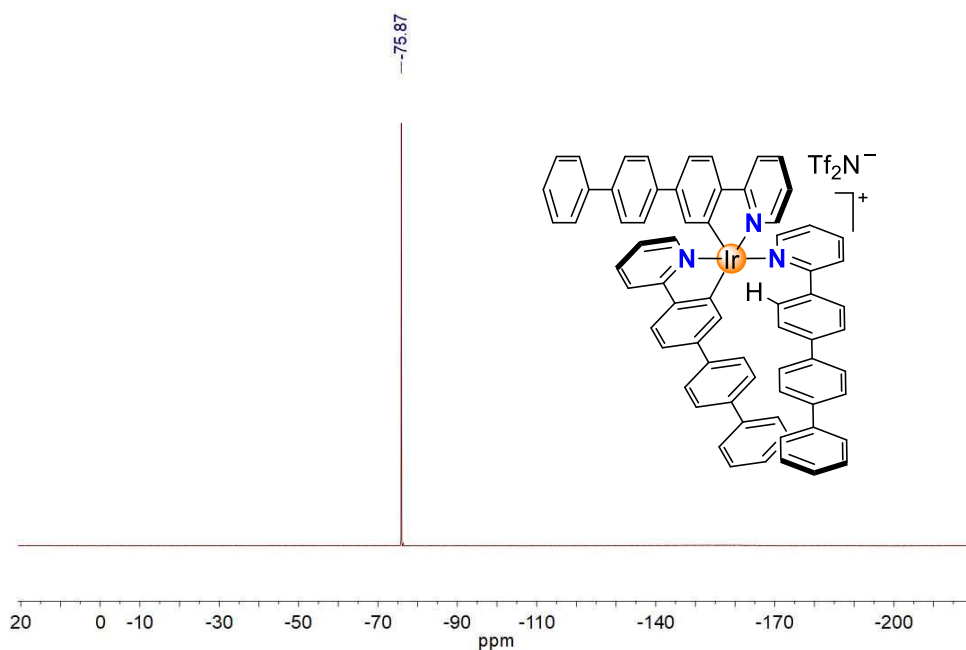
^1H - ^1H COSY NMR (400 MHz, CD_2Cl_2 , 273 K) spectrum of $[\text{Ir}(\text{dfppy})_2(\text{Hdfppy})](\text{NTf}_2)$



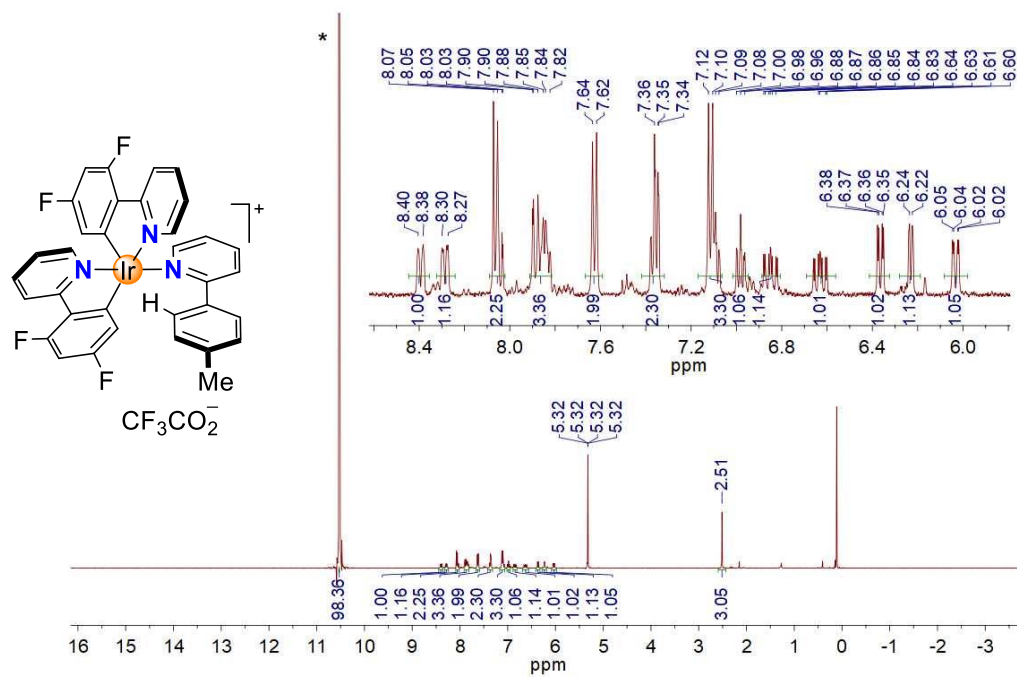
^{19}F NMR (376 MHz, CD_2Cl_2 , 298 K) spectrum of $[\text{Ir}(\text{dfppy})_2(\text{Hdfppy})](\text{NTf}_2)$. The Tf_2NH signal is marked by an asterisk.



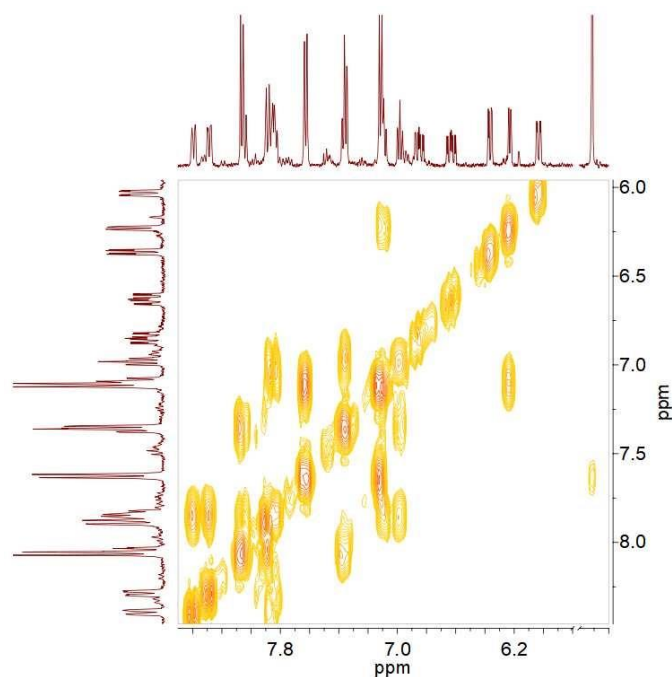
^1H NMR (400 MHz, CD_2Cl_2 , 298 K) spectrum of $[\text{Ir}(\text{tppy})_2(\text{Htppy})](\text{O}_2\text{CCF}_3)$. The TFA signal is marked by an asterisk.



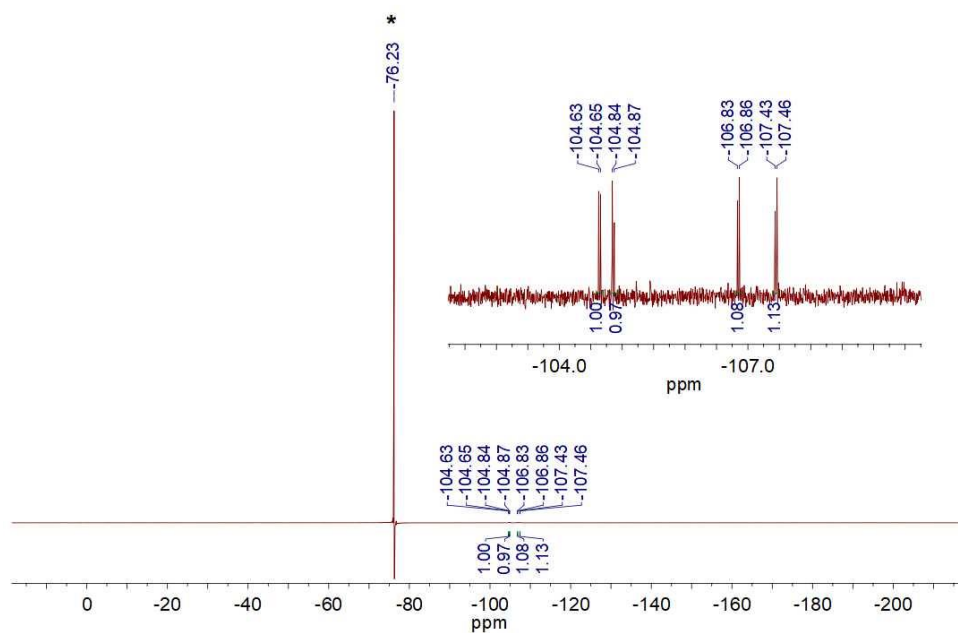
^{19}F NMR (376 MHz, CD_2Cl_2 , 298 K) spectrum of $[\text{Ir}(\text{tppy})_2(\text{Htppy})](\text{O}_2\text{CCF}_3)$



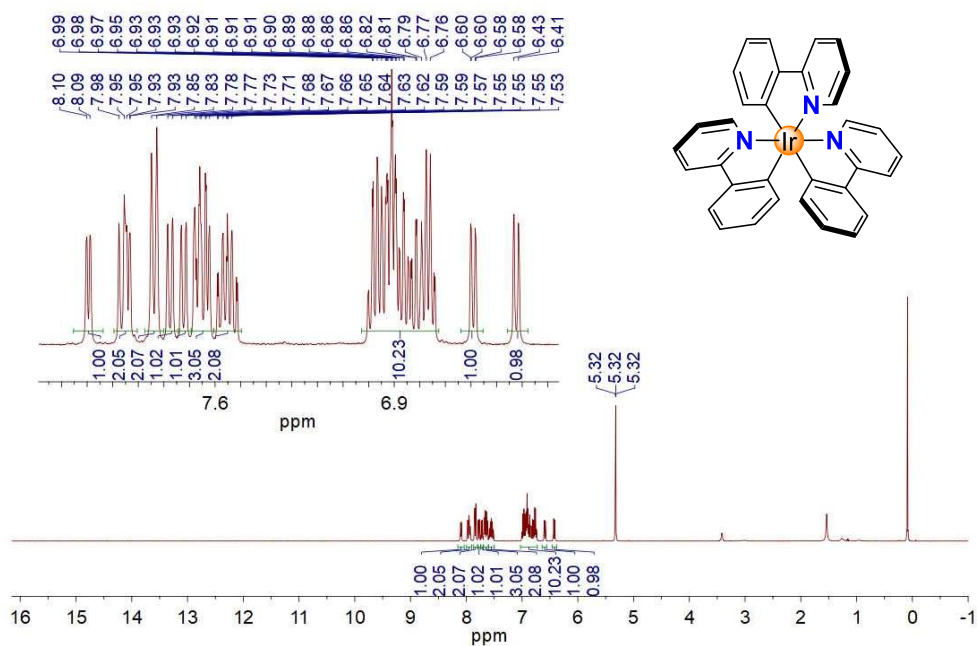
^1H NMR (400 MHz, CD_2Cl_2 , 298 K) spectrum of $[\text{Ir}(\text{dfppy})_2(\text{Htpy})](\text{O}_2\text{CCF}_3)$. The TFA signal is marked by an asterisk.



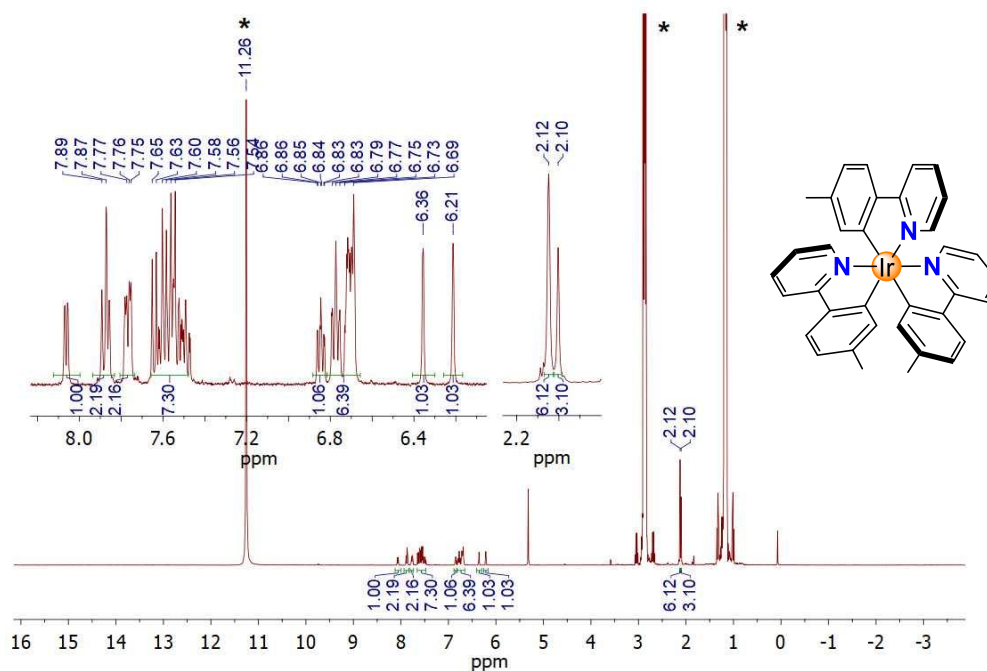
^1H - ^1H COSY NMR (400 MHz, CD_2Cl_2 , 273 K) spectrum of $[\text{Ir}(\text{dfppy})_2(\text{Htpy})](\text{O}_2\text{CCF}_3)$

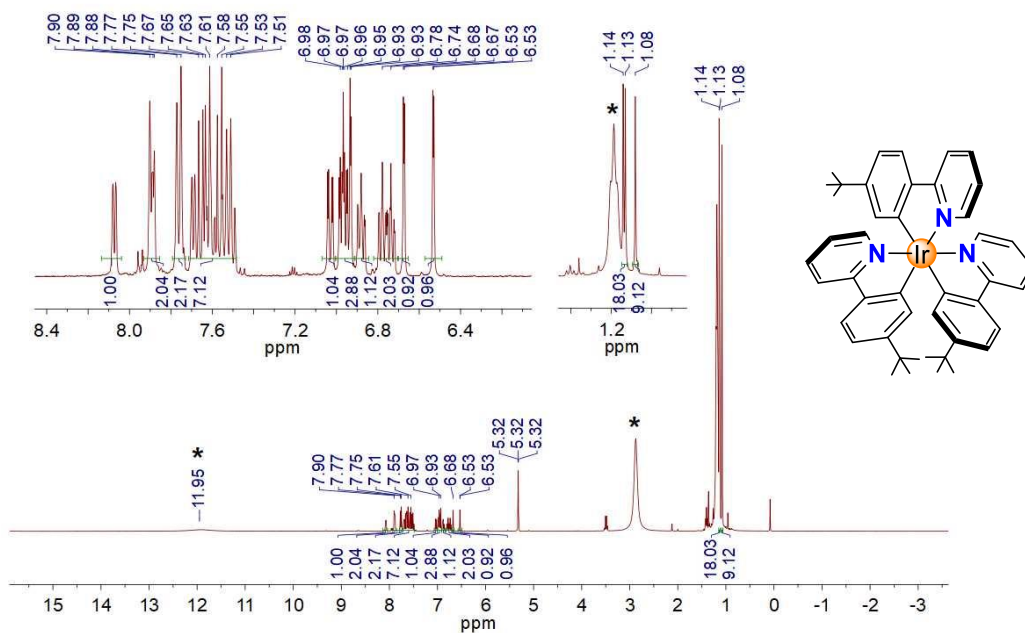


^{19}F NMR (376 MHz, CD_2Cl_2 , 298 K) spectrum of $[\text{Ir}(\text{dfppy})_2(\text{Htpy})](\text{O}_2\text{CCF}_3)$. The TFA signal is marked by an asterisk.

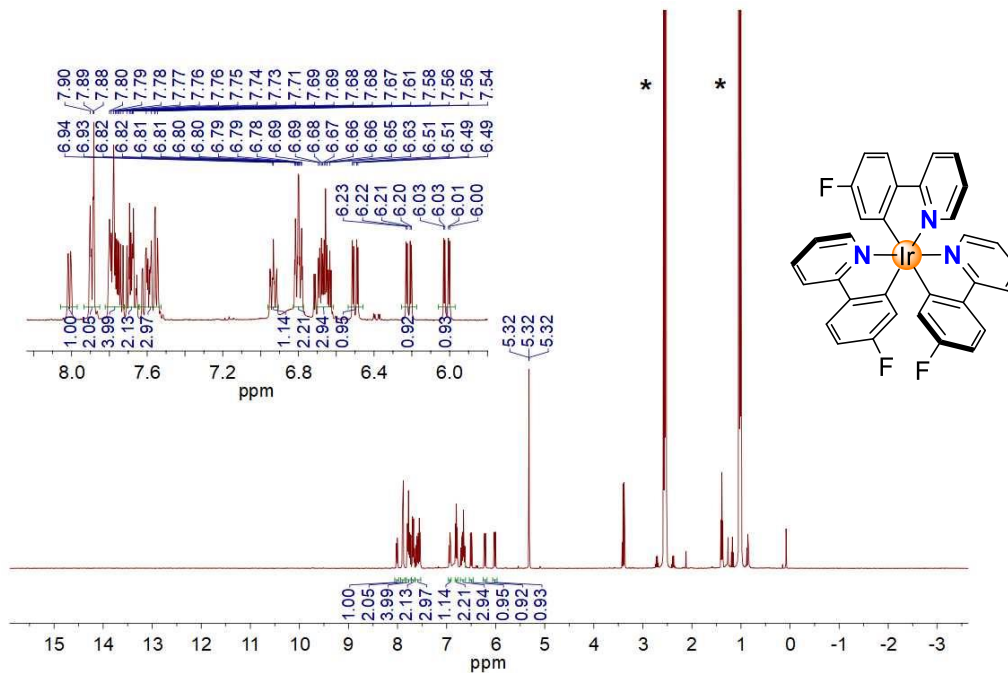


^1H NMR (400 MHz, CD_2Cl_2 , 298 K) spectrum of *mer*- $\text{Ir}(\text{ppy})_3$ obtained in large-scale synthesis from *fac*- $\text{Ir}(\text{ppy})_3$

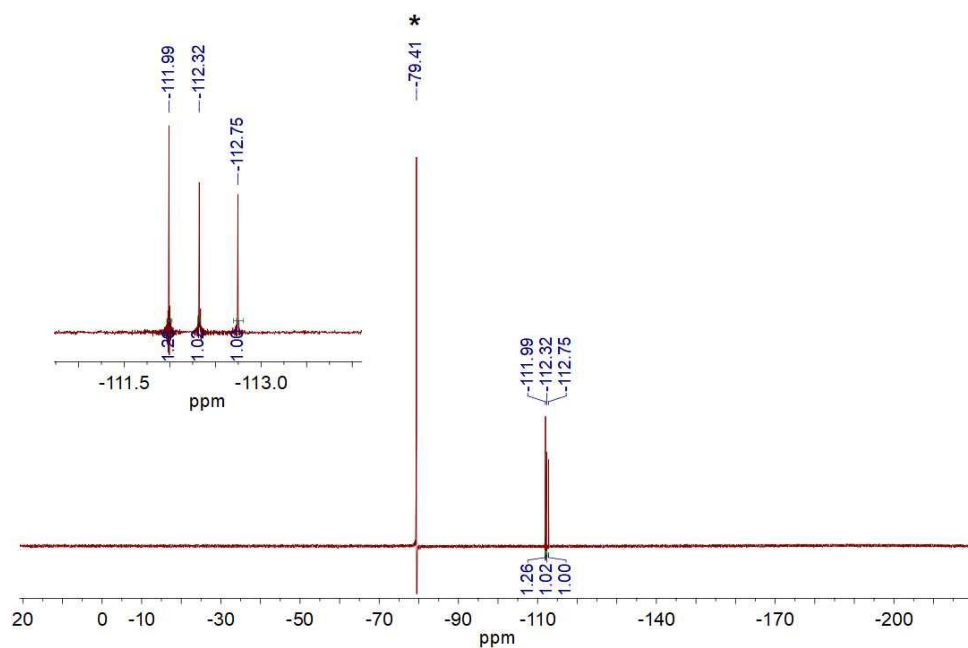




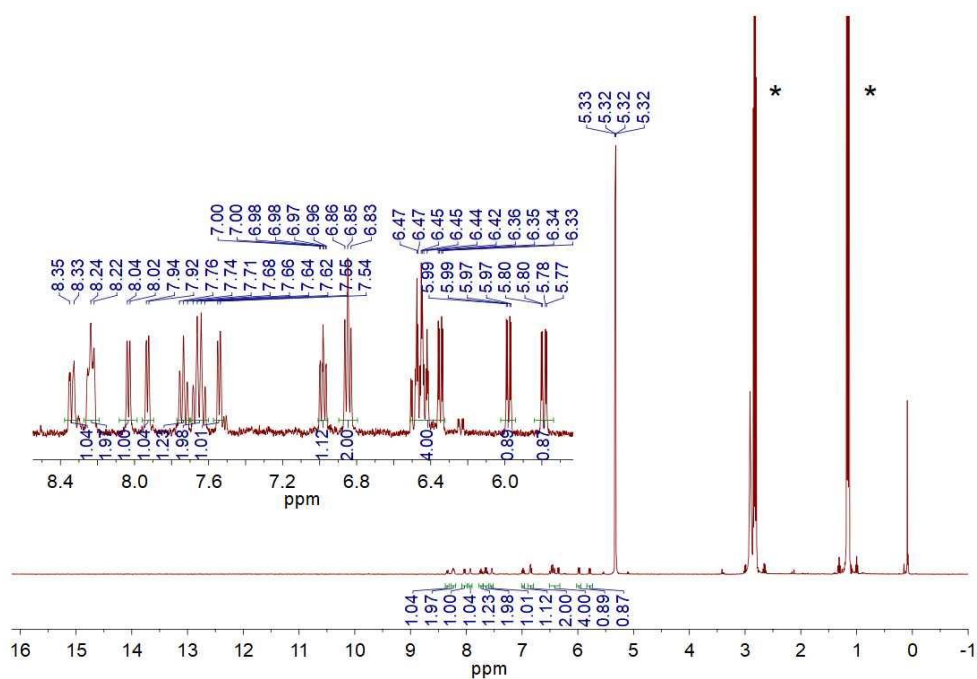
¹H NMR (400 MHz, CD₂Cl₂, 298 K) spectrum of *mer*-Ir(buppy)₃ obtained from *fac*-Ir(buppy)₃ using the General Procedure. The peaks of HNEt₃(O₂CCF₃) are marked by asterisks.



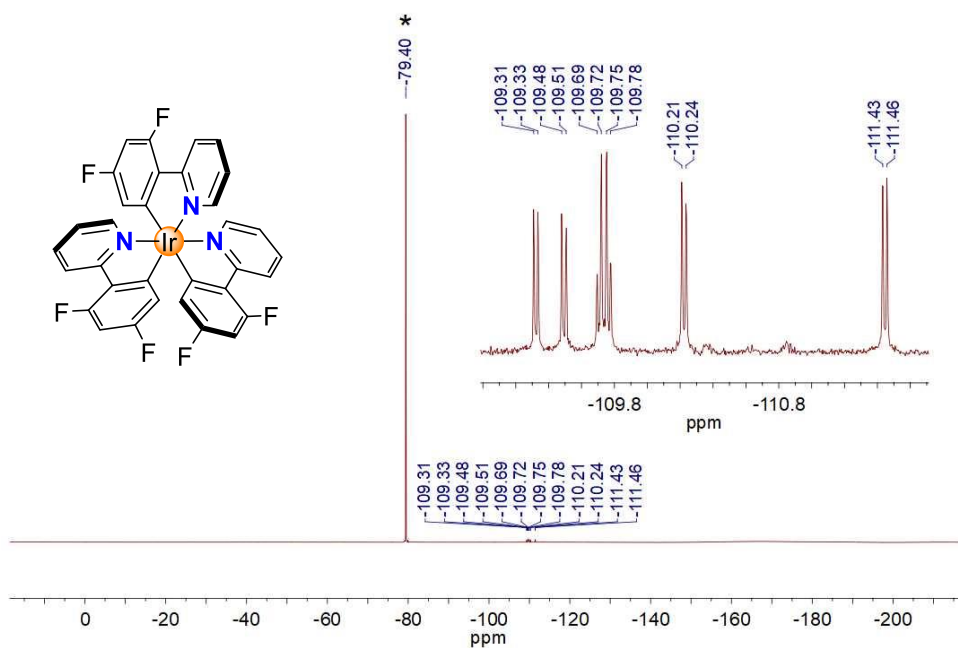
¹H NMR (400 MHz, CD₂Cl₂, 298 K) spectrum of *mer*-Ir(fppy)₃ obtained from *fac*-Ir(fppy)₃ using the General Procedure. The signals of NEt₃ excess are marked by asterisks.



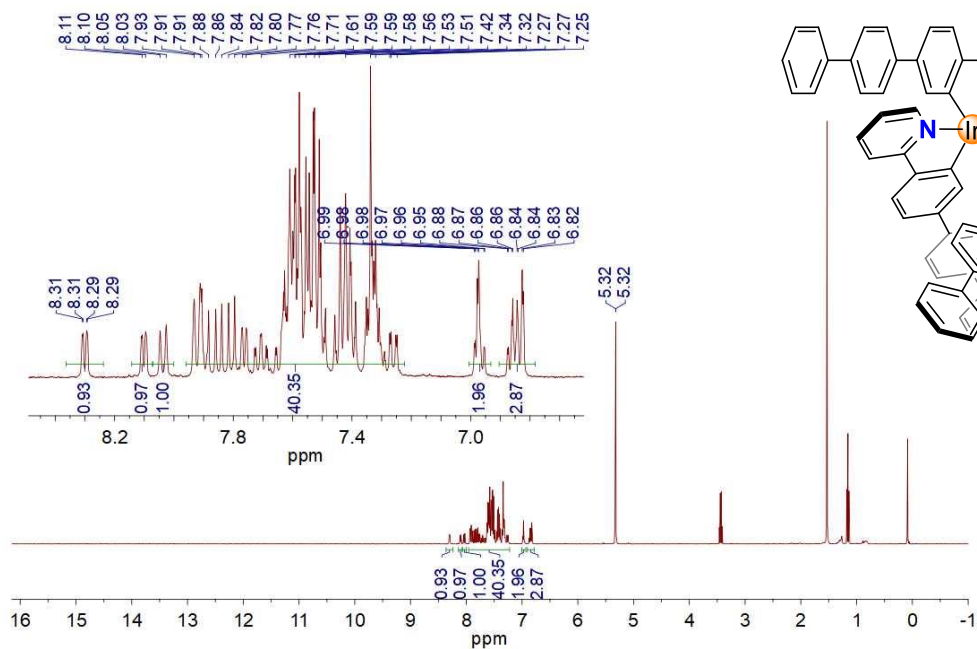
^{19}F NMR (376 MHz, CD_2Cl_2 , 298 K) spectrum of *mer*-Ir(fppy) $_3$ obtained from *fac*-Ir(fppy) $_3$ using the General Procedure. The signal of $\text{HNEt}_3(\text{NTf}_2)$ is marked by an asterisk.



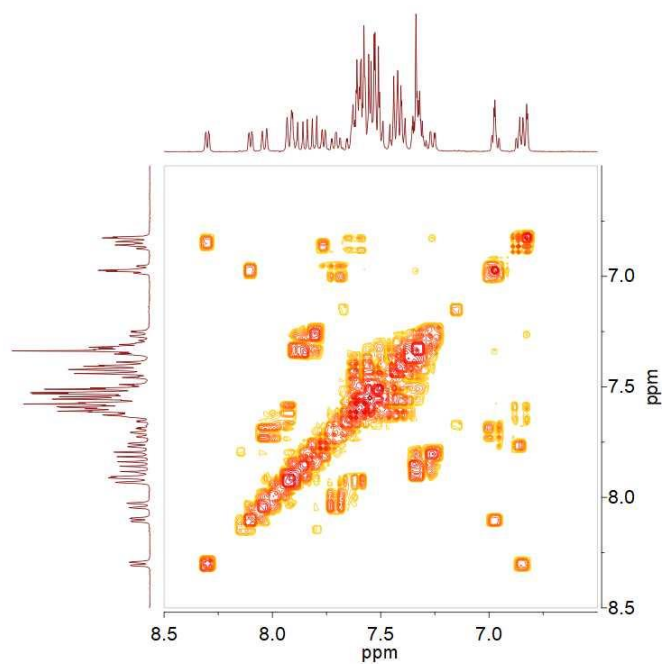
^1H NMR (400 MHz, CD_2Cl_2 , 298 K) spectrum of *mer*-Ir(dfppy) $_3$ obtained from *fac*-Ir(dfppy) $_3$ using the General Procedure. The signals of $\text{HNEt}_3(\text{NTf}_2)$ are marked by asterisks.



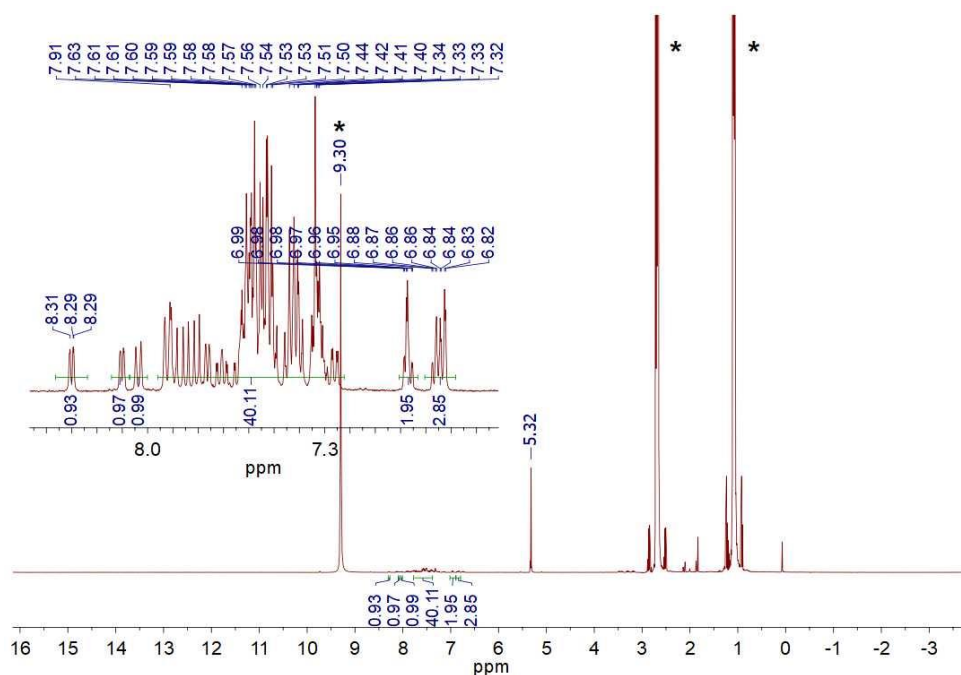
^{19}F NMR (376 MHz, CD_2Cl_2 , 298 K) spectrum of $mer\text{-Ir}(\text{dfppy})_3$ obtained from $fac\text{-Ir}(\text{dfppy})_3$ using the General Procedure. The signal of $\text{HNEt}_3(\text{NTf}_2)$ is marked by an asterisk.



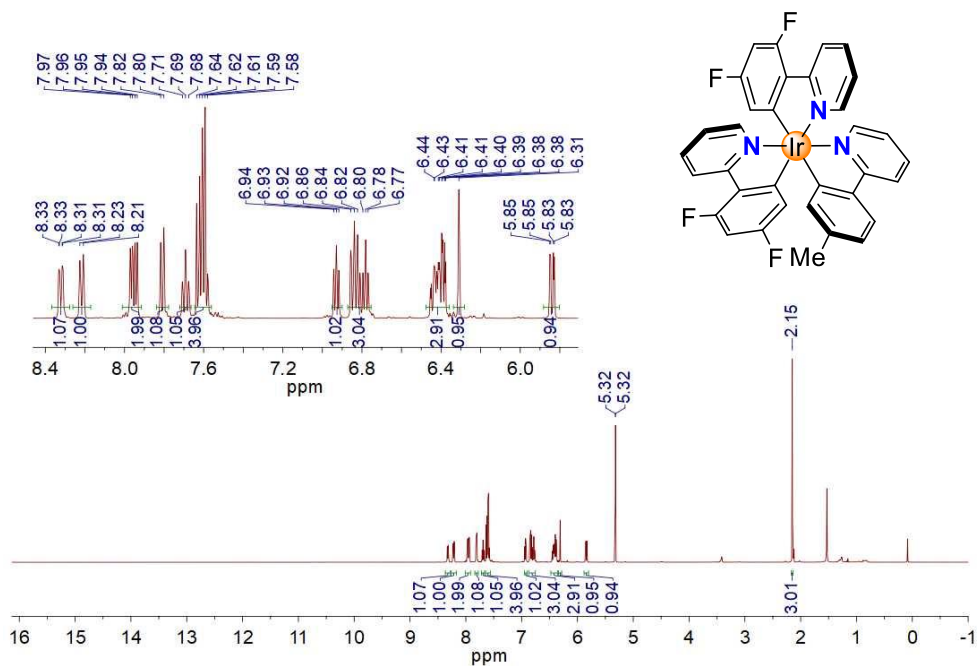
^1H NMR (400 MHz, CD_2Cl_2 , 298 K) spectrum of $mer\text{-Ir}(\text{tppy})_3$ synthesized from $[\text{Ir}(\text{tppy})_2(\mu\text{-Cl})]_2$ and Htppy



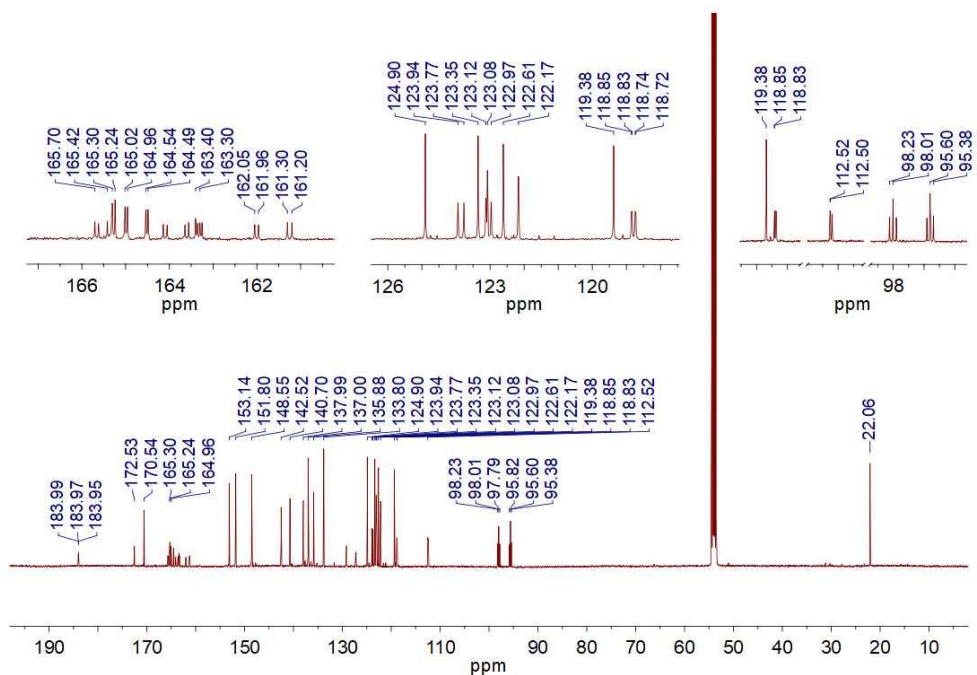
^1H - ^1H COSY NMR (400 MHz, CD_2Cl_2 , 273 K) spectrum of *mer*- $\text{Ir}(\text{tppy})_3$ synthesized from $[\text{Ir}(\text{tppy})_2(\mu\text{-Cl})]_2$ and Htppy



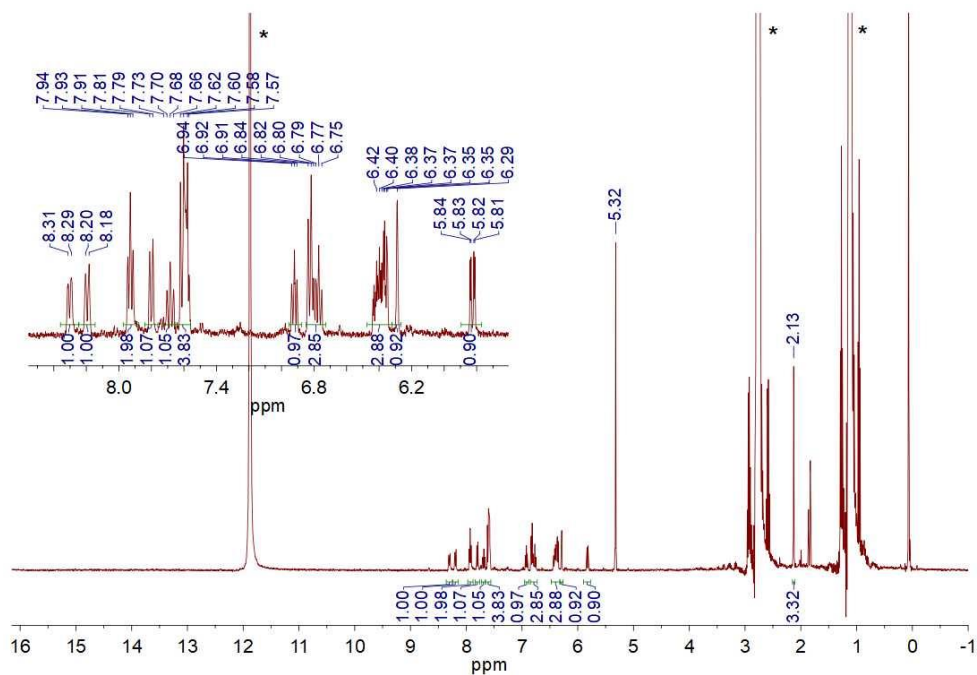
^1H NMR (400 MHz, CD_2Cl_2 , 298 K) spectrum of *mer*- $\text{Ir}(\text{tppy})_3$ obtained from *fac*- $\text{Ir}(\text{tppy})_3$ using the General Procedure. The signals of $\text{HNEt}_3(\text{O}_2\text{CCF}_3)$ are marked by asterisks.



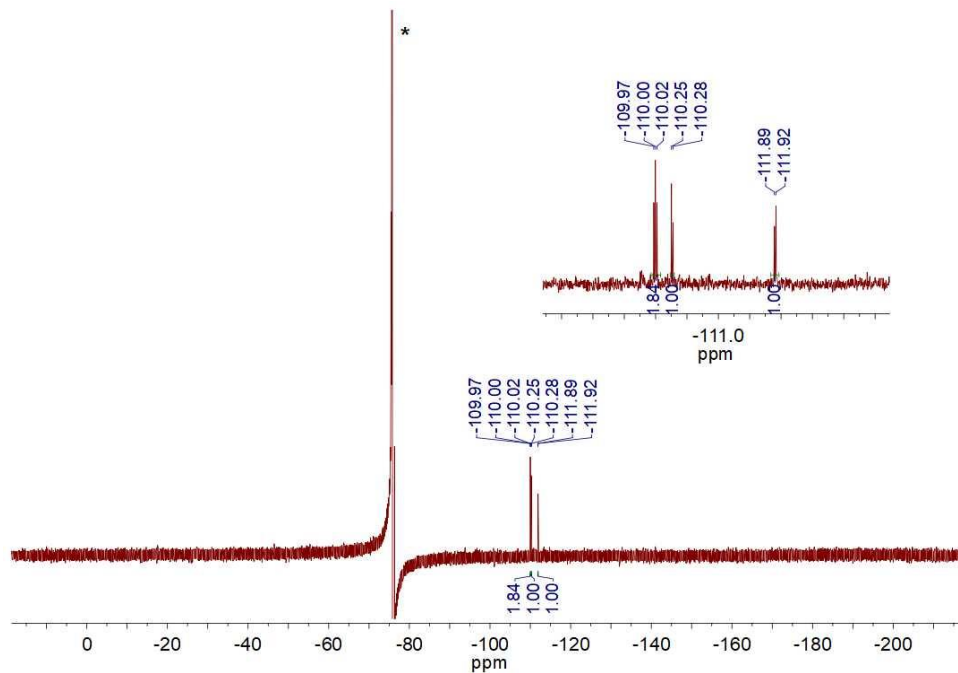
¹H NMR (500 MHz, CD₂Cl₂, 298 K) spectrum of *mer*-Ir(dfppy)₂(tpy) obtained in large-scale synthesis from *fac*-Ir(dfppy)₂(tpy)



¹³C NMR (126 MHz, CD₂Cl₂, 298 K) spectrum of *mer*-Ir(dfppy)₂(tpy) obtained in large-scale synthesis from *fac*-Ir(dfppy)₂(tpy)

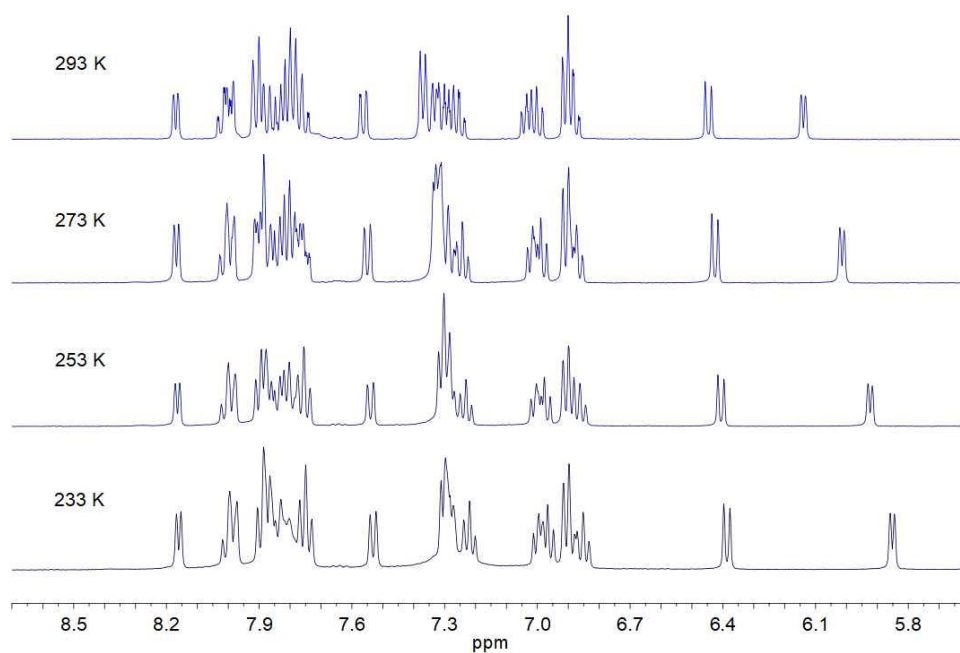


^1H NMR (400 MHz, CD_2Cl_2 , 298 K) spectrum of *mer*-Ir(dfppy) $_2$ (tpy) obtained from *fac*-Ir(dfppy) $_2$ (tpy) using the General Procedure. The signals of $\text{HNEt}_3(\text{O}_2\text{CCF}_3)$ are marked by an asterisk.

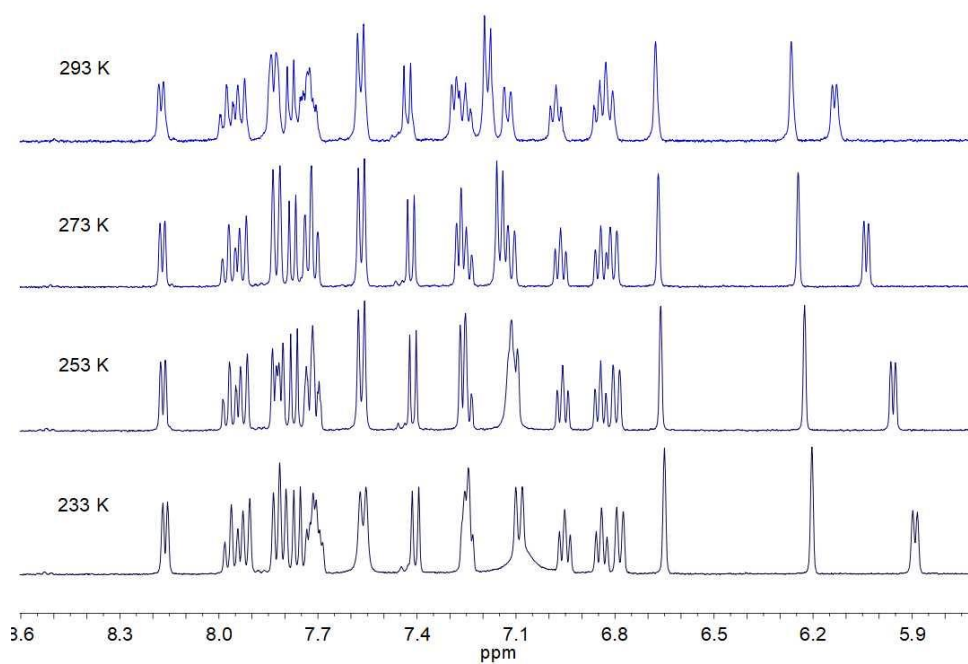


^{19}F NMR (376 MHz, CD_2Cl_2 , 298 K) spectrum of *mer*-Ir(dfppy) $_2$ (tpy) obtained from *fac*-Ir(dfppy) $_2$ (tpy) using the General Procedure. The signals of $\text{HNEt}_3(\text{O}_2\text{CCF}_3)$ are marked by an asterisk.

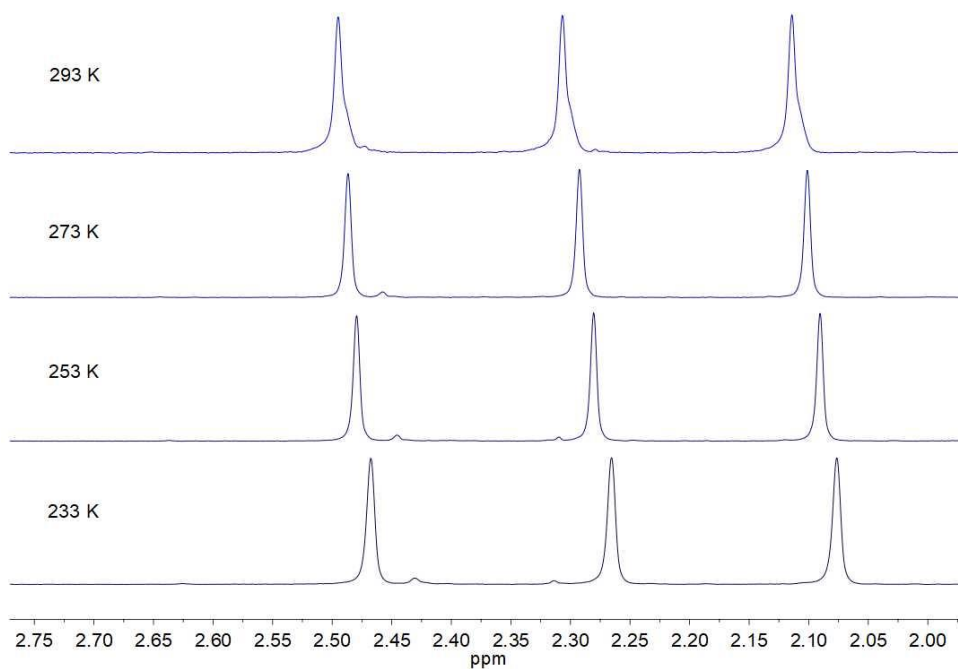
6.3.14 Variable-Temperature (VT) NMR Spectra



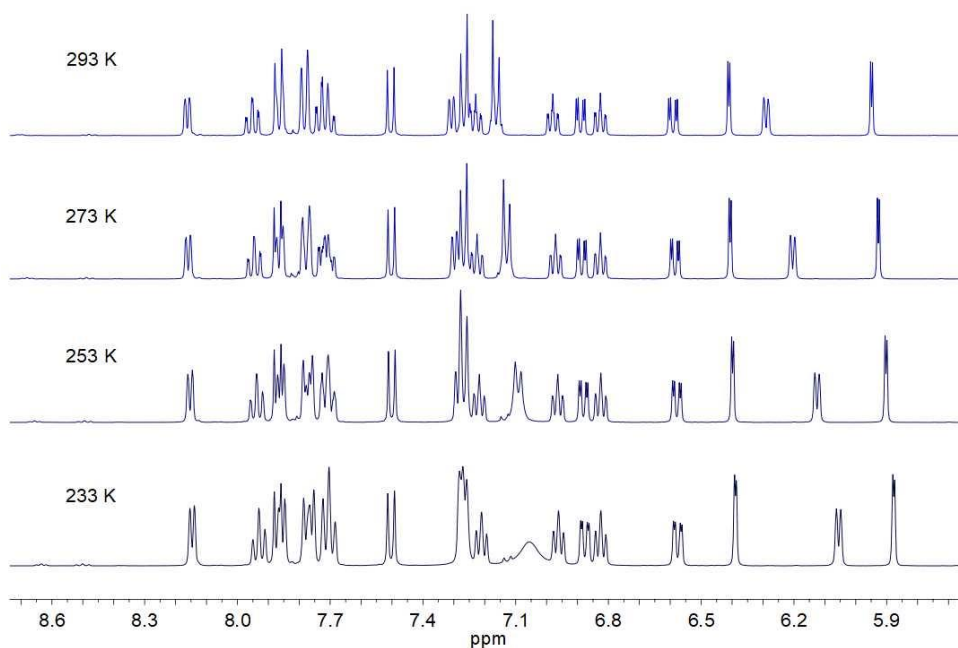
VT ^1H NMR (400 MHz, CD_2Cl_2) spectra of $[\text{Ir}(\text{ppy})_2(\text{Hppy})](\text{O}_2\text{CCF}_3)$



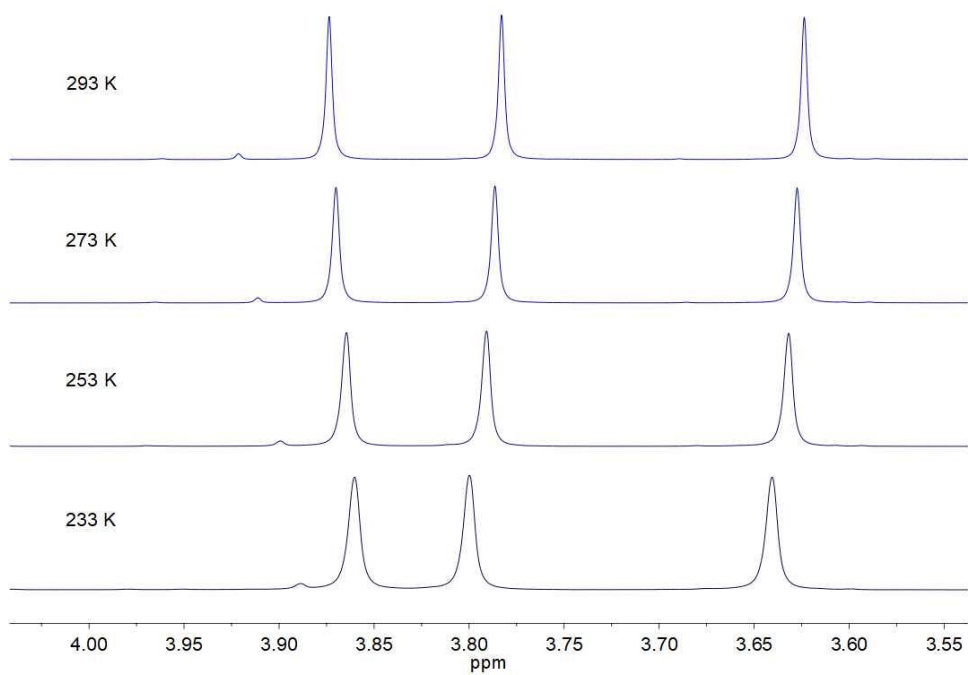
Aromatic region of VT ^1H NMR (400 MHz, CD_2Cl_2) spectra of $[\text{Ir}(\text{tpy})_2(\text{Htpy})](\text{O}_2\text{CCF}_3)$



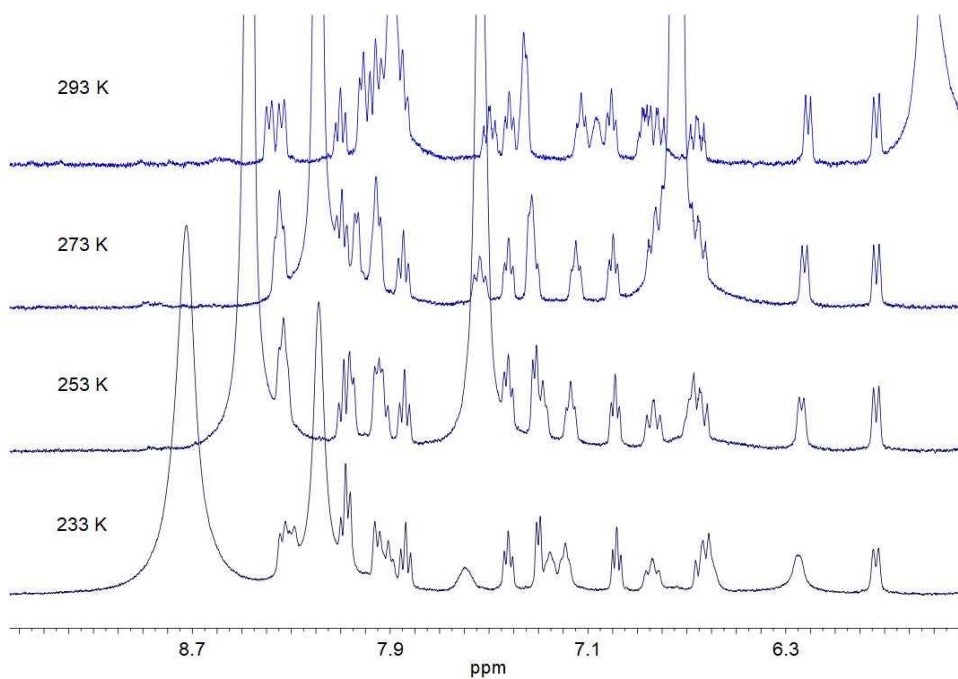
Aliphatic region of VT ^1H NMR (400 MHz, CD_2Cl_2) spectra of $[\text{Ir}(\text{tpy})_2(\text{Htpy})](\text{O}_2\text{CCF}_3)$



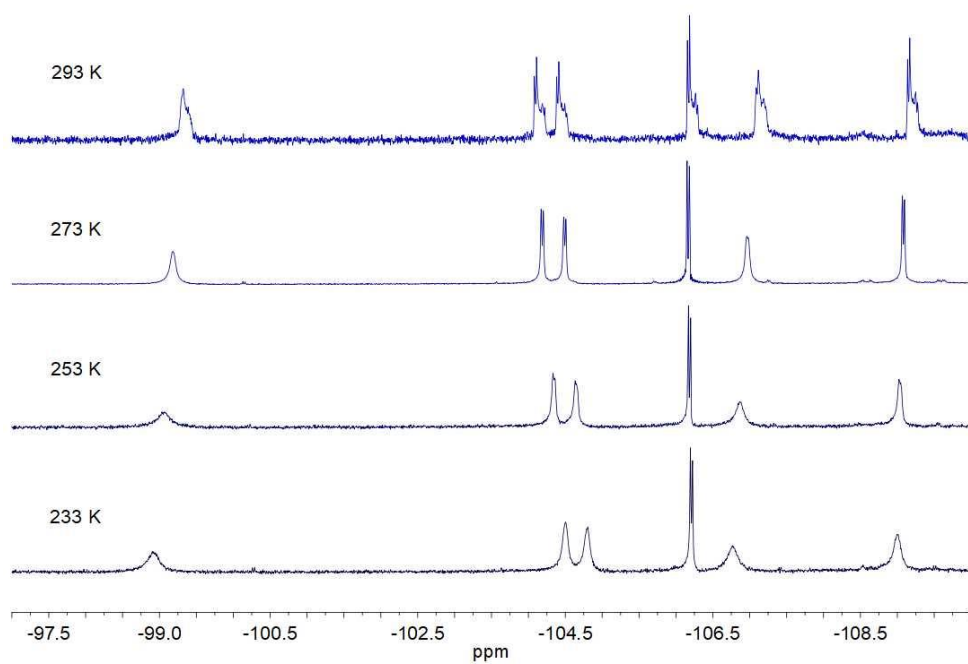
Aromatic region of VT ^1H NMR (400 MHz, CD_2Cl_2) spectra of $[\text{Ir}(\text{meppy})_2(\text{Hmeppy})](\text{O}_2\text{CCF}_3)$



Aliphatic region of VT ^1H NMR (400 MHz, CD_2Cl_2) spectra of $[\text{Ir}(\text{meppy})_2(\text{Hmeppy})](\text{O}_2\text{CCF}_3)$

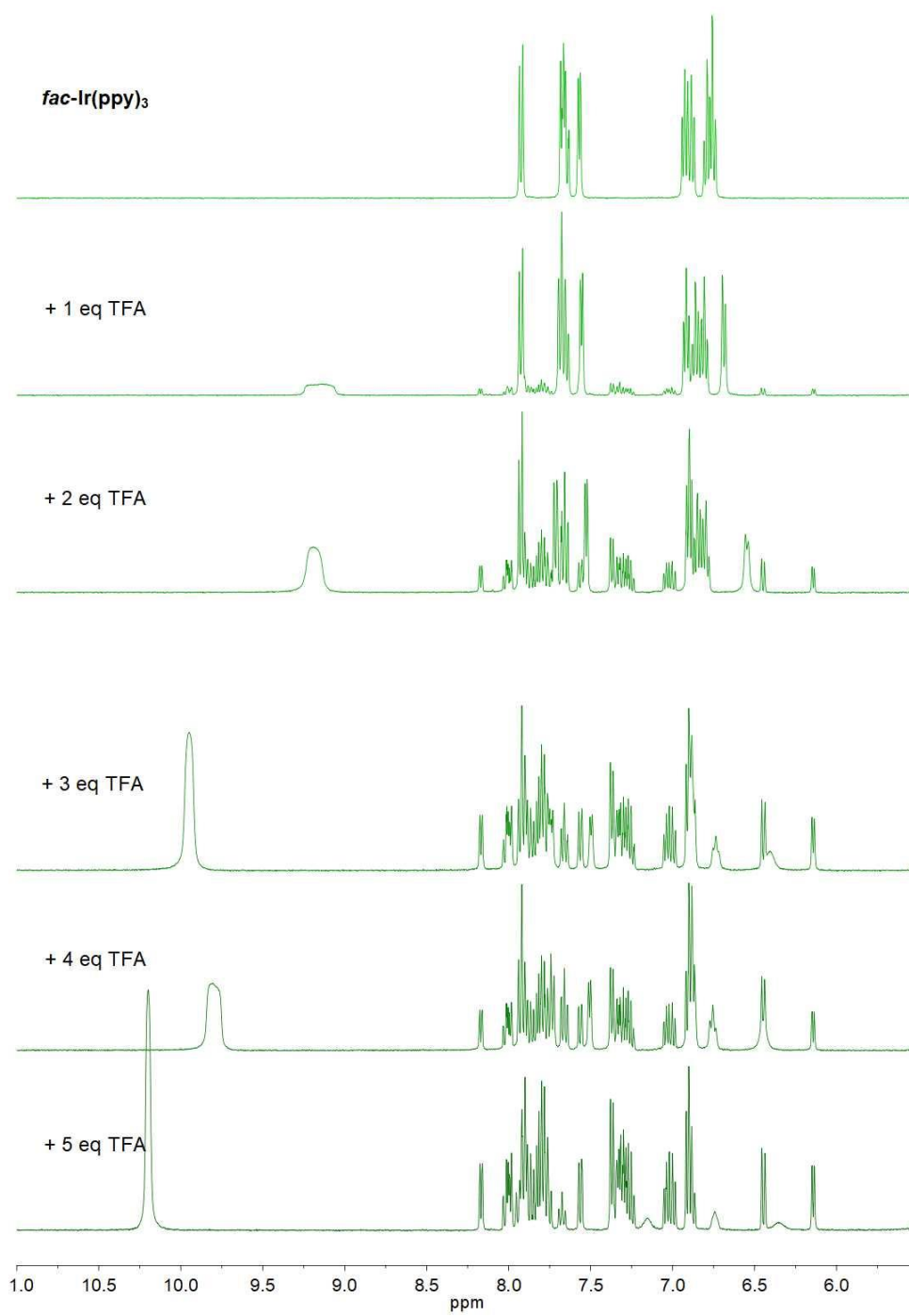


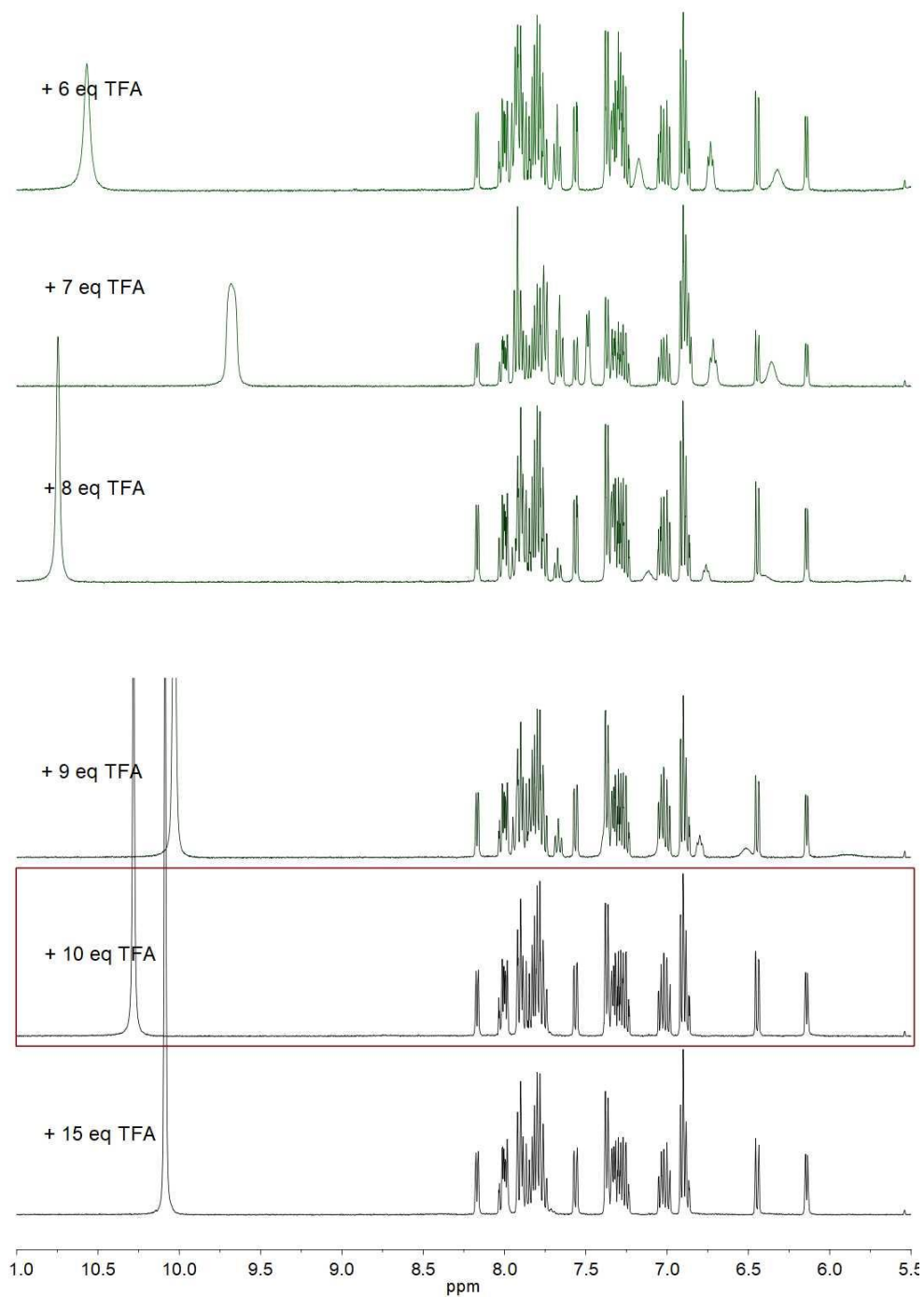
VT ^1H NMR (400 MHz, CD_2Cl_2) spectra of $[\text{Ir}(\text{dfppy})_2(\text{Hdfppy})](\text{NTf}_2)$



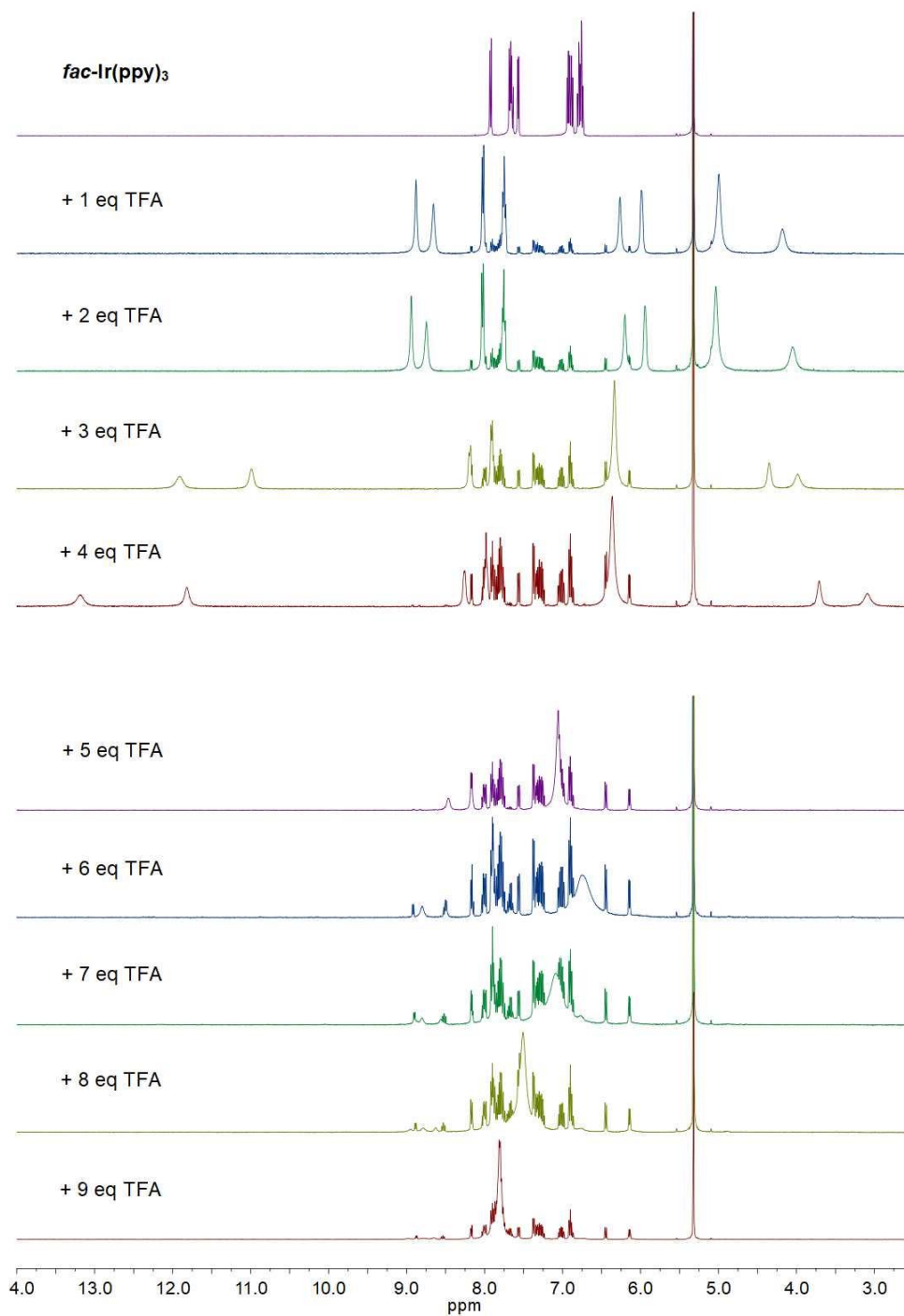
VT ^{19}F NMR (376 MHz, CD_2Cl_2) spectra of $[\text{Ir}(\text{dfppy})_2(\text{Hdfppy})](\text{NTf}_2)$

6.3.15 Optimization Details

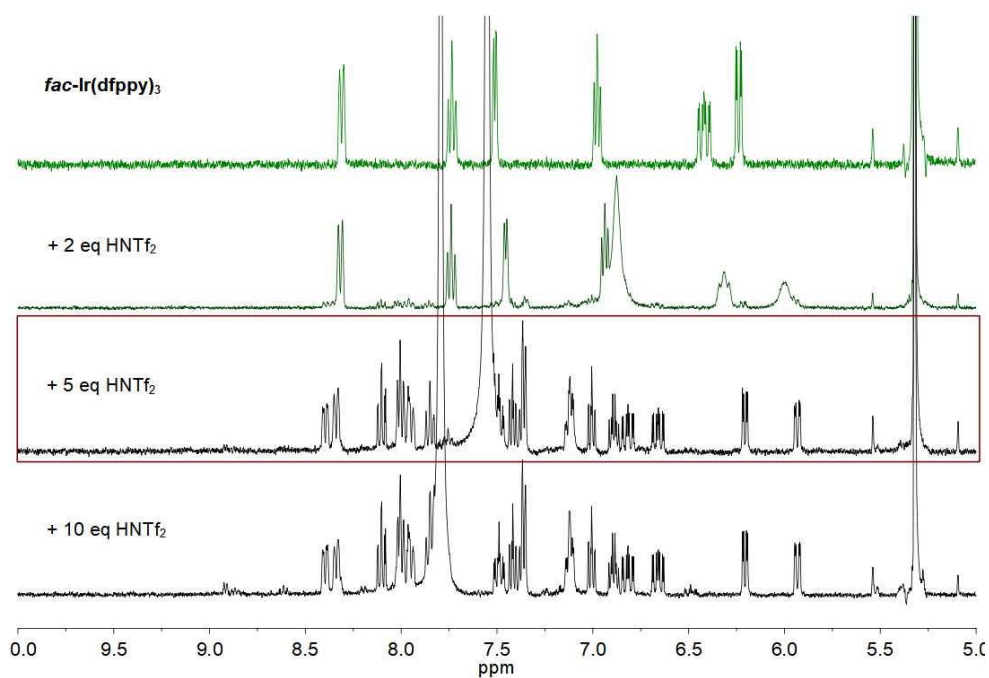




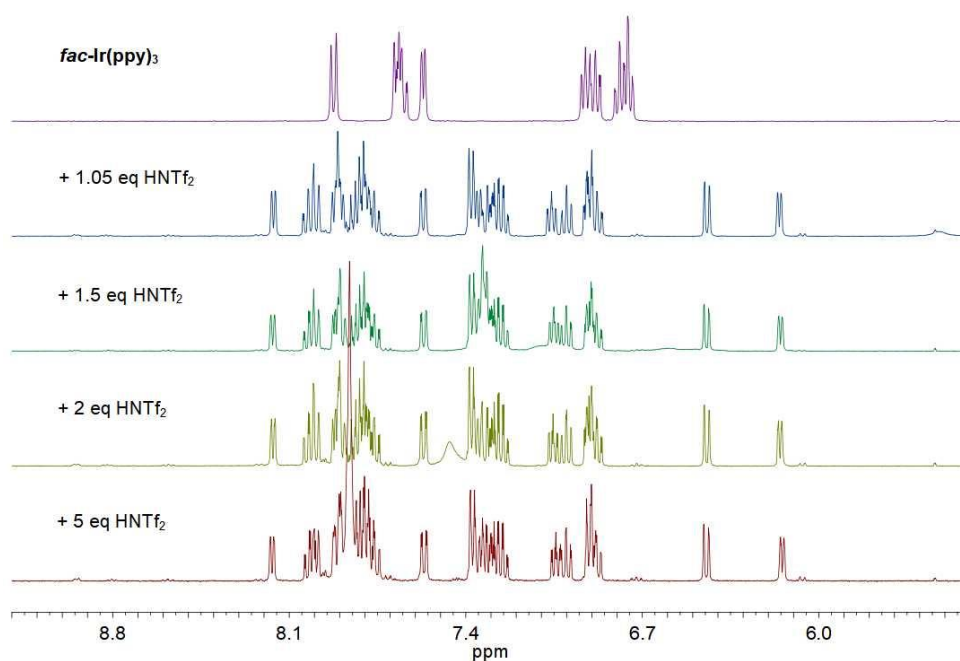
¹H NMR (400 MHz, CD₂Cl₂, 298 K) study of the influence of the TFA concentration on the reaction *fac*-Ir(ppy)₃ → [Ir(ppy)₂(Hppy)](O₂CCF₃). The spectra were measured after the addition of the indicated amount of TFA to a fresh sample of *fac*-Ir(ppy)₃. The conditions used for the General Procedure are highlighted with a red rectangle.



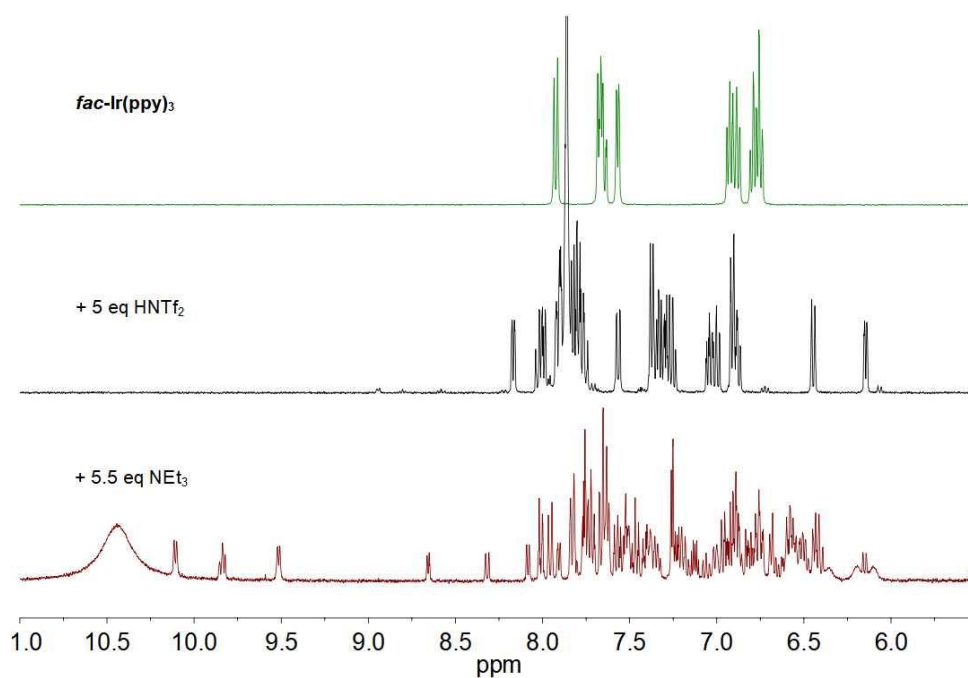
¹H NMR (400 MHz, CD₂Cl₂, 298 K) study of the influence of the TFA concentration on the reaction *fac*-Ir(ppy)₃ → [Ir(ppy)₂(Hppy)](O₂CCF₃). Increasing amounts of TFA were added to the same sample of *fac*-Ir(ppy)₃.



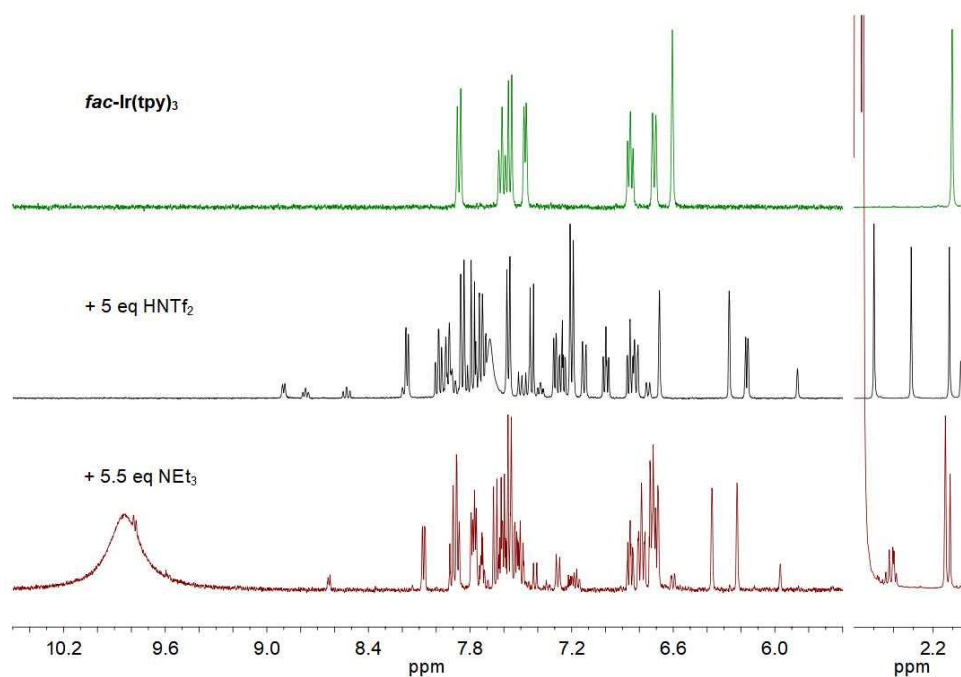
^1H NMR (400 MHz, CD_2Cl_2 , 298 K) study of HNTf_2 concentration effect on reaction $\text{fac-Ir}(\text{dfppy})_3 \rightarrow [\text{Ir}(\text{dfppy})_2(\text{Hdfppy})](\text{NTf}_2)$. The spectra were measured after the addition of indicated amount of HNTf_2 to a fresh sample of $\text{fac-Ir}(\text{dfppy})_3$. The conditions used for the General Procedure are highlighted with a red rectangle.



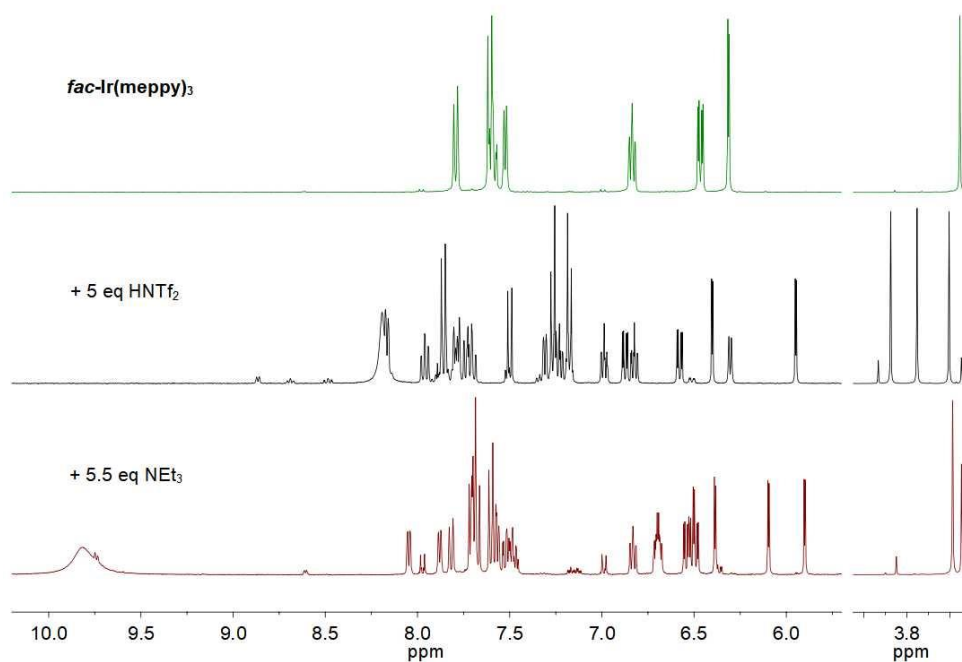
^1H NMR (400 MHz, CD_2Cl_2 , 298 K) study of the influence of the HNTf_2 concentration on reaction $\text{fac-Ir}(\text{ppy})_3 \rightarrow [\text{Ir}(\text{ppy})_2(\text{Hppy})](\text{NTf}_2)$. The spectra were measured after the addition of the indicated amount of HNTf_2 to a fresh sample of $\text{fac-Ir}(\text{dfppy})_3$.



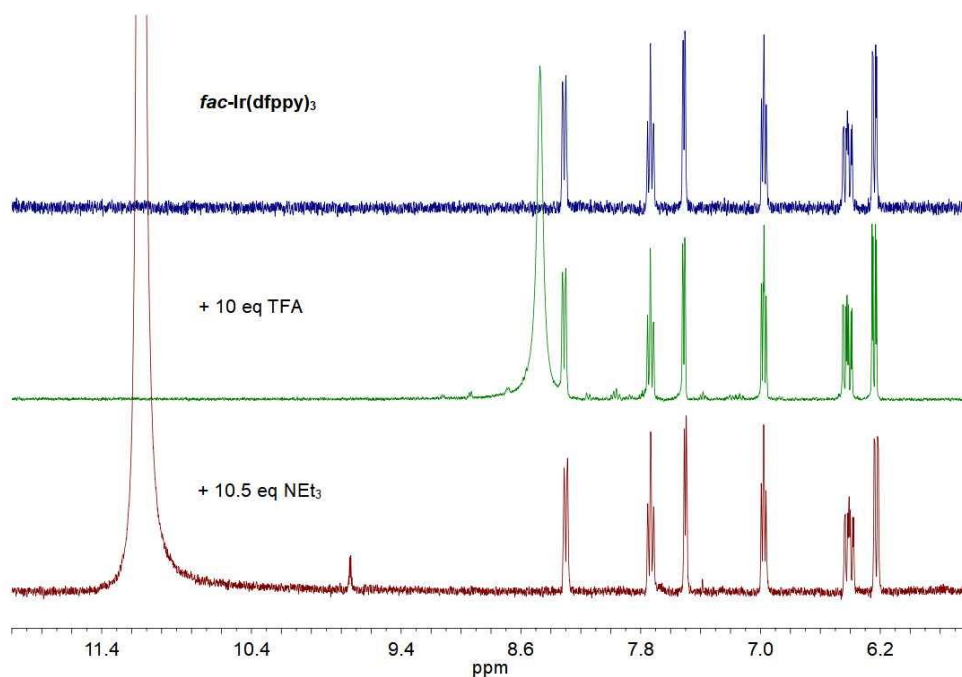
¹H NMR (400 MHz, CD₂Cl₂, 298 K) spectra of a solution of *fac*-Ir(ppy)₃ upon addition of first HNTf₂ and then NEt₃.



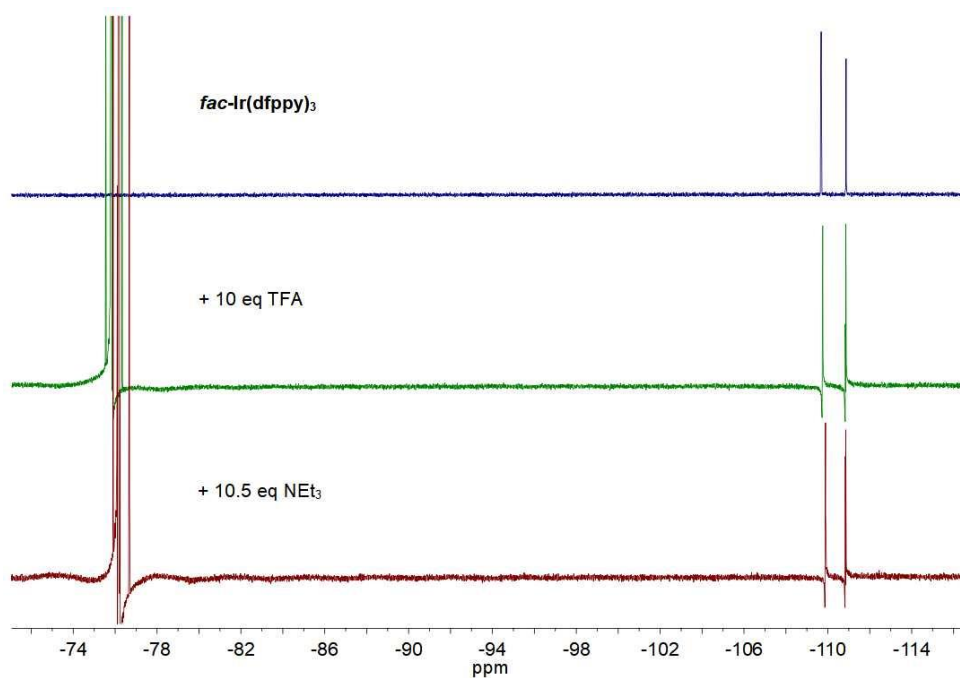
¹H NMR (400 MHz, CD₂Cl₂, 298 K) spectra of a solution of *fac*-Ir(tpy)₃ upon addition of first HNTf₂ and then NEt₃.



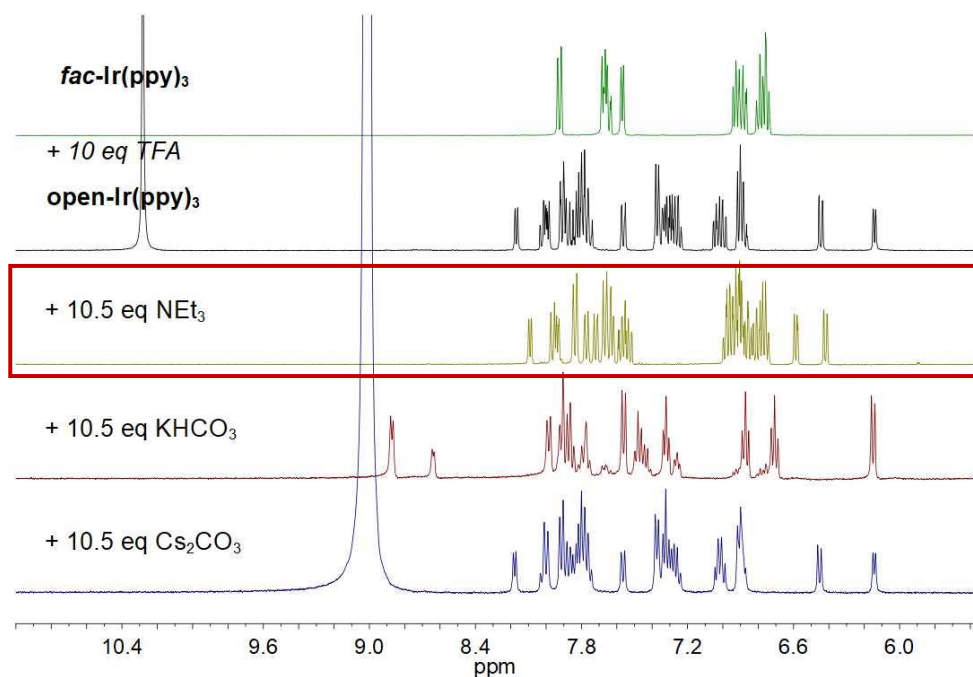
¹H NMR (400 MHz, CD₂Cl₂, 298 K) spectra of a solution of *fac*-Ir(meppy)₃ upon addition of first HNTf₂ and then NEt₃.



¹H NMR (400 MHz, CD₂Cl₂, 298 K) spectra of a solution of *fac*-Ir(dfppy)₃ upon addition of first TFA and then NEt₃.



^{19}F NMR (376 MHz, CD_2Cl_2 , 298 K) spectra of a solution of fac-Ir(dfppy)_3 upon addition of first TFA and then NEt_3

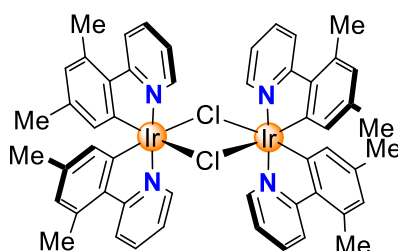


^1H NMR (400 MHz, CD_2Cl_2 , 298 K) study of base effect on reaction $[\text{Ir(ppy)}_2(\text{Hppy})](\text{O}_2\text{CCF}_3) \rightarrow \text{fac-Ir(dfppy)}_3$. The spectra were measured after the addition of indicated amount of base to a fresh sample of $[\text{Ir(ppy)}_2(\text{Hppy})](\text{O}_2\text{CCF}_3)$. The conditions used for the General Procedure are highlighted with a red rectangle.

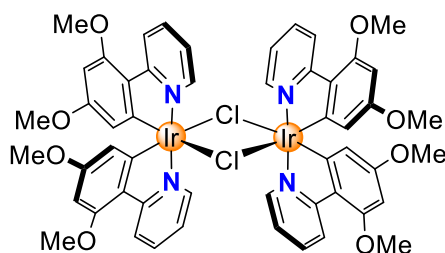
6.3.16 Towards Autonomous Switching

2-(2,4-dimethylphenyl)pyridine, 2-(2,4-dimethoxyphenyl)pyridine, 2-(3-methoxyphenyl)pyridine, and 2-(3,4-dimethoxyphenyl)pyridine ligands have been obtained following the typical conditions for Suzuki-Miyaura cross-coupling reaction using the published procedures.^{229–231} The NMR spectra of the obtained ligands are in agreement with the published ones.

The chloro-bridged dimers $[\text{Ir}(\text{C}^{\wedge}\text{N})_2(\mu\text{-Cl})_2]$ were obtained following the procedure described by B. Orwat and co-workers for the microwave synthesis of the complexes $[\text{Ir}(\text{ppy})_2(\mu\text{-Cl})_2]$ and $[\text{Ir}(\text{dfppy})_2(\mu\text{-Cl})_2]$ with some modifications (for procedure details, see subchapter 6.3.2).¹¹⁰

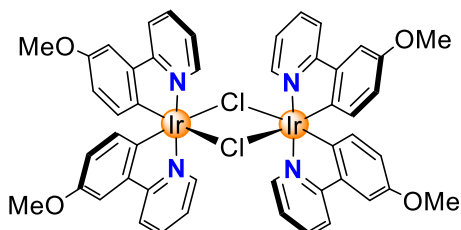


Dichlorotetrakis(2-(2,4-dimethylphenyl)pyridyl)diiridium(III). Obtained from $\text{IrCl}_3 \cdot x\text{H}_2\text{O}$ (500 mg, 1.42 mmol) and 2-(2,4-dimethylphenyl)pyridine (571 mg, 3.12 mmol). Yellow powder, 594 mg (71%). ^1H NMR (400 MHz, acetone- d_6 , 298 K) δ 9.18 (dd, $J = 5.8, 1.7$ Hz, 1H), 8.09 (d, $J = 8.4$ Hz, 1H), 7.80 (ddd, $J = 8.6, 7.4, 1.8$ Hz, 1H), 6.76 (ddd, $J = 7.3, 5.7, 1.4$ Hz, 1H), 6.22 (m, 1H), 5.33 (m, 1H), 2.53 (s, 3H), 1.68 (s, 3H). Single crystals of dichlorotetrakis(2-(2,4-dimethylphenyl)pyridyl)diiridium(III) were obtained by evaporation of a solution of dichlorotetrakis(2-(2,4-dimethylphenyl)pyridyl)diiridium(III) in CHCl_3 at room temperature.

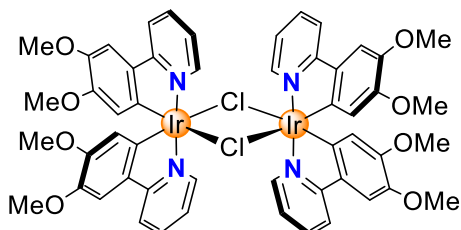


Dichlorotetrakis(2-(2,4-dimethoxyphenyl)pyridyl)diiridium(III). Obtained from $\text{IrCl}_3 \cdot x\text{H}_2\text{O}$ (417 mg, 1.18 mmol) and 2-(2,4-dimethoxyphenyl)pyridine (559 mg, 2.60

mmol). Yellow powder, 530 mg (68%). ^1H NMR (400 MHz, acetone- d_6 , 298 K) δ 9.25 (d, $J = 5.3$ Hz, 1H), 8.63 (d, $J = 8.2$ Hz, 1H), 7.82 (ddd, $J = 8.6, 7.3, 1.7$ Hz, 1H), 6.81 (ddd, $J = 7.3, 5.7, 1.5$ Hz, 1H), 6.01 (d, $J = 2.3$ Hz, 1H), 5.01 (d, $J = 2.2$ Hz, 1H), 3.89 (s, 3H), 3.35 (s, 3H). The NMR data is in agreement with what reported in the literature.²²⁹

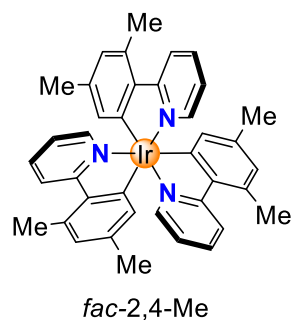


Dichlorotetrakis(2-(3-methoxyphenyl)pyridyl)diiridium(III). Obtained from $\text{IrCl}_3 \cdot x\text{H}_2\text{O}$ (500 mg, 1.42 mmol) and 2-(3-methoxyphenyl)pyridine (577 mg, 3.12 mmol). Yellow powder, 590 mg (70%). ^1H NMR (400 MHz, acetone- d_6 , 298 K) δ 9.32 – 9.23 (m, 1H), 8.14 (t, $J = 8.0$ Hz, 1H), 7.97 – 7.93 (m, 1H), 7.29 – 7.22 (m, 1H), 6.98 (ddd, $J = 7.3, 5.7, 1.4$ Hz, 1H), 6.29 – 6.22 (m, 1H), 5.72 (d, $J = 8.5$ Hz, 1H), 3.65 (d, $J = 2.1$ Hz, 3H). The NMR spectrum is in agreement with what reported in the literature.²³²

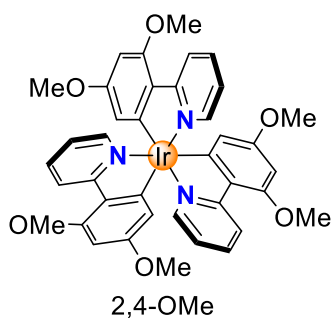


Dichlorotetrakis(2-(3,4-dimethoxyphenyl)pyridyl)diiridium(III). Obtained from $\text{IrCl}_3 \cdot x\text{H}_2\text{O}$ (500 mg, 1.42 mmol) and 2-(3,4-dimethoxyphenyl)pyridine (671 mg, 3.12 mmol). Yellow powder, 582 mg (63%). ^1H NMR (400 MHz, CDCl_3 , 298 K) δ 9.24 (dd, $J = 5.7, 1.4$ Hz, 1H), 7.74 – 7.67 (m, 2H), 7.06 (s, 1H), 6.70 (td, $J = 6.2, 2.2$ Hz, 1H), 5.45 (s, 1H), 3.78 (s, 3H), 3.36 (s, 3H).

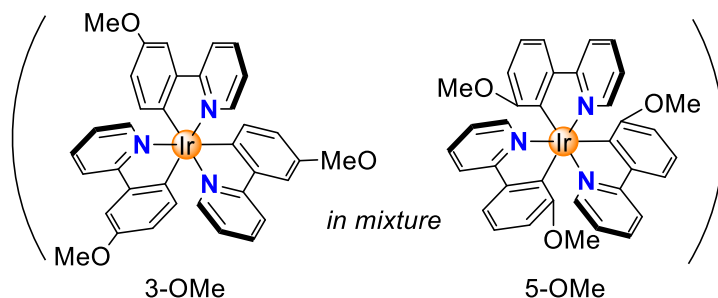
The facial complexes 2,4-Me, 2,4-OMe, 3-OMe, 5-OMe and 3,4-OMe have been synthesized using both the conventional method¹⁰³ and the microwave method (for procedure details, see subchapter 6.3.2).



fac-2,4-Me. Obtained by the microwave method from $\text{IrCl}_3 \cdot x\text{H}_2\text{O}$ and 2-(2,4-dimethylphenyl)pyridine (2.60 g, 14.2 mmol). Yellow crystals, 4 mg (4%). ^1H NMR (400 MHz, CD_2Cl_2 , 298 K) δ 8.10 (d, $J = 8.5$ Hz, 1H), 7.60 (s, 1H), 7.45 (d, $J = 4.4$ Hz, 1H), 6.81 (s, 1H), 6.52 (d, $J = 2.7$ Hz, 2H), 2.70 (s, 3H), 2.04 (s, 3H).

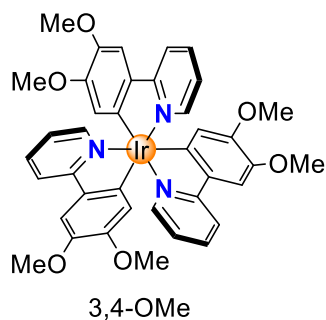


fac-2,4-OMe. Obtained by the microwave method from $\text{IrCl}_3 \cdot x\text{H}_2\text{O}$ (43.0 mg, 1.22 mmol) and 2-(2,4-dimethoxyphenyl)pyridine (2.63 g, 12.2 mmol). Pale yellow crystals, 90.7 mg (89%). ^1H NMR (400 MHz, CD_2Cl_2 , 298 K) δ 7.74 (m, 1H), 7.60 (ddd, $J = 8.4$, 7.3, 1.6 Hz, 1H), 7.53 (d, $J = 5.5$ Hz, 1H), 7.22 (s, 1H), 6.83 (ddd, $J = 7.1$, 5.5, 1.3 Hz, 1H), 6.39 (s, 1H), 3.80 (s, 3H), 3.47 (s, 3H). ^{13}C NMR (101 MHz, CD_2Cl_2 , 298 K) δ 168.0, 165.8, 161.8, 160.5, 147.0, 136.1, 125.6, 123.4, 120.3, 113.8, 91.1, 55.2, 54.9.

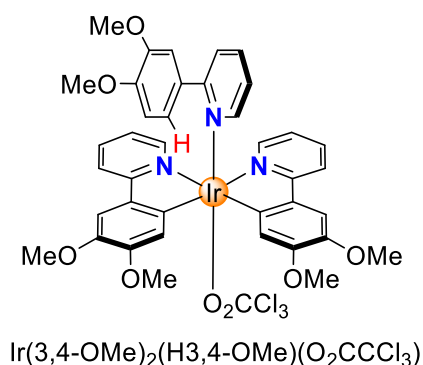


fac-3-OMe. Due to the two possible positions for *ortho*-metalation in 2-(3-methoxyphenyl)pyridine ligand, *fac*-3-OMe has been obtained in a mixture with *fac*-5-

OMe by the convenient method from dichlorotetrakis(2-(3-methoxyphenyl)pyridyl)diiridium(III) (590 mg, 0.50 mmol), 2-(3-methoxyphenyl)pyridine (230 mg, 1.24 mmol) and K_2CO_3 (683 mg, 4.95 mmol). Orange crystals, 336 mg (46%, *fac*-3-OMe : *fac*-5-OMe = 3:1). 1H NMR (400 MHz, CD_2Cl_2 , 298 K) spectrum of the mixture is shown below.

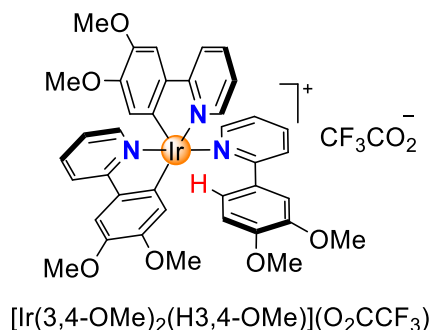


fac-3,4-OMe. Obtained by the convenient method from dichlorotetrakis(2-(3,4-dimethoxyphenyl)pyridyl)diiridium(III) (582 mg, 0.44 mmol), 2-(3,4-dimethoxyphenyl)pyridine (238 mg, 1.11 mmol) and K_2CO_3 (612 mg, 4.44 mmol). Orange crystals, 368 mg (53%). 1H NMR (400 MHz, CD_2Cl_2 , 298 K) δ 7.74 (m, 1H), 7.59 (ddd, $J = 8.3, 7.3, 1.7$ Hz, 1H), 7.53 (d, $J = 5.6$ Hz, 1H), 7.22 (s, 1H), 6.83 (ddd, $J = 7.1, 5.5, 1.3$ Hz, 1H), 6.39 (s, 1H), 3.80 (s, 3H), 3.47 (s, 3H). ^{13}C NMR (101 MHz, CD_2Cl_2 , 298 K) δ 168.0, 155.0, 151.8, 147.6, 144.2, 136.3, 135.5, 121.0, 118.9, 118.4, 109.3, 56.7, 55.5. Single crystals of *fac*-3,4-OMe were obtained by slow gas phase diffusion of hexane into a solution of *fac*-3,4-OMe in DCM at r.t.

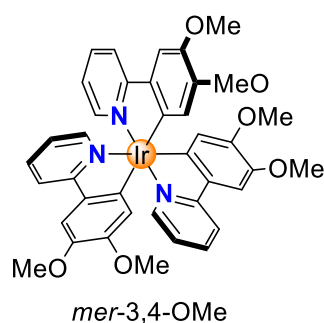


$Ir(3,4-OMe)_2(H3,4-OMe)(O_2CCCl_3)$. A solution of the open form was obtained upon addition of an aliquot of a stock solution of HO_2CCCl_3 in CD_2Cl_2 (0.2 M, 74.9 μL , 15.0 μmol , 1.0 equiv.) to a solution of *fac*-3,4-OMe (12.5 mg, 15.0 μmol , 1.0 equiv.) in 0.5 mL of CD_2Cl_2 . 1H NMR (400 MHz, CD_2Cl_2 , 298 K) δ 9.22 (dt, $J = 5.8, 1.2$ Hz, 2H), 9.10

– 9.00 (m, 2H), 8.30 (td, $J = 7.8, 1.7$ Hz, 1H), 8.04 (dt, $J = 8.3, 1.0$ Hz, 1H), 7.82 – 7.59 (m, 7H), 7.54 (dd, $J = 8.5, 2.3$ Hz, 1H), 7.12 (s, 2H), 7.06 (d, $J = 8.5$ Hz, 1H), 6.79 – 6.69 (m, 2H), 4.01 (s, 3H), 3.93 (s, 3H), 3.78 (s, 6H), 3.33 (s, 6H).



$[\text{Ir}(3,4\text{-OMe})_2(\text{H}3,4\text{-OMe})](\text{O}_2\text{CCF}_3)$. A solution of the open form was obtained upon addition of an aliquot of a stock solution of TFA in CD_2Cl_2 (0.5 M, 59.9 μL , 29.9 μmol , 5.0 equiv.) to a solution of *fac*-3,4-OMe (5.00 mg, 5.99 μmol , 1.0 equiv.) in 0.5 mL of CD_2Cl_2 . ^1H NMR (400 MHz, CD_2Cl_2 , 298 K) δ 8.09 (ddd, $J = 5.9, 1.6, 0.7$ Hz, 1H), 7.98 (td, $J = 7.9, 1.5$ Hz, 1H), 7.80 – 7.74 (m, 4H), 7.70 – 7.66 (m, 1H), 7.38 (s, 1H), 7.32 (ddd, $J = 5.9, 1.6, 0.7$ Hz, 1H), 7.25 (ddd, $J = 7.5, 5.8, 1.5$ Hz, 1H), 7.13 – 7.01 (m, 3H), 7.00 – 6.91 (m, 2H), 6.81 (ddd, $J = 7.4, 5.9, 1.5$ Hz, 1H), 6.67 (dt, $J = 5.7, 1.3$ Hz, 1H), 6.25 (s, 1H), 5.89 (s, 1H), 3.95 (s, 3H), 3.83 – 3.77 (m, 9H), 3.62 (s, 3H), 3.47 (s, 3H).

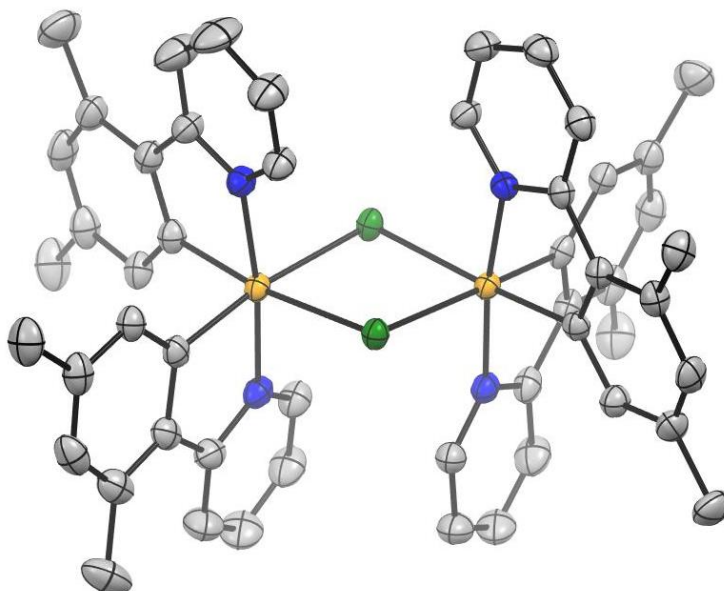


mer-3,4-OMe. A solution of the *mer* isomer was obtained upon addition of an aliquot of a stock solution of NEt_3 in CD_2Cl_2 (0.5 M, 65.9 μL , 32.9 μmol , 5.5 equiv.) to the solution of $[\text{Ir}(3,4\text{-OMe})_2(\text{H}3,4\text{-OMe})](\text{O}_2\text{CCF}_3)$. ^1H NMR (400 MHz, CD_2Cl_2 , 298 K) δ 7.78 – 7.74 (m, 1H), 7.67 – 7.57 (m, 4H), 7.50 (dtd, $J = 11.1, 7.8, 1.6$ Hz, 2H), 7.29 (d, $J = 7.2$ Hz, 2H), 7.24 (s, 1H), 6.83 (ddd, $J = 7.1, 5.6, 1.3$ Hz, 1H), 6.69 (ddt, $J = 7.4,$

5.9, 1.8 Hz, 2H), 6.41 (s, 1H), 6.07 (s, 1H), 5.94 (s, 1H), 3.83 – 3.80 (m, 9H), 3.55 – 3.44 (m, 9H).

Crystallographic Data

Dichlorotetrakis(2-(2,4-dimethylphenyl)pyridyl)diiridium(III) (dimer)



ORTEP view of dichlorotetrakis(2-(2,4-dimethylphenyl)pyridyl)diiridium(III) at the 50% probability level. Hydrogen atoms are omitted for clarity.

A clear, intense yellow prism-shaped crystal with dimensions of 0.27×0.16×0.05 mm³ was mounted. Data were collected using a XtaLAB Synergy R, DW system, HyPix-Arc 150 diffractometer operating at $T = 140.00(10)$ K.

Data were measured using ω scans with CuK α radiation. The diffraction pattern was indexed and the total number of runs and images was based on the strategy calculation from the program CrysAlis^{Pro} 1.171.42.53a (CrysAlis^{Pro} Software System, Rigaku Oxford Diffraction, 2022). The maximum resolution that was achieved was $\theta = 75.563^\circ$ (0.80 Å).

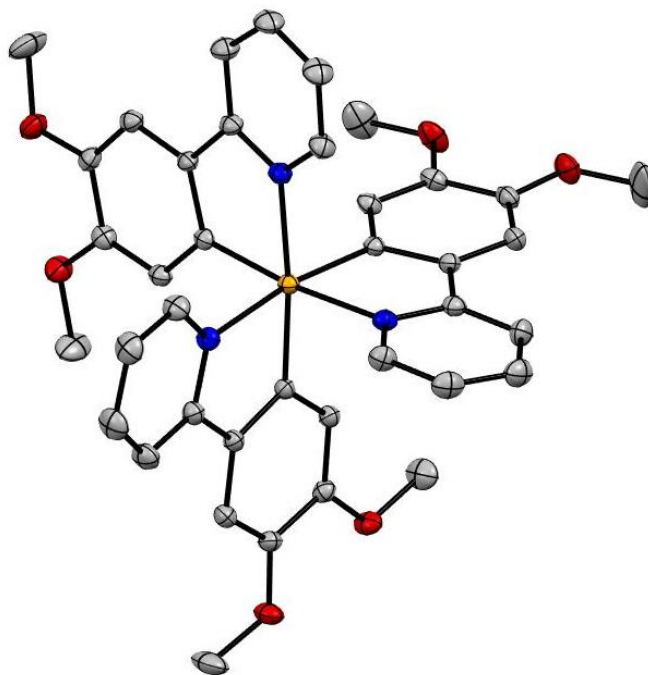
The unit cell was refined using CrysAlis^{Pro} 1.171.42.53a on 58809 reflections, 69% of the observed reflections.

Data reduction, scaling and absorption corrections were performed using CrysAlis^{Pro} 1.171.42.53a. The final completeness is 99.80% out to 75.563° in θ . A Gaussian absorption correction was performed using CrysAlis^{Pro} 1.171.42.53a. Numerical absorption correction based on Gaussian integration over a multifaceted crystal model. Empirical absorption correction using spherical harmonics as implemented in SCALE3 ABSPACK scaling algorithm. The absorption coefficient μ of this material is 10.541 mm⁻¹ at this wavelength ($\lambda = 1.54184\text{\AA}$) and the minimum and maximum transmissions are 0.120 and 0.995.

The structure was solved in the space group P-1 (№ 2) by the ShelXT 2018/2²²⁶ structure solution program using dual methods and refined by full-matrix least-squares minimization on F^2 using version 2018/3 of ShelXL 2018/3.²²⁷ All non-hydrogen atoms were refined anisotropically. Hydrogen atom positions were calculated geometrically and refined using the riding model.

There is a single molecule in the asymmetric unit, which is represented by the reported sum formula. In other words: Z is 2 and Z' is 1.

fac-3,4-OMe



ORTEP view of *fac*-3,4-OMe at the 50% probability level. Hydrogen atoms are omitted for clarity.

A clear, intense yellow prism-shaped crystal with dimensions 0.50×0.39×0.30 mm³ was mounted. Data were collected using a SuperNova, Dual, Cu at home/near Atlas diffractometer operating at $T = 139.99(10)$ K.

Data were measured using ω scans with MoK α radiation. The diffraction pattern was indexed, and the total number of runs and images was based on the strategy calculation from the program CrysAlis^{Pro} 1.171.42.53a (CrysAlis^{Pro} Software System, Rigaku Oxford Diffraction, 2022). The maximum resolution achieved was $\theta = 32.707^\circ$ (0.66 Å).

The unit cell was refined using CrysAlis^{Pro} 1.171.42.53a on 22859 reflections, 62% of the observed reflections.

Data reduction, scaling, and absorption corrections were performed using CrysAlis^{Pro} 1.171.42.53a. The final completeness is 99.90% out to 32.707° in θ . A Gaussian absorption correction was performed using CrysAlisPro 1.171.42.53a. Numerical absorption correction was based on Gaussian integration over a multifaceted crystal model. Empirical absorption correction using spherical harmonics as implemented in SCALE3 ABSPACK scaling algorithm. The absorption coefficient μ of this material is 3.270 mm⁻¹ at this wavelength ($\lambda = 0.71073\text{Å}$), and the minimum and maximum transmissions are 0.143 and 1.000.

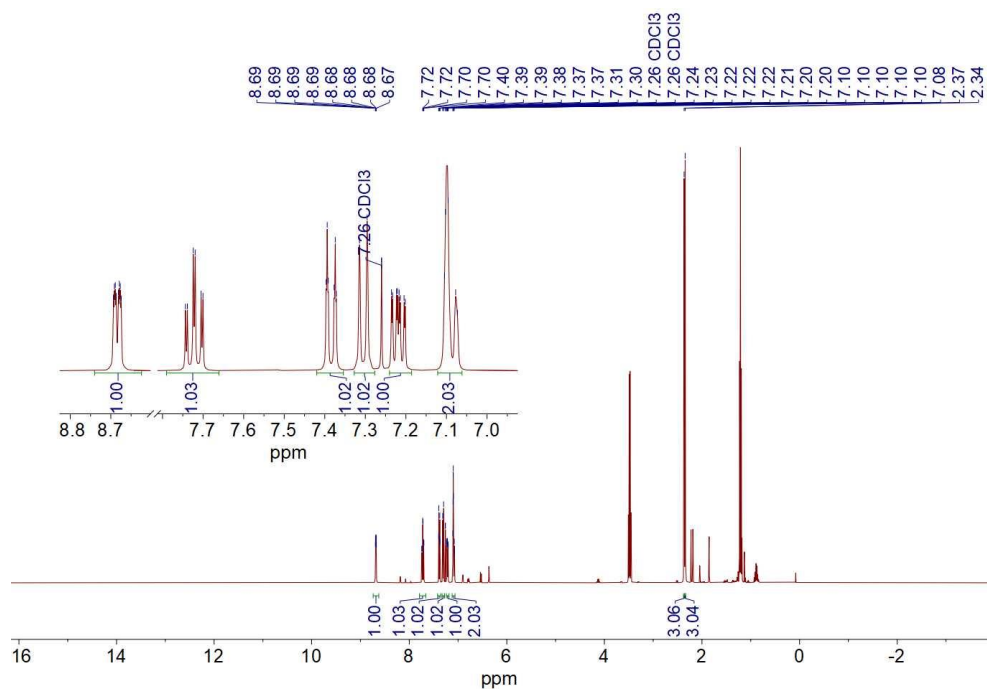
The structure was solved in the space group P-1 (No 2) by the ShelXT 2018/2²²⁶ structure solution program using dual methods and refined by full-matrix least-squares minimization on F^2 using version 2018/3 of ShelXL 2018/3.²²⁷ All non-hydrogen atoms were refined anisotropically. Hydrogen atom positions were calculated geometrically and refined using the riding model.

There is a single molecule in the asymmetric unit, which is represented by the reported sum formula. In other words: Z is 2 and Z' is 1.

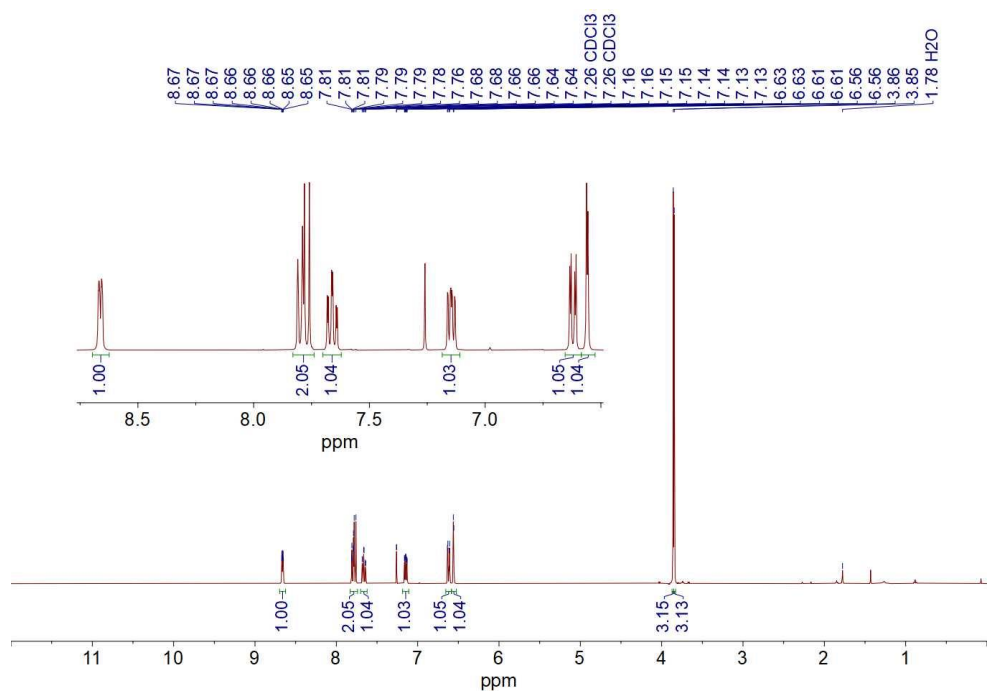
Crystallographic data for the compounds

Compound	Dimer	fac-3,4-OMe
Formula	C ₆₂ H ₆₉ Cl ₂ Ir ₂ N ₄ O ₃	C _{42.5} H ₄₃ Cl ₇ IrN ₃ O ₆
Formula Weight	1.664	1.592
<i>D</i> _{calc.} , g cm ⁻³	10.541	3.270
μ , mm ⁻¹	1373.51	1132.15
Colour	Clear, intense yellow	clear intense yellow
Shape	prism-shaped	prism-shaped
Size, mm ³	0.27×0.16×0.05	0.50×0.39×0.30
<i>T</i> , K	140.00(10)	139.99(10)
Crystal System	triclinic	triclinic
Space Group	<i>P</i> $\bar{1}$	<i>P</i> $\bar{1}$
<i>a</i> , Å	12.86489(14)	14.3801(4)
<i>b</i> , Å	14.95910(14)	14.7781(5)
<i>c</i> , Å	15.16772(7)	14.9497(4)
α , °	88.0133(6)	93.758(2)
β , °	87.8469(7)	116.289(3)
γ , °	70.0784(10)	117.959(3)
<i>V</i> , Å ³	2741.63(5)	2361.48(14)
<i>Z</i>	2	2
<i>Z'</i>	1	1
λ , Å	1.54184	0.71073
Radiation type	CuK α	MoK α
θ_{min} , °	2.916	2.691
θ_{max} , °	75.563	32.707
Measured Refl.	85527	37167
Independent Refl.	10825	15734
Refl. $I \geq 2\sigma(I)$	10294	14232
<i>R</i> _{int}	0.0364	0.0319
Parameters	740	613
Restraints	199	122
Largest Peak, e Å ⁻³	1.097	1.338
Deepest Hole, e Å ⁻³	-0.888	-1.159
GooF	1.062	1.051
<i>wR</i> ₂ (all data)	0.0614	0.0724
<i>wR</i> ₂	0.0607	0.0694
<i>R</i> ₁ (all data)	0.0244	0.0380
<i>R</i> ₁	0.0231	0.0316
CCDC number	2173942	2175392

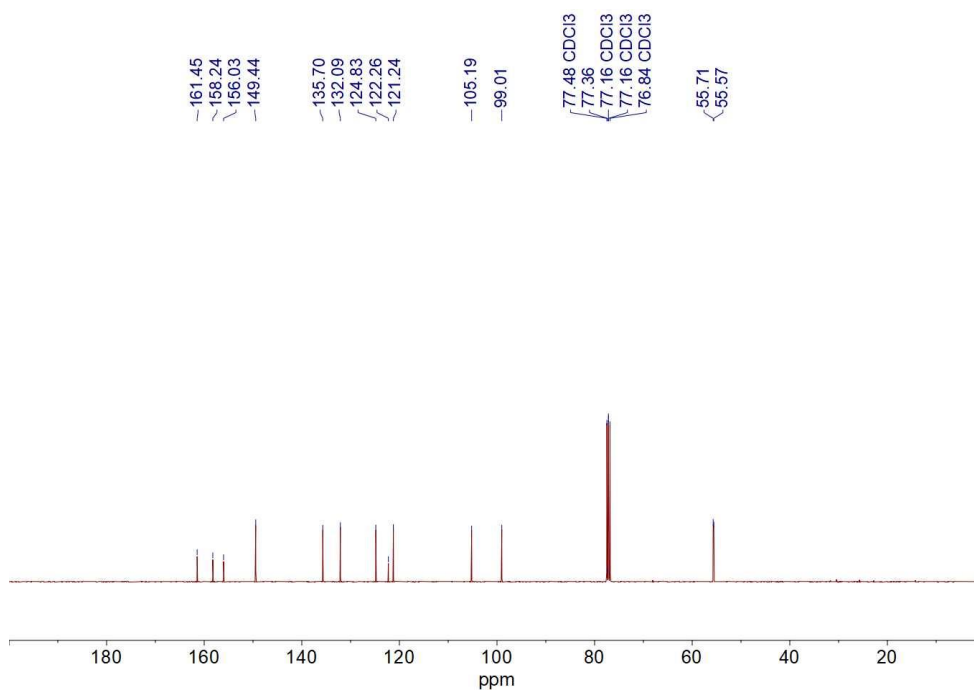
NMR Spectra



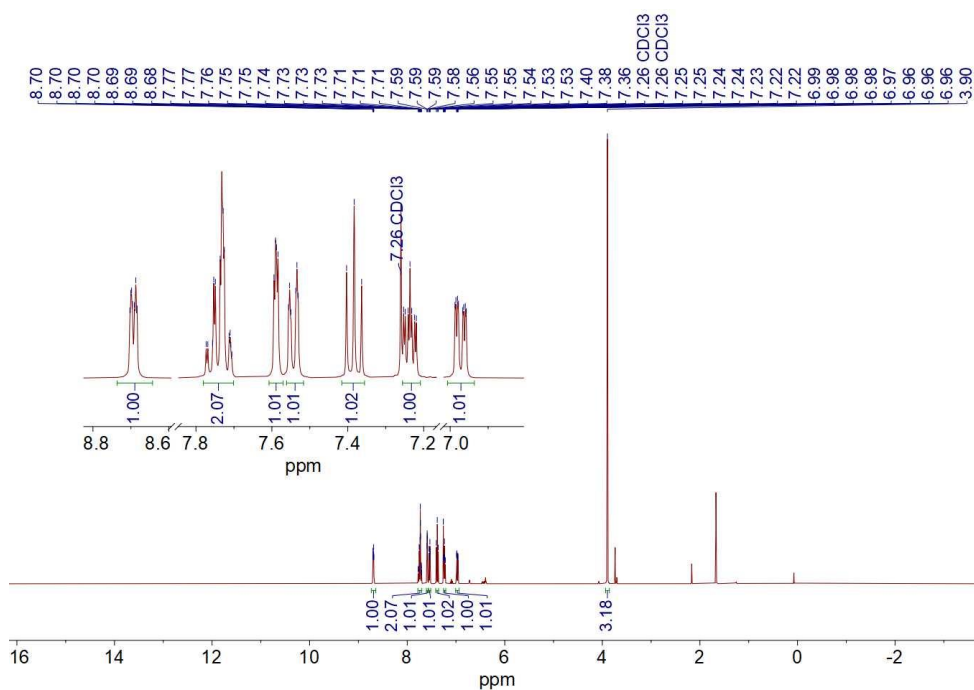
¹H NMR (400 MHz, CDCl₃, 298 K) spectrum of 2-(2,4-dimethylphenyl)pyridine



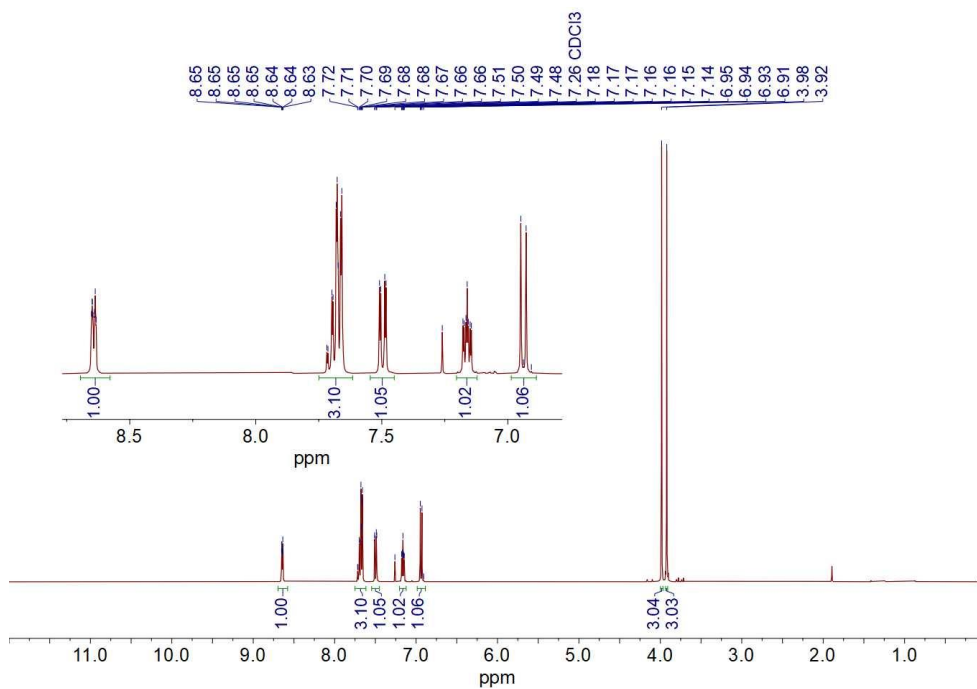
¹H NMR (400 MHz, CDCl₃, 298 K) spectrum of 2-(2,4-dimethoxyphenyl)pyridine



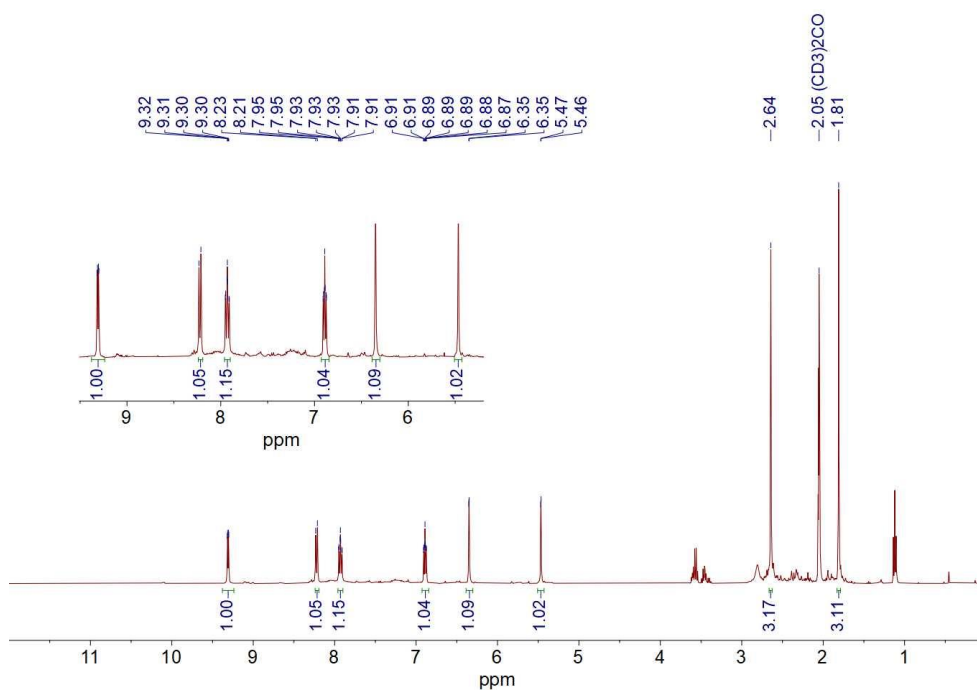
^{13}C NMR (101 MHz, CDCl_3 , 298 K) spectrum of 2-(2,4-dimethoxyphenyl)pyridine



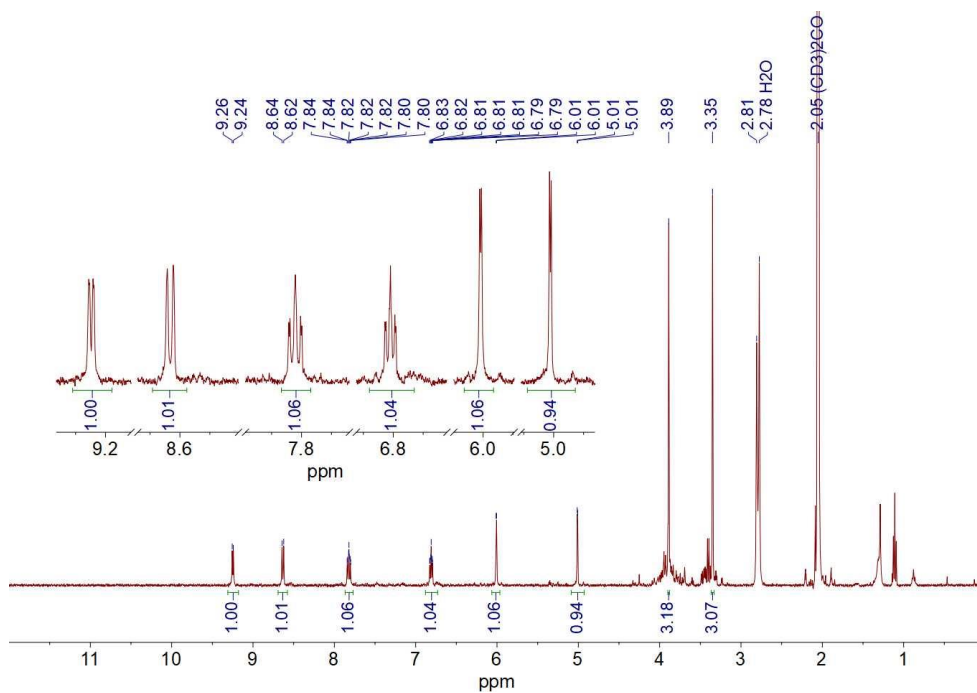
^1H NMR (400 MHz, CDCl_3 , 298 K) spectrum of 2-(3-methoxyphenyl)pyridine



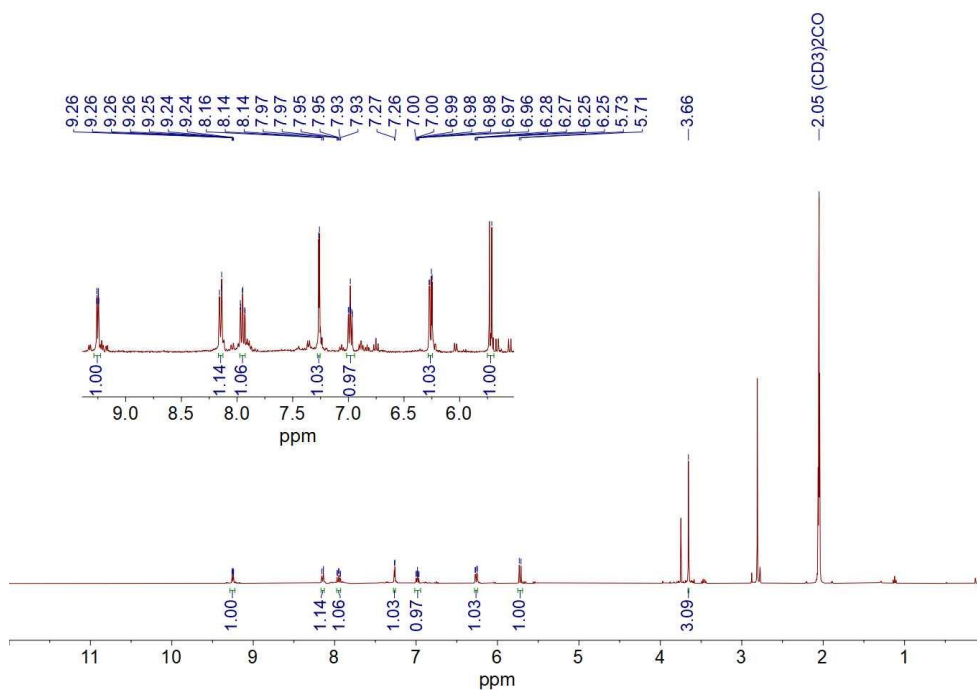
¹H NMR (400 MHz, CDCl₃, 298 K) spectrum of 2-(3,4-dimethoxyphenyl)pyridine



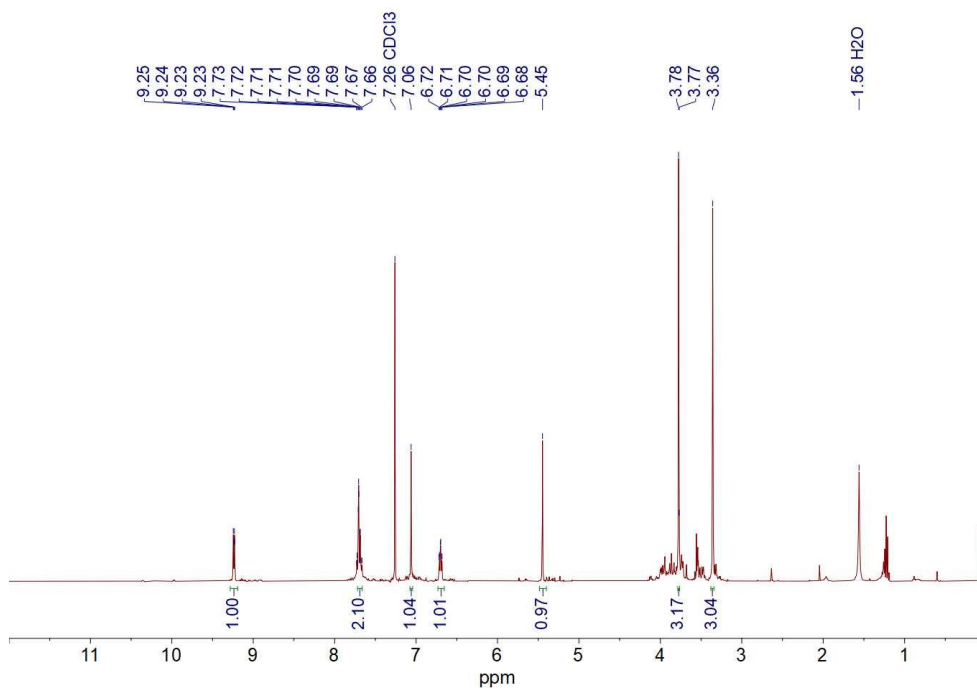
¹H NMR (400 MHz, acetone-d₆, 298 K) spectrum of dichlorotetrakis(2-(2,4-dimethylphenyl)pyridyl)diiridium(III)



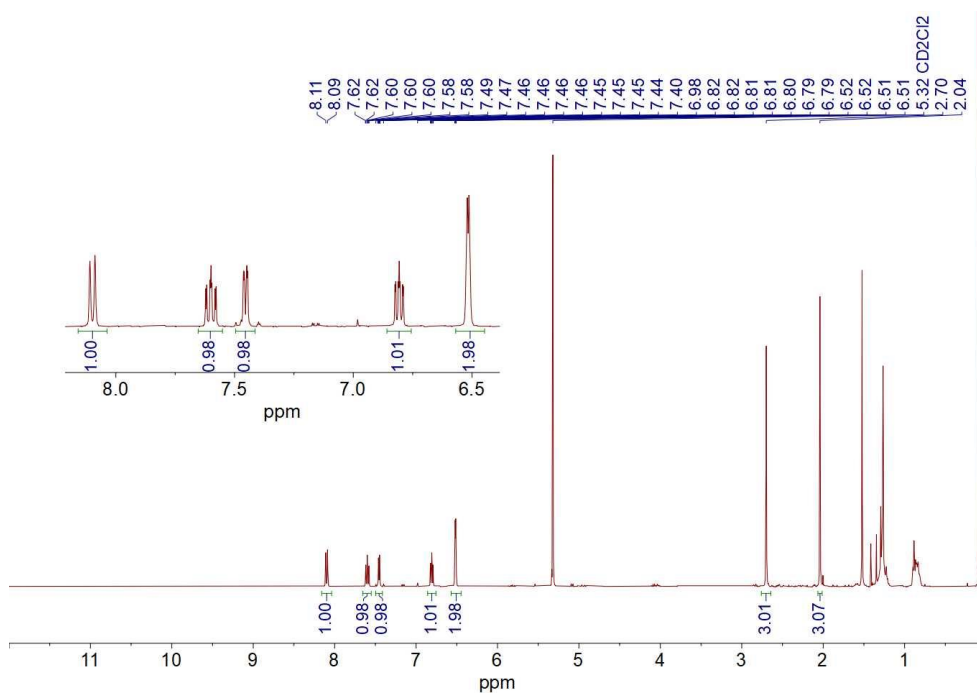
¹H NMR (400 MHz, acetone-d₆, 298 K) spectrum of dichlorotetrakis(2-(2,4-dimethoxyphenyl)pyridyl)diiridium(III).



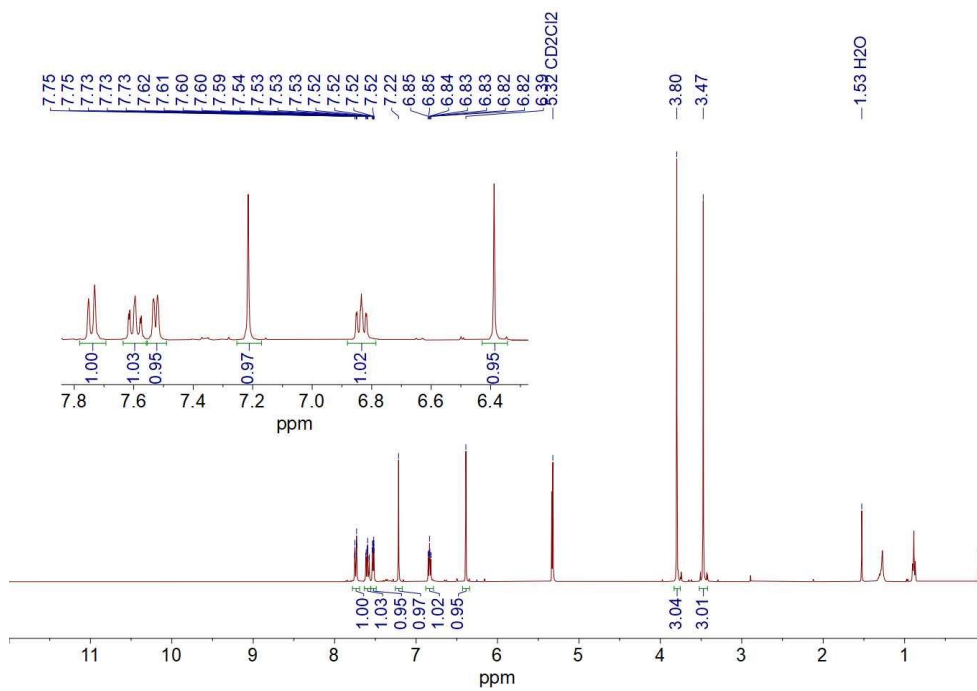
¹H NMR (400 MHz, acetone-d₆, 298 K) spectrum of dichlorotetrakis(2-(3-methoxyphenyl)pyridyl)diiridium(III).



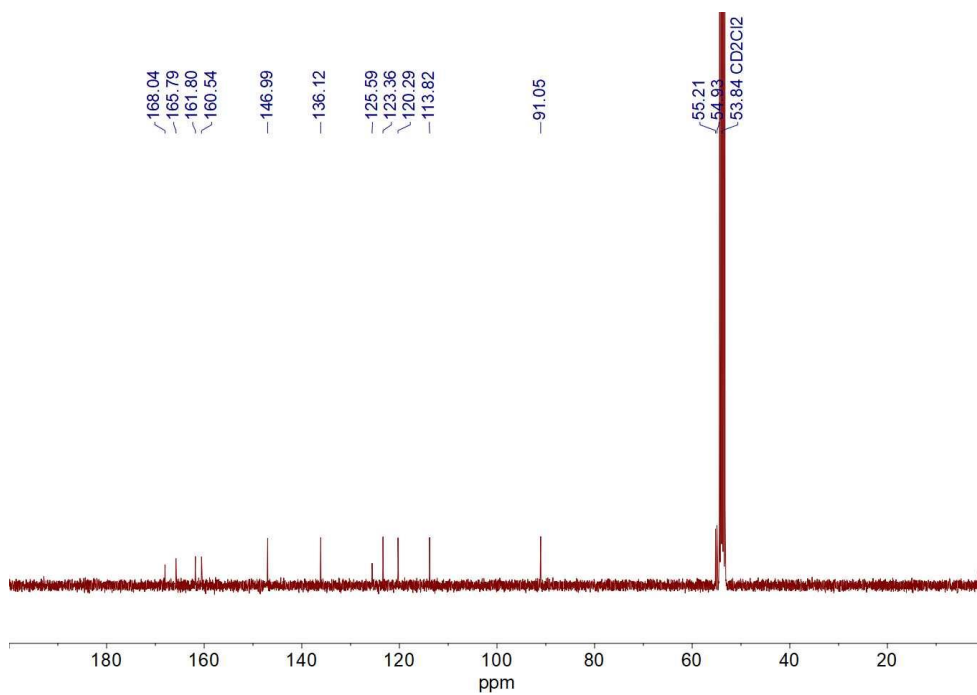
¹H NMR (400 MHz, CDCl₃, 298 K) spectrum of dichlorotetrakis(2-(3,4-dimethoxyphenyl)pyridyl)diiridium(III)



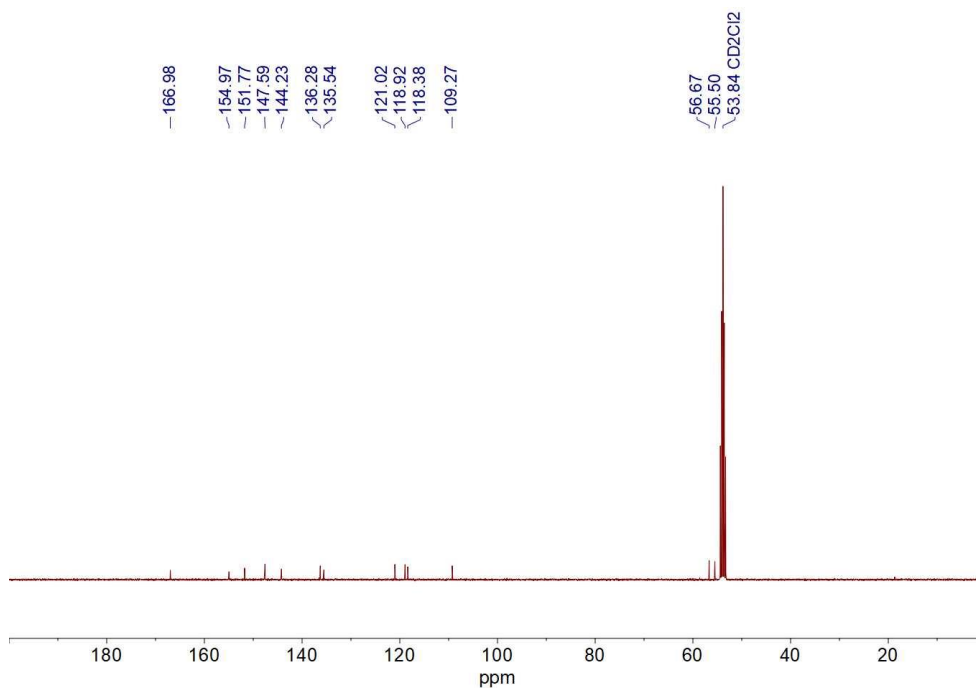
¹H NMR (400 MHz, CD₂Cl₂, 298 K) spectrum of *fac*-2,4-Me



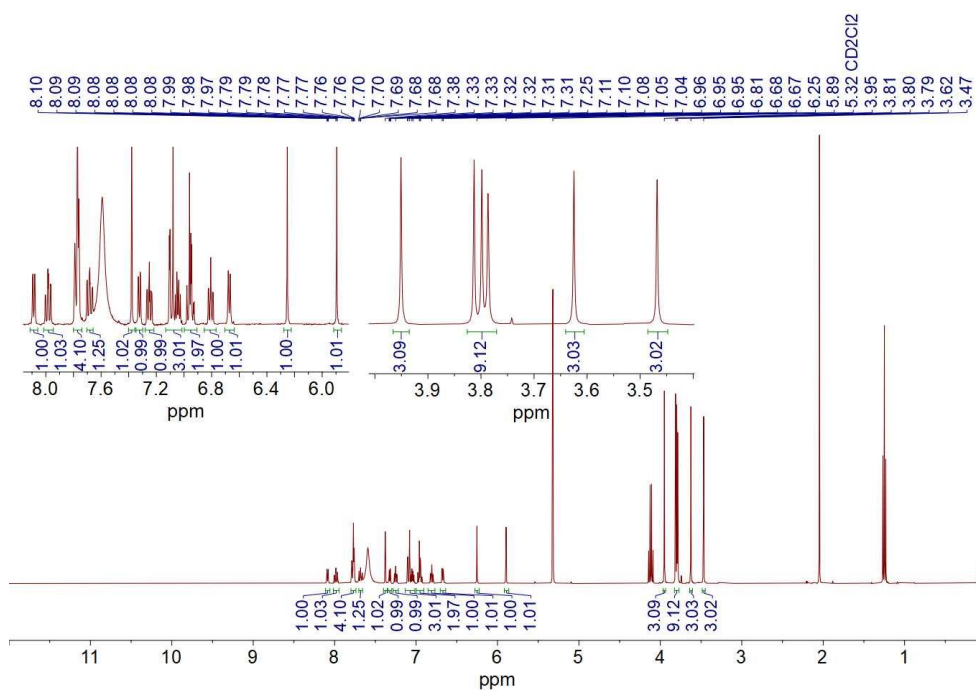
¹H NMR (400 MHz, CD₂Cl₂, 298 K) spectrum of *fac*-2,4-OMe



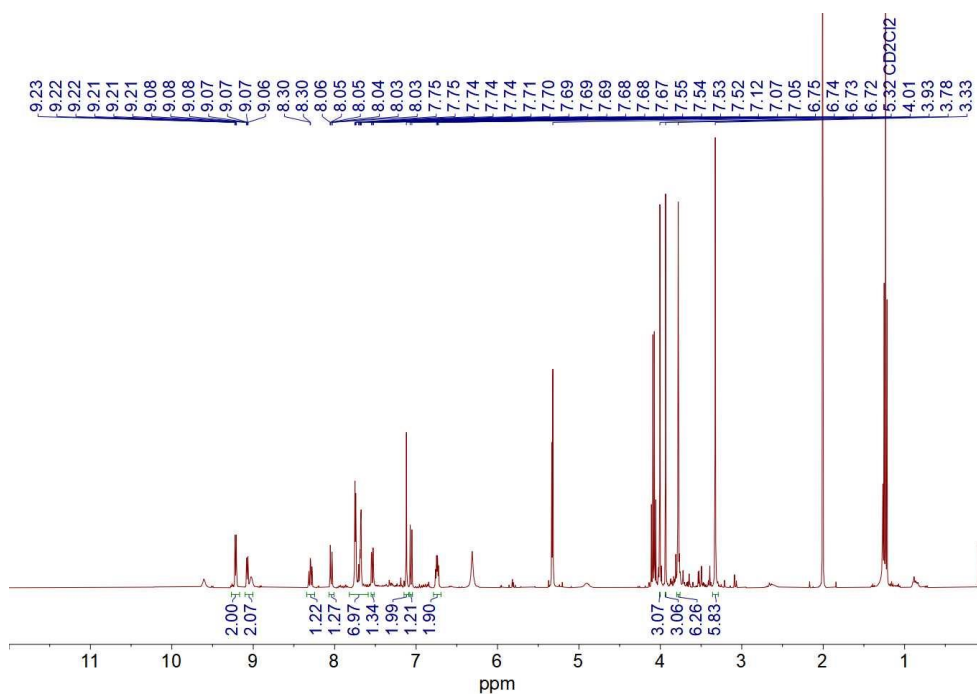
¹³C NMR (101 MHz, CD₂Cl₂, 298 K) spectrum of *fac*-2,4-OMe



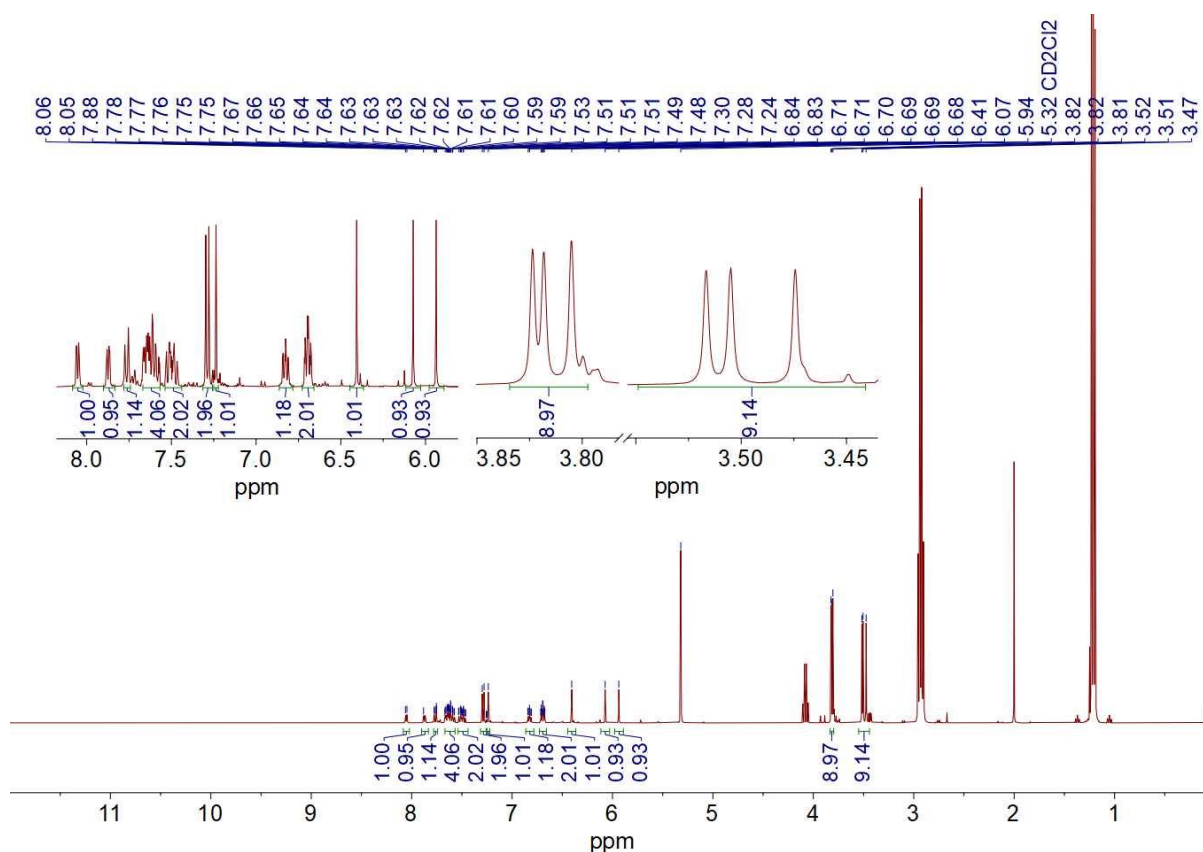
¹³C NMR (101 MHz, CD₂Cl₂, 298 K) spectrum of *fac*-3,4-OMe



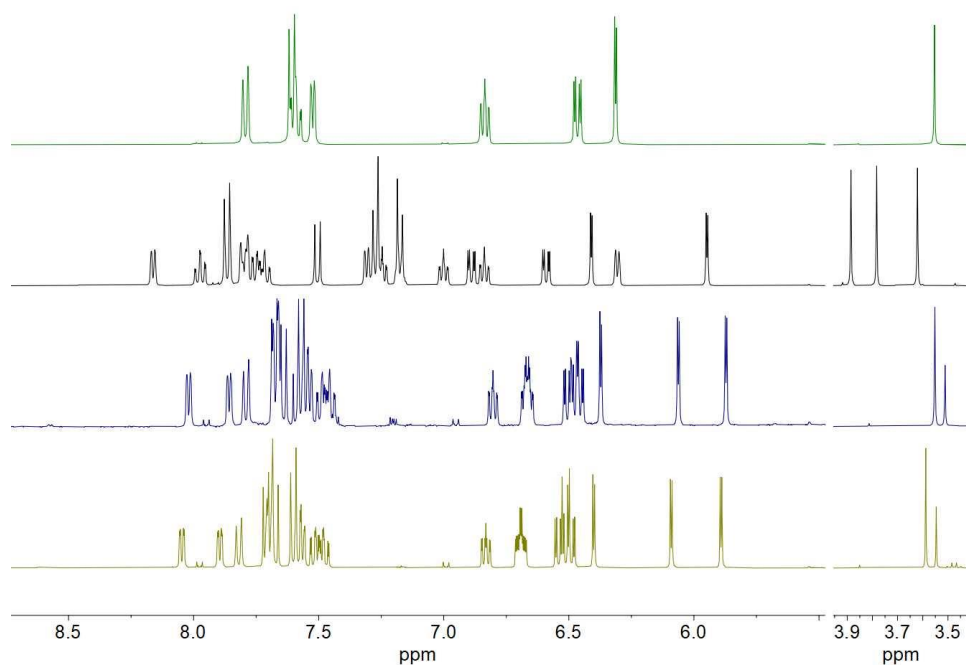
¹H NMR (400 MHz, CD₂Cl₂, 298 K) spectrum of [Ir(3,4-OMe)₂(H_{3,4}-OMe)](CF₃CO₂)



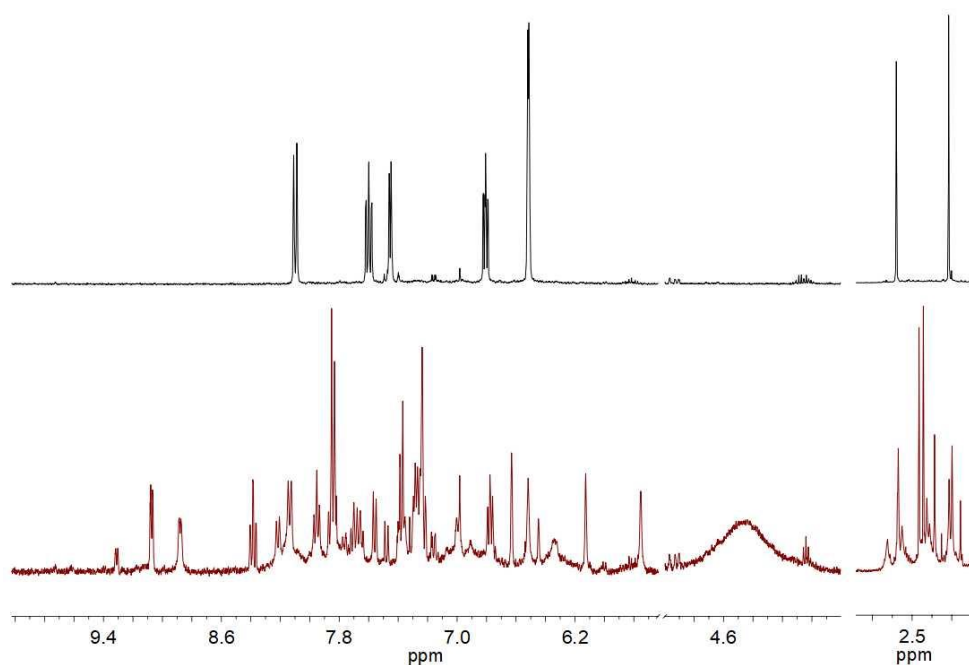
^1H NMR (400 MHz, CD_2Cl_2 , 298 K) spectrum of $\text{Ir}(\text{3,4-OMe})_2(\text{H}_{3,4}\text{-OMe})(\text{CCl}_3\text{CO}_2)$



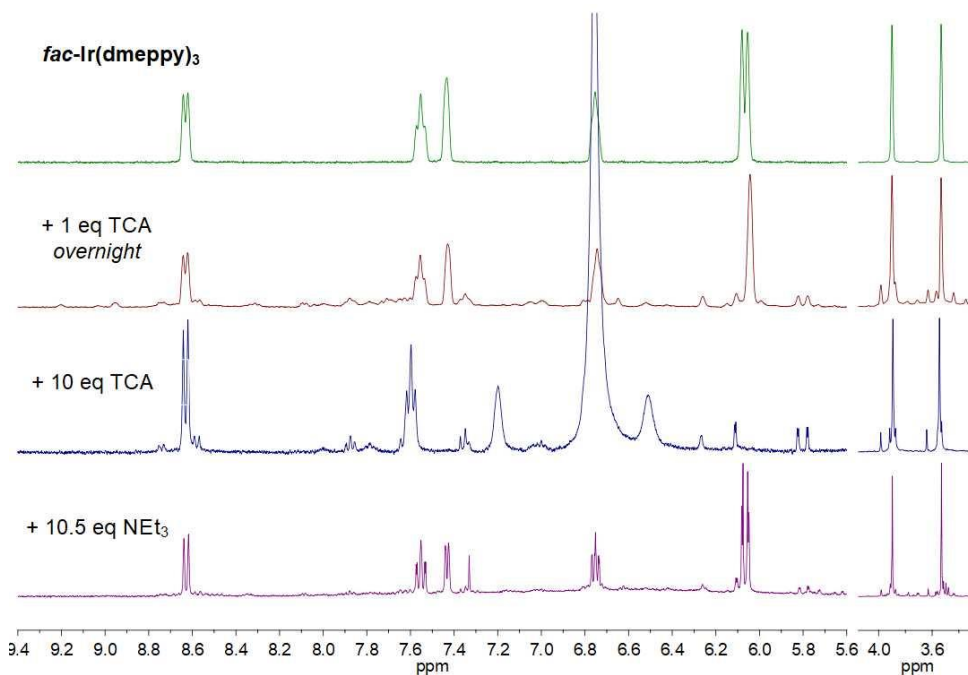
^1H NMR (400 MHz, CD_2Cl_2 , 298 K) spectrum of *mer*-3,4-OMe obtained from *fac*-3,4-OMe using General Procedure for acid-base *fac* \rightarrow *mer* isomerization



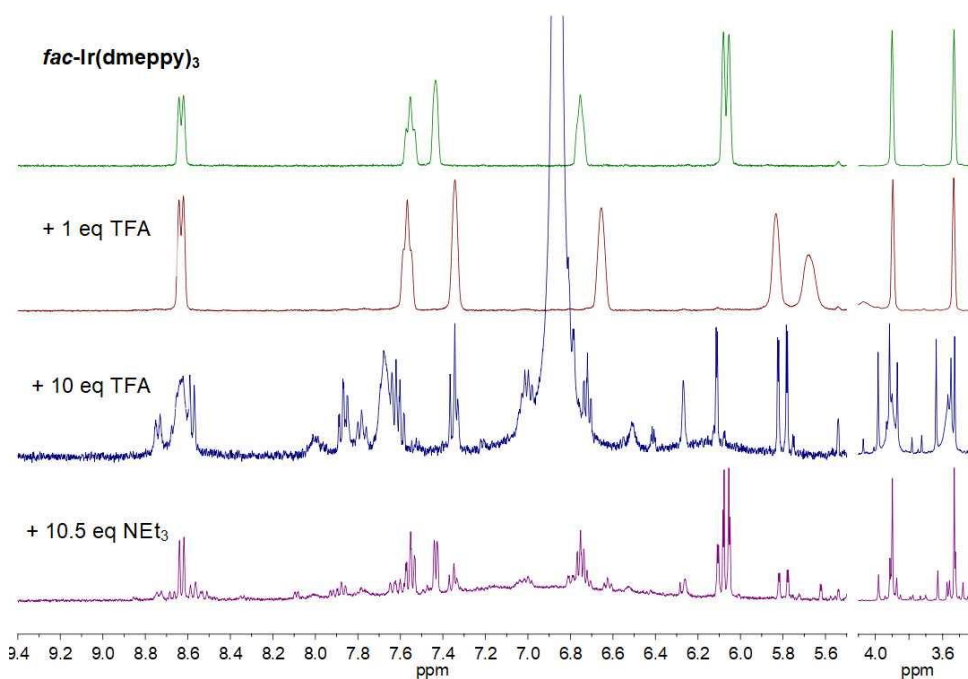
^1H NMR (400 MHz, 298 K) spectra for *fac*-Ir(meppy)₃ and *mer*-Ir(meppy)₃ in CD₂Cl₂ in CD₂Cl₂ (spectra in green and yellow, respectively), and after sequential addition of 10 equiv. HO₂CCCl₃ (spectrum in black) and 10.5 equiv. NEt₃ (spectrum in navy) to *fac*-Ir(meppy)₃



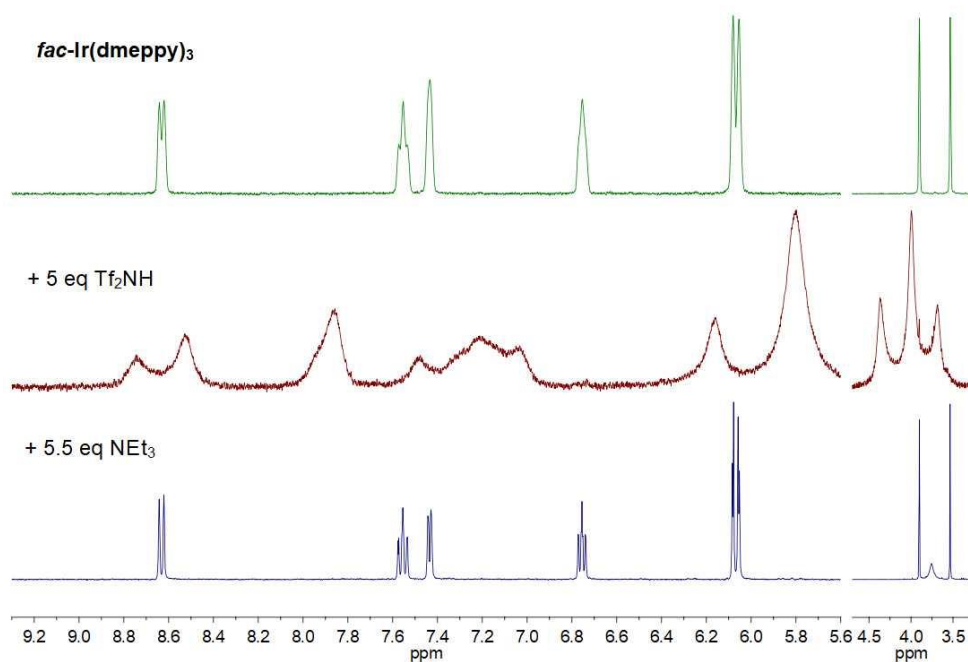
^1H NMR (400 MHz, 298 K) spectra for *fac*-2,4-Me in CD₂Cl₂ (spectrum in black) and after addition of 1 equiv. HO₂CCCl₃ (spectrum in maroon)



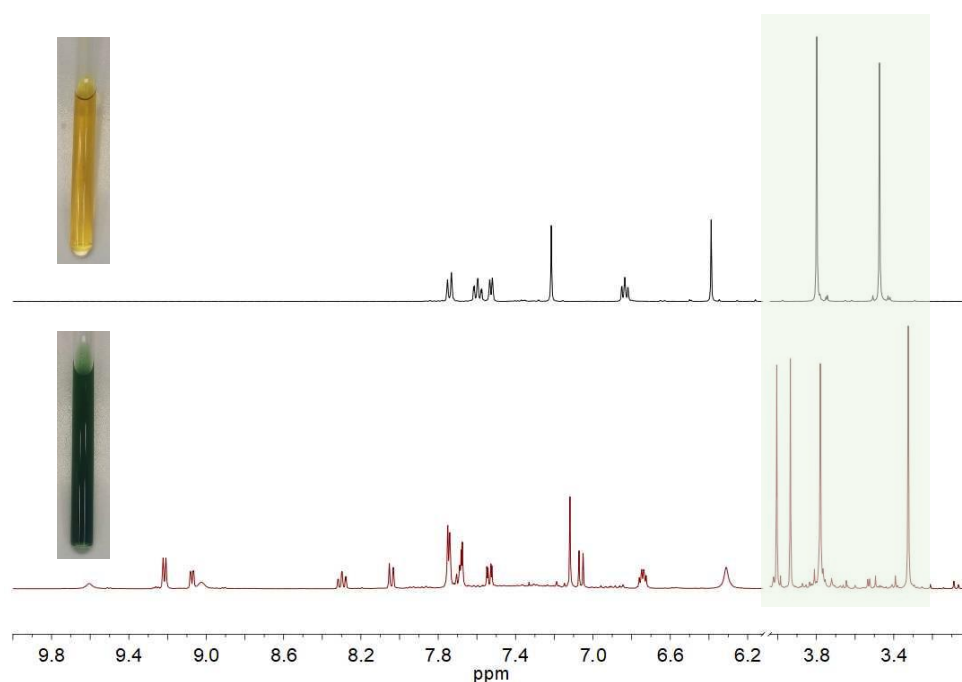
¹H NMR (400 MHz, 298 K) spectra for *fac-2,4-OMe* in CD₂Cl₂ (spectrum in green), after addition of 1 equiv. (spectrum in orange) and 10 equiv. (spectrum in navy) HO₂CCl₃, and after the following addition of 10.5 equiv. NEt₃ (spectrum in purple)



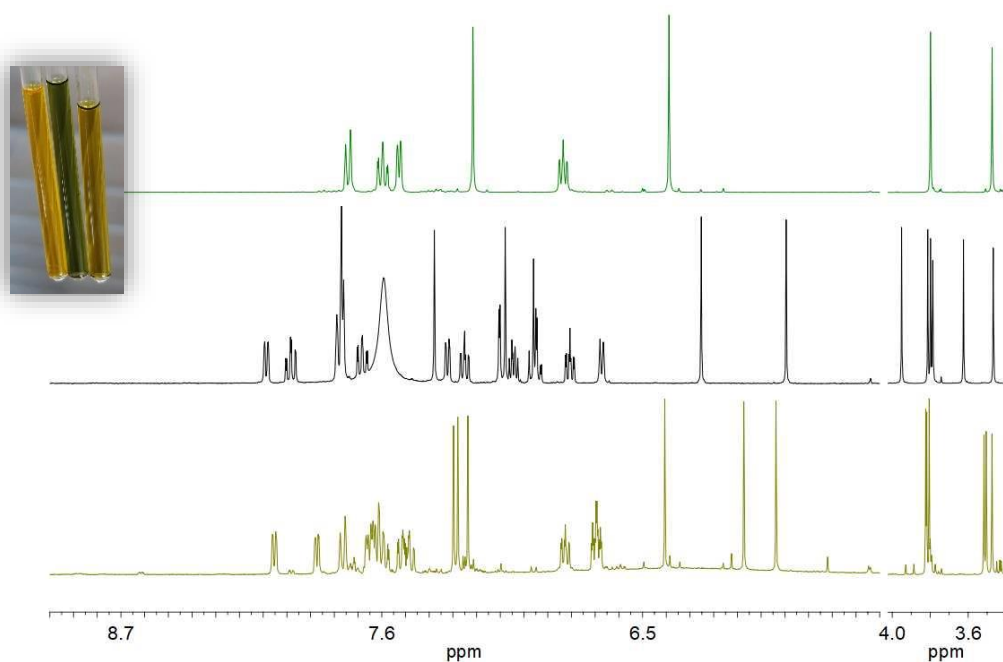
¹H NMR (400 MHz, 298 K) spectra for *fac-2,4-OMe* in CD₂Cl₂ (spectrum in green), after addition of 1 equiv. (spectrum in orange) and 10 equiv. (spectrum in navy) TFA, and after the following addition of 10.5 equiv. NEt₃ (spectrum in purple)



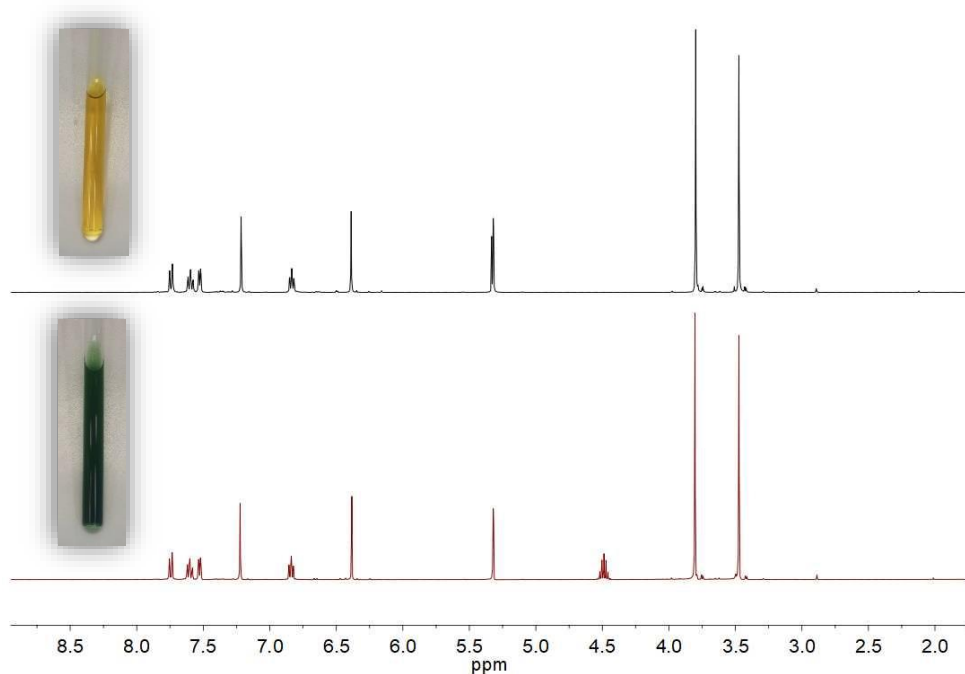
¹H NMR (400 MHz, 298 K) spectra for *fac*-2,4-OMe in CD₂Cl₂ (spectrum in green), after addition of 5 equiv. HNTf₂ (spectrum in maroon), and after the following addition of 5.5 equiv. NEt₃ (spectrum in navy)



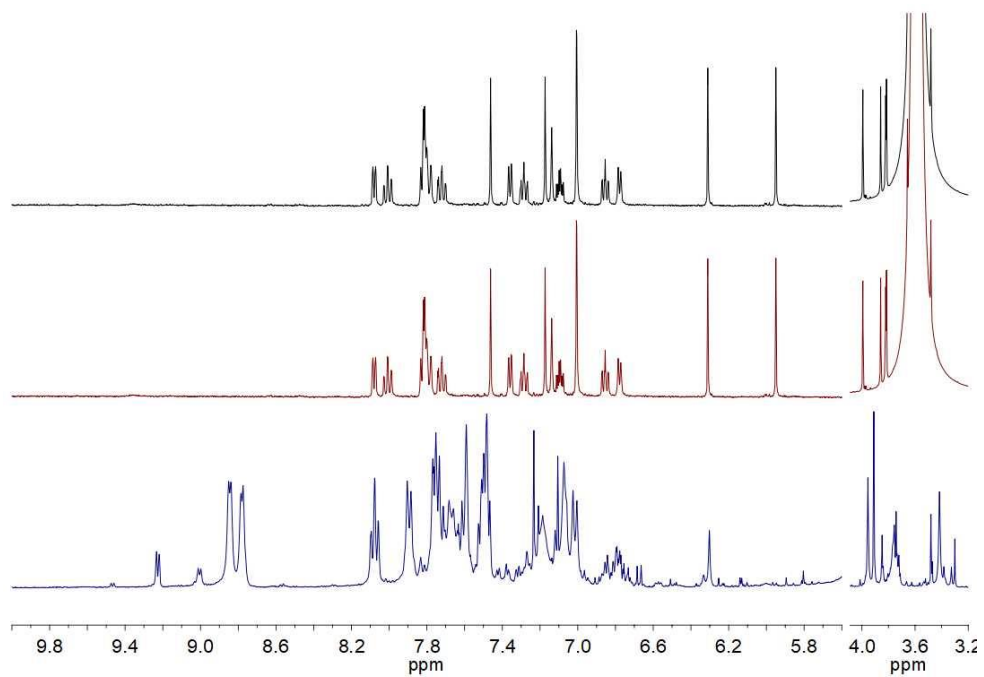
¹H NMR (400 MHz, 298 K) spectra for *fac*-3,4-OMe in CD₂Cl₂ (spectrum in black) and after addition of 1 equiv. HNTf₂ (spectrum in maroon) with photos of samples and ratio of integral intensity in aliphatic region



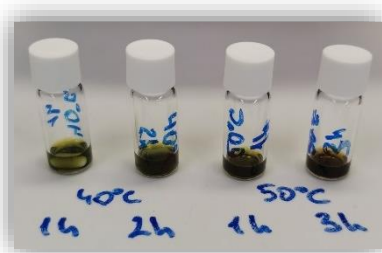
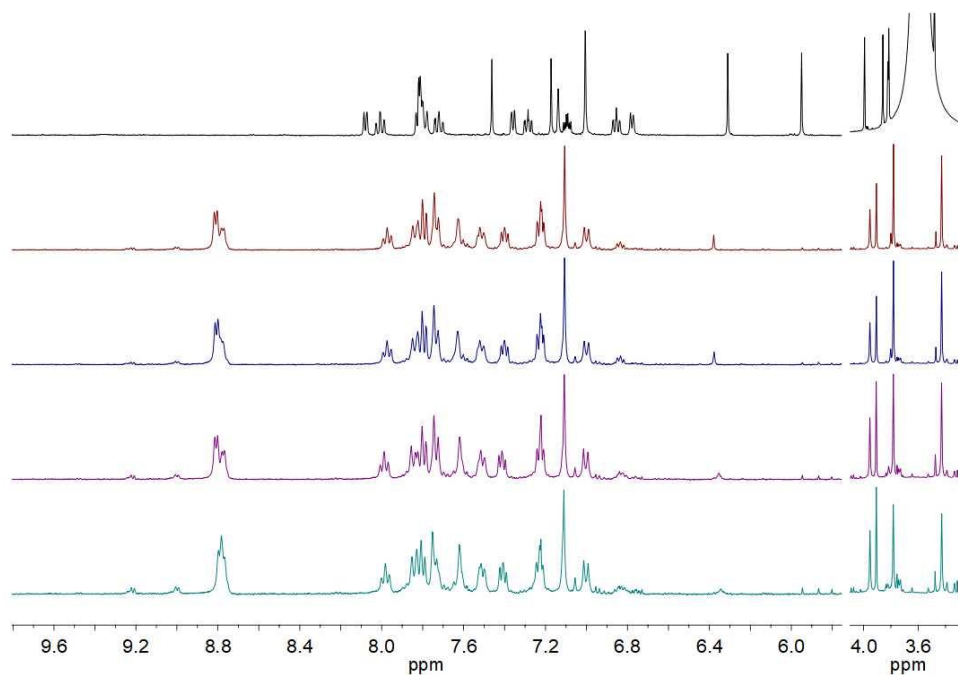
^1H NMR (400 MHz, 298 K) spectra for *fac*-3,4-OMe in CD_2Cl_2 (spectrum in green), after addition of 5 equiv. TFA (spectrum in black), and after the following addition of 5.5 equiv. NEt_3 (spectrum in yellow) showing *fac*→*mer* isomerization of *fac*-3,4-OMe. Inset: photos of samples corresponding to the spectra (from left to right, respectively)



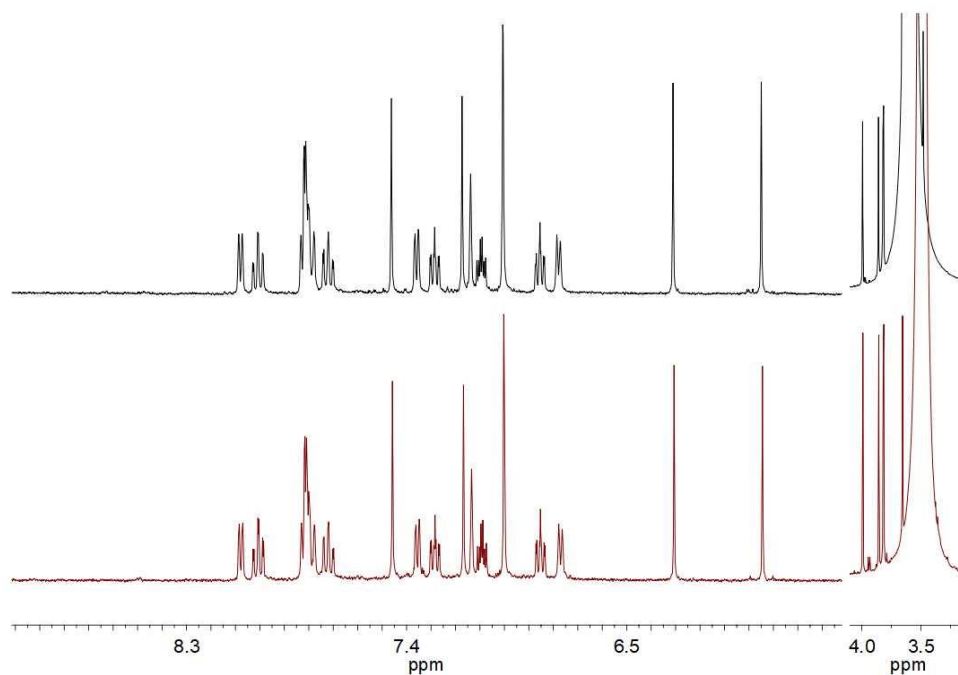
^1H NMR (400 MHz) spectra for *fac*-3,4-OMe in CD_2Cl_2 (spectrum in black) and in HFIP-d_2 (spectrum in maroon) with photos of samples showing strong solvatochromism



Evolution of ^1H NMR (400 MHz, CD_2Cl_2 locked, 298 K) spectrum of the 'open form' obtained by the addition of 1 equiv. HO_2CCCl_3 to *fac*-3,4-OMe in HFIP- d_2 : 1 day (spectrum in black), 2 days (spectrum in maroon), and 7 days (spectrum in navy) provided to follow if decarboxylation of trichloroacetate anion happens



Top: ¹H NMR (400 MHz, CD₂Cl₂ locked, 298 K) spectra for the heating of the 'open form' obtained by the addition of 1 equiv. HO₂CCCl₃ to *fac*-3,4-OMe in HFIP-d₂ (spectrum in black): 40 °C for 1 h (spectrum in maroon) and 2 h (spectrum in navy), 50 °C for 1 h (spectrum in purple) and 3 h (spectrum in teal) attempted to facilitate decarboxylation of trichloroacetate anion. Bottom: photos of samples.

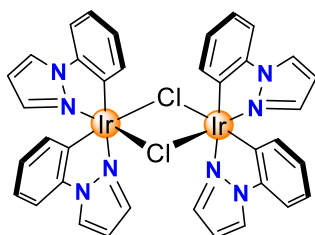


^1H NMR (400 MHz, CD_2Cl_2 locked, 298 K) spectrum of the 'open form' obtained by the addition of 1 equiv. HO_2CCCl_3 to *fac*-3,4-OMe in HFIP- d_2 (spectrum in black) and after addition of 10 mol.% NEt_3 (spectrum in maroon) attempted to facilitate decarboxylation of trichloroacetate anion

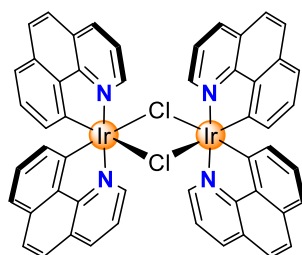
6.3.17 Attempted *fac*→*mer* Isomerization of Other Ir Complexes

1-phenylpyrazole (Hppz), benzo[*h*]quinoline (Hbzq) and 2,2'-bipyridine (Hbpy) were purchased from chemical suppliers and used as received. 2-(benzo[*b*]thiophen-2-yl)pyridine (Hbtpy) was synthesized following the conditions for Suzuki-Miyaura cross-coupling reaction using the published procedure.²³³ The ^1H NMR spectrum of the obtained ligand is in agreement with the published one.

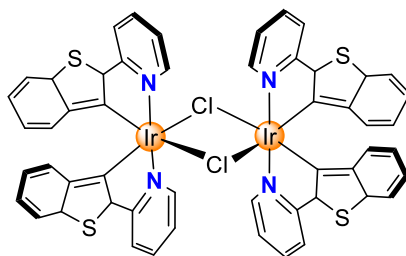
The chloro-bridged dimers $[\text{Ir}(\text{C}^{\wedge}\text{N})_2(\mu\text{-Cl})_2]$ were obtained following the procedure described by B. Orwat and co-workers for the microwave synthesis of the complexes $[\text{Ir}(\text{ppy})_2(\mu\text{-Cl})_2]$ and $[\text{Ir}(\text{dfppy})_2(\mu\text{-Cl})_2]$ with some modifications (for procedure details, see subchapter 6.3.2).¹¹⁰



Dichlorotetrakis(1-phenylpyrazolyl)diiridium(III). Obtained from $\text{IrCl}_3 \cdot x\text{H}_2\text{O}$ (500 mg, 1.42 mmol) and 1-phenylpyrazole (511 mg, 3.55 mmol). White powder, 600 mg (82%). ^1H NMR (400 MHz, acetone- d_6 , 298 K) δ 8.71 (dd, $J = 2.9, 0.8$ Hz, 1H), 7.81 (dd, $J = 2.2, 0.7$ Hz, 1H), 7.40 (dd, $J = 7.8, 1.3$ Hz, 1H), 6.87 (dd, $J = 2.9, 2.1$ Hz, 1H), 6.75 (td, $J = 7.6, 1.3$ Hz, 1H), 6.48 (td, $J = 7.4, 1.3$ Hz, 1H), 5.94 (dd, $J = 7.6, 1.3$ Hz, 1H). ^{13}C NMR (101 MHz, acetone- d_6 , 298 K) δ 206.1, 144.5, 141.2, 133.3, 128.7, 128.1, 125.7, 122.5, 111.6, 107.7. The NMR data are in agreement with those reported in the literature.²³⁴

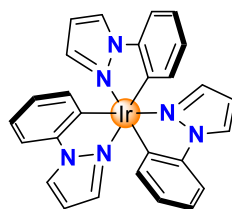


Dichlorotetrakis(benzo[*h*]quinoliny)diiridium(III). Obtained from $\text{IrCl}_3 \cdot x\text{H}_2\text{O}$ (500 mg, 1.42 mmol) and benzo[*h*]quinoline (559 mg, 3.12 mmol). Yellow powder, 828 mg (81%). ^1H NMR (400 MHz, CD_2Cl_2 , 298 K) δ 9.39 (dd, $J = 5.3, 1.3$ Hz, 1H), 8.36 (dd, $J = 8.1, 1.4$ Hz, 1H), 7.83 – 7.75 (m, 2H), 7.33 – 7.19 (m, 2H), 6.85 (t, $J = 7.6$ Hz, 1H), 5.91 (dd, $J = 7.5, 0.9$ Hz, 1H). The NMR data is in agreement with what reported in the literature.²³⁵



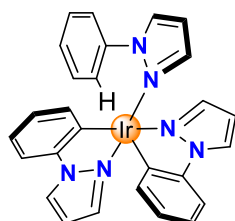
Dichlorotetrakis(2-(benzo[b]thiophen-2-yl)pyridyl)diiridium(III). Obtained from $\text{IrCl}_3 \cdot x\text{H}_2\text{O}$ (200 mg, 0.57 mmol) and 2-(benzo[b]thiophen-2-yl)pyridine (263 mg, 1.25 mmol). Red powder, 365 mg (quant). Used further without characterization.

fac-Ir(ppz)₃, *mer*-Ir(bzq)₃ and *mer*-Ir(btpy)₃ were obtained following the standard conditions for the synthesis of facial isomers of homoleptic iridium(III) complexes from the corresponding chloro-bridged dimers in glycerol (for procedure details, see subchapter 6.3.2).¹⁰³ *fac*-Ir(bzq)₃ and *fac*-Ir(btpy)₃ were synthesized from *mer*-Ir(bzq)₃ and *mer*-Ir(btpy)₃ by thermal *mer*-to-*fac* isomerization in presence of phenol using the conditions described by G. van Koten and co-workers (for procedure details, see subchapter 6.3.2).¹⁷⁸ [Ir(ppy)₂(bpy)]PF₆ was synthesized from [Ir(ppy)₂(μ-Cl)]₂, Hbpy and KPF₆ following the published procedure.²³⁶



fac-Ir(ppz)₃

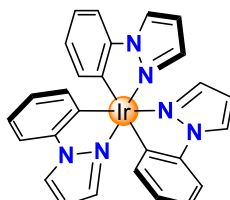
fac-Ir(ppz)₃. Obtained by the conventional method from dichlorotetrakis(1-phenylpyrazolyl)diiridium(III) (200 mg, 0.20 mmol) and 1-phenylpyrazole (70.0 mg, 0.49 mmol). White crystals, 242 mg (74%). *Note: the compound is piezoelectric, do not grind!* ¹H NMR (400 MHz, CD₂Cl₂, 298 K) δ 8.05 (dd, *J* = 2.8, 0.7 Hz, 1H), 7.29 – 7.19 (m, 1H), 7.04 (dd, *J* = 2.1, 0.7 Hz, 1H), 6.92 (ddd, *J* = 7.9, 6.3, 2.5 Hz, 1H), 6.79 – 6.69 (m, 2H), 6.46 (dd, *J* = 2.7, 2.1 Hz, 1H). The NMR data is in agreement with what reported in the literature.¹⁰³



[Ir(ppz)₂(Hppz)](NTf₂)

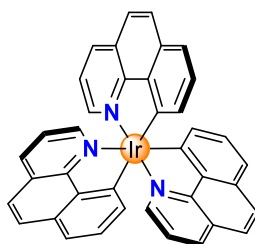
[Ir(ppz)₂(Hppz)](NTf₂). A solution of the open form was obtained upon addition of HNTf₂ (11.3 mg, 40.3 μmol, 5.0 equiv.) to a solution of *fac*-Ir(ppz)₃ (5.00 mg, 8.01 μmol, 1.0

equiv.) in 0.5 mL of CD₂Cl₂. ¹H NMR (400 MHz, CD₂Cl₂, 298 K) δ 8.36 (dd, *J* = 3.0, 0.9 Hz, 1H), 8.20 (t, *J* = 2.8 Hz, 3H), 8.05 (d, *J* = 2.4 Hz, 2H), 7.71 – 7.65 (m, 3H), 7.62 (qd, *J* = 4.1, 2.4 Hz, 2H), 7.21 (dd, *J* = 8.0, 1.3 Hz, 2H), 6.98 (t, *J* = 2.9 Hz, 1H), 6.96 – 6.91 (m, 2H), 6.85 (t, *J* = 2.6 Hz, 2H), 6.68 (td, *J* = 7.5, 1.3 Hz, 2H), 6.07 (d, *J* = 7.7 Hz, 2H).



mer-Ir(ppz)₃

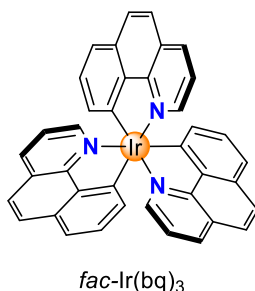
mer-Ir(ppz)₃. Obtained from *fac*-Ir(ppz)₃ (50.0 mg, 0.08 mmol) by the acid-base *fac*→*mer* isomerization *via* sequential addition of HNTf₂ (226 mg, 0.81 mmol) and NEt₃ (122 mg, 168 μL, 1.21 mmol) with following work-up and purification. White powder, 27 mg (54%). ¹H NMR (400 MHz, CD₂Cl₂, 298 K) δ 8.06 (d, *J* = 2.7 Hz, 1H), 8.04 – 7.96 (m, 2H), 7.36 – 7.31 (m, 1H), 7.28 (dd, *J* = 7.9, 1.1 Hz, 1H), 7.23 (dd, *J* = 7.9, 1.3 Hz, 1H), 7.12 (d, *J* = 2.1 Hz, 1H), 7.03 – 6.93 (m, 4H), 6.93 – 6.81 (m, 4H), 6.77 (td, *J* = 7.4, 1.3 Hz, 2H), 6.51 – 6.30 (m, 4H). The NMR data is in agreement with what reported in the literature.¹⁰³



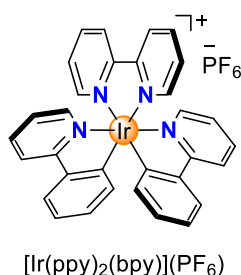
mer-Ir(bq)₃

mer-Ir(bzq)₃. Obtained by the conventional method from dichlortetrakis(benzo[*h*]quinolyl)diiridium(III) (400 mg, 0.34 mmol), benzo[*h*]quinoline (153 mg, 0.86 mmol) and K₂CO₃ (473 mg, 3.43 mmol). Red powder, 404 mg (81%). ¹H NMR (400 MHz, CD₂Cl₂, 298 K) δ 8.32 (dd, *J* = 5.4, 1.4 Hz, 1H), 8.20 (dd, *J* = 5.1, 1.5 Hz, 1H), 8.13 (dd, *J* = 8.1, 1.7 Hz, 1H), 8.03 (ddd, *J* = 13.8, 8.0, 1.4 Hz, 2H), 7.87 – 7.80 (m, 5H), 7.65 – 7.56 (m, 3H), 7.51 – 7.44 (m, 2H), 7.40 (t, *J* =

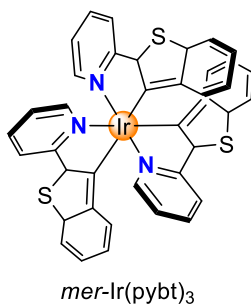
6.9 Hz, 1H), 7.31 – 6.99 (m, 8H), 6.82 (dd, $J = 6.9, 1.1$ Hz, 1H), 6.57 (dd, $J = 7.4, 0.9$ Hz, 1H).



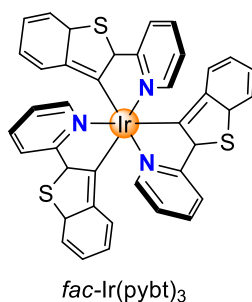
fac-Ir(bzq)₃. Obtained from *mer*-Ir(bzq)₃ (100 mg, 0.14 mmol) by refluxing in phenol. Red powder, 100 mg (quant). ¹H NMR (400 MHz, CD₂Cl₂, 298 K) δ 8.13 (dd, $J = 8.0, 1.4$ Hz, 1H), 7.88 – 7.79 (m, 2H), 7.60 (m, 1H), 7.39 (d, $J = 6.7$ Hz, 1H), 7.22 (dd, $J = 8.0, 5.1$ Hz, 1H), 7.12 (m, 1H), 6.86 (d, $J = 7.1$ Hz, 1H). The NMR data is in agreement with what reported in the literature.²³⁷



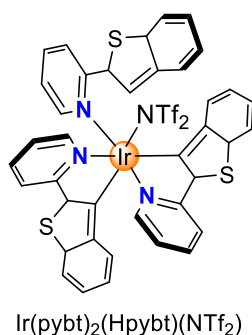
[Ir(ppy)₂(bpy)]PF₆. Obtained from [Ir(ppy)₂(μ -Cl)]₂ (134 mg, 0.13 mmol), Hbpy (43 mg, 0.28 mmol) and KPF₆ (230 mg, 1.25 mmol). Yellow powder, 198 mg (quant.). ¹H NMR (400 MHz, CD₂Cl₂, 298 K) δ 8.66 (dt, $J = 8.2, 1.1$ Hz, 1H), 8.15 (td, $J = 7.9, 1.6$ Hz, 1H), 8.06 – 7.92 (m, 2H), 7.85 – 7.70 (m, 2H), 7.54 – 7.42 (m, 2H), 7.08 (td, $J = 7.5, 1.2$ Hz, 1H), 7.03 – 6.90 (m, 2H), 6.32 (dd, $J = 7.6, 1.2$ Hz, 1H). The NMR data is in agreement with what reported in the literature.²³⁶



mer-Ir(btpy)₃. Obtained by the conventional method from dichlorotetrakis(2-(2-pyridyl)benzothiophenyl)diiridium(III) (365 mg, 0.28 mmol), 2-(2-pyridyl)benzothiophene (150 mg, 0.71 mmol) and K₂CO₃ (972 mg, 7.05 mmol). Red powder, 376 mg (81%). ¹H NMR (400 MHz, CD₂Cl₂, 298 K) δ 8.01 (dt, *J* = 5.8, 1.3 Hz, 1H), 7.86 – 7.74 (m, 3H), 7.72 (dt, *J* = 5.6, 1.2 Hz, 2H), 7.69 – 7.48 (m, 6H), 7.21 – 7.03 (m, 3H), 6.84 (ddt, *J* = 8.2, 7.0, 1.1 Hz, 2H), 6.77 (ddd, *J* = 6.5, 5.6, 2.4 Hz, 1H), 6.74 – 6.60 (m, 3H), 6.52 (dd, *J* = 8.0, 1.1 Hz, 1H), 6.25 – 6.14 (m, 2H).

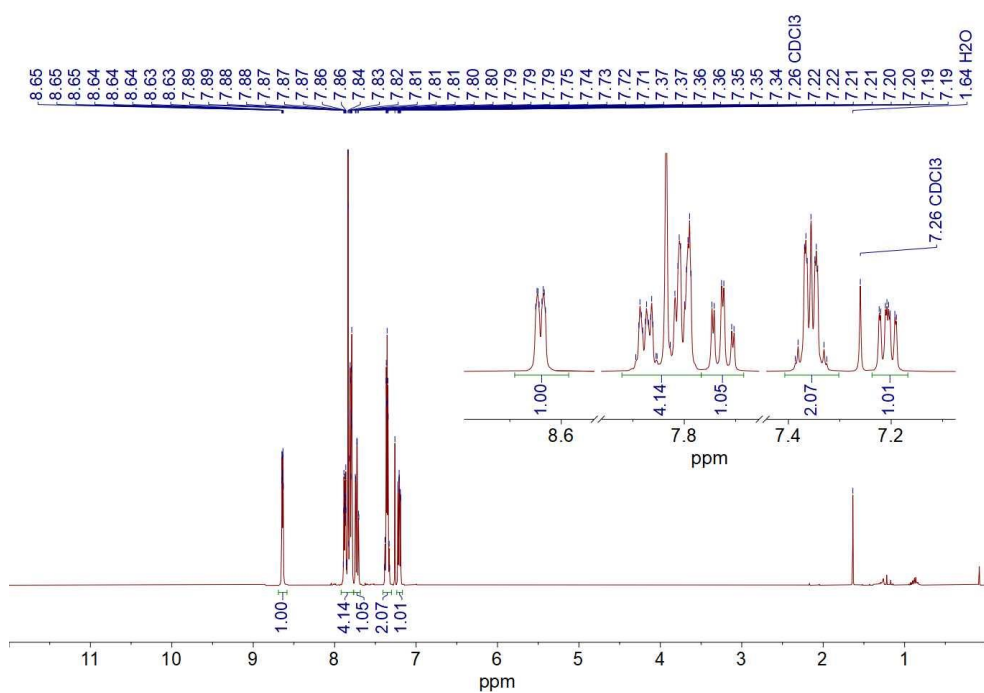


fac-Ir(btpy)₃. Obtained from *mer*-Ir(btpy)₃ (100 mg, 0.12 mmol) by refluxing in phenol. Red powder, 100 mg (quant). ¹H NMR (400 MHz, CD₂Cl₂, 298 K) δ 7.76 (d, *J* = 8.0 Hz, 1H), 7.58 (d, *J* = 12.4 Hz, 2H), 7.38 (d, *J* = 5.4 Hz, 1H), 7.09 (t, *J* = 7.9 Hz, 1H), 6.84 – 6.75 (m, 1H), 6.65 (d, *J* = 7.6 Hz, 1H), 6.59 (d, *J* = 8.5 Hz, 1H). ¹³C NMR (101 MHz, CD₂Cl₂, 298 K) δ 163.2, 156.9, 148.9, 147.9, 142.8, 137.8, 134.8, 128.7, 125.4, 123.9, 122.59, 120.4, 118.7. The NMR data are in agreement with those reported in the literature.²³⁸

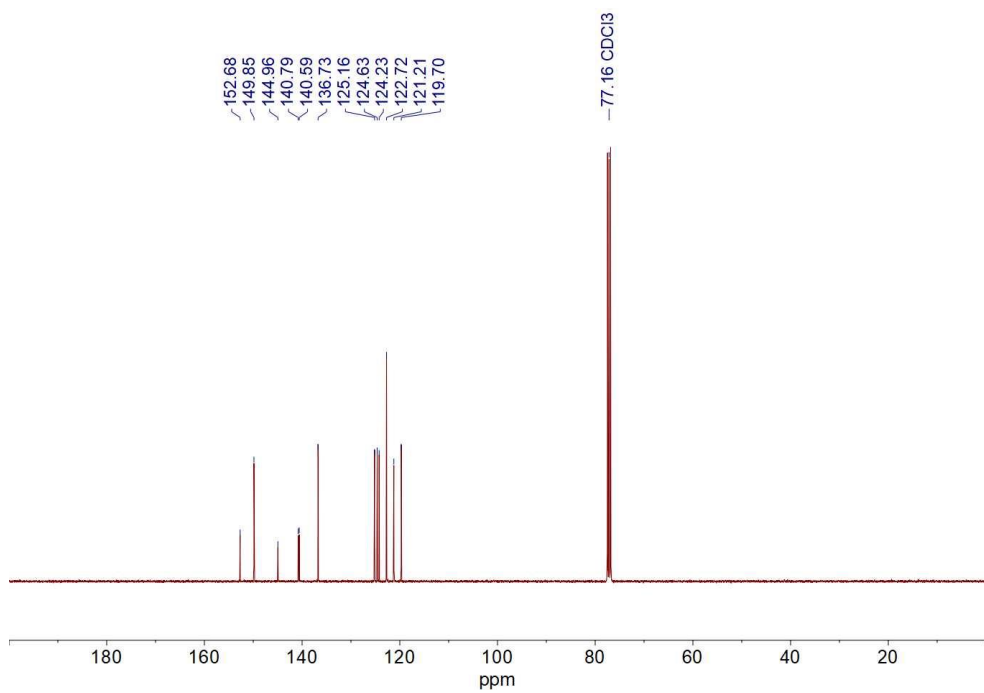


Ir(btpy)₂(Hbtpy)(NTf₂). A solution of the open form was obtained upon addition of a solution of HNTf₂ in CD₂Cl₂ (0.2 M, 125 μL, 24.9 μmol, 5.0 equiv.) to a solution of *fac*-Ir(btpy)₃ (4.1 mg, 5.0 μmol, 1.0 equiv.) in 0.5 mL of CD₂Cl₂. ¹H NMR (400 MHz, CD₂Cl₂, 298 K) δ 8.68 (d, *J* = 8.2 Hz, 1H), 8.22 – 8.11 (m, 2H), 8.06 (d, *J* = 8.1 Hz, 1H), 7.83 – 7.72 (m, 4H), 7.65 (d, *J* = 7.2 Hz, 1H), 7.55 – 7.43 (m, 4H), 7.36 – 7.17 (m, 6H), 7.13

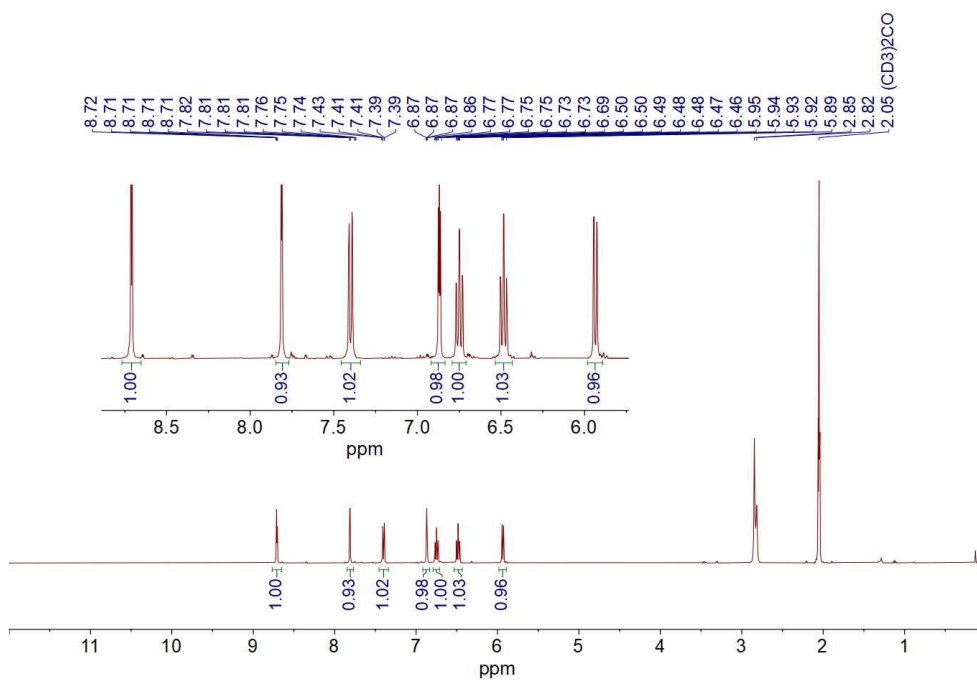
– 7.05 (m, 1H), 6.90 (ddd, $J = 7.2, 5.6, 1.3$ Hz, 1H), 6.84 – 6.76 (m, 2H), 6.63 (dd, $J = 12.3, 8.1$ Hz, 2H).



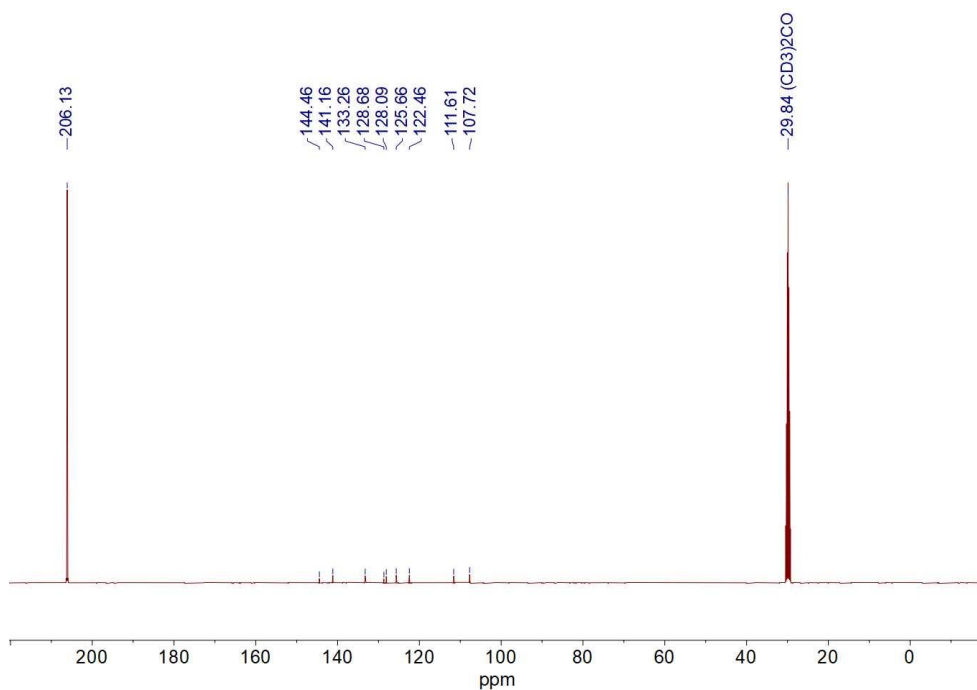
^1H NMR (400 MHz, CDCl_3 , 298 K) spectrum of 2-(benzo[b]thiophen-2-yl)pyridine (Hbtpy)



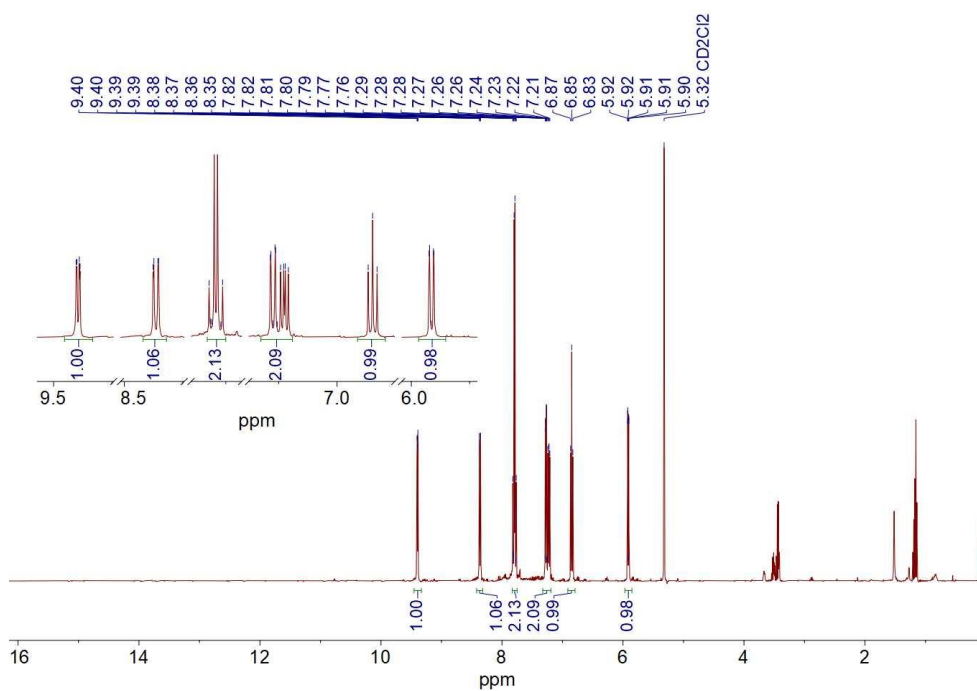
^{13}C NMR (101 MHz, CDCl_3 , 298 K) spectrum of 2-(benzo[b]thiophen-2-yl)pyridine (Hbtpy)



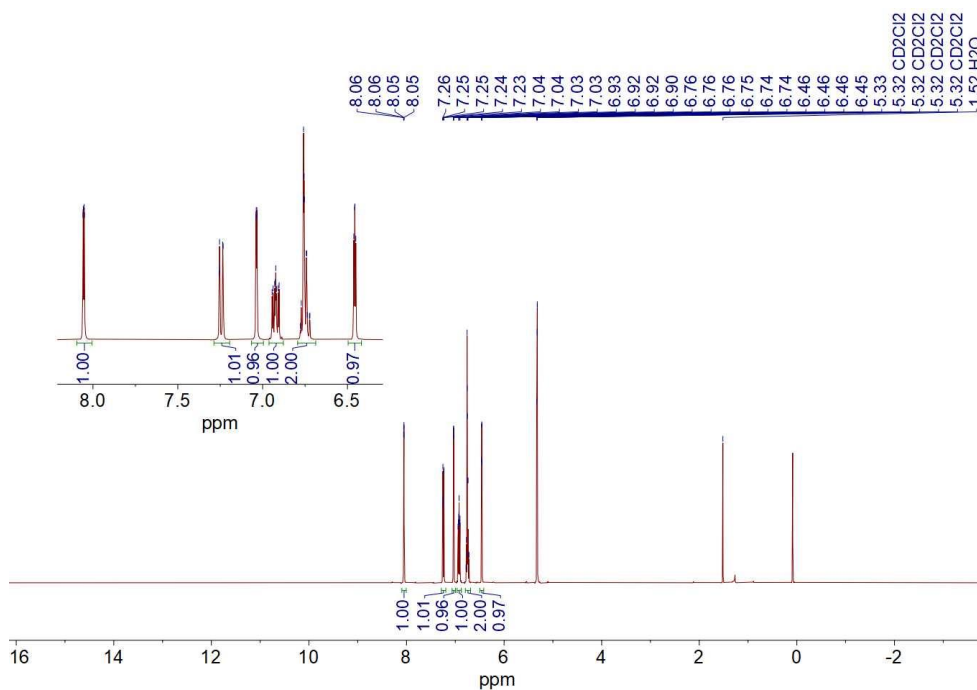
^1H NMR (400 MHz, acetone- d_6 , 298 K) spectrum of dichlorotetrakis(1-phenylpyrazolyl)diiridium(III)



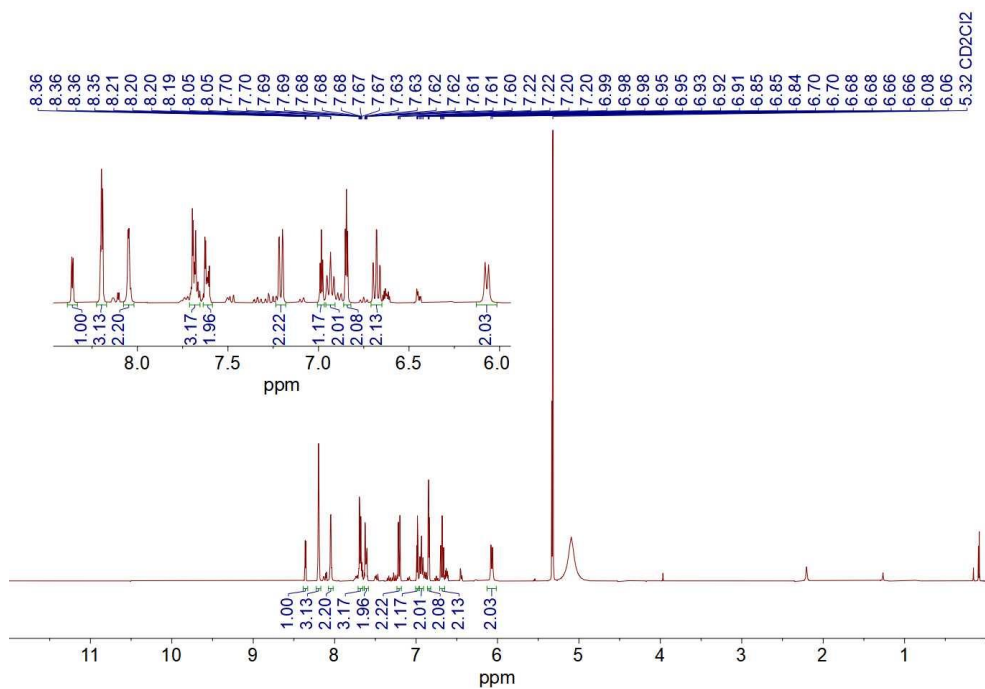
^{13}C NMR (101 MHz, acetone- d_6 , 298 K) spectrum of dichlorotetrakis(1-phenylpyrazolyl)diiridium(III)



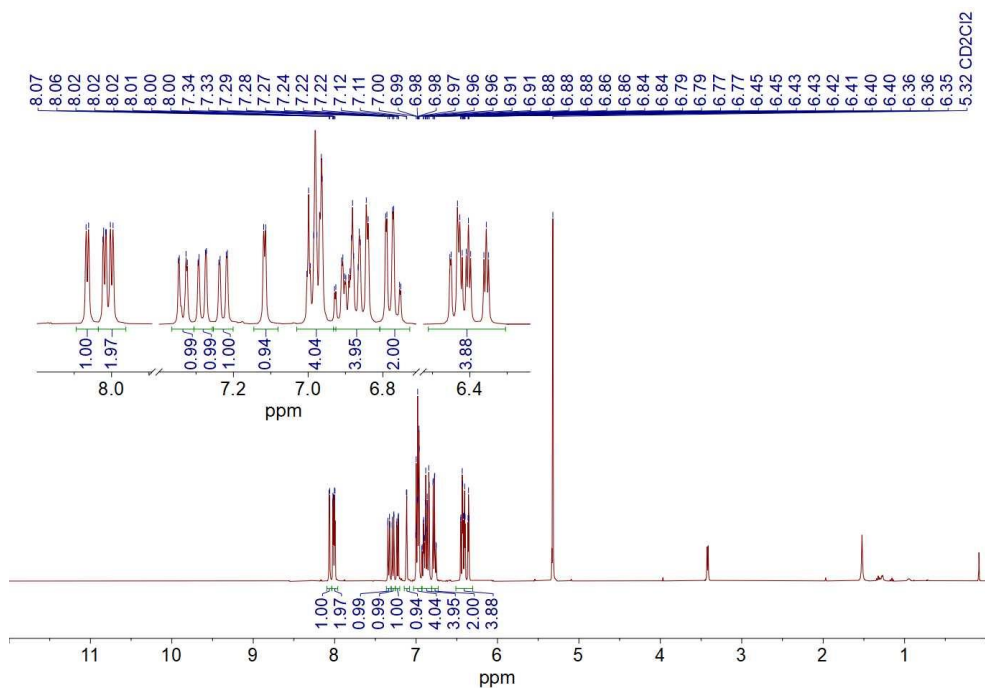
¹H NMR (400 MHz, CD₂Cl₂, 298 K) spectrum of dichlorotetrakis(benzo[*h*]quinolinyl)diiridium(III)



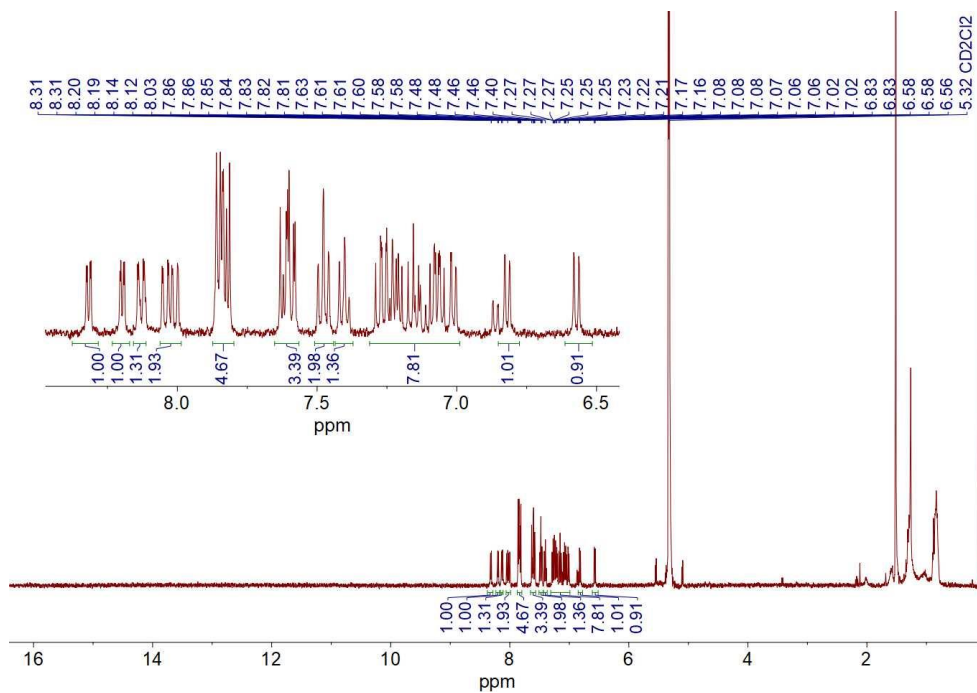
¹H NMR (400 MHz, CD₂Cl₂, 298 K) spectrum of *fac*-Ir(ppz)₃



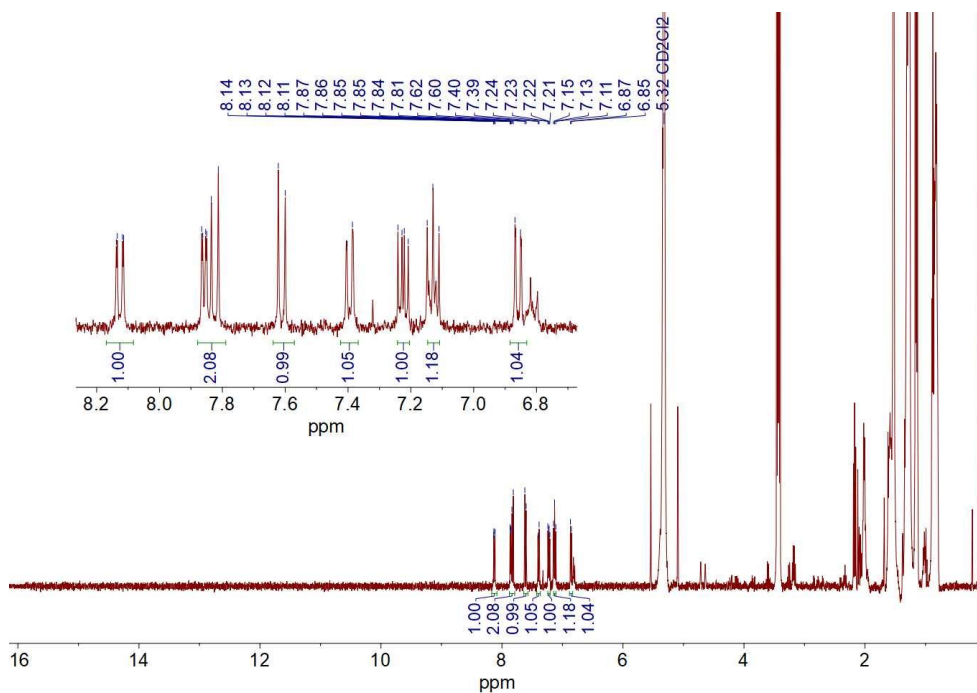
^1H NMR (400 MHz, CD_2Cl_2 , 298 K) spectrum of $[\text{Ir}(\text{ppz})_2(\text{Hppz})](\text{NTf}_2)$



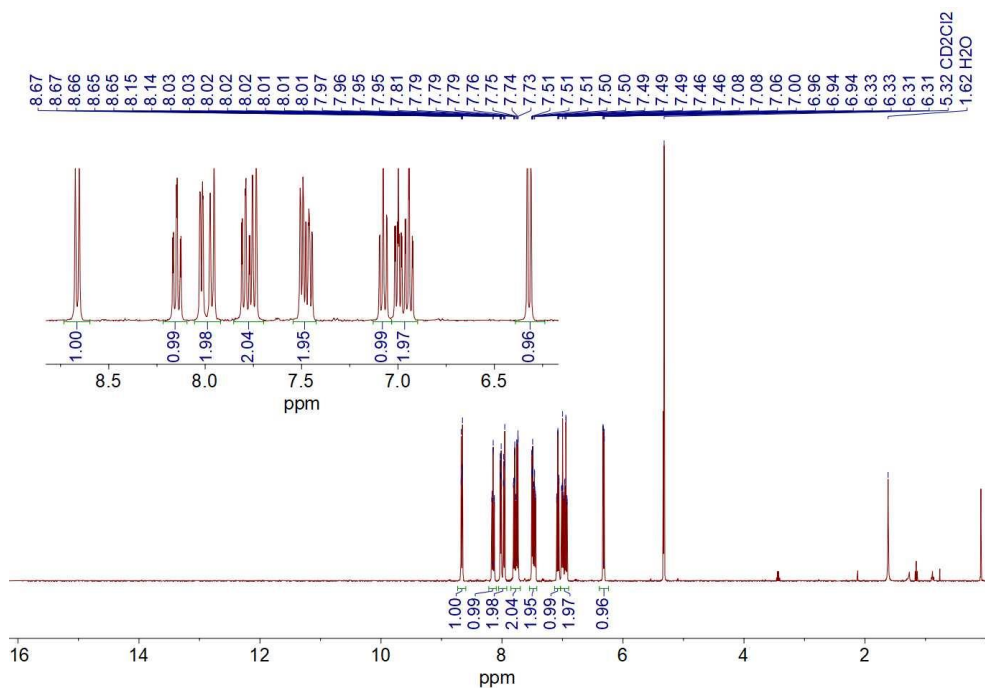
^1H NMR (400 MHz, CD_2Cl_2 , 298 K) spectrum of *mer*- $\text{Ir}(\text{ppz})_3$



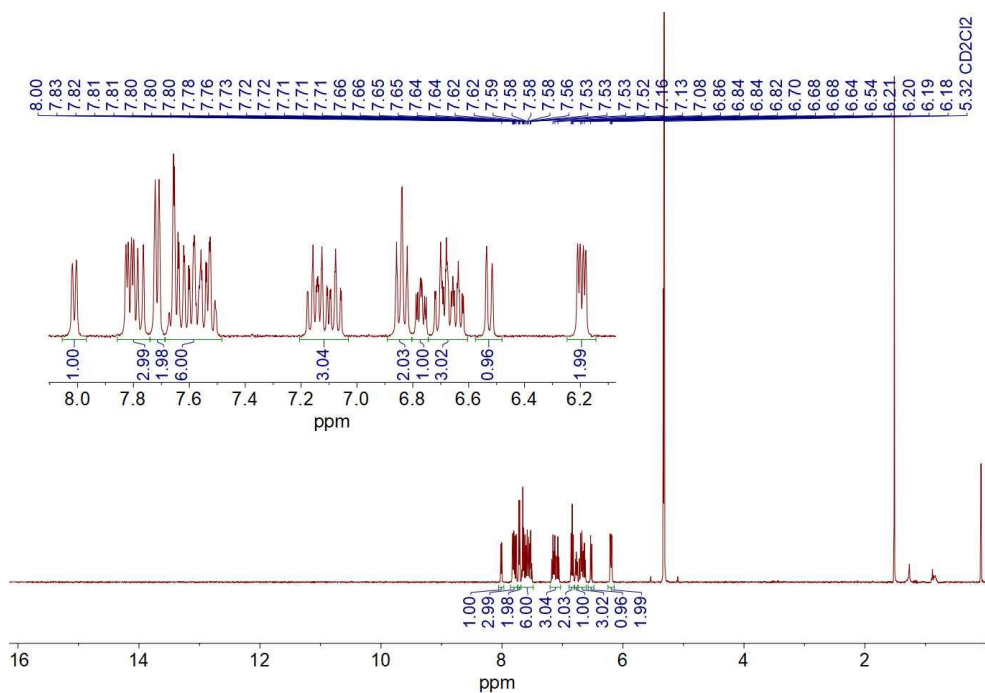
^1H NMR (400 MHz, CD_2Cl_2 , 298 K) spectrum of *mer*-Ir(bzq) $_3$



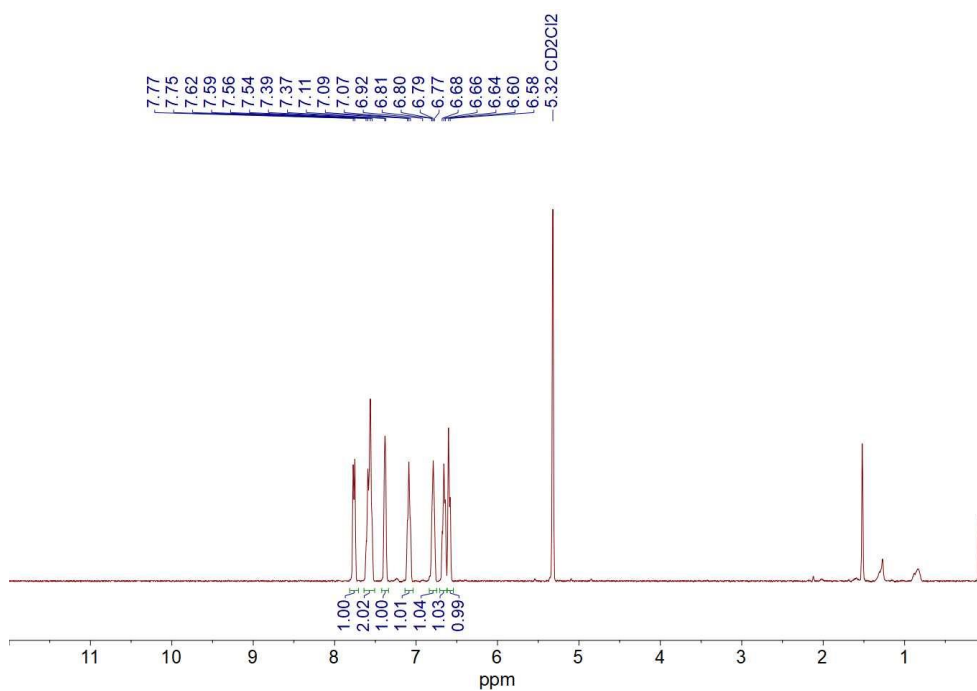
^1H NMR (400 MHz, CD_2Cl_2 , 298 K) spectrum of *fac*-Ir(bzq) $_3$



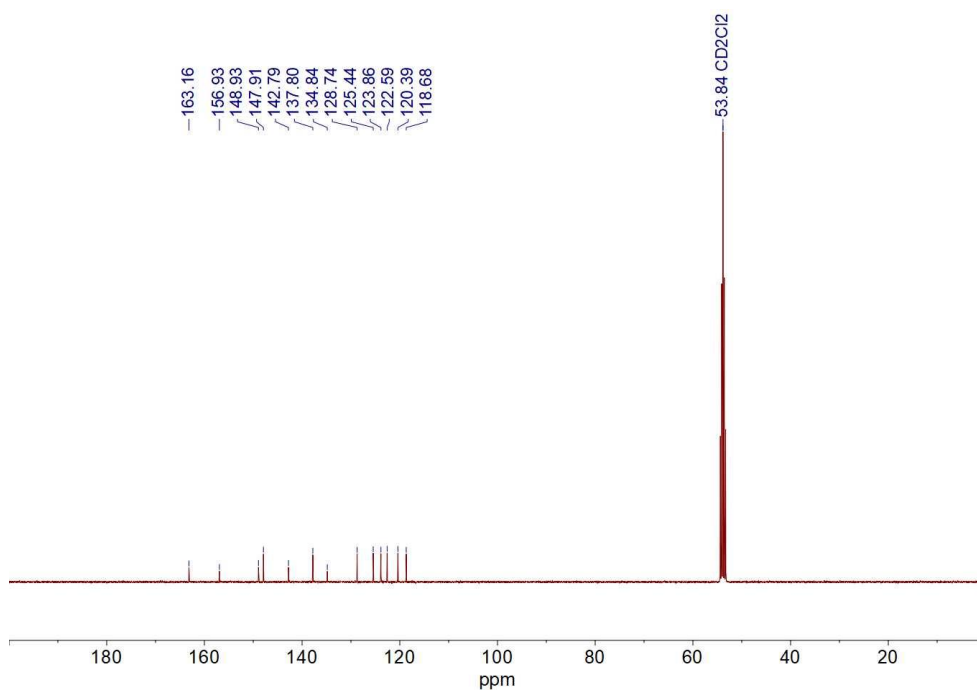
¹H NMR (400 MHz, CD₂Cl₂, 298 K) spectrum of [Ir(ppy)₂(bpy)]PF₆



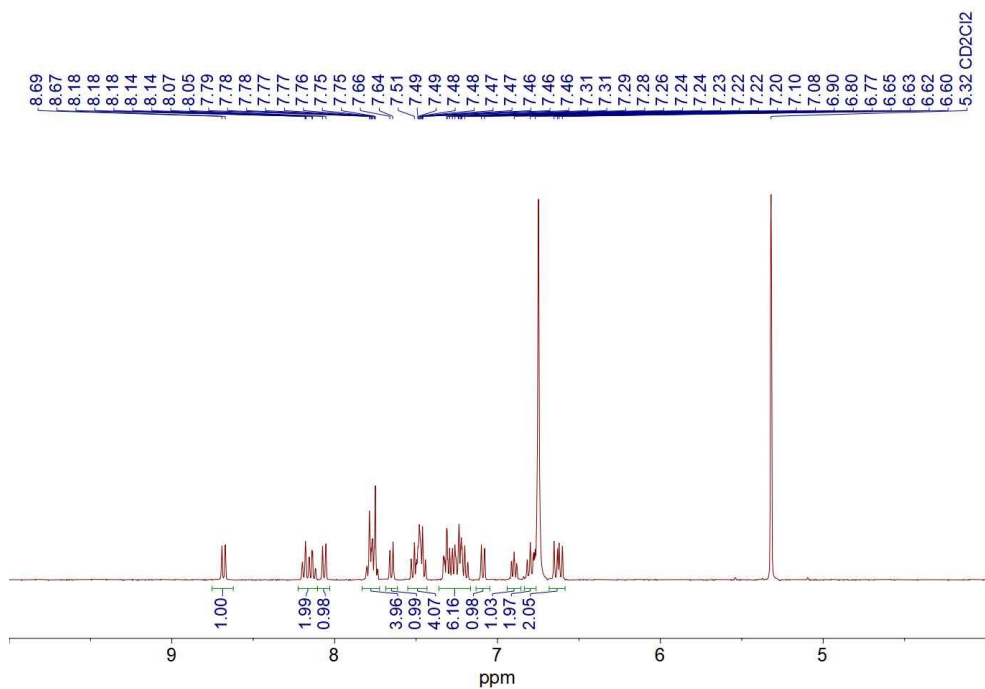
¹H NMR (400 MHz, CD₂Cl₂, 298 K) spectrum of *mer*-Ir(btpy)₃



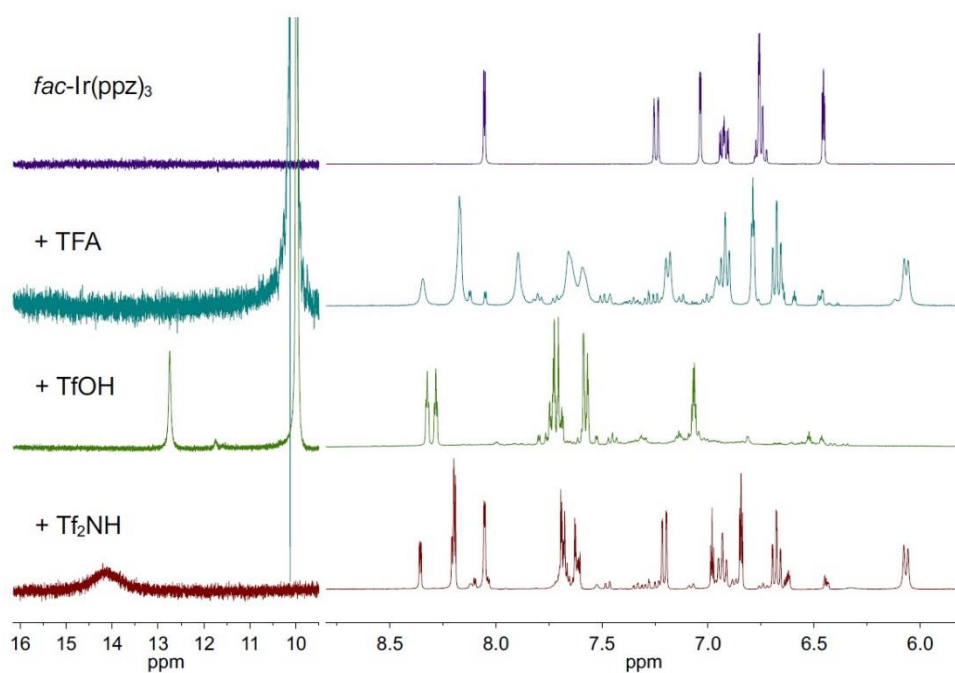
¹H NMR (400 MHz, CD₂Cl₂, 298 K) spectrum of *fac*-Ir(btpy)₃



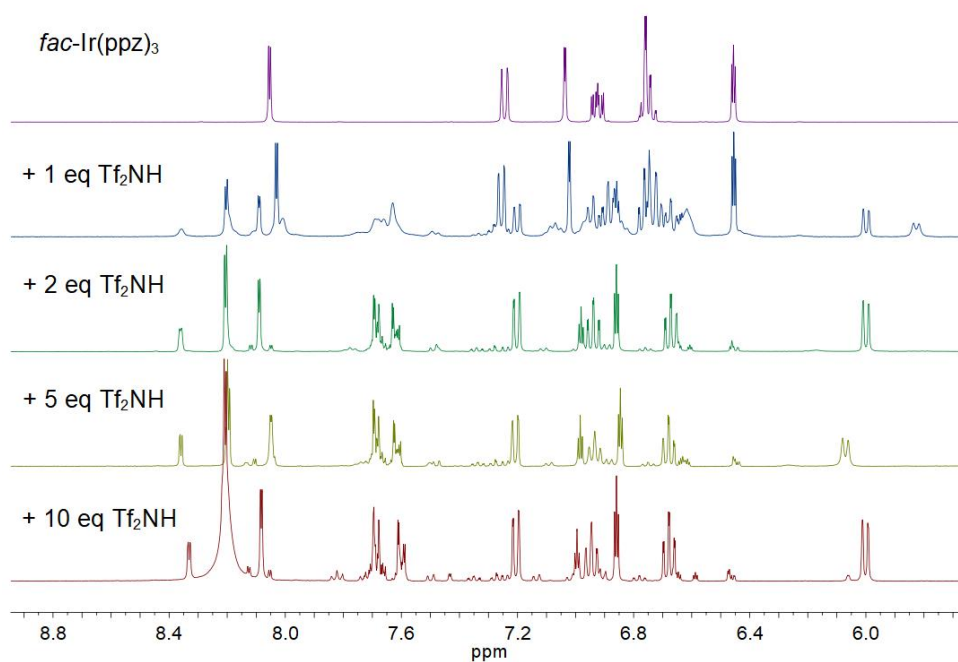
¹³C NMR (101 MHz, CD₂Cl₂, 298 K) spectrum of *fac*-Ir(btpy)₃



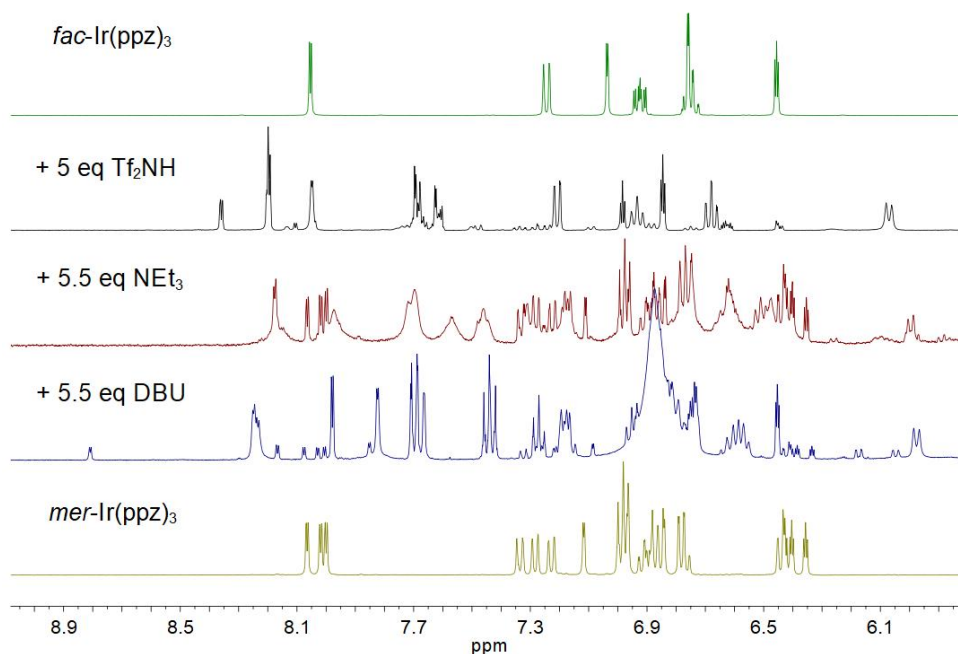
^1H NMR (400 MHz, CD_2Cl_2 , 298 K) spectrum of $\text{Ir}(\text{btpy})_2(\text{Hbtpy})(\text{NTf}_2)$



^1H NMR (400 MHz, 298 K) spectra for $\text{fac-Ir}(\text{ppz})_3$ in CD_2Cl_2 and after addition of 10 equiv. TFA, 10 equiv. HOTf and 5 equiv. HNTf₂



¹H NMR (400 MHz, 298 K) spectra for *fac*-Ir(ppz)₃ in CD₂Cl₂ and after addition of different amount of HNTf₂. Addition of 5 equiv. HNTf₂ was found optimal for conversion to the corresponding 'open form'.

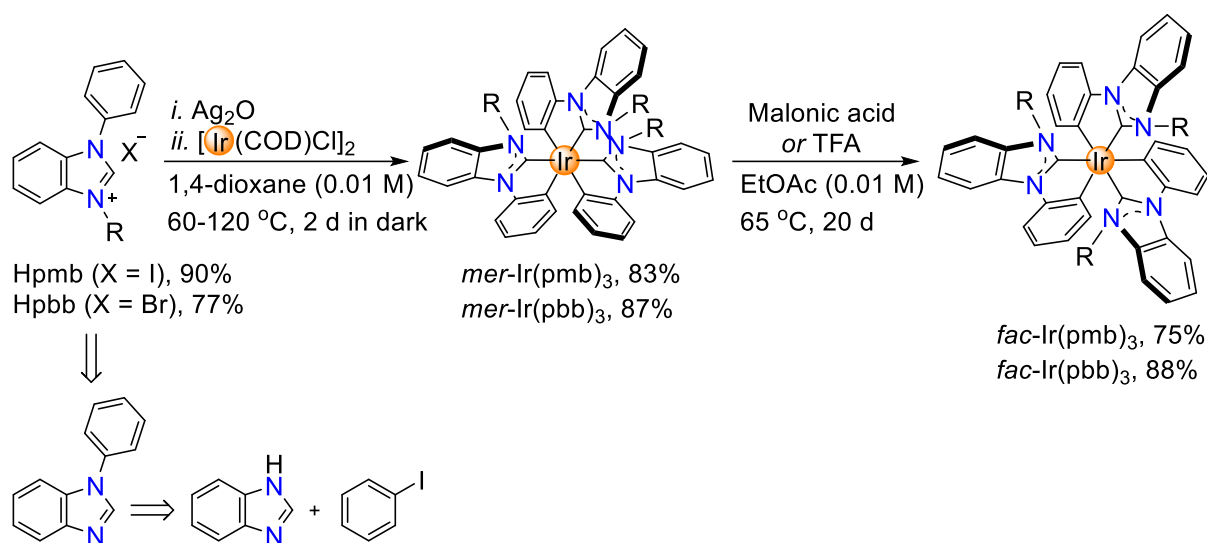


¹H NMR (400 MHz, 298 K) spectra for *fac*-Ir(ppz)₃ in CD₂Cl₂, after addition of 5 equiv. HNTf₂, and after the following addition of NEt₃ and 1,8-diazabicyclo(5.4.0)undec-7-ene (DBU). The use of DBU did not lead to the clean formation of *mer*-Ir(ppz)₃.

6.4 Experimental Part for Chapter 4

6.4.1 Synthesis of Facial Complexes

Facial isomers of complexes $\text{Ir}(\text{pmb})_3$ and $\text{Ir}(\text{pbb})_3$, where pmb is metalated 1-phenyl-3-methylbenzimidazolin-2-ylidene and pbb is 1-phenyl-3-benzylbenzimidazolin-2-ylidene, were prepared following the procedure described by H.-H. Johannes and co-workers with slightly modified conditions.¹³¹



$\text{mer-Ir}(\text{pmb})_3$. Obtained from $[\text{Ir}(\text{COD})\text{Cl}]_2$ (750 mg, 1.12 mmol, 1 equiv.), Ag_2O (1.29 g, 5.58 mmol, 5 equiv.) and Hpmc (3.75 g, 11.2 mmol, 10 equiv.). White powder, 1.51 g (83%). ^1H NMR (400 MHz, CD_2Cl_2 , 298 K) δ 8.19 (t, $J = 8.5$ Hz, 2H), 8.12 (d, $J = 8.1$ Hz, 1H), 7.89 (dd, $J = 7.4, 1.9$ Hz, 2H), 7.84 (d, $J = 8.0$ Hz, 1H), 7.39 – 7.21 (m, 9H), 7.06 – 6.96 (m, 3H), 6.86 (dt, $J = 7.1, 1.7$ Hz, 2H), 6.70 – 6.58 (m, 4H), 3.31 (s, 3H), 3.26 (s, 3H), 3.20 (s, 3H). ^{13}C $\{^1\text{H}\}$ NMR (101 MHz, CD_2Cl_2 , 298 K) δ 188.9, 186.3, 185.3, 151.7, 150.3, 150.1, 149.4, 148.4, 148.0, 139.4, 139.2, 137.2, 137.2, 136.7, 133.0, 132.9, 125.2, 124.9, 124.6, 123.1, 123.1, 122.4, 122.3, 122.2, 121.2, 120.8, 120.8, 113.0, 112.9, 112.5, 111.6, 111.5, 110.2, 110.2, 110.2, 33.8, 33.7, 33.2.

$\text{mer-Ir}(\text{pbb})_3$. Obtained from $[\text{Ir}(\text{COD})\text{Cl}]_2$ (243 mg, 0.36 mmol, 1 equiv.), Ag_2O (419 mg, 1.81 mmol, 5 equiv.) and Hpbc (1.32 g, 3.62 mmol, 10 equiv.). White powder, 656 mg (87%). ^1H NMR (400 MHz, CD_2Cl_2 , 298 K) δ 8.17 (d, $J = 8.4$ Hz, 1H), 7.89 (d, $J = 7.8$ Hz, 1H), 7.84 – 7.77 (m, 1H), 7.48 – 7.39 (m, 2H), 7.31 (ddd, $J = 8.4, 7.3, 1.2$ Hz, 1H), 7.23 (ddd, $J = 8.4, 7.3, 1.3$ Hz, 1H), 7.19 (d, $J = 7.9$ Hz, 1H), 7.14 (tdd, $J = 7.3,$

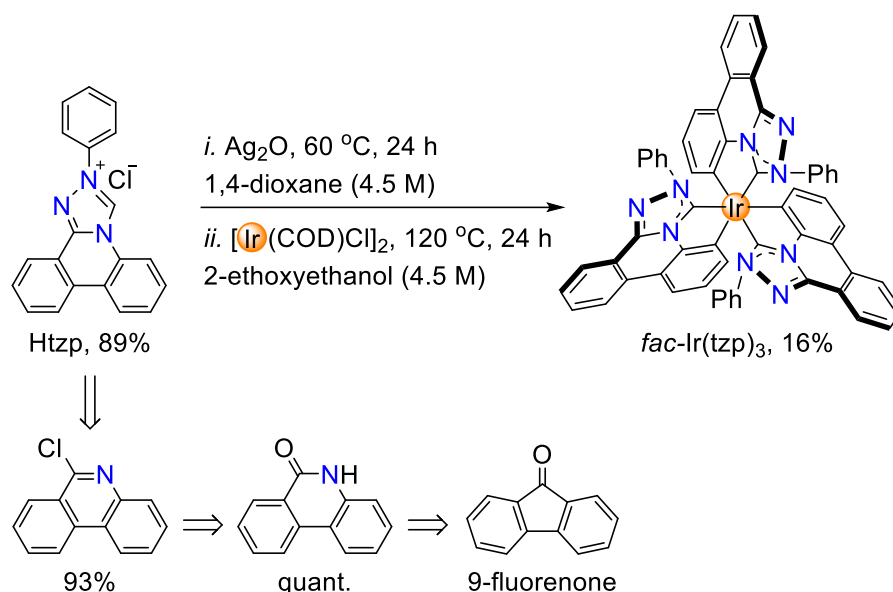
2.8, 0.9 Hz, 2H), 7.10 – 7.00 (m, 5H), 6.96 (dd, $J = 7.1, 1.5$ Hz, 1H), 6.93 – 6.74 (m, 9H), 6.72 – 6.58 (m, 8H), 6.38 – 6.32 (m, 2H), 6.24 (dd, $J = 11.8, 8.3$ Hz, 4H), 5.54 – 5.33 (m, 3H), 5.03 (d, $J = 16.7$ Hz, 1H), 4.93 (d, $J = 16.2$ Hz, 1H), 4.69 (d, $J = 16.3$ Hz, 1H). ^{13}C $\{^1\text{H}\}$ NMR (101 MHz, CD_2Cl_2 , 298 K) δ 190.3, 185.8, 185.6, 151.6, 150.3, 149.2, 148.5, 146.7, 139.1, 138.3, 137.3, 136.8, 136.7, 136.5, 136.3, 136.2, 135.3, 133.3, 133.2, 132.9, 128.3, 128.0, 128.0, 127.2, 126.9, 125.9, 125.6, 125.4, 125.2, 124.9, 124.5, 123.3, 123.1, 122.6, 122.4, 122.3, 122.0, 121.1, 120.9, 120.7, 113.5, 113.3, 113.0, 112.1, 112.1, 111.8, 110.9, 110.8, 110.4, 51.0, 50.9, 50.8.

fac-Ir(pmb)₃. Obtained by malonic acid-mediated (1 M in deionized water, 5.30 mL, 10 equiv.) isomerization of *mer*-Ir(pmb)₃ (433 mg, 0.53 mmol, 1.00 equiv.) with a reaction time of 20 d. White powder, 325 mg (75%). ^1H NMR (400 MHz, CD_2Cl_2 , 298 K) δ 8.15 (dt, $J = 8.3, 0.9$ Hz, 1H), 7.87 (dd, $J = 8.0, 1.1$ Hz, 1H), 7.35 – 7.29 (m, 1H), 7.28 – 7.18 (m, 2H), 7.03 (ddd, $J = 7.9, 7.3, 1.6$ Hz, 1H), 6.65 (td, $J = 7.3, 1.1$ Hz, 1H), 6.55 (dd, $J = 7.2, 1.6$ Hz, 1H), 3.28 (s, 3H). ^{13}C $\{^1\text{H}\}$ NMR (126 MHz, CD_2Cl_2 , 298 K) δ 190.1, 149.3, 148.9, 137.0, 136.7, 133.0, 124.7, 123.1, 122.2, 121.4, 112.5, 111.5, 110.2, 33.9.

fac-Ir(pbb)₃. Obtained by trifluoroacetic acid-mediated (TFA, 1 M in deionized water, 5.00 mL, 10 equiv.) isomerization of *mer*-Ir(pbb)₃ (521 mg, 0.50 mmol, 1 equiv.) with a reaction time of 20 d. White powder, 458 mg (88%). ^1H NMR (400 MHz, CD_2Cl_2 , 298 K) δ 7.78 (d, $J = 8.3$ Hz, 1H), 7.61 (d, $J = 8.0$ Hz, 1H), 7.13 (ddd, $J = 8.4, 7.3, 1.2$ Hz, 1H), 7.05 – 7.00 (m, 2H), 6.99 – 6.94 (m, 1H), 6.88 (d, $J = 8.0$ Hz, 1H), 6.83 – 6.75 (m, 2H), 6.66 (td, $J = 7.3, 1.1$ Hz, 1H), 6.55 (dd, $J = 7.3, 1.6$ Hz, 1H), 6.21 – 6.13 (m, 2H), 5.27 (d, $J = 16.4$ Hz, 1H), 4.82 (d, $J = 16.4$ Hz, 1H). ^{13}C $\{^1\text{H}\}$ NMR (126 MHz, CD_2Cl_2 , 298 K) δ 190.6, 149.5, 148.7, 136.5, 135.9, 135.2, 133.1, 128.4, 127.3, 125.5, 125.2, 124.6, 122.9, 122.1, 121.3, 113.1, 111.7, 110.4, 51.7.

The NMR spectra of *fac* and *mer* isomers of Ir(pmb)₃ and Ir(pbb)₃ are in agreement with those reported in the literature.¹³¹

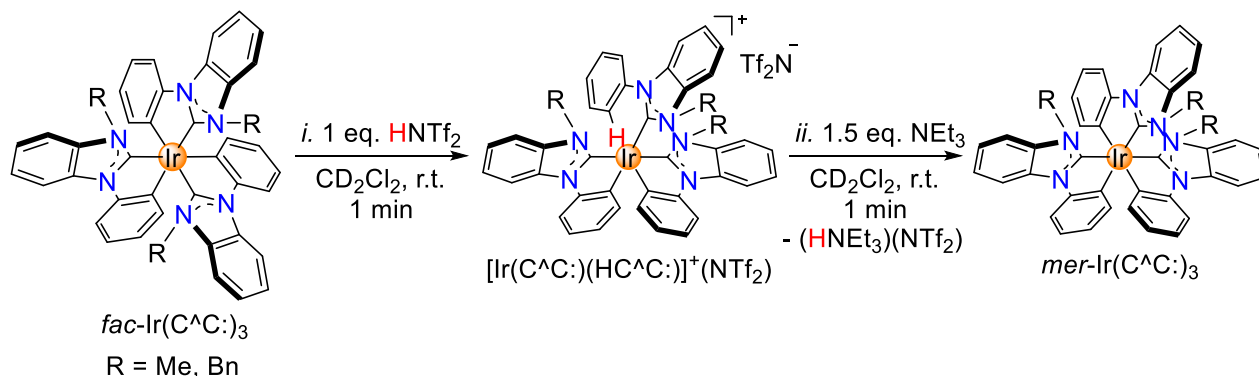
fac-Ir(tzp)₃, where tzp is metalated 1-phenyl-1,2,4-triazolo[4,3-*f*]phenanthridilin-2-ylidene, was prepared following the procedure described by Kang and co-workers with slightly modified conditions.²¹² The precursor for the cyclometalated carbene ligand was obtained in two steps from 9-fluorenone.²³⁹



fac- $\text{Ir}(\text{tzp})_3$. Obtained from $[\text{Ir}(\text{COD})\text{Cl}]_2$ (2.84 g, 4.22 mmol, 1 equiv.), Ag_2O (4.89 g, 21.1 mmol, 5 equiv.) and Htzp (14.0 g, 42.2 mmol, 10 equiv.). Cream-coloured powder, 1.45 g (16%). ^1H NMR (400 MHz, CD_2Cl_2 , 298 K) δ 8.48 (d, $J = 8.0$ Hz, 1H), 8.35 (dd, $J = 8.0, 1.3$ Hz, 1H), 7.87 (dd, $J = 8.1, 1.0$ Hz, 1H), 7.79 (ddd, $J = 8.4, 7.2, 1.4$ Hz, 1H), 7.63 (ddd, $J = 8.1, 7.2, 1.1$ Hz, 1H), 7.26 (tt, $J = 7.5, 1.2$ Hz, 1H), 7.11 (dd, $J = 8.0, 7.2$ Hz, 1H), 6.99 – 6.81 (m, 3H), 6.24 – 6.07 (m, 2H). ^{13}C $\{^1\text{H}\}$ NMR (101 MHz, CD_2Cl_2 , 298 K) δ 169.0, 146.4, 144.4, 140.3, 139.8, 138.2, 134.4, 131.4, 128.7, 128.7, 128.1, 127.0, 125.4, 125.2, 124.5, 119.6, 118.9, 115.7.

6.4.2 General Procedure for the $\text{HNTf}_2/\text{NEt}_3$ *fac*→*mer* Isomerization

The general procedure for the $\text{HNTf}_2/\text{NEt}_3$ -induced *fac*→*mer* isomerization of $\text{Ir}(\text{C}^{\wedge}\text{C}:)_3$ complexes ($\text{C}^{\wedge}\text{C}: = \text{pmb}, \text{pbb}$) is shown below.



fac-Ir(C[^]C:)₃ (1 equiv.) was placed in a 5 mL vial equipped with a stirring bar and dissolved in 0.5 mL of CD₂Cl₂ resulting in a colourless solution. Subsequently, a stock solution of HNTf₂ (0.2 M in CD₂Cl₂, 1 equiv.) was added in one portion under vigorous stirring (1100 rpm). The reaction was accompanied by a change of colour to yellow. After 1 min of stirring at RT, the solution was transferred to an NMR tube, and a spectrum of the protonated complex [Ir(C[^]C:)₂(HC[^]C:)](NTf₂) was recorded. Then, the solution of [Ir(C[^]C:)₂(HC[^]C:)](NTf₂) was transferred back to the vial, and a stock solution of NEt₃ (0.5 M in CD₂Cl₂, 1.5 equiv.) was added slowly dropwise under vigorous stirring (1100 rpm). The reaction was accompanied by a change of solution colour back to colourless. After 1 min of stirring at RT, the solution was transferred to an NMR tube, and a spectrum of *mer*-Ir(C[^]C:)₃ was recorded.

Additionally, ¹H, ¹⁹F {¹H} and ¹³C {¹H} NMR spectra of HNTf₂ in CD₂Cl₂ were recorded to distinguish the signals of counter anion NTf₂ in ¹³C spectra of [Ir(C[^]C:)₂(HC[^]C:)](NTf₂) complexes and follow the shifts in ¹H and ¹⁹F spectra.

HNTf₂. ¹H NMR (400 MHz, CD₂Cl₂, 298 K) δ 8.03 (s). ¹⁹F {¹H} NMR (376 MHz, CD₂Cl₂, 298 K) δ -75.3 (s). ¹³C {¹H} NMR (101 MHz, CD₂Cl₂, 298 K) δ 119.1 (q, *J* = 322.1 Hz).

[Ir(pmb)₂(Hpmb)](NTf₂). A solution of the protonated complex was obtained by the addition of a stock solution of HNTf₂ (0.2 M in CD₂Cl₂, 91.3 μL, 18.3 μmol, 1 equiv.) to a solution of *fac*-Ir(pmb)₃ (14.9 mg, 18.3 μmol, 1 equiv.) in 0.5 mL of CD₂Cl₂. ¹H NMR (500 MHz, CD₂Cl₂, 298 K) δ 8.34 – 8.26 (m, 1H), 8.10 (d, *J* = 8.2 Hz, 1H), 8.03 (d, *J* = 7.6 Hz, 1H), 7.91 (dd, *J* = 7.9, 1.3 Hz, 1H), 7.83 (dd, *J* = 8.1, 1.1 Hz, 1H), 7.67 (m, 1H), 7.60 – 7.34 (m, 10H), 7.17 – 7.07 (m, 3H), 6.79 (td, *J* = 7.4, 1.0 Hz, 1H), 6.59 (td, *J* = 7.6, 1.3 Hz, 1H), 6.55 (dd, *J* = 7.2, 1.4 Hz, 1H), 6.24 (dd, *J* = 7.8, 1.3 Hz, 1H), 6.06 (broad s, 2H), 3.91 (s, 3H), 3.27 (s, 3H), 3.10 (s, 3H). ¹⁹F {¹H} NMR (471 MHz, CD₂Cl₂, 298 K) δ -79.5 (s). ¹³C {¹H} NMR (126 MHz, CD₂Cl₂, 298 K) δ 183.4 (s), 182.9 (s), 179.5 (s), 149.6 (s), 146.7 (s), 144.9 (s), 139.1 (s), 137.8 (s), 136.5 (s), 136.2 (s), 135.9 (s), 135.6 (s), 134.5 (s), 132.5 (s), 131.9 (s), 131.8 (s), 129.4 (s), 126.4 (s), 125.8 (s), 125.5 (s), 125.5 (s), 125.3 (s), 125.2 (s), 125.0 (s), 124.6 (s), 124.2 (s), 123.9 (s), 123.7 (s), 120.3 (q, *J* = 321.8 Hz), 114.8 (s), 113.8 (s), 112.6 (s), 112.5 (s), 112.4 (s), 111.8 (s), 111.8 (s), 111.8 (s), 35.0 (s), 33.8 (s), 33.0 (s). HRMS (nanochip-ESI/LTQ-Orbitrap) *m/z*: [M]⁺ calcd. for C₄₂H₃₄IrN₆⁺ 815.2469; found 815.2449.

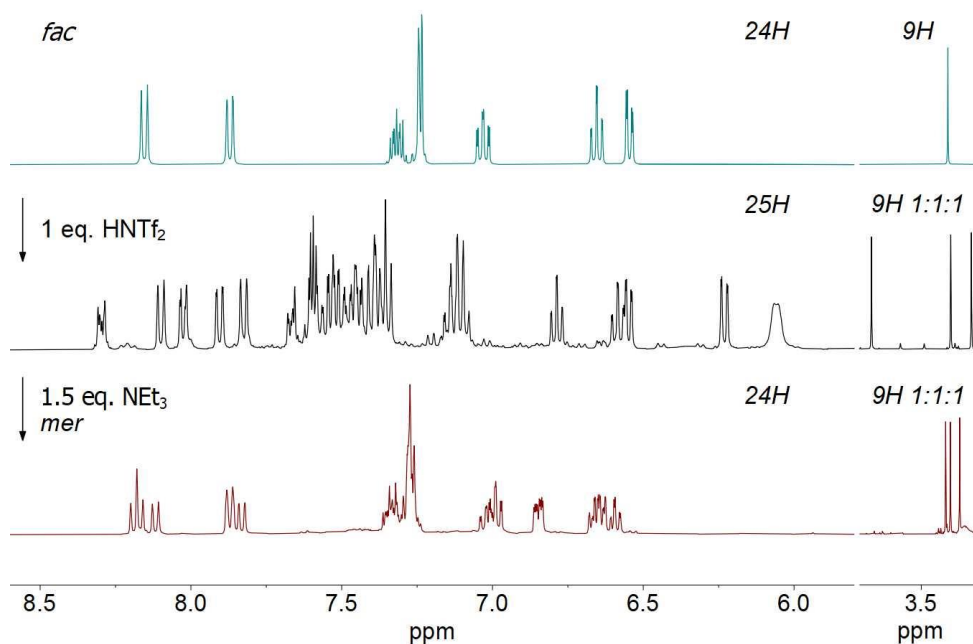
mer-Ir(pmb)₃. A solution of the *mer* isomer was obtained by the addition of a stock solution of NEt₃ (0.5 M in CD₂Cl₂, 54.8 μL, 27.4 μmol, 1.5 equiv.) to the solution of [Ir(pmb)₂(Hpmb)](NTf₂). The ¹H NMR spectrum of *mer*-Ir(pmb)₃ obtained *in situ* is in agreement with the one obtained by conventional synthesis and with the published one.¹³¹

[Ir(pbb)₂(Hpbb)](NTf₂). A solution of the protonated complex was obtained by the addition of a stock solution of HNTf₂ (0.2 M in CD₂Cl₂, 53.7 μL, 10.7 μmol, 1 equiv.) to a solution of *fac*-Ir(pbb)₃ (11.2 mg, 10.7 μmol, 1 equiv.) in 0.5 mL of CD₂Cl₂. ¹H NMR (500 MHz, CD₂Cl₂, 298 K) δ 8.18 (dd, *J* = 15.3, 8.4 Hz, 1H), 7.87 – 7.59 (m, 3H), 7.51 – 7.27 (m, 9H), 7.22 – 6.71 (m, 17H), 6.68 – 6.35 (m, 5H), 6.26 – 6.13 (m, 4H), 5.36 (d, *J* = 2.7 Hz, 1H), 5.29 – 5.17 (m, 2H), 5.13 – 4.94 (m, 2H), 4.88 – 4.80 (m, 1H), 4.74 – 4.42 (m, 1H). ¹⁹F {¹H} NMR (376 MHz, CD₂Cl₂, 273 K) δ –79.5 (s). ¹³C {¹H} NMR (126 MHz, CD₂Cl₂, 273 K) δ 183.7, 181.1, 179.1, 149.0, 147.7, 146.7, 146.6, 145.4, 145.1, 144.4, 139.0, 136.7, 135.9, 135.7, 135.5, 135.3, 135.2, 134.5, 134.5, 134.3, 133.8, 133.6, 133.5, 133.5, 132.0, 131.9, 131.0, 129.1, 128.8, 128.7, 128.5, 128.4, 128.1, 128.0, 127.9, 127.5, 127.1, 126.1, 126.1, 125.8, 125.3, 125.3, 125.2, 125.2, 125.1, 125.0, 124.9, 124.8, 124.6, 124.5, 124.4, 124.2, 124.1, 123.3, 121.1, 118.5, 115.2, 114.8, 113.9, 113.5, 112.7, 112.7, 112.5, 111.9, 111.7, 111.6, 111.3, 51.4, 51.2, 49.7. HRMS (nanochip-ESI/LTQ-Orbitrap) *m/z*: [M]⁺ calcd. for C₆₀H₄₆IrN₆⁺ 1043.3408; found 1043.3388. Single crystals of [Ir(pbb)₂(Hpbb)](NTf₂) were obtained by slow gas phase diffusion of pentane into a solution of the mixture of *fac*-Ir(pbb)₃ (40.0 mg, 1 equiv.) and HNTf₂ (10.8 mg, 1 equiv.) in dichloromethane at room temperature.

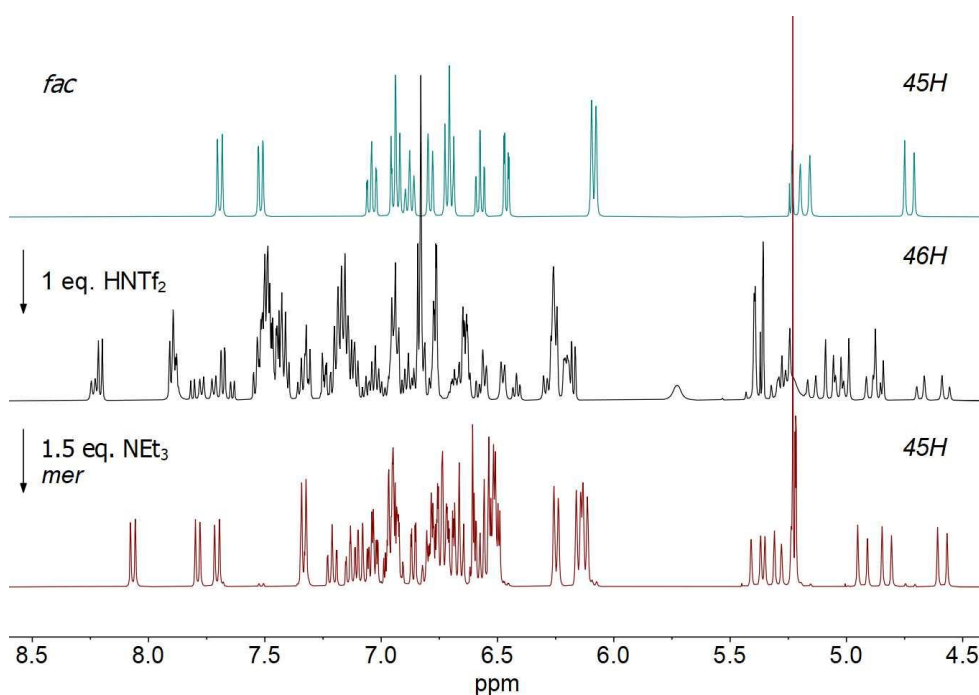
mer-Ir(pbb)₃. A solution of the *mer* isomer was obtained by addition of a stock solution of NEt₃ (0.5 M in CD₂Cl₂, 60.3 μL, 30.1 μmol, 10.5 equiv.) to a solution of [Ir(pbb)₂(Hpbb)](NTf₂). The ¹H NMR spectrum of *mer*-Ir(pbb)₃ obtained by *fac*→*mer* isomerization is in agreement with the one obtained by conventional synthesis and with the published one.¹³¹

6.4.3 NMR Control of *fac*→*mer* Isomerization

The *fac*→*mer* isomerization of the complexes Ir(pmb)₃ and Ir(pbb)₃ was monitored by ¹H NMR spectra (400 MHz, CD₂Cl₂, 298 K).



¹H NMR spectra for *fac*→*mer* isomerization for Ir(pmb)₃

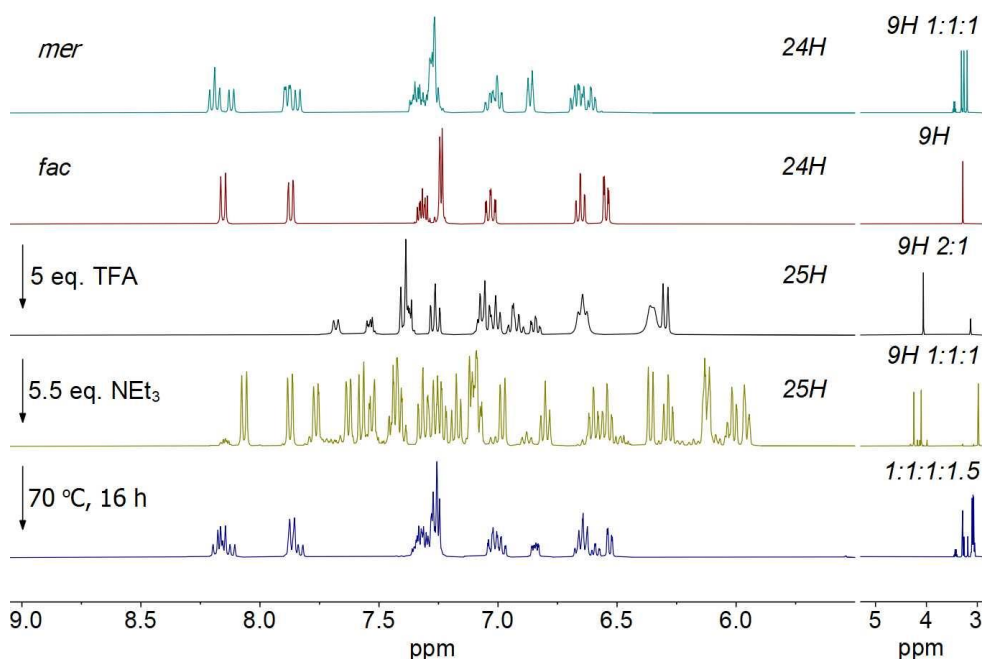


¹H NMR spectra for *fac*→*mer* isomerization for Ir(pbb)₃

6.4.4 TFA/NEt₃ Treatment of *fac*-Ir(pmb)₃

The addition of TFA to *fac*-Ir(pmb)₃ (spectrum in maroon) leads to a quantitative conversion to a protonated complex [Ir(pmb)₃+TFA] of undefined structure with high symmetry (spectrum in black). The NEt₃ treatment of [Ir(pmb)₃+TFA] results in a

quantitative conversion to a monoprotonated complex of the structure $\text{Ir}(\text{pmb})_2(\text{Hpmb})(\text{CF}_3\text{CO}_2)$ (spectrum in yellow). Further heating of $\text{Ir}(\text{pmb})_2(\text{Hpmb})(\text{CO}_2\text{CF}_3)$ at 70 °C overnight gives a mixture of *fac*- $\text{Ir}(\text{pmb})_3$ and *mer*- $\text{Ir}(\text{pmb})_3$ in the ratio 1:1.5 (spectrum in navy).



^1H (400 MHz, CD_2Cl_2) NMR spectra of *mer*- $\text{Ir}(\text{pmb})_3$ and the conversion of *fac*- $\text{Ir}(\text{pmb})_3$ to a mixture of *fac* and *mer* isomers

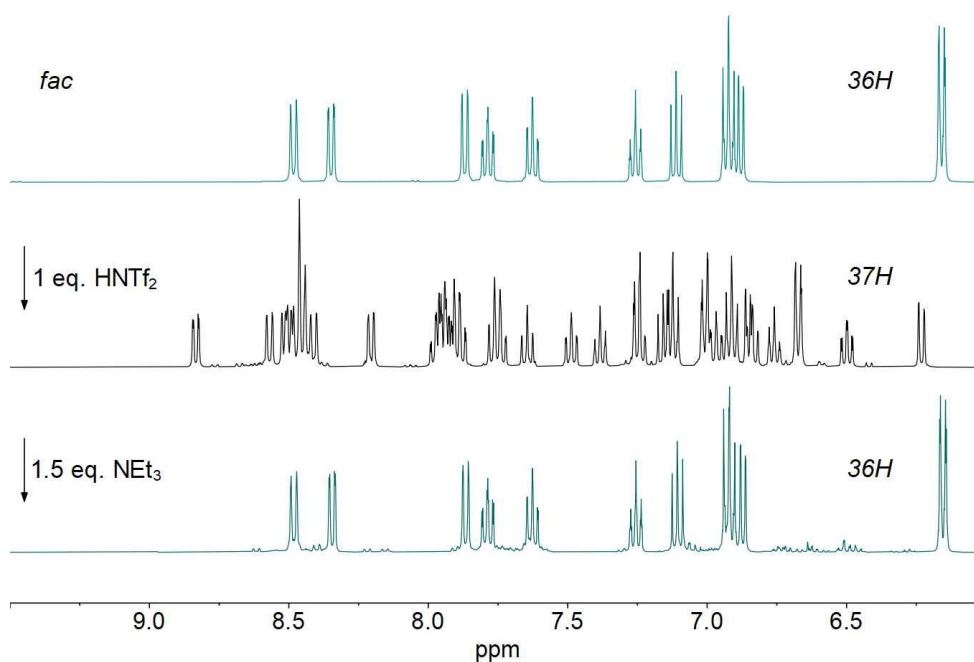
$[\text{Ir}(\text{pmb})_3+\text{TFA}]$. *fac*- $\text{Ir}(\text{pmb})_3$ (4.16 mg, 5.11 mmol, 1 equiv.) was placed in a 5 mL glass vial equipped with a stirring bar and dissolved in 0.5 mL of CD_2Cl_2 resulting in a colourless solution. Then, a stock solution of TFA (0.5 M in CD_2Cl_2 , 51.1 μL , 25.6 μmol , 5 equiv.) was added to the vial in one portion under vigorous stirring (1100 rpm). The reaction was accompanied by a change of colour to yellow. After 1 min of stirring at RT, the solution was transferred to an NMR tube, and a spectrum of the protonated complex $[\text{Ir}(\text{pmb})_3+\text{TFA}]$ was recorded. ^1H NMR (400 MHz, CD_2Cl_2 , 298 K) δ 7.68 (d, $J = 7.6$ Hz, 1H), 7.57 – 7.51 (m, 1H), 7.47 – 7.32 (m, 4H), 7.32 – 7.20 (m, 2H), 7.14 – 6.96 (m, 5H), 6.97 – 6.88 (m, 2H), 6.84 (td, $J = 7.3, 1.8$ Hz, 1H), 6.64 (broad t, $J = 7.7$ Hz, 4H), 6.35 (broad d, $J = 7.7$ Hz, 3H), 6.30 (d, $J = 8.2$ Hz, 2H), 4.06 (s, 6H), 3.13 (s, 3H). HRMS (nanochip-ESI/LTQ-Orbitrap) m/z : $[\text{Ir}(\text{pmb})_3+\text{H}]^+$ calcd. for $\text{C}_{42}\text{H}_{34}\text{IrN}_6^+$ 815.2469; found 815.2444; $[\text{Ir}(\text{pmb})_3-\text{pmb}]^+$ calcd. for

$C_{28}H_{22}IrN_4^+$ 607.1474; found 607.1451; $[Ir(pmb)_3+2H]^{2+}$ calcd. for $C_{42}H_{35}IrN_6^{2+}$ 408.1271; found 408.1259.

$Ir(pmb)_2(Hpmb)(CF_3CO_2)$. The solution of $[Ir(pmb)_3+TFA]$ was transferred back to the vial, and a stock solution of NEt_3 (0.5 M in CD_2Cl_2 , 56.2 μL , 28.1 μmol , 5.5 equiv.) was added slowly dropwise under vigorous stirring (1100 rpm). The reaction was accompanied by a change of colour back to colourless. After 1 min of stirring at r.t., the solution was transferred to an NMR tube, and a spectrum of $Ir(pmb)_2(Hpmb)(CO_2CF_3)$ was recorded. 1H NMR (400 MHz, CD_2Cl_2 , 298 K) δ 8.07 (d, $J = 8.2$ Hz, 1H), 7.87 (dd, $J = 8.0, 1.2$ Hz, 1H), 7.78 – 7.74 (m, 1H), 7.63 (dd, $J = 7.4, 1.6$ Hz, 1H), 7.57 (d, $J = 8.1$ Hz, 1H), 7.53 (m, 1H), 7.45 – 7.40 (m, 2H), 7.35 – 7.29 (m, 1H), 7.29 – 7.22 (m, 2H), 7.18 (t, $J = 7.7$ Hz, 1H), 7.13 – 7.05 (m, 3H), 6.98 (dd, $J = 8.0, 1.3$ Hz, 1H), 6.84 – 6.77 (m, 1H), 6.60 (td, $J = 7.6, 1.5$ Hz, 1H), 6.54 (td, $J = 7.7, 1.5$ Hz, 1H), 6.36 (d, $J = 8.1$ Hz, 1H), 6.28 (td, $J = 7.5, 1.3$ Hz, 1H), 6.16 – 6.10 (m, 2H), 6.02 (td, $J = 7.6, 1.5$ Hz, 1H), 5.95 (m, 1H), 4.25 (s, 3H), 4.10 (s, 3H), 2.98 (s, 3H). Single crystals of $Ir(pmb)_2(Hpmb)(CF_3CO_2)$ were obtained by slow gas phase diffusion of pentane into a solution of $Ir(pmb)_2(Hpmb)(CF_3CO_2)$ in DCM at r.t.

6.4.5 HNTf₂/NEt₃ Treatment of *fac*-Ir(tzp)₃

The addition of HNTf₂ to *fac*-Ir(tzp)₃ (top spectrum in teal) leads to a quantitative conversion to a monoprotonated complex '*fac*'-[Ir(tzp)₂(Htzp)](NTf₂) (spectrum in black). The quick NEt₃ treatment of '*fac*'-[Ir(tzp)₂(Htzp)](NTf₂) results in a nearly quantitative back-conversion to *fac*-Ir(tzp)₃ (bottom spectrum in teal).

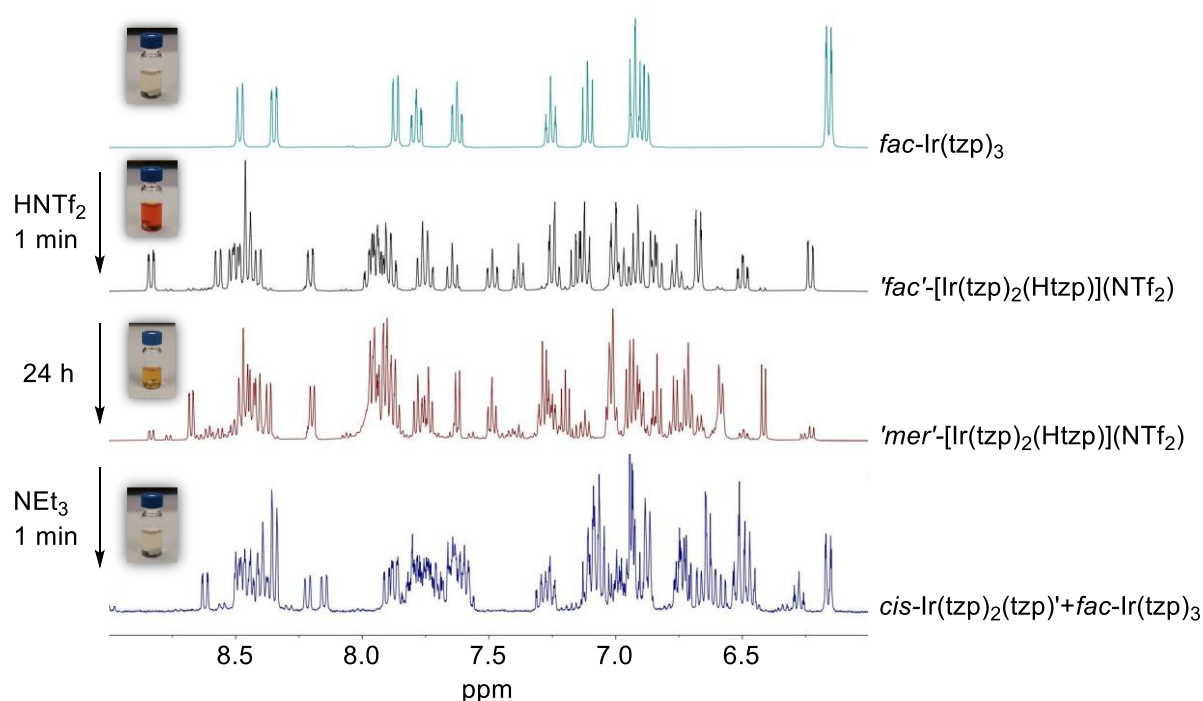


^1H (400 MHz, CD_2Cl_2) NMR spectra for the conversion of *fac*- $\text{Ir}(\text{tzp})_3$ to $[\text{Ir}(\text{tzp})_2(\text{Htzp})](\text{NTf}_2)$ by the acid treatment and then back to *fac* by the quick base addition.

'fac'- $[\text{Ir}(\text{tzp})_2(\text{Htzp})](\text{NTf}_2)$. *fac*- $\text{Ir}(\text{tzp})_3$ (16.8 mg, 15.6 μmol , 1 equiv.) was placed in a 5 mL glass vial equipped with a stirring bar and dissolved in 0.5 mL of CD_2Cl_2 resulting in a colourless solution. Then, HNTf_2 (0.2 M, 78.1 μL , 15.6 μmol , 1 equiv.) was added in one portion under vigorous stirring (1100 rpm). The reaction was accompanied by a change of colour to dark red. After 1 min of stirring at r.t., the solution was transferred to an NMR tube, and a spectrum of the protonated complex *'fac'*- $[\text{Ir}(\text{tzp})_2(\text{Htzp})](\text{NTf}_2)$ was recorded. ^1H NMR (400 MHz, CD_2Cl_2 , 298 K) δ 8.88 – 8.79 (m, 1H), 8.57 (d, J = 8.4 Hz, 1H), 8.53 – 8.44 (m, 5H), 8.41 (d, J = 8.3 Hz, 1H), 8.21 (dd, J = 8.0, 1.3 Hz, 1H), 8.01 – 7.84 (m, 6H), 7.78 – 7.72 (m, 2H), 7.67 – 7.62 (m, 1H), 7.49 (ddd, J = 8.3, 7.3, 1.2 Hz, 1H), 7.41 – 7.36 (m, 1H), 7.24 (m, 2H), 7.14 (m, 3H), 7.01 (dd, J = 8.6, 1.3 Hz, 2H), 6.99 – 6.95 (m, 1H), 6.93 – 6.89 (m, 2H), 6.87 – 6.81 (m, 2H), 6.79 – 6.73 (m, 1H), 6.69 – 6.65 (m, 2H), 6.50 (td, J = 7.7, 1.6 Hz, 1H), 6.23 (dd, J = 8.0, 1.1 Hz, 1H). ^{13}C $\{^1\text{H}\}$ NMR (126 MHz, CD_2Cl_2 , 260 K) δ 169.6, 164.5, 164.1, 147.7, 147.2, 146.8, 140.5, 140.1, 139.7, 138.0, 137.6, 137.3, 133.1, 132.9, 132.7, 132.6, 132.4, 130.9, 130.6, 130.5, 130.2, 129.5, 129.5, 129.3, 129.2, 129.1, 129.1, 128.8, 128.5, 128.4, 128.3, 127.0, 126.3, 125.4, 125.3, 125.2, 125.1, 124.3, 124.3, 124.0, 123.5, 123.2,

121.2, 119.9, 119.9, 119.7, 118.9, 118.6, 118.5, 118.3, 116.0, 114.5, 110.9. HRMS (nanochip-ESI/LTQ-Orbitrap) m/z : $[M]^+$ calcd. for $C_{60}H_{37}IrN_9^+$ 1076.2796; found 1076.2788.

When the monoprotonated complex '*fac*'-[Ir(tzp)₂(Htzp)](NTf₂) (spectrum in black) was left at r.t. overnight, it isomerized to a monoprotonated complex '*mer*'-[Ir(tzp)₂(Htzp)](NTf₂) (spectrum in maroon). The NEt₃ treatment of '*mer*'-[Ir(tzp)₂(Htzp)](NTf₂) results in a mixture of '*fac*'-Ir(tzp)₃ and '*cis*'-Ir(tzp)₂(tzp)' (spectrum in navy).

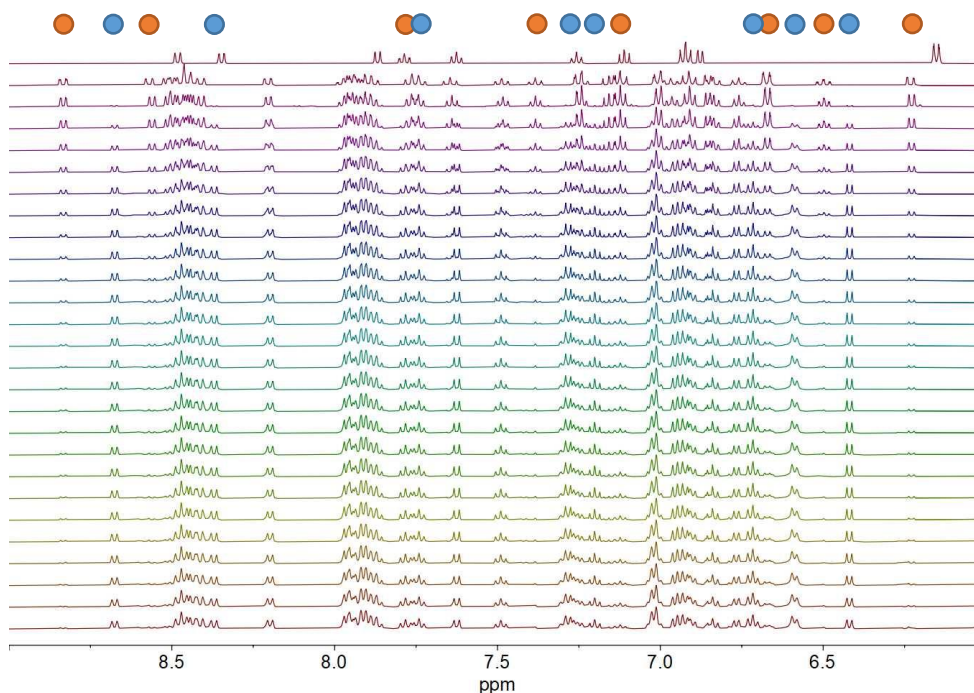


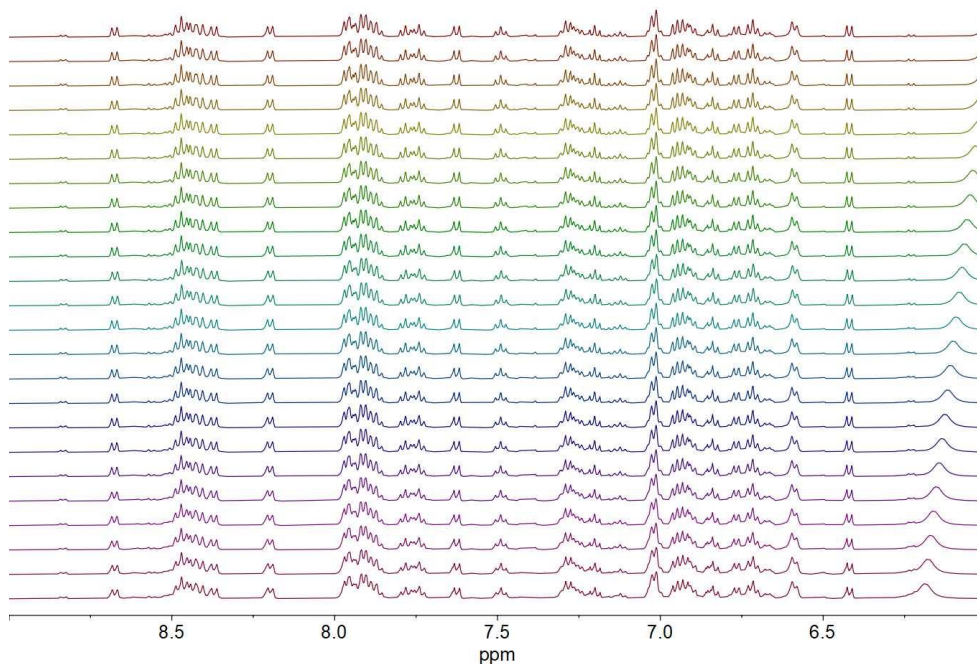
¹H NMR spectra (400 MHz) of a solution of *fac*-Ir(tzp)₃ in CD₂Cl₂ (spectrum in teal), after quick addition of HNTf₂ (1 equiv.; spectrum in black), leaving this mixture for overnight (spectrum in maroon), and after addition of NEt₃ (1.5 equiv., spectrum in navy).

'*mer*'-[Ir(tzp)₂(Htzp)](NTf₂). The solution of '*fac*'-[Ir(tzp)₂(Htzp)](NTf₂) was transferred back to the vial. The reaction was accompanied by a change of colour from dark red to yellow. After 24 h, the solution was transferred to an NMR tube, and a spectrum of '*mer*'-[Ir(tzp)₂(Htzp)](NTf₂) was recorded. ¹H NMR (500 MHz, CD₂Cl₂, 298 K) δ 8.71 – 8.63 (m, 1H), 8.53 – 8.35 (m, 5H), 8.20 (dd, J = 7.9, 2.0 Hz, 1H), 8.04 – 7.80 (m, 8H), 7.82 – 7.71 (m, 2H), 7.67 – 7.59 (m, 1H), 7.54 – 7.46 (m, 1H), 7.36 – 7.16 (m, 4H),

7.08 – 6.97 (m, 3H), 6.99 – 6.85 (m, 4H), 6.87 – 6.81 (m, 1H), 6.80 – 6.75 (m, 1H), 6.74 – 6.66 (m, 2H), 6.59 (m, 2H), 6.42 (d, $J = 7.5$ Hz, 1H). Single crystals of '*mer*'-[Ir(tzp)₂(Htzp)](NTf₂) with different polymorphic structure were obtained by slow gas phase diffusion of pentane into a solution of '*mer*'-[Ir(tzp)₂(Htzp)](NTf₂) in DCM at r.t.

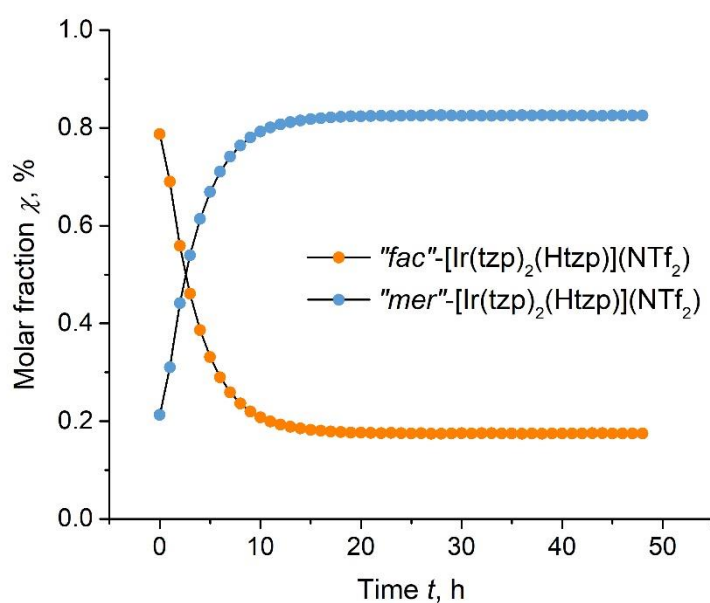
To define the time and yield of the reaction '*fac*'-[Ir(tzp)₂(Htzp)](NTf₂) → '*mer*'-[Ir(tzp)₂(Htzp)](NTf₂), kinetic studies using ¹H NMR spectroscopy were performed. A sample containing *fac*-Ir(tzp)₃ and 1 equiv. of HNTf₂ has been prepared and ¹H NMR (500 MHz, 298 K) were being measured every 1 h within 48 hours. The spectra are shown below. To visualize the conversion better, some signals belonging to '*fac*'-[Ir(tzp)₂(Htzp)](NTf₂) and '*mer*'-[Ir(tzp)₂(Htzp)](NTf₂) have been highlighted by orange and blue balls, respectively. According to the spectra, within 48 h the signals of '*fac*'-[Ir(tzp)₂(Htzp)](NTf₂) almost disappeared, while the intensity of the signals of '*mer*'-[Ir(tzp)₂(Htzp)](NTf₂) increased.





^1H NMR spectra (500 MHz, 298 K) of a solution of *fac*-Ir(tzp)₃ in CD₂Cl₂ (top spectrum), and a mixture of *fac*-Ir(tzp)₃ and 1 equiv. HNTf₂ measured every 1 h within 48 hours. Spectra from top to bottom correspond to 0 h → 48 h.

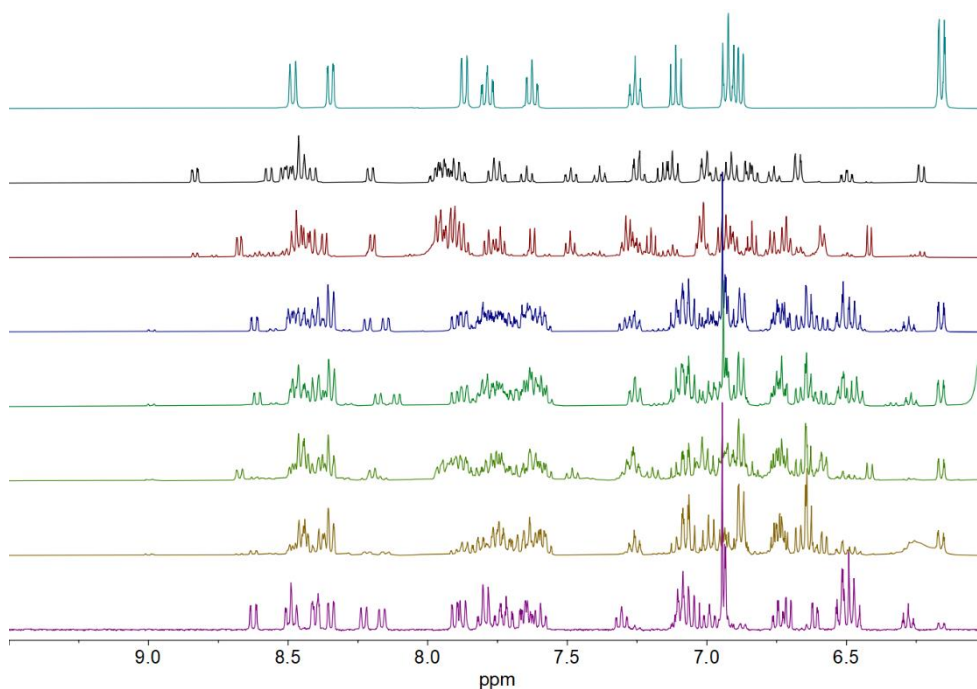
The kinetic profiles of '*fac*' and '*mer*' open forms are presented below. According to the graphics, the full conversion is 82.5%, and it can be achieved in 15 h, while the half conversion time is 2.6 h.



Kinetic profiles for the isomerization $\text{'fac'-[Ir(tzp)}_2(\text{Htzp)](NTf}_2) \rightarrow \text{'mer'-[Ir(tzp)}_2(\text{Htzp)](NTf}_2)$

$\text{cis-Ir(tzp)}_2(\text{tzp})'$. The solution of $\text{'mer'-[Ir(tzp)}_2(\text{Htzp)](NTf}_2)$ was transferred back to the vial, and a stock solution of NEt_3 (0.5 M in CD_2Cl_2 , 65.2 μL , 23.4 μmol , 1.5 equiv.) was added slowly dropwise under vigorous stirring (1100 rpm). The reaction was accompanied by a change of colour back to colourless. After 1 min of stirring at r.t, the solution was transferred to an NMR tube, and a spectrum of fac-Ir(tzp)_3 and $\text{cis-Ir(tzp)}_2(\text{tzp})'$ was recorded. Single crystals of $\text{cis-Ir(tzp)}_2(\text{tzp})'$ were obtained by slow gas phase diffusion of diethyl ether into a solution of fac-Ir(tzp)_3 and $\text{cis-Ir(tzp)}_2(\text{tzp})'$ in DCM at r.t. $\text{cis-Ir(tzp)}_2(\text{tzp})'$. $^1\text{H NMR}$ (400 MHz, CD_2Cl_2 , 298 K) δ 8.51 – 8.46 (m, 2H), 8.40 (dd, $J = 8.0, 2.0$ Hz, 2H), 8.35 (dd, $J = 7.9, 1.4$ Hz, 1H), 8.23 (d, $J = 8.1$ Hz, 1H), 8.19 – 8.14 (m, 1H), 7.91 – 7.85 (m, 2H), 7.81 – 7.70 (m, 4H), 7.67 – 7.58 (m, 3H), 7.31 (td, $J = 7.8, 1.3$ Hz, 1H), 7.07 (ddd, $J = 8.1, 6.7, 5.8$ Hz, 4H), 6.95 – 6.93 (m, 4H), 6.55 – 6.45 (m, 5H), 6.32 – 6.23 (m, 1H).

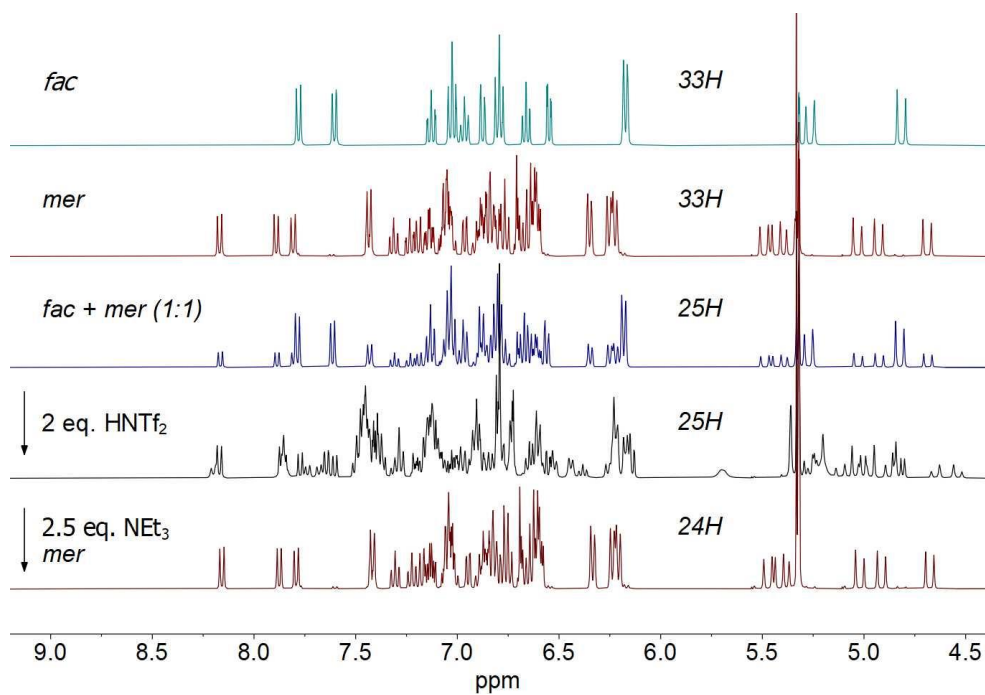
In order to check if the conditions of the base-induced re-metalation direct the reaction towards mer-Ir(tzp)_3 , we attempted the optimization of this step. We attempted: a) NEt_3 addition at low temperature, b) NEt_3 diffusion at low temperature and c) NEt_3 diffusion at room temperature to a solution of $\text{'mer'-[Ir(tzp)}_2(\text{Htzp)](NTf}_2)$ in DCM. Unfortunately, the NMR spectroscopy showed that varying the conditions did not lead to the desired product.



^1H NMR spectra (400 MHz) of a solution of *fac*-Ir(tzp)₃ in CD₂Cl₂ (spectrum in teal), '*fac*'-[Ir(tzp)₂(Htzp)](NTf₂) (spectrum in black), '*mer*'-[Ir(tzp)₂(Htzp)](NTf₂) (spectrum in maroon), a mixture of *fac*-Ir(tzp)₃ and *cis*-Ir(tzp)₂(tzp)' (spectrum in navy), *cis*-Ir(tzp)₂(tzp)' (spectrum in purple), and after addition of NEt₃ to '*mer*'-[Ir(tzp)₂(Htzp)](NTf₂) following the conditions a–c (spectra in green, greenish-yellow and yellow, respectively)

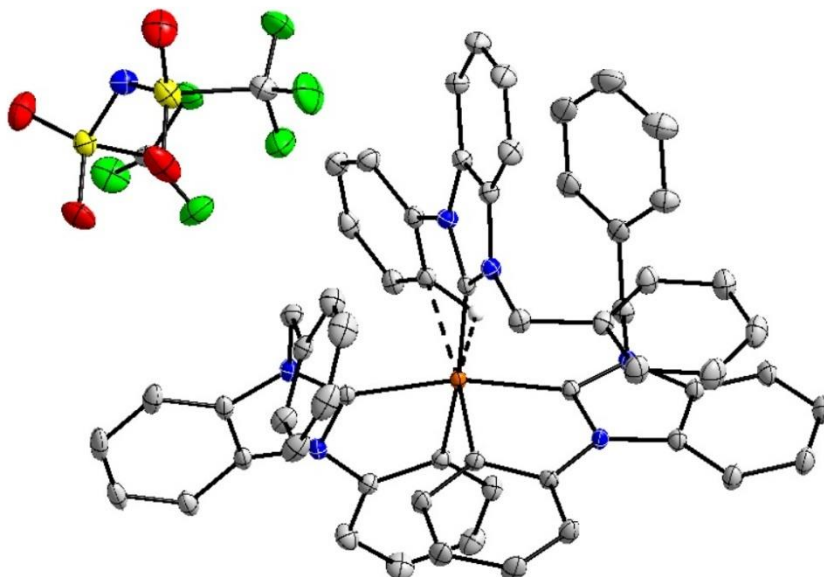
6.4.6 Conversion of the Mixture of *fac* and *mer* to *mer*

The equimolar mixture of *fac*-Ir(pbb)₃ (spectrum in teal) and *mer*-Ir(pbb)₃ (top spectrum in maroon) was prepared (spectrum in navy). The treatment of the mixture by HNTf₂ leads to quantitative conversion to the complex [Ir(pbb)₂(Hpbb)](NTf₂) (spectrum in black). The NEt₃ addition to [Ir(pbb)₂(Hpbb)](NTf₂) results in a quantitative conversion to *mer*-Ir(pbb)₃ (bottom spectrum in maroon).



^1H (400 MHz, CD_2Cl_2) NMR spectra of *fac* and *mer* isomers of $\text{Ir}(\text{pbb})_3$ and the conversion of mixture of *fac* and *mer* to *mer* through $[\text{Ir}(\text{pbb})_2(\text{Hpbb})](\text{NTf}_2)$.

6.4.7 Crystallographic Data



ORTEP view of $[\text{Ir}(\text{pmb})_2(\text{Hpmb})](\text{NTf}_2)$ at the 50% probability level. Most hydrogen atoms are omitted for clarity.

A clear intense yellow prism-shaped crystal with dimensions of 0.16×0.09×0.04 mm³ was mounted. Data were collected using an XtaLAB Synergy R, DW system, HyPix-Arc 150 diffractometer operating at $T = 140.00(10)$ K.

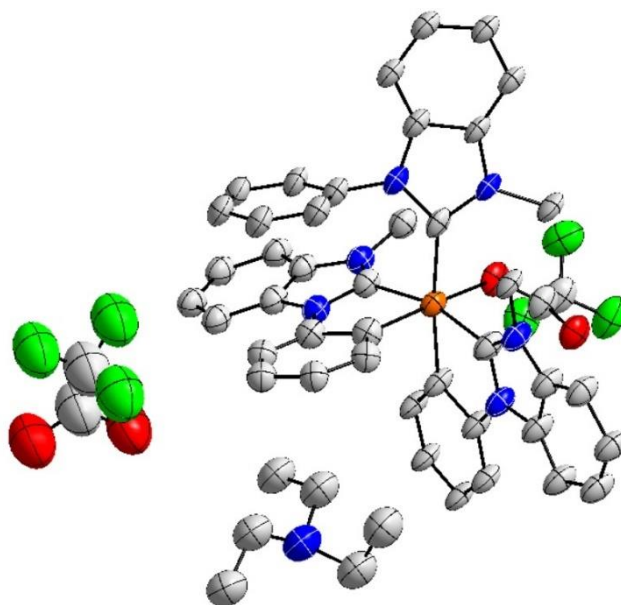
Data were measured using ω scans using MoK α radiation. The diffraction pattern was indexed and the total number of runs and images was based on the strategy calculation from the program CrysAlis^{Pro} 1.171.42.70a (CrysAlis^{Pro} Software System, Rigaku Oxford Diffraction, 2022). The maximum resolution that was achieved was $\theta = 36.319^\circ$ (0.60 Å).

The unit cell was refined using CrysAlis^{Pro} 1.171.42.70a on 36919 reflections, 46 % of the observed reflections.

Data reduction, scaling and absorption corrections were performed using CrysAlis^{Pro} 1.171.42.70a. The final completeness is 99.90 % out to 36.319° in θ . A Gaussian absorption correction was performed using CrysAlis^{Pro} 1.171.42.70a. Numerical absorption correction based on gaussian integration over a multifaceted crystal model Empirical absorption correction using spherical harmonics, implemented in SCALE3 ABSPACK scaling algorithm. The absorption coefficient μ of this material is 2.748 mm⁻¹ at this wavelength ($\lambda = 0.71073$ Å) and the minimum and maximum transmissions are 0.770 and 0.991.

The structure was solved in the space group $P\bar{1}$ (№ 2) by the ShelXT 2018/2²²⁶ structure solution program using dual methods and refined by full-matrix least-squares minimization on F^2 using version 2018/3 of ShelXL 2018/3.²²⁷ All non-hydrogen atoms were refined anisotropically. The hydrogen atom positions were calculated geometrically and refined using the riding model, but the hydride was found in a difference map and refined freely.

There is a single molecule in the asymmetric unit, which is represented by the reported sum formula. In other words: Z is 2 and Z' is 1.



ORTEP view of *Ir(pmb)₂(Hpmb)(CF₃CO₂)* with (NHET₃)(CF₃CO₂) trapped in the crystal cell at the 50% probability level. Hydrogen atoms are omitted for clarity.

A colourless plate-shaped crystal with dimensions of 0.20×0.06×0.03 mm³ was mounted. Data were collected using an XtaLAB Synergy R, DW system, HyPix-Arc 150 diffractometer operating at $T = 140.00(10)$ K.

Data were measured using ω scans using CuK α radiation. The diffraction pattern was indexed and the total number of runs and images was based on the strategy calculation from the program CrysAlis^{Pro} 1.171.41.122a (CrysAlis^{Pro} Software System, Rigaku Oxford Diffraction, 2021). The maximum resolution that was achieved was $\theta = 66.599^\circ$ (0.84 Å).

The unit cell was refined using CrysAlis^{Pro} 1.171.41.122a on 4526 reflections, 14 % of the observed reflections.

Data reduction, scaling and absorption corrections were performed using CrysAlis^{Pro} 1.171.41.122a. The final completeness is 99.30 % out to 66.599° in θ . A Gaussian absorption correction was performed using CrysAlis^{Pro} 1.171.41.122a. Numerical absorption correction based on gaussian integration over a multifaceted crystal model Empirical absorption correction using spherical harmonics, implemented in SCALE3

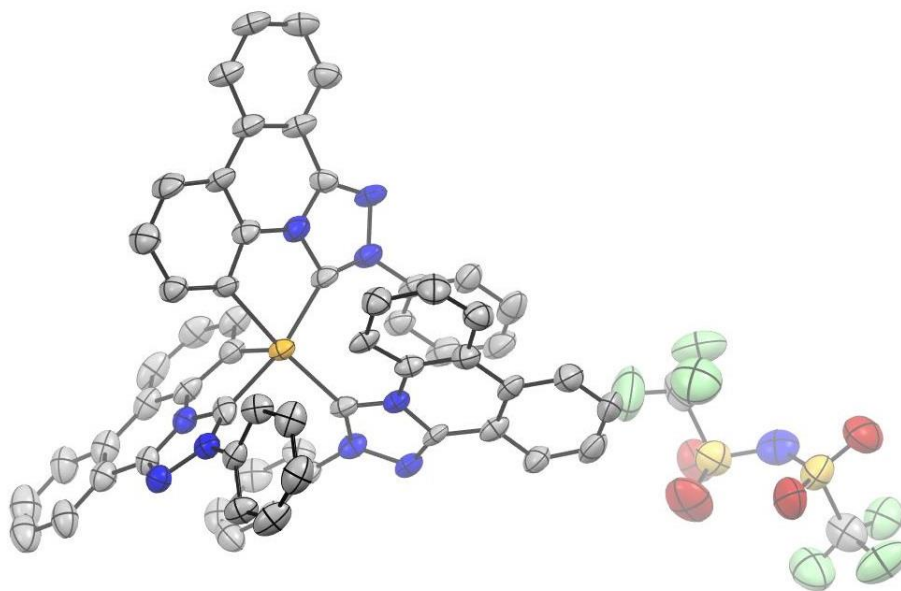
ABSPACK scaling algorithm. The absorption coefficient μ of this material is 5.124 mm^{-1} at this wavelength ($\lambda = 1.54184 \text{ \AA}$) and the minimum and maximum transmissions are 0.472 and 1.000.

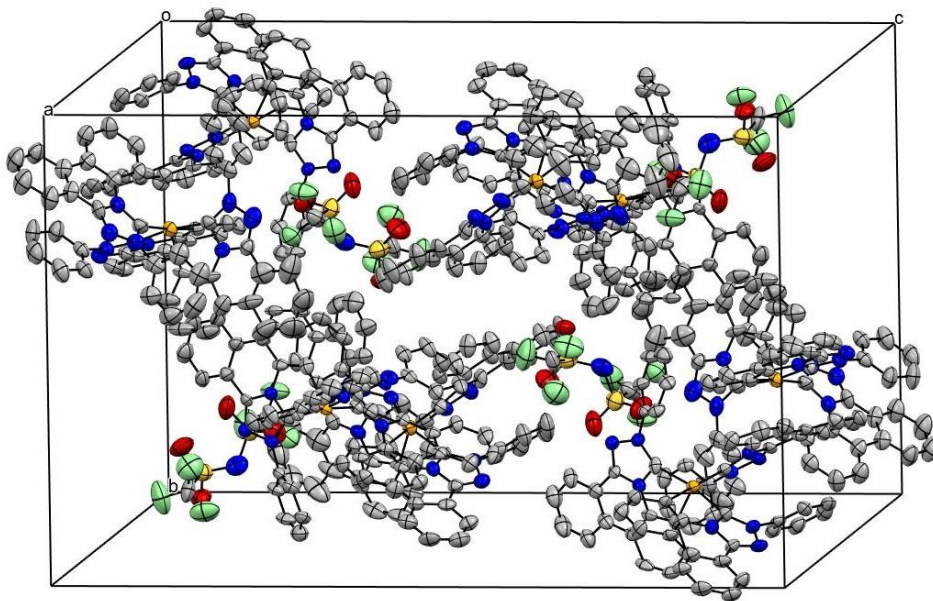
The structure was solved in the space group $P2_1/c$ (№ 14) by the ShelXT 2018/2²²⁶ structure solution program using dual methods and refined by full-matrix least-squares minimization on F^2 using version 2018/3 of ShelXL 2018/3.²²⁷ All non-hydrogen atoms were refined anisotropically. The hydrogen atom positions were calculated geometrically and refined using the riding model.

A solvent mask was calculated, and 416 electrons were found in a volume of 1216 \AA^3 in one void per unit cell. This is consistent with the presence of 2.5 solvent molecules of pentane per asymmetric unit which account for 420 electrons per unit cell.

There is a single molecule in the asymmetric unit, which is represented by the reported sum formula. In other words: Z is 4 and Z' is 1.

'mer'-[Ir(tzp)₂(Htzp)](NTf₂) monoclinic





ORTEP view of '*mer*'-[Ir(tzp)₂(Htzp)](NTf₂) at the 50% probability level. Hydrogen atoms are omitted for clarity. Packing of '*mer*'-[Ir(tzp)₂(Htzp)](NTf₂) forming a monoclinic crystal system.

A clear intense yellow plate-shaped crystal with dimensions 0.56×0.05×0.02 mm³ was mounted. Data were collected using an XtaLAB Synergy R, DW system, HyPix-Arc 150 diffractometer operating at $T = 139.99(10)$ K.

Data were measured using ω scans with CuK α radiation. The diffraction pattern was indexed and the total number of runs and images was based on a strategy calculation from the program CrysAlis^{Pro} 1.171.42.75a (CrysAlis^{Pro} Software System, Rigaku Oxford Diffraction, 2022). The maximum resolution achieved was $\theta = 74.789^\circ$ (0.80 Å).

The unit cell was refined using CrysAlis^{Pro} 1.171.42.75a on 29678 reflections, 32 % of the observed reflections.

Data reduction, scaling and absorption corrections were performed using CrysAlis^{Pro} 1.171.42.75a. The final completeness is 99.70 % out to 74.789° in θ . A Gaussian absorption correction was performed using CrysAlis^{Pro} 1.171.42.75a. Numerical absorption correction based on Gaussian integration over a multifaceted crystal model. Empirical absorption correction using spherical harmonics as implemented in SCALE3 ABSPACK scaling algorithm. The absorption coefficient μ of this material is

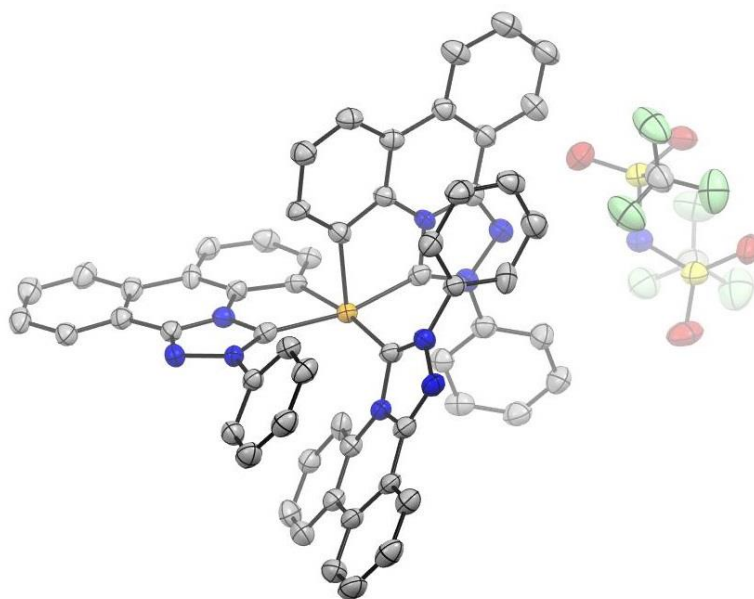
5.515 mm⁻¹ at this wavelength ($\lambda = 1.54184\text{\AA}$) and the minimum and maximum transmissions are 0.120 and 1.000.

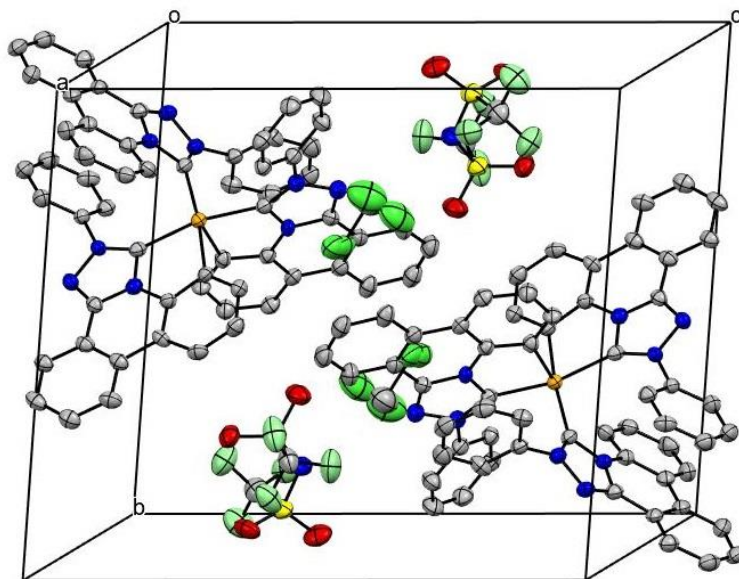
The structure was solved in the space group P21/c (№ 14) by the ShelXT 2018/2²²⁶ structure solution program using dual methods and refined by full-matrix least-squares minimization on F^2 using version 2018/3 of ShelXL 2018/3.²²⁷ All non-hydrogen atoms were refined anisotropically. Hydrogen atom positions were calculated geometrically and refined using the riding model.

The second NTf₂ anion was too highly disordered to be modelled and was considered by using the solvent mask program in Olex2.

There is a single molecule in the asymmetric unit, which is represented by the reported sum formula. In other words: Z is 4 and Z' is 1.

'mer'-[Ir(tzp)₂(Htzp)](NTf₂) triclinic





ORTEP view of '*mer*'-[Ir(tzp)₂(Htzp)](NTf₂) at the 50% probability level. Hydrogen atoms are omitted for clarity. Packing of '*mer*'-[Ir(tzp)₂(Htzp)](NTf₂) forming a triclinic crystal system.

A clear intense yellow plate-shaped crystal with dimensions 0.10×0.07×0.01 mm³ was mounted. Data were collected using an XtaLAB Synergy R, DW system, HyPix-Arc 150 diffractometer operating at $T = 140.00(10)$ K.

Data were measured using ω scans with CuK α radiation. The diffraction pattern was indexed and the total number of runs and images was based on a strategy calculation from the program CrysAlisPro 1.171.42.75a (CrysAlis^{Pro} Software System, Rigaku Oxford Diffraction, 2022). The maximum resolution achieved was $\theta = 75.776^\circ$ (0.80 Å).

The unit cell was refined using CrysAlisPro 1.171.42.75a (Rigaku OD, 2022) on 26272 reflections, 42% of the observed reflections.

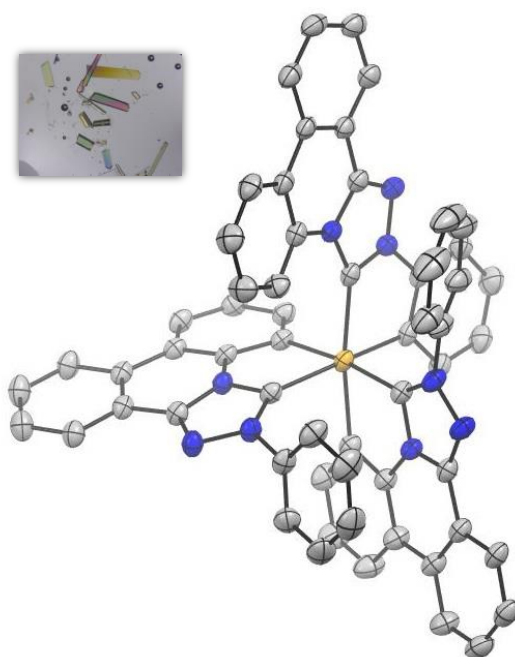
Data reduction, scaling and absorption corrections were performed using CrysAlis^{Pro} 1.171.42.75a. The final completeness is 99.50 % out to 75.776° in θ . A Gaussian absorption correction was performed using CrysAlis^{Pro} 1.171.42.75a. Numerical absorption correction based on Gaussian integration over a multifaceted crystal model. Empirical absorption correction using spherical harmonics as implemented in SCALE3 ABSPACK scaling algorithm. The absorption coefficient μ of this material is

6.769 mm⁻¹ at this wavelength ($\lambda = 1.54184\text{\AA}$) and the minimum and maximum transmissions are 0.584 and 0.973.

The structure was solved in the space group P (№ 2) by the ShelXT 2018/2²²⁶ structure solution program using dual methods and refined by full matrix least squares minimization on F^2 using version 2019/3 of ShelXL 2019/3.²²⁷ All non-hydrogen atoms were refined anisotropically. Hydrogen atom positions were calculated geometrically and refined using the riding model.

There is a single formula unit in the asymmetric unit, which is represented by the reported sum formula. In other words: Z is 2 and Z' is 1. The moiety formula is C₆₀H₃₇IrN₉, C₂F₆NO₄S₂, CH₂Cl₂.

cis-Ir(tzp)₂(tzp)'



ORTEP view of *cis-Ir(tzp)₂(tzp)'* at the 50% probability level. Hydrogen atoms are omitted for clarity.

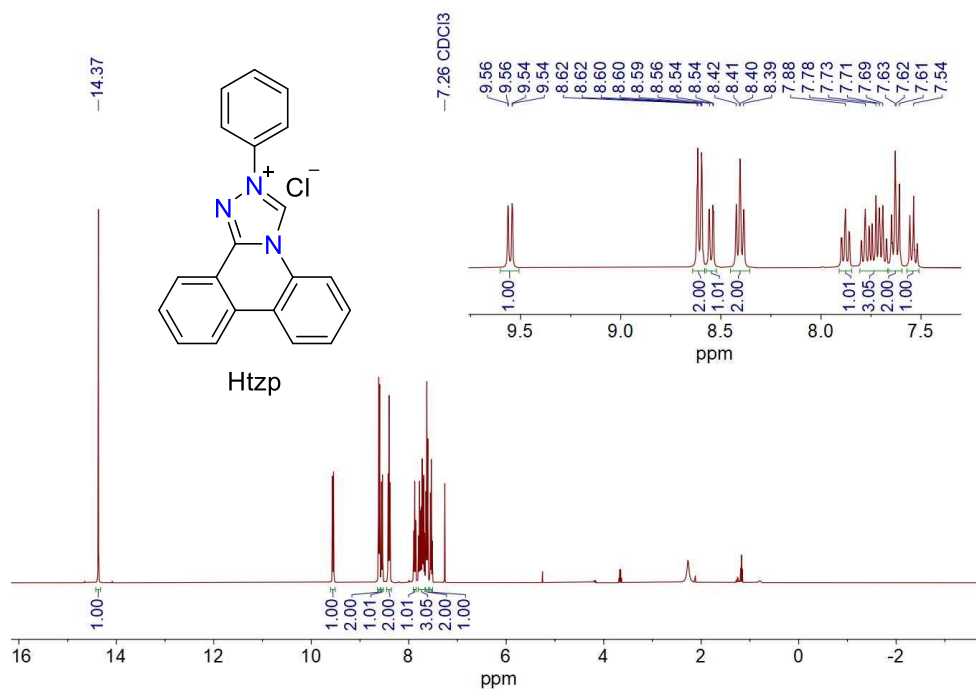
The crystal structure of *cis-Ir(tzp)₂(tzp)'* has been published (CCDC 2003242) in the work of H.-J. Son and S. O. Kang and co-workers,²¹² and the crystallographic data can be found in the Supporting Information for this publication.

Crystallographic data of the compounds

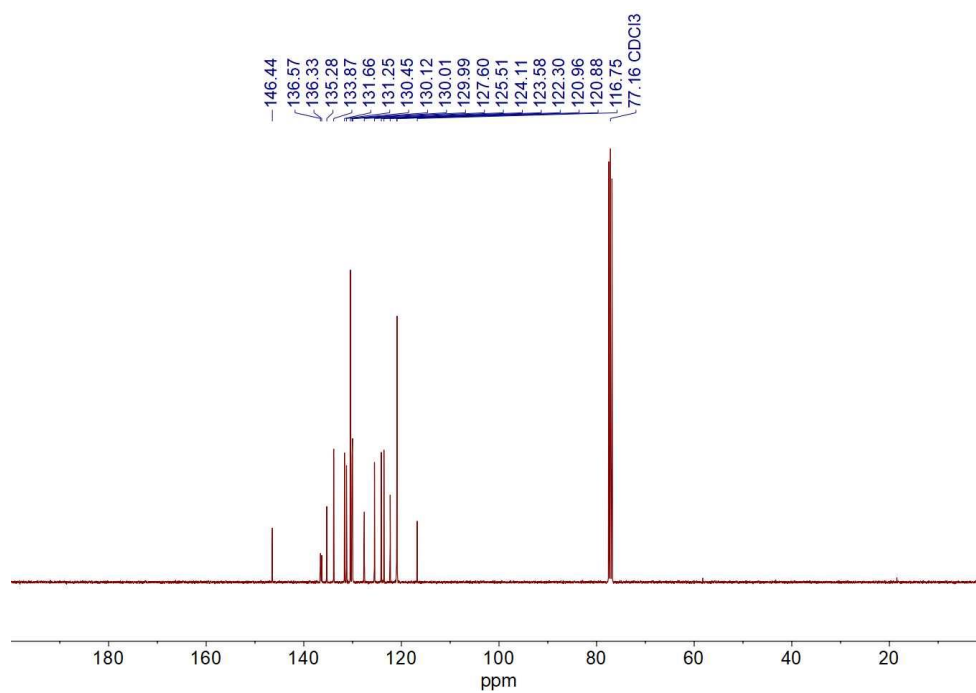
Compound	[Ir(pmb) ₂ (Hpmb)](NTf ₂)	Ir(pmb) ₂ (Hpmb)(CO ₂ CF ₃)
Formula	C ₆₂ H ₄₆ F ₆ IrN ₇ O ₄ S ₂	C ₅₂ H ₅₀ F ₆ IrN ₇ O ₄
Formula Weight	1.702	1.341
<i>D</i> _{calc.} , g cm ⁻³	2.748	5.124
<i>μ</i> , mm ⁻¹	1323.38	1143.19
Colour	clear intense yellow	colourless
Shape	prism-shaped	plate-shaped
Size, mm ³	0.16×0.09×0.04	0.20×0.06×0.03
<i>T</i> , K	140.00(10)	140.00(10)
Crystal System	triclinic	monoclinic
Space Group	<i>P</i> $\bar{1}$	<i>P</i> 2 ₁ / <i>c</i>
<i>a</i> , Å	11.63227(10)	9.2810(9)
<i>b</i> , Å	13.80526(10)	37.482(3)
<i>c</i> , Å	16.19706(13)	16.6684(13)
<i>α</i> , °	85.2923(6)	90
<i>β</i> , °	87.1337(7)	102.498(9)
<i>γ</i> , °	85.6362(7)	90
<i>V</i> , Å ³	2582.23(4)	5661.1(9)
<i>Z</i>	2	4
<i>Z'</i>	1	1
<i>λ</i> , Å	0.71073	1.54184
Radiation type	MoK α	CuK α
<i>θ</i> _{min} , °	2.023	2.358
<i>θ</i> _{max} , °	36.319	66.599
Measured Refl.	80489	31825
Independent Refl.	24306	9922
Refl. <i>I</i> ≥ 2σ(<i>I</i>)	21440	5020
<i>R</i> _{int}	0.0345	0.1607
Parameters	743	631
Restraints	0	1034
Largest Peak, e Å ⁻³	1.568	2.262
Deepest Hole, e Å ⁻³	-0.982	-2.881
GooF	1.032	1.054
<i>wR</i> ₂ (all data)	0.0608	0.3251
<i>wR</i> ₂	0.0590	0.2892
<i>R</i> ₁ (all data)	0.0373	0.1951
<i>R</i> ₁	0.0288	0.1206
CCDC number	2210250	2225294

Compound	'mer'-[Ir(tzp) ₂ (Htzp)](NTf ₂) monoclinic	'mer'-[Ir(tzp) ₂ (Htzp)](NTf ₂) triclinic
Formula	C ₁₂₂ H ₇₄ F ₆ Ir ₂ N ₁₉ O ₄ S ₂	C ₆₃ H ₃₉ Cl ₂ F ₆ IrN ₁₀ O ₄ S ₂
Formula Weight	1.454	1.680
<i>D</i> _{calc.} , g cm ⁻³	5.515	6.769
<i>μ</i> , mm ⁻¹	2432.52	1441.26
Colour	clear intense yellow	clear intense yellow
Shape	plate-shaped	plate-shaped
Size, mm ³	0.56×0.05×0.02	0.10×0.07×0.01
<i>T</i> , K	139.99(10)	140.00(10)
Crystal System	monoclinic	triclinic
Space Group	<i>P</i> 2 ₁ / <i>c</i>	<i>P</i> $\bar{1}$
<i>a</i> , Å	17.09143(17)	10.71577(13)
<i>b</i> , Å	21.0201(4)	15.9001(3)
<i>c</i> , Å	31.7845(5)	17.3167(3)
<i>α</i> , °	90	95.8693(14)
<i>β</i> , °	103.2670(13)	102.1257(12)
<i>γ</i> , °	90	95.3533(12)
<i>V</i> , Å ³	11114.2(3)	2849.45(8)
<i>Z</i>	4	2
<i>Z'</i>	1	1
<i>λ</i> , Å	1.54184	1.54184
Radiation type	CuKα	CuKα
<i>θ</i> _{min} , °	2.541	2.631
<i>θ</i> _{max} , °	74.789	75.776
Measured Refl.	93702	62916
Independent Refl.	21877	11482
Refl. <i>I</i> ≥ 2σ(<i>I</i>)	15655	9898
<i>R</i> _{int}	0.0604	0.0478
Parameters	1390	812
Restraints	0	41
Largest Peak, e Å ⁻³	4.556	2.469
Deepest Hole, e Å ⁻³	-2.827	-3.027
GooF	1.043	1.055
<i>wR</i> ₂ (all data)	0.1968	0.1435
<i>wR</i> ₂	0.1849	0.1383
<i>R</i> ₁ (all data)	0.1094	0.0635
<i>R</i> ₁	0.0824	0.0536
CCDC number	2233207	2297932

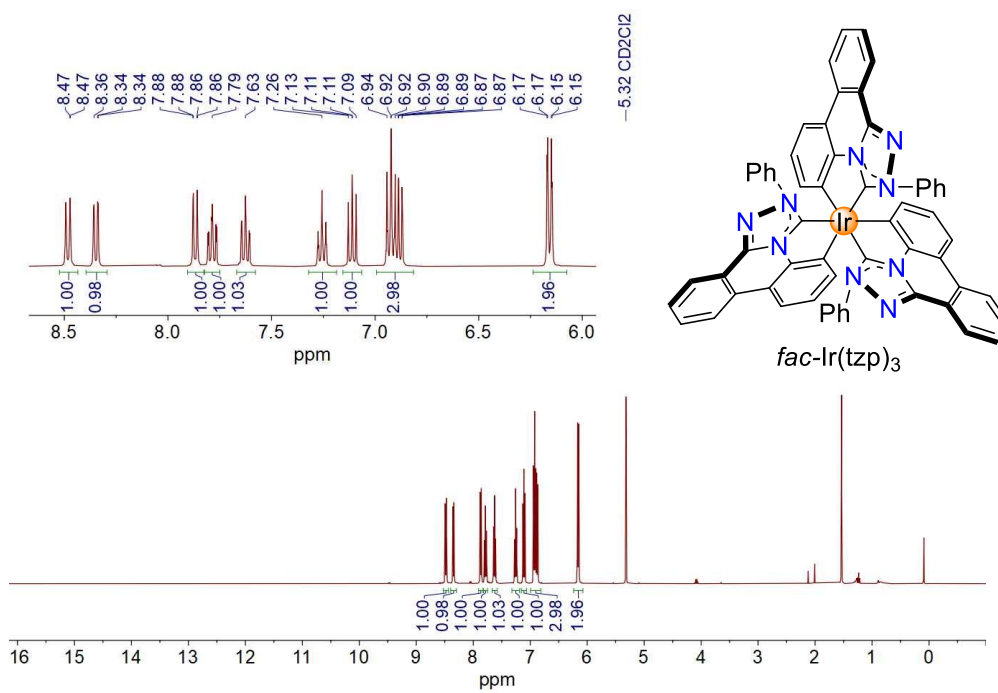
6.4.8 NMR Spectra



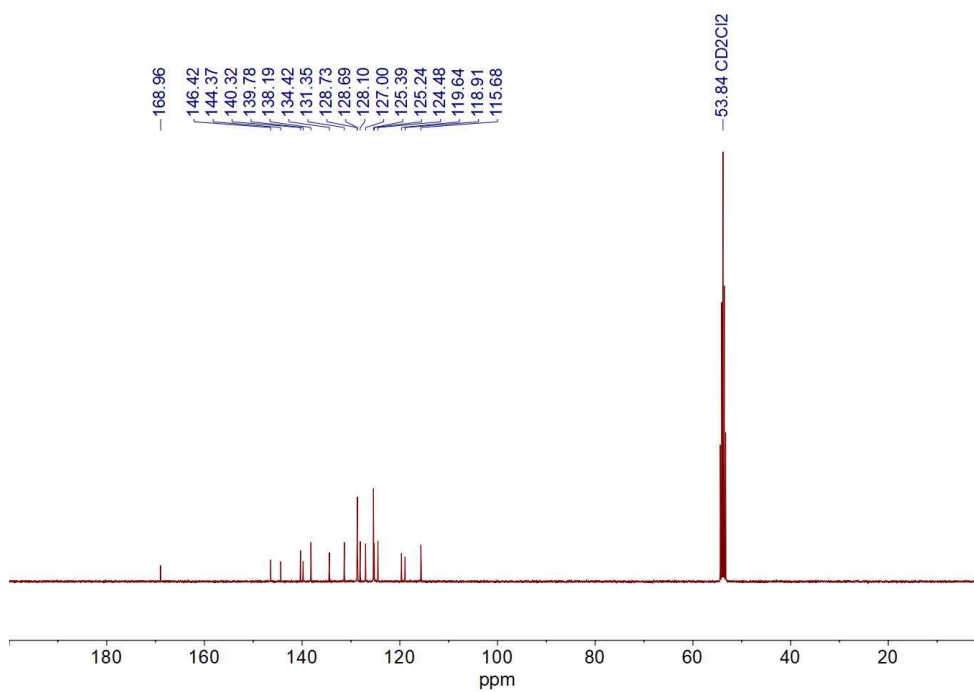
¹H NMR (400 MHz, CDCl₃, 298 K) spectrum of Htzp



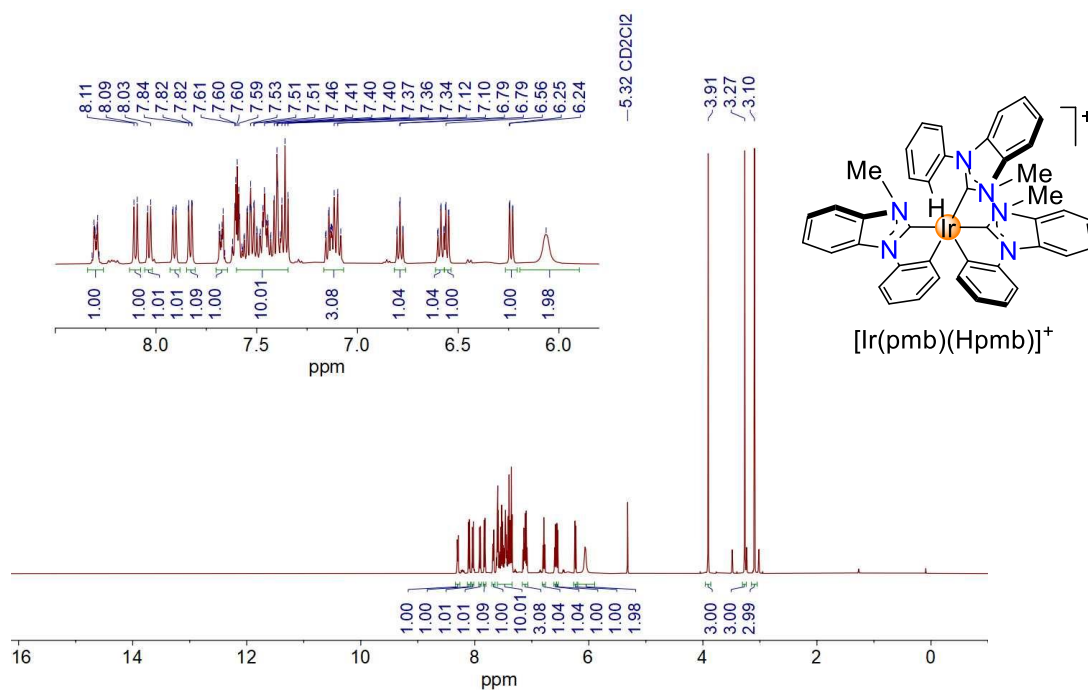
¹³C NMR (101 MHz, CDCl₃, 298 K) spectrum of Htzp



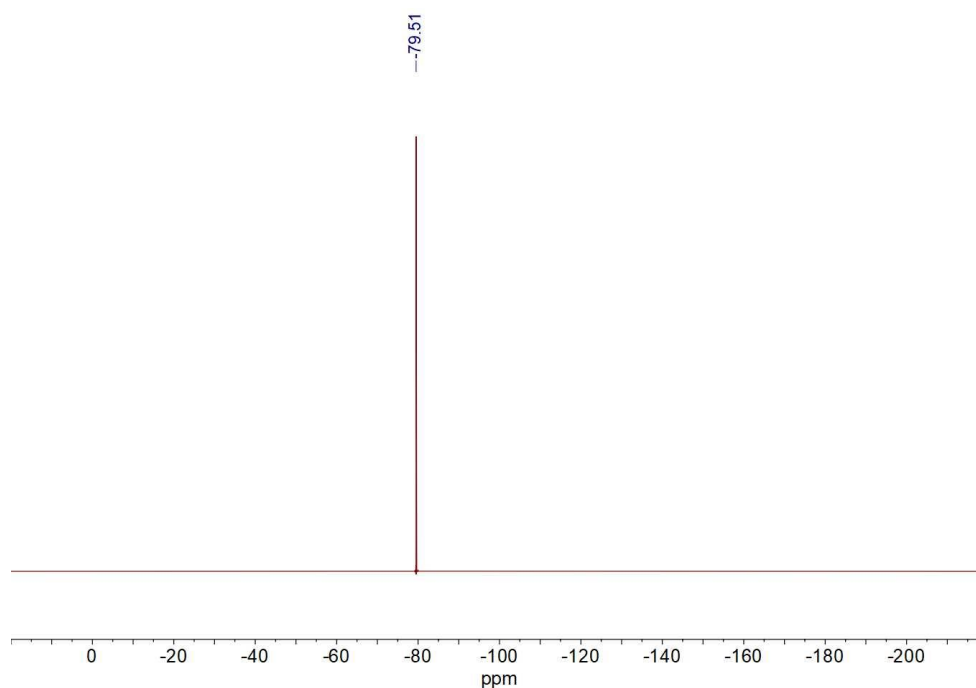
^1H NMR (400 MHz, CD_2Cl_2 , 298 K) spectrum of *fac*-Ir(tzp)₃



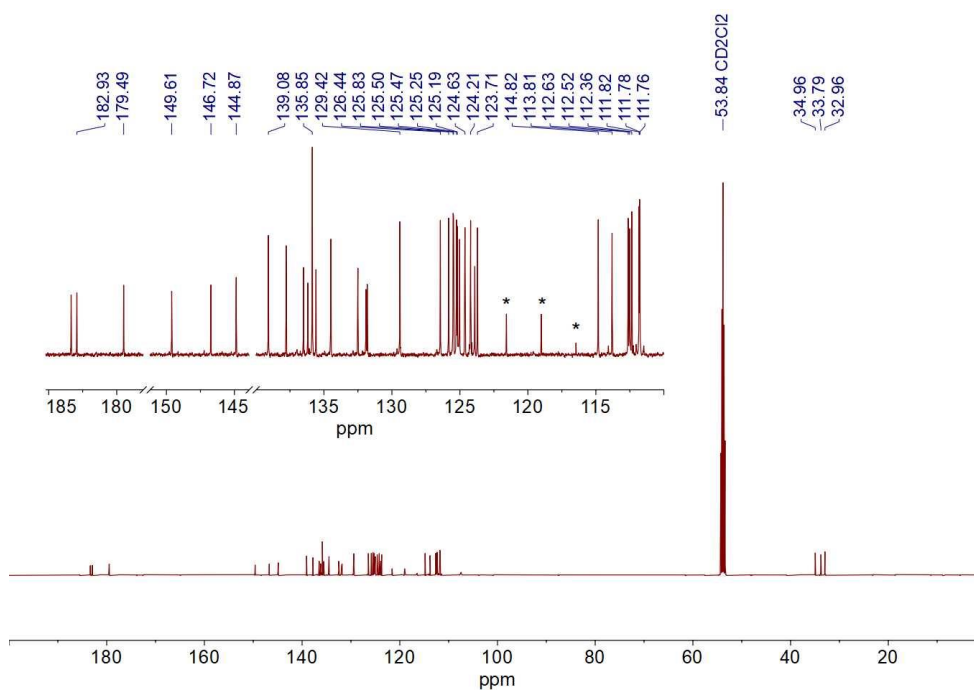
^{13}C NMR (101 MHz, CD_2Cl_2 , 298 K) spectrum of *fac*-Ir(tzp)₃



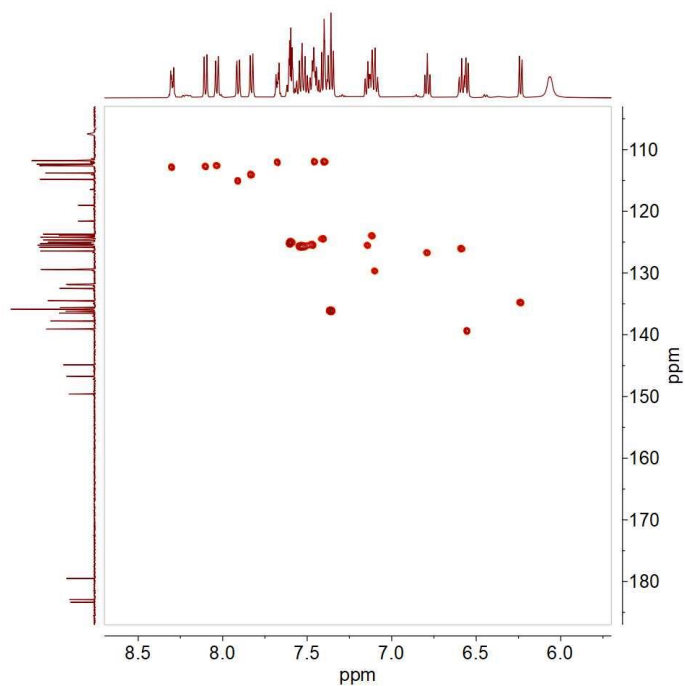
^1H NMR (500 MHz, CD_2Cl_2 , 298 K) spectrum of $[\text{Ir}(\text{pmb})_2(\text{Hpmb})](\text{NTf}_2)$. The NTf_2 anion is omitted for clarity.



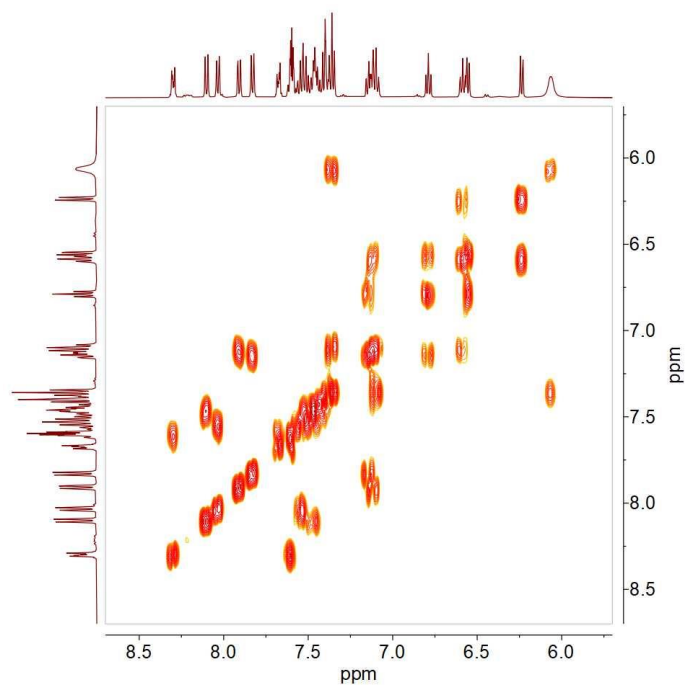
^{19}F NMR (376 MHz, CD_2Cl_2 , 298 K) spectrum of $[\text{Ir}(\text{pmb})_2(\text{Hpmb})](\text{NTf}_2)$



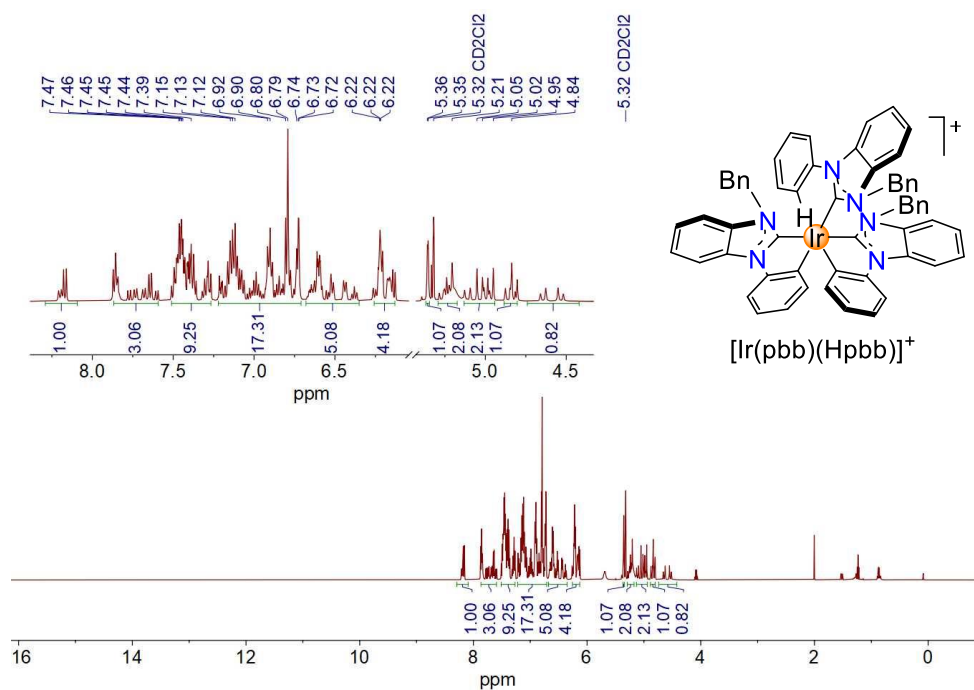
^{13}C NMR (126 MHz, CD_2Cl_2 , 298 K) spectrum of $[\text{Ir}(\text{pmb})_2(\text{Hpmb})](\text{NTf}_2)$. The signals of NTf_2 anion are marked by asterisks.



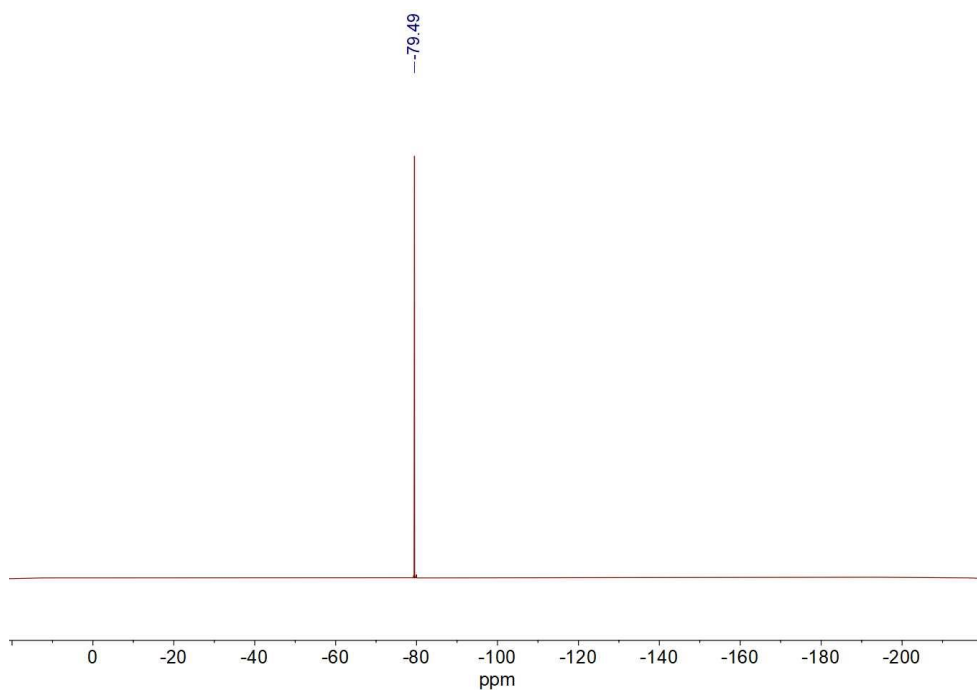
HSQC NMR (500 MHz, CD_2Cl_2 , 298 K) spectrum of $[\text{Ir}(\text{pmb})_2(\text{Hpmb})](\text{NTf}_2)$



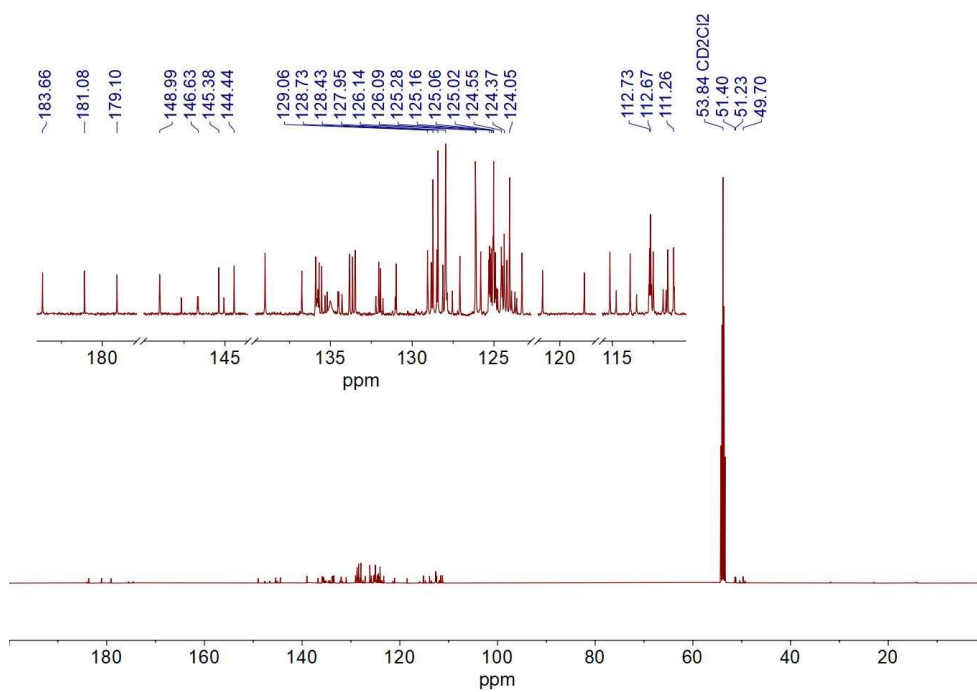
^1H - ^1H COSY NMR (500 MHz, CD_2Cl_2 , 298 K) spectrum of $[\text{Ir}(\text{pmb})_2(\text{Hpmb})](\text{NTf}_2)$



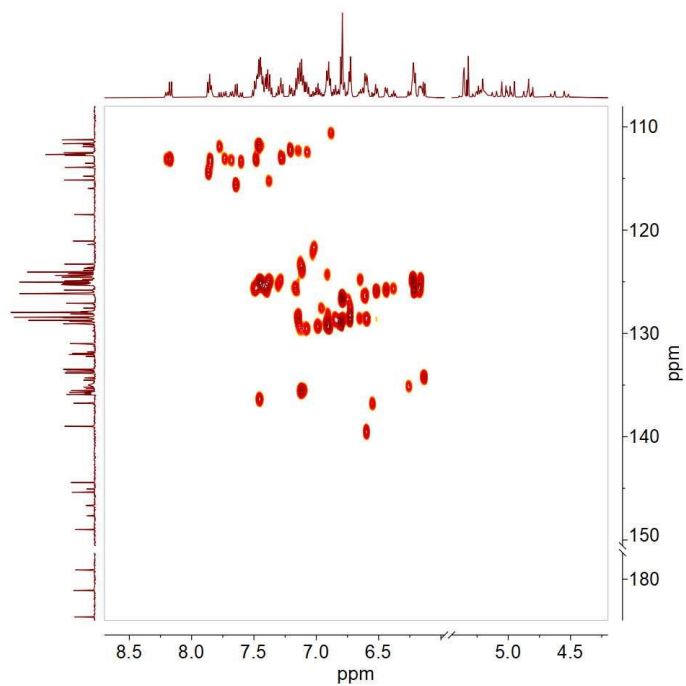
^1H NMR (500 MHz, CD_2Cl_2 , 298 K) spectrum of $[\text{Ir}(\text{pbb})_2(\text{Hpbb})](\text{NTf}_2)$. The NTf_2 anion is omitted for clarity.



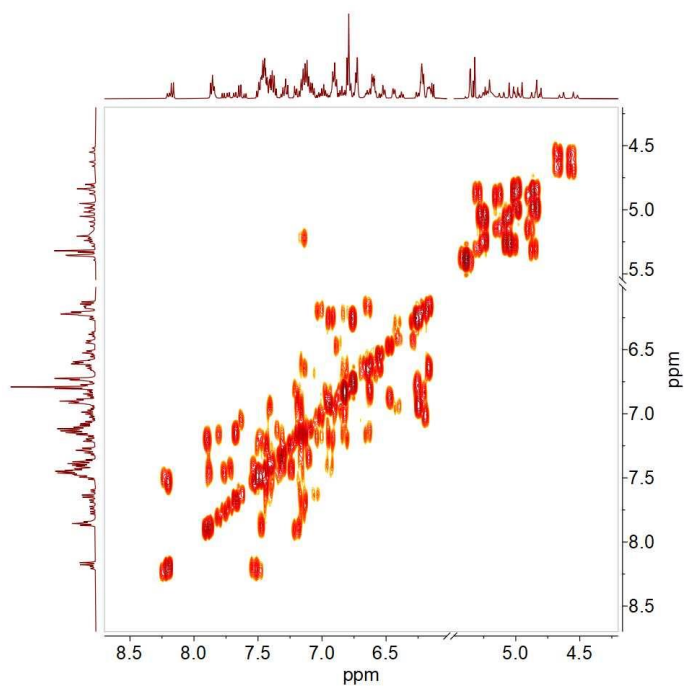
^{19}F NMR (376 MHz, CD_2Cl_2 , 298 K) spectrum of $[\text{Ir}(\text{pbb})_2(\text{Hpbb})](\text{NTf}_2)$



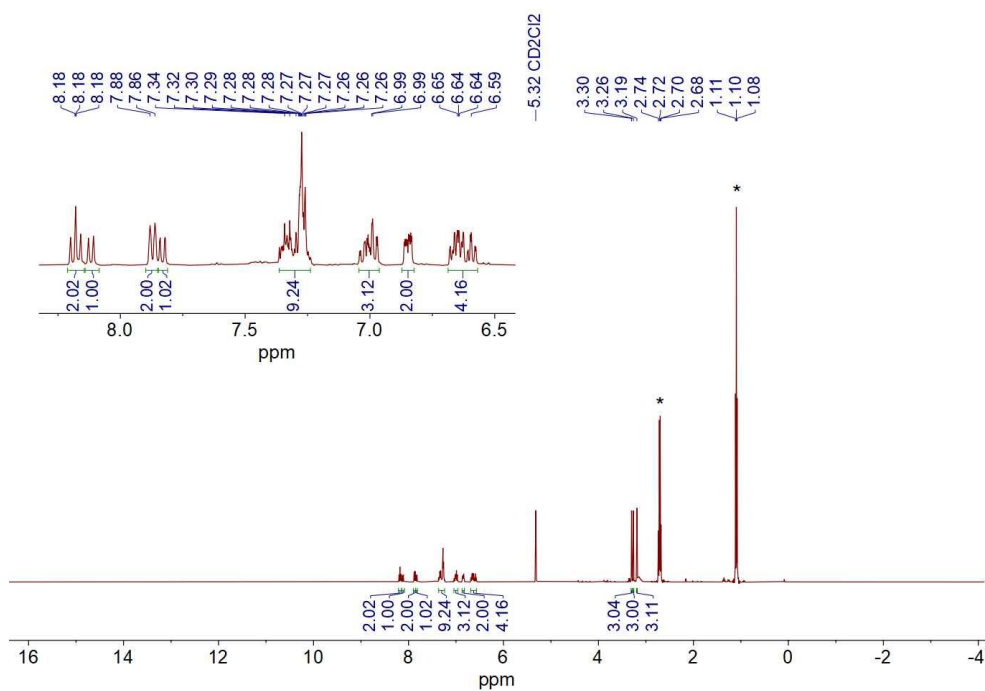
^{13}C NMR (126 MHz, CD_2Cl_2 , 260 K) spectrum of $[\text{Ir}(\text{pbb})_2(\text{Hpbb})](\text{NTf}_2)$



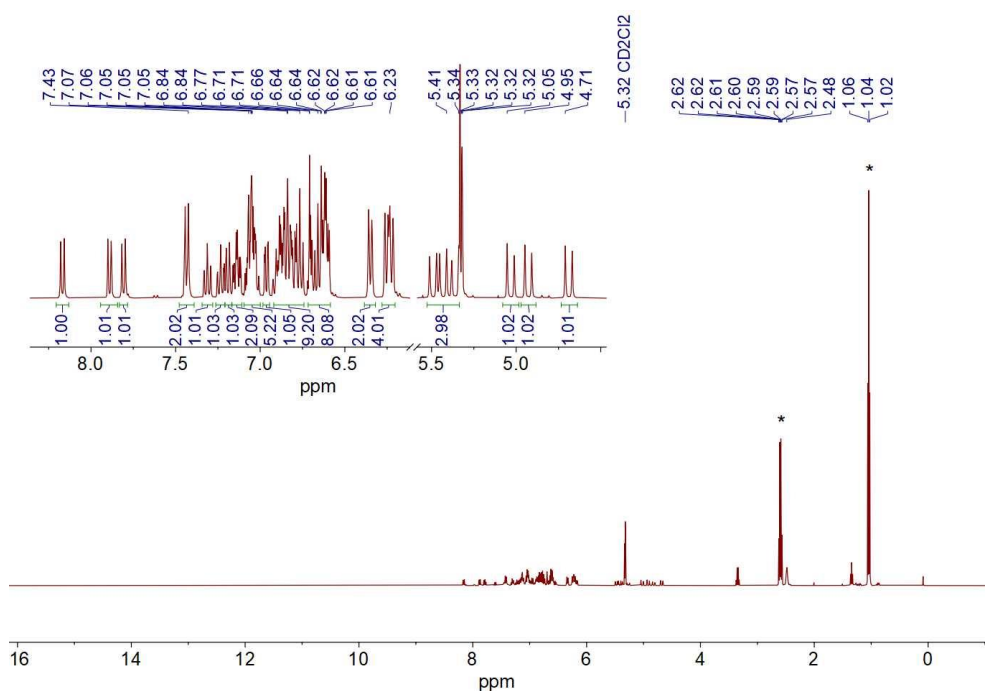
HSQC NMR (500 MHz, CD_2Cl_2 , 260 K) spectrum of $[\text{Ir}(\text{pbb})_2(\text{Hpbb})](\text{NTf}_2)$



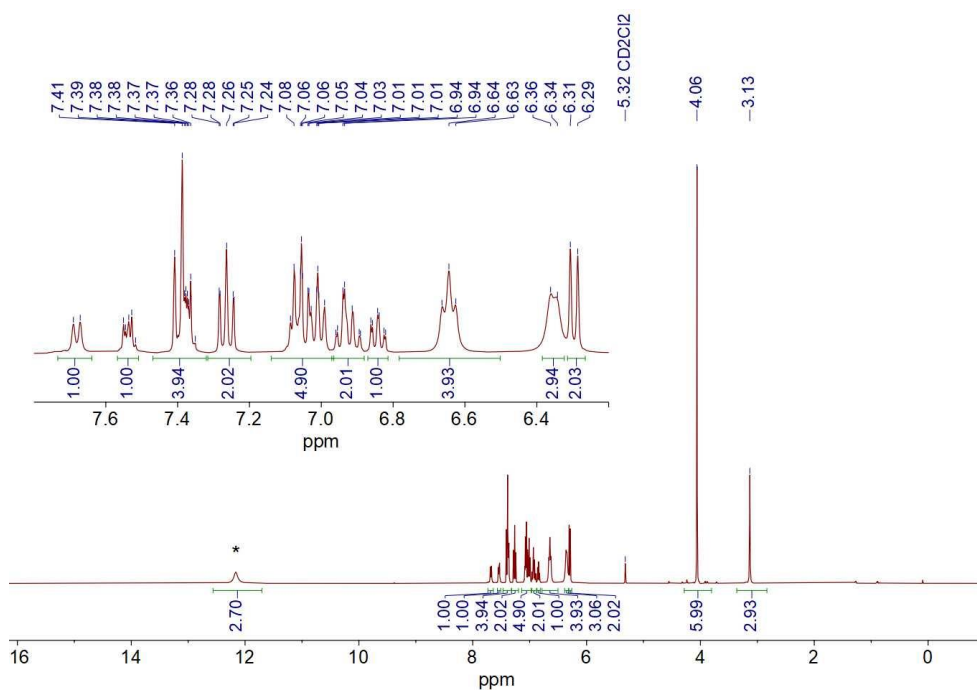
^1H - ^1H COSY NMR (500 MHz, CD_2Cl_2 , 298 K) spectrum of $[\text{Ir}(\text{pbb})_2(\text{Hpbb})](\text{NTf}_2)$



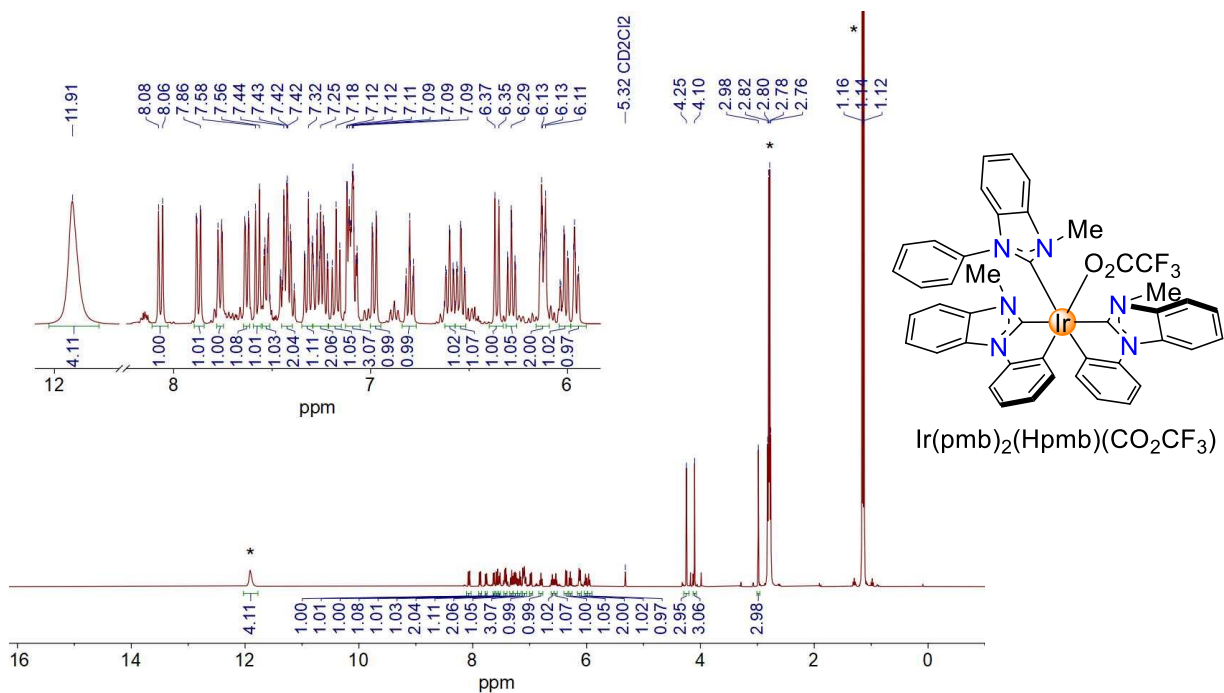
^1H NMR (400 MHz, CD_2Cl_2 , 298 K) spectrum of *mer*-Ir(pmb)₃ obtained from *fac*-Ir(pmb)₃ by acid-base-induced *fac*→*mer* isomerization. The signals of (NHET₃)(NTf₂) are marked by asterisks.



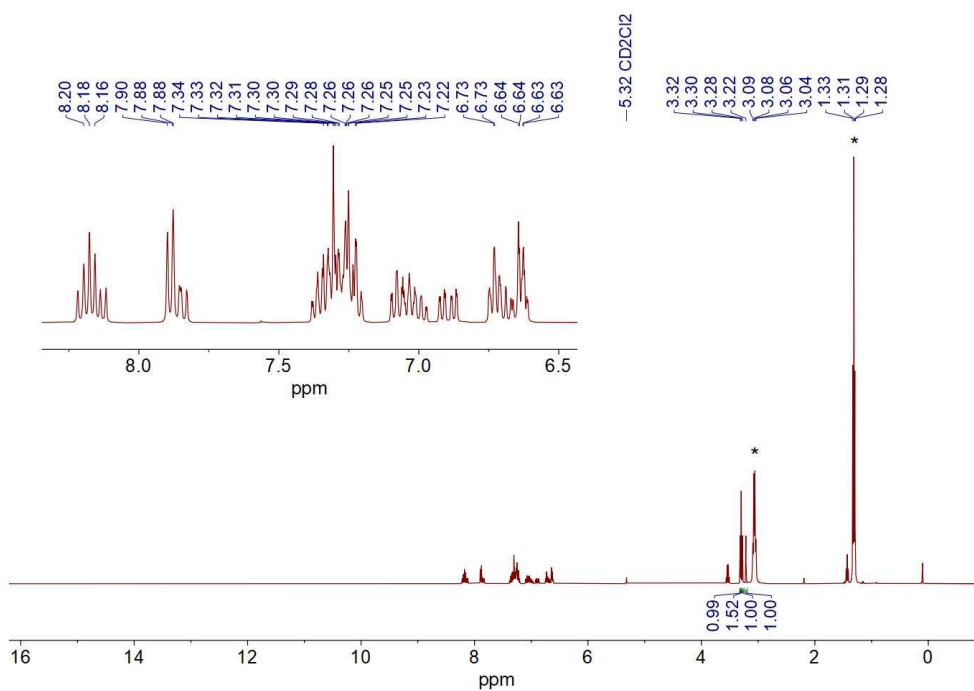
^1H NMR (400 MHz, CD_2Cl_2 , 298 K) spectrum of *mer*-Ir(pbb)₃ obtained from *fac*-Ir(pbb)₃ by acid-base-induced *fac*→*mer* isomerization. The signals of (NHET₃)(NTf₂) are marked by asterisks.



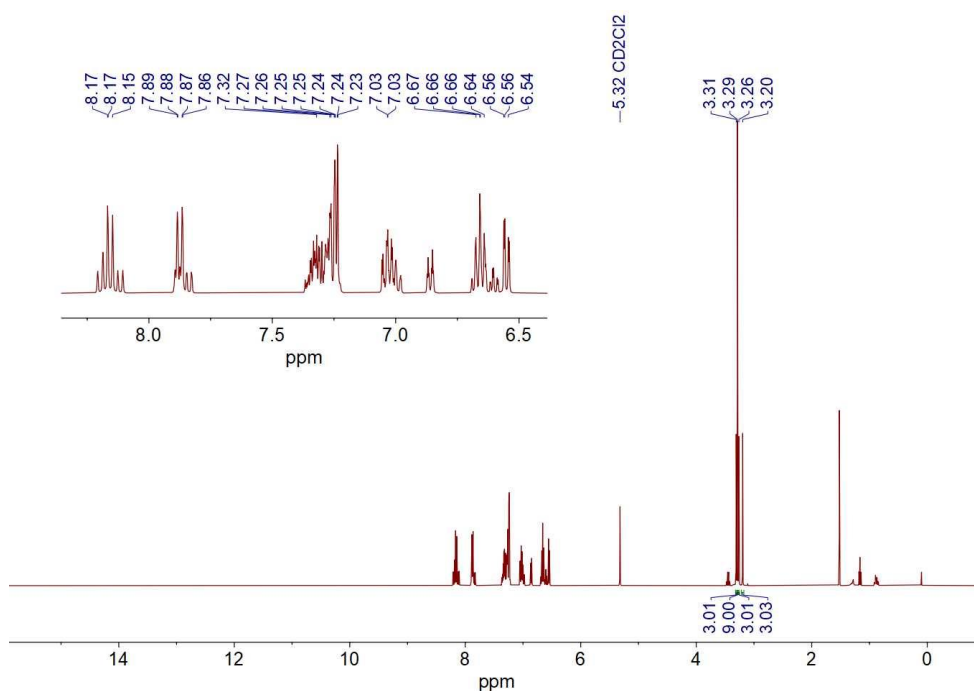
^1H NMR (400 MHz, CD_2Cl_2 , 298 K) spectrum of $[\text{Ir}(\text{pmb})_3+\text{TFA}]$. The signal of TFA is marked by an asterisk.



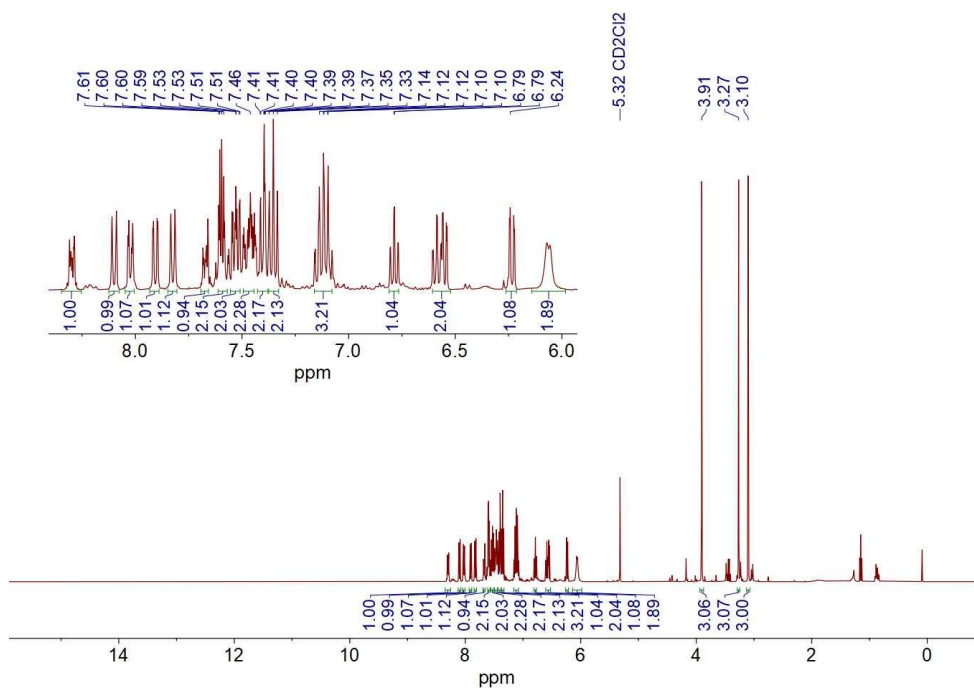
^1H NMR (400 MHz, CD_2Cl_2 , 298 K) spectrum of $\text{Ir}(\text{pmb})_2(\text{Hpmb})(\text{CO}_2\text{CF}_3)$. The signals of $(\text{NH}_4)_3(\text{CO}_2\text{CF}_3)$ are marked by asterisks.



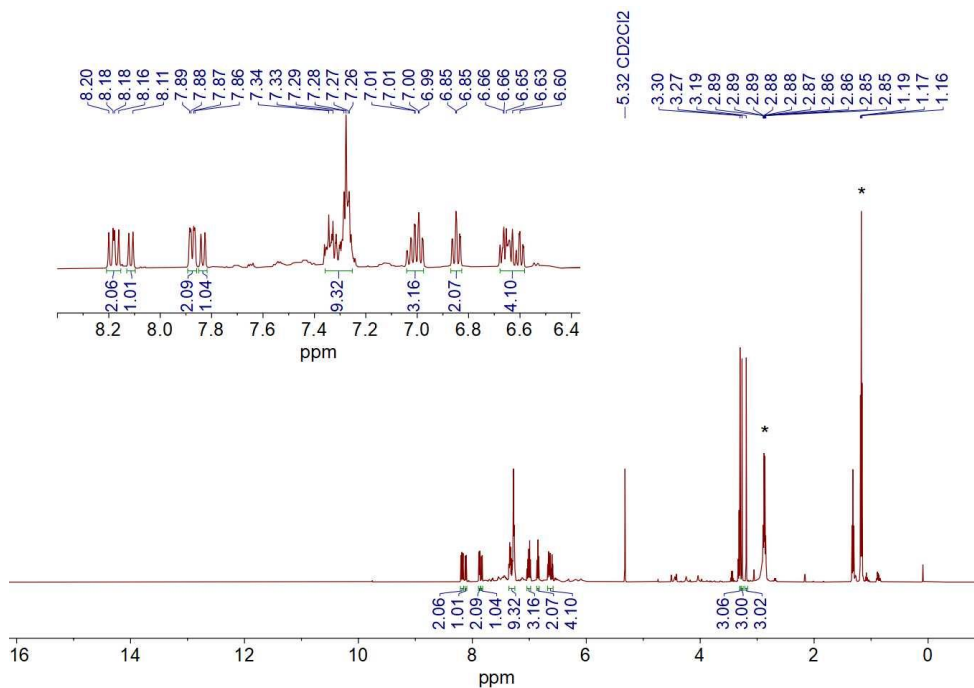
^1H NMR (400 MHz, CD_2Cl_2 , 298 K) spectrum of the mixture of *fac*- $\text{Ir}(\text{pmb})_3$ and *mer*- $\text{Ir}(\text{pmb})_3$ obtained by the heating of $\text{Ir}(\text{pmb})_2(\text{Hpmb})(\text{CO}_2\text{CF}_3)$ at 70 °C for 16 h. The signals of $(\text{NHET}_3)(\text{CO}_2\text{CF}_3)$ are marked by asterisks.



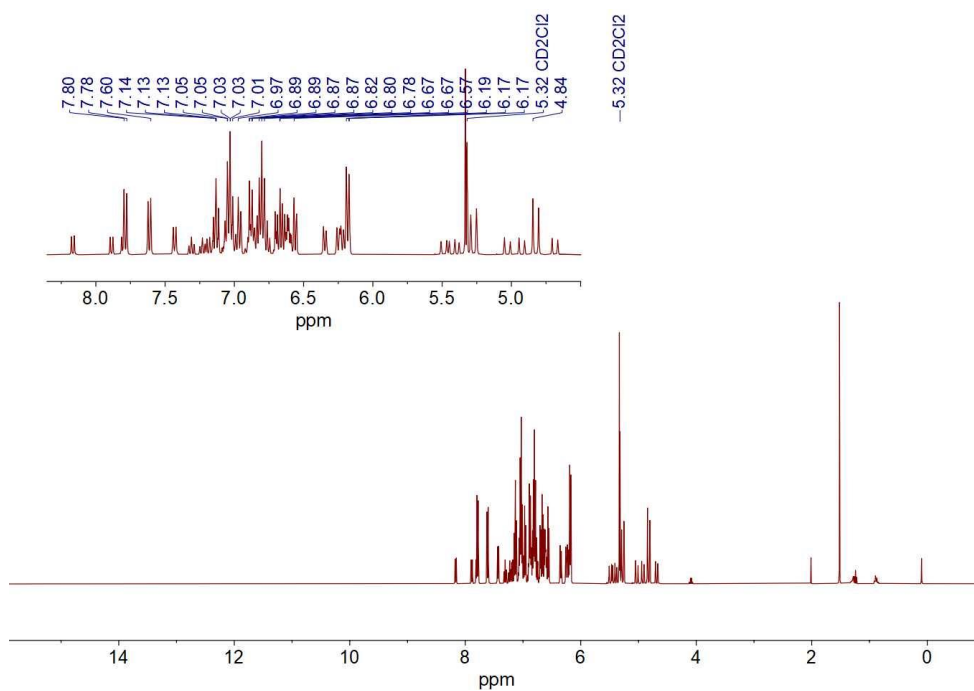
^1H NMR (400 MHz, CD_2Cl_2 , 298 K) spectrum of the equimolar mixture of *fac*- $\text{Ir}(\text{pmb})_3$ and *mer*- $\text{Ir}(\text{pmb})_3$



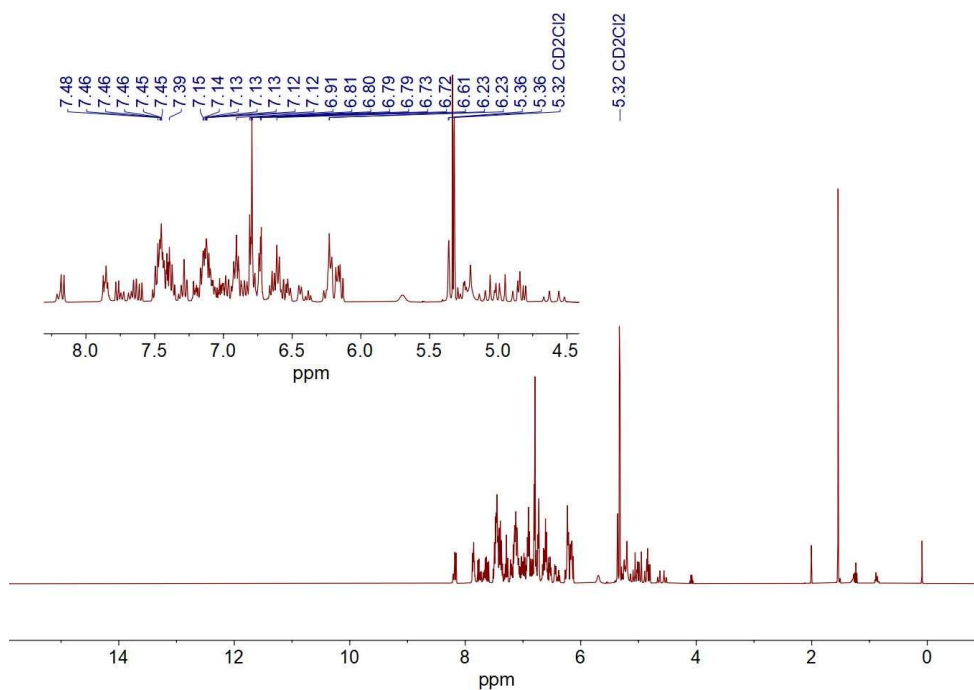
^1H NMR (400 MHz, CD_2Cl_2 , 298 K) spectrum of $[\text{Ir}(\text{pmb})_2(\text{Hpmb})](\text{NTf}_2)$ obtained by the treatment of the equimolar mixture of *fac*- $\text{Ir}(\text{pmb})_3$ and *mer*- $\text{Ir}(\text{pmb})_3$ with HNTf_2



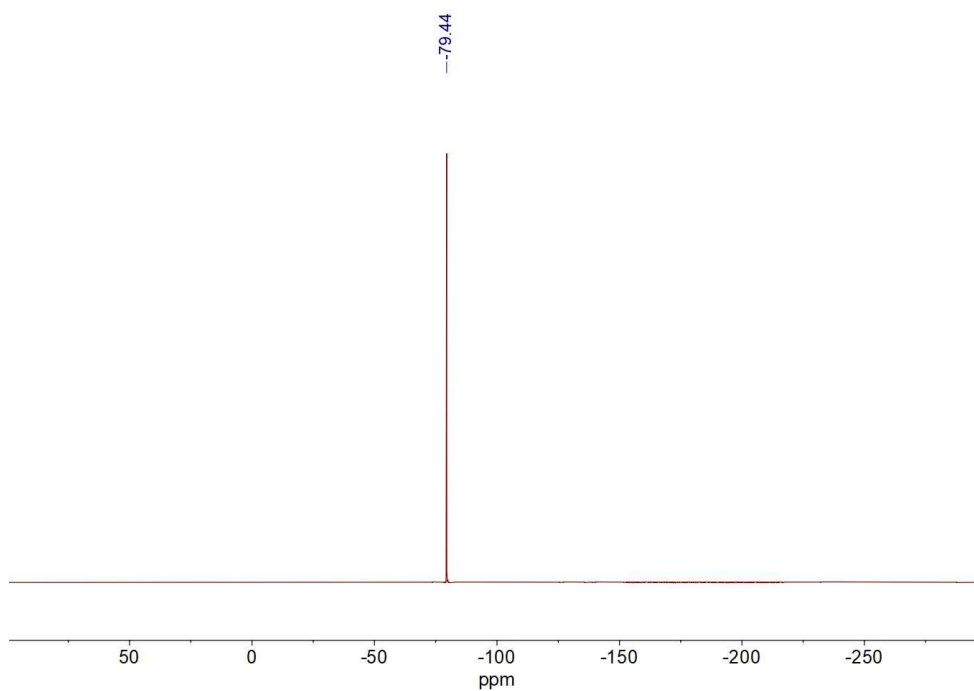
^1H NMR (400 MHz, CD_2Cl_2 , 298 K) spectrum of *mer*- $\text{Ir}(\text{pmb})_3$ obtained by the sequential treatment of the equimolar mixture of *fac*- $\text{Ir}(\text{pmb})_3$ and *mer*- $\text{Ir}(\text{pmb})_3$ by HNTf_2 and then NEt_3



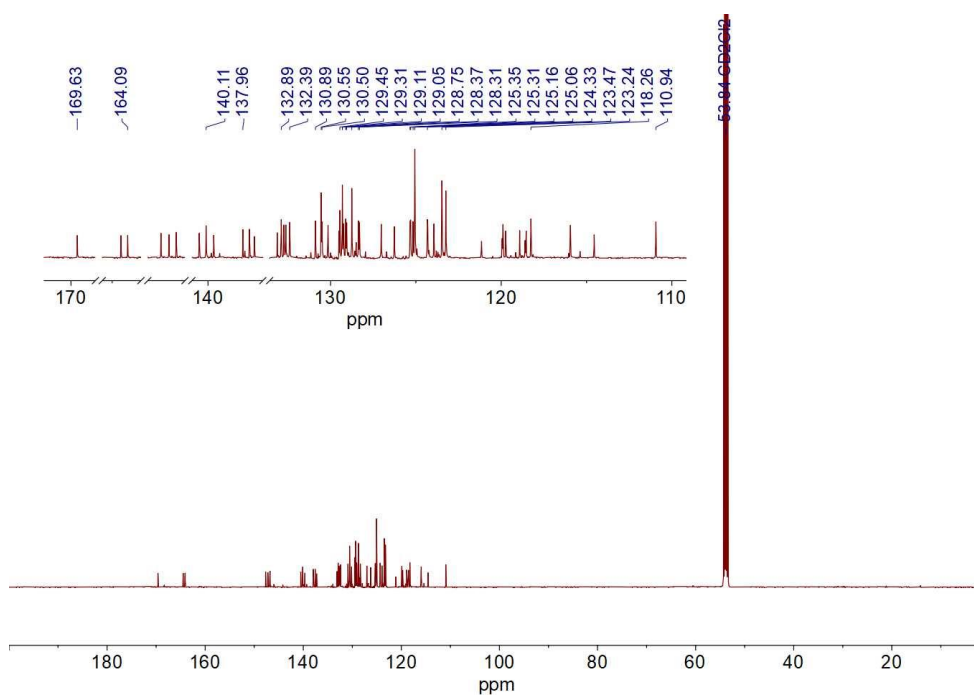
^1H NMR (400 MHz, CD_2Cl_2 , 298 K) spectrum of the equimolar mixture of *fac*- $\text{Ir}(\text{pbb})_3$ and *mer*- $\text{Ir}(\text{pbb})_3$



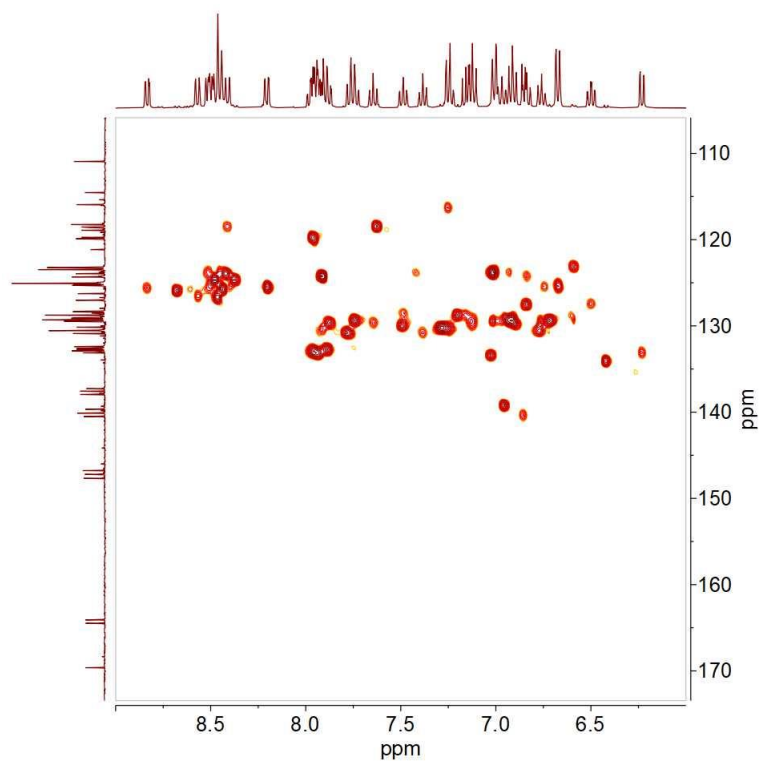
^1H NMR (400 MHz, CD_2Cl_2 , 298 K) spectrum of $[\text{Ir}(\text{pbb})_2(\text{Hpbb})](\text{NTf}_2)$ obtained by the treatment of the equimolar mixture of *fac*- $\text{Ir}(\text{pbb})_3$ and *mer*- $\text{Ir}(\text{pbb})_3$ with HNTf_2



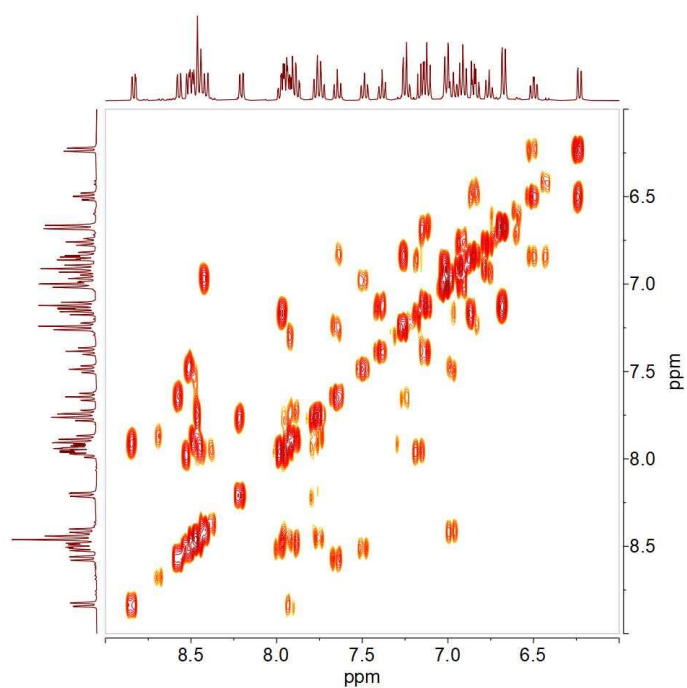
^{19}F NMR (376 MHz, CD_2Cl_2 , 260 K) spectrum of *fac*- $[\text{Ir}(\text{tzp})_2(\text{Htzp})](\text{NTf}_2)$



^{13}C NMR (126 MHz, CD_2Cl_2 , 260 K) spectrum of *fac*- $[\text{Ir}(\text{tzp})_2(\text{Htzp})](\text{NTf}_2)$

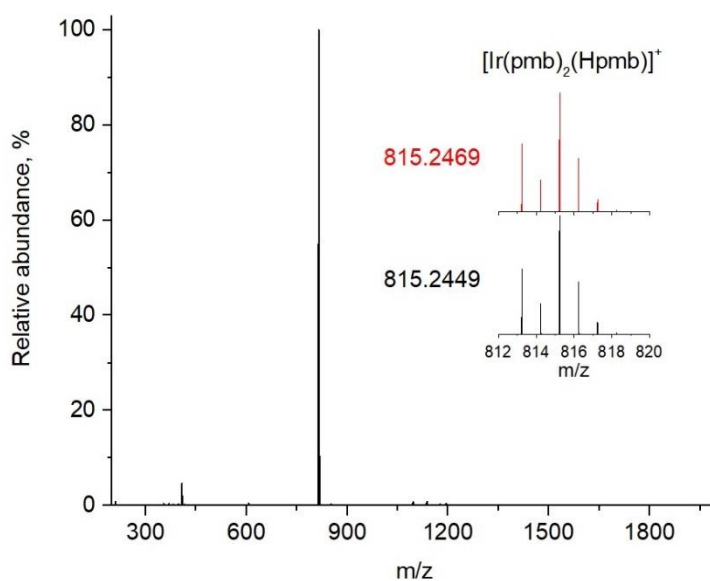


HSQC NMR (500 MHz, CD_2Cl_2 , 260 K) spectrum of *fac*'-[Ir(tzp)₂(Htzp)](NTf₂)

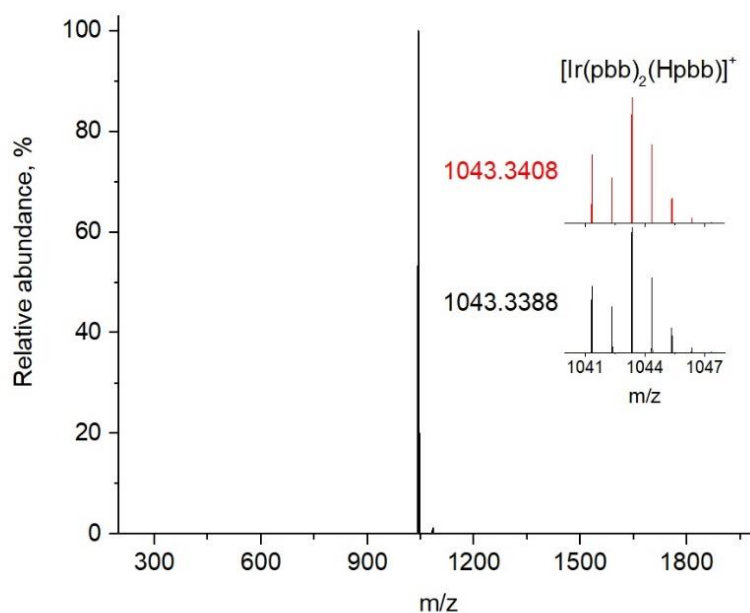


^1H - ^1H COSY NMR (500 MHz, CD_2Cl_2 , 298 K) spectrum of *fac*'-[Ir(tzp)₂(Htzp)](NTf₂)

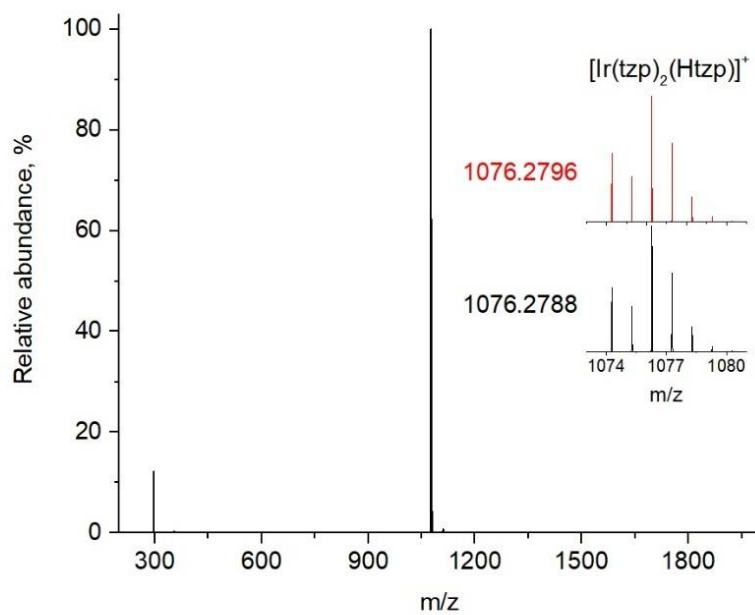
6.4.9 Mass Spectra



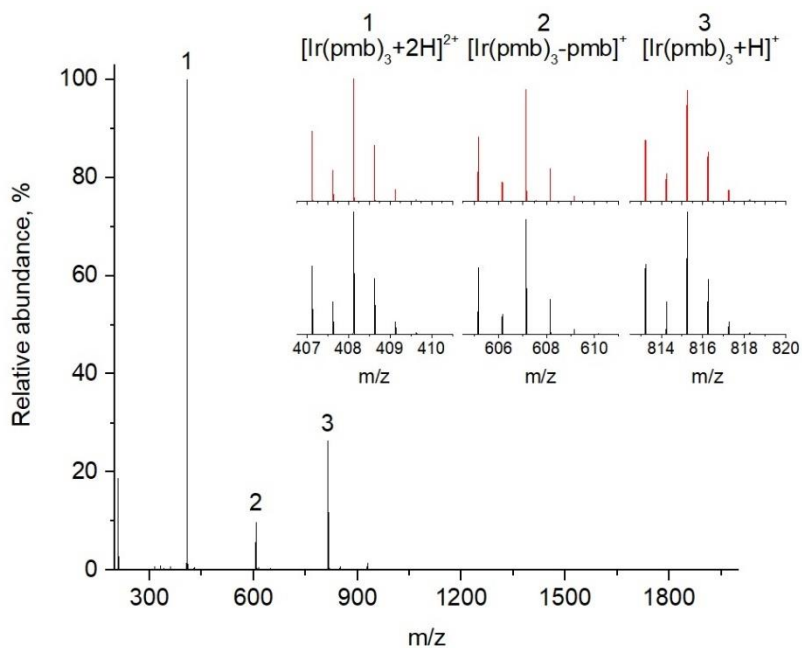
Nanochip-ESI⁺ HRMS of $[\text{Ir}(\text{pmb})_2(\text{Hpmb})](\text{NTf}_2)$. The simulated spectrum is shown in red.



Nanochip-ESI⁺ HRMS of $[\text{Ir}(\text{pbb})_2(\text{Hpbb})](\text{NTf}_2)$. The simulated spectrum is shown in red.



Nanochip-ESI⁺ HRMS of $[\text{Ir}(\text{tzp})_2(\text{Htzip})](\text{NTf}_2)$. The simulated spectrum is shown in red.



Nanochip-ESI⁺ HRMS of the adduct of $[\text{Ir}(\text{pmb})_3+\text{TFA}]$. Simulated spectra are shown in red.

References

- 1 J. Mei, N. L. C. Leung, R. T. K. Kwok, J. W. Y. Lam and B. Z. Tang, *Chem. Rev.*, 2015, **115**, 11718–11940.
- 2 H. Zhang, Z. Zhao, A. T. Turley, L. Wang, P. R. McGonigal, Y. Tu, Y. Li, Z. Wang, R. T. K. Kwok, J. W. Y. Lam and B. Z. Tang, *Adv. Mater.*, 2020, **32**, 1–25.
- 3 S. Xu, Y. Duan and B. Liu, *Adv. Mater.*, 2020, **32**, 1–31.
- 4 G. R. Suman, M. Pandey and A. S. J. Chakravarthy, *Mater. Chem. Front.*, 2021, **5**, 1541–1584.
- 5 F. Würthner, *Angew. Chemie - Int. Ed.*, 2020, **59**, 14192–14196.
- 6 Q. Xia, Y. Zhang, Y. Li, Y. Li, Y. Li, Z. Feng, X. Fan, J. Qian and H. Lin, *Aggregate*, 2022, **3**, 1–16.
- 7 T. Förster and K. Kasper, *Z. Phys. Chem. (Muenchen, Ger.)*, 1954, **1**, 275–277.
- 8 J. B. Birks, *Photophysics of Aromatic Molecules*, Wiley—Interscience, London, 1970.
- 9 B. Andreiuk, A. Reisch, E. Bernhardt and A. S. Klymchenko, *Chem. - An Asian J.*, 2019, **14**, 836–846.
- 10 T. Liang, Q. Wang, Z. Li, P. Wang, J. Wu, M. Zuo and Z. Liu, *Adv. Funct. Mater.*, 2020, **30**, 1910765.
- 11 X. Li, M. Li, Y. Chen, G. Qiao, Q. Liu, Z. Zhou, W. Liu and Q. Wang, *Chem. Eng. J.*, 2021, **415**, 128975.
- 12 J. Luo, Z. Xie, Z. Xie, J. W. Y. Lam, L. Cheng, H. Chen, C. Qiu, H. S. Kwok, X. Zhan, Y. Liu, D. Zhu and B. Z. Tang, *Chem. Commun.*, 2001, **18**, 1740–1741.
- 13 Y. Dong, J. W. Y. Lam, A. Qin, J. Liu, Z. Li, B. Z. Tang, J. Sun and H. S. Kwok, *Appl. Phys. Lett.*, 2007, **91**, 011111.

- 14 Y. Hong, J. W. Y. Lam and B. Z. Tang, *Chem. Commun.*, 2009, 4332–4353.
- 15 Z. Li, Y. Dong, B. Mi, Y. Tang, M. Häussler, H. Tong, Y. Dong, J. W. Y. Lam, Y. Ren, H. H. Y. Sung, K. S. Wong, P. Gao, I. D. Williams, H. S. Kwok and B. Z. Tang, *J. Phys. Chem. B*, 2005, **109**, 10061–10066.
- 16 G. F. Zhang, Z. Q. Chen, M. P. Aldred, Z. Hu, T. Chen, Z. Huang, X. Meng and M. Q. Zhu, *Chem. Commun.*, 2014, **50**, 12058–12060.
- 17 J. Shi, N. Chang, C. Li, J. Mei, C. Deng, X. Luo, Z. Liu, Z. Bo, Y. Q. Dong and B. Z. Tang, *Chem. Commun.*, 2012, **48**, 10675–10677.
- 18 B. P. Jiang, D. S. Guo, Y. C. Liu, K. P. Wang and Y. Liu, *ACS Nano*, 2014, **8**, 1609–1618.
- 19 J. Luo, K. Song, F. L. Gu and Q. Miao, *Chem. Sci.*, 2011, **2**, 2029–2034.
- 20 N. L. C. Leung, N. Xie, W. Yuan, Y. Liu, Q. Wu, Q. Peng, Q. Miao, J. W. Y. Lam and B. Z. Tang, *Chem. - A Eur. J.*, 2014, **20**, 15349–15353.
- 21 T. Nishiuchi, K. Tanaka, Y. Kuwatani, J. Sung, T. Nishinaga, D. Kim and M. Iyoda, *Chem. - A Eur. J.*, 2013, **19**, 4110–4116.
- 22 C. Yuan, S. Saito, C. Camacho, T. Kowalczyk, S. Irle and S. Yamaguchi, *Chem. - A Eur. J.*, 2014, **20**, 2193–2200.
- 23 Y. Tang and B. Z. Tang, *Principles and Applications of Aggregation-Induced Emission*, Springer Nature Switzerland AG 2019, 2019.
- 24 Z. Yang, W. Qin, N. L. C. Leung, M. Arseneault, J. W. Y. Lam, G. Liang, H. H. Y. Sung, I. D. Williams and B. Z. Tang, *J. Mater. Chem. C*, 2015, **4**, 99–107.
- 25 A. Prlj, N. Došlić and C. Corminboeuf, *Phys. Chem. Chem. Phys.*, 2016, **18**, 11606–11609.
- 26 T. Tran, A. Prlj, K. H. Lin, D. Hollas and C. Corminboeuf, *Phys. Chem. Chem. Phys.*, 2019, **21**, 9026–9035.
- 27 J. Guan, R. Wei, A. Prlj, J. Peng, K. H. Lin, J. Liu, H. Han, C. Corminboeuf, D.

- Zhao, Z. Yu and J. Zheng, *Angew. Chemie - Int. Ed.*, 2020, **59**, 14903–14909.
- 28 F. B. Mallory, C. S. Wood and J. T. Gordon, *J. Am. Chem. Soc.*, 1964, **86**, 3094–3102.
- 29 R. J. Olsen and R. E. Buckles, *J. Photochem.*, 1979, **10**, 215–220.
- 30 M. P. Aldred, C. Li and M. Q. Zhu, *Chem. - A Eur. J.*, 2012, **18**, 16037–16045.
- 31 M. A. Robb, M. Garavelli, M. Olivucci and F. Bernardi, in *Reviews in Computational Chemistry*, ed. K. B. Lipkowitz and D. B. Boyd, John Wiley & Sons, Inc., New Jersey, 2007, vol. 15, p. Ch. 2, 87–146.
- 32 M. Gao and B. Z. Tang, *ACS Sensors*, 2017, **2**, 1382–1399.
- 33 M. Yu, R. Huang, J. Guo, Z. Zhao and B. Z. Tang, *PhotoniX*, 2020, **1**, 1–33.
- 34 C. Zhu, R. T. K. Kwok, J. W. Y. Lam and B. Z. Tang, *ACS Appl. Bio Mater.*, 2018, **1**, 1768–1786.
- 35 X. Cai and B. Liu, *Angew. Chemie - Int. Ed.*, 2020, **59**, 9868–9886.
- 36 H. T. Feng, Y. X. Yuan, J. Bin Xiong, Y. S. Zheng and B. Z. Tang, *Chem. Soc. Rev.*, 2018, **47**, 7452–7476.
- 37 D. D. La, S. V. Bhosale, L. A. Jones and S. V. Bhosale, *ACS Appl. Mater. Interfaces*, 2018, **10**, 12189–12216.
- 38 K. S. Sharath Kumar, Y. R. Girish, M. Ashrafizadeh, S. Mirzaei, K. P. Rakesh, M. Hossein Gholami, A. Zabolian, K. Hushmandi, G. Orive, F. B. Kadumudi, A. Dolatshahi-Pirouz, V. K. Thakur, A. Zarrabi, P. Makvandi and K. S. Rangappa, *Coord. Chem. Rev.*, 2021, **447**, 214135.
- 39 L. Bian, Y. Liang and Z. Liu, *ACS Appl. Nano Mater.*, 2022, **5**, 13940–13958.
- 40 Y. Liu, C. Deng, L. Tang, A. Qin, R. Hu, J. Z. Sun and B. Z. Tang, *J. Am. Chem. Soc.*, 2011, **133**, 660–663.
- 41 E. Zhao, Y. Hong, S. Chen, C. W. T. Leung, C. Y. K. Chan, R. T. K. Kwok, J. W.

- Y. Lam and B. Z. Tang, *Adv. Healthc. Mater.*, 2014, **3**, 88–96.
- 42 J. Tong, Y. Wang, J. Mei, J. Wang, A. Qin, J. Z. Sun and B. Z. Tang, *Chem. - A Eur. J.*, 2014, **20**, 4661–4670.
- 43 Y. Li, R. T. K. Kwok, B. Z. Tang and B. Liu, *RSC Adv.*, 2013, **3**, 10135–10138.
- 44 R. Hu, J. L. Maldonado, M. Rodriguez, C. Deng, C. K. W. Jim, J. W. Y. Lam, M. M. F. Yuen, G. Ramos-Ortiz and B. Z. Tang, *J. Mater. Chem.*, 2012, **22**, 232–240.
- 45 Y. Li, L. Xu and B. Su, *Chem. Commun.*, 2012, **48**, 4109–4111.
- 46 Z. Zhao, S. Chen, X. Shen, F. Mahtab, Y. Yu, P. Lu, J. W. Y. Lam, H. S. Kwok and B. Z. Tang, *Chem. Commun.*, 2010, **46**, 686–688.
- 47 Y. Cai, C. Gui, K. Samedov, H. Su, X. Gu, S. Li, W. Luo, H. H. Y. Sung, J. W. Y. Lam, R. T. K. Kwok, I. D. Williams, A. Qin and B. Z. Tang, *Chem. Sci.*, 2017, **8**, 7593–7603.
- 48 N. Zhao, M. Li, Y. Yan, J. W. Y. Lam, Y. L. Zhang, Y. S. Zhao, K. S. Wong and B. Z. Tang, *J. Mater. Chem. C*, 2013, **1**, 4640–4646.
- 49 A. A. Suleymanov, M. Doll, A. Ruggi, R. Scopelliti, F. Fadaei-Tirani and K. Severin, *Angew. Chemie - Int. Ed.*, 2020, **59**, 9957–9961.
- 50 J. E. McMurry, *Acc. Chem. Res.*, 1983, **16**, 405–411.
- 51 M. Zhang, X. Yin, T. Tian, Y. Liang, W. Li, Y. Lan, J. Li, M. Zhou, Y. Ju and G. Li, *Chem. Commun.*, 2015, **51**, 10210–10213.
- 52 G. Wittig and U. Schöllkopf, *Chem. Ber.*, 1954, **87**, 1318–1330.
- 53 G. Wittig and W. Haag, *Chem. Ber.*, 1955, **88**, 1654–1666.
- 54 H. Li, Z. Chi, B. Xu, X. Zhang, X. Li, S. Liu, Y. Zhang and J. Xu, *J. Mater. Chem.*, 2011, **21**, 3760–3767.
- 55 R. Rathore, C. L. Burns and S. A. Abdelwahed, *Org. Lett.*, 2004, **6**, 1689–1692.

- 56 M. Banerjee, S. J. Emond, S. V. Lindeman and R. Rathore, *J. Org. Chem.*, 2007, **72**, 8054–8061.
- 57 D. Tselikhovsky and J. Blum, *European J. Org. Chem.*, 2008, 2417–2422.
- 58 G. Tan, L. Zhu, X. Liao, Y. Lan and J. You, *J. Am. Chem. Soc.*, 2017, **139**, 15724–15737.
- 59 W. M. Jones and F. W. Miller, *J. Am. Chem. Soc.*, 1967, **89**, 1960–1962.
- 60 L. de Koninck and G. Smets, *J. Polym. Sci., Part A Polym. Chem.*, 1969, **7**, 3313–3328.
- 61 T. Nagai, H. Namikoshi and N. Tokura, *Tetrahedron*, 1968, **24**, 3267–3272.
- 62 L. de Koninck and G. Smets, *J. Polym. Sci., Part A Polym. Chem.*, 1969, **7**, 3313–3328.
- 63 H.-H. Hörhold, J. Gottschaldt and J. Opfermann, *J. Prakt. Chem.*, 1977, **319**, 611–621.
- 64 H.-H. Hörhold D. Raabe, *Acta Polym.*, 1979, **30**, 86–92.
- 65 N. Tsutsumi, *Polym. J.*, 2016, **48**, 571–588.
- 66 D. M. Johansson, M. Theander, O. Inganas and M. R. Andersson, *Synth. Met.*, 2000, **113**, 293–297.
- 67 S. Baysec, E. Preis, S. Allard and U. Scherf, *Macromol. Rapid Commun.*, 2016, **37**, 1802–1806.
- 68 H. Zhou, X. Wang, T. T. Lin, J. Song, B. Z. Tang and J. Xu, *Polym. Chem.*, 2016, **7**, 6309–6317.
- 69 C. Belton, D. F. O'Brien, W. J. Blau, A. J. Cadby, P. A. Lane, D. D. C. Bradley, H. J. Byrne, R. Stockmann and H. H. Hörhold, *Appl. Phys. Lett.*, 2001, **78**, 1059–1061.
- 70 Y. Xu, L. Chen, Z. Guo, A. Nagai and D. Jiang, *J. Am. Chem. Soc.*, 2011, **133**,

- 17622–17625.
- 71 R. Hu, J. L. Maldonado, M. Rodriguez, C. Deng, C. K. W. Jim, J. W. Y. Lam, M. M. F. Yuen, G. Ramos-Ortiz and B. Z. Tang, *J. Mater. Chem.*, 2012, **22**, 232–240.
- 72 E. Preis, W. Dong, G. Brunklaus and U. Scherf, *J. Mater. Chem. C*, 2015, **3**, 1582–1587.
- 73 P. Chem, R. Hu, J. W. Y. Lam, J. Liu, H. H. Y. Sung, I. D. Williams, Z. Yue, K. S. Wong, M. F. Yuen and B. Z. Tang, *Polym. Chem.*, 2012, **3**, 1481–1489.
- 74 Y. Liu, J. Roose, J. W. Y. Lam and B. Z. Tang, *Macromolecules*, 2015, **48**, 8098–8107.
- 75 G. Lyu, J. Kendall, I. Meazzini, E. Preis, S. Baysec, U. Scherf, I. Charles, G. Montpellier, U. De Montpellier and P. Euge, *ACS Appl. Polym. Mater*, 2019, **1**, 3039–3047.
- 76 Q. Chen, J.-X. Wang, F. Yang, D. Zhou, N. Bian, X.-J. Zhang, C.-G. Yan and B.-H. Han, *J. Mater. Chem.*, 2011, **21**, 13554–13560.
- 77 J. L. Comstock, *Elements of Chemistry (In Which the Recent Discoveries in the Science Are Included and the Doctrines Familiably Explained)*, Robinson, Pratt, and Co., New York, 1838.
- 78 G. Wang, M. Zhou, J. T. Goettel, G. J. Schrobilgen, J. Su, J. Li, T. Schlöder and S. Riedel, *Nature*, 2014, **514**, 475–477.
- 79 K. K.-W. Lo and K. Y. Zhang, *RSC Adv.*, 2012, 12069–12083.
- 80 S. Abbas, I. ud D. Din, A. Raheel and A. Tameez ud Din, *Appl. Organomet. Chem.*, 2019, **34**, 1–16.
- 81 L. L. Tinker, N. D. McDaniel and S. Bernhard, *J. Mater. Chem.*, 2009, **19**, 3328–3337.
- 82 D. N. Tritton, F. K. Tang, G. B. Bodedla, F. W. Lee, C. S. Kwan, K. C. F. Leung, X. Zhu and W. Y. Wong, *Coord. Chem. Rev.*, 2022, **459**, 214390.

- 83 K. Teegardin, J. I. Day, J. Chan and J. Weaver, *Org. Process Res. Dev.*, 2016, **20**, 1156–1163.
- 84 J. D. Bell and J. A. Murphy, *Chem. Soc. Rev.*, 2021, **50**, 9540–9685.
- 85 J. C. Bawden, P. S. Francis, S. DiLuzio, D. J. Hayne, E. H. Doeven, J. Truong, R. Alexander, L. C. Henderson, D. E. Gómez, M. Massi, B. I. Armstrong, F. A. Draper, S. Bernhard and T. U. Connell, *J. Am. Chem. Soc.*, 2022, **144**, 11189–11202.
- 86 D. Ashen-Garry and M. Selke, *Photochem. Photobiol. Sci.*, 2014, **90**, 257–274.
- 87 P. I. Djurovich, D. Murphy, M. E. Thompson, B. Hernandez, R. Gao, P. L. Hunt and M. Selke, *Dalt. Trans.*, 2007, 3763–3770.
- 88 R. Gao, D. G. Ho, B. Hernandez, M. Selke, D. Murphy, P. I. Djurovich and M. E. Thompson, *J. Am. Chem. Soc.*, 2002, **124**, 14828–14829.
- 89 K. Y. Zhang, P. Gao, G. Sun, T. Zhang, X. Li, S. Liu, Q. Zhao, K. K. W. Lo and W. Huang, *J. Am. Chem. Soc.*, 2018, **140**, 7827–7834.
- 90 D. L. Ma, H. Z. He, D. S. H. Chan, C. Y. Wong and C. H. Leung, *PLoS One*, 2014, **9**, e99930.
- 91 V. Guerchais and J. L. Fillaut, *Coord. Chem. Rev.*, 2011, **255**, 2448–2457.
- 92 D. L. Ma, S. Lin, W. Wang, C. Yang and C. H. Leung, *Chem. Sci.*, 2017, **8**, 878–889.
- 93 H. Shi, Y. Wang, S. Lin, J. Lou and Q. Zhang, *Dalt. Trans.*, 2021, **50**, 6410–6417.
- 94 Q. Zhao, F. Li and C. Huang, *Chem. Soc. Rev.*, 2010, **39**, 3007–3030.
- 95 A. F. Henwood and E. Zysman-Colman, *Iridium(III) in Optoelectronic and Photonics Applications*, John Wiley & Sons Ltd, Chichester, West Sussex, 2017.
- 96 T. Y. Li, J. Wu, Z. G. Wu, Y. X. Zheng, J. L. Zuo and Y. Pan, *Coord. Chem. Rev.*, 2018, **374**, 55–92.

- 97 M. Savitha Lakshmi and S. Mahalakshmi, *Mol. Syst. Des. Eng.*, 2022, **7**, 1172–1206.
- 98 G. Bähr and G. E. Müller, *Chem. Ber.*, 1955, **88**, 251–264.
- 99 S. Trofimenko, *Inorg. Chem.*, 1973, **12**, 1215–1221.
- 100 M. Leist, C. Kerner, L. T. Ghoochany, S. Farsadpour, A. Fizia, J. P. Neu, F. Schön, Y. Sun, B. Oelkers, J. Lang, F. Menges, G. Niedner-Schatteburg, K. S. M. Salih and W. R. Thiel, *J. Organomet. Chem.*, 2018, **863**, 30–43.
- 101 M. Nonoyama, *Bull. Chem. Soc. Jpn.*, 1974, **47**, 767–768.
- 102 S. Sprouse, K. A. King, P. J. Spellane and R. J. Watts, *J. Am. Chem. Soc.*, 1984, **106**, 6647–6653.
- 103 A. B. Tamayo, B. D. Alleyne, P. I. Djurovich, S. Lamansky, I. Tsyba, N. N. Ho, R. Bau and M. E. Thompson, *J. Am. Chem. Soc.*, 2003, **125**, 7377–7387.
- 104 G. A. Carlson, P. I. Djurovich and R. J. Watts, *Inorg. Chem.*, 1993, **32**, 20–21.
- 105 F. O. Garces, K. A. King and R. J. Watts, *Inorg. Chem.*, 1988, **27**, 3464–3471.
- 106 J. L. Herde, J. C. Lambert, C. V. Senoff and M. A. Cushing, in *Inorganic Syntheses*, 1974, vol. 15, pp. 18–20.
- 107 PCT International Patent Application, WO 2004/043974A1, 2004, 81.
- 108 H. Böttcher, M. Graf, K. Sünkel, P. Mayer and H. Krüger, *Inorganica Chim. Acta*, 2011, **365**, 103–107.
- 109 E. Baranoff, B. F. E. Curchod, J. Frey, R. Scopelliti, F. Kessler, I. Tavernelli, U. Rothlisberger, M. Grätzel and M. K. Nazeeruddin, *Inorg. Chem.*, 2011, **51**, 215–224.
- 110 B. Orwat, M. J. Oh, M. Zaranek, M. Kubicki, R. Januszewski and I. Kownacki, *Inorg. Chem.*, 2020, **59**, 9163–9176.
- 111 K. A. King, P. J. Spellane and R. J. Watts, *J. Am. Chem. Soc.*, 1985, **107**, 1431–

- 1432.
- 112 M. G. Colombo, T. C. Brunold, T. Riedener, H. U. Giidel, I. F. Anorganische, P. Chemie, U. Bern, M. Fortsch, H. Biirgi, M. Kristallographie and U. Bern, *Inorg. Chem.*, 1994, **33**, 545–550.
- 113 US Patent, 6,870,054 B1, 2005, 21.
- 114 M. C. DeRosa, D. J. Hodgson, G. D. Enright, B. Dawson, C. E. B. Evans and R. J. Crutchley, *J. Am. Chem. Soc.*, 2004, **126**, 7619–7626.
- 115 V. V. Grushin, N. Herron, D. D. Lecloux, W. J. Marshall, A. Viacheslav and Y. Wang, *Chem. Commun.*, 2001, 1494–1495.
- 116 H. Konno and Y. Sasaki, *Chem. Lett.*, 2003, **32**, 252–253.
- 117 K. Dedeian, P. I. Djurovich, F. O. Garces, G. Carlson and R. J. Watts, *Inorg. Chem.*, 1991, **30**, 1685–1687.
- 118 A. Tsuboyama, H. Iwawaki, M. Furugori, T. Mukaide, J. Kamatani, S. Igawa, T. Moriyama, S. Miura, T. Takiguchi, S. Okada, M. Hoshino and K. Ueno, 2003, 1053–1059.
- 119 F. P. Dwyer and A. M. Sargeson, *J. Am. Chem. Soc.*, 1953, **75**, 984–985.
- 120 P. B. Hitchcock, M. F. Lappert and P. Terreros, *J. Organomet. Chem.*, 1982, **239**, C26–C30.
- 121 T. Sajoto, P. I. Djurovich, A. Tamayo, M. Yousufuddin, R. Bau, M. E. Thompson, R. J. Holmes and S. R. Forrest, *Inorg. Chem.*, 2005, **44**, 7992–8003.
- 122 H. M. J. Wang and I. J. B. Lin, *Organometallics*, 1998, **17**, 972–975.
- 123 A. R. Chianese, X. Li, M. C. Janzen, J. W. Faller, R. H. Crabtree and W. A. J. Organomet, *Organometallics*, 2003, **22**, 1663–1667.
- 124 D. Transactions, C. Chien, S. Fujita, S. Yamoto, T. Hara and T. Yamagata, *Dalt. Trans.*, 2008, 916–923.

- 125 F. Monti, M. Grazia, I. La Placa, N. Armaroli, R. Scopelliti and M. Gra, *Inorg. Chem.*, 2015, **54**, 3031–3042.
- 126 A. R. McDonald, M. Lutz, L. S. Von Chrzanowski, G. P. M. Van Klink, A. L. Spek and G. Van Koten, *Inorg. Chem.*, 2008, **47**, 6681–6691.
- 127 T. Karatsu, T. Nakamura, S. Yagai, A. Kitamura, K. Yamaguchi, Y. Matsushima, T. Iwata, Y. Hori and T. Hagiwara, *Chem. Lett.*, 2003, **32**, 886–887.
- 128 K. Tsuchiya, E. Ito, S. Yagai, A. Kitamura and T. Karatsu, *Eur. J. Inorg. Chem.*, 2009, 2104–2109.
- 129 B. Wu, M. Huang, C. Lai, C. Cheng and I. Chen, *Inorg. Chem.*, 2018, **57**, 4448–4455.
- 130 D. Escudero, *ChemPhotoChem*, 2019, **3**, 697–701.
- 131 J. G. Osiak, T. Setzer, P. G. Jones, C. Lennartz, A. Dreuw, W. Kowalsky and H. H. Johannes, *Chem. Commun.*, 2017, **53**, 3295–3298.
- 132 Y. Qin, X. Yang, J. Jin, D. Li, X. Zhou, Z. Zheng, Y. Sun, W. Y. Wong, Y. Chi and S. J. Su, *Adv. Opt. Mater.*, 2022, **10**, 2201633.
- 133 X. Yang, X. Zhou, Y. X. Zhang, D. Li, C. Li, C. You, T. C. Chou, S. J. Su, P. T. Chou and Y. Chi, *Adv. Sci.*, 2022, **9**, 1–11.
- 134 M. Idris, S. C. Kapper, A. C. Tadle, T. Batagoda, D. S. Muthiah Ravinson, O. Abimbola, P. I. Djurovich, J. Kim, C. Coburn, S. R. Forrest and M. E. Thompson, *Adv. Opt. Mater.*, 2021, **9**, 2001994.
- 135 C. You, X. Q. Wang, X. Zhou, Y. Yuan, L. S. Liao, Y. C. Liao, P. T. Chou and Y. Chi, *ACS Appl. Mater. Interfaces*, 2021, **13**, 59023–59034.
- 136 J. Yan, Q. Xue, H. Yang, S. M. Yiu, Y. X. Zhang, G. Xie and Y. Chi, *Inorg. Chem.*, 2022, **61**, 8797–8805.
- 137 C. F. R. Mackenzie, L. Zhang, D. B. Cordes, A. M. Z. Slawin, I. D. W. Samuel and E. Zysman-colman, *Adv. Opt. Mater.*, 2023, **11**, 2201495.

- 138 B. Yun, S. Kim, J. Kim, S. Lee and H. Son, *J. Mater. Chem. C*, 2022, **10**, 4196–4207.
- 139 N. Kandoth, J. Pérez Hernández, E. Palomares and J. Lloret-Fillol, *Sustain. Energy Fuels*, 2021, **5**, 638–665.
- 140 R. Tsuchida, *Bull. Chem. Soc. Jpn.*, 1938, **13**, 388–400.
- 141 T. Hofbeck and H. Yersin, *Inorg. Chem.*, 2010, **49**, 9290–9299.
- 142 Y. You and W. Nam, *Chem. Soc. Rev.*, 2012, **41**, 7061–7084.
- 143 M. G. Colombo, A. Hauser and H. U. Güdel, in *Electronic and Vibronic Spectra of Transition Metal Complexes I*, 1994, pp. 143–171.
- 144 Y. Zhang and J. Qiao, *iScience*, 2021, **24**, 102858.
- 145 B. D. Stringer, L. M. Quan, P. J. Barnard, D. J. D. Wilson and C. F. Hogan, *Organometallics*, 2014, **33**, 4860–4872.
- 146 J. Lee, H. F. Chen, T. Batagoda, C. Coburn, P. I. Djurovich, M. E. Thompson and S. R. Forrest, *Nat. Mater.*, 2016, **15**, 92–98.
- 147 A. K. Pal, S. Krotkus, M. Fontani, C. F. R. Mackenzie, D. B. Cordes, A. M. Z. Slawin, I. D. W. Samuel and E. Zysman-Colman, *Adv. Mater.*, 2018, **30**, 1–10.
- 148 M. H. Shaw, J. Twilton and D. W. C. MacMillan, *J. Org. Chem.*, 2016, **81**, 6898–6926.
- 149 R. C. McAtee, E. J. McClain and C. R. J. Stephenson, *Trends Chem.*, 2019, **1**, 111–125.
- 150 P. Y. Ho, C. L. Ho and W. Y. Wong, *Coord. Chem. Rev.*, 2020, **413**, 213267.
- 151 D. L. Ma, V. P. Y. Ma, D. S. H. Chan, K. H. Leung, H. Z. He and C. H. Leung, *Coord. Chem. Rev.*, 2012, **256**, 3087–3113.
- 152 D. Rota Martir and E. Zysman-Colman, *Coord. Chem. Rev.*, 2018, **364**, 86–117.
- 153 D. Rota Martir and E. Zysman-Colman, *Chem. Commun.*, 2019, **55**, 139–158.

- 154 H. Hörhold, M. Helbig, D. Raabe, J. Opfermann, U. Scherf, R. Stockmann and D. Weiß, *Zeitschrift für Chemie*, 1987, **27**, 126–137.
- 155 H.-H. Hörhold and M. Helbig, *Makromol. Chem., Macromol. Symp.*, 1987, **12**, 229–258.
- 156 Z. Zhao, J. W. Y. Lam and B. Zhong Tang, *Curr. Org. Chem.*, 2010, **14**, 2109–2132.
- 157 G. Pelletier, S. Lie, J. J. Mousseau and A. B. Charette, *Org. Lett.*, 2012, **14**, 5464–5467.
- 158 R. Koller, Q. Huchet, P. Battaglia, J. M. Welch and A. Togni, *Chem. Commun.*, 2009, 5993–5995.
- 159 P. Nimnual, J. Tummatorn, B. Boekfa, C. Thongsornkleeb, S. Ruchirawat, P. Piyachat and K. Punjajom, *J. Org. Chem.*, 2019, **84**, 5603–5613.
- 160 J. Shi, N. Chang, C. Li, J. Mei, C. Deng, X. Luo, Z. Luo, Z. Bo, Y. Q. Dong and B. Z. Tang, *Chem. Commun.*, 2012, **48**, 10675–10677.
- 161 M. Zhu, Q. Zhou, H. Cheng, Z. Meng, L. Xiang, Y. Sha, H. Yan and X. Li, *New J. Chem.*, 2022, **46**, 11382–11388.
- 162 J. Guan, R. Wei, A. Prlj, J. Peng, K. Lin, J. Liu, H. Han, C. Corminboeuf, D. Zhao, Z. Yu and J. Zheng, *Angew. Chemie Int. Ed.*, 2020, **59**, 14903–14909.
- 163 J. Rouillon, C. Monnereau and C. Andraud, *Chem. Eur. J.*, 2021, **27**, 8003–8007.
- 164 Y. Qi, Y. Li, M. Tan, F. Yuan, N. Murthy, Y. Duan, H. Zhu and S. Yang, *Coord. Chem. Rev.*, 2023, **486**, 215130.
- 165 H. Jin, X. Jiang, Z. Sun and R. Gui, *Coord. Chem. Rev.*, 2021, **431**, 213694.
- 166 A. Bigdeli, F. Ghasemi, S. Abbasi-moayed, M. Shahrajabian, S. Jafarinejad, M. A. Farahmand and M. R. Hormozi-nezhad, *Anal. Chim. Acta*, 2019, **1079**, 30–58.

- 167 M. H. Lee, J. S. Kim and J. L. Sessler, *Chem. Soc. Rev.*, 2015, **44**, 4185–4191.
- 168 L. Mei, C. Li, P. Zhao, T. Chen, R. Tian and J. Guo, *Macromol. Rapid Commun.*, 2022, **43**, 2100899.
- 169 H. Hamada, H. Tsuji and E. Nakamura, *Mater. Chem. Front.*, 2018, **2**, 296–299.
- 170 Y. Hang, J. Wang, T. Jiang, N. Lu and J. Hua, *Anal. Chem.*, 2016, **88**, 1696–1703.
- 171 Y. Takeda, R. Kohno, Y. Kudo and N. Fukada, *Bull. Chem. Soc. Jpn.*, 1989, **62**, 999–1003.
- 172 P. Alam, C. Climent, P. Alemany and R. I. Laskar, *J. Photochem. Photobiol. C Photochem.*, 2019, **41**, 100317.
- 173 X. L. Xin, M. Chen, Y. B. Ai, F. L. Yang, X. L. Li and F. Li, *Inorg. Chem.*, 2014, **53**, 2922–2931.
- 174 Y. Tian, Z. Y. Wang, S. Q. Zang, D. Li and T. C. W. Mak, *Dalt. Trans.*, 2019, **48**, 2275–2279.
- 175 D. Wang, S. M. Li, J. Q. Zheng, D. Y. Kong, X. J. Zheng, D. C. Fang and L. P. Jin, *Inorg. Chem.*, 2017, **56**, 984–990.
- 176 Y. Z. Xie, G. G. Shan, P. Li, Z. Y. Zhou and Z. M. Su, *Dye. Pigment.*, 2013, **96**, 467–474.
- 177 S. Greed, *Nat. Rev. Chem.*, 2022, **6**, 676.
- 178 A. R. McDonald, M. Lutz, L. S. Von Chrzanowski, G. P. M. Van Klink, A. L. Spek and G. Van Koten, *Inorg. Chem.*, 2008, **47**, 6681–6691.
- 179 C. H. Yang, K. H. Fang, C. H. Chen and I. W. Sun, *Chem. Commun.*, 2004, **19**, 2232–2233.
- 180 S. Huo, J. C. Deaton, M. Rajeswaran and W. C. Lenhart, *Inorg. Chem.*, 2006, **45**, 3155–3157.

- 181 A. Maity, B. L. Anderson, N. Deligonul and T. G. Gray, *Chem. Sci.*, 2013, **4**, 1175–1181.
- 182 D. Arntz, A. Fischer, M. Höpp, S. Jacobi, J. Sauer, T. Ohara, T. Sato, N. Shimizu and H. Schwind, in *Ullmann's Encyclopedia of Industrial Chemistry*, 2007, pp. 329–346.
- 183 M. Brookhart, M. L. H. Green and G. Parkin, *Proc. Natl. Acad. Sci. U. S. A.*, 2007, **104**, 6908–6914.
- 184 T. Y. Li, Y. M. Jing, X. Liu, Y. Zhao, L. Shi, Z. Tang, Y. X. Zheng and J. L. Zuo, *Sci. Rep.*, 2015, **5**, 1–9.
- 185 F. J. Coughlin, M. S. Westrol, K. D. Oyler, N. Byrne, C. Kraml, E. Zysman-Colman, M. S. Lowry and S. Bernhard, *Inorg. Chem.*, 2008, **47**, 2039–2048.
- 186 X. Chen, Y. Okamoto, T. Yano and J. Otsuki, *J. Sep. Sci.*, 2007, **30**, 713–716.
- 187 H. E. Kim, N. H. Seo and M. H. Hyun, *Bull. Korean Chem. Soc.*, 2016, **37**, 2094–2097.
- 188 D. Dattler, G. Fuks, J. Heiser, E. Moulin, A. Perrot, X. Yao and N. Giuseppone, *Chem. Rev.*, 2020, **120**, 310–433.
- 189 E. R. Kay, D. A. Leigh and F. Zerbetto, *Angew. Chemie - Int. Ed.*, 2007, **46**, 72–191.
- 190 J. D. Harris, M. J. Moran and I. Aprahamian, *Proc. Natl. Acad. Sci. U. S. A.*, 2018, **115**, 9414–9422.
- 191 W. Wang, Y. X. Wang and H. B. Yang, *Chem. Soc. Rev.*, 2016, **45**, 2656–2693.
- 192 B. L. Feringa and W. R. Browne, *Molecular Switches*, Wiley-VCH, 2nd Ed., 2011.
- 193 Y. Tamura, Y. Hisamatsu, S. Kumar, T. Itoh, K. Sato, R. Kuroda and S. Aoki, *Inorg. Chem.*, 2017, **56**, 812–833.
- 194 J. Haribabu, Y. Tamura, K. Yokoi, C. Balachandran, M. Umezawa, K. Tsuchiya,

- Y. Yamada, R. Karvembu and S. Aoki, *Eur. J. Inorg. Chem.*, 2021, **2021**, 1796–1814.
- 195 H. Wang, X. Ji, Z. A. Page and J. L. Sessler, *Mater. Chem. Front.*, 2020, **4**, 1024–1039.
- 196 J. Andréasson and U. Pischel, *Isr. J. Chem.*, 2013, **53**, 236–246.
- 197 C. Biagini and S. Di Stefano, *Angew. Chemie Int. Ed.*, 2020, **59**, 8344–8354.
- 198 B. L. Feringa, *Angew. Chemie - Int. Ed.*, 2017, **56**, 11060–11078.
- 199 J. P. Sauvage, *Angew. Chemie - Int. Ed.*, 2017, **56**, 11080–11093.
- 200 J. F. Stoddart, *Angew. Chemie - Int. Ed.*, 2017, **56**, 11094–11125.
- 201 R. A. Van Delden, M. K. J. Ter Wiel, M. M. Pollard, J. Vicario, N. Koumura and B. L. Feringa, *Nature*, 2005, **437**, 1337–1340.
- 202 G. Ragazzon, M. Baroncini, S. Silvi, M. Venturi and A. Credi, *Nat. Nanotechnol.*, 2015, **10**, 70–75.
- 203 M. Baroncini, S. Silvi and A. Credi, *Chem. Rev.*, 2020, **120**, 200–268.
- 204 B. Hesseler, M. Zindler, R. Herges and U. Lüning, *European J. Org. Chem.*, 2014, **2014**, 3885–3901.
- 205 G. Du, E. Moulin, N. Jouault, E. Buhler and N. Giuseppone, *Angew. Chemie*, 2012, **124**, 12672–12676.
- 206 V. V. Samoshin, V. A. Chertkov, L. P. Vatlina, E. K. Dobretsova, N. A. Simonov, L. P. Kastorsky, D. E. Gremyachinsky and H. J. Schneider, *Tetrahedron Lett.*, 1996, **37**, 3981–3984.
- 207 S. Erbas-Cakmak, S. D. P. Fielden, U. Karaca, D. A. Leigh, C. T. McTernan, D. J. Tetlow and M. R. Wilson, *Science (80-.)*, 2017, **358**, 340–343.
- 208 H. Amouri, *Chem. Rev.*, 2023, **123**, 230–270.
- 209 B. S. Yun, S. Y. Kim, J. H. Kim, S. Lee, H. J. Son and S. O. Kang, *J. Mater.*

- Chem. C*, 2022, **10**, 4196–4207.
- 210 A. Yu. Gitlina, F. Fadaei-Tirani, A. Ruggi, C. Plaice and K. Severin, *Chem. Sci.*, 2022, **13**, 10370–10374.
- 211 T. Setzer, C. Lennartz and A. Dreuw, *Dalt. Trans.*, 2017, **46**, 7194–7209.
- 212 B. Yun, S. Kim, J. Kim, S. Choi, S. Lee and H. Son, *ACS Appl. Electron. Mater.*, 2022, **4**, 2699–2710.
- 213 G. R. Fulmer, A. J. M. Miller, N. H. Sherden, H. E. Gottlieb, A. Nudelman, B. M. Stoltz, J. E. Bercaw, K. I. Goldberg, R. Gan and H. Apiezon, *Organometallics*, 2010, **29**, 2176–2179.
- 214 K. L. Wong, J. C. G. Bünzli and P. A. Tanner, *J. Lumin.*, 2020, **224**, 117256.
- 215 J. R. Lakowicz, *Principles of fluorescence spectroscopy, 3rd Edition*, Springer, 2006.
- 216 A. M. Brouwer, *Pure Appl. Chem.*, 2011, **83**, 2213–2228.
- 217 I. M. Smallwood, *Handbook of Organic Solvent Properties*, John Wiley & Sons, Inc., 1996.
- 218 C. Redshaw, M. R. J. Elsegood, J. W. A. Frese, S. Ashby, Y. Chao and A. Mueller, *Chem. Commun.*, 2012, **48**, 6627–6629.
- 219 C. Reichardt, in *Solvents and Solvent Effects in Organic Chemistry*, 2004, pp. 389–469.
- 220 Y. Hisamatsu and S. Aoki, *Eur. J. Inorg. Chem.*, 2011, **35**, 5360–5369.
- 221 K. A. Teegardin and J. D. Weaver, *Org. Synth.*, 2002, **95**, 29–45.
- 222 R. H. Wiley, P. X. Callahan, C. H. Jarboe and J. T. Nielsen, *J. Org. Chem.*, 1960, **25**, 366–371.
- 223 A. F. Henwood, A. K. Bansal, D. B. Cordes, A. M. Z. Slawin, I. D. W. Samuel and E. Zysman-Colman, *J. Mater. Chem. C*, 2016, **4**, 3726–3737.

- 224 A. Kazama, Y. Imai, Y. Okayasu, Y. Yamada, J. Yuasa and S. Aoki, *Inorg. Chem.*, 2020, **59**, 6905–6922.
- 225 M. Montalti, A. Credi, L. Prodi and M. T. Gandolfi, *Handbook of Photochemistry*, CRC Press, 3rd ed., 2006.
- 226 G. M. Sheldrick, *Acta Crystallogr. Sect. A*, 2015, **A71**, 3–8.
- 227 G. M. Sheldrick, *Acta Crystallogr. Sect. C*, 2015, **C71**, 3–8.
- 228 B. Y. F. O. Garces, K. Dedeian, N. L. Keder and R. J. Watts, *Acta Crystallogr. Sect. C*, 1993, **C49**, 1117–1120.
- 229 J. Frey, B. F. E. Curchod, R. Scopelliti, I. Tavernelli, U. Rothlisberger, M. K. Nazeeruddin and E. Baranoff, *Dalt. Trans.*, 2014, **43**, 5667–5679.
- 230 C. O'Brien, M. Y. Wong, D. B. Cordes, A. M. Z. Slawin and E. Zysman-Colman, *Organometallics*, 2015, **34**, 13–22.
- 231 Y. Zhang, Y. Zhao, Y. Luo, L. Xiao, Y. Huang, X. Li, Q. Peng, Y. Liu, B. Yang, C. Zhu, X. Zhou and J. Zhang, *Org. Lett.*, 2017, **19**, 6470–6473.
- 232 E. D. Nacsa and D. W. C. MacMillan, *J. Am. Chem. Soc.*, 2018, **140**, 3322–3330.
- 233 D. Wang, X. Chen, H. Yang, D. Zhong, B. Liu, X. Yang, L. Yue, G. Zhou, M. Ma and Z. Wu, *Dalt. Trans.*, 2020, **49**, 15633–15645.
- 234 C. Momblona, C. D. Ertl, A. Pertegás, J. M. Junquera-Hernández, H. J. Bolink, E. C. Constable, M. Sessolo, E. Ortí and C. E. Housecroft, *J. Mater. Chem. C*, 2018, **6**, 12679–12688.
- 235 K. Takimoto, Y. Watanabe, J. Yoshida and H. Sato, *Dalt. Trans.*, 2021, **50**, 13256–13263.
- 236 E. Sauvageot, P. Lafite, E. Duverger, R. Marion, M. Hamel, S. Gaillard, J. L. Renaud and R. Daniellou, *J. Organomet. Chem.*, 2016, **808**, 122–127.
- 237 S. Lamansky, P. Djurovich, D. Murphy, F. Abdel-Razzaq, R. Kwong, I. Tsyba,

- M. Bortz, B. Mui, R. Bau and M. E. Thompson, *Inorg. Chem.*, 2001, **40**, 1701–1711.
- 238 A. Tsuboyama, H. Iwawaki, M. Furugori, T. Mukaide, J. Kamatani, S. Igawa, T. Moriyama, S. Miura, T. Takiguchi, S. Okada, M. Hoshino and K. Ueno, *J. Am. Chem. Soc.*, 2003, **125**, 12971–12979.
- 239 G. K. Sterligov, A. N. Lysenko, E. A. Drokin, L. I. Minaeva, M. A. Topchiy, A. A. Agheshina, S. A. Rzhhevskiy, M. S. Nechaev and A. F. Asachenko, *Russ. Chem. Bull.*, 2022, **71**, 479–483.

Curriculum Vitae

Anastasia Yu. Gitlina

Born: April 20th, 1995 in Luga, Russia

 +41766291550

Languages: English, French, Russian

✉ anastasia.gitlina@gmail.com

 [Anastasiia Yu. Gitlina](#)

 [0000-0002-4934-9524](#)

Education

- 2019 – 2023 **PhD** in Chemistry and Chemical Engineering
École Polytechnique Fédérale de Lausanne (EPFL), Switzerland
Thesis director: Prof. Kay Severin
- 2017 – 2019 **MSc** in Chemistry, St. Petersburg State University (SPbSU), Russia
Grade: 4.9/5.0, *honours degree*
Supervisor: Prof. Elena Grachova
Academic scholarship of SPbSU (*top 10% students*)
- 2013 – 2017 **BSc** in Chemistry, specialty in Organic Chemistry, SPbSU, Russia
Grade: 4.76/5.0, *honours degree*
Supervisor: Prof. Elena Grachova

Professional Experience

- 09.2019 – 04.2024 **Doctoral assistant**
Laboratory of Supramolecular Chemistry, EPFL, Switzerland
- 02.2015 – 06.2019 **Research assistant**
Luminescent Transition Metal Complexes Group, SPbSU, St. Petersburg, Russia
- 09.2018 – 12.2018 **Visiting researcher** (*sponsored by a travel grant*)
and
08.2016 – 10.2016 Organometallic synthesis group, University of Eastern Finland (UEF), Joensuu, Finland

Extra-Curricular Activities

- **Teaching assistant** at the chemistry courses for students at EPFL and SPbSU (550 hours, 2017 – 2022), organizer of chemistry exams
- **Scientific supervisor** of a master student at EPFL (6 months, 2021) and of a bachelor student at SPbSU (5 months, 2018)

- **Member of the Organization committee** of St. Petersburg School Chemistry Olympiad (2019)
- **Jury member** of XLII All-Russian Scientific and Practical Conference of Schoolchildren in Chemistry at SPbSU (2018)

Awards & Achievements

- **Postdoc.Mobility fellowship**, SNSF (2024 – 2026)
- **Runner-up poster presentation award** in the Inorganic Chemistry session, SCS Fall Meeting, Zurich, Switzerland (2022)
- **Best poster communication** in the Coordination Chemistry session, 44th International Conference on Coordination Chemistry, Rimini, Italy (2022)
- **Best oral presentation** in the Chemistry session, International Student Conference “Science and Progress”, St. Petersburg, Russia (2016)
- **Government Science Scholarship**, St. Petersburg, Russia (2018 – 2019)
- **Enhanced Academic Scholarship**, SPbSU (top 10% students, 2018 – 2019)
- **Travel grant** “Internships for students and young scientists”, IN №7398/1, SPbSU (2016)
- **Best research** among 1st year bachelor students in chemistry, SPbSU (2014)
- **Winner** and **prize-winner** on regional stages of the All-Russian **Chemistry Olympiad** for schoolchildren (2011 – 2013)

Publications

11. A.Yu. Gitlina, S. Petrovskii, M. Luginin, A. Melnikov, E. Rychagova, S. Ketkov, E. Grachova “X/Y platinum(II) complexes: some features of supramolecular assembly *via* halogen bonding”, *Dalton Trans.* **2023**, 52 (43), 16005–16017.
[DOI:10.1039/D3DT02970K](https://doi.org/10.1039/D3DT02970K)

10. A.Yu. Gitlina, A. Ruggi, K. Severin “Synthesis of hyperbranched polyarylethenes by consecutive C–H vinylation reactions”, *Polym. Chem.* **2023**, 14 (36), 4182–4187.
[DOI: 10.1039/D3PY00803G](https://doi.org/10.1039/D3PY00803G)

9. A.Yu. Gitlina, V. Khistiaeva, A. Melnikov, M. Ivonina, V. Sizov, D. Spiridonova, A. Makarova, D. Vyalikh, E. Grachova “Organometallic Ir(III) complexes: post-synthetic

modification, photophysical properties and binuclear complex construction”, *Dalton Trans.* **2023**, 52 (26), 8986–8997. [DOI: 10.1039/D3DT00901G](https://doi.org/10.1039/D3DT00901G)

8. P. Varava, T.H. Wong, Z. Dong, **A.Yu. Gitlina**, A. Sienkiewicz, W. Feuerstein, R. Scopelliti, F. Fadaei-Tirani, K. Severin “Head-to-tail dimerization of *N*-heterocyclic diazoolefins”, *Angew. Chem. Int. Ed.* **2023**, 62 (25), e202303375. [DOI: 10.1002/anie.202303375](https://doi.org/10.1002/anie.202303375)

7. **A.Yu. Gitlina**, F. Fadaei-Tirani, K. Severin “The acid-mediated isomerization of iridium(III) complexes with cyclometalated NHC ligands: kinetic vs thermodynamic control”, *Dalton Trans.* **2023**, 52 (9), 2833–2837. [DOI: 10.1039/D2DT04039E](https://doi.org/10.1039/D2DT04039E)

6. **A.Yu. Gitlina**, F. Fadaei-Tirani, A. Ruggi, C. Plaice, K. Severin “Acid-base-induced *fac*→*mer* isomerization of luminescent iridium(III) complexes”, *Chem. Sci.* **2022**, 13 (35), 10370 – 10374. [DOI: 10.1039/D2SC02808E](https://doi.org/10.1039/D2SC02808E)

This article is part of the themed collection: [Most popular 2022 main group, inorganic and organometallic chemistry articles](#)

Highlighted by S. Greed “Making a mer-isomer”, *Nat. Rev. Chem.* **2022**, 6, 676. [DOI: 10.1038/s41570-022-00429-y](https://doi.org/10.1038/s41570-022-00429-y)

5. E. Abramova, A. Paderina, S. Slavova, E. Kostenko, E. Eliseenkov, S. Petrovskii, **A.Yu. Gitlina**, V. Boyarskiy, E. Grachova “Just add the gold: aggregation-induced-emission properties of alkynylphosphinegold(I) complexes functionalized with phenylene-terpyridine subunits”, *Inorg. Chem.* **2021**, 60 (24), 18715–18725. [DOI: 10.1021/acs.inorgchem.1c02125](https://doi.org/10.1021/acs.inorgchem.1c02125)

4. A. Vasileva, S. Haschke, V. Mikhailovskii, **A. Gitlina**, J. Bachmann, A. Manshina “Direct laser-induced deposition of AgPt@C nanoparticles on 2D and 3D substrates for electrocatalytic glucose oxidation”, *Nano-Struct. Nano-Objects* **2020**, 24, 100547. [DOI: 10.1016/j.nanoso.2020.100547](https://doi.org/10.1016/j.nanoso.2020.100547)

3. **A.Yu. Gitlina**, A. Surkova, M. Ivonina, V. Sizov, S. Petrovskii, A. Legin, G. Starova, I. Koshevoy, E. Grachova, D. Kirsanov “Cyclometalated Ir(III) complexes as tuneable multiband light sources for optical multisensory systems: Feasibility study”, *Dyes Pigm.* **2020**, 180, 108428. [DOI: 10.1016/j.dyepig.2020.108428](https://doi.org/10.1016/j.dyepig.2020.108428)

2. I. Krytchankou, **A.Yu. Gitlina**, I. Koshevoy, A. Melnikov, S. Tunik “Luminescent Ag–Cu “hourglass” hepta- and decanuclear alkynyl-phosphine clusters”, *Eur. J. Inorg. Chem.* **2018**, 34, 3822–3828. [DOI: 10.1002/ejic.201800631](https://doi.org/10.1002/ejic.201800631)

1. **A.Yu. Gitlina**, M. Ivonina, V. Sizov, G. Starova, A. Pushkarev, D. Volyniuk, S. Tunik, I. Koshevoy, E. Grachova “The rare example of compact heteroleptic cyclometalated iridium(III) complex demonstrating well-separated dual emission”, *Dalton Trans.* **2018**, 47 (22), 7578–7586. [DOI: 10.1039/C8DT01336E](https://doi.org/10.1039/C8DT01336E)

Conferences

17. **A. Gitlina**, K. Severin

Poster: Hyperbranched polyarylethenes synthesized by successive C–H vinylation
SCS Fall Meeting 2023, Bern, Switzerland (24-25.08.2023).

16. **A. Gitlina**, F. Fadaei-Tirani, K. Severin

Poster: X-Ray diffraction analysis of Ir(III) complexes protonated by strong acids
8th European Crystallography School 2023, Berlin, Germany (18-24.06.2023).

15. **A. Gitlina**, K. Severin

Online poster: Acid-base-induced *fac*→*mer* isomerization of luminescent iridium(III) complexes

Chem. Sci. Symposium: Sustainable Synthesis and Catalysis 2022, London, UK (10-11.11.2022).

14. **A. Gitlina**, K. Severin

Poster: Reversible *fac-mer* isomerization of luminescent Ir(III) complexes (Runner-up poster prize)

SCS Fall Meeting 2022, Zurich, Switzerland (08.09.2022).

13. **A. Gitlina**, K. Severin

Poster: “Reversible *fac-mer* isomerization of luminescent Ir(III) complexes (Best poster prize)

44th International Conference on Coordination Chemistry 2022, Rimini, Italy (28.08-02.09.2022).

12. **A. Gitlina**, K. Severin

Short **speech** and **poster**: Reversible switching of luminescence of Ir(III) complexes
Swiss Photochemistry symposium 2022, Fribourg, Switzerland (17.06.2022).

11. C. Plaice, **A. Gitlina**, K. Severin

Poster: Heteroleptic iridium complexes as molecular motors (3rd best poster of 2021 graduates)

Poster session of Master students at EPFL 2021, Lausanne, Switzerland (02.10.2021).

10. *5th EuChemS Inorganic Chemistry Conference 2019, Moscow, Russia (24-28.06.2019).*

A. Gitlina, I. Koshevoy, E. Grachova

Poster: Solid-state organization of novel cyclometalated Pt(II) complexes through weak interactions

V. Khistiaeva, **A. Gitlina**, E. Grachova

Poster: Click-chemistry as a convenient way for binding of metalloblocks: design principles for the construction of multimetallic systems containing Ln(III)

E. Abramova, E. Kostenko, **A. Gitlina**, V. Boyarskiy, E. Eliseenkov, E. Grachova.

Poster: Gold(I) complexes decorated by flexible alkynyl-terpyridine ligands: some features of luminescence

9. E. Abramova, D. Barkhatova, E. Kostenko, **A. Gitlina**

Poster: Novel gold(I) complexes decorated by phosphine and terpyridine ligands

International Student Conference "Science and Progress" 2018, Peterhof, Russia (12-14.11.2018).

8. E. Grachova, **A. Gitlina**, V. Khistiaeva, V. Sizov

Oral presentation: Molecular d-f emitters based on heterofunctional polytope ligands: design features and photophysical properties

IV Russian Rare Earths Day 2018, Moscow, Russia (15-16.02.2018).

7. *International Student Conference "Science and Progress" 2017, Peterhof, Russia (13-17.11.2017).*

A. Gitlina, E. Grachova

Oral presentation: Novel "prolongated" Ir(III) complexes as d-blocks for multiple emissive materials: synthesis and photophysical properties

M. Ivonina, **A. Gitlina**, V. Sizov

Poster: Mechanism of the rare example of dual emission in heteroleptic cyclometalated Ir(III) complexes: DFT study

6. A. Gitlina, E. Grachova

Poster: Novel cyclometalated Ir(III) complexes as blocks for dual emission material: synthesis and photophysical properties

4th EuChemS Inorganic Chemistry Conference 2017, Copenhagen, Denmark (02-05.07.2017).

5. X International conference of young scientists in Chemistry “Mendeleev 2017” 2017, St. Petersburg, Russia (04-07.04.2017).

A. Gitlina, I. Solovjov, A. Solomatina

Poster: Novel cyclometalated Ir(III) complexes as blocks for dual emissive materials

I. Krytchankou, **A. Gitlina**, I. Koshevoy, S. Tunik

Poster: Luminescent Ag(I)-Cu(I) alkynyl-phosphine clusters

4. E. Grachova, A. Gitlina, V. Khistiaeva, I. Solovjov

Oral presentation: Design of d-f molecular emitters: mononuclear Au(I) complexes as lanthanide sensitizers

III Russian Rare Earths Day 2017, Novosibirsk, Russia (20-21.02.2017).

3. A. Gitlina, I. Krytchankou, I. Koshevoy

Oral presentation: Synthesis of novel alkynyl-phosphine cluster complexes with {Ag₆Cu_x} metal core (x = 1, 4) (Best oral presentation prize)

International Student Conference “Science and Progress” 2016, Peterhof, Russia (17-21.10.2016).

2. A. Gitlina, J. Shakirova, E. Grachova

Poster: Synthesis, characterization and photophysical properties of a novel cyclometalated complexes of Ir(III)

Cluster Conference on Organic Chemistry 2016, Repino, Russia (27.06-01.07.2016).

1. A. Gitlina, J. Shakirova

Poster: Phosphine-alkynyl heterometallic hybrid systems Au–M (M = Cu, Ag) as the precursors for synthesis of self-organizing surfaces and nanoparticles Au–Ag@C

International Student Conference “Science and Progress” 2015, Peterhof, Russia (09-13.11.2015).